Fall 2000

Transition metal complexes of novel ligands derived from the cis,cis-1,3,5-triaminocyclohexane (TACH) framework: Structural and biological studies

Gyungse Park
University of New Hampshire, Durham

TRANSITION METAL COMPLEXES OF NOVEL LIGANDS DERIVED FROM THE *CIS,CIS*-1,3,5-TRIAMINOCYCLOHEXANE (TACH) FRAMEWORK: STRUCTURAL AND BIOLOGICAL STUDIES

BY

GYUNGSE PARK

B.S., KOREA UNIVERSITY, 1991
M.S., WAYNE STATE UNIVERSITY, 1995

DISSERTATION

Volume 1

Chapter 1 and Chapter 2

Submitted to the University of New Hampshire
In Partial Fulfillment of
the Requirements for the Degree of

Doctor of Philosophy

in

Chemistry

September, 2000

This dissertation has been examined and approved.

Dissertation Director, Dr. Roy P. Planalp
Associate Professor of Chemistry

Dr. Edward H. Wong
Professor of Chemistry

Dr. N. Dennis Chasteen
Waite Professor of Chemistry

Dr. Glen P. Miller
Assistant Professor of Chemistry

Dr. Dale P. Barkey
Professor of Chemical Engineering

July 20, 2000

DEDICATION

This work I dedicate
to my Lord, Jesus Christ, for everything

To my parents, Ki-Tai Park and Hee-Ja Lim,
for eternal love,
forgiveness, and
sacrifice
in
whole my life,

To my parents in law, Hyun-Jin Nam and Hee-Young Kim,
for their understanding,
prayers, and
love,

To my loving wife, Hyeran,
for her patience,
love,
understanding, and
support
during the pursuit of my graduate study,

To my son, Sunghyun,
for his love and understanding.

ACKNOWLEDGEMENTS

My heartfelt acknowledgement and grateful appreciation are made to my advisor, Dr. Roy P. Planalp, for his sincere guidance, patience, support, direction, assist, and invaluable help during the pursuit of my graduate study.

I'd also like to acknowledge our collaborators, Dr. Brechbiel at NIH for ligand syntheses, FAB-Mass spectra, and hydrolysis study, Dr. Chasteen and Dr. Shao for their excellent and enormous efforts in EPR measurements and helpful discussions, Dr. Rogers for his excellent work in solving the X-ray structures, and Dr. Torti for Iron chelation in cancer therapy.

I'd also like to acknowledge my graduation committee, Dr. Wong, Dr. Chasteen, Dr. Miller, and Dr. Barkey, for their time and concern.

I'm very grateful to Kathleen S. Gallagher for her professional instruction and to John Wilderman for his professional technical assistance in the use of NMR and UV-vis spectroscopy.

My special thanks go to Cindi Rohwer, Peg Torch, Sabrina Kirwan, and Robert Constantine for their helps and support.

The encouragement, friendship, and understanding of Xiankai Sun, Dr. Ken Miller, Neng Ye, Jeff Condon, Dan Widlicka, and Dr. Planalp's group members are very much appreciated.

I also really appreciate proofreaders of this dissertation, Jeff Condon, Dan Widlicka, Matt Ronsheim, and Anne Przyborowska, for their effort and time in making it much better.

TABLE OF CONTENTS

LIST OF TABLES

LIST OF SCHEMES

LIST OF FIGURES

ABSTRACT

TRANSITION METAL COMPLEXES OF NOVEL LIGANDS DERIVED FROM THE *CIS,CIS*-1,3,5-TRIAMINOCYCLOHEXANE (TACH) FRAMEWORK: STRUCTURAL AND BIOLOGICAL STUDIES

by

GYUNGSE PARK

University of New Hampshire, September, 2000

Transition and Group IIB metal complexes of novel ligands derived from *cis,cis*-1,3,5-triaminocyclohexane (tach) were prepared for structural and biological activity study. Copper(II) complexes of *N,N',N''*-trialkylated derivatives of tach [Cu(tach-R_3)Cl_2] (R = Me, Et, Pr, furanyl, and thiophenyl) were prepared from $CuCl_2$ in MeOH or MeOH/Et_2O solvent. The structures of [Cu(tach-R_3)Cl_2] in the solid and solution (aqueous and methanolic) states were extensively studied by UV-vis and EPR spectroscopies and were consistent to X-ray structure of [Cu(tach-Et_3)$Br_{0.8}Cl_{1.2}$] which reveals a slightly distorted square-based pyramidal geometry. Displacement of halide ions with water molecules in aqueous media was observed by the band shift to high-energy transition. Catalytic behavior of $[Cu(tach\text{-}Me_3)]^{2+}$ in the hydrolysis of activated phosphate diesters in aqueous medium is different from other labile metal complex. Hydrolysis is first-order in phosphate ester and second-order in $[Cu(tach\text{-}Me_3)]^{2+}$, suggesting a binuclear complex in which a substrate bridges two Cu(II) ions. Iron-mediated oxidative dehydrogenation of a coordinated ligand was observed in the reactions of Fe(II) and Fe(III) with tachpyr and (+/-)tach(C-$Me)_3$pyr in the

presence of O_2 resulting in the formation of a mixture of corresponding mono- and di-imino Fe(II) complexes characterized by ^1H NMR, IR, and UV-vis spectroscopies. Further oxidation can be achieved by adding H_2O_2 in the case of tachpyr, and by longer exposure of the complex to air, for (+/-)tach(C-Me)$_3$pyr, affording the tris-imino complex. Tachpyr also reveals cytotoxicity toward cancer cells through an iron depletion mechanism. The abilities of tachpyr to complex iron, to reduce intracellular Fe(III) to Fe(II), and to produce hydroxyl radicals is believed to correlate to its cytotoxic effect. First-row transition and Group IIB metal complexes of tachpyr, *N,N',N''*-tris(2-pyridylmethyl)-*cis,cis*-1,3,5-triaminocyclohexane, exhibit a metal radius effects on coordination geometry. The tachpyr ligand forms a nearly octahedral complex with the Zn(II) and Ni(II), a tetragonally distorted octahedral complex with Cu(II), an intermediate between octahedron and trigonal prismatic complex with Cd(II), while it forms a nearly trigonal prism complexes with Mn(II) and Hg(II). Tach-Me$_3$pyr, *N,N',N''*-trimethyl-*N,N',N''*-tris(2-methylpyridyl)-*cis,cis*-1,3,5-triaminocyclohexane, forms a distorted octahedral complexes with Ni(II) and Zn(II), while it forms a Jahn-Teller distorted Cu(II) complex. The steric effects of methyl groups govern the coordination of metal complexes of tach-6-Mepyr, *N,N',N''*-tris(6-methyl-2-methylpyridyl)-*cis,cis*-1,3,5-triaminocyclohexane, affording a nearly octahedral geometry with the Zn(II), Ni(II), Co(II) and Mn(II) metal ions, while it forms a distorted trigonal bipyramidal complexes with Cu(II) as a consequence of a twisted pendent arm away from Cu(II) ion.

GENERAL INTRODUCTION

This dissertation is divided into three chapters: 1) Structural and biological property study of Cu(II) complexes with *N*-alkylated tach 2) Iron-mediated ligand oxidation and biochemical properties of iron complexes and chelators based on tach ligands 3) Transition (M = Mn(II), Fe(II), Co(II), Co(III), Ni(II), and Cu(II)) and Group IIB (Zn(II), Cd(II), and Hg(II)) metal complexes of novel ligands derived from *cis,cis*-1,3,5-triaminocyclohexane framework. Because of diversity of material covered, each chapter is self-contained with its own introduction, experimental section, results, discussion, and conclusion.

The *N*-alkylated tachpyr ligands were previously reported as (N-Me)$_3$tachpyr and (N-Et)$_3$tachpyr[1] but will be referred as tach-Me$_3$pyr and tach-Et$_3$pyr in this study in order to be consistent with names of the precursors (tach-Me$_3$•3HBr and tach-Et$_3$•3HBr) used to synthesize these ligands.

CHAPTER 1

STRUCTURAL AND BIOLOGICAL PROPERTY STUDY OF CU(II) COMPLEXES OF *N*-ALKYLATED TACH

Summary

In this chapter, the collaboration study described herein with Professor Chasteen and Junlong Shao at University of New Hampshire focuses on the synthesis and characterization of the Cu(II) with *N,N,N"*-trialkyltach derivatives $[Cu(tach\text{-}R_3)X_2]^{n+}$ (X = Cl^-, Br^-, H_2O, or OH^- and n = 0 - 2) to investigate their structures and bonding properties as the catalytically active Cu(II) complexes for the hydrolysis of phosphodiesters. By using visible-near IR optical spectra, X-band and Q-band EPR spectra and X-ray crystallography, the structures of $[Cu(tach\text{-}R_3)X_2]^{n+}$ complexes were analyzed in solution and solid states. The catalytic activity study of a Cu(II) complex $[Cu(tach\text{-}Me_3)Cl_2]$ in the hydrolysis of the phosphate diesters has been undertaken in collaboration with Dr. Brechbiel and Dr. Kim Deal at NIH. Professor Rogers at University of the Alabama provided the X-ray structure analysis of $[Cu(tach\text{-}Et_3)Cl_{1.2}Br_{0.8}]$.

Introduction

In this introduction, the structural properties of five-coordinate Cu(II) complexes and the metal complex-promoted hydrolysis of phosphate diesters will be addressed.

A. Five Coordinate Cu(II) Complexes

The copper(II) ion readily forms coordination complexes with a higher affinity than other transition metal ions but is reluctant to form a regular octahedral or tetrahedral complex because of Jahn-Teller distortion.[2] Five-coordinate copper(II) complexes are as common as the six-coordinate elongated rhombic octahedral complexes. The five-coordinate $Cu(II)L_5$ rarely forms a regular trigonal bipyramidal (D_{3h} symmetry) or a square pyramidal (C_{4v} symmetry) geometry (**Scheme 1.1 (a)**), but generally involves a distorted square pyramidal or a distorted trigonal bipyramidal geometry, which may be connected by the Berry twist mechanism (which retains a C_2 axis of symmetry) (**Scheme 1.1(b)**).[3]

square-based pyramidal trigonal bipyramidal **(a)**

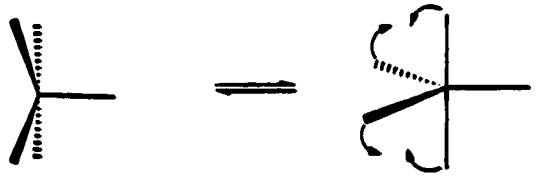

(b)

Scheme 1.1. (a) Regular trigonal bipyramidal and square pyramidal geometry; (b) Berry twist mechanism.

In the regular square-based pyramidal structures (**Fig. 1.1 (a)**) the four in-plane distances are of normal length, ca. 2.0 Å for O and N ligands and ca. 2.3 Å for Cl, but the fifth ligand distance is 0.2-0.5 Å longer as a result of Jahn-Teller distorted Cu(II). Interestingly, the Cu(II) ion is also lifted out of plane of square-basal plane by a distance of 0.1-0.5 Å, represented by ρ Å, with an inverse relationship to the fifth ligand distance *i. e.* longer Cu-L bond length less lifting (**Fig. 1.2 (a)**).

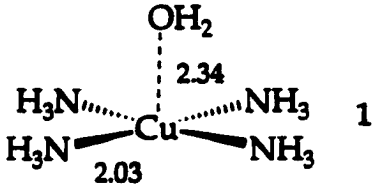

1

$[Cu(NH_3)_4(OH_2)](SO_4)$

(a)

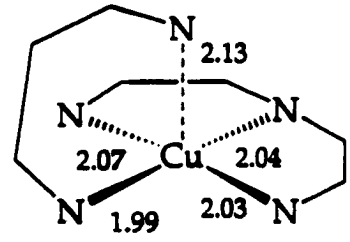

2

$[Cu(dien)(bipyam)](ClO_4)$

(b)

Figure 1.1. (a) Regular square-based pyramid; (b) Distorted square-based pyramid.

The largest group of five-coordinate geometries of the Cu(II) ion involves distortion from the regular square-based pyramid (**Fig. 1.1 (b)**). The bond length change can be described by the tetragonality T^5 defined as the ratio of the four in-plane Cu-L distances and the single long Cu-L distance. In general the T^5 values are in the range 0.90-0.96, for example 0.925 of T^5 in $K[Cu(NH_3)_5](PF_6)_3$[4] (**Fig. 1.3**), and show a proportional relationship with an angular difference, τ value (**Fig. 1.2 (b)**).

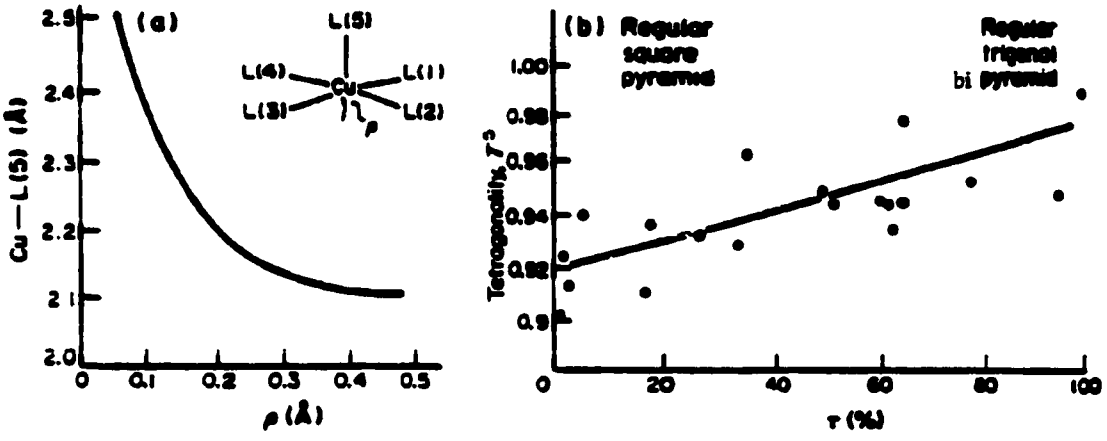

(a) (b)

Figure 1.2. (a) Correlation of the Cu-L_5 distance with the distance ρ that Cu(II) is lifted out of the plane of the four square-based ligands; (b) tetragonality, T^5, *vs.* angular difference, τ.[3]

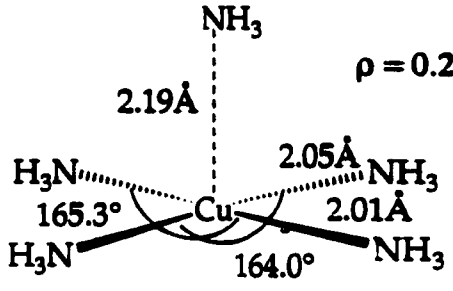

3

Figure 1.3. $K[Cu(NH_3)_5](PF_6)_3$.

The in-plane angular distortions can be described by the ratio τ (**Fig. 1.4**), representing a percentage trigonal distortion of a square pyramidal stereochemistry (when τ is100 its geometry is a regular trigonal bipyramid and when τ is 0 its geometry is a regular square-based pyramid). Structural data of five-coordinated Cu(II) complexes are presented in **Table 1.1.**

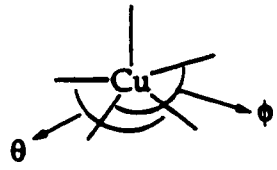

$$\tau = \frac{\theta - \phi}{60} \times 100$$

Figure 1.4. τ (percentage trigonal distortion of a square pyramid).

Table 1.1. Structural data of five-coordinated Cu(II)N_5 complexes correlating the square pyramidal and trigonal bipyramidal geometries.[3]

Complex	mean Cu-L_4 (Å)	mean Cu-L_5 (Å)	T^3	ρ (Å)	τ(%)
$[Cu(cyclops)py]^+$	1.972	2.171	0.908	0.40	0.5
$[Cu(dibenzocyclam)(N_3)]^+$	2.082	2.160	0.964	0.21	1.8
$K[Cu(NH_3)_5]^{2+}$	2.029	2.193	0.925	0.27	2.2
$[Cu(en)_2NH_3]^{2+}$	2.01	2.21	0.910	0.22	7.0
$[Cu(Me_5dien)(NCBH_3)_2]$	2.038	2.153	0.947	0.36	18
$[Cu(tren)(NCS)]^+$	2.025	2.144	0.945		51
$[Cu(dien)(bipyam)]^{2+}$	2.033	2.150	0.946	0.44	60
$[Cu(bipy)_2(NH_3)]^{2+}$	2.104	2.112	0.954		77
$[Cu(tren)(NH_3)]^{2+}$	2.057	2.082	0.988		100
$[Cu(NH_3)Ag(NCS)_3]$	1.96	1.92	1.02		100

The Cu(II) complexes are generally colored. This color normally originates from the maximum of four electronic transitions between the ground

state and the excited states of the crystal-field levels.[5] These transitions occur in the range 4.0-30.0 kK (kK = 1000 cm^{-1}) and are (1) pure *d-d* transitions below 20 kK; (2) charge-transfer transitions above 20-30 kK; (3) internal ligand transitions between 20-30 kK; (4) combination and overtone vibrations of the ligands below 10 kK. The intensities of types 2) and 3) are much greater than type 1) and may well mask the less intense d-d transition when they are of low energies. Among these transitions, only *d-d* transitions show dependence on the Cu(II) stereochemistry present, although MLCT (metal to ligand charge transfer) and LMCT (ligand to metal charge transfer) bands may also related to the Cu(II) stereochemistry.[6] Most copper(II) *d-d* spectra show a single broad band with an occasional shoulder or two bands, with rarely evidence of further resolved bands, even though there are four possible transitions.[7]

Electronic spectra of the Cu(II) complexes have been measured in three ways, in solution, as reflectance spectra, and as polarized single-crystal spectra. The solution spectra provide accurate extinction coefficient data with the uncertainty of actual species present in solution. The reflectance and single-crystal spectra provide the information for the crystal structure in the solid state with a low certainty in the extinction coefficient. The large half-width of all these spectra cause problems in determining the positions of the underlying transitions. In solution, Gaussian analysis is used to determine the exact positions of transitions. Polarized single-crystal electronic spectra are the most accurate method for resolving of a Cu(II) electronic spectrum into its component. They are recorded in the three mutually perpendicular directions determined by the crystal indices.[7]

The ligand type, the particular CuL_n coordination number, and geometries are variations that make the determination of the band position and one-electron energy levels of a Cu(II) ion in the complexes more difficult. Even though electronic spectra of Cu(II) complexes are a wealth of variety, they provide little definitive information about the structures because of the above reasons.

The *d-d* transition of the copper(II) ions are governed by two selection rules: the spin multiplicity rule which is redundant for Cu(II) (d^9) configuration (always yields doublet states) and Laporte rule which forbid the transitions between states of the same parity (symmetry with respect to a center of inversion). Three mechanisms are available to account for the breakdown of the Laporte rule.[8]

- In non-centrosymmetric complexes, *d-p* mixing may occur affording increased electronic intensity from allowed *d* -> *p* transition.
- In C_{4v} complexes, a vibronic mechanism is invoked, which allows an ungerade mode of vibration of the molecule, coupling with the electronic excited state.
- Less commonly, intensity borrowing from a low-energy charge transfer band can occur.

As mentioned above, two coordination geometries, trigonal bipyramidal (D_{3h} symmetry) and square pyramidal (C_{4v} symmetry), may be involved for five-coordinated Cu(II) complexes. However, Berry pseudorotation relates these two geometries (D_{3h} and C_{4v}) extremes by a pathway maintaining C_{2v} symmetry. The correlation diagram of one-electron energy levels between D_{3h} and C_{4v} is depicted in **Figure 1.5.** The correlation between the range of energies of the *d-d* transitions

of a five-coordinated Cu(II) complex and the two possible stereochemistries are presented (**Fig. 1.6**). Since the square pyramidal geometry has C_{4v} symmetry and lacks of centro-symmetry, the *d-p* mixing provides higher energies for the *d-d* transitions in the square pyramidal complex than those in the trigonal bipyramidal complex. According to the correlation diagram of the one-electron energy levels of the square pyramid, a total of three *d-d* transitions, d_{xz} or d_{yz} -> d_{x2-y2}, d_{xy} -> d_{x2-y2}, and d_{z2} -> d_{x2-y2}, are expected to occur, while only two *d-d* transitions, d_{xz} or d_{yz} -> d_{z2} and d_{x2-y2} or d_{xy} -> d_{z2}, are possible in the trigonal bipyramidal geometry.

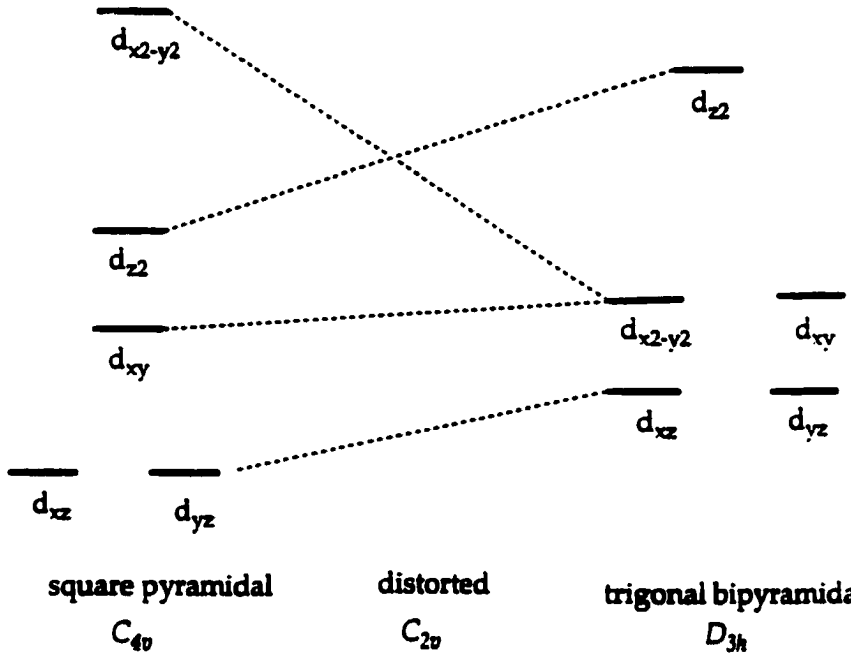

Figure 1.5. Correlation diagram of one-electron energy levels for five-coordinated Cu(II) complexes.

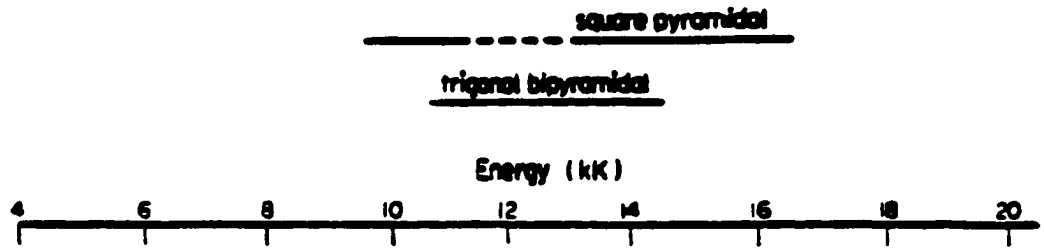

Figure 1.6. The range of energies of *d-d* transitions for a square pyramid and a trigonal bipyramid.

The location of the shoulder is very informative in characterizing the stereochemistry of the five-coordinated Cu(II) complexes that can adopt two possible geometries, a trigonal bipyramid and a square pyramid. Two electronic spectra of $[Cu(tren)(NH_3)](ClO_4)_2$ (tren = tris(2-aminoethyl)amine) and $K[Cu(NH_3)_5](PF_6)_3$ are presented in **Figure 1.7**. The coordination sphere of the $[Cu(tren)(NH_3)](ClO_4)_2$ complex is a trigonal bipyramid, while $K[Cu(NH_3)_5](PF_6)_3$ has a square pyramidal molecular structure.[4] The $[Cu(tren)(NH_3)](ClO_4)_2$ complex has a higher-energy shoulder at 15,200 cm^{-1} with a band maximum at 11,400 cm^{-1}, on the other hand the $K[Cu(NH_3)_5](PF_6)_3$ complex has a low-energy shoulder at 11,000 cm^{-1} with a band maximum at 15,200 cm^{-1}.

Karlin et al.[9] also reported a low-energy shoulder (967 nm) with a band maximum at 665 nm for a square pyramidal Cu(II) complex $[Cu(tepa)Cl]^+$ (tepa = tris-(2-(2-pyridyl)ethyl)amine) and reversed appearance for a trigonal pyramid $[Cu(tmpa)Cl]^+$ (tmpa = tris(2-pyridyl) methylamine) with a high-energy shoulder (632 nm) and a band maximum at 962 nm. Wei et al. observed identical trends from UV-vis spectrum of a trigonal bipyramidal Cu(II) complex $[(TMPA)CuCl]^+$ (TMPA = tris[((2-pyridyl)methyl)-methyl]amine) and of a square pyramidal

Cu(II) complex [(TMQA)CuCl]$^+$ (TEQA = tris(2-quinolylmethyl)amine).[10]

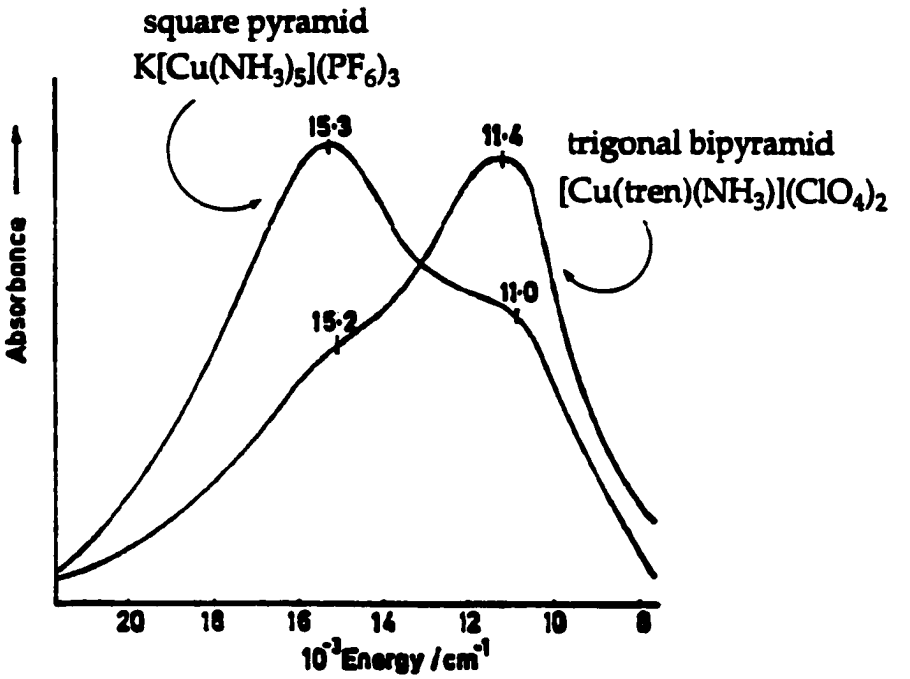

Figure 1.7. Electronic spectra of $[Cu(tren)(NH_3)](ClO_4)_2$ and $K[Cu(NH_3)_5](PF_6)_3$.

B. Hydrolysis of Phosphodiester

Tridentate ligands with nitrogen donors are of interests in bond cleavage of biological molecules, especially phosphodiesters bonds. Novel ligands based on *cis,cis*-1,3,5-triaminocyclohexane (tach) **238** (**Scheme 3.6**) have not only three nitrogen donor atoms, but also facial coordinational configuration so that they have shown versatility in binding metal ions with varied charges and sizes.[11, 12, 13] The face-capping N_3 nature of tach form the basis of many ligand systems, particularly in modeling of metal enzyme active sites[14] and as a basis for an *in vivo* metal chelator.[15]

Phosphodiester linkages join adjacent nucleosides in DNA, deoxyribonucleic acid, and RNA, ribonucleic acid, to form a sugar-phosphate polymer backbone (**Fig. 1.8 (a)**). Proteins consist of unbranched chains of amino acids linked by peptide bonds that are planar units that usually exist in the *trans* configuration (**Fig. 1.8 (b)**).

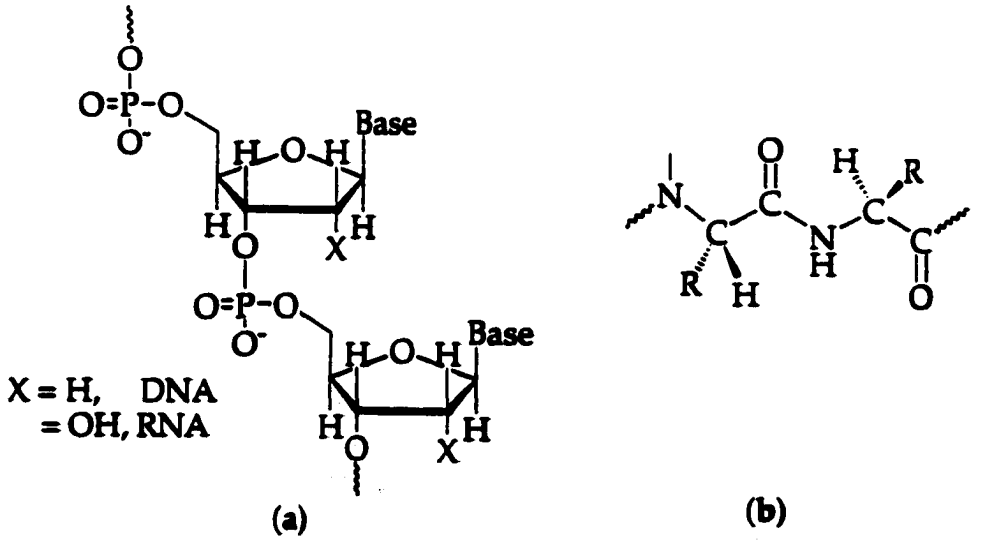

Figure 1.8. (a) Phosphodiester bond link the nucleosides of DNA and RNA; (b) Peptide bonds link amino acids in protein and polypeptides.

Phosphodiesters are exceptionally stable to maintain the integrity of the genetic code and the proper function of the proteins. A single mutation in any of DNA, RNA, or degradation of an essential protein could lead to serious problems. In a neutral solution at room temperature, hydrolysis of the dimethyl phosphate backbone in DNA takes a long time, an estimated half-life of 130,000 years.[16] The hydrolysis of the phosphodiester bonds in RNA is much faster compared to that in DNA because of the presence of the 2′-hydroxy group on the ribose ring in RNA and takes an estimated half-life of four years under the same conditions.[17] The stability of the phosphodiester bond in DNA and RNA is attributed to the repulsion between the negatively charged phosphodiester backbone and potential nucleophiles. Since the delocalization of the electron density in the peptide bond makes the carbonyl a poor electrophile, the half-life in hydrolysis of the peptide bonds connecting amino acids in proteins takes at least seven years at neutral pH and 25 °C.[18] Ironically, the stability of phosphodiester linkages and peptide bonds can be a problem because efficient hydrolysis for these bonds is necessary in DNA repair and at many different stages of transcriptions and translations.

There are significant kinetic barriers to hydrolyze peptide or phosphate ester bonds, even though these bonds are unstable to hydrolysis.[19] Nature utilizes a class of enzymes called hydrolases[20] to destroy foreign DNA and proteins. Other functions of hydrolases are to excise and repair a mutated DNA, to hydrolyze *m*RNA so that the proteins it encodes are not synthesized unnecessarily, and to degrade native proteins into their corresponding amino

acids once they have served their function and are no longer needed. Natural nucleases are able to catalyze the hydrolysis of P-O bonds of phosphodiester with rate enhancement over un-catalyzed reaction exceeding 10^{16} under physiological conditions.[21] These hydrolytic enzymes are in fact metalloenzymes with metal ions present at the active site and utilize one or multiple catalytic metal ions as cofactors to hydrolyze phosphodiester and phosphomonoester bonds. The positions of these ions have been determined, with respect to the phosphate residues, by X-ray crystal structures. However, the exact role of the most frequently employed metal ions, Mg(II), Zn(II), Mn(II), Ca(II), and Fe(II), in the hydrolytic process is not well known.[22]

The hydrolytic cleavage of peptide or phosphate ester bonds is an important step in metabolic and biochemical pathways. Therefore, a lot of effort on degradation of the phosphodiester backbone by synthetic hydrolases have concentrated on the oxidative degradation of DNA or hydrolysis of activated substrates during last two decades. Unlike synthetic hydrolases, which catalyze the nucleophilic attack of water on the phosphorus atom of a substrate, nonhydrolytic DNA nucleases cleave DNA or RNA by H abstraction, an oxidative degradation, which will be discussed in **Chapter 2.**

Since the study of natural metallohydrolases provides a better understanding of the precise function of metal ions and strategies for designing synthetic metallohydrolases, a discussion on natural hydrolases and synthetic hydrolases are presented in this section.

B.1 Natural Peptide Hydrolases and Phosphohydrolases

Peptidases catalyze the hydrolysis of peptide bonds in proteins (**Scheme. 1.2 (a)**), while phosphatases and nucleases catalyze the hydrolysis of phosphate ester bonds in phosphorylated amino acids, nucleotides, DNA, or RNA (**Scheme. 1.2 (b)**) effectively under physiological conditions.

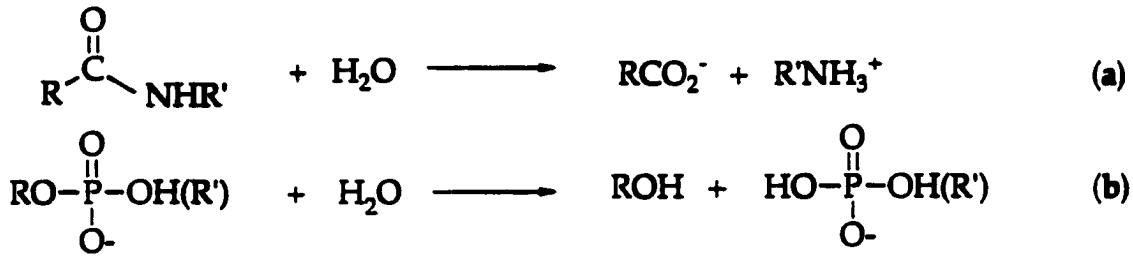

Scheme 1.2. Hydrolysis of peptide bonds and phosphate ester bonds.

Three different types of peptidases are known. The first type uses a serine or cysteine nucleophilic attack at carbonyl carbon, resulting in acyl-enzyme intermediate that is attacked by water. The second type utilizes two-carboxylate functional groups in general acid-base catalysis with no enzyme-bound intermediates. The third type uses the Lewis acidity of metal ions to increase the electrophilicity of carbonyl carbon and increase the nucleophilicity of water. Phosphatases and nucleases use the functional groups of amino acids and/or the Lewis acidity of metal ions. Ribonuclease, which hydrolyzes RNA with a concerted acid-base mechanism using two histidine residues, and staphylococcal nucleases, which uses the electrostatic properties of a protein-bound Ca(II) ion and general-base catalysis to hydrolyze DNA, are two of the best characterized enzymes that catalyze the hydrolysis of phosphate ester bonds.[19]

B.1.1 Carboxypeptidase A and Thermolysin

Carboxypeptidase A and thermolysin utilize the zinc ion in similar ways and their structures and mechanisms are well understood. In order to catalyze peptide hydrolysis, an enzyme must facilitate the nucleophilic attack on the peptide carbonyl group by a nucleophile and stabilize the tetrahedral intermediate or transition state that is generated by nucleophilic attack. It also must stabilize the amide nitrogen atom to make it a good leaving group, so that the tetrahedral intermediate can break down upon C-N bond cleavage.[23]

Carboxypeptidase A is a metallopeptidase and contains one zinc ion bound to a single polypeptide chain (~300 amino acids and ~34,000 molecular weight), and its biological function is the hydrolysis of C-terminal amino acids from polypeptide substrates. It shows a preference toward substrates that possess large hydrophobic C-terminal side chain such as phenylalanine.[24] This preference toward the C-terminal carboxylate of substrates is provided by hydrogen-bond interactions with a triad of residues. Three forms of bovine carboxypeptidase A, designated A_α, A_β, and A_γ with 307, 305, and 300 amino-acid residues, have been obtained. The structure of carboxypeptidase A has been determined in a high-resolution X-ray crystal structure study. The important residues for catalysis and binding are Glu-270, Arg-127, Arg-71, Asn-144, Arg-145, Tyr-248, Zn(II), and the zinc-bound water molecule.[24] The zinc ion is seated well inside the protein surface and is coordinated by two imidazole side chains, from His-69 and His-196, and to the bidentate carboxylate group of Glu-72 (Fig. 1.9). A penta-coordination of Zn(II) is completed by an additional coordination

of a water molecule. The Glu-72 becomes nearly unidentate in the presence of substrates or inhibitors. The ability of Glu or Asp residues to rearrange, called the carboxylate shift, allows a nearly constant penta-coordination of the Zn(II) ion.

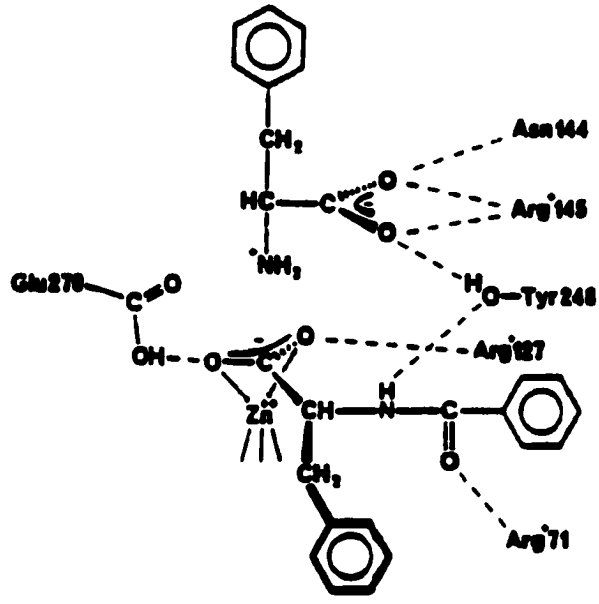

Figure. 1.9. The active site of carboxypeptidase A with a bound inhibitor.[24]

Thermolysin is a thermostable calcium-binding zinc endopeptidase of molecular weight 34,600. The amino acid sequence and three-dimensional structure of the endopeptidase thermolysin has also been determined by X-ray crystal-refinement with support from oscillation photography.[25] Closer investigation of the active site of thermolysin reveals many similarities to that of carboxypeptidase A. In native thermolysin, three ligands, from His-142, His-146, and Glu-166, and a water molecule coordinate zinc ion (**Fig. 1.10**). The coordination sphere of Zn(II) is an approximate tetrahedral coordination.[26] The non-coordinating amino-acid side chains, Glu-143 and His-231, in the

thermolysin are also similar to that of Glu-270 and Arg-127 in carboxypeptidase A.[23]

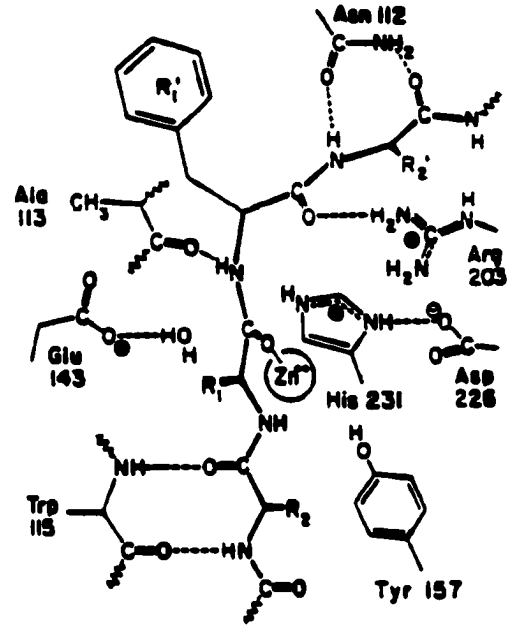

Figure 1.10. The active site of thermolysin with a bound substrate.[27]

Thermolysin and carboxypeptidase A employ essentially the same catalytic mechanism, a water-promoted pathway in the hydrolysis of peptide substrate.[24] The deprotonation of a coordinated water molecule generates a nucleophile, zinc-bound hydroxide ion. The p*K*a of a zinc-bound water molecule is as low as 7, and zinc-bound water molecule can be hydroxide-like or nucleophilic at neutral pH.[28] The nucleophilicity of zinc-bound hydroxide is further enhanced through a hydrogen bond with nearby glutamate, Glu-143 in thermolysin and Glu-279 in carboxypeptidase A. The incoming substrate leads the zinc-bound water molecule toward glutamate, and the nucleophilicity of this water could be enhanced through the hydrogen bond to glutamate and the

coordination of the carbonyl oxygen from substrate to zinc ion. This interaction directs the remaining lone pair of the zinc-bound water molecule toward the carbonyl carbon of the substrate and is aligned for nucleophilic attack. Then, the water attacks the carbonyl carbon to form the penta-coordinate intermediate.[27] The glutamate immediately transfers the accepted proton to the leaving amino group. The main role of the zinc is presumably not ground-state effects, polarization, but the transition-state stabilization through charge neutralization.[24] The proposed mechanisms for the thermolysin and carboxypeptidase A catalyzed cleavage of peptides are depicted in **Scheme 1.3** and **Scheme 1.4.**

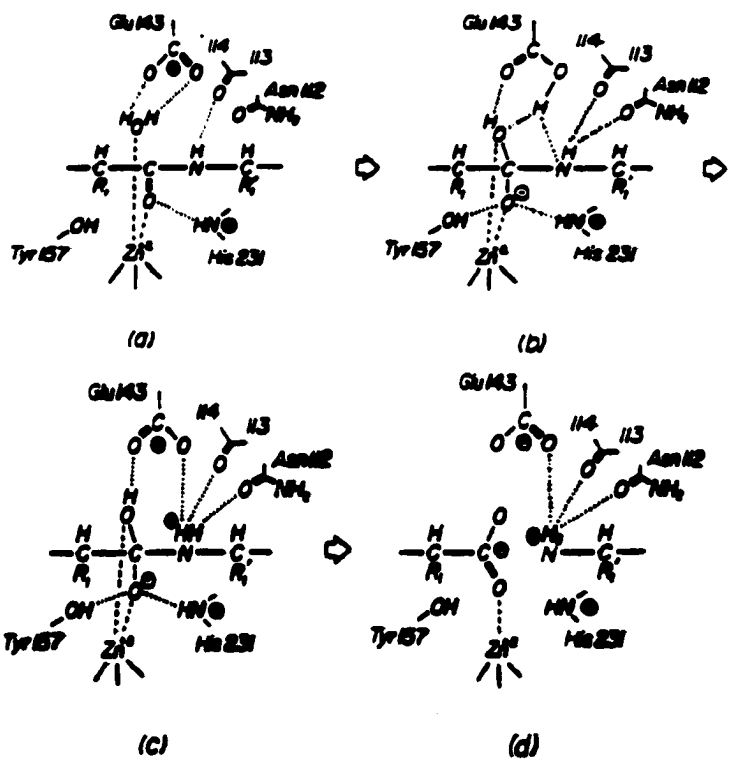

Scheme 1.3. Proposed mechanism for the thermolysin-catalyzed cleavage of peptides.[26]

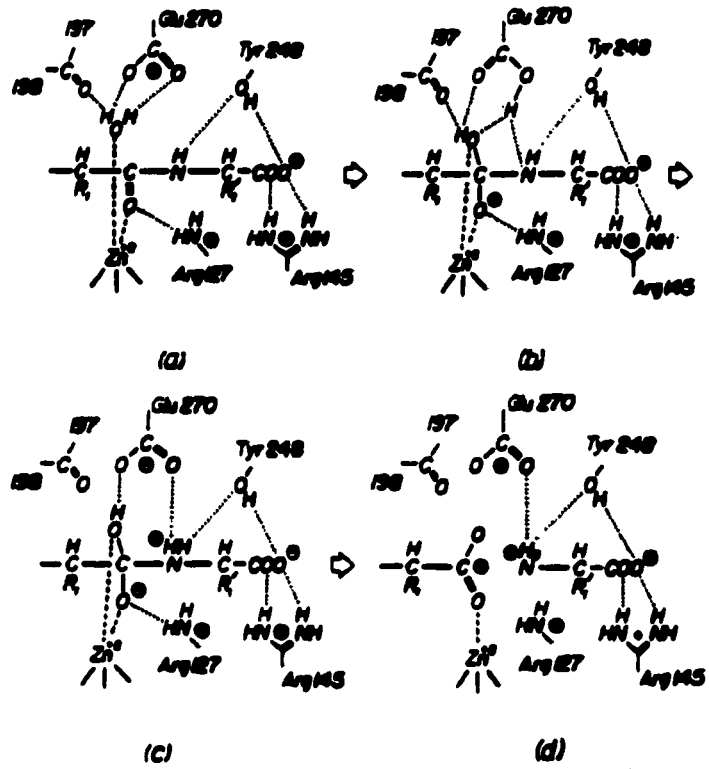

Scheme 1.4. Proposed mechanisms for the carboxypeptidase A catalyzed hydrolysis of peptide bonds.[26]

B.1.2. Alkaline Phosphatase and Purple Acid Phosphatases (PAP)

The alkaline[23] and purple acid phosphatases[29] catalyze the removal of a phosphate group from phosphomonoester. Alkaline phosphatase contains a three-metal cluster comprised of two zinc ions and one magnesium ion. The two zinc ions are essentially involved in the hydrolysis reaction, the magnesium is not required but enhances the reactivity. Kim and Wyckoff[30] proposed a mechanism for the hydrolase activity of alkaline phosphatase via a two-step nucleophilic displacement mechanism. The zinc ion activates the nucleophile, a serine residue, to attack the phosphomonoester allowing a water molecule to displace the phosphate group from the serine residue in each displacement step. Inversions at the phosphorus center in each nucleophilic attack lead to retention

of configuration. Active site structure and proposed mechanism for the hydrolase of alkaline phosphatases are depicted in **Scheme 1.5.**

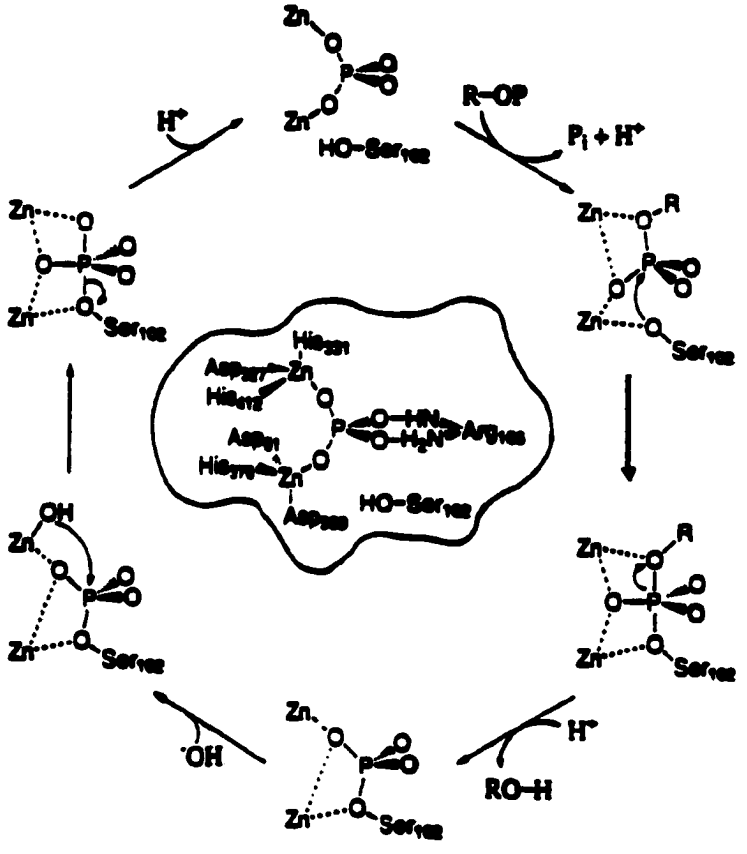

Scheme 1.5. Active site structure and proposed mechanism for the hydrolysis of alkaline phosphates.[30]

Purple acid phosphatases (PAP) are enzymes that exhibit a characteristic purple color (λ_{max} ~ 550 nm), a tyrosine -> Fe(III) charge transfer transition, in inactive oxidized form and a pink color (λ_{max} ~ 510 nm) in active reduced form. These enzymes catalyze the hydrolysis of phosphate esters under acidic conditions (pH range 4.9 – 6.0).[19] Purple acid phosphatases also employ bimetallic catalytic sites in which one Fe(III) and a second divalent metal ion, usually Zn(II) or Fe (II), work together. The presence of binuclear metal ion site

in PAP was initially proven by magnetic susceptibility and EPR measurements. The X-ray crystal structure of kidney bean PAP shows that aspartate-164 residue provide a monoatomic carboxylate bridge between metal ions, Fe(III) and Zn(II).[31] Based on the geometry of the coordination sphere of the metal ions, three additional ligands were added to the active site of structure, a bridging hydroxide, a terminal water on the Zn(II), and a terminal hydroxide on the Fe(III). This model suggests that both metal ions are six-coordinated with each ion retaining one open coordinate site occupied by an exchangeable solvent ligand, water. The bridging hydroxide and the hydroxide bound to the Fe(III) ion were not observed in the crystal structure even at 2.65 Å resolution, but their existence has been postulated based on spectroscopic and kinetic evidence.[22] PAP hydrolysis of phosphate ester occurs with inversion of configuration at the phosphorus. This fact suggests a mechanism involving attack of a metal-bound hydroxide ligand on the phosphate ester and formation of a trigonal-bipyramidal phosphorus intermediate.[32] The pH-dependence of these enzymes is attributed to the deprotonation of a Fe(III)-bound water molecule that has a p*K*a of 4.8.[19] The proposed mechanism for hydrolysis of phosphomonoester by purple acid phosphatase is shown in **Scheme 1.6.**

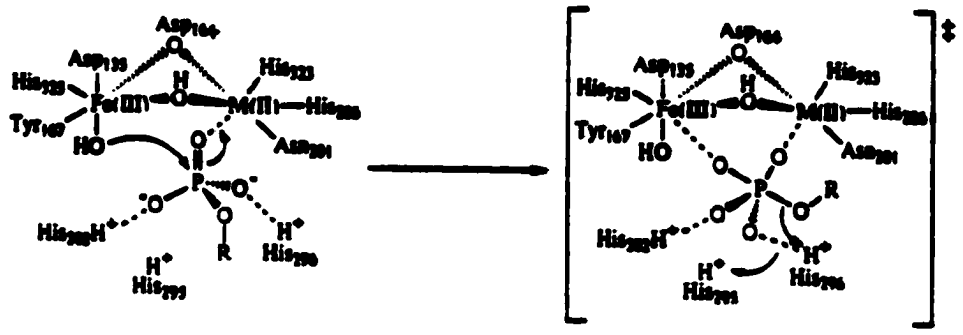

Scheme 1.6. Proposed mechanism for hydrolysis of phosphomonoester by purple acid phosphatase. M (II) is Zn on the crystal structure of kidney bean purple acid phosphatase.[22]

B.1.3. Inositol Monophosphatase and Fructose-1,6-bisphosphatase

The enzyme inositol monophosphatase (IMP) catalyzes hydrolysis of the phosphate ester bond of inositol-1-phosphate (I-1-P, 4), product of inositol biosynthesis. IMP requires Mg(II) and a partial activity of Mn(II), Zn(II) or Co(II). IMP binds two metal ions with different rates and exhibits cooperative Mg(II) activation of enzyme activity.[33]

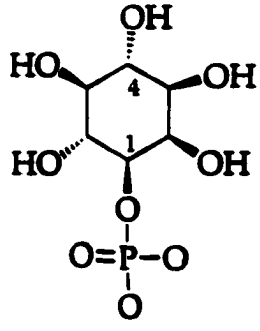

4

Figure 1.11. D-*myo*-Inositol-1-phosphate

Recent X-ray crystal structures of human IMP in the presence of 5 mM $MnCl_2$ showed the metal ion coordination and revealed a binuclear Mn(II) site.[34] Without phosphate, the coordination sphere of one Mn(II) (site 1) is distorted between trigonal bipyramidal and square pyramidal with five ligands, Glu70, the carbonyl oxygen of Ile92 , water, Asp 90 and Cl^-, in which last two ligands bridge the second Mn(II) (site 2) that has a tetrahedral geometry coordinated by Asp93 and Asp220. There is the third Mn(II) (site 3) which weakly binds to protein by the coordination to the other oxygen of Glu70, catalytically important, and three water. In the phosphate complex (**Fig. 1.12**), the Mn(II) (site 3) and the Cl^- are displaced and the phosphate links the two strongly bound Mn(II) ions through one oxygen and coordinate to Mn(II) (site 1) through another oxygen giving octahedral coordination with retention of water ligand.

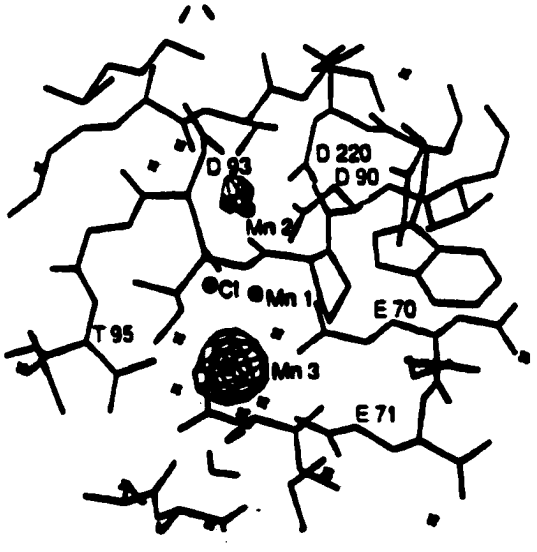

Figure 1.12. The active site of the complex of IMP with Mn(II) and phosphate (DI1P = D-*myo*-inositol-1-phosphate.[34]

A mechanism of IMP hydrolysis promoted by two Mg(II) ions was proposed by Bone et al.[35] In the proposed mechanism (**Scheme 1.7**), metal ions participate in binding substrate, activating a nucleophile, stabilizing the trigonal-bipyramidal phosphorus intermediate, and interacting with the product. It was also proposed that one Mg(II) is strongly bound through the entire catalytic cycle while the other Mg(II) enters the catalytic cycle with the substrate to form catalytically active site but then released with products.

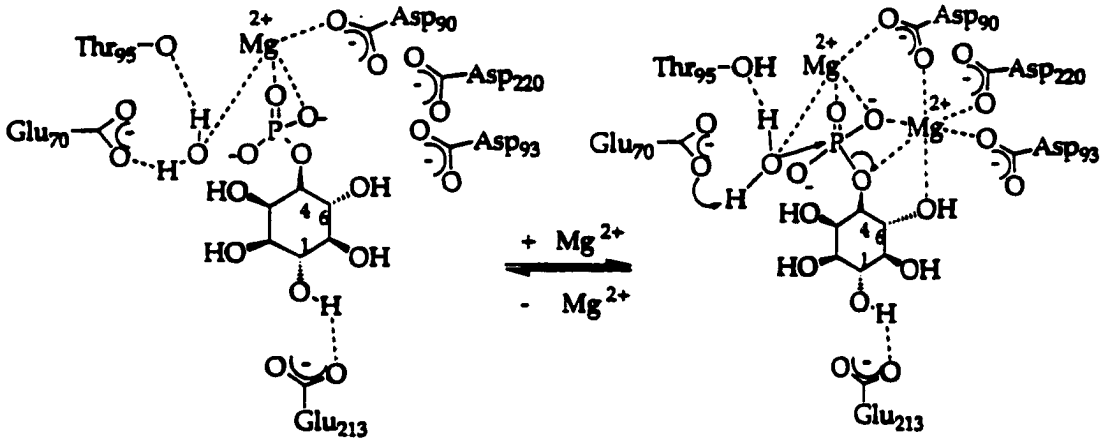

Scheme 1.7. Proposed mechanism for inositol-1-phosphate hydrolysis at IMP active site.[35]

Fructose-1,6-bisphosphatase (FBPase) catalyze the hydrolysis of 1-phosphate from D-fructose 1,6-bisphosphate (Fru-1,6-P_2) to give D-fructose 6-bisphosphate in the gluconeogenesis. This enzyme requires two divalent metal ions which may consist of Mg(II), Mn(II), Zn(II), or Co(II). X-ray crystal structure of FBPase complex with substrate, fructose 1,6-bisphosphate, and inhibitors, AhG-1,6-P_2 and AhM-1,6-P_2, has shown the presence of Mg(II) and one of Mn(II) or Zn(II).[36] Because AhG-1,6-P_2 inhibitor is an analog of Fru-1,6-P_2, the Mn(II)

and Zn(II) complex with this inhibitor give a fundamental principle for substrate binding and a mechanism for the hydrolysis of 1-phosphate from Fru-1,6-P_2. In the proposed mechanism (**Scheme 1.8**), both metal ions bind and position the substrate, activate a water molecule for a nucleophilic attack, and stabilize the trigonal bipyramidal phosphorus intermediate. Inversion of phosphorus stereochemistry supports the proposed mechanism.[37]

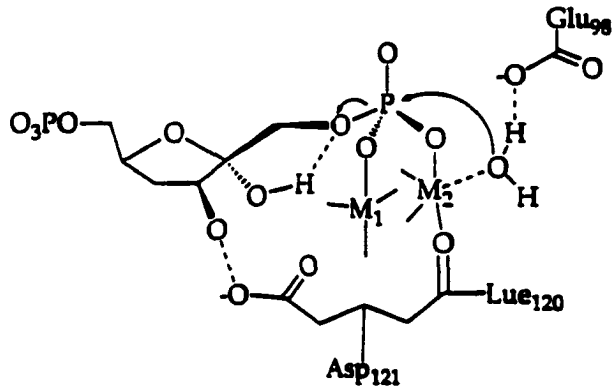

Scheme 1.8 Propose mechanism for fructose 1,6-bisphosphate hydrolysis at the FBP binuclear metal ion site.[36]

B.1.4. Inorganic Pyrophosphatase (IP)

Inorganic pyrophosphatase is one of the best examples of an ubiquitous cytoplasmic enzyme that will hydrolyze pyrophosphate, maintaining the intracellular level of phosphate and removing the pyrophosphatase product of nucleotide coupling reactions.[19]

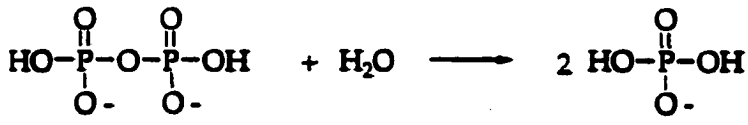

Scheme 1.9. Hydrolysis of pyrophosphate.

All pyrophosphatase contain metal ions. Pyrophosphatase with Mg(II) provides the highest activity and specificity for pyrophosphate, while with other activating metal ions, Zn(II), Mn(II), and Co(II), the enzyme become less specific and hydrolyze a number of phosphate esters with appreciable rates.[38] Multiple binding sites in close proximity in IP were found by physical characterization methods, especially EPR and NMR, with different metal ions. EPR studies of the active Mn(II) form of IP show magnetic interaction between the two Mn(II) ions[39] while NMR studies of ^{113}Cd substituted IP show three different ^{113}Cd resonances.[40] X-ray crystal structures for a variety of IP's indicated that one metal ion is chelated by the substrate and at least one other divalent metal ion is necessary for activity.

The proposed mechanisms for hydrolysis of pyrophosphate by IP have common facts; the metal ions bind to a substrate pyrophosphate, for the optimal activity the substrate is stabilized by interaction with residue, and a metal bound hydroxide ion is essential for catalysis either as the attacking nucleophile or as a general base.

B.1.5. DNA Polymerase I (Pol I)

The enzyme DNA Polymerase I catalyzes the transfer of nucleotides to the 3′ end of template-primer DNA and the hydrolysis of the 3′ terminal nucleotide of single-stranded DNA (3′-5′exonuclease activity). An unpaired 3′-terminal nucleotide with a free OH group activates the 3′-5′exonuclease activity. If Pol I erroneously incorporates a wrong nucleotide at the end of growing DNA chain,

the polymerase activity is stopped and the 3′-5′exonuclease activity starts to correct the offending nucleotide (**Fig. 1.13**).[20]

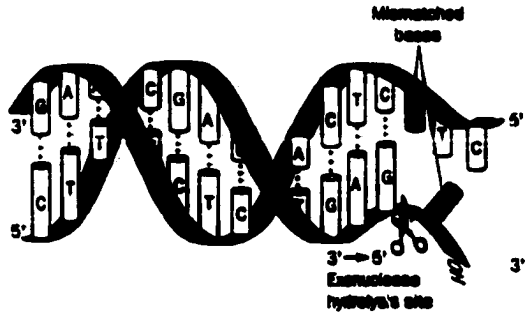

Figure 1.13. The 3′-5′exonuclease function of DNA polymerase I excises mispaired nucleotide from the 3′ end of the growing DNA strand.

The products of the 3′-5′exonuclease activity of DNA polymerase I are a deoxynucleoside 5′-monophosphate and a free 3′ hydroxyl of the shortened DNA polymer. According to high-resolution X-ray crystal structures, the 3′-5′exonuclease site of DNA polymerase I contains two Mg^{2+} ions.[41] Later, cooperative binding of three metal ions has been reported for Co(II), Mn(II), and Mg(II) in the activation of 3′-5′exonuclease activity of DNA polymerase I.[42] One metal ion (M_1) is tightly bound to enzyme affording coordination through five sites with Asp355, Glu357, Asp501, a phosphate oxygen, and a hydroxide ligand. The second metal ion (M_2) has octahedral coordination geometry with a bridging carboxylate from Asp355, two of the phosphate oxygens, and three water molecules.

A mechanism (**Scheme 1.10**) for 3′-5′exonuclease activity of DNA polymerase I proposed that a $metal_2$-bound water is correctly positioned for

nucleophilic attack on the phosphate, resulting the inversion of phosphorus stereochemistry.[43] The p*Ka* of metal-bound water is lowered by the interaction with Glu357 and Tyr497 when the metal ion is Mn(II) or Mg(II). It is suggested that the two metal ions together enhance solvent nucleophilicity providing a potent nucleophile at neutral pH. This metal-bound hydroxide stabilizes the trigonal-bipyramidal phosphorus intermediate and assists in removal of the 3′ hydroxyl of the DNA product.

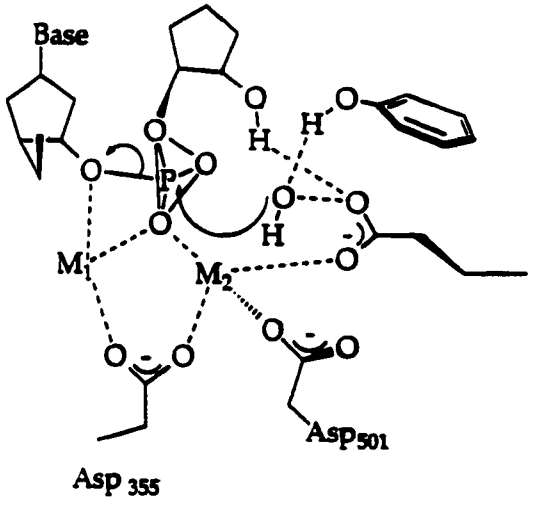

Scheme 1.10. Proposed mechanism for DNA hydrolysis at the 3′-5′ exonuclease active site of DNA polymerase I.

B.1.6. Other Nucleases

Ribonuclease H (RNase H) hydrolyzes the RNA of RNA-DNA hybrids and requires Mg(II) (or Mn(II)) for activity. It is know that RNase H activity occurs at a binuclear Mn(II) site that is similar to the 3′-5′ exonuclease active sites of DNA polymerase I and shows a similar mechanism for oligonucleotide hydrolysis.[44]

P1 nuclease preferentially catalyzes the hydrolysis of single-stranded DNA or RNA and then hydrolyzes the 5′ terminal phosphate from the initial oligonucleotide cleavage. It requires three Zn(II) ions and hydrolyzes phosphate esters with inversion of the phosphorus stereochemistry.[45] P1 nuclease has a low optimal pH (4.6-6) similar to that of purple acid phosphatases. EcoRV endonuclease catalyzes the hydrolysis of the phosphodiester backbone of double-stranded DNA with sequence specificity and requires two Mg(II) ions for hydrolysis activity.[46]

Nature continually uses the same metal ions, Mg(II) and Zn(II), in different enzymes as described above. The choice of Mg(II) as the catalytically active metal ions comes from its high charge density and hard Lewis acidity compared to other metal ions in biological systems, allowing it to bind hard oxygen anions of the negatively charged phosphodiester back bone in nucleic acids. Zn(II) is a strong acid and is effective at polarizing carbonyl bonds. Zn(II) is labile in the ligand substitution reactions which is a important property in catalysis. Zn(II) can also adopt different geometry with no cost of energy stabilizing the transition state.[22]

B.2. Synthetic Hydrolases

The design, modeling, and development of synthetic nucleases and peptidases have been a challenge for chemists to create artificial nucleases capable of competing with natural ones. A synthetic hydrolase could be used as an artificial restriction enzyme by encoding sequence specificity into the cleavage agent or by linking it to an appropriate DNA binding agent.[47] An example of this is endonucleases, which recognize short sequences in double-helical DNA and catalyze the double-stranded hydrolysis of the DNA at those sites. An artificial restriction enzyme would be useful to cleave at a site, not recognized by currently available endonucleases, and to investigate the sequence of the human genome. Synthetic hydrolases could also be used as conformational probes in obtaining the three-dimensional structure information for nucleic acids or proteins.[22] The most conventional and powerful techniques used, NMR spectroscopy or X-ray crystallography, require a large amount of material, and it is hard to get X-ray quality of crystals of protein and nucleic acids. Synthetic metallonucleases and metallopeptidase would have great potential to elucidate the exact role of metal ions in natural hydrolases.

The knowledge obtained by studying natural hydrolase has been an impetus for many scientists in the design, modeling, and development of synthetic nucleases. This section will focus on recent success in the synthesis of a number of metal complexes, the report of synthetic hydrolases utilizing substitution-inert metal ions, more than one metal ions, and labile metal ions.

B.2.1. Synthetic Peptidase

The hydrolysis of amides by metal complexes is less certain compared to the hydrolysis of phosphate esters. Mechanistic studies with substitutionally inert Co(III) complexes propose that amide hydrolysis can be promoted both through activation of the carbonyl and intramolecular attack of a metal bound hydroxide.[48, 49] Five different mechanisms for the hydrolysis of amides were proposed by Sayre, three of which are similar to the mechanism proposed for phosphodiester hydrolysis. According to his mechanisms, a substrate binds to a metal ion with activation of the carbonyl followed by attack from the metal-bound hydroxide. Groves et al. reported the hydrolysis of unactivated amide bonds promoted by Cu(II) and Zn(II). They proposed that a metal-bound hydroxide is a catalytically active species.[50] The involvement of metal-bound hydroxides and the importance of avoiding deprotonation of the amide NH for rate increase were observed in the hydrolysis of various picoliamides mediated by divalent metal ions.[51, 52]

B.2.2. Synthetic Hydrolases Using Substitution–inert Metal Ions

The fact that polyphosphate and phosphate ester hydrolysis is promoted by simple metal ions has been known since 1963.[53] The problems encountered with divalent metal ions in the study of hydrolysis are that the divalent metal ions are substitutionally labile and form numerous complexes in rapid equilibrium. These problems can be resolved by the use of well-defined substitution-inert complexes to get important information. The required

substitutionally inert metal ions in synthetic hydrolases can be obtained from the literature on the hydrolysis of activated phosphodiester.

Butcher and Westheimer[54] investigated the hydrolysis of a variety of phosphates and showed that the hydrolysis rate was enhanced by up to 10^3-fold by using Lanthanide hydroxide gels, $La(OH)_3$ gels. They were, however, unable to identify the complexes responsible for the activation.

Sargeson et al.[55] examined the efficiency of the intramolecular nucleophilic attack of the hydroxide ion in the hydrolysis of the 4-nitrophenylphosphate ion by using the Co(III) complex, *cis*-$[(en)_2Co(OH_2)(NPP)]^+$ (5). In that study, it was observed that the labeled *cis*-coordinated hydroxide ion attacked the P center to yield 4-nitrophenolate and the chelated phosphate ion as the P-containing product. There was an initial increase in rate over the pH range 6-8 that is consistent with deprotonation of the coordinated water molecule to give the coordinated hydroxide ion. The nucleophilic attack of hydroxide ion at P center initially forms the intermediate five-coordinate phosphorane 8 that exchanges oxygen with solvent water to form a six-coordinate species 9 as an activated complex or intermediate. The five-coordinate phosphorane complex 8 then decays rapidly to the chelated phosphate complex 10 followed by ring opening at pH>9 to yield some of the monodentate phosphato complex 12 (**Scheme 1.11**). The rapid hydrolysis of the ester moiety by the intramolecular nucleophilic attack of the hydroxide ion at near neutral condition occurs despite the formation of a strained four-membered ring and the reduced basicity of OH^- by the coordination to the metal ion.

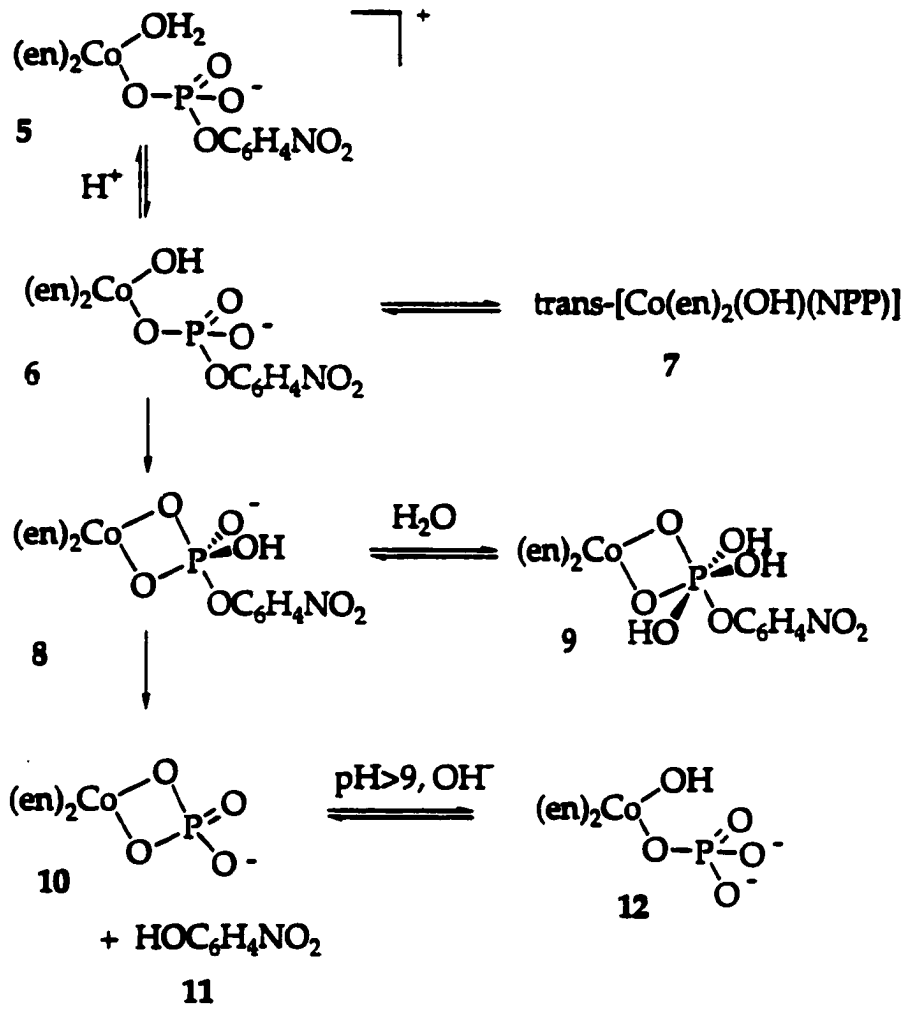

Scheme 1.11. Proposed mechanism of the hydrolysis of *cis*-$[(en)_2Co(OH_2)(NPP)]^+$.

Various cobalt(III) complexes of the general formula $[N_4Co(OH)(OH_2)]^{2+}$ (N_4 = bis-bidentate or tetradentate N donor ligand, 1,3-propanediamine (tn), 2,3-dimethyl-2,3-butanediamine (tmen), 1,8-diamino-3,6-diazaoctane (trien), 2,2'-bipyridine (bipy)) have been used to hydrolyze 4-nitrophenyl-methylphosphonate and ethyl-4-nitrophenyl-methylphosphonate **13** by Kenley et al.[56, 57] The rate of reaction in producing 4-nitrophenolate (NP) from both phosphonates is exactly consistent with the reactivity of the complexes in

exchanging the coordinated water with the substrates. An increasing rate of the reaction is observed in the order of $bipy_2$, trien, tn_2, and $tmen_2$. This indicates that the rate-determining step in the reaction is probably the substitution of the coordinated water by the phosphate esters and intramolecular attack of the *cis*-coordinated hydroxide ion on the P center proceeds rapidly (**Scheme 1.12**).

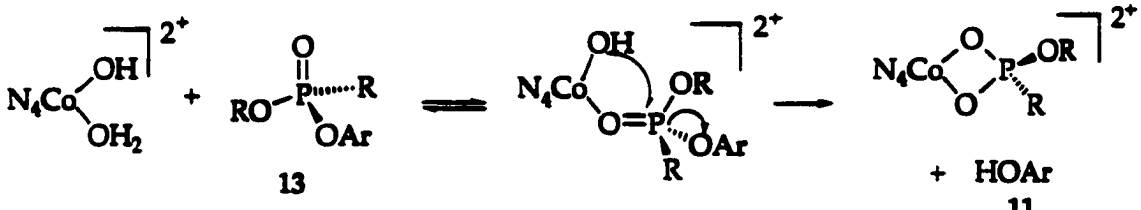

Scheme 1.12. Proposed mechanism of hydrolysis of the phosphate esters by the $[N_4Co(OH)(OH_2)]^{2+}$ complexes.

Chin et al. also[56, 58] used several complexes of the type of $[N_4Co(OH)(OH_2)]^{2+}$ in the hydrolysis of a number of phosphate esters. In their results, the hydrolysis of cyclic-AMP is 10^8 times faster in the presence of the $[(trien)Co(OH)(OH_2)]^{2+}$ complex than without the complex at pH 7 and 50°C. They proposed a similar mechanism as postulated in **Scheme 1.12.** The effect of the ligands, N_4, was also investigated by using the cyclen, tren, and trpn that form *cis* complexes.[59] Those ligands hydrolyzed BNNP, bis(4-nitrophenyl)phosphate with apparent second-order rate constant which parallel their rates of the phosphate ion coordination.

Hendry and Sargeson synthesized Ir(III) bound phosphate esters, **14** and **15**, and studied their catalytic hydrolysis behavior caused by an intramolecular nucleophile attack of coordinated hydroxide ion over a pH range 5-7[57, 58] As

the pH increased from 5 for both complexes, the rate of release of nitrophenolate increased as the aqua group was deprotonated. The kinetic p*K*a values of the coordinated water for both complexes were around pH 7 as expected for dicationic Ir(III) complexes. The reaction rate reaches a plateau region above pH 8 and rate of production of NP is independent of pH. Above a pH of 11 the rate of release of NP increases again as the concentration of hydroxide ion increases.

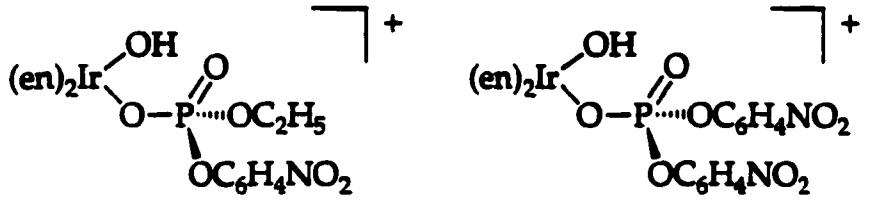

14 15

Figure 1.14. [(en)$_2$Ir(III)(OH)(substrates)] complexes.

^{31}P NMR spectra recorded while the reaction was in progress indicated that a single species was produced over the entire pH range unlike the reactions of Co(III) complexes. Since Ir(III) is extremely inert to ligand exchange, no *cis*-to-*trans* isomerization was observed. An ^{18}O tracer study was used to determine whether the ring opening of the chelate ester occurred with P-O or Ir-O bond cleavage, and proved that reaction predominantly occurred by P-O cleavage. They proposed a mechanism (**Scheme 1.13**) for this reaction in which the two open sites must be oriented *cis* to one other, the corresponding substrate binds to the metal ion, and the substrate is attacked by a metal-coordinated hydroxide. This mechanism was supported by further mechanistic work by Chin et al.[57, 58,

[59] with LCo(III) complexes. This has become a paradigm for metal-ion promoted phosphodiester hydrolysis.

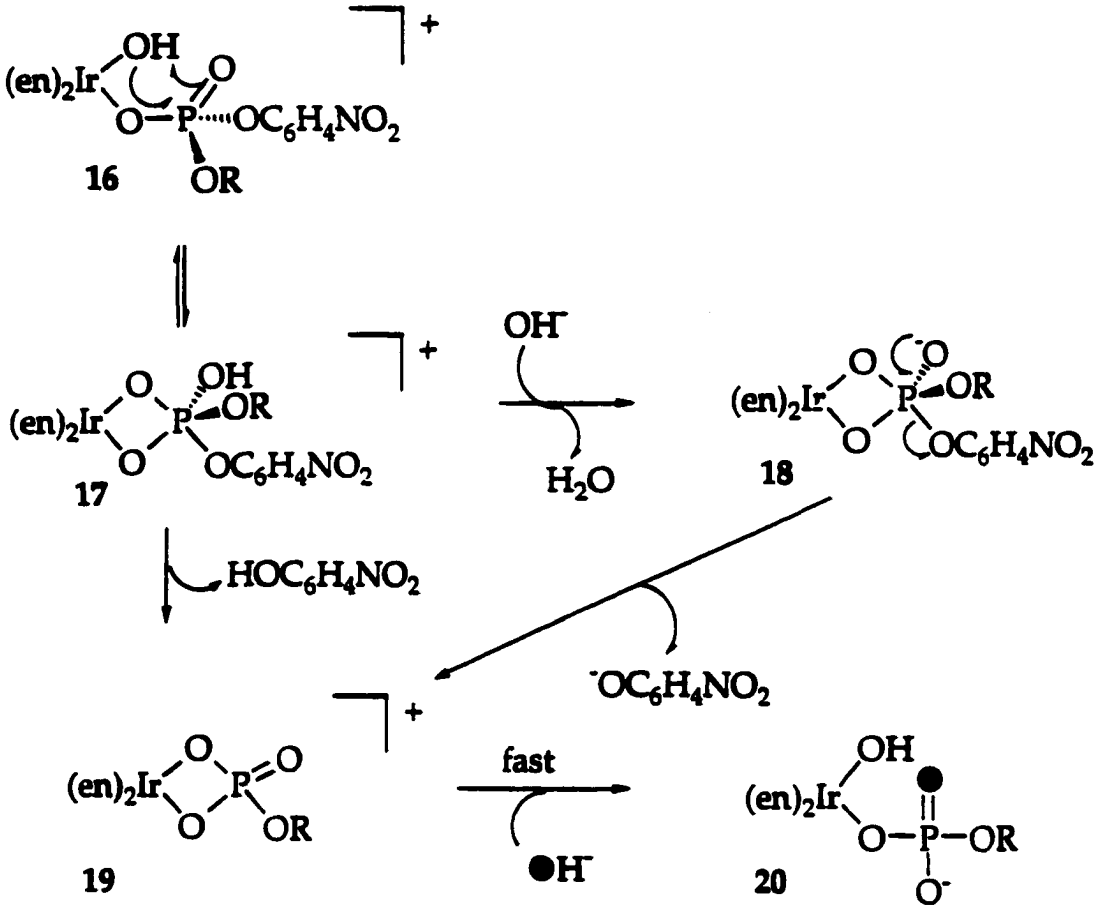

Scheme 1.13. Proposed mechanism for the Ir(III)-promoted hydrolysis of phosphodiester.[57]

A facile transfer of a phosphoryl group from an oxygen to nitrogen is one of the important biological pathways and was demonstrated in the hydrolysis of phosphate, 4-nitrophenylphosphate and 2,4-dinitrophenylphosphate, coordinated to the pentaamminecobalt(III) complex.[60, 61] The reactions (**Scheme 1.14**) proceed via two competing pathways, the $S_N1(cb)$, conjugate base dissociative mechanism, resulting in the liberation of substrate, and the other

involving the attack of coordinated amido ion (NH_2^-) at the P center. Rapid reaction rates and ester hydrolysis were achieved by the deprotonation of an ammonia *cis* to the ester. After attack of the coordinated amido ion at the P center, the aminophosphorane decays to the chelate phosphoamidate monoester that contains a very strained chelating ring including the phosphorus atom and an exocyclic ester group. The presence of the elusive chelate phosphoamidate **23** as an intermediate was observed by using an even more reactive analogue, $[(NH_3)_5Co(DNPP)]^+$.

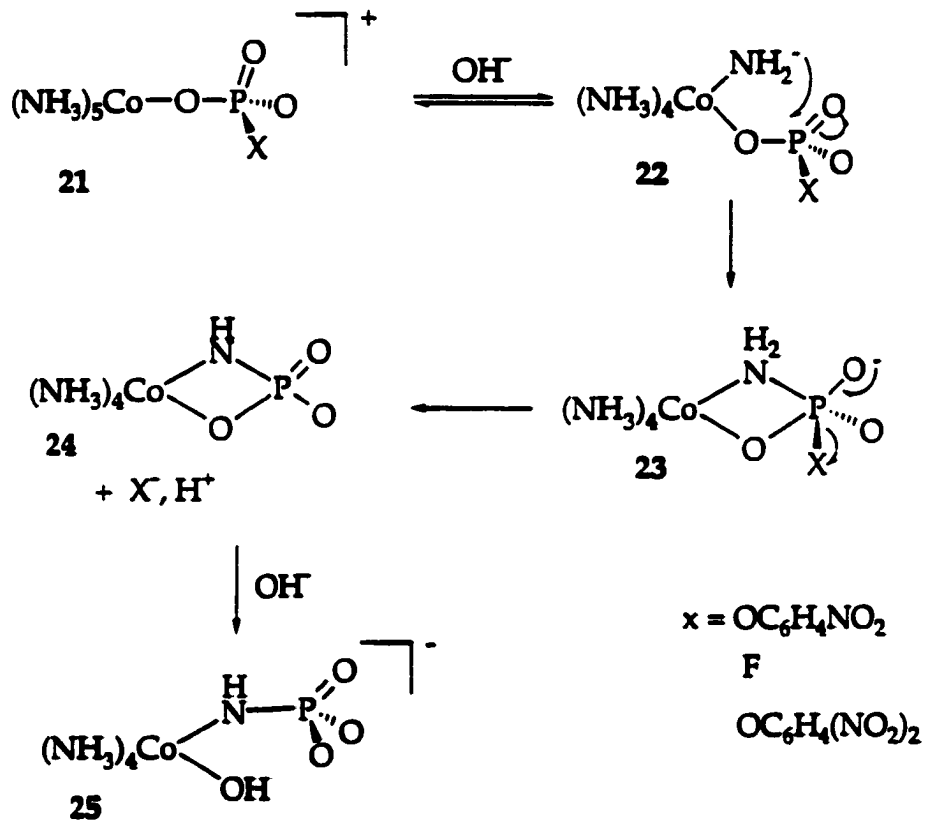

Scheme 1.14. Proposed mechanism of hydrolysis of Co(III)-bound phosphate esters.

Similarly, the reactivity of two pentaammine Ir(III) phosphodiester complexes was investigated and found to be 10^3-fold slower than the reaction of the analogous Co(III) complex.[62] The major product of the reaction is obviously produced by the attack of a *cis* coordinated amido ion on the P center of the phosphate ester.

Chin et al. found that in order to efficiently hydrolyze esters, amides, nitriles, and phosphates *cis*-diaqua Co(III) complexes should easily form four-membered ring complexes with carboxylates.[63] They used $[(tren)Co(OH_2)_2]^{3+}$ (tren = tris(2-aminoethyl)amine), $[(cyclen)Co(OH_2)_2]^{3+}$ (cyclen = 1,4,7,10-teraazacyclododecane), and $[(trpn)Co(OH_2)_2]^{3+}$ (trpn = tris(3-aminopropyl)amine) to investigate steric, electronic, and solvent effects in the chelation reaction.

B.2.3. Synthetic Hydrolases with More Than One Metal Ion

While there have been a considerable number of structural models to mimic multinuclear synthetic hydrolases, until now there have only been a few functional models. The phosphate hydrolysis with bis(Co^{III}-cyclen) complexes (cyclen = 1,4,7,10-tetraazacyclododecane) **26** and **27** has been studied by Czarnik et al.[64, 65]

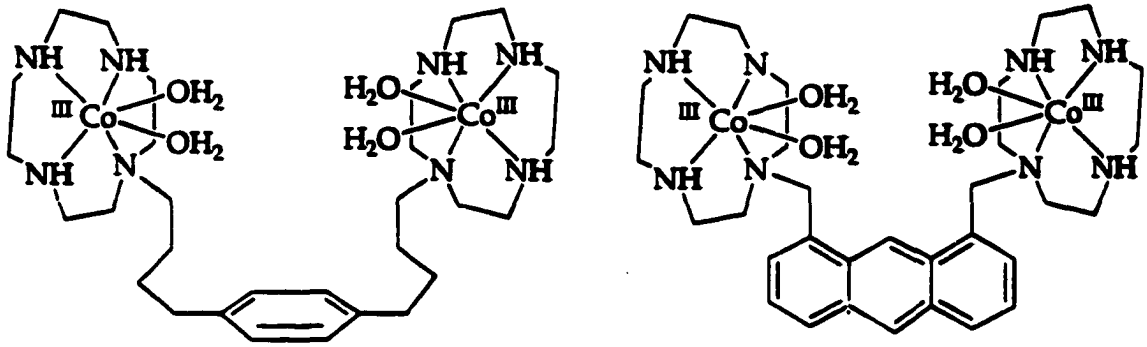

26 27

Figure 1.15. Bis(Co^{III}-cyclen) complexes.

The reactivity of the flexible binuclear Co(III) complex **26** (1 mM) in hydrolysis of bis(4-nitrophenyl)phosphate ion (BNPP) (0.05 mM) at pH 7 and 25°C was 3.2 times faster than with the parent Co(III)-cyclen complex. In order to accommodate inorganic phosphate in the internuclear pocket and to prevent formation of an intramolecular μ–oxo dinuclear complex the more rigid complex **27** was designed. The dinuclear complex **27** (1 mM) hydrolyzed 4-nitrophenyl phosphate dianion (NPP) (0.025 mM) at pH 7 and 25°C ten times faster than the Co(III)-cyclen (2 mM) complex. In this reaction, one Co(III) ion probably provide a nucleophilic water molecule, while the second Co(II) binds the phosphoryl group forming a four-membered ring (**Scheme 1.15**).

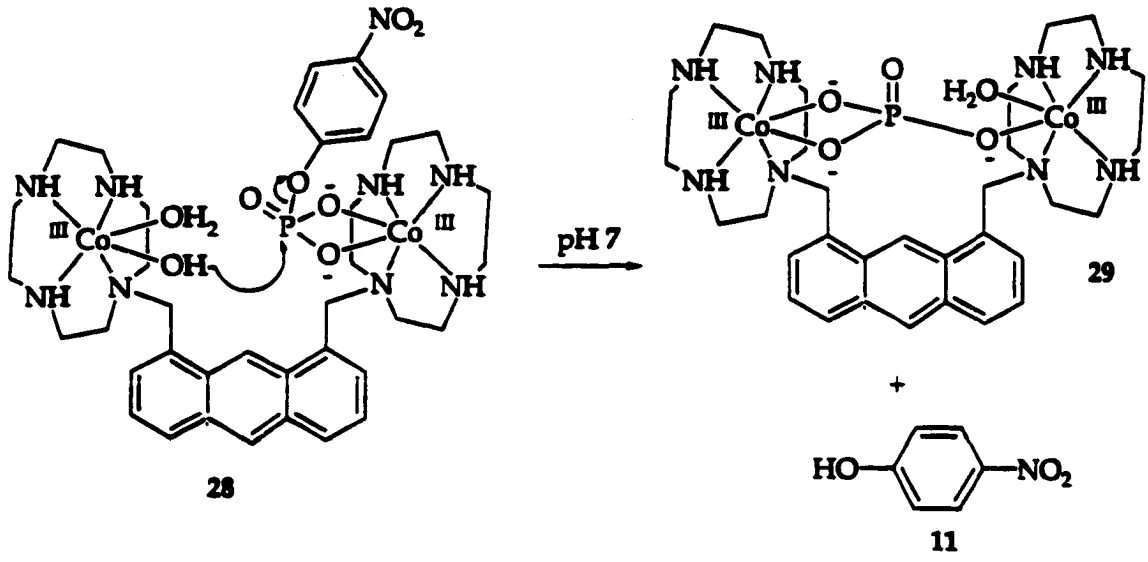

Scheme 1.15. Proposed mechanism of hydrolysis of NPP by bis(Co(III)-cyclen) complex.

Wall et al. have demonstrated double Lewis-acid activation on the intramolecular transesterification of 2-hydroxypropyl-4-nitrophenyl phosphate (HPNP) using binuclear copper(II) complex **30**, in which each Cu^{2+} is suggested to ligate to both oxygen atoms of the phosphate group.[66] The alcohol group of the substrate attacks the Cu(II)-activated P center intramolecularly as a nucleophile for a ring closure reaction like the first step of the hydrolysis of RNA. The rate of hydrolysis by binuclear Cu(II) was compared to an analogous mononuclear complex **31** and was ca. 50 times faster at 25°C and pH 7 implying that the two metal ions probably cooperate in the hydrolysis reaction.[67]

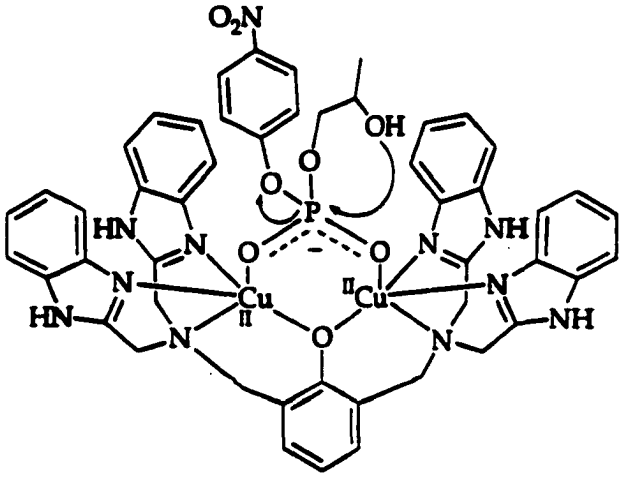

30

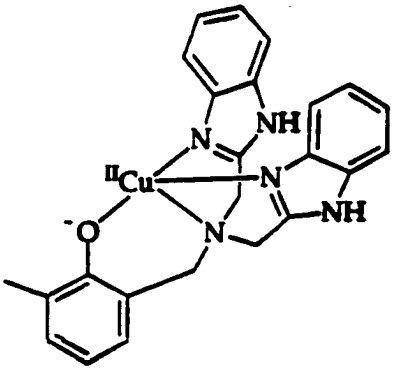

31

Scheme 1.16. Binuclear Cu(II) complex (a) and mononuclear Cu(II) complex (b).

Remarkable rate enhancement (*ca.* 10^{13}) in phosphonate ester hydrolysis catalyzed by two La(III) ions was reported by Tsubouchi and Bruice.[58, 67] They synthesized (8-hydroxy-2-quinoyl)methyl ((8-hydroxy-2-quinoyl)methylphosphonate as a model to hold two metal ions and examine complexation with La^{3+}, Al^{3+}, Zn^{2+}, Ni^{2+}, Co^{2+}, and Cu^{2+} and hydrolytic activity of their metal complexes. The phosphonate ester forms a hydrolytically active 1:2 complex with La^{3+} (**Scheme 1.17**) but inert 1:1 complexes with Al^{3+}, Zn^{2+}, Ni^{2+}, Co^{2+}, and Cu^{2+}. The hydrolytically active 1:2 complex of La(III) shows double metal ion cooperatively: (i) facile formation of metal ligated hydroxide (p*Ka* = 7.2 at 30°C) as an intramolecular nucleophile; (ii) stabilization of the transition state of the hydrolysis by neutralization of the phosphonate negative charge; (iii) interaction with the incipient oxyanion of the leaving alcohol. The first-order rate constant for the phosphonate hydrolysis of binuclear La(III) complex **29** was determined as 1.36×10^{-3} sec^{-1} at 30°C.

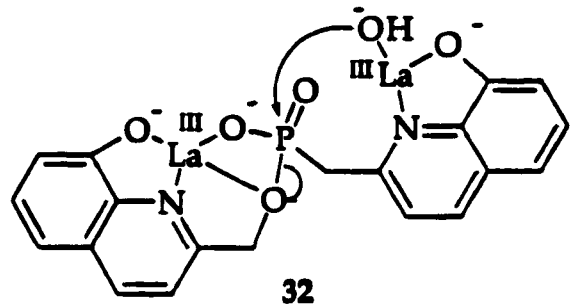

32

Scheme 1.17. Proposed mechanism of phosphonate hydrolysis by the binuclear La(III) complex.

Zinc complexes of monomer and dimers derived from 1,4,7-triazacyclododecane with phenyl **33** and 4,4'-biphenyl linkers **34** were synthesized by Chapman and Breslow.[68] Their catalytic activities in the hydrolysis of 4-nitrophenyl phosphate dianion (NPP) and bis(4-nitrophenyl)phosphate ion (BNPP) in 20% (v/v) DMSO at 55°C were examined. The distance between the metal binding sites determines the catalytic activity. The binuclear Zn(II) complex **33** with shorter 1,3-phenyl and 1,4-phenyl spacer is better for the hydrolysis of monoester (NPP), whereas the longer biphenyl spacer **34** favors the hydrolysis of diester (DNPP). Double binding of a single phosphate group by the two metal ions is only favored by the phenyl spacers and is essentially impossible with the biphenyl spacer.

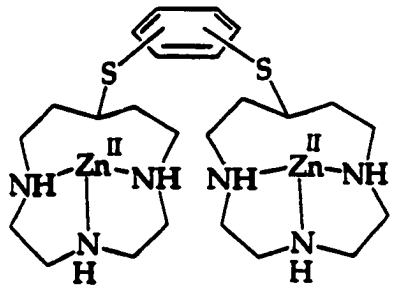

33

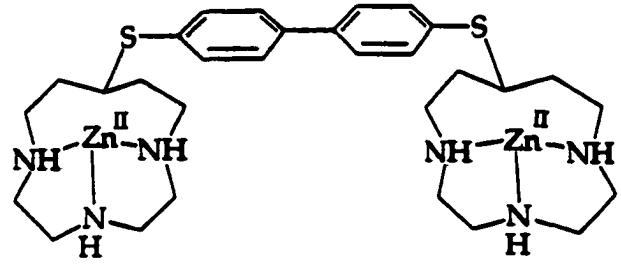

34

Figure 1.16. Zinc complexes of monomer and dimers derived from 1,4,7-triazacyclo dodecane with phenyl (a) and 4,4'-biphenyl linkers (b).

In the NPP hydrolysis by 1,3-phenyl-spaced dimer **33**, a bell-shaped pH versus rate profile, with a maximum rate at pH 7.8, was obtained. Since the phosphomonoester NPP prefers the two zinc(II) ions to be in close proximity, two alternative mechanisms **35** and **36** were proposed for hydrolysis. The catalytic activity of (a) decreases with increasing pH and was lost at pH > 12 accounting for the formation of a double OH^--bridged zinc(II) species.

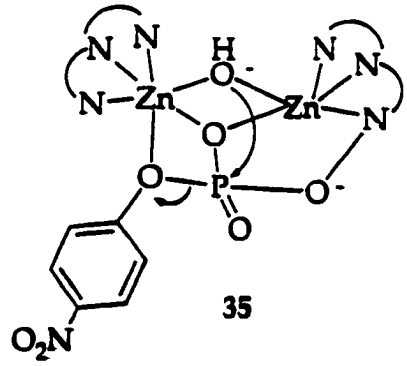

35

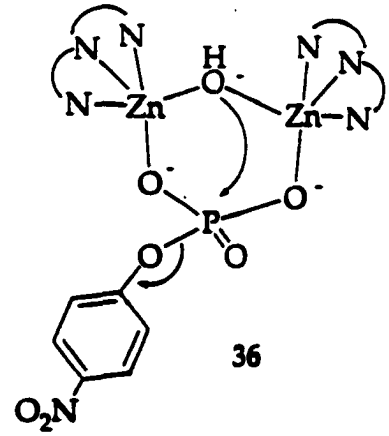

36

Scheme 1.18. Two alternative mechanisms for the hydrolysis of 4-nitrophenyl phosphate catalyzed by the binuclear Zn(II) complex of 1,4,7-triazacyclodododecane with phenyl spacer.

For BNPP hydrolysis, a greater Zn-Zn separation was preferred. In the proposed mechanism, one zinc(II) binds to the phosphate and act as a Lewis acid, while the other delivers a nucleophilic bound OH^-. They also obtained a bell-shaped pH versus rate profile, with the ascending leg corresponding to a p*K*a of 8 and the descending leg to a p*K*a of 12. The lower one was assumed to be a deprotonation of a water molecule on the zinc(II) that does not bind to the phosphate group, whose p*K*a is essentially the same as that for the catalyst with out bound substrate. The second one was considered to be the binding of a OH^- to the second Zn(II), that carries the bound phosphate leading to loss of catalytic activity by displacing substrate or diminishing the Lewis acidity of that zinc. As a result, a similar mechanism to that for bis(Co(III)-cyclen) complex and binuclear La(III) complex was proposed (**Scheme 1.19**).

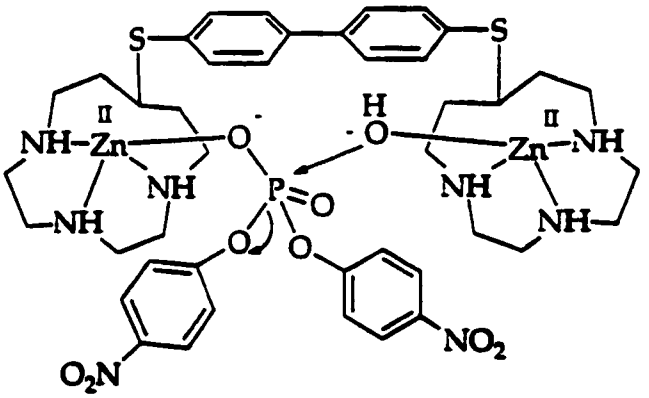

Scheme 1.19. Proposed mechanism for the hydrolysis of the BNPP by the binuclear zinc(II) complex with 1,4,7-triazacyclododecane with 4,4′-biphenyl linkers (b).

Koike et al.[69] synthesized a propanol-bridged octaazacryptand (26-hydroxy-1,4,7,10,13,16,19,22-octaazabicyclo[11.11.3]heptacosane **37** (HL) which

forms a novel binuclear zinc(II) complex of an alkoxide-bridged octaazacryptate Zn_2L **38** (L = alkoxide form of HL) at pH > 4.

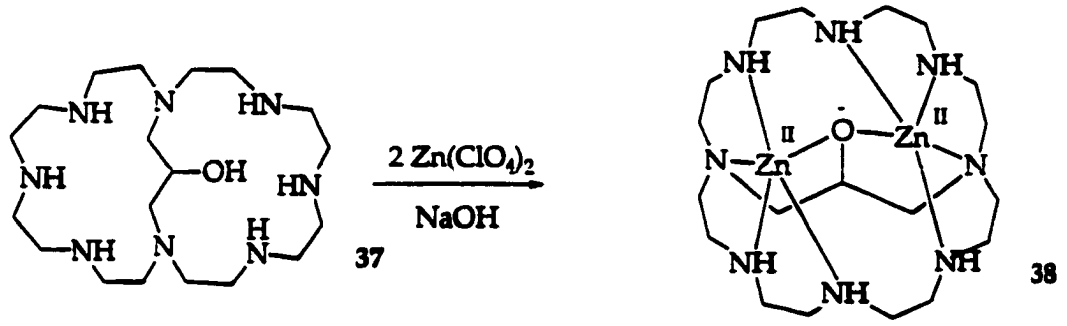

Scheme 1.20. (a) New cryptand (b) binuclear zinc(II) cryptate.

The structure of **38** was analyzed by X-ray and shows that each zinc(II) ion is in a distorted trigonal-bipyramidal environment involving two NH's and an alkoxide O^- anion in the equatorial positions and tertiary amine and a NH stand in apical positions. Although the two zinc(II) ions in **38** appeared to be coordinately saturated and hence were assumed unreactive, they were shown to work together to selectively recognize a phosphomonoester, 4-nitrophenyl phosphate dianion (NPP), and promote the cleavage of its P-O ester bond by the nucleophilic attack of one of the apically coordinated NH's at pH 4.9-9.5 in aqueous solution (**Scheme 1.21**). The reaction product was isolated as a phosphonamide derivative (Zn_2L-PO_3H) **41** from aqueous solution at pH 3 and characterized by X-ray crystal analysis. A proposed mechanism for phosphate P-O bond cleavage is that as a substrate NPP approaches in order to bridge both zinc(II) ions, the apical NH's dissociate and one of them attacks the incoming P center to perform a phosphoryl-transfer reaction (i.e. a phosphoryl group

migrates from 4-nitrophenyl to the amine), yielding 4-nitrophenol and **41**. The phosphoryl transfer by the binuclear zinc(II) cryptate stops after formation of an extremely stable **41**, hence the reaction is not a catalytic process. However, when the zinc(II) ions were removed with EDTA, ethylenediaminetetraacetic acid, at pH 7 in aqueous solution at ca. 50°C, the P-N bond was hydrolyzed to yield the starting material **37** and an inorganic phosphate.

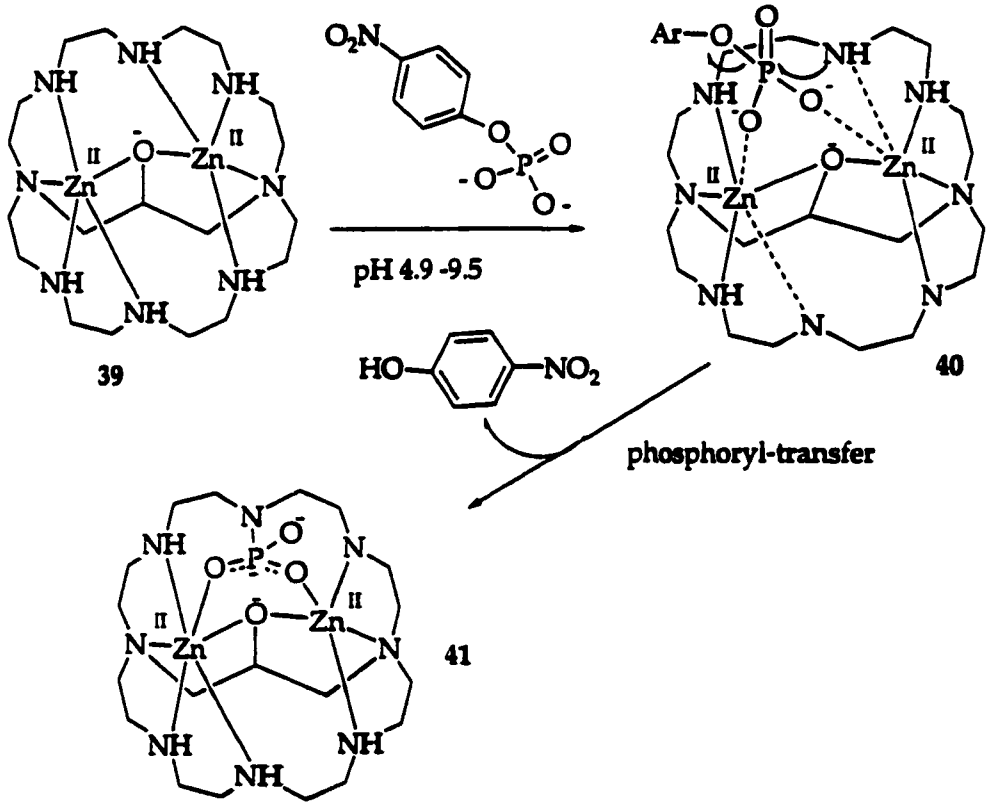

39 40 41

Scheme 1.21. Proposed mechanism for hydrolysis of NPP by binuclear zinc(II) cryptate.

The dinuclear Zn(II) complex $[Zn_2L(\mu\text{-}OH)](ClO_4)_2$ (L =α,α′-bis(bis(2-pyridylethyl)amino)-*m*-xylene **42** has been synthesized by Gultneh et al.[70] The p*Ka* of the zinc-bound water is 7.55, and rate of hydrolysis of bis(4-

nitrophenyl)phosphate catalyzed by the binuclear Zn(II) complex was shown to increase from pH 7 to 8. The detailed mechanism, however, was not proposed. Later, Gultneh et al.[71] also reported the hydrolysis of bis(4-nitrophenyl)phosphate (BNPP) by Zn(II) complexes of chelating pyridyl donor ligands, bis(2-pyridyl-2-ethyl)amine **43** (bpea), bis(2-pyridylmethyl)amine **44** (bpa), 2,2'-dipyridylamine **45** (dipyam), and 2,2'-dipyridyl **46** (bipy). The p*Ka* values of zinc-bound water molecules in a binuclear Zn(II) complex $[Zn_2(bpea)_2(\mu\text{-}OH](ClO_4)_3$ and mononuclear Zn(II) complexes $[Zn(bpa)(H_2O)_2](ClO_4)_2$, $[Zn(dipyam)_2](BF_4)_2$, and $[Zn(dipy)_2(H_2O)](BF_4)_2$ are 8.35, 9.85, 8.00 and 9.01 respectively. At pH values up to 9.5 the rate of hydrolysis of BNPP increases by a factor from 100 to 200 times the non-catalyzed rate in the presence of those Zn(II) complexes. The metal-bound hydroxide was proposed as the reactive nucleophile, which is consistent with the widely accepted mechanism for many hydrolytic reactions catalyzed by metal complexes.

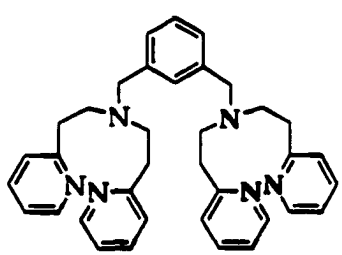

42

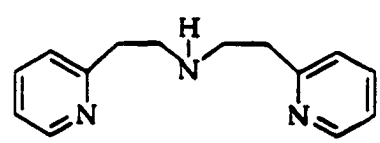

43

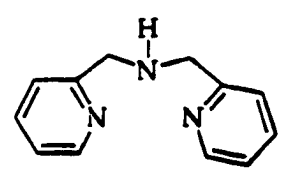

44

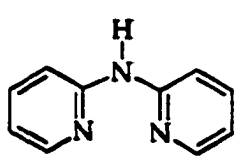

45

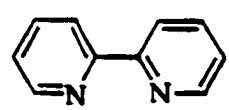

46

Figure 1.17. **42** = α,α'-bis(bis(2-pyridylethyl)amino)-*m*-xylene (*m*-xybpea); **43** = bis(2-pyridyl-2-ethyl)amine (bpea); **44** = bis(2-pyridylmethyl)amine (bpa); **45** = 2,2'-dipyridylamine (dipyam); and **46** = 2,2'-dipyridyl (dipy).

Bazzicalupi et al. measured the hydrolysis rates of bis (4-nitrophenyl) phosphate promoted by mononuclear Zn(II) and binuclear Zn(II) complex.[72] The dinuclear monohydroxo $[Zn_2L_1OH]^{3+}$ and dihydroxo $[Zn_2L_1(OH)_2]^{2+}$ (L_1 = [30]aneN_6O_4, **47**) complexes were formed in aqueous solution from neutral and alkaline pH. The hydrolysis rate of BNPP was enhanced 10-fold by the binuclear $[Zn_2L_1(OH)]^{2+}$ complex with respect to the mononuclear $[L_2\text{-Zn-OH}]^{+}$ (L_2 = [15]aneN_3O_2, **48**) complex indicating a cooperative role of the two metals in the hydrolytic mechanism. In the proposed mechanism (**Scheme 1.22**), a bridging of the two Zn(II) ions by the substrate was proposed and supported by the crystal structure of $[Zn_2L_1(\mu\text{-}PP_2)_2(MeOH)_2](ClO_4)_2$ (PP = diphenyl phosphate).

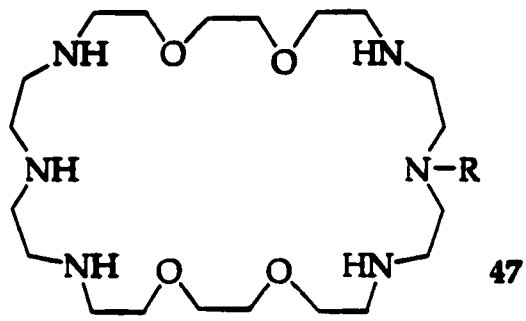

47

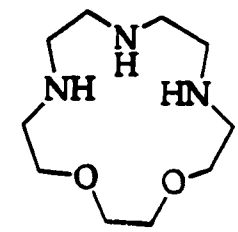

48

L_1: R = H

ap-L_1: R = CH_2CH_2OH

Figure 1.18. (a) [30]aneN_6O_4; (b) [15]aneN_3O_2.

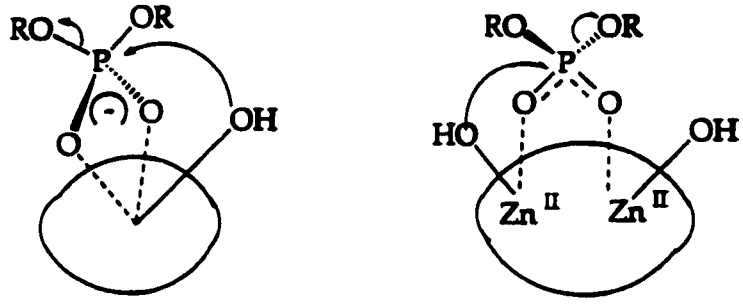

(a) (b)

Scheme 1.22. Proposed mechanism for hydrolysis of BNPP by $[L_2\text{-Zn-OH}]^+$ (a), and by $[Zn_2L_1(OH)_2]^{2+}$ (b).[72]

Bazzicalupi et al.[73] also reported an alcohol-pendented-L_1 (**ap-L_1**) and hydrolysis of BNPP promoted by the dinuclear Zn(II) complex (Zn_2(**ap-L_1-H)OH**$]^{2+}$ which contains both a Zn(II)-bound alkoxide and a Zn(II)-OH nucleophile function.

B.2.4. Synthetic Hydrolases with Labile Metal Ions

Since substitution lability is an essential requirement for efficient catalysis, first-row divalent metal ions are commonly chosen as cofactors for natural enzymes used to promote hydrolysis. Among of the first-row divalent metal ions, Cu(II) and Zn(II) are the metal ions that are not only substitutionally labile but also strong Lewis acids. Because of the strong Lewis acidity of these metal ions, they can activate phosphodiester bonds toward nucleophilic attack through charge neutralization and polarization of the bonds and also can lower the p*K*a of a coordinated water providing metal-bound hydroxide as a nucleophile at near-natural pH.[23] Because of well-studied coordination chemistry of Cu(II) and

Zn(II) and spectroscopically richness of Cu(II) complexes, recently Cu(II) and Zn(II) complexes have been studied extensively to provide information for the detailed reaction mechanism and the exact role of metal ions in the hydrolysis. Lanthanide metal complexes have also attracted attention as synthetic hydrolases due to their high Lewis acidity and substitution liability. In this section, synthetic hydrolases with substitution labile metal ions, especially Cu(II) and Zn(II), will be discussed.

Sigel et al. have investigated the hydrolysis of a variety of nucleoside 5'-triphosphates and the effects of divalent metal ions. In the hydrolysis of ε-ATP, N^6-ethenoadenosine 5'-triphosphates, they observed that the most active species is a 2:1 complex, metal ion: ε-ATP, and the effect of metal bound OH^- ion on the hydrolysis. The change in rate for dephosphorlyation of nucleotide triphosphates for different metal ions was also investigated. The order, Cu^{2+}> Cd^{2+}> Zn^{2+}> Ni^{2+}> Mn^{2+}> Mg^{2+}, was parallel to the ease of formation of hydroxo complexes of corresponding metal ions. This suggests that a metal bound hydroxide ion is involved in the reaction through an intramolecular attack.[74]

Breslow et al.[75] studied hydrolysis of diphenyl-4-nitro-phenylphosphate **49** (DPNPP) induced by the Zn^{2+} complex of tetraaza macrocycle **50**. The formation of a catalytically active species was achieved by the removal of a relatively acidic proton, which in turn implicates LZn-OH (L = ligand), mono-hydroxo metal complex, as the active species.

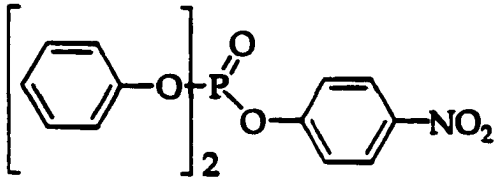

49

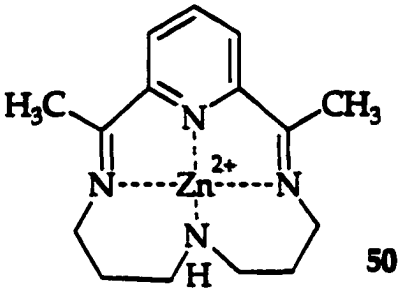

50

Figure 1.19. (a) DPNPP; (b) Tetraaza macrocycle Zn(II) complex.

Norman reported the synthesis of a zinc(II) complex of the cyclen 1,4,7,10-tetra-azacyclododecane **51** and its catalytic activity in the hydrolysis of ethyl(2,4-dinitrophenyl)-methylphosphonate **52** (DNPEMP) and diethyl(2,4-dinitrophenyl) phosphate **53** (DNPDEP).[76] Substantially enhanced rates of release of 2,4-dinitrophenoxide from both esters were observed for hydrolysis promoted by **51**. The catalytic effect of **51** increased markedly as the pH of the reaction approached and passed the p*Ka* (7.9) of the coordinated water molecule of the complex providing a higher concentration of the metal-bound hydroxide as a nucleophilic reagent.

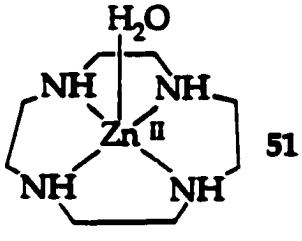

51

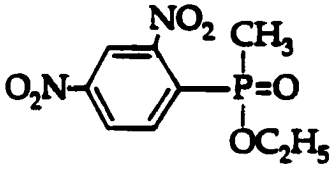

52

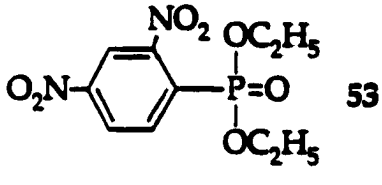

53

Figure 1.20. (a) Zinc(II) cyclen complex with coordinated water molecule; (b) DNPEMP; (c) DNPDEP.

In 1989, Zn(II) and Cu(II) complexes of *N,N,N',N''*-tetrakis(1-methylimidazol-2-ylmethyl)pentane-1,5-diamine **54** and (bis(1-methylimidazol-2-ylmethyl)ethylamine **55** were prepared and their catalytic activity in the hydrolysis of tris-4-nitrophenyl phosphate in 33% ethanol-water were reported.[77] The deprotonation of a metal-bound water molecule was observed in all the binuclear ($L_1M_2^{2+}$) and mononuclear (L_2M^{2+}) complexes. They observed order of activity, $L_2Cu^{2+} > L_2Zn^{2+} > L_1Cu_2^{2+} > L_1Zn_2^{2+}$, which is a result of the nucleophilicity of the metal-bound hydroxide ion decreasing as the p*K*a decreases. The formation of stabilized hydroxide ion **56** via bridging binuclear metal ions in the $L_1Cu_2^{2+}$ and $L_1Zn_2^{2+}$ complexes was suggested to explain the loss in activity of those complexes.

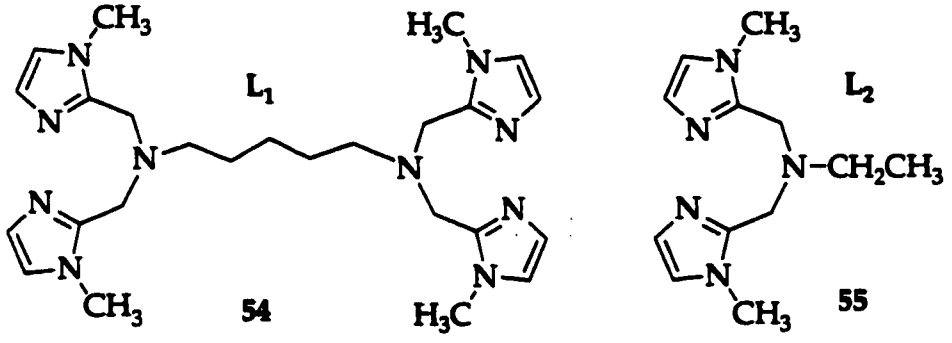

Figure 1.21. (a) *N,N,N',N''*-tetrakis(1-methylimidazol-2-ylmethyl)pentane-1,5-diamine; (b) (bis(1-methylimidazol-2-ylmethyl)ethylamine.

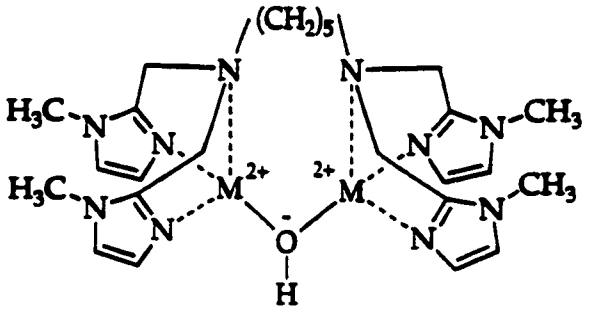

56

Figure 1.22. Proposed binuclear $L_1M_2^{2+}$ complex.

A zinc(II) complex with a tridentate ligand, 1,5,9-triazacyclododecane [12]aneN$_3$ **57**, and a tetradentate ligand, 1,4,7,10-tetra-azacyclododecane [12]aneN$_4$ **51**, were synthesized and their catalytic activity in the hydrolysis of tris(4-nitrophenyl) phosphate (TNPP) and bis(4-nitrophenyl)phosphate anion (BNPP) were compared by Koike et al.[78] Kinetic studies showed that the reactive species were commonly L-Zn(II)-OH$^-$. For both the neutral phosphotriester TNPP and the anionic phosphodiester BNPP, a catalytic activity of the Zn(II)[12]aneN$_3^{2+}$ complex were greater than Zn(II)[12]aneN$_4^{2+}$. This observation correlates with the lower p*K*a (7.3) for the coordinated water in of Zn(II)[12]aneN$_3^{2+}$ than that of Zn(II)[12]aneN$_4^{2+}$ and greater Lewis acidity of the zinc(II) with fewer nitrogen donors. They also proposed an intramolecular attack of the metal-bound hydroxide on the coordinated substrate as a proposed mechanism for hydrolysis by Zn(II)[12]aneN$_3^{2+}$ (**Fig. 1.23**).

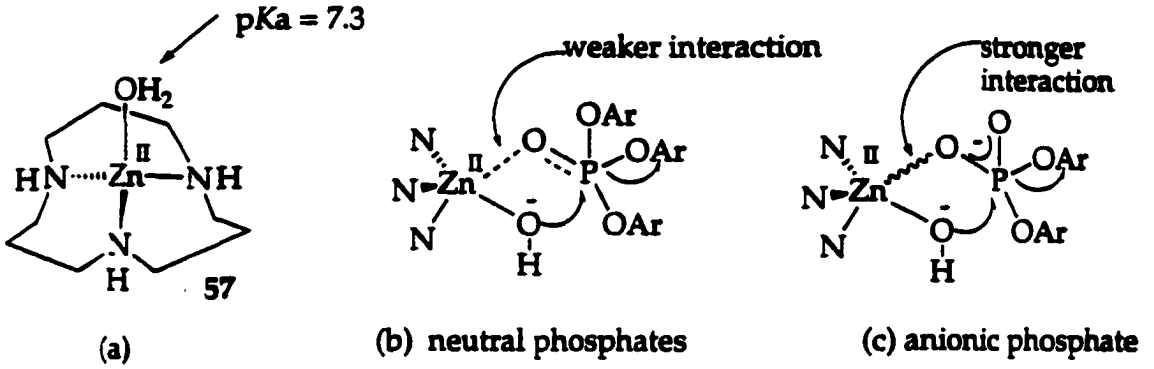

Figure 1.23. (a) $[Zn(II)[12]aneN_3]^{2+}$ complex; (b) proposed mechanism for the hydrolysis of neutral phosphotriester TNPP by $[Zn(II)[12]aneN_3]^{2+}$; (c) proposed mechanism for the hydrolysis of the anionic phosphodiester BNPP by $[Zn(II)[12]aneN_3]^{2+}$.

Kimura et al.[79] synthesized a new macrocycle tetraamine (cyclen) (**Scheme 1.23**) with a strategically appended benzyl alcohol group, (s)-1-(2-hydroxy-2-phenylethyl)-1,4,7,10-tetraazacyclododecane **58**. The complexation of **58** with Zn(II) yielded a 1:1 five-coordinated complex, either a protonated ZnL complex **59** at acidic condition (pH 6) or a deprotonated ZnL complex **60** at basic condition (pH 9.5). The X-ray crystal structure of the deprotonated ZnL complex showed that the alkoxide is closely coordinated to Zn(II) at the fifth coordination site. The zinc(II)-bound alkoxide anion in the deprotonated ZnL complex was proven to be a more reactive nucleophile than a reference *N*-methylcyclen-Zn(II)-OH^- species. The product of the nucleophilic attack by a metal-bound alkoxide is the alcohol-phosphorylated species **62**, which was isolated as a crystalline with ClO_4 salts. The kinetic study of the hydrolysis of bis(4-nitrophenyl)phosphate with the deprotonated ZnL complex in aqueous solution (pH 6.0-10.3) at 35°C with $I = 0.10$ gave a sigmoidal curve with an inflection point at pH 7.3 which is consistent with the p*K*a value of the protonated ZnL complex.

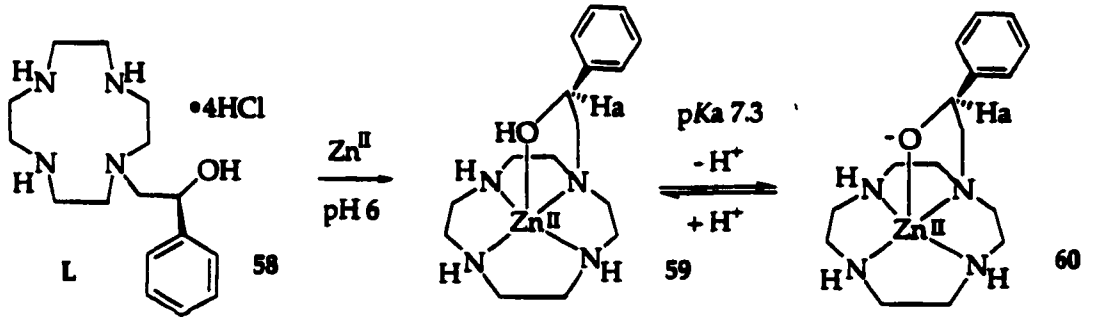

Scheme 1.23. (a) 1-(2-hydroxyethyl)-1,4,7,10-tetraazacyclododecane; (b) undissociated ZnL complex; (c) dissociated ZnL complex.

The potentiometric pH titration of the alcohol-phosphorylated **62** with NaOH shows the mono-deprotonation, with a p*Ka* value of 9.1, giving the pendent phosphodiester **64** which undergoes spontaneous hydrolysis in alkaline buffer to yield a phosphomonoester pendent zinc(II) complex **65**.. The proposed mechanism is postulate in **Scheme 1.24.**

Kady et al. reported the hydrolysis of another phosphate ester by a Zn(II)-activated alcohol.[80] They synthesized alcohol-bearing polyamine **66** and studied the catalytic activity of Zn(II) complex, L_1-Zn(II) **68** (**Scheme 1.25**). The hydrolysis of phosphate esters was compared to that of L_2-Zn(II) which lacks an alcohol pendent to elucidate possible participation of neighboring alcohol groups **67**. They found that L_1-Zn(II) was more than 10^4 fold more effective in promoting the release of 4-nitrophenol from diethyl(4-nitrophenyl)phosphate than the L_2-Zn(II) complex.

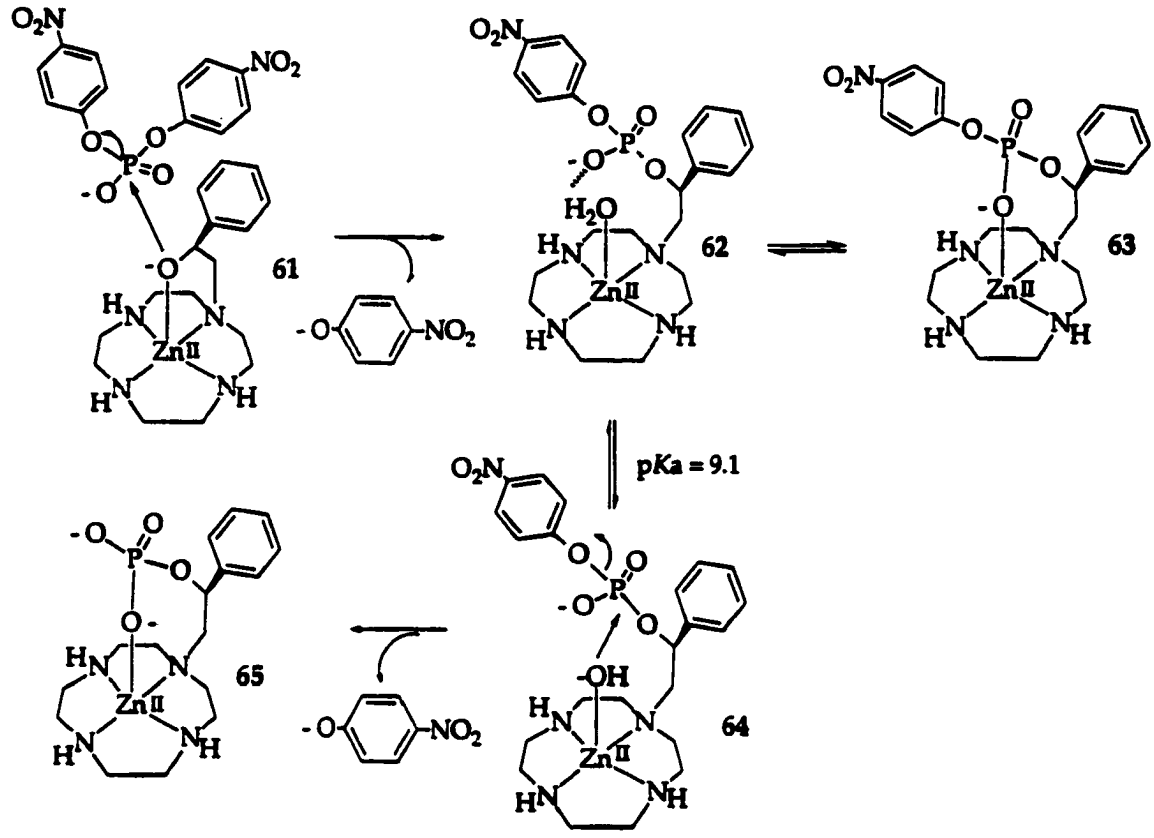

Scheme 1.24. Reaction mechanism for P-O ester bond cleavage of bis(4-nitrophenyl) phosphate by alkoxide-pendent cyclen zinc(II) complex.

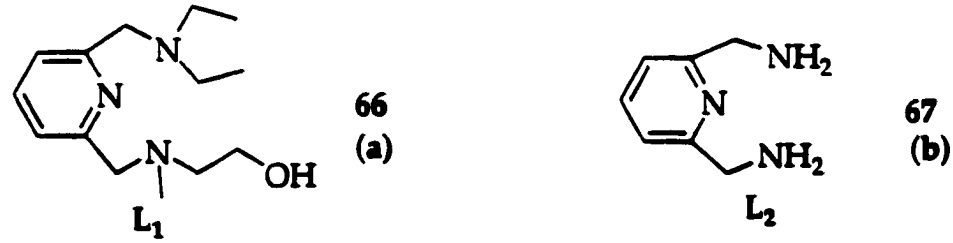

Figure 1.24. (a) Polyamine ligand with an alcohol pendent group; (b) polyamine ligand without an alcohol pendent group.

The alcoholic OH was deprotonated with p*Ka* of 8.6 yielding alkoxide-bound Zn(II) complex 69. The reaction of alkoxide bound with a diethyl(4-nitrophenyl) phosphate in TAPS buffer (pH 8.6) at 25°C promoted a phosphoryl transfer reaction to phosphotriester 71. The mechanism of the subsequent

hydrolysis step 71 -> 69 was not clarified. The pH dependence of the first-order rate constant gave a sigmoidal curve with an inflection point around the p*K*a value of 8.6.

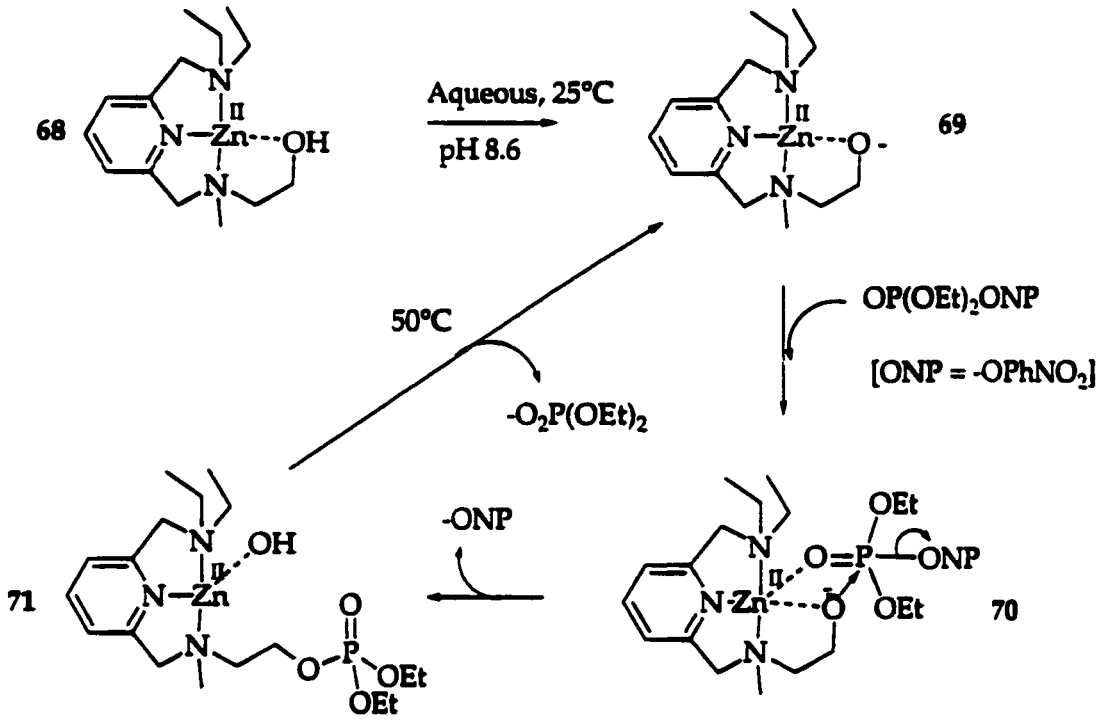

Scheme 1.25. Propose mechanism for the hydrolysis of a diethyl(4-nitrophenyl) phosphate by the alcohol-bearing polyamine.

The hydrolysis of bis(4-nitrophenyl)phosphate (BNPP) and ethyl-4-nitrophenylphosphate (ENPP) by $[Cu(bipy)]^{2+}$ (bipy = 2,2'-bipyridine, **46**), in aqueous solution at 75°C in the pH range 5.8-8.3, was studied by Morrow and Trogler in 1988.[81] The rate increased dramatically with pH indicates the participation of a Cu(II)-bound hydroxide in the hydrolysis mechanism. The hydrolysis mechanism (**Scheme 1.26**) was proposed to proceed via coordination of the diester to the $[Cu(bipy)]^{2+}$ complex followed by the nucleophilic attack of a cis coordinated OH^- ion at the P center. Observing a single ^{18}O label in the

product ethylphosphate supports this mechanism when the reaction is conducted in ^{18}O labeled water.

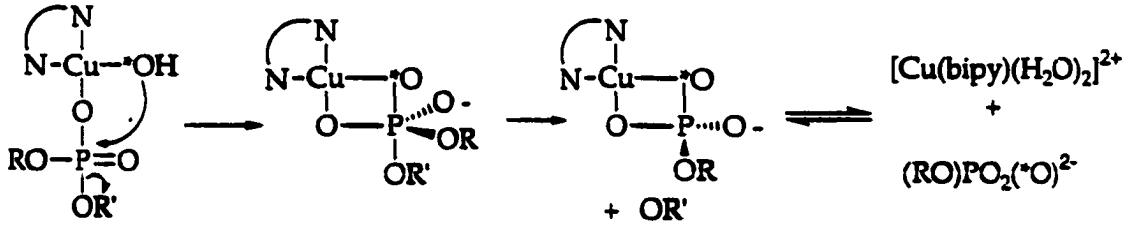

Scheme 1.26. Proposed mechanism for the hydrolysis of phosphate diester by $[Cu(bipy)]^{2+}$.[81]

Fife et al.[82] investigated the hydrolysis of 2-(1,10-phenanthrolyl)phosphate by a variety of the first-row transition metal ions Cu(II), Ni(II), Co(II), and Zn(II). A larger effect by Cu(II) on the rate of its hydrolysis was reported. The reaction mechanism was proposed to proceed via attack of a water on the Cu(II) complex or attack of a hydroxide ion on the protonated form of the Cu complex. Second mechanism is unlikely since the OH^- ion coordinated to Cu(II) is sterically restrained from attacking at the P center when it is formed at ~pH 7 (**Scheme 1.27**).

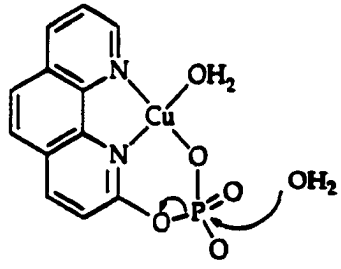

Scheme 1.27. Proposed mechanism of hydrolysis of 2-(1,10-phenanthrolyl) phosphate.

Chin et al.[83] compared the reactivities of three cis-diaqua Cu(II) complexes, $[Cu(dipyam)(OH_2)_2]^{2+}$ **71** (dipyam = 2,2′-dipyridylamine), $[Cu(bispicam)(OH_2)_2]^{2+}$ **72** (bispicam = *N,N′*-bis(2-pyridylmethyl)amine, and $[Cu(NH(CH_2C_7H_5N_2)_2(OH_2)_2]^{2+}$ **73** ($NH(CH_2C_7H_5N_2)$ = bis(2-benzimidazolyl-methyl)amine), for promoting the intramolecular transesterification of 2-hydroxypropyl-*p*-nitrophenylphosphate (HPNP, **74**). Release of the p-nitrophenolate ion cleaved from the barium(II) salt of HPNP was detected by monitoring the increase in the visible absorbance at 400 nm. The reported pKa values of the metal-bound water molecules in **71**, **72**, **73** are 7.2, 8.2, and 6.8 respectively. Compound **73** became more reactive with increasing concentrations unlike **71** and **72** that became less reactive. They proposed that **73** dimerizes to a highly reactive monohydroxide-bridging complex, while **71** and **72** dimerize to inactive dihydroxide bridging complexes. The rate of transesterification promoted by **73** increases with increasing pH up to 7 and then levels off indicating that the aqua-hydroxy form of **73** or its kinetic equivalent is the active species. They proposed a double Lewis-acid activation mechanism based on the binuclear **75** complex (**Scheme 1.28**).

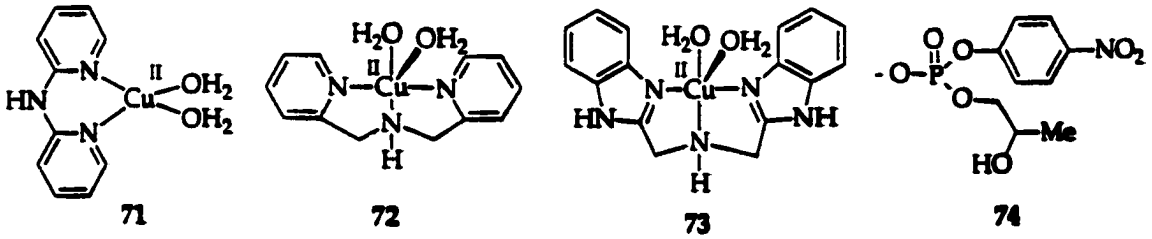

71 72 73 74

Figure 1.25. Three *cis*-diaqua Cu(II) complexes and HPNP **74**.

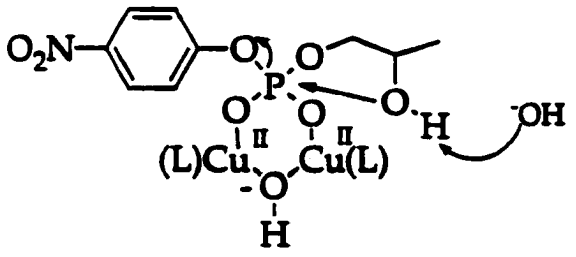

75

Scheme 1.28. Proposed hydrolysis of HPNP by **73**.

To mimic a metal-ammonium promoted phosphodiester hydrolysis, ammonium-functionalized ligand **76** [6,6′-($Me_2HNCH_2C \equiv C)_2$bipy]$^{2+}$ which has two NMe_2H^+ group linked to a metal binding 2,2′-bipyridine (bipy) was synthesized. The activity of Cu(II)-**76** complex in the hydrolysis of BNPP was compared with related Cu(II) complexes which do not contain such functional groups.[84] The hydrolytic activity of the Cu(II)-**76** system shows a maximum at pH 6.1 and greater efficiency compared to Cu(II)-**77**. The observed pH dependence of Cu(II)-**76** indicated the generation of a nucleophilic Cu(II)-OH species. It was suggested that the positively charged ammonium groups should make a Cu(II)-bound water molecule even more acidic. A double electrophilic activation of the phosphodiester by coordination to metal ion and hydrogen bonding to one of the ammonium groups were proposed as well as an intramolecular attack of Cu(II)-bound hydroxide ion to a coordinated phosphodiester (**Scheme 1.29**).

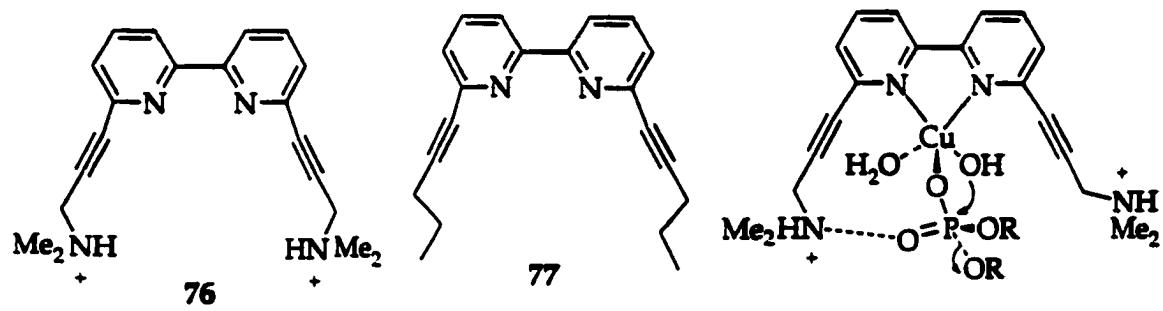

Scheme 1.29. Ammonium-functionalized ligand **76**, without ammonium-functionalized ligand **77**, and proposed hydrolysis promoted by Cu(II)-**76** .

Chin et al.[85] compared the reactivities and mechanism of Cu(II) complexes of (bis(pyridyl)amine **78** (**Scheme 1.30**), (*N*-(2-hydroxyethyl)bis(pyridylmethyl) amine) **79**, and (*N*-(3-hydroxypropyl)bis(pyridylmethyl)amine) **80** for cleaving bis(2,4-dinitrophenyl) phosphate (BDNPP). The Cu(II) complex **81** with the hydroxypropyl group was deprotonated at a pKa value of 8.8 to yield **82**, which cleaves BDNPP by transesterification to produce **83** at 25°C. On the other hand the analogous complexes with a hydroxyethyl pendent (Cu(II)-**79**) and without any pendent group (Cu(II)-**78**) cleave the diester predominantly by hydrolysis indicating that the reactive species is not Cu(II)-alkoxide, but Cu(II)-OH^-. An increase of two orders of magnitude in the activity of Cu(II)-**80** for cleaving BDNPP was reported compared to Cu(II)-**78** and Cu(II)-**79**. This copper model study shows that metal-alkoxide species may be more effective nucleophiles, compared to the zinc(II)-model complex **61**.

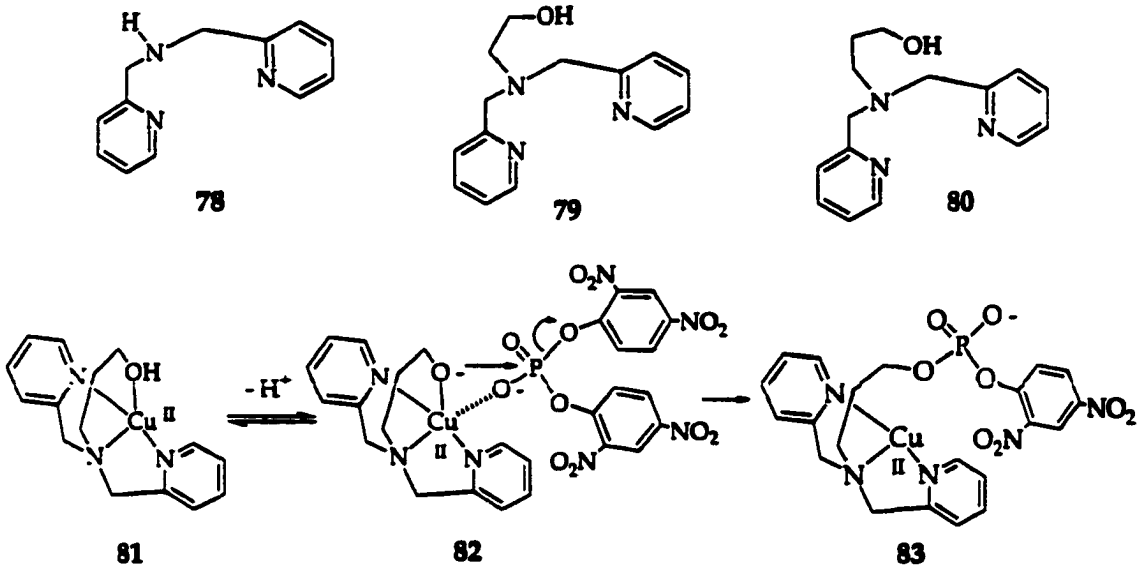

Scheme 1.30. Bis(pyridyl)amine **78**, *N*-(2-hydroxyethyl)bis(pyridylmethyl)amine **79**, and *N*-(3-hydroxypropyl)bis(pyridylmethyl)amine **80** and proposed mechanism for hydrolysis of the BDNPP by **81**.

The micellar rate effects on the catalytic hydrolysis of diphenyl-4-nitrophosphate (DPNPP, **49**) were investigated by using Cu(II) complexes with 2-(dimethylaminomethyl)-6-(alkylaminomethyl)pyridines of various lipophilicities (**84**, **85**, **86**).[86] The rate constants were compared to those of Cu(II) complexes with *N*-alkyl-*N*,*N*',*N*''-triethyl-1,2-diaminoethane (**87**, **88**, **89**). The formation of metallomicelles and rate enhancement in the hydrolysis by metallomicelles were reported when the alkyl group is a C_{12} (or longer) chain complexes, **85**, **86**, **88**, and **89**. The p*K*a values of Cu(II)-bound water are ca. 8 for **85**, **86** and ca. 6 and ca. 7 for **88** and **89** respectively.

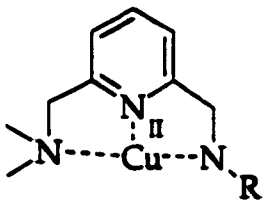

84: R = CH_3
85: R = $C_{14}H_{29}$
86: R = $C_{16}H_{33}$

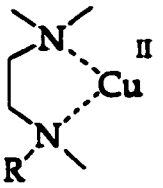

87: R = CH_3
88: R = $C_{14}H_{29}$
89: R = $C_{16}H_{33}$

Figure 1.26. Cu(II) metallomicells and monomeric Cu(II) complexes used in the hydrolysis of DPNPP.

Deal and Burstyn[87, 88] reported catalytic hydrolysis of activated bis(4-nitrophenyl)phosphate (BNPP) and ethyl-4-nitrophenylphosphate (ENPP) by [Cu([9]aneN_3)Cl_2] **90** (**Scheme 1.31**). In addition to hydrolyzing phosphodiesters, **90** also hydrolyzes both RNA[89] and DNA[90].

The metal ion in **90** are hydrolyzed when the complex is dissolved in aqueous media. In comparison with hydroxide ion mediated hydrolysis, a rate enhancement by a factor of 2000 was reported for **90**. They observed a half-order dependence on the concentration of metal complex indicating that **90** is in a monomer-dimer equilibrium with the monomer as the active catalyst in a solution (**Scheme 1.31**). However, because of monomer-dimer equilibrium, the p*K*a obtained by titration is not the p*K*a of the coordinated water.

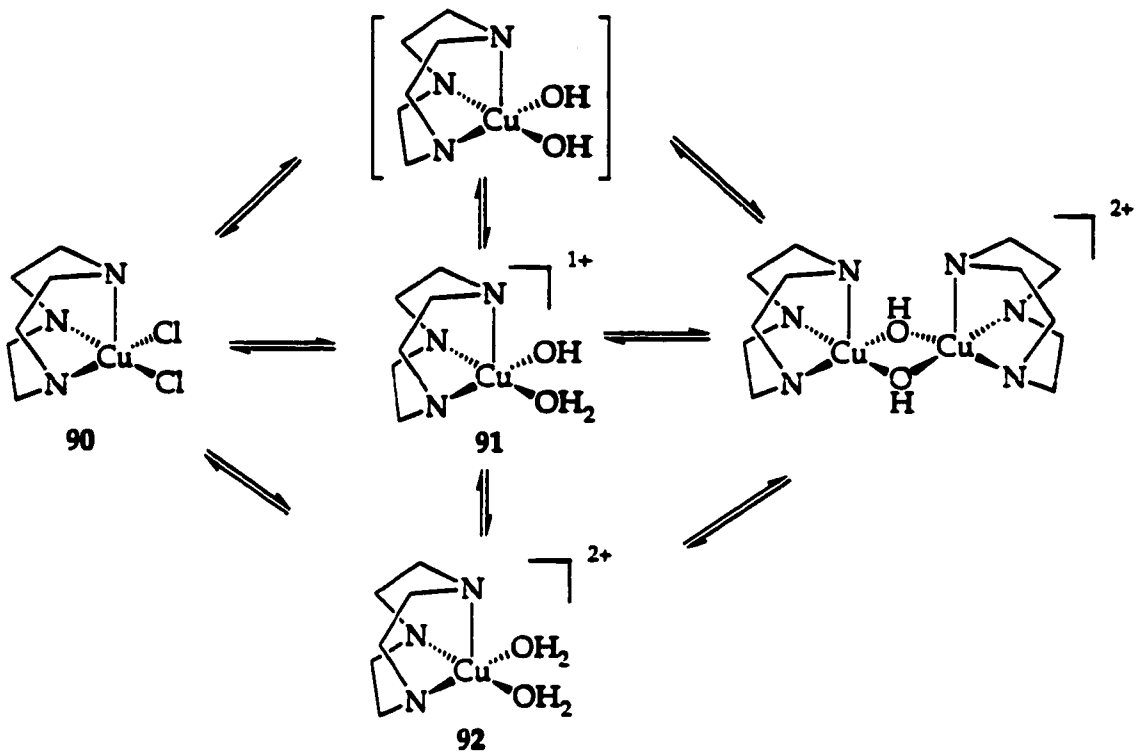

Scheme 1.31. $Cu([9]aneN_3)Cl_2$ **90 and proton equilibria for 90.**[22]

Deal and Burstyn[87, 88] proposed a concerted mechanism (**Scheme 1.32**) in detail involving direct nucleophilic attack by a metal-coordinated hydroxide through a phosphorane-like transition state. In order to distinguish between a general base mechanism (attack of the activated water) and direct nucleophilic attacks of the metal-coordinated hydroxide, solvent deuterium isotope effects were used. No proton transfer during the hydrolysis of the phosphodiesters was observed and is consistent with an intramolecular attack by a metal-coordinated hydroxide. Secondary ^{15}N isotope effects were also used to distinguish between a penta-coordinated phosphorane intermediate and a phosphorane-like transition state **93** as a result of the intramolecular attack by the metal-bound hydroxide.. No secondary ^{15}N isotope effects were observed indicating that the

mechanism proceeds via a concerted pathway with approximately 50% bond formation and 50% bond cleavage in the transition state.

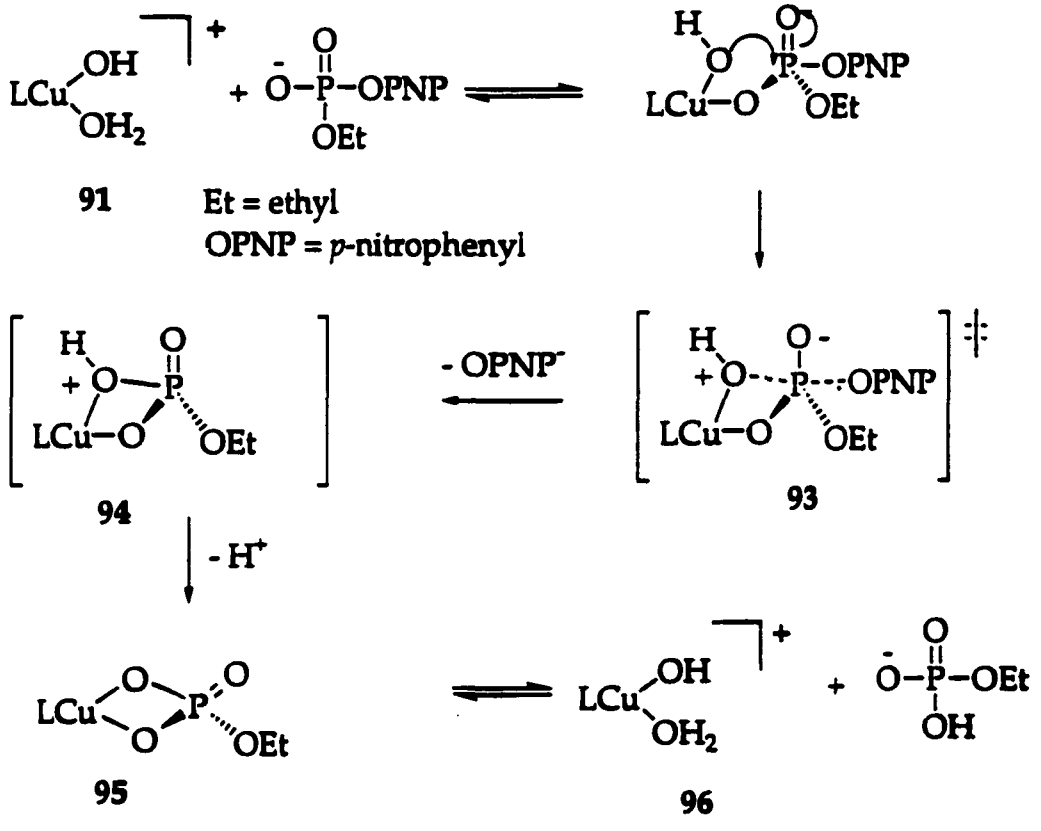

Scheme 1.32. A detailed mechanism in the [Cu([9]aneN$_3$)Cl$_2$]-catalyzed hydrolysis of activated phosphodiesters.[88]

Fujii et al.[91] investigated the hydrolysis of lithium 2,4-dinitrophenyl ethyl phosphate **97** and 2,4-dinitrophenyl diethyl phosphate **98** catalyzed by Cu(II)-triamine complexes (triamine = *cis,cis*-triaminocyclohexane **99**, 1,5,9-triazacycododecane **100**, 1,4,7-triazacyclononane **92**, dipropylenetriamine **101**, *N*-(2-aminoethyl)-1,3-propanediamine **102**, and diethylenetriamine **103**) at pH 7.0-9.5. The reactivity in the hydrolysis increases in the order **102**~**103**~**101** < **92** < **99** < **100** and corresponds closely to the decreasing order in the coordination

strength of the triamine ligands. The Cu(II)-bound hydroxide was proposed as an active species for all catalysts based on the pH dependence of the rate constants and the deprotonation constant (p*Ka*) of coordinated water. A reaction mechanism (**Scheme 1.33**) was proposed and is similar to the mechanism suggested by Burstyn et al.[87, 88]

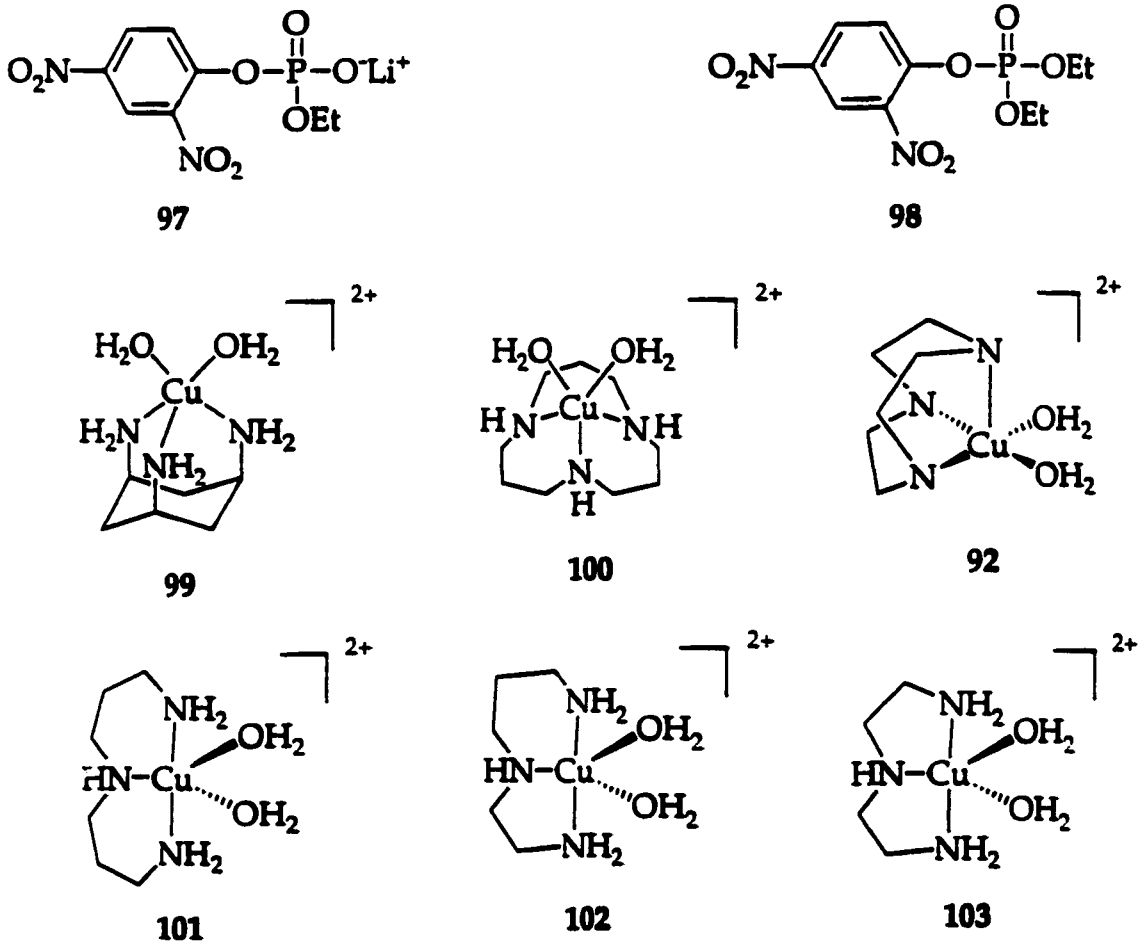

Figure 1.27. Lithium 2,4-dinitrophenyl ethyl phosphate **97** and 2,4-dinitrophenyl diethyl phosphate **98** and Cu(II)-triamine complexes.

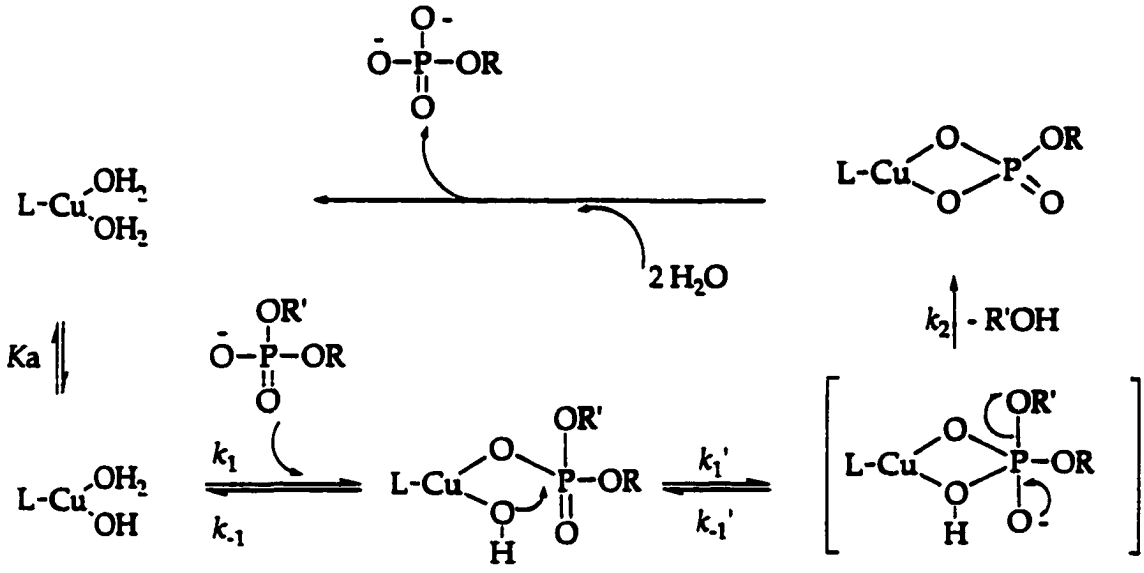

Scheme 1.33. Proposed mechanism of the hydrolysis by Cu(II)-triamine complexes.

The catalytic hydrolysis of the 2,4-dinitrophenyl diethyl phosphate **98** by $[Cu(tmen)(OH)(OH_2)]^+$ (tmen = *N,N,N',N'*-tetramethylethyleneamine, **87** in **Figure 1.26** in the pH range 6.5-8.0 with a rate enhancement ca. 10^4 compared to base hydrolysis (OH^-) at pH 7 were reported by Govan and Hay.[92] The p*Ka* (7.58) of Cu(II)-bound water at 25°C and the pH dependence of the catalysis indicate that the hydroxoaqua complex is an active species. A bifunctional "push-pull" mechanism in which metal center delivers a coordinated hydroxide ion to the substrate while simultaneously withdrawing electron density from the phosphorus atom by interacting with the phosphoryl oxygen was proposed. They also reported the hydrolysis of 2,4-dinitrophenyl diethyl phosphate **98** by $[Cu([9]aneN_3)(OH)(OH_2)]^+$ **91** (**Scheme 1.31**) and the p*Ka* (7.5) at 35°C for Cu(II)-coordinated water.[93] Again the hydroxoaqua Cu(II) complex was suggested as an active species in this study.

The structure of three related Cu(II) complexes $[Cu[9\text{-}11]aneN_3]X_2$ (X = Cl or Br) (**92**, **104**, and **105**) and their catalytic reactivity in the hydrolysis of BNPP and ENPP were investigated by Burstyn et al.[21] They found that the rate constant for the hydrolysis of BNPP increases by an order of magnitude with increasing ligand sizes from **92** to **104** and then to **105**. That trend was explained by the fact that the formation of catalytically inactive dihydroxo-bridged Cu(II) dimer decreases as the ligand size increases and increases the concentration of catalytically-active monomer species.

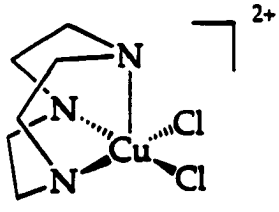

92

$[Cu[9]aneN_3]Cl_2$

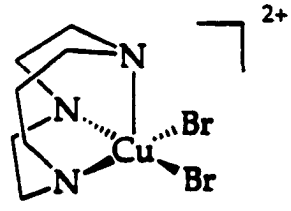

104

$[Cu[10]aneN_3]Br_2$

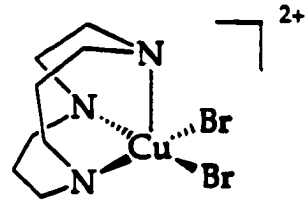

105

$[Cu[11]aneN_3]Br_2$

Figure 1.28. Cu(II) complexes $[Cu[9\text{-}11]aneN_3]X_2$ (X = Cl or Br).

The hydrolysis studies using synthetic hydrolases with substitution –inert metal ions, more than one metal ion, and labile metal ions were described in this section and indicate the following;

- Provision of two *cis*-oriented labile sites to accommodate both the substrate and a water molecule is important.
- One of the most effective ways that metal ion can promote a reaction with phosphate esters is to provide an intramolecular nucleophile, in an accessible position, which can attack the phosphate. This effect is dependent on the

nature of the metal ion and the ease of formation of the required four-membered ring after nucleophile attack.

- Supplying an available nucleophile, at a physiological pH level, is an important role for the metal ion that reduces the p*K*a of the coordinated water.
- Addition of multiple metal ions may enhance the reactivity of phosphate esters by a variety of methods. For example, one metal ion may be able to provide the intramolecular nucleophile and electrophile activation while another metal ion activates the phosphate ester by further withdrawal of electron density and charge neutralization.
- The metal ion at the catalytically active site should be able to release the products at a reasonable rate.

Experimental Section

A. Materials and Methods

All the materials listed below were of a research grade or a spectroquality grade in the highest purity available and were generally used without further purification except Et_2O. Et_2O was distilled from Na/K and used immediately.

Hepes (*N*-(2-hydroxyethyl)piperazine-*N'*-ethylsulfonic acid) and Caps (3-[cyclohexyamino]-1-propanesulfonic acid) were purchased from Sigma Chemical Co. ^{63}Cu , glycerol-d_3, and D_2O , were obtained from Cambridge Isotope Laboratories. DCl and NaOD were obtained from Alfa Products. BNPP (sodium bis(*p*-nitrophenyl)phosphate, $Na_4P_2O_7$ (sodium pyrophosphate decahydrate), Cu(II)Cl_2, Cu(II)Br_2, anhydrous MeOH, $Na_2CO_3 \bullet H_2O$, glycerol and DMSO were purchased from Aldrich. NaOH and benzene were obtained from Fisher Scientific. EtOH was purchased from Pharmco. CH_2Cl_2 and $CHCl_3$ were obtained from EM Science. Deionized water was obtained through reversed-osmosis followed by anion and cation exchange on an E-pure from Barnstend.

All ligands used in this study were synthesized by Dr. Brechbiel et al. at NIH and kindly donated to this group for the purpose of metal complex syntheses in order to investigate biological applications and structural studies.

All of the visible-near IR electronic spectra were measured using a Cary 5 Varian UV-vis spectrometer with 1 mL or 3 mL quartz cuvettes (1cm path-length). All of the vibrational spectra were measured using a Nicolet 205 FT-IR spectrometer with KBr pellets. An Orion Model 210A pH meter equipped with a 9106 non-refillable combination pH electrode was used for pH measurements. Fast atom bombardment (FAB-MS) mass spectra were taken on an Extrel 4000 at NIH. ^1H and ^{13}C NMR spectra were obtained using a Bruker AM360 instrument.

Elemental analysis was performed by Atlantic Microlabs (Atlanta, Georgia) or by Galbraith Laboratories (Knoxville, Tennessee).

B. Preparation of Cu(II) complexes of *N*-alkylated tach derivatives

[Cu(tach-Me_3)Cl_2] (106A). An aqueous solution (3 mL) of tach-Me_3•3HBr (0.143 g, 3.44×10^{-4} mol) was neutralized by adding of 0.1N NaOH solution (10.3 mL, 1.03×10^{-4} mol, 3 equiv). The neutralized ligand was dried under reduced pressure for 10h and extracted into $CHCl_3$ (2 mL). To a pale green solution of $CuCl_2$ (0.0471 g, 3.44×10^{-4} mol) in anhydrous MeOH (2 mL) was added a pale yellow solution of the neutralized tach-Me_3 ligand in $CHCl_3$ (2 mL) affording green precipitates and a dark green solution. After drying the mixture under reduced pressure, the green solid was taken up in CH_2Cl_2 (8 mL) and dried under reduced pressure. The crude product was washed with anhydrous Et_2O and dried again under reduced pressure giving a green solid in 38% yield (0.0403 g, 1.32×10^{-4} mol). Anal. Calcd for $C_9H_{21}Cl_2CuN_3$ [Cu(tach-Me_3)Cl_2]: C, 35.36; H, 6.92; N, 13.74. Found: C, 35.46; H, 6.83; N, 13.60. UV (MeOH) 700 nm (ε = 157.3). MS (FAB/glycerol): 234 ($M-2Cl^-$)

[Cu(tach-Me_3)Cl_2] (106B). A mixture of tach-Me_3•3HBr (0.12 g, 2.9×10^{-4} mol) in water (5 mL), Na_2CO_3•H_2O (0.054 g, 4.4×10^{-4} mol, 1.5 equiv) in water (5 mL), and benzene (100 mL) was stirred and heated in a 250 mL round-bottomed flask fitted with a Dean-Stark trap with a water-cooled condenser. Benzene-water azeotrope was distilled for 14 h with collection of ca. 11.7 mL of water. The benzene layer was transferred to an another 250 mL round-bottomed flask and dried under reduced pressure to give tach-Me_3 as a white solid. The solid was dissolved in a mixture of chloroform/Et_2O (2 mL/4 mL) and added to a green solution of $CuCl_2$ (0.040 g, 2.9×10^{-4} mol) in a mixture of MeOH/Et_2O (2 mL/4

mL) immediately affording a green precipitate. Decanting the supernatant and extracting the solid with CH_2Cl_2 (5 mL) followed by drying under reduced pressure afforded a green solid (0.056 g, 1.8 x 10^{-4} mol, 63%). Anal. Calcd for $C_9H_{21}Cl_2CuN_3$ [Cu(tach-Me_3)Cl_2]: C, 35.36; H, 6.92; N, 13.74. Found: C, 35.16; H, 6.85; N, 13.62. UV (MeOH) 687 nm (ε = 111.7). MS (FAB/DMSO/glycerol): 234 (M-Cl_2^-)

[Cu(tach-Me_3)Br_2] (107). A mixture of tach-Me_3•3HBr (0.191 g, 4.61 x 10^{-4} mol) in water (10 mL), Na_2CO_3•H_2O (0.0857 g, 6.91 x 10^{-4} mol, 1.5 equiv) in water (10 mL), and Benzene (100 mL) was stirred and heated in a 250 mL round-bottomed flask fitted with Dean-Stark trap with a water-cooled condenser. The mixture was heated for 14 h over which time the temperature was raised to 170°C in stages, and water was collected in the Dean-Stark trap and discarded. The benzene layer was transferred to another 500 mL round bottomed flask and dried under reduced pressure to give a white solid. To a brown solution of $CuBr_2$ (0.163 g, 4.6 x 10-4 mol) in MeOH (2 mL) was added a pale yellow solution of tach-Me_3 (0.0788 g, 4.60 x 10^{-4} mol) in MeOH (2 mL) affording a dark green solution. After standing for 1 hour, green microcrystals were deposited and the mixture was cooled at 5°C for overnight to form more crystals. Crystals were isolated and taken up in CH_2Cl_2 (12 mL) followed by drying under reduced pressure affording a green solid in 42.2% yield (0.102 g, 2.58 x 10^{-4} mol). Anal. Calcd for $C_9H_{21}Br_2CuN_3$ [Cu(tach-Me_3)Br_2]: C, 27.39; H, 5.36; N, 10.65. Found: C, 27.67; H, 5.26; N, 10.25. UV (MeOH) 691 nm (ε = 117.34). MS (FAB/glycerol): 234 (M-2Br^-)

[Cu(tach-Et_3)$Br_{0.8}Cl_{1.2}$] (108). An aqueous solution (3 mL) of tach-Et_3•3HBr (0.193 g, 4.26 x 10^{-4} mol) was neutralized by adding 0.100 N NaOH solution (12.8 mL, 1.03 x 10^{-4} mol, 3 equiv). This was dried under reduced pressure for 10 h and extracted into of $CHCl_3$ (12 mL), filtered, and dried under reduced pressure. The resulting pale-yellow solid was taken up in $CHCl_3$ (3 mL) and added to a pale green solution of $CuCl_2$ (0.0573 g, 4.26 x 10^{-4} mol) in anhydrous MeOH (2 mL) affording a dark green solution. This was filtered and dried under reduced pressure. The dried crude product was dissolved in anhydrous MeOH (5 mL), and anhydrous Et_2O was diffused into MeOH solution giving green crystals (0.0541 g, 1.56 x 10^{-4} mol, 35.5%). Anal. Calcd for $C_{12}H_{27}Br_{0.7}Cl_{1.3}CuN_3$ [Cu(tach-Et_3)$Br_{0.7}Cl_{1.3}$]: C, 38.04; H, 7.18; N, 11.09. Found: C, 38.47; H, 6.71; N, 10.45. UV (MeOH) 716 nm (ε = 132.8). MS (FAB/glycerol): 276 ($M-2X^+$)

[Cu(tach-Et_3)Cl_2] (109). A mixture of tach-Et_3•3HBr (0.17 g, 3.7 x 10^{-4} mol) in water (5 mL), Na_2CO_3•H_2O (0.073 g, 5.9 x 10^{-4} mol, 1.5 equiv) in water (5 mL), and benzene (100 mL) was stirred and heated in a 250 mL round-bottomed flask fitted with a Dean-Stark trap with a water-cooled condenser. Benzene-water azeotrope was distilled for 14h with collection of ca. 11.9 mL of water. The benzene layer was dried under reduced pressure to give tach-Et_3 as a white solid. To a pale green solution of $CuCl_2$ (0.050 g, 3.7 x 10^{-4} mol) in a mixture of MeOH/Et_2O (3 mL/6 mL) was added a pale yellow solution of tach-Et_3 (0.079 g, 3.7 x 10^{-4} mol) in a mixture of MeOH/Et_2O (2 mL/4 mL) affording a dark green solution and a brown precipitate. The brown precipitate was filtered away, and the dark green filtrate was dried under reduced pressure affording a green solid.

This was dissolved in CH_2Cl_2 (4 mL) and Et_2O was diffused into the solution affording green prisms (0.053 g, 1.5×10^{-4} mol, 43%). Anal. Calcd for $C_{12}H_{27}Cl_2CuN_3$ [Cu(tach-Et_3)Cl_2]: C, 41.44; H, 7.82; N, 12.08. Found: C, 41.22; H, 7.83; N, 11.94. UV (MeOH) 718 nm (ε = 97.0). MS (FAB/glycerol): 276 (M-2Cl$^-$).

[Cu(tach-Pr_3)Cl_2] (110). A mixture of tach-Pr_3•3HBr (0.250 g, 5.05×10^{-4} mol) in deionized (5 mL), Na_2CO_3•H_2O (0.200 g, 1.62×10^{-3} mol, 1.6 equiv) in deionized (5 mL), and benzene (100 mL) was stirred and heated in a 250 mL round-bottomed flask fitted with Dean-Stark trap with a water-cooled condenser. Benzene-water azeotrope was distilled for 14h with collection of ca. 11.7 mL of water. The benzene layer was dried under reduced pressure to give tach-Pr_3 as a white solid. To a pale green solution of $CuCl_2$ (0.0678 g, 5.05×10^{-4} mol) in a mixture of MeOH/Et_2O (2 mL/6 mL) was added a pale yellow solution of tach-Pr_3 (0.1274 g, 5.05×10^{-4} mol) in a mixture of MeOH/Et_2O (2 mL/6 mL) affording a dark green solution. The turquoise feather-like crystals were formed while standing and isolated by decanting supernatant. Crystals were dried under reduced pressure, extracted into CH_2Cl_2 (5 ml) and filtered, and dried again under reduced pressure to afford a turquoise solid (0.140 g, 3.63×10^{-4} mol, 72%). Anal. Calcd for $C_{15}H_{33}Cl_2CuN_3$ [Cu(tach-Pr_3)Cl_2]: C, 46.21; H, 8.53; N, 10.78. Found: C, 46.33; H, 8.36; N, 10.63. UV (MeOH) 703 nm (ε = 95.9). MS (FAB/glycerol/DMSO/EtOH): 318 (M-2Cl$^-$).

[Cu(tach)Cl_2]•1/2H_2O (111). A mixture of tach•3HBr (0.073 g, 2.0×10^{-4} mol) in water (5 mL), Na_2CO_3•H_2O (0.039 g, 3.2×10^{-4} mol, 1.6 equiv) in water (5 mL),

and benzene (100 mL) was stirred and heated in a 250 mL round-bottomed flask fitted with a Dean-Stark trap with a water-cooled condenser. Benzene-water azeotrope was distilled for 14h with collection of ca. 11.7 mL of water. The benzene layer was transferred to another 250 mL round-bottomed flask and dried under reduced pressure to give tach as a white solid. The solid was dissolved in EtOH (4 mL) and added to a green solution of $CuCl_2$ (0.024 g, 1.8 x 10^{-4} mol, 0.9 equiv) in a mixture of MeOH/Et_2O (2 mL/4 mL) immediately affording a green suspension. Et_2O was added to a mixture to force the formation of a green precipitate. After standing 1 h, the mixture was dried under reduced pressure giving a turquoise powder and a dirty green solid. The turquoise powder was taken up in MeOH (5 mL) and filtered. Et_2O was diffused into MeOH solution of a crude product giving blue prisms and small amount of dirty green precipitates. Prisms were isolated, dissolved in MeOH (3 mL), and dried under reduced pressure giving a green solid (0.0095 g, 3.6 x 10^{-5} mol, 63%). Anal. Calcd for $C_6H_{15}Cl_2CuN_3 \bullet 1/2H_2O$ [Cu(tach)Cl_2]$\bullet$1/2H_2O: C, 26.43; H, 5.91; N, 15.41. Found: C, 26.87; H, 5.88; N, 15.16.

C. *In Situ* Preparation of [Cu(tach-R_3)X_2] for EPR study

$[Cu(tach\text{-}Me_3)]^{2+}$ - To a blue solution of 0.1M $CuCl_2$ in water (1.49 mL) is added a clear solution of 0.1M tach-Me_3 in water (1.5 mL), prepared by neutralization of tach-$Me_3 \bullet 3HBr$ (0.06210 g, 1.5 x 10^{-4} mol) in water (1.0365 mL) with three equiv of 1.02 N NaOH (0.4635 mL), affording a deep blue 50 mM $[Cu(tach\text{-}Me_3)]^{2+}$ solution. Occasionally, a faint blue-green precipitate formed, presumably insoluble Cu(II) hydroxide, which was removed by filtration. From this was

prepared 5 mM $[Cu(tach\text{-}Me_3)]^{2+}$ solution by further dilution with a mixture 50 mM Hepes/glycerol (2:1), pH 7.4 at 25°C.

$[^{63}Cu(tach\text{-}Me_3)]^{2+}$. To a clear solution of tach-Me_3•3DCl (0.014 g, 5.0×10^{-6} mol) in a mixture of 50 mM Hepes in D_2O/glycerol-d_3 (2:1), pH 7.4 at 25°C, (0.75 mL) is added a pale blue solution of 20 mM $^{63}CuCl_2$/DCl (0.25 mL, 5.0×10^{-6} mol) affording 5 mM $[^{63}Cu(tach\text{-}Me_3)]^{2+}$ with pH of 7.4.

$[Cu(tach\text{-}Et_3)]^{2+}$. To a blue solution of $CuCl_2$ (0.0201 g, 1.50×10^{-4} mol) in water (1.5 mL) is added a clear solution of tach-Et_3, neutralized by 3 equiv of 1.0 N NaOH, (0.0681 g, 1.50×10^{-4} mol) in water (1.5 mL) to form a sky blue solution with small amount of a faint blue-green precipitate, presumably insoluble Cu(II) hydroxides, which was removed by filtration. From this was prepared 5 mM $[Cu(tach\text{-}Et_3)]^{2+}$ solution by further dilution with a mixture 50 mM Hepes/glycerol (2:1), pH 7.4 at 25°C.

$[Cu(tach\text{-}Me_3)]^{2+}$ and BNPP (BNPP = bis(4-nitrophenyl)phosphate). A 50 mM $[Cu(tach\text{-}Me_3)]^{2+}$ solution prepared as above was diluted by mixing with 50 mM Hepes (pH 7.4) affording a final concentration of 2 mM. To a blue solution of 2 mM $[Cu(tach\text{-}Me_3)]^{2+}$ in Hepes (1 mL) is added 20 mM BNPP (1 mL) affording the final concentration of 1 mM $[Cu(tach\text{-}Me_3)]^{2+}$ and 10 mM BNPP.

$[Cu(tach\text{-}Me_3)]^{2+}$ and Inhibitor ($Na_4P_2O_7$•$10H_2O$, sodium pyrophosphate decahydrate). A 50 mM $[Cu(tach\text{-}Me_3)]^{2+}$ solution prepared as above was diluted by mixing with 50 mM Hepes (pH 7.4) affording final concentration of 1 mM. To

a blue solution of 1 mM $[Cu(tach\text{-}Me_3)]^{2+}$ in Hepes (1 mL) is added 10 mM $Na_4P_2O_7 \bullet 10H_2O$ (1 mL) affording a final concentration of 0.5 mM $[Cu(tach\text{-}Me_3)]^{2+}$ and 5 mM $Na_4P_2O_7 \bullet 10H_2O$.

D. Preparation of $[Cu(tach\text{-}R_3)]^{2+}$ for EPR study

$[Cu(tach\text{-}Pr_3)]^{2+}$. The turquoise solid of $[Cu(tach\text{-}Pr_3)Cl_2]$ (0.012 g, 3.0×10^{-5} mol) was dissolved in a mixture of 50 mM Hepes/glycerol (2:1) (3 mL), pH 7.4 at 25°C, affording turquoise cloudy solution which became a clear turquoise 5 mM $[Cu(tach\text{-}Pr_3)]^{2+}$ solution by adding MeOH (3 mL).

$[Cu(tach\text{-}thioph_3)]^{2+}$. A green solid $[Cu(tach\text{-}thioph_3)Cl_2]$ prepared by Neng Ye with the literature method[94] (0.017 g, 3.0×10^{-5} mol) was dissolved in a mixture of 50 mM Hepes/glycerol (2:1) (3 mL), pH 7.4 at 25°C, affording greenish cloudy solution which became a clear green 5 mM $[Cu(tach\text{-}thioph_3)]^{2+}$ solution by adding EtOH (3 mL).

E. EPR Measurements

Junlong Shao of Professor Chasteen's research group (UNH) measured all EPR spectra at either X-band or Q-band frequency. All the solution samples of $[Cu(tach\text{-}R_3)]^{2+}$ were prepared *in situ* as described above or dissolving corresponding solids in a mixture of Hepes/glycerol (2:1) or only Hepes or in anhydrous MeOH affording the final concentration of 5 mM Cu(II) ion. The

powder samples of [Cu(tach-R_3)X_2] were prepared by grinding corresponding crystalline samples.

F. Product Analysis and Kinetic Measurements of Hydrolysis study

Product analysis. A 3.00 mL solution 1 mM [Cu(tach-Me_3)]$^{2+}$, 1 mM bis(*p*-nitropneyl)phosphate and 50 mM HEPES, pH 7.24 at 50°C, was incubated at 50°C for one hour. An aliquot was withdrawn and analyzed by reverse-phase HPLC, elute with a linear gradient from 100% 50 mM acetic acid/50mM triethylamine to 100% methanol over 25 minutes. Products were confirmed by co-injection of standard.

Kinetic measurements. The initial rate of formation of *p*-nitrophenolate was monitored spectrophotometrically at 400 nm. The concentration of *p*-nitrophenolate was calculated from the absorbance at 400 nm (ε = 18700 L mol^{-1} cm^{-1}). The initial rate was obtained from the slope of the plots of *p*-nitrophenolate concentration versus time.

In a typical reaction, 1mM freshly prepared [Cu(tach-Me_3)]$^{2+}$ was added to 50mM HEPES, pH 7.24 and heated to 50°C in a Teflon sealed screw capped cuvette. A reference was prepared identical to the reaction mixtures without metal complex. An aliquot of 20 mM bis(*p*-nitrophenyl)phosphate was added to yield a 2mM substrate concentration in a 3 mL reaction mixture. The increase in absorbance at 400 nm was followed for 60 minutes, or for less than 10% conversion of bis(*p*-nitrophenyl)phosphate to products.

Catalytic hydrolysis of phosphate diesters promoted by [Cu(tach-Me_3)]$^{2+}$ were investigated by Dr. Kim Deal at NIH.

Results

A. Synthesis of Cu(II) Metal Complexes with (N-R)$_3$tach Derivatives

Until recently the availability of the tach ligand and its derivatives have been limited because of previously problematic syntheses and poor yields. The synthesis of the high-yield tach[95] and new families of trialkyl derivatives of tach have become successful by modification of the synthetic route, making them readily available now (see introduction of **Chapter 3**).[1, 94, 96, 97]

The tach-R_3•3HBr ligands are hydrobromide salts. Neutralization of the hydrobromide should be fulfilled before complexation can take place because the protonated nitrogens do not have the ability to donate and coordinate to the metal ions. In early attempts at synthesizing [M(II)(tach-R_3)X_2] (M = Cu or Zn and X = Cl or Br), the tach-R_3•3HBr ligands were neutralized by adding three equiv of NaOH. The neutralized ligands with NaOH were dried under reduced pressure, extracted into a reaction medium, EtOH, and filtered. To a solution of metal ion in MeOH is added a solution of neutralized ligand in EtOH affording a precipitate of metal complexes with a low yield and composition ambiguity. After purification, all the complexes were analyzed by elemental analyses and fast atom bombardment (FAB-MS) mass spectra. In the attempted synthesis of [Cu(tach-Me_3)Cl_2] and [Cu(tach-Et_3)Cl_2], the products obtained, however, were actually [Cu(tach-Me_3)Br_xCl_{2-x}] and [Cu(tach-Et_3)Br_xCl_{2-x}] complexes according to the elemental analysis and X-ray structural analysis.

The composition ambiguity of the anions in the synthesis of [M(II)(tach-R_3)X_2] (M = Cu or Zn and X = Cl or Br) complexes was avoided by using benzene-water azeotropic distillation as a neutralization method. In the

benzene-water azeotropic-distillation, a mixture of a tach-R_3•3HBr ligand in water, metal ions in water, and benzene was stirred and heated in a round-bottomed flask fitted with a Dean-Stark trap with a water-cooled condenser. Teflon sleeves were used to connect the Dean-stark trap and a round-bottomed flask and a water-cooled condenser in order to prevent the problem caused by conventional greases with high temperature reactions. The round-bottom flask was placed in a sand bath for better transfer of heat and wrapped with glass wool in order to prevent loss of the heat thus facilitating the collection of the water at the Dean-stark trap. Benzene-water azeotrope was distilled for at least 14 h with collection of water. The benzene layer which contains the neutralized ligand was transferred to another round-bottomed flask while it was still hot and dried under reduced pressure at the pump (10^{-2} torr) or rotary evaporator (water aspirator) to give the neutralized ligand as a white solid or yellowish oil depending on the method of drying. The dried neutralized ligand was taken up in MeOH and added to a MeOH solution of a metal ion affording a precipitate of the desired product. Usually Et_2O was added to force the formation of additional precipitate.[98] After decanting the supernatant, the isolated crude product was dried under reduced pressure, taken up in CH_2Cl_2, and recrystallized by vapor diffusion of Et_2O into a CH_2Cl_2 solution of the product.

Results of elemental analysis and FAB-MS spectra of [Cu(tach-R_3)X_2] are presented in **Table 1.1.** Elemental analysis and FAB-MS spectra indicate that the synthesis of [Cu(tach-R_3)X_2] have been successful giving pure products with reasonable yields (35.5 ~ 72.0 %). Attempts in preparing [Cu(tach-Np_3)Cl_2] (Np = neopentyl) have been unsuccessful. It seems that it forms impure substances,

presumable a polymeric material with N_L-Cu-N_L, bridging unit, with poor solubility in the conventional solvents because of the large steric effect of neopentyl groups.

Table 1.2. Results of elemental analysis and FAB-MS of $[Cu(tach\text{-}R_3)X_2]$ complexes where X is Cl except in $[Cu(tach\text{-}Et_3)Br_{0.7}Cl_{1.3}]$

Metal Complex	Anal.Calcd (%)	Found (%)	FAB-Mass Spec.
$[Cu(tach\text{-}Me_3)Cl_2]$	C, 35.36 H, 6.92 N, 13.74	C, 35.16 H, 6.85 N, 13.62	234 ($M\text{-}2Cl^-$)
$[Cu(tach\text{-}Me_3)Br_2]$	C, 27.39 H, 5.36 N, 10.65	C, 27.67 H, 5.26 N, 10.25	234 ($M\text{-}2Cl^-$)
$[Cu(tach\text{-}Et_3)Br_{0.7}Cl_{1.3}]$	C, 38.04 H, 7.11 N, 11.09	C, 38.47 H, 6.71 N, 10.45	276 ($M\text{-}2X^-$)
$[Cu(tach\text{-}Et_3)Cl_2]$	C, 41.44 H, 7.82 N, 12.08	C, 41.22 H, 7.83 N, 11.94	276 ($M\text{-}2Cl^-$)
$[Cu(tach\text{-}Pr_3)Cl_2]$	C, 46.21 H, 8.53 N, 10.78	C, 46.33 H, 8.36 N, 10.63	318 ($M\text{-}2Cl^-$)
$[Cu(tach\text{-}furanyl_3)Cl_2]$	C, 50.05 H, 5.40 N, 8.34	C, 49.84 H, 5.39 N, 8.22	432 ($M\text{-}2Cl^-$)

B. Solid Structural Study of $[Cu(tach\text{-}Et_3)Cl_{1.2}Br_{0.8}]$

X-ray quality crystals of $[Cu(tach\text{-}Et_3)Cl_{1.2}Br_{0.8}]$ were obtained by vapor phase diffusion of Et_2O into a CH_2Cl_2 solution of product. ORTEP view of $[Cu(tach\text{-}Et_3)\ Cl_{1.2}Br_{0.8}]$ (**108**) is depicted in **Figure 1.29**, and Chem 3D view showing a mirror plane in **108** is depicted in **Figure 1.30**. A crystallographic mirror plane in **108** generates the atoms N2A, ClBrA, C2A, C3A, C7A, and C8A by a reflection of atoms N2, ClBr, C2, C3, C7, and C8. One of $NH\text{-}CH_2$ groups around the mirror plane also generates the atoms N(1A)and C(5A), which correspond to the atoms N(1) and C(5). Selected bond distances and angles of **108** are in **Table 1.3**. A summary of crystallographic and data collection parameters for **108** are given in **Appendix A-1**.

The coordination geometry of **108** (**Fig. 1.31 (b)**) is best described in terms of a distorted square pyramid. In **108**, N(1) or N(1A) is located in the apical position, and N(2) and N(2A) and the two halides form the square pyramidal base. However, the N(1) or N(1A) atom is not located in an apical position of a normal square pyramidal geometry but slightly tilts (*ca.* 6.1°) toward the basal nitrogens N(2) and N(2A) (**Fig. 1.31 (a)**).

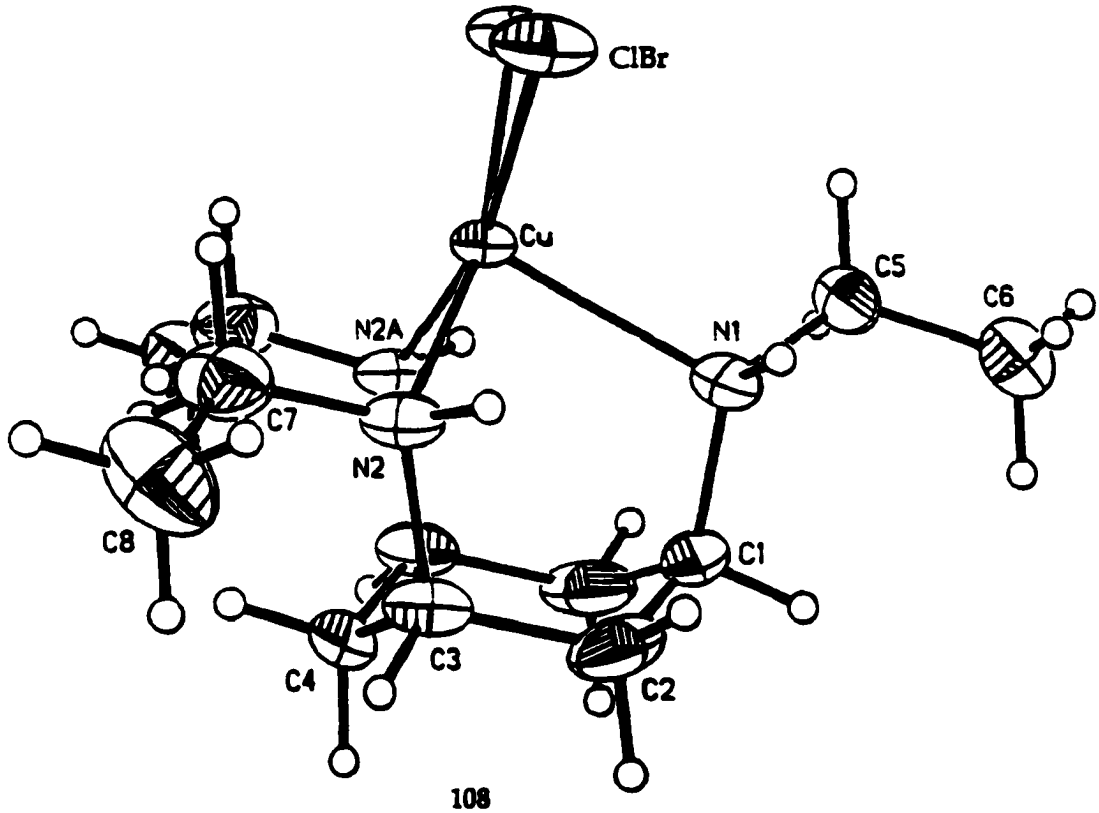

108

Figure 1.29. ORTEP view of $[Cu(tach\text{-}Et_3)Cl_{1.2}Br_{0.8}]$ **(108)** showing 50% probability of thermal ellipsoids.

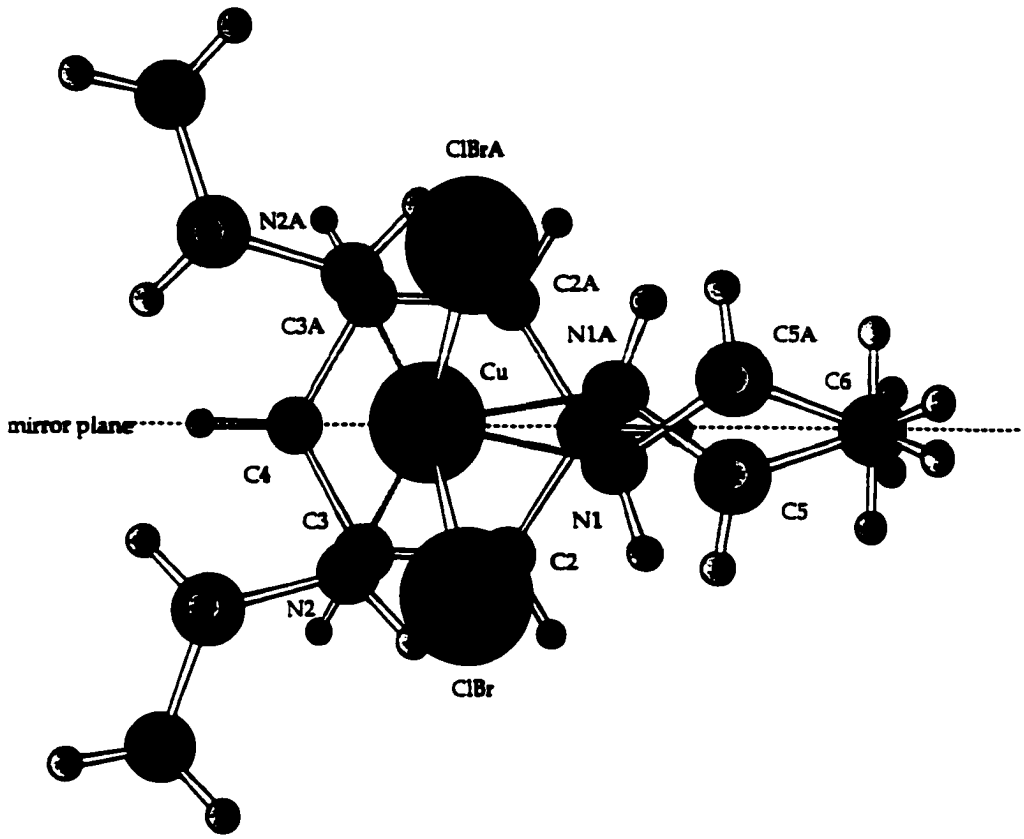

Figure 1.30. Chem 3D view of $[Cu(tach\text{-}Et_3)Cl_{1.2}Br_{0.8}]$ with a mirror plane.

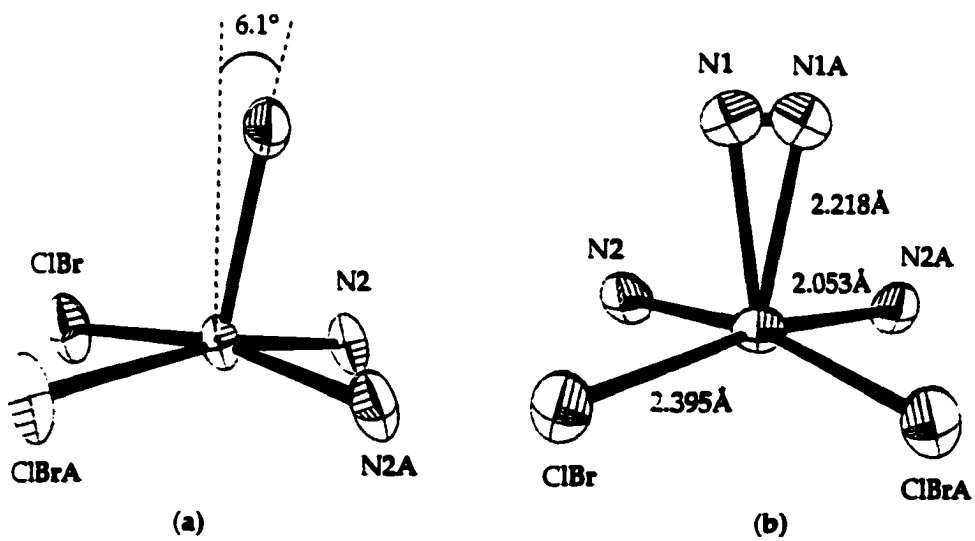

Figure 1.31. Square pyramidal geometry of **108**.

Table 1.3. Selected Bond lengths and angles for of [Cu(tach-Et_3) $Cl_{1.2}Br_{0.8}$] (108)

Cu-N(2)	2.053(2)	Cu-N(1)	2.218(5)
Cu-ClBr	2.3948(6)	N(1)-C(5)	1.478(7)
N(l)-C(1)	1.524(6)	N(2)-C(7)	1.484(4)
N(2)-C(3)	1.498(4)	C(1)-C(2)	1.519(5)
C(2)-C(3)	1.517(5)	C(3)-C(4)	1.515(4)
C(5)-C(6)	1.528(7)	C(7)-C(8)	1.506(5)

N(2)-Cu-N(2A)#	91.98(14)	N(2)-Cu-N(1A)#	96.75(14)
N(2)-Cu-N(l)	83.94(14)	N(2)-Cu-ClBr	86.24(7)
N(2A)#-Cu-ClBr	167.63(8)	N(1A)#-Cu-ClBr	108.42(12)
N(1)-Cu-ClBr	95.24(12)	ClBr-Cu-ClBr(A)#	92.89(3)
C(5)-N(l)-C(l)	109.6(4)	C(5)-N(1)-Cu 1	11.0(3)
C(1)-N(1)-Cu	109.5(3)	C(7)-N(2)-C(3)	114.2(2)
C(7)-N(2)-Cu	111.7(2)	C(3)-N(2)-Cu	115.7(2)
C(2)-C(l)-C(2A)#	110.2(4)	C(2)-C(l)-N(1)	99.7(3)
C(2)-C(l)-N(1A)#	122.6(3)	C(3)-C(2)-C(1)	114.6(3)
N(2)-C(3)-C(4)	112.0(3)	N(2)-C(3)-C(2)	110.7(3)
C(4)-C(3)-C(2)	110.9(3)	C(3A)#-C(4)-C(3)	112.9(4)
N(l)-C(5)-C(6)	113.0(4)	N(2)-C(7)-C(8)	114.7(3)

Equivalent atoms with the suffix "A" are generated by the symmetry transformation:
x, -y=1/2, z

C. Structural Study of [Cu(tach-R_3)X_2] in Solution

C.1. Structural Study of [Cu(tach-R_3)X_2] in Anhydrous MeOH Solution

Electronic spectra of the [Cu(tach-R_3)X_2] complexes were obtained to investigate the structures of the corresponding complexes in the solution and to compare those with the solid structure of [Cu(tach-Et_3)$Cl_{1.2}Br_{0.8}$] (**108**). Electronic spectra of the [Cu(tach-R_3)Cl_2] complexes in anhydrous MeOH are presented in **Figure 1.32.** Samples for electronic spectra were prepared by dissolving each purified solid products of [Cu(tach-R_3)Cl_2] complexes in anhydrous MeOH. The molar absorptivity (ε, L mol^{-1} cm^{-1}) of each sample was obtained and presented in **Table 1.4.** The green solids [Cu(tach-$thioph_3$)Cl_2] and [Cu(tach-$furanyl_3$)Cl_2] synthesized by Neng Ye and Su-jen Lai were purified by recrystallization, and used to obtain the corresponding electronic spectrum.

All visible-near IR spectra of [Cu(tach-R_3)Cl_2] contain a band maximum around 700 nm (~14,500 cm^{-1}) with a low-energy shoulder and a band around 1,100 nm (~9,000 cm^{-1}), suggesting identical structures in anhydrous MeOH solution. The location of the shoulder at low-energy is indicative of the coordination spheres of [Cu(tach-R_3)Cl_2] complexes as a square pyramidal geometry in MeOH solution and of rigidity of their coordination spheres under a time scale of the visible-near IR spectrum. This is consistent with the observed solid structure of [Cu(tach-$Et_3Cl_{1.2}Br_{0.8}$] (**108**), described above. The unsymmetrical band maximum around 700 nm (~14,500 cm^{-1}) is considered as a result of a superimposition of two d-d transition, d_{xz} or d_{yz} -> $d_{x^2-y^2}$ and d_{xy} -> $d_{x^2-y^2}$, while the broad band around 1,100 nm (~9,000 cm^{-1}) is attributed to the

low energy d-d transition d_{z2} -> d_{x2-y2}. However, the exact wavenumber (or wavelength) of the each transitions and the positions of the underlying transitions could not be determined without further analysis because of the superimposition and the large half-width of all these spectra.

Solid visible-near IR spectra of the [Cu(tach-Et_3)Cl_2] complex were obtained as well. The samples were prepared by grinding the green solid with either nujol or KBr. An unsymmetrical band maximum around 690 nm was observed, however, a low energy transition assigned for a d_{z2} -> d_{x2-y2} transition in the solution spectra was not observed due to a very broad band width. The location of this low-energy shoulder on the band maximum in the solid visible-near IR spectra of the [Cu(tach-Et_3)Cl_2] indicates a square pyramidal geometry of the complex which is consistent with X-ray structure of [Cu(tach-Et_3)$Cl_{1.2}Br_{0.8}$] **108.**

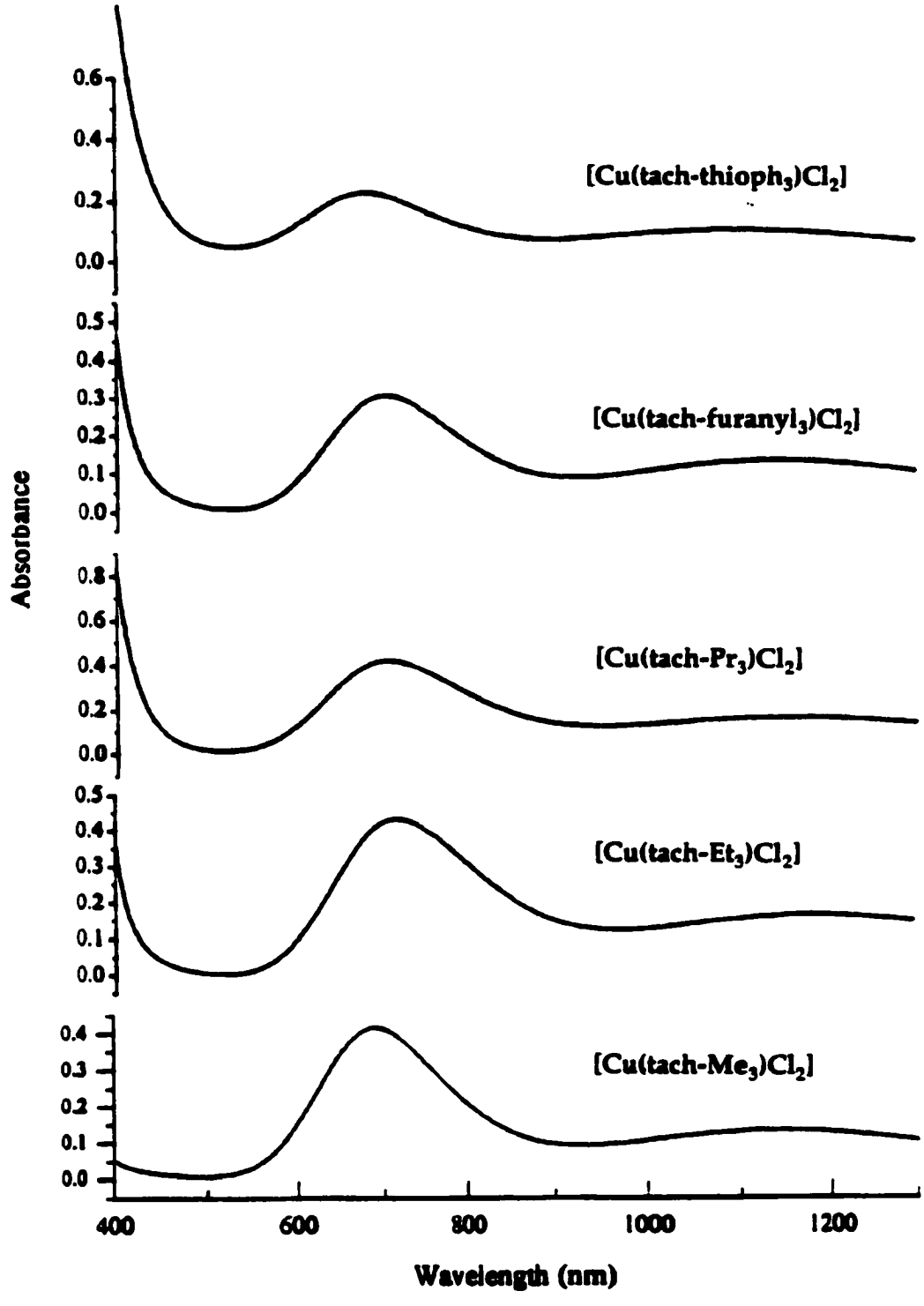

Figure 1.32. Electronic spectra of [Cu(tach-R_3)X_2]complexes in analytical grade MeOH. The concentration of each sample is 5 mM.

Table 1.4. Results of the electronic spectra of $[Cu(tach\text{-}R_3)X_2]$ and their molar absorptivity in anhydrous MeOH.

Metal Complex	Concentration 10^{-3} M	Max (nm)	ε(L mol^{-1} cm^{-1})
$[Cu(tach\text{-}Me_3)Cl_2]$	3.71	687	111.7
$[Cu(tach\text{-}Me_3)Br_2]$	3.55	691	117.3
$[Cu(tach\text{-}Et_3)Br_{0.7}Cl_{1.3}]$	5.00 *	716	132.8
$[Cu(tach\text{-}Et_3)Cl_2]$	5.00	718	97.0
$[Cu(tach\text{-}Pr_3)Cl_2]$	4.36	703	95.9
$[Cu(tach\text{-}thioph_3)Cl_2]$	3.56	693	105.5
$[Cu(tach\text{-}furanyl_3)Cl_2]$	3.04	700	100.9

*Concentration was calculated with a previous elemental analysis.

C.2. Structural Study of $[Cu(tach\text{-}Et_3)]^{2+}$ in Aqueous Medium

The Cu(II) complexes of *N*-alkylated tach derivatives $[Cu(tach\text{-}R_3)]^{2+}$ are substitution-labile in nature. The structures and chemical species of the $[Cu(tach\text{-}R_3)]^{2+}$ complexes in a aqueous solution, especially the $[Cu(tach\text{-}Et_3)]^{2+}$ complex, were investigated by using potentiometric titration, visible-near IR spectroscopy, and EPR spectroscopy.

A typical pH-metric determination was performed. An aqueous solution (10 mL) of 1 mM tach-Et_3•3HBr was titrated with a 0.05 N NaOH solution in the absence of the Cu(II) ion for determination of the ligand deprotonation constants (K_1, K_2, and K_3, **Scheme 1.34**). The samples were kept under a nitrogen gas atmosphere, and the solution was at room temperature. The ionic strength was adjusted to 0.1 M with $NaClO_4$. Three independent titrations were made for the determination.

Two marginally steep inflections at a = 1 and 2 correspond to the loss of two acidic protons from amine salt (where a indicates the moles of base added per mole of the ligand present). The first acid dissociation is of a strong acid, and was not detected. Acid dissociation constants of tach-Et_3•3HBr are listed and compared to other tridentate amine ligands in **Table 1.5**. The lower p*K*a values for tach-Et_3•3HBr compared to tach are presumably a result of the presence of an electron donating ethyl group attached to the amine nitrogens.

$$H_3L^{3+} \xrightleftharpoons{K_1} H_2L^{2+} + H^+$$

$$H_2L^{2+} \xrightleftharpoons{K_2} HL^+ + H^+$$

$$HL^+ \xrightleftharpoons{K_3} L + H^+$$

Scheme 1.34. Acid dissociation reactions for the tach-Et_3•3HBr ligand.

Table 1.5. Acid dissociation constants of the tach-Et_3•3HBr ligand and other tridentate amines.

	$(N\text{-}Et)_3$tach	[9]aneN_3[99]	tach[91]
pK_{a1}	strong	strong	7.15
pK_{a2}	7.44	6.82	8.95
pK_{a3}	9.14	10.42	10.68

The Cu(II)-tach-Et_3•3HBr ligand (L) 1:1 titration (**Fig. 1.33**) was also performed to investigate the deprotonation constant of the coordinated water in Cu(II)-L complex. A sample was prepared by adding a clear solution of 1 mM $CuCl_2$ in water (5 mL) into a clear solution of 1 mM tach-Et_3•3HBr in water affording a clear solution of 0.5 mM $[Cu(\text{tach-}Et_3)]^{2+}$ with a pH around 5 and was titrated with a 0.05 N NaOH solution. The ionic strength was also adjusted to 0.1 M with $NaClO_4$. The clear mixture became a pale blue colored solution around pH 6.8 with a = 2.0 indicating formation of a Cu-L complex. Beyond a = 2.5 the pH of a mixture increases gradually without an inflection up to pH 10.4 instead of showing two separate inflections at a = 3 and 4, which correspond to reactions (1) and (2) in **Scheme 1.35.**

$$Cu^{2+} + L \underset{}{\overset{Ka}{\rightleftharpoons}} CuL^{2+} \quad (1)$$

$$CuL^{2+} \underset{}{\overset{Ka}{\rightleftharpoons}} CuL(OH)^{+} + H^{+} \quad (2)$$

Scheme 1.35. Reactions for a complex formation (1) and deprotonation of a coordinated water molecule (2).

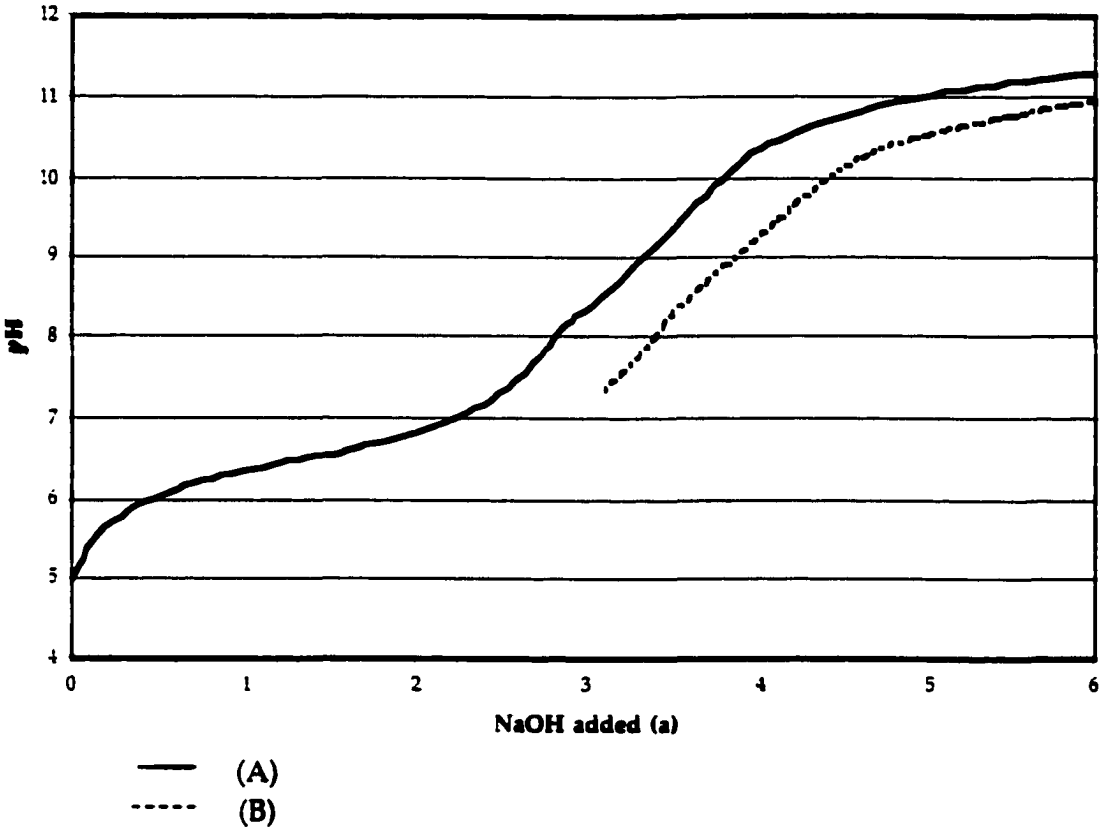

Figure 1.33. Titration curve for Cu(II)-L (1:1) system and [Cu(tach-Et_3)Cl_2] in water.

A structural study of the [Cu(tach-R_3)X_2] complexes in aqueous medium by visible-near IR spectroscopy was undertaken to detect a replacement of coordinated halide ligands by a water molecule in aqueous medium and to investigate the chemical species of a Cu(II) complex at different pH. The [Cu(tach-Et_3)Cl_2] complex was chosen for this study because of an available X-ray structure, a corresponding visible near IR spectrum in MeOH, and a solid visible-near IR spectrum for comparison purpose. Samples for the visible-near IR spectra were prepared either by direct dissolution of a green solid of [Cu(tach-Et_3)Cl_2] and filtration of the pale blue precipitates, by diluting a concentrated [Cu(tach-Et_3)Cl_2] solution in anhydrous MeOH with a 50 mM buffer solution

(Hepes or Caps), or by generating samples *in situ.*, mixing $CuCl_2$ and tach-Et_3•3HBr in a buffer solution and raising the pH of the mixture up to a desired point, in order to avoid the formation of a polymeric species.

Visible-near IR spectra of $[Cu(tach\text{-}Et_3)]^{2+}$ in MeOH and 50 mM Caps solution (pH = 10.2) are presented in **Figure 1.34.** All visible-near IR spectra of the $[Cu(tach\text{-}Et_3)]^{2+}$ in aqueous medium contain a band maximum around 670 nm with a low-energy shoulder and a broad band around 1050 nm, suggesting that the stereochemistry of $[Cu(tach\text{-}Et_3)]^{2+}$ is maintained as a square pyramid in aqueous medium with bands shifted to higher energy compared to those in anhydrous MeOH. Since H_2O is a stronger field ligand than halides ion in the spectrochemical series,[100] the observed band shifts to higher energy (718 nm to 669 nm for a band maximum and 1190nm to 1050 mm for a broad low-energy band) suggest that H_2O molecules displace the coordinated Cl^- ligand affording a larger splitting of the energy levels and consequently higher energy *d-d* transitions. The wavenumbers obtained by the simulation for each of the three *d-d* transitions for the $[Cu(N\text{-}Et)_3tachCl_2]$ complex in MeOH and Hepes buffer are listed in **Table 1.6.**

Bands shift toward higher energy were also observed in a visible-near IR spectrum obtained by adding a $[Cu(tach\text{-}Et_3)Br_{0.7}Cl_{1.3}]$ solution in MeOH (3 mL) into water (1 mL). The band maximum at 702 nm and a low-energy band at 1180 nm in MeOH were observed and shifted to higher energy 687 nm and 1120 nm in a mixture with water.

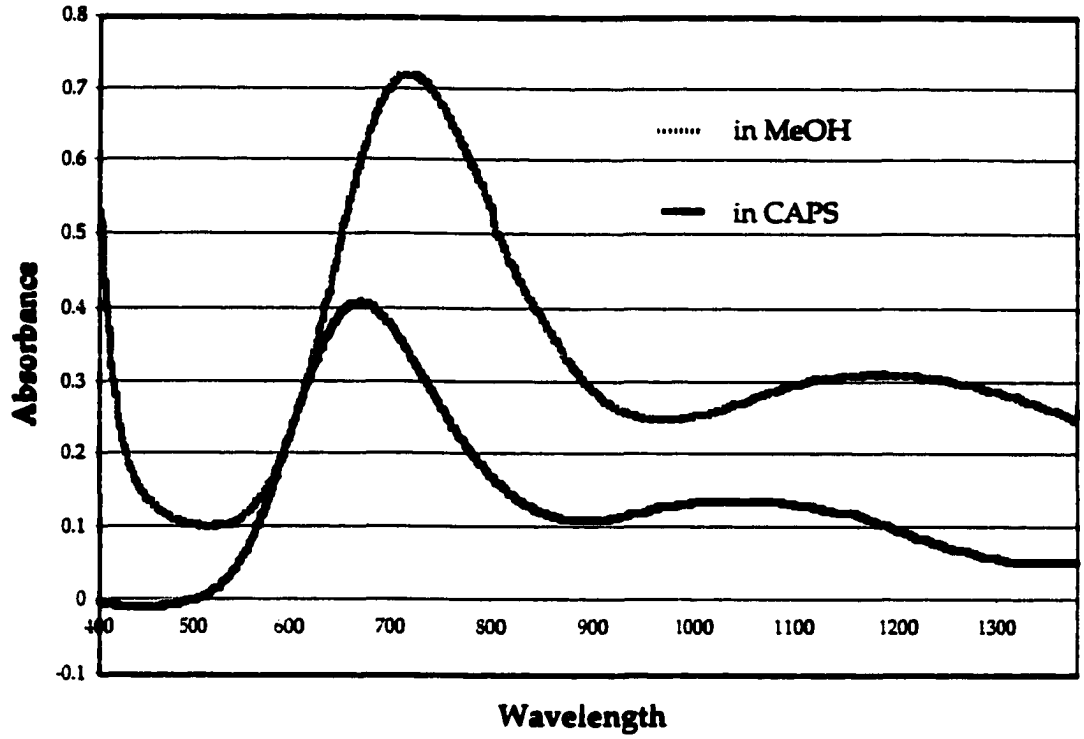

Figure 1.34. Visible-near IR spectra of $[Cu(N\text{-}Et)_3tachCl_2]$ in anhydrous MeOH and in Caps buffer (pH 10.2).

Table 1.6. The *d-d* transitions (wavenumbers) of $[Cu(tach\text{-}Et_3)Cl_2]$ complex in MeOH and Hepes buffer solutions. All values are taken from the Gaussian function analyses.[101]

Medium	Anticipated species in medium	$\Delta E_{xz, yz}$[a]	ΔE_{xy}[a]	ΔE_{z^2}[a]
Hepes buffer	$[Cu(N\text{-}Et)_3tach(OH_2)_2]^{2+}$	15075(54.4)	14214(17.8)	8670(22.0)
MeOH	$[Cu(N\text{-}Et)_3tachCl_2]$	14252(76.2)	12321(23.8)	8398(31.8)

Molar absorptivity, (ε, L mol-1 cm-1), in parentheses.

[a] $\Delta E_{xz, yz} = E_{x^2-y^2} \rightarrow E_{xz, yz}$; $\Delta E_{xy} = E_{x^2-y^2} \rightarrow E_{xy}$; $\Delta E_{z^2} = E_{x^2-y^2} \rightarrow E_{z^2}$

Discussion

A. Solid Structural Study of $[Cu(tach\text{-}Et_3)Cl_{1.2}Br_{0.8}]$ (108)

X-ray data of **108** indicate a slightly distorted square pyramidal geometry. The tetragonality T^5 defined as the ratio of the four in-plane Cu-L distances and the single long Cu-L distance may give insight into the coordination sphere of **108** even though **108** does not have four nitrogen ligands for a square base. By taking 2.053(2) Å as a distance of the in-plane Cu-L distance and 2.218(5) Å the single long Cu-L distance, the tetragonality, T^5, of **108** is 0.926 which is comparable to 0.925 in $K[Cu(NH_3)_5](PF_6)_3$.[4] However, the τ(%) value, percentage of trigonal distortion from a square pyramid, of **108** is meaningless because the crystallographic mirror plane in **108** generates identical dihedral angles for N(2)-Cu-ClBr(A) and N(2A)-Cu-ClBr which provide a regular square-based pyramid for the coordination sphere of **108**.

The copper(II) ion in **108** seems to be lifted marginally above the mean plane fitted to the four basal atoms, two nitrogens and two halogens, in the direction towards the apical nitrogen atom, N(1) or N(1A). This results in the out-of-plane angles of N(1)-Cu-N(2), N(1)-Cu-N(2A), N(1)-Cu-ClBr, and N(1)-Cu-ClBr(A) of 83.94(12), 96.75(14), 95.24(12), and 108.42(12)° (average 96.1(3)°) respectively. Additionally, the significantly small corresponding basal angle of N(2A)-Cu-ClBr or N(2)-Cu-ClBr(A) (167.63(8)°) also can be explained by this fact. By adding a centroid in the basal plane of **108**, it was estimated that Cu(II) ion is lifted *ca.* 0.51 Å above the base of the square pyramid in **108**, which is slightly larger than the ρ values of the $Cu\text{-}N_5$ complexes in **Table 1.1**. Adding a centroid for the base of the pyramid in **108** which contains two halogen atoms with long

bonds (2.3948(6) Å) and two nitrogen donors with shorter bonds (2.218(5) Å) locates the centroid a little bit closer to the halogens. However, the exact location of the centroid (adjusted centroid) can be calculated from the centroid before adjustment and so as the distance between the adjusted centroid and Cu(II) ion (**Fig 1.35**). The calculated X is 0.032 Å, therefore the distances between N(2) and the adjusted centroid is 2.087 Å and between ClBr and the adjusted centroid is 2.339 Å. The distance between the Cu(II) ion and the adjusted centroid, Y, is calculated giving 0.51Å.

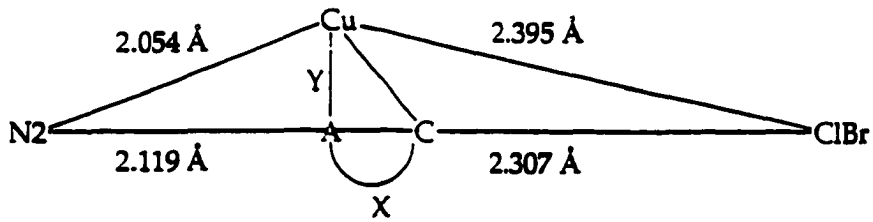

Figure 1.35. Locating the exact position of the centroid. A = adjusted position of the centroid; C = position of centroid before adjustment; bond length between centroid and ClBr = 2.307 Å; bond length between N2 and centroid = 2.119 Å; X = distance between adjusted centroid and centroid before adjustment Y = the distance between the centroid and Cu(II) ion.

The coordination sphere of **108** is comparable to those of [Cu(tach-thioph$_3$)Cl$_2$] and *r*-1[(Z)-(X-benzylidene)amino-k*N*]-*c*-3,*c*-5-diamino-k^2*N*,*N*'-cyclohexane bis(Y)Cu(II) complexes (X = H **113**, 3-hydroxo **114**, and 3,5-dimethoxy **115**, and Y = acetato-*kO* and dichloro),[102] which are Cu(II) complexes of tach based ligands. The coordination sphere of [Cu(tach-thioph$_3$)Cl$_2$] complex **112** (**Fig. 1.36**)[94] can also be described as a distorted square pyramid, with N(3) Cl(2) in the apical positions and N(2), N(3), Cl(1) and Cl(2) forming the square base. The distortion of the coordination sphere in **112** locates N(1) and Cl(2)

toward the apical sites in a trigonal bipyramid and N(2), N(3), and Cl(1) toward the equatorial sites. The structures of **113**, **114**, and **115** all show a five-coordinate Cu(II) centers ligated by two anions and by three nitrogen atoms of the tach ligand. The coordination sphere of these Cu(II) complexes is described as a distorted square pyramid.

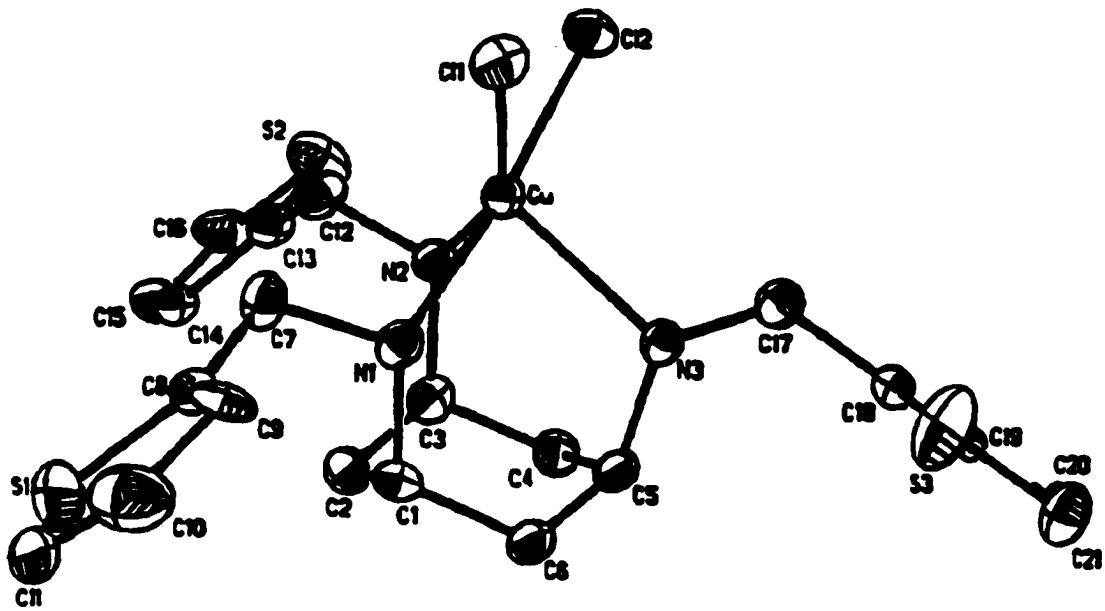

112

Figure 1.36. ORTEP view of [Cu(N-CH_2-2-thienyl)$_3$tachCl_2] showing 50% probability of thermal ellipsoids.[94]

The apical Cu-N(1)bond distance in **108** of 2.218(5) Å is significantly longer than basal bond distance Cu-N(2) of 2.053(2) Å as is typical for a Jahn-Teller distorted copper(II) complex. The apical Cu-N(1) bond distance in **108** of 2.218(5) Å is significantly shorter than the apical Cu-N(3) bond distance, 2.288(3) Å, in **112**, which is presumably the result of the steric effect of a bulky ethyl group in **108** and the fact that the "apical" nitrogen does not lie at a purely apical

position but is distorted toward the basal nitrogens. The bond distance is also considerably shorter than those of 2.246(4), 2.231(4), 2.401(7), 2.395(4), and 2.446(3) Å in [Cu([9]aneN$_3$)Cl$_2$] **90**,[103] [Cu([9]aneN$_3$)Br$_2$],[104] **113**, **114**, and **115**,[102] respectively.

The basal Cu-N(2)bond distance of 2.053(2) Å in **108** is, however, comparable to those of 2.065(3) and 2.069(3) Å in **112**, 2.046(4) and 2.047(4) Å in [Cu([9]aneN$_3$)Br$_2$], and 2.038(4) and 2.063(4) Å in **90**. The basal bond distance in **108** is slightly longer than those 2.006(4) in **113**, 1.990(3) in **114**, and 2.000(3) and 2.013(3) Å in **115**, respectively.

B. Electronic Spectra of [Cu(tach-R_3)X_2]

Colors of [Cu(tach-R_3)X_2] complexes in MeOH or in aqueous solutions are either blue or greenish blue, typical for the Cu(II)N_n complexes.[3] The color of the solid complex [Cu(tach-Et_3)Cl_2] in KBr is also blue. All visible-near IR spectra of [Cu(tach-R_3)X_2] complexes in solution and solid [Cu(tach-Et_3)Cl_2] complex contain a band maximum around 700 nm (~14,500 cm^{-1}) with a low-energy shoulder, this indicates that the coordination geometry of the complexes is square pyramidal.

In order to obtain the exact wavenumber (or wavelength) of the each three transitions, d_{xz} or d_{yz} -> d_{x2-y2}, d_{xy} -> d_{x2-y2}, and d_{z2} -> d_{x2-y2}, and the positions of the underlying transitions, Gaussian function analyses of the spectra were undertaken by Junlong Shao. The three simulated individual peaks correspond to the three *d-d* transitions mentioned earlier, and the final simulated spectrum was generated by the summation of the three simulated peaks. All simulated spectra match the experimental spectra very well. The experimental visible-near IR spectrum and simulated spectrum of [Cu(tach-Et_3)Cl_2] are presented in **Figure 1.37.** The wavenumbers obtained by simulation of the three *d-d* transitions of [Cu(tach-R_3)Cl_2] complexes are listed in **Table 1.7.**

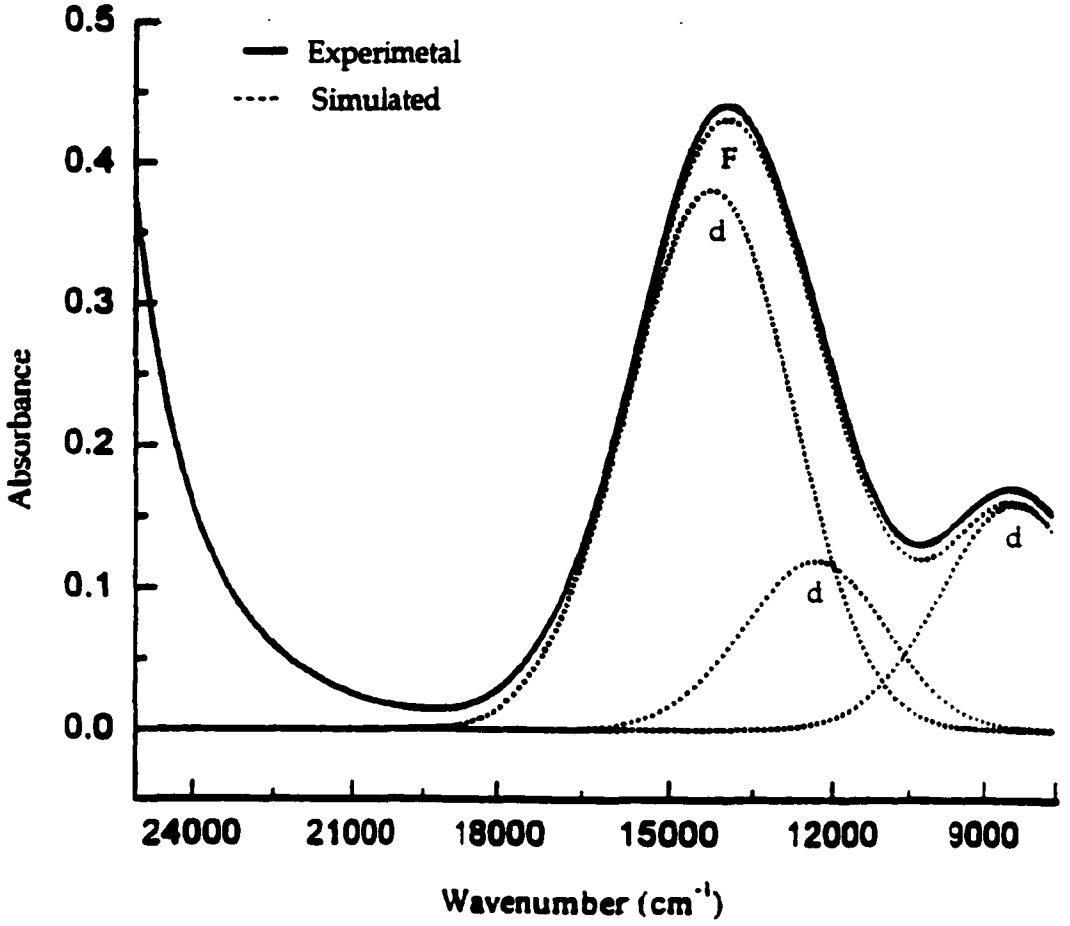

Figure 1.37. The simulated and experimental electronic spectrum of $[Cu(tach\text{-}Et_3)Cl_2]$, F = finally simulated spectrum generated by the summation of the individually simulated three *d-d* transitions (d).[101, 105]

Table 1.7. Height A_i, bandwidths B_i, and wavenumbers υ_i of the three *d-d* transitions in the visible-near IR spectra of $[Cu(tach\text{-}R_3)Cl_2]$ complexes in MeOH. All values are taken from the Gaussian function analyses.[101]

Metal complex	*d-d* transition	υ_i (cm^{-1})	A_i	$2B_i$ (cm^{-1})
$[Cu(tach\text{-}Me_3)Cl_2]$	1	14252	0.381	1731
	2	12316	0.122	1593
	3	8388	0.159	1755
$[Cu(tach\text{-}Et_3)Cl_2]$	1	14252	0.381	1731
	2	12321	0.119	1603
	3	8398	0.159	1755
$[Cu(tach\text{-}Pr_3)Cl_2]$	1	14482	0.375	1862
	2	12491	0.097	1703
	3	8588	0.159	1765
$[Cu(tach\text{-}furanyl_3)Cl_2]$	1	14472	0.281	1732
	2	12481	0.059	1703
	3	8698	0.131	1755
$[Cu(tach\text{-}thioph_3)Cl_2]$	1	14892	0.215	2001
	2	12656	0.022	2103
	3	9128	0.096	1825

d-d transition: 1, d_{xz} or d_{yz} -> d_{x2-y2}; 2, d_{xy} -> d_{x2-y2}; 3, d_{z2} -> d_{x2-y2}.

C. Structural Study of $[Cu(tach\text{-}Et_3)]^{2+}$ in Aqueous Medium

The titration of a 1:1 mixture of Cu(II) and the ligand, tach-Et_3•3HBr over the pH range 4.9 to 11.0 indicates that the complex does not undergo appreciable hydrolysis up to pH 10.4. The titration data also indicate the formation of $[Cu(tach\text{-}Et_3)H_2]^{4+}$ **116** and $[Cu(tach\text{-}Et_3)H]^{3+}$ **117** in the region of $a = 0$ to $a = 2$ (pH 6.82) of the titration curve. The titration curve data indicates the formation of a $[Cu(tach\text{-}Et_3)(H_2O)_2]^{2+}$ species beyond a = 2; the $[Cu(tach\text{-}Et_3)(H_2O)_2]^{2+}$ species is the only species in solution until the titration curve started to flatten around a pH of 10.4. The titration curve for the Cu(II)-L system is presented in **Figure 1.33 (A)**.

The final concentration of 0.5 mM for Cu(II)-L was used in this titration study because a pale blue precipitate forms around pH 6.7 (around $a = 2$) with a higher concentration ($\geq$ 0.5 mM) of the samples. Even though there is the formation of a precipitate, the titration curve obtained with a higher concentration (> 1.0 mM) was almost identical to those obtained with the 0.5 mM sample concentration. The pale blue precipitate is assumed to be either an insoluble Cu(II) hydroxide ($Cu(OH)_2$) or a polymeric species, however, further characterization was not attempted. The proposed mechanism for the formation of the polymeric species is presented in **Scheme 1.36**. After two equivalents of base ($a = 2$) is added, a proton equilibrium exists. A conformation change from a chair form to a twist boat form of a cyclohexane ring allow the uncoordinated nitrogen atoms in **118 (Scheme 1.36)** to coordinate to an adjacent Cu(II) complex affording a polymeric species.

The attempt to obtaining a titration curve by directly dissolving the green solid $[Cu(tach\text{-}Et_3)Cl_2]$ has been unsuccessful due to the formation of a pale blue

precipitate at concentrations above *ca.* 1.0 mM. Dilution of a concentrated solution of $[Cu(tach\text{-}Et_3)Cl_2]$ in MeOH with water avoids the formation of a precipitate, and its titration curve is similar to that obtained from the sample generated *in situ.* (**Figure 1.33 (B)**).

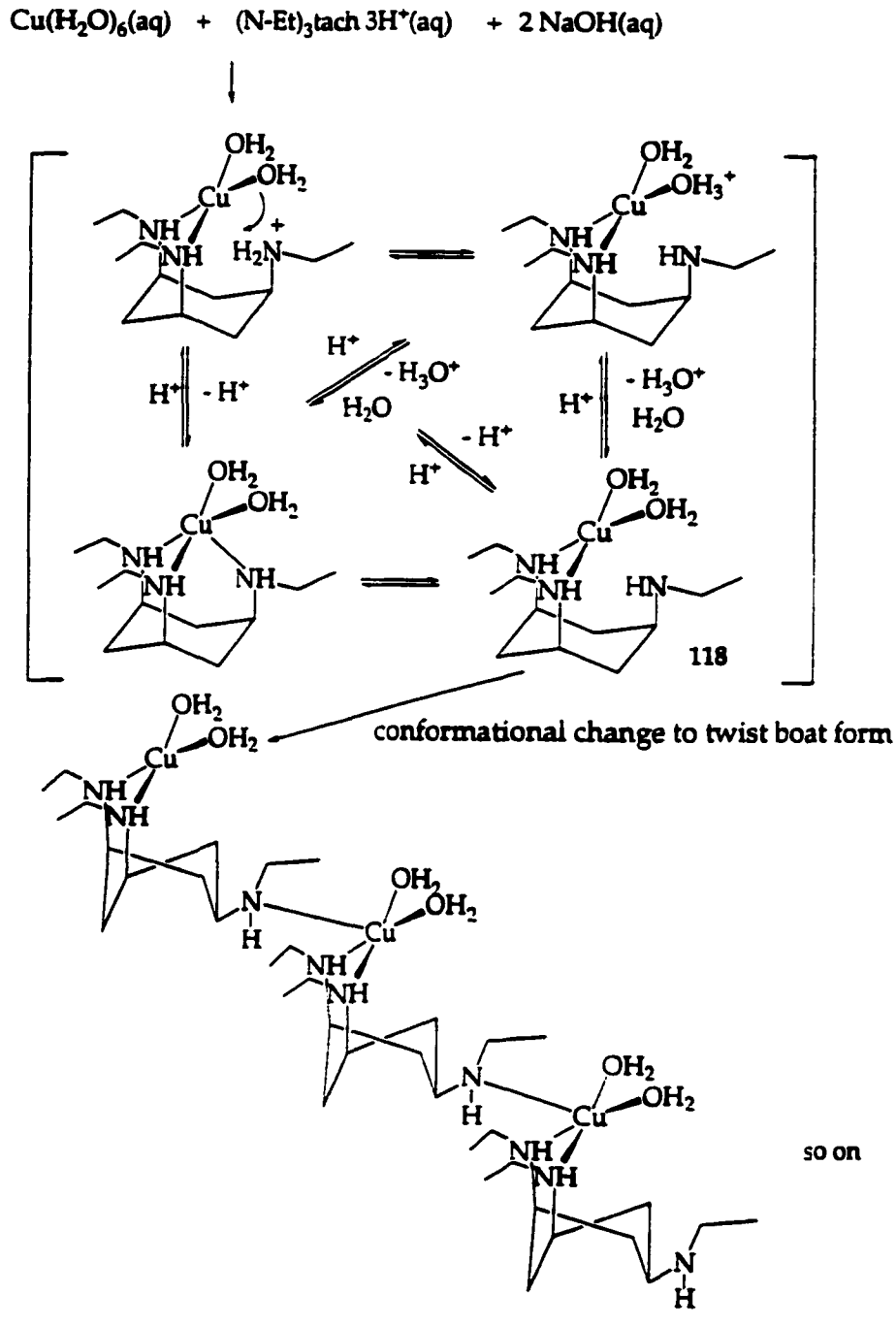

Scheme 1.36. Proposed mechanism for the formation of a polymeric species.

The change in the chemical species with the pH of the solution was investigated by visible-near IR spectra. Samples were prepared by diluting a concentrated solution (40 mM [Cu(tach-Et_3)$Br_{0.8}Cl_{1.2}$]) in anhydrous MeOH with a

50 mM Hepes solution affording the final concentration of 0.5 mM with pH values of 5.0, 6.7, 7.4, and 11.0. The Visible-near IR spectra at each pH were obtained by running samples against Hepes solutions as a reference with the identical pH. In order to identify the chemical species at pH 5.0, the sample spectrum obtained at pH 5.0 was compared to that of $CuCl_2$ in water, pH 5.0. **Table 1.8** lists the electronic absorption spectral data for each pH and a proposed chemical species for $[Cu(tach\text{-}Et_3)Br_{0.8}Cl_{1.2}]$ dissolved in buffer at that pH.

Visible-near IR electronic spectra data suggest that a protonated (on one of nitrogen atoms) species $[Cu(tach\text{-}Et_3)H(H_2O)_2]^{3+}$ (**119**) is the only species present at pH 6.7 (a = 2). Beyond a = 2.6 (pH 7.4) the diaqua species $[Cu(tach\text{-}Et_3)(H_2O)_2]^{2+}$ (**120**) is the only species in solution. All visible-near IR electronic spectra data and the proposed species at different pH are consistent with the titration data (**Fig. 1.37**). The wavelength of a band maximum for $[Cu(tach\text{-}Et_3)H(H_2O)_2]^{3+}$, in which two nitrogen atoms are coordinated to Cu(II), is 710 nm and higher than the diaqua complex, $[Cu(tach\text{-}Et_3)(H_2O)_2]^{2+}$, in which three nitrogen atoms coordinated. $[Cu(tach\text{-}Et_3)(H_2O)_2]^{2+}$ has a band maximum at 670 nm with a low-energy shoulder and is comparable to those of $[Cu(tach)(H_2O)_2]^{2+}$ and $[Cu([9]aneN_3)(H_2O)_2]^{2+}$ species, 680 nm and 658 nm respectively.[91] The blue shift, a band maximum shift to higher energy, observed between two species $[Cu(tach)(H_2O)_2]^{2+}$ and $[Cu(tach)(OH)(H_2O)]^{+}$ and $[Cu([9]aneN_3)(H_2O)_2]^{2+}$ and $[Cu([9]aneN_3)(OH)(H_2O)_2]^{+}$ complexes, 39 nm and 36 nm respectively,[91] was not observed indicating the hydroxo-aqua species $[Cu(N\text{-}Et)_3tach(OH)(OH_2)]^{+}$ does not form in this system.

Table 1.8. Band maximums of $[Cu(tach\text{-}Et_3)X_2]$ and proposed chemical species at different pH.

pH	5	6.7	7.4	11.0
Wavelength of a band maximum	810 nm	710 nm	672 nm	666 nm
Proposed species	$Cu(H_2O)_6(aq)$	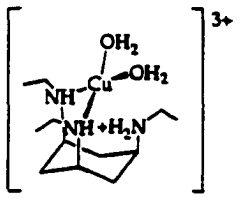 119	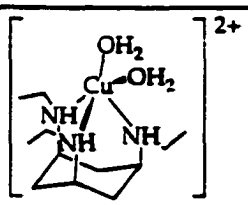 and small amount of 119	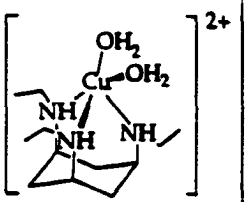 120

D. EPR and ENDOR Studies of $[Cu(tach\text{-}R_3)X_2]$

The X-band and Q-band EPR spectra of $[Cu(tach\text{-}R_3)]^{2+}$ complexes in aqueous or in MeOH solutions and the Q-band EPR of powder samples of $[Cu(tach\text{-}R_3)Cl_2]$ were measured by Junlong Shao to investigate the structure around a copper(II) ion and to determine the orbital bonding coefficients.

The low temperature (100 K) Q-band EPR spectra of the powder $[Cu(tach\text{-}R_3)]^{2+}$ complexes indicate that only the $[Cu(tach\text{-}Et_3)Cl_2]$ has an EPR spectrum of a single species. The other powdered samples have spectra indicating the presence of more than one species (**Fig. 138A**).[101] At 100 K, the Q-band spectrum of the powder $[Cu(tach\text{-}Et_3)Cl_2]$ did not show evidence for rhombicity. A clear rhombic feature of this complex, consistent with its distorted square pyramidal geometry in X-ray structure, was obtained at room temperature giving three peaks with $g_x = 2.061 \pm 0.001$, $g_y = 2.071 \pm 0.001$, and $g_z = 2.262 \pm 0.001$.

The frozen (77 K) X-band EPR spectra of the $[Cu(tach\text{-}R_3)]^{2+}$ complexes in a mixture 50 mM Hepes/glycerol (2:1) with pH 7.4 indicated that all $[Cu(tach\text{-}R_3)]^{2+}$ complexes have similar structures with no indication of a rhombicity within the resolution of the spectral lines. The loss of rhombicity in the solution EPR spectra may be a result of an increased flexibility of the Cu(II) complexes, causing a slight structural change, in the solution environment. The ^{63}Cu EPR spectra at X-band are characteristic for monomeric copper(II) species in solution, however, no evidence of ligand $^{14}N(I=1)$ superhyperfine coupling was observed because of broad low-field parallel peaks.

One of the parallel peaks was superimposed on a perpendicular peak in

the X-band spectra of these samples. Therefore Q-band EPR spectra were measured in order to obtain the spin Hamiltonian parameters for these complexes. The Q-band EPR spectra of frozen samples of 5 mM $[Cu(tach\text{-}R_3)]^{2+}$ complexes in a mixture 50 mM Hepes/glycerol (2:1) with a pH of 7.4 were obtained giving the completely separated parallel and perpendicular peaks and are presented in **Figure 1.38.**

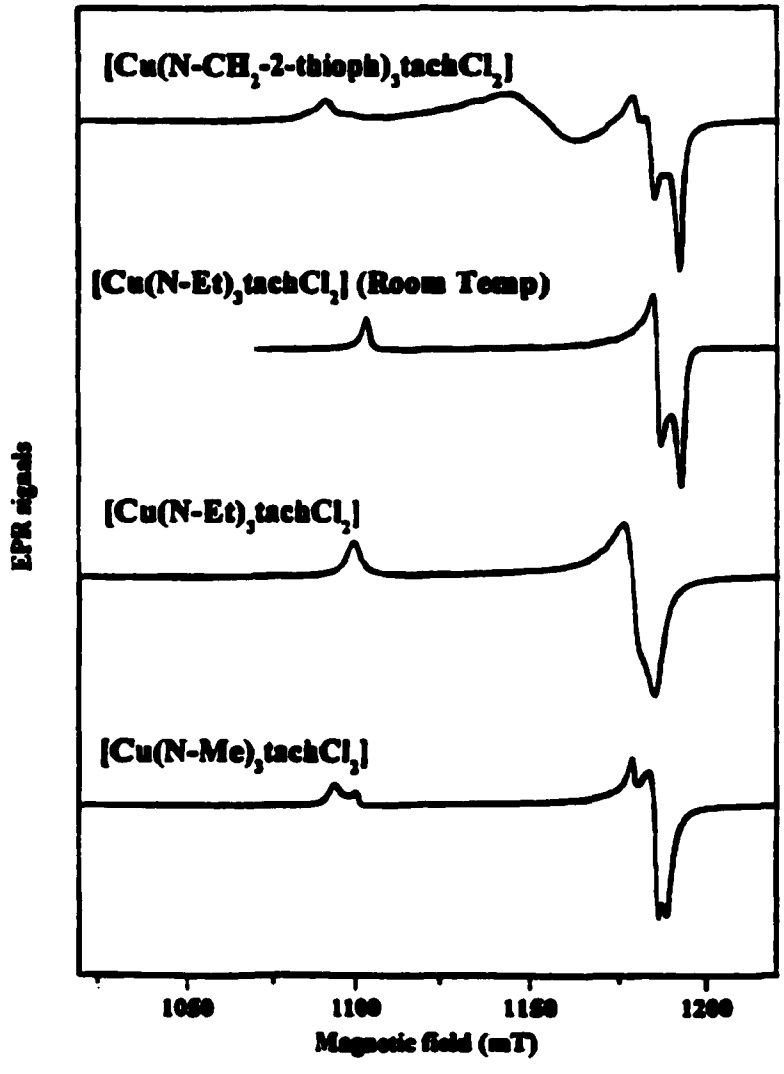

Figure 1.38A. The Q-band powder EPR spectra of $[Cu(tach\text{-}R_3)Cl_2]$

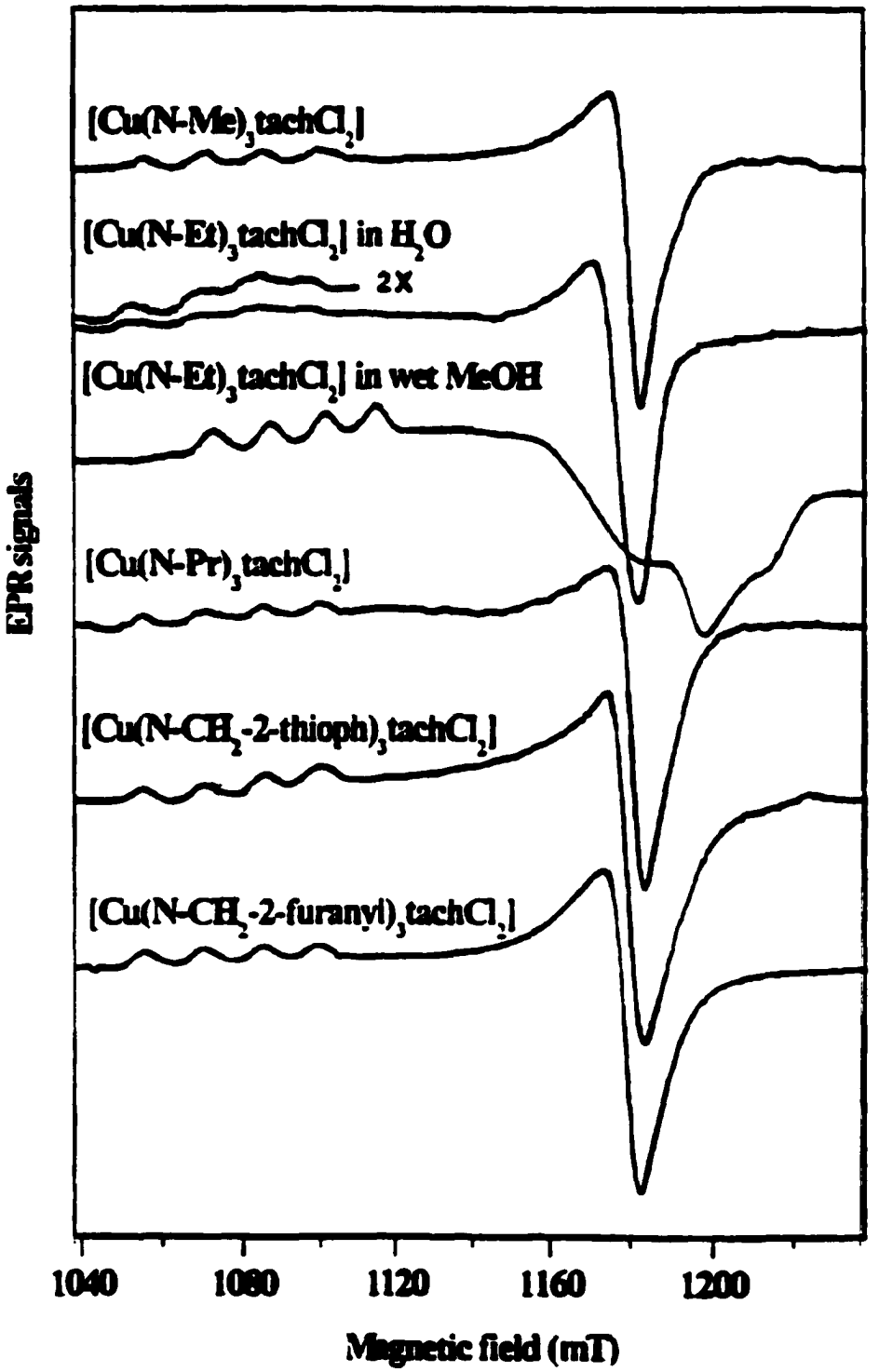

Figure 1.38. The Q-band EPR spectra of the frozen $[Cu(tach\text{-}R_3)]^{2+}$ complexes at 100 K.[96]

Table 1.9. The spin Hamiltonian parameters obtained by 100 K Q-band and R.T. X-band of the $[Cu(tach\text{-}R_3)]^{2+}$ complexes.[96]

Metal complex	g_o	$g_{//}$	$g_\perp$	$A_o(10^{-4}\ cm^{-1})$	$A_{//}(10^{-4}\ cm^{-1})$	$A_\perp(10^{-4}\ cm^{-1})$
$[Cu(tach\text{-}Me_3)]^{2+}$ in Hepes	2.127	2.264	2.066	58	166.9	3.5
$[^{63}Cu(tach\text{-}Me_3)]^{2+}$ in Hepes	2.132	2.265	2.066		164	
$[Cu(tach\text{-}Et_3)]^{2+}$ in Hepes	2.128	2.266	2.066	55.5	164.3	1.2
$[Cu(tach\text{-}Et_3)]^{2+}$ in Caps	2.128	2.263	2.061		165	
$[Cu(tach\text{-}Et_3)Cl_2]$ powder	2.131	$g_z = 2.262$	$g_x = 2.061$ $g_y = 2.061$			
$[Cu(tach\text{-}Pr_3)]^{2+}$ in Hepes	2.127	2.266	2.065	59.3	164.0	6.7
$[Cu(tach\text{-}furanyl_3)Cl_2]^{2+}$ in Hepes	2.127	2.261	2.064	58.8	164.0	6.2
$[Cu(tach\text{-}thioph_3)Cl_2]^{2+}$ in Hepes	2.124	2.261	2.063	60.5	165.7	8.0

- All the g-values have an error of ± 0.001 and all the hyperfine couplings have an error of ± 0.2 x 10^{-4}
- The concentrations of $[Cu(tach\text{-}R_3)]^{2+}$ complexes in Hepes are 5 mM with a pH of 7.4.
- The concentration of $[Cu(tach\text{-}Et_3)]^{2+}$ complex in Caps is 2.5 mM with a pH of 10.1.
- All the⊥ values are calculated by $A_o = 1/3\ A_{//} + 2/3\ A_\perp$.
- The powder EPR of $[Cu(tach\text{-}Et_3)Cl_2]$ complex shows a rhombic symmetry in its g-values.

The $g_{//}$ and $A_{//}$ were calculated from the four parallel peaks. Only a $g_{\perp}$ value was measured from the perpendicular peak since the perpendicular peak did not show any hyperfine splitting. The spin Hamiltonian parameters of $[Cu(N\text{-}R)_3tach]^{2+}$ complexes are listed in **Table 1.9**. The g-values ($g_{//} > g_{\perp} > 2.0$) indicate that the coordination geometries of those samples in solution are identical and are square pyramidal with nitrogen ligands which is known to give a $g_{//}$ value around 2.230 and a $g_{\perp}$ value around 2.060.[7] The steric effects of substituents on the coordinated nitrogen seem to have no effect on the first coordination sphere of the complexes according to their g-values and hyperfine couplings.

The displacement of the coordinated halide ions by water molecules is expected to occur when the EPR samples of the $[Cu(tach\text{-}R_3)]^{2+}$ complexes were prepared by dissolving solid in buffered solution or by generating the material *in situ*. A result of the halide displacement, smaller $g_{//}$ and $A_{//}$ values in an aqueous sample compared to those in MeOH or in the powder sample were anticipated and observed since H_2O is a stronger field ligand than halides ion in the spectrochemical series.[100] This theory could be used to distinguish different chemical species of the Cu(II) complex $[Cu(tach\text{-}Et_3)(H_2O)_2]^{2+}$ and $[Cu(tach\text{-}Et_3)(OH)(H_2O)]^{+}$ at a given pH. The similar spin Hamiltonian parameters, obtained from EPR spectra of the $[Cu(N\text{-}Et)_3tach]^{2+}$ complex at pH 7.8 and 10.1, indicates the presence of one species at both pH values.

The LCAO-MO bonding parameters of $[Cu(tach\text{-}Et_3)]^{2+}$ in aqueous media were calculated by Junlong Shao from the visible-near IR electronic spectra and the EPR spin Hamiltonian parameters. The calculation yields α^2 of ~ 0.78 (in-

plane σ bond), β^2 of ~ 0.92 (in-plane π bond), and β_1^2 of 0.88 (out-of-plane π bond)[101], the squares of MO coefficients of the metal centered d_{x2-y2}, $d_{xz, yz}$ and d_{xy} orbitals, respectively. Bonding parameters of 0.5 and 1.0 indicate a pure covalent bond and a pure ionic bond, respectively. Therefore, the α^2 (0.78) value shows moderate in-plane σ bonding, while β^2 (0.92)and β_1^2 (0.88) bonding parameters indicate rather ionic in-plane π and out-of-plane π bond character; this is consistent with the substitution of Cl^- by H_2O in the equatorial plane of the complex. All of the results described above support $[Cu(tach\text{-}Et_3)(H_2O)_2]^{2+}$ as the main species in aqueous media in the pH range of 7.4 – 10.1.

E. Catalytic Hydrolysis of Phosphate Diester Promoted by $[Cu(tach\text{-}Me_3)]^{2+}$

Product analysis and kinetic measurements for the catalytic hydrolysis of phosphate diesters promoted by $[Cu(tach\text{-}Me_3)]^{2+}$ were investigated by Dr. Kim Deal at NIH. The results of the catalytic activity study are summarized herein.

A solution of $[Cu(tach\text{-}Me_3)]^{2+}$ (**121**) was prepared *in situ* due to availability and efficiency of highly concentrated samples compared to dissolving an appropriate quantity of a solid. Reversed-phase HPLC was used to determine the products, *p*-nitrophenyl phosphate and *p*-nitrophenolate , of the hydrolysis of BNPP by **121** in comparison with co-injected authentic standards. The reaction kinetics of **121** with BNPP were studied using the method of initial rates, a convenient method for slow reactions. The only significant spectral change occurred at 400 nm, which corresponds to the formation of p-nitrophenolate. When the [Cu(II)]:[tach-Me_3] ratio (*r*) is one, the maximum rate is obtained. The formation of an uncharacterized blue solid with a decrease in rate was observed as *r* exceeded one.

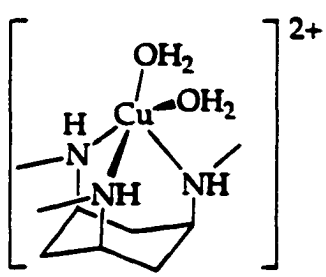

121

Figure 1.39. $[Cu(tach\text{-}Me_3)(H_2O)_2]^{2+}$ complex.

Dr. Deal observed the second-order dependence on the concentration of the metal complex in the hydrolysis of BNPP by **121**. The initial rate of the hydrolysis of BNPP by **121** increases with increasing pH (**Fig. 1.40 (a)**), and a plot of log(initial rate) versus pH yields two linear regions, which intersects at a kinetic p*K*a of 7.3 (**Fig. 1.40 (b)**).

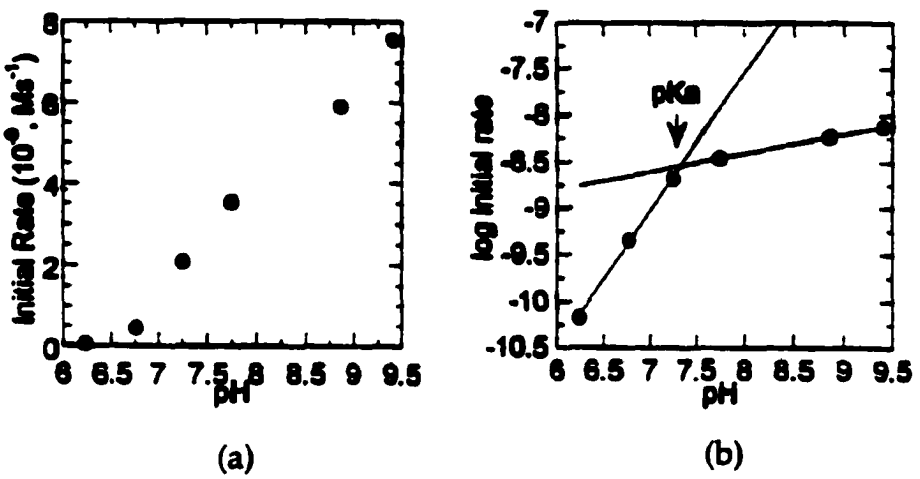

Figure 1.40. (a) pH dependence; (b) plot of log(initial rate) versus pH.[105]

The following mechanism is proposed based on mechanistic analysis and is consistent with observed reaction orders. The $[Cu(tach\text{-}Me_3)]^{2+}$ complex in aqueous media is denoted by LCu and substrate (BNPP) by S:

$$LCu + S \rightleftharpoons LCu\text{-}S \qquad K_1 \qquad (1)$$

$$LCu\text{-}S + LCu \rightleftharpoons LCu\text{-}S\text{-}CuL \text{ (122a, b, or c)} \qquad K_2 \qquad (2)$$

$$\text{122a, b, or c} \longrightarrow \text{products} \qquad k_3 \qquad (3)$$

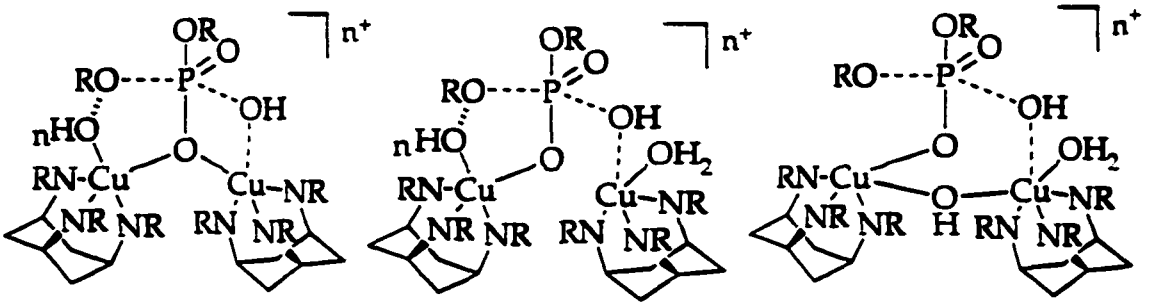

122a, n = 1 or 2 **122b**, n = 1 or 2 **122c**

Scheme 1.37. Proposed mechanism and dinuclear LCu-S-CuL intermediates.

The rate of reaction in terms of the product formation is derived by assuming that the first two steps are in pre-equilibrium:

$$V = d[\text{products}]/dt = K_1K_2k_3[LCu]^2[S] \qquad (4)$$

Equation (1) and (2) is combined for the formation of the $[Cu(tach\text{-}Me_3)^{2+}]_2$-phosphate diester complex in one step, and equation (4) is reduced to equation (6):

$$2\,LCu + S \rightleftharpoons LCu\text{-}S\text{-}CuL \qquad K_o \qquad (5)$$

$$V = d[\text{products}]/dt = Kok_3[LCu]^2[S] \qquad (6)$$

The rate of the phosphate diester hydrolysis promoted by $[Cu(tach\text{-}Me_3)]^{2+}$ ($8.0 \times 10^{-6} s^{-1}$) is approximately 6.5 times faster compared to that of $[Cu[9]aneN_3]^{2+}$ ($1.6 \times 10^{-6} s^{-1}$)[87] with same substrate. The formation of a dimeric intermediate prior to the hydrolysis of substrate in the $[Cu(tach\text{-}Me_3)]^{2+}$ system was proposed

(**Scheme 1.37**) and is consistent with kinetic data; being second-order in metal complex. It is clear that the substrate must bind to monomeric $[Cu(tach\text{-}Me_3)]^{2+}$ (step (1)), to form a dimer complex. EPR studies clearly indicate that there is no formation of a binuclear complex $[Cu(tach\text{-}Me_3)_2]^{2+}$ in aqueous media without the substrate, while in presence of substrate, the formation of an antiferromagnetically coupled dimeric complex was observed affording 21% and 37% reduced EPR signal intensity. Thus, the possibility of structure **122b** as an intermediate was ignored since it would not give a strong exchanged-coupled signal in EPR. Both **122a**, n=1 and **122c** require the deprotonations of two coordinated water ligands from the dimer, suggesting that two kinetic p*K*a's would be observed in the pH-rate profile (**Fig. 1.40 (b)**). Since only one kinetic p*K*a (7.3) is observed in $[Cu(tach\text{-}Me_3)]^{2+}$ system, the **122a**, n=1 and **122c** intermediates are unlikely.

The markedly higher affinity of **121** (230 M^{-1}) for the phosphate diester was observed in saturation kinetics and suggests a greater Lewis acidity for **121** relative to $[Cu(bipy)_2]^{2+}$ or $[Cu[9]aneN_3]^{2+}$ which have affinity constant of 20 M^{-1} and 15 M^{-1}, respectively.[81, 87] The intermediates **122** show a concerted process of intramolecular attack of the coordinated hydroxide at the phosphorus center with a penta-coordinated phosphorane intermediate (see Chapter 1 introduction). Furthermore, the intermediate **122** proposed in this study resembles those for the hydrolysis of the 3′ terminal nucleotide in single-stranded DNA 3′-5′exonuclease activity promoted by DNA polymerase I.[41] The overall similarity of the proposed mechanism of $[Cu(tach\text{-}Me_3)]^{2+}$ with DNA polymerase I suggests $[Cu(tach\text{-}Me_3)]^{2+}$ may have significant biological activity.

Conclusion

The structures of $[Cu(tach\text{-}R_3)X_2]$ complexes were investigated in this study. X-ray structure of $[Cu(tach\text{-}Et_3)Cl_{1.2}Br_{0.8}]$ shows a slightly distorted square pyramidal geometry with an elongated apical nitrogen bond due to the John-Teller distortion about Cu(II) center. The powder EPR study supports the stereochemistry of the same complex by showing rhombicity. Contrary to the solid structure, the coordination spheres of $[Cu(tach\text{-}R_3)X_2]$ in solution are more symmetrical but maintain a square pyramidal geometry according to EPR and visible-near IR spectra. Displacement of halide ions with water molecules occurs in aqueous media and can be detected by EPR and visible-near IR spectra. $[Cu(tach\text{-}Me_3)]^{2+}$ promotes the hydrolysis of activated phosphate diesters in aqueous medium at pH 7.24. A kinetic p*K*a of 7.3 is consistent with the deprotonation of a metal-bound water to form a hydroxide ion which attacks the phosphorus center in the rate-determining step of the ester cleavage. The hydrolysis is first-order in phosphate ester and second-order in $[Cu(tach\text{-}Me_3)]^{2+}$, suggesting a binuclear complex in which a substrate bridges two Cu(II) ions. The similarity of $[Cu(tach\text{-}Me_3)]^{2+}$ to DNA polymerase I suggests $[Cu(tach\text{-}Me_3)]^{2+}$ would be a promising synthetic DNA nucleases.

CHAPTER 2

IRON-MEDIATED LIGAND OXIDATION, BIOCHEMICAL PROPERTIES OF IRON COMPLEXES, AND NOVEL IRON CHELATORS BASED ON TACH LIGANDS

Summary

In this chapter of my dissertation, the iron complexation study of novel hexadentate tachpyr derivatives, and the oxidative dehydrogenation of the tachpyr and the (+/-)tach(C-Me)$_3$pyr ligands leading to the formation of corresponding imino species have been presented. Attempts for formation of a hydroxyl radical which causes oxidative damage to DNA in the presence of iron complexes of the tachpyr derivatives, and preliminary competition studies between Zn(II) and Fe(II) for complexation with tachpyr ligand have been investigated. The collaborate study described herein with Professor Suzy Torti at Wake Forest University of School of Medicine focuses on the iron chelation study and tumor cell cytotoxicity of the tachpyr chelator.

Introduction

In this introduction, pathways of iron uptake and regulation in cells, oxidative degradations of DNA through H-abstraction, transition metal induced oxidative dehydrogenation, and iron chelators will be discussed to understand structural, iron-mediated ligand oxidation, and biochemical properties of novel hexadentate tachpyr derivatives.

A. Uptake and Storage of Iron

Iron is the second most abundant metal after aluminum and the fourth most abundant element in the Earth's crust (approximately 5%).[2] Its great abundance and two readily interconvertible redox states have led to incorporation of iron at the active centers for an astonishing array of biological reactions. Iron is ubiquitous in the form of many non-heme Fe-containing proteins or as the Fe-protoporphyrin complex of heme-proteins. Iron plays essential roles in cell growth and replication since many Fe-containing proteins catalyze important reactions involved in energy metabolism (cytochromes, mitochondrial aconitase, Fe-S proteins of the electron transport chain), respiration (hemoglobin and myoglobin), and DNA synthesis (ribonucleotide reductase).[106]

The intracellular concentration of iron, not bound to organic ligands, is tightly controlled in animals, plants, and microbes. Under physiological conditions, free iron exists as an oxidized form, the ferric state, and ferric salts form insoluble ferric hydroxide polymers at neutral pH and aerobic conditions within cells. An additional reason for tight control of the level of free iron is that

iron can readily participate in one-electron transfer reactions that produce very harmful free radicals (**Scheme 2.1**) such as the hydroxyl radical which can damage cells by initiating autooxidative chain reactions.

$$O_2^{\cdot-} + Fe^{3+} \longrightarrow O_2 + Fe^{2+}$$

$$2O_2^{\cdot-} + 2H^+ \longrightarrow O_2 + H_2O_2$$

$$Fe^{2+} + H_2O_2 \longrightarrow Fe^{3+} + OH^- + OH\bullet$$

Scheme 2.1. Haber-Weiss reaction.

Free ion, whether in solution or precipitated as a polymeric hydroxide, as well as some iron-ligand complexes, can participate in this reaction.[107] Microorganisms secrete Fe-chelating molecules with high affinity known as siderophores[23], while higher organisms have developed Fe-binding proteins known as the transferrins (Tfs) in order to overcome these problems above. Biological organisms control intracellular iron concentrations at a number of process including uptake into the organism, transport, and reversible storage within it.

A.1 Uptake of Iron

Many microorganisms acquire iron by using siderophores secreted by the bacteria (**Fig. 2.1**) which are small molecules with the ability to chelate iron tightly. These bind iron, and resulting iron-siderophore complexes are then absorbed through specific receptors in their outer membrane by the bacteria.

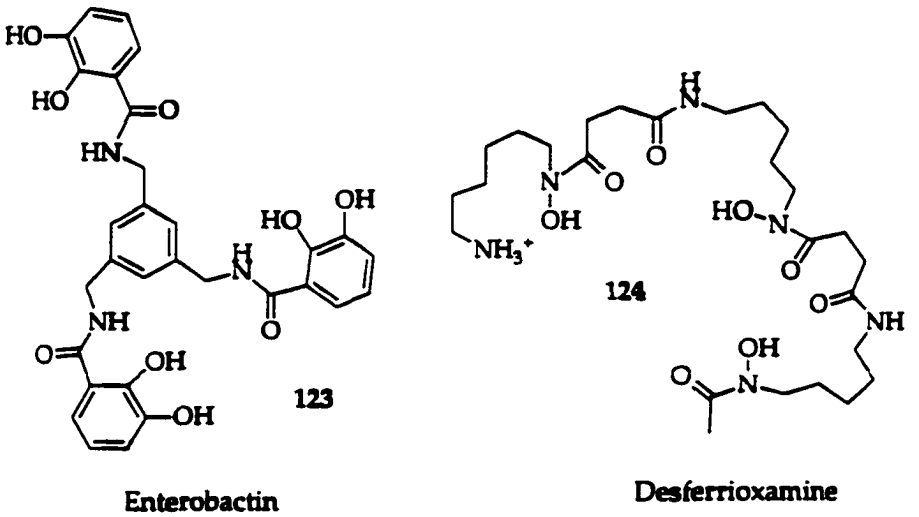

Figure 2.1. Example of siderophores.

After the absorbed iron-siderophore complexes are broken down, iron is released as a reduced form Fe^{2+}, which binds much less tightly to the siderophores. However, some appear to release their iron following enzymatic degradation of the siderophore itself. The deferrated siderophore must be either stored, rapidly excreted, or altered when the metal is released.[108]

Unlike plants and microorganisms, which use small molecules as iron carriers, animal usually use iron transport proteins, the transferrins Tf, which provides iron for cells and tissues utilizing this metal. The transferrins are member of a family of proteins that include serum Tf, lactoferrin, ovotransferrin, and melanotransferrin.[106] Transferrin binds two atoms of Fe(III) with high affinity ($K_d = 10^{-23}$ M), and binding of Fe to Tf is a pH-dependent process, a property that is involved in the physiological mechanism of Fe release from the protein.[109]

The X-ray structure of lactoferrin and transferrin have been determined and showed bi-lobed proteins with each lobe possessing a binding site for a single iron atom. Under physiological conditions, the iron binds in the Fe^{3+} oxidation state with extremely high affinity that occurs only with a carbonate anion binding with each Fe^{3+}.[23]

The coordination sphere of iron in transferrin is distorted octahedral, consisting of two phenolate oxygens from tyrosine, one imidazole nitrogen from histidine, one carboxylate oxygen from aspartic acid, and two oxygens from bound carbonate. The carbonate is also hydrogen-bound to side chains from arginine and threonine and to two peptides NH groups (**Fig. 2.2**). The protein provides a binding site for carbonate that consists of the hydrogen-bonding units. After carbonates binds in this pocket, the metal binding site is fully organized for a coordination of Fe(III) since oxygen-rich environment of ligands prefer a relatively hard metal ion like Fe(III).

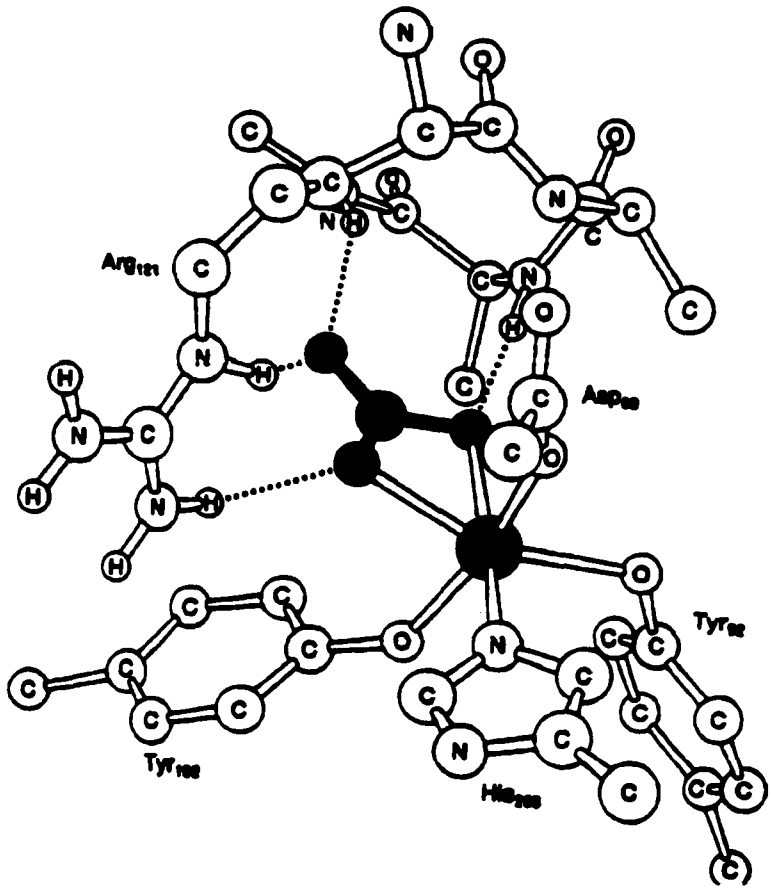

Figure 2.2. Active site structure of lactoferrin, showing the coordination of the iron and bound carbonate.[23]

The iron is carried across cell membranes via receptor-mediated endocytosis (**Figure 2.3**). This process involves the iron-transferrin complex binding to a specific receptor on the cell surface and then being taken into the cell where the iron is released in the acidic environment (pH 5.5) of the endosome.[110] The transferrin receptor is a large dimeric glycoprotein that binds iron-containing transferrin but not apotransferrin.

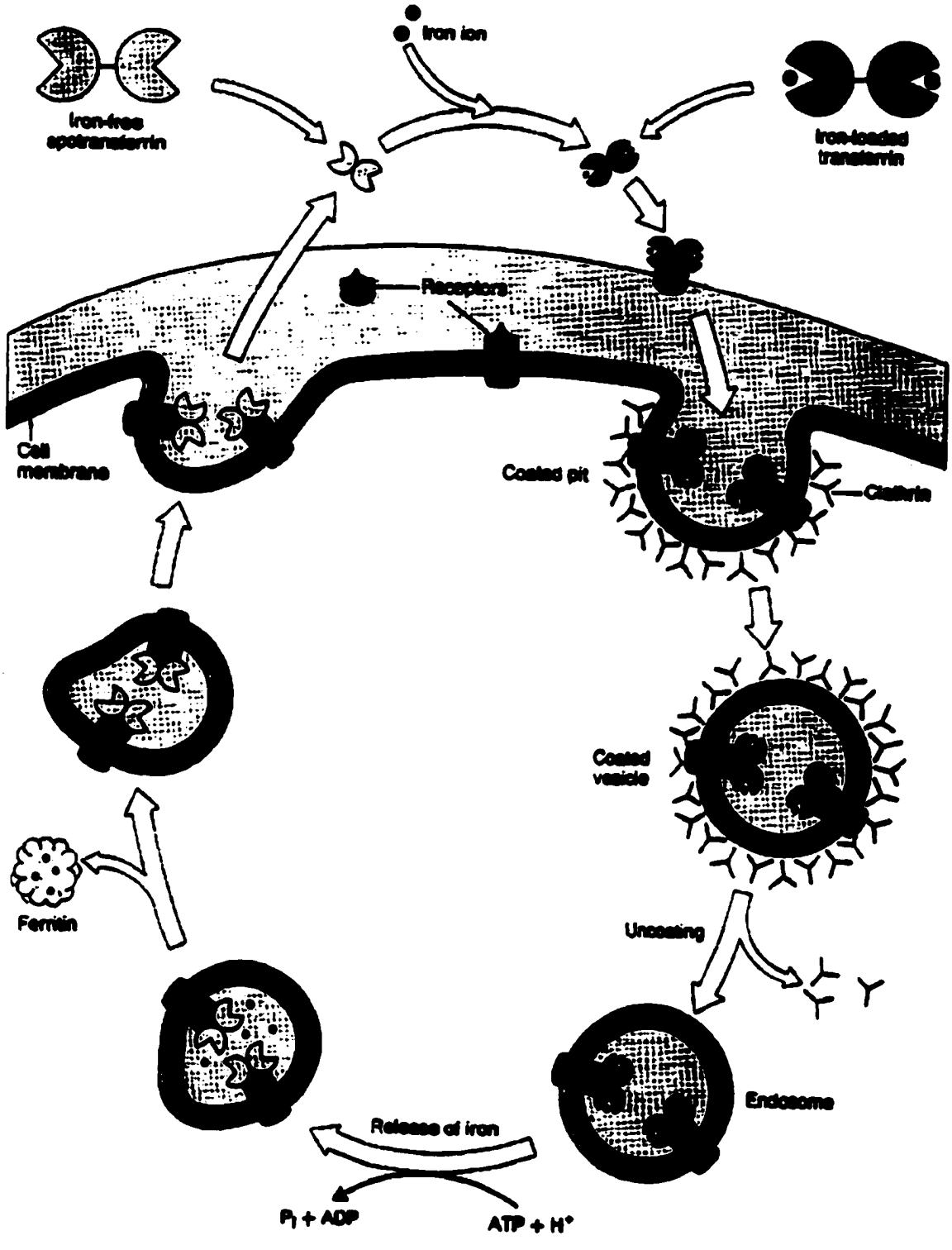

Figure 2.3. The extracellular binding of iron to transferrin, receptor-mediated endocytosis, ATP-driven release of iron into the endosome, and loading of the metal ion into ferritin.[23]

The large conformational changes in transferrin that happen upon binding carbonate and iron are essential to this differentiation between loaded and unloaded transferrin.[23] Once the receptor binds transferrin, a portion of the membrane containing the receptor pinches off to form a "coated" vesicle. Inside the cell, this vesicle uncoats to form an endosome. The membrane of the endosome has ATP-driven proton pumps that provide protons into the endosome to lower the pH between 5 and 6. At this low pH, the iron is released as a result of protonation of the carbonate and tyrosine ligands.

Iron released from a transferrin/transferrin-receptor complex is entered into a poorly characterized "regulatory" or "labile" iron pool where it is probably bound to low molecular weight ligands.[111] The identities of the ligands and the nature of their iron complexes have not yet been clearly established. However, glutamate, aspartate, and ATP have been identified as possible ligands, and a μ_3-oxytriiron(III) cluster **125** (**Fig 2.4**) has been proposed as an essential component of the low molecular weight pool.[112, 113] The complexes forming this low molecular weight pool of iron may have only short lifetimes, but during that time they function as intracellular iron transporters, and may be involved directly in iron uptake and release by ferritin.

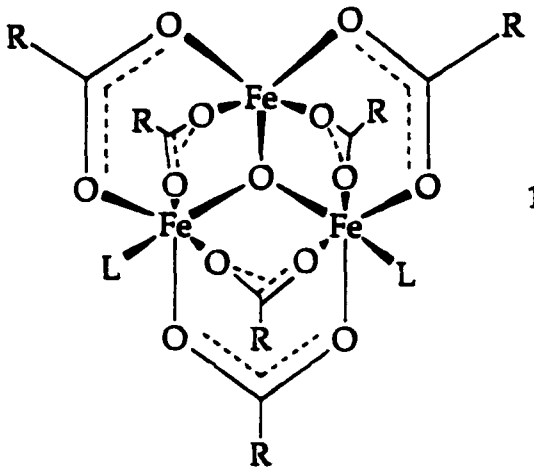

125

Figure 2.4. Structure formula of a μ_3-oxytriiron(III) cluster. R may be glutamate or aspartate and L may be H_2O or OH^-.[113]

A.2. Storage of Iron

The principal iron storage in animals is the protein ferritin in which 4500 Fe atoms can be stored in its internal cavity. The ferritin consists of a protein shell composed of 24 symmetrically related subunits of two types, a light subunit (L-subunit) of about 19 KDa and a heavy subunit (H-subunit) of about 21 KDa. The overall structure of the protein is highly symmetric and roughly spherical with an outside diameter of 130 Å and an inside diameter of 75 Å. The entry and exit of Fe may occur via channels connecting the interior of the assembly with the outside lie along the three-fold and four-fold symmetry axes. Six four-fold channels are lined with hydrophobic residues, while eight three-fold channels are lined with hydrophilic aspartate and glutamate residues (**Fig. 2.5**). All of these channels are approximately 3-4 Å in diameter.[114] Those three-fold channels are most plausible sites for metal entry and exit. The hydrophilic residues are also lined up inside of the protein shell.

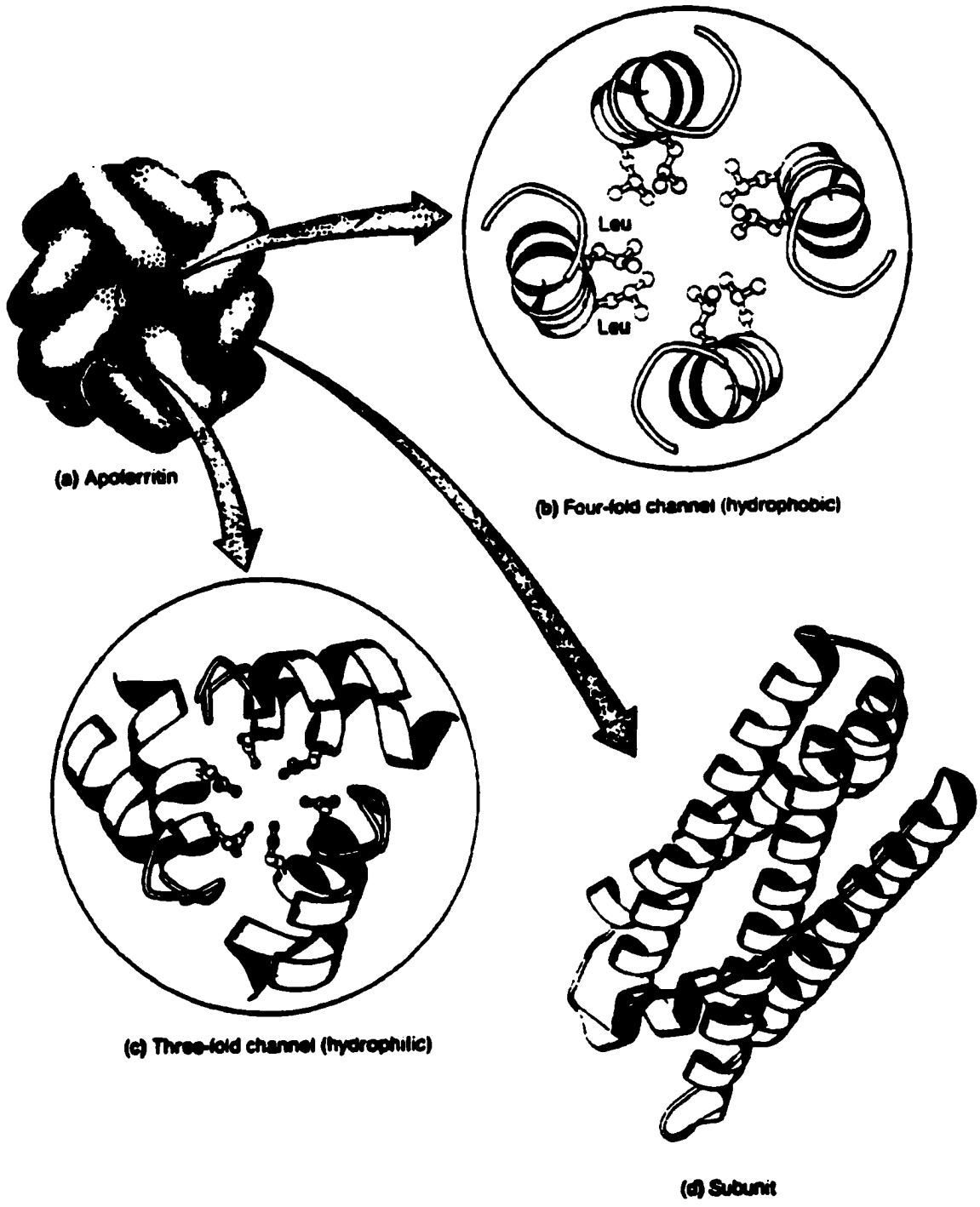

Figure 2.5. Structure of apoferritin, including (a) the overall organization of 24 subunits in the apo protein; (b) hydrophobic channel of four-fold symmetry; (c) hydrophilic channel of three-fold symmetry; (d) fold of an individual subunit.[23]

The mechanism in which Fe is obtained by ferritin remains obscure, but *in vitro* experiments suggest that Fe(II) is more rapidly incorporated into ferritin than Fe(III), and the protein shell plays an essential role in the initial oxidation of the incoming Fe(II).[115] A shell in the inner surface of ferritin subunits has catalytic site for the conversion of Fe(II) to Fe(III). However, Chasteen et al. have shown that a spin-coupled Fe(II)-Fe(III) dimer is produced at low iron:protein ratios.[116] It has also been suggested that initial Fe(II) binding and oxidation occurs in the three-fold channels,[117] or on the external surface of ferritin.[118]

$$4Fe^{2+} + O_2 + 6H_2O \longrightarrow 4FeOOH + 8H^+$$

Scheme 2.2. Possible oxidation of Fe(II) to Fe(III).

The structure of the iron core of ferritin has been investigated by a variety of spectroscopic techniques, including EXAFS, Mössbauer, and optical spectroscopy. The iron in ferritin is octahedrally coordinated ferric state as ferric-oxyhydroxide phosphate of approximate composition $(FeOOH)_8$ $(FeO:OPO_3H_2)$.[115, 119] The EXAFS spectra showed iron-oxygen distance of 1.95 Å and iron-iron distance of 3.3 Å, with approximately seven iron neighbors at this distance.[120] The structure is consistent with a close-packed array of oxygen atoms with iron atoms partially occupying the octahedral interstices, and the vacant octahedral site may be arranged irregularly. The structure could be described as two-dimensional sheets built up of interconnected FeO_6 units that fold back on themselves to fill the three-dimensional core. However, there is need for more definitive work on the core geometry as well as the mechanism of

iron entry and release.[23]

As the process of Fe uptake into ferritin remains unknown, the mechanism of Fe release is still mysterious. *In vitro*, Fe is released from ferritin only when it is in the Fe(II) state.[121] Therefore the process of Fe release from ferritin may involve Fe reduction and/or chelation. A plausible mechanism for Fe release under physiological condition is shown in **Scheme 2. 3.** In this mechanism, iron enters ferritin (**F**) as Fe^{2+}, binds an iron donor molecule (**IDM**), and then becomes Fe^{3+} by an oxidation in the protein with O_2 that is the terminal electron acceptor. Iron must be in the Fe^{2+} state in order to be released. Therefore an electron donor to ferritin, ferritin reductase (**FR**) is required. Once reduced, the Fe^{2+} is released to an iron acceptor molecule (**IAM**). The important feature in this proposed mechanism is a requirement of a ferritin reductase since core iron Fe^{3+} needs to be reduced to Fe^{2+}. However, the identity of **IAM**, **IDM**, and **FR** are not known.

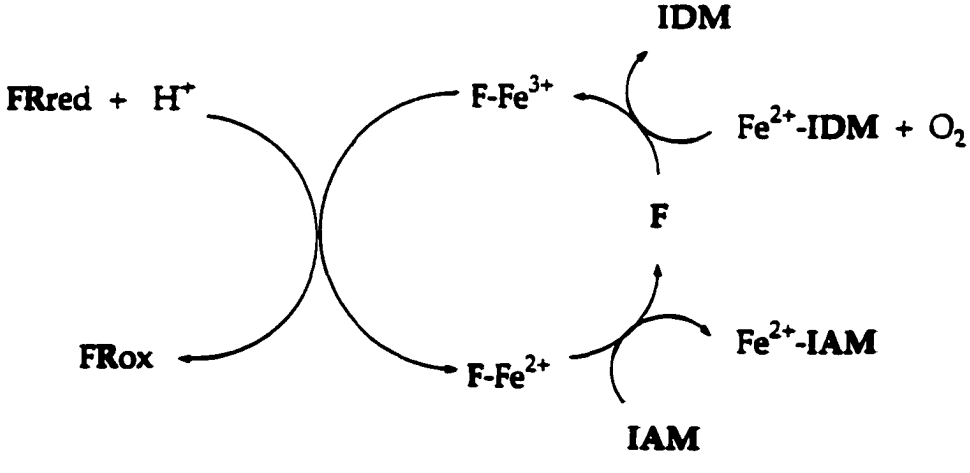

Scheme 2.3. Proposed mechanism of Fe release from ferritin.[122]

A.3 Coordinate Regulation of Iron Uptake, Storage and Utilization

The concentration of the iron uptake, transport and storage proteins are under tight genetic control. Too little Fe can lead to cell death, while an excess of Fe results in cellular toxicity that is probably mediated by the generation of free radicals. Sensitive control mechanisms that monitor intracellular Fe levels have been developed through evolution because cells are very sensitive to their level of iron. In the past 15 years, understanding of these mechanisms has been greatly accelerated by the discovery of the iron regulatory protein 1 (IRP 1; formerly known as IRF, IRE-BP, FRP, or p90).[123] This monomeric cytoplasmic protein is identical to cytoplasmic aconitase, a mitochodrial enzyme that catalyzes the conversion of citrate to iso-citrate.[106]

Both transferrin and ferritin are regulated at the post-transcriptional level, and the mRNA for ferritin and the transferrin receptor (TfR) protein contain non-translated regions known as "iron-responsive elements" (IRE) that are recognized by IRP1. The IREs are stem-loop structures that are located in the 5′ non-translated region (UTR) of ferritin and mRNA and the 3′ non-translated region of TfR mRNA. Under low level of intracellular iron, the mRNA translation of ferritin is prevented once IRP1 binds to the IRE of ferritin mRNA, but IRP1 binding to the TfR mRNA prevents the TfR mRNA from being degraded while also allowing it to be translated. A relatively large amount of TfR protein formation and lack of ferritin formation occurred when IRP1 is bound to mRNA. With an increased iron level, the bound IRP1 dissociates from the mRNA leading to an increase in ferritin synthesis and a decrease in the synthesis of TfR protein (**Scheme 2.4**). Recent work has demonstrated that high

level of Fe IPR1 possesses a cubane 4Fe-4S cluster that prevents IRE binding, but in low level of Fe, the Fe-S cluster is not present allowing the IRP1 to bind to the IRE with high affinity.[124] The effect of level of iron on the synthesis of ferritin and transferrin receptor and iron uptake and storage is summarized in **Table 2.1.**

Table 2.1. Effect of iron level.

	low level of iron	high level of iron
Iron uptake	Increases	Decreases
Transferrin receptor synthesis	Increases	Decreases
Transferrin receptor mRNA concentration	Increases	Decreases
Iron storage	Decreases	Increases
Ferritin synthesis	Decreases	Increases
Ferritin mRNA concentration	No change	No change

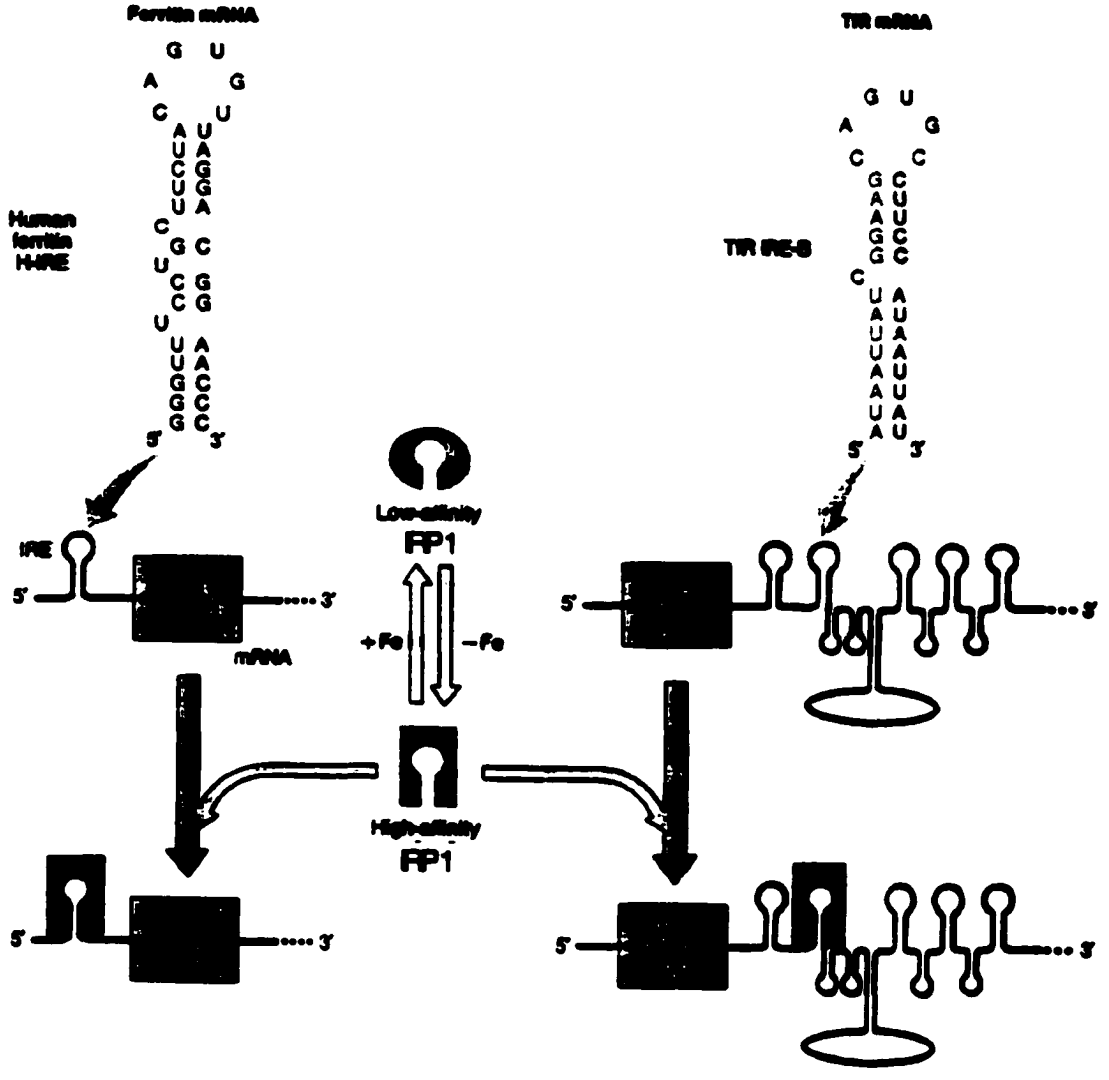

Scheme 2.4. Regulation of ferritin and transferrin receptor expression by the iron responsive element binding protein (IRP1).[23]

B. Oxidative DNA and RNA Cleavage Mediated by Transition Metal

Iron is one of the transition metal ions that can perform autooxidation of organic substance in aqueous media, especially as a ferric state in complex form. A brief review on oxidative degradation of DNA promoted by transition metal ions will be necessary to understand the role of Fe ions in biological system.

Presently, developing of synthetic hydrolases has attracted a lot of attention in the field of molecular genetics and genetic engineering to elucidate the solution structure of proteins and the sequencing of large proteins. A lot of efforts have concentrated on oxidative degradation of DNA or hydrolysis of activated substrates during the last two decades.[125] The oxidative degradation of DNA utilizes redox-active transition metal ions for nicking DNA. Sequence-specific DNA binding agents are attached to Fenton reagent analogues, which produce hydroxide radicals and cleave DNA by the oxidation of deoxyribose moiety by hydrogen atom abstraction followed by breakage of the sugar-phosphate backbone. Depending on the nature, structure, type of activation, or mode of DNA interaction of DNA-cleaver, five different oxidative C-H bond cleavages are known.[126] Oxidative degradation processes by many highly cytotoxic drugs or synthetic nucleases are undertaken by H abstraction since a oxidation by electron abstraction is not favored by the aliphatic nature of deoxyribose. Although the homolysis of a C-H bond depends on the substituents on the carbon, less energy from tertiary carbon than secondary, the relative orientation of C-H to drugs is more important.[126] Two tertiary C-H bonds, C4'-H and C1'-H, from the minor groove of DNA and one tertiary C-H bond, C3'-H, from major groove are accessible for the interaction with drugs. For

secondary C-H bonds, C2'-H_R and C5'-H_S bonds from minor groove and C2'-H and C5'-H bonds from major groove are available for interaction with drugs. The different arrangement of deoxyribose C-H bonds with respect to the minor groove is depicted in **Figure 2.6.**

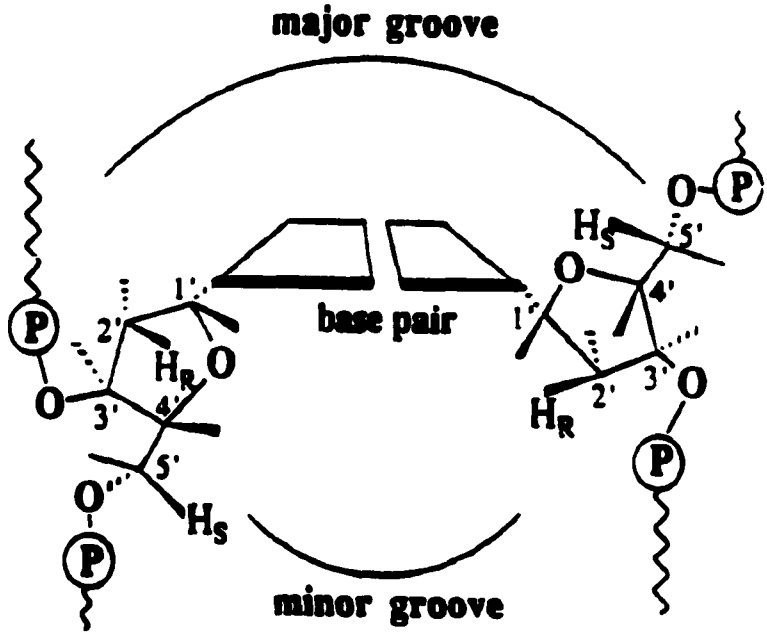

Figure 2.6. Seven possible targets, C-H bonds of deoxyribose, for oxidative activation. Four point into the minor groove (indicated by wedge-shaped bonds), and three into the major groove (H_R and H_S refer to the absolute configuration (pro-*R* or pro-*S*) of hydrogen atoms at C2' and C5').[126]

The molecular aspects of the oxidative DNA cleavage, the modes of activation, and DNA binding by synthetic nucleases, and utilize transition metal complexes that are endowed with redox properties and DNA binding affinity will be discussed in this section.

B.1. Bis(1,10-phenanthroline)copper(I) Complex, $Cu(I)(phen)_2$

Sigman *et al.* synthesized the first chemical nucleases in 1979, $Cu(I)(phen)_2$ **117** (**Fig. 2.7**).[127] The $Cu(I)(phen)_2$ complex and hydrogen peroxide are two essential co-reactants in the cleavage of double-stranded DNA.

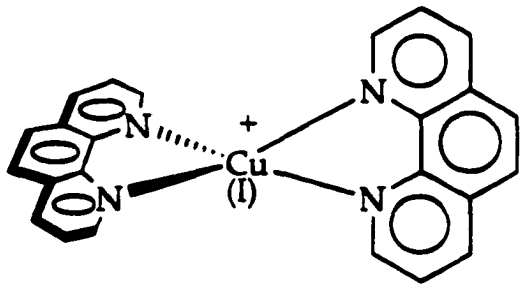

126

Figure 2.7. Structure of Bis(1,10-phenanthroline)copper(I) complex, $Cu(I)(phen)_2$.

Despite the frequent use of **126** as a cleaving agent, the exact nature of the reactive species involved in DNA cleavage is still a matter of debate. The mostly accepted mechanism is that the hydrophobic cation complex **126** (or $Cu(II)(phen)_2$ before being reduced) freely diffuses along with double-stranded DNA, binds to DNA , and then reacts with H_2O_2 to generate hydroxyl radicals and to cleave DNA.[128] Since the DNA damage caused by activated $Cu(I)(phen)_2$ is typical of processes induced by hydroxyl radicals, it is presumed that at least a minor reaction pathway involves free hydroxyl radicals. Williams *et al.* concluded that the DNA damaging species can diffuse over a limited range from the binding site of $Cu(I)(phen)_2$ and suggested that it is unlikely to be an oxo-copper complex.[129]

The one-electron reduction of starting complex $Cu(II)(phen)_2$ to $Cu(I)(phen)_2$ can be achieved by adding reducing agents such as ascorbate, thiol

like mercaptopropionic acid, and mercaptoethanol or by superoxide (**Scheme 2.5** (1) and (2)). The reduced $Cu(I)(phen)_2$ complex binds to DNA (3). This non-covalently bound Cu(I) complex is then oxidized by hydrogen peroxide to generate the reactive species responsible for DNA cleavage (4).

$$2[Cu(phen)_2]^{2+} + 2RS^- \longrightarrow 2[Cu(phen)_2]^+ + RSSR \quad (1)$$

$$[Cu(phen)_2]^{2+} + O_2^{\bullet -} \longrightarrow [Cu(phen)_2]^+ + O_2 \quad (2)$$

$$[Cu(phen)_2]^+ + DNA \longrightarrow [Cu(phen)_2\text{-}DNA]^+ \quad (3)$$

$$[Cu(phen)_2\text{-}DNA]^+ + H_2O_2 \longrightarrow ([Cu(III)(phen)_2\text{-}OH]DNA)^{2+} + OH^- \quad (4)$$

Scheme 2.5. Formation of reactive species for DNA cleavage by a reaction between the $Cu(I)(phen)_2$ and a reducing agent.

The inhibition study of DNA cleavage by activated $Cu(I)(phen)_2$ suggests that $Cu(I)(phen)_2$ interacts with double-stranded DNA through an intercalation mode in the minor groove of a right-handed double helix.[130, 131] Since the coordination geometry of $Cu(I)(phen)_2$ is tetrahedral, a partial intercalation of one phenanthroline ligand is more likely to occur than a full intercalation. Since $Cu(I)(phen)_2$ attacks DNA from a binding site within the minor groove, the geometry of the structure govern the cleavage specificity by the complex. A predominant preference for binding at 5'-TAT triplets in the minor groove is believed to be responsible for the observed cleavage specificity.[132] The main targets of activated $Cu(I)(phen)_2$ as a minor-groove binder are C-H bonds at C1' and C4' of deoxyriboses, two sugar C-H bonds accessible from the minor groove. Sigman *et al.*[127] isolated 3'-phosphoglycolates as a minor degradation product from a C4' chemistry compared to those generated by a C1' chemistry, which is

responsible for 80-90% of the DNA damage. After abstraction of H atom and oxidation at the C1′ position, attached base is leased, followed by first β–elimination to liberate a 5′-phosphate end (the single-strand break). A damaged sugar residue is still attached to the 3′ end of the DNA strand, and the 5-methylene-2(5H)-furanone (5MF) is released by a thermal treatment, 90° C for 1 min, or a piperidine treatment which facilitate the second β–elimination (**Scheme 2.6**).

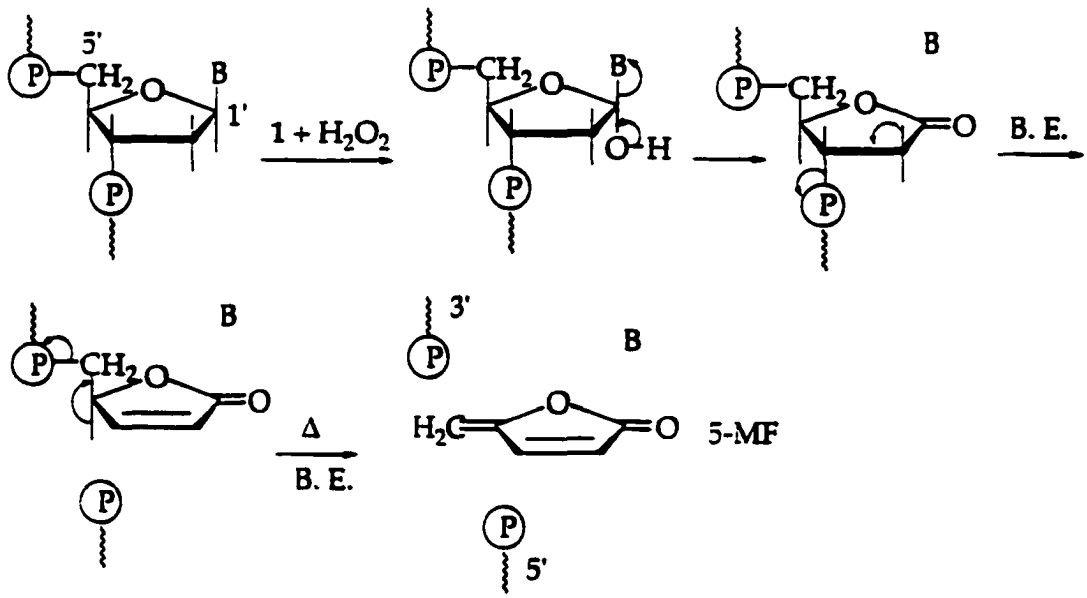

Scheme 2.6. Proposed mechanism of DNA cleavage after hydroxylation of the C-H bond on the 1′ position of deoxyribose by $Cu(phen)_2/H_2O_2$ (Δ = thermal treatment, B. E. = β–elimination, B = base).

B.2. Bleomycin

The bleomycins, referred as BLMs, are family of glycopeptide antitumoral antibiotics that have been used in chemotherapy in association with other drugs for treatments of non-Hodgkin lymphomas, head and neck cancers, and

testicular tumors.[128] Their ability to bind to and cleave DNA are assumed as main reasons for their cytotoxic activity. Two BLMs, A_2 and B_2, are known, and their structures are depicted in **Figure 2.8.** Several metal ions, such as iron, manganese, cobalt, copper, and zinc, can bind strongly to five nitrogen atoms of BLM. However, only redox-active metal ions, iron, cobalt, and copper, can mediate BLM-induced DNA cleavage through a strong chelation to nitrogen atoms of the peptide moiety of BLM and a reaction with molecular oxygen.[133]

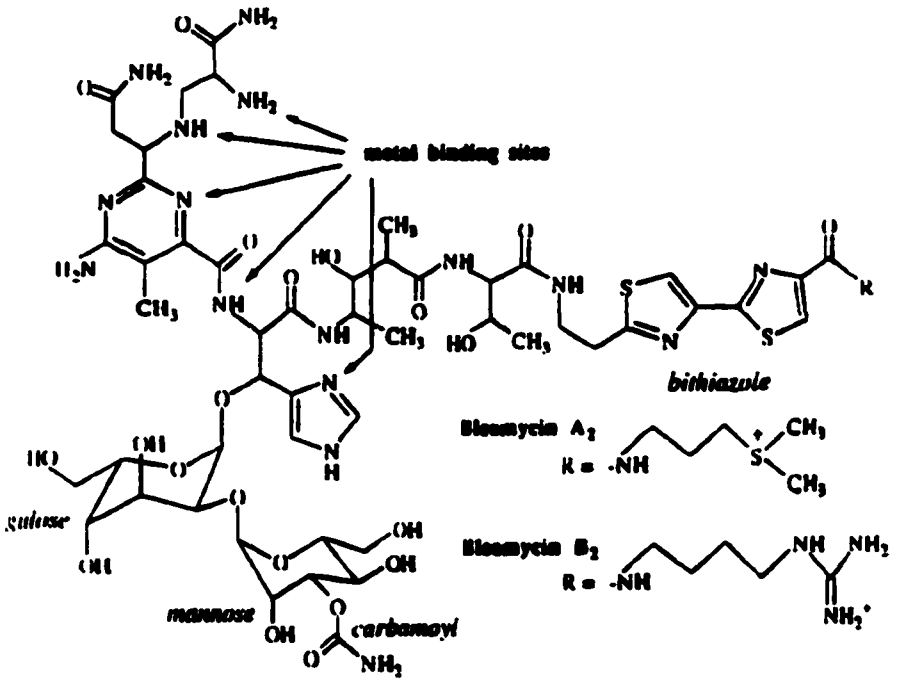

Figure 2.8. Structure of bleomycins A_2 and B_2.[126]

The oxidative degradation of DNA by BLM involves abstraction of the hydrogen atom attached to the C'4 of deoxyribose units by an activated bleomycin,[133] a high-valent iron-oxo complex generated by a reductive activation of molecular oxygen.[134] The precursor of the activated BLM is the

hydroperoxo complex, BLM-Fe^{III}-OOH, which can be generated by two different ways (**Scheme 2.7** (a)). This intermediate has been prepared from Fe^{II}-BLM and hydrogen peroxide and characterized by electrospray mass spectrometry[135] and electron spin resonance spectrum.[134, 136] The heterolysis of the O-O bond of an iron-peroxo complex forms the activated BLM, perferryl complex (**Scheme 2.7** (**b**)). The perferryl complex, BLM-Fe^{V}=O, is capable of H-abstraction from deoxyribose to give a carbon-centered radical at C'4 position.

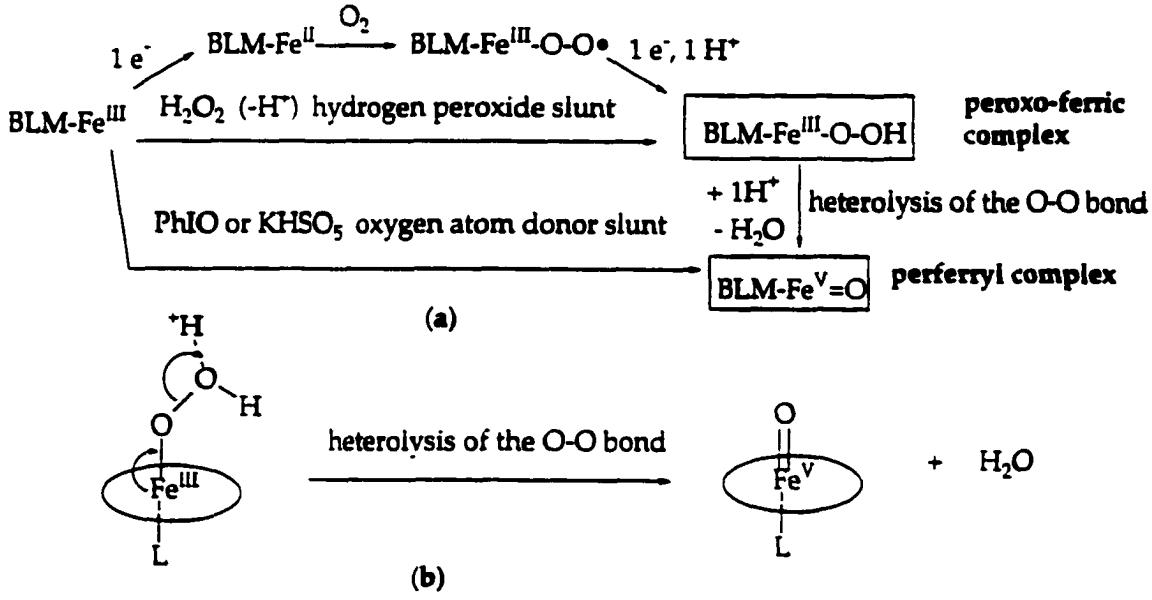

Scheme 2.7. (a) Different routes for the formation of activated BLM; (b) Heterolysis of the O-O bond of iron-peroxo complex.

In the presence of either Fe(III) and hydrogen peroxide or Fe(III) ions, molecular oxygen, and a reducing agent, DNA cleavage is efficiently performed by BLM. The simultaneous release of free bases, base propenal derivatives **A**, 3'-phosphoglycolates **B**, 5'-phosphate ends **C**, and alkali-labile 4'-hydroxylated abasic sites **D** was observed in the Fe-BLM induced DNA-cleavage. The radical

at C4′ position of a deoxyribose unit can react with molecular oxygen to generate an unstable hydroperoxide at C4′, which can break down into the corresponding base propenal, 3′-phosphoglycolates, and 5′-phosphate derivatives via Criegee-type rearrangement. The reaction of radical with the coordinated OH group of BLM-Fe^{IV}-OH generates the 4′-hydroxylated site E through a oxygen-rebound mechanism. It also can react BLM-Fe^{IV}-OH via an electron transfer to produce an intermediate cation F which react with water to give E (**Scheme 2.8**).[128]

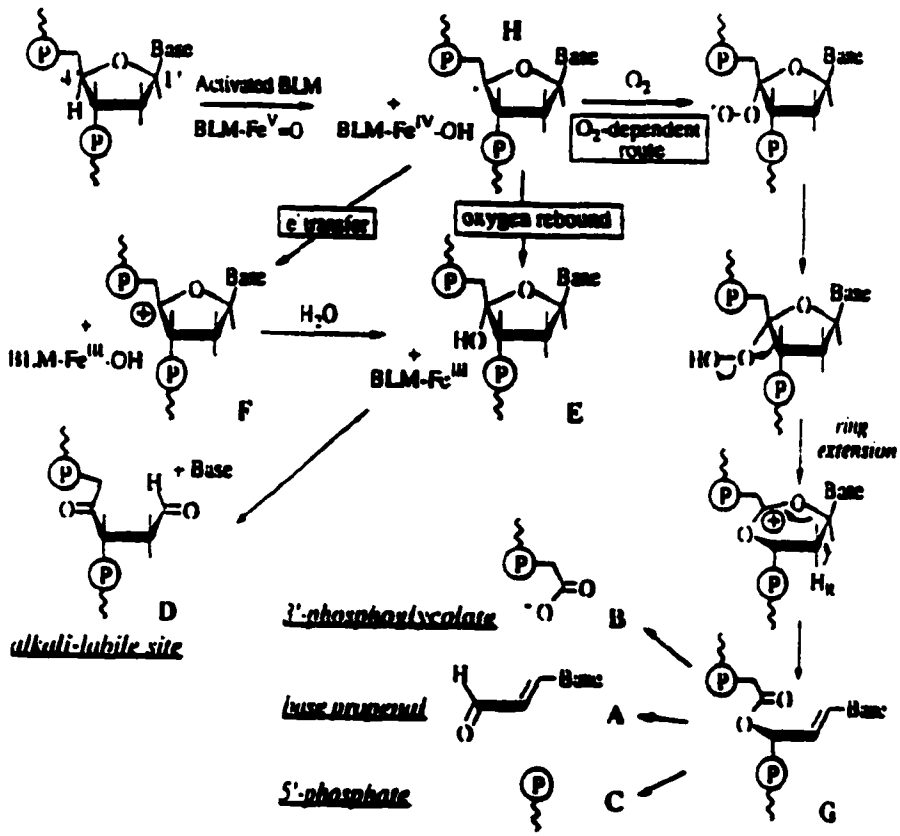

Scheme 2.8. Mechanism of the oxidative DNA cleavage by activated Fe-BLM.

B.3. Fe-EDTA and Fe-MPE

Fe(II) salts, even without chelators, can bind to DNA and cleave DNA by the formation of hydroxyl radicals from H_2O_2 through the Fenton reaction.[137, 138] An Fe(II) complex, Fe-L, must be able to undergo the Fenton reaction in order to produce hydroxyl radical (**Scheme 2.9** (1)). However, in order for Fe(II) complex to be able to catalyze the production of HO• radicals the oxidized Fe(III) complex must be reduced back to the Fe(II) form, which is accomplished by superoxide in the metal catalyzed Haber-Weiss reaction (**Scheme 2.9** (2)).

$$Fe^{II}\text{-}L + H_2O_2 \longrightarrow Fe^{III}\text{-}L + OH^- + HO\bullet \quad (1)$$

$$Fe^{III}\text{-}L + O_2^{\bullet -} \longrightarrow Fe^{II}\text{-}L + O_2 \quad (2)$$

Scheme 2.9. Oxidation of Fe(II) complex by Fenton reaction and reduction of Fe(III) complex by Haber-Weiss reaction.

When Fe^{2+} is chelated by EDTA, it forms a negatively charged metal complex, $[Fe(EDTA)]^{2-}$. This complex would be repelled by the DNA phosphodiester back-bone and is also hard to make an electrostatic interaction with DNA.[139] This fact could be an advantage of Fe(II)-EDTA/H_2O_2 system in generating the HO• radical in the vicinity of DNA and cleaving DNA without or with little sequence specificity.[128] There has been debate regarding the identity of DNA-oxidizing species, either hydroxyl radicals or an iron-oxo species. Tullius *et al*[137] compared DNA cleavage patters formed by γ-radiolysis of water or by Fe(II)-EDTA/H_2O_2 and confirmed that hydroxyl radicals rather than a

high-valent iron-oxo species are responsible for DNA strand scission with presence of a reducing agent, ascorbate. The hydroxyl radicals are formed by the catalysis reaction of Fe(II)-EDTA with H_2O_2 in the presence of ascorbate, which reduced an iron specie oxidized, Fe(III)-EDTA, back to the Fe(II) state according to equations (**Scheme 2.10** (1) and (2)).[137]

$$[Fe^{II}\text{-EDTA}]^{2-} + H_2O_2 \longrightarrow [Fe^{III}\text{-EDTA}]^{-} + OH^{-} + HO\bullet \quad (1)$$

$$[Fe^{III}\text{-EDTA}]^{-} + \text{ascorbate} \longrightarrow [Fe^{II}\text{-EDTA}]^{2-} \quad (2)$$

Scheme 2.10. Catalytic cycle reaction of Fe(II)-EDTA with H_2O_2 in the presence of ascorbate.

The freely diffusible neutral hydroxyl radicals react with DNA bases by a diffusion-controlled rate and cleave DNA not at a single nucleotide in the binding site but over several positions by the H-abstraction of deoxyriboses. Iron-methidiumpropyl-EDTA, MPE, **127** (**Fig. 2.9**) was first designed by Dervan et al. This simple bifunctional molecule which contains the DNA intercalator methidium can be covalently bound by a short hydrocarbon tether to the metal chelator, EDTA. In the presence of Fe(II) ion, molecular oxygen, and a reducing agent, usually dithiothreitol (DTT), MPE efficiently produces single-strand breaks and some double-strand breaks in double helical DNA at low concentration (10^{-6} M), compared to that used with bleomycin.[140]

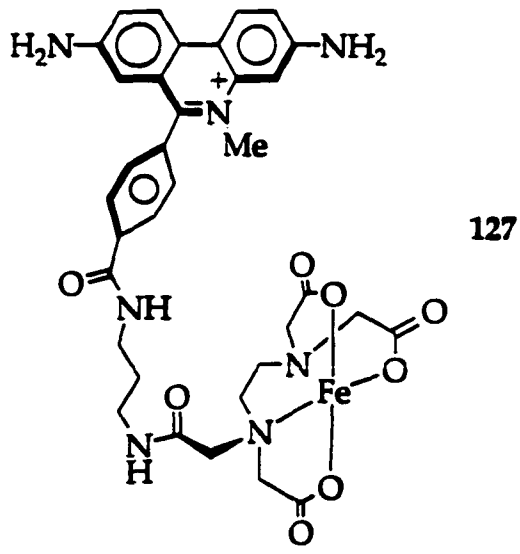

127

Figure 2.9. Structure of the Fe(II) complex of MPE.

In the mechanism of DNA cleavages induced by **127**, the chelated Fe(II) react with molecular oxygen to give Fe(III) and $O_2^{-\bullet}$ (**Scheme 2.11** (1)). Superoxide anions are quickly disproportionated into hydrogen peroxide and dioxygen in protic media (2). The H_2O_2 then reacts with Fe(II)-MPE to generate HO• radicals via a Fenton reaction (3). In the presence of a reducing agent, an oxidized Fe(III)-MPE is reduced to the active Fe(II)-MPE, making possible the catalytic production of hydroxyl radicals (4).

$$Fe^{II}\text{-MPE} + O_2 \longrightarrow Fe^{III}\text{-MPE} + O_2^{\bullet -} \quad (1)$$

$$2\,O_2^{\bullet -} + 2H^{+} \longrightarrow H_2O_2 + O_2 \quad (2)$$

$$Fe^{II}\text{-MPE} + H_2O_2 \longrightarrow Fe^{III}\text{-MPE} + OH^{-} + HO\bullet \quad (3)$$

$$Fe^{III}\text{-MPE} + \text{reductant} \longrightarrow Fe^{II}\text{-MPE} \quad (4)$$

Scheme 2.11. Catalytic production of hydroxyl radicals induced by Fe(II)-MPE and molecular oxygen.

Unlike bleomycin-Fe(II), MPE-Fe(II) cleaves DNA non-sequence-specifically. The free nucleotide bases and 5′-phosphate termini, with equal amount of 3′-phosphate and 3′-phosphoglycolate ends are the released products of DNA cleavage by Fe(II)-MPE and suggest that the deoxyriboses are degraded by hydroxyl radicals via H atom abstraction at C4′, C1′, and C3′.[141]

The attachment of Fe-EDTA to sequence-specific DNA binding molecules such as antibiotics, polypeptides, oligonucleotides, or proteins provides a new class of DNA affinity cleaving molecules. This strategy is the basis for the design of artificial restriction endonucleases with defined target sequences and binding-site sizes.[141] Consequently, tethering EDTA to distamycin,[142] chiral derivatives of netropsin[143], oligopeptides[144], or oligonucleotides have been synthesized to cleave single-stranded DNA or double-stranded DNA.

B.4. Cationic Metalloporphyrins

In the field of chemical and photochemical cleavage of DNA, porphyrins and metalloporphyrin derivatives have attracted lots of attention of scientists because of their ability to intercalate to the DNA and to cleave the DNA. Synthetic derivatives based on the porphyrin core containing hydrophobic, anionic, or cationic functional groups in the meso positions are the mostly studied compounds except natural products.[145, 146]

Depending on the nature of the metal ions, its size and charge on the location of different substituents at the porphyrin periphery, binding modes of the porphyrins to DNA would be different. For cationic porphyrins, only half of the

porphyrin ring is required to intercalate to the DNA, and most of the porphyrins are capable of intercalative binding through at least two *meso*-pyridiniumyl substituents which can freely rotate and come in-plane with the porphyrin macrocycle.[145, 146] However, hydrophobic or anionic porphyrin derivatives do not exhibit any affinity for DNA. They induce oxidative damage to the DNA by staying close to DNA, either by linking to DNA vectors, by using dicationic metal salts in order to form porphyrin/metallic cation/DNA ternary attractions, or by working at high concentrations to generate diffusing active species.[128] Fiel *et al.*[147] first demonstrated the oxidative cleavage of DNA with cationic water-soluble porphyrin, Fe-TMPyP (**Fig. 2.10**) which is activated by a reducing agent in the presence of molecular oxygen.

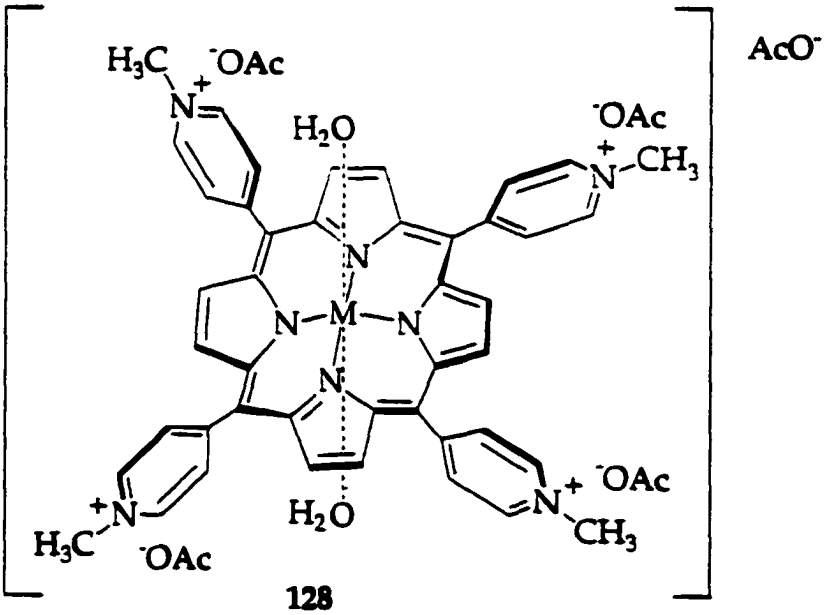

128

Figure 2.10. Structure of M-TMPyP pentaacetate (M = Fe(III) or Mn(III) **128** and TMPyP = *meso*-tetra(4-*N*-methylpyridiniumyl) porphyrins.

The Fe(III)-TMPyP can be activated by not only reducing agents such as ascorbate or superoxide anion in the presence of oxygen but also by oxygen donors such as iodosylbenzene with an efficiency depending on the metal.[148, 149] Several other activating agents such as potassium monopersulfate ($KHSO_5$)[149], magnesium monoperphthalate (MMPP), and peroxynitrite ($ONOO^-$)[150] have been investigated. A catalytically-active species is formed by a direct reaction between the metalloporphyrin and those single-oxygen-atom donors and is thought to be a high valent oxo intermediate Por-M^V=O. Reductive activation of O_2 by Mn(III) and Fe(III) porphyrins can also generate high-valent metal oxo species in the presence of ascorbate, as dose cytochrome P-450.

The most efficient method of oxidative DNA cleavage can be accomplished by the oxidation of cationic Mn(III)-porphyrins by $KHSO_5$.[151, 152] It is believed that the diffusible radical species is not involved in this reaction because the breaks are well-defined and H_2O_2 is at least three orders of magnitude less efficient in generating the active species resulting to cleavage.[151] A proposed activation and reaction cycle is presented in **Scheme 2.12.** The high valent TMPyP-Mn^V=O species that cleaves DNA is too reactive to be characterized.

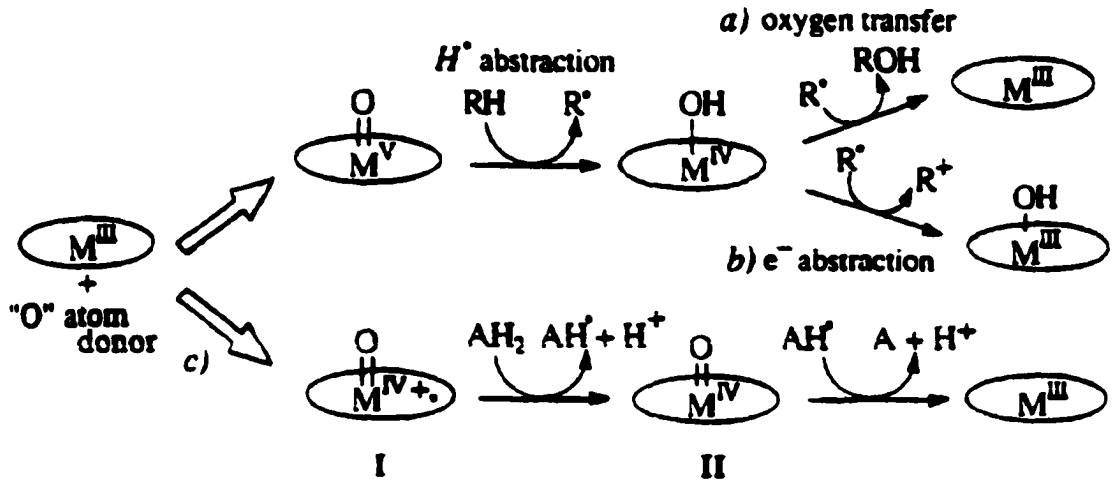

Scheme 2.12. Three possible oxidative pathways for M(III)-porphyrin complex (M = Fe or Mn): a) P-450 route (oxygen-bound mechanism), b) diverted P-450 route, and c) peroxidase route.

The Mn(III)-TMPyP **128** does not intercalate between DNA base-pairs but binds in the minor groove of A•T-rich regions of DNA via an electrostatic or a steric interaction.[153] This cationic metalloporphyrin is attracted by the high negative potential at the surface of the minor groove of A•T-rich sequences (**Fig. 2. 11**). This **128** can span over five to six base-pairs in the minor groove of DNA, but preferred cleaving site consists of three consecutive A•T base-pairs creating a suitable pocket for highly selective DNA cleavage. At this site, **128** strictly mediates C5′ oxidation on nucleosides on both 3′ sides of the AT box: one single-strand break on each strand leads to double-strand cleavage with four base-pair shift to the 3′ end of the opposite DNA strand. Molecule **128** is also able to degrade G•C-rich sequences with a reactivity two orders of magnitude weaker than A•T degradation sites. The mechanism of DNA cleavage in these regions is not fully understood and may involve sugar oxidation and/or base oxidations. DNA cleavage by **128** through C1′ and/or C5′ oxidation also occurs.[126]

Oxidative damage to DNA can also be initiated by photooxidation (ultraviolet or visible light with or without photosentitizers) of metal complexes, especially Ru(II) polypyridyl complexes.[154]

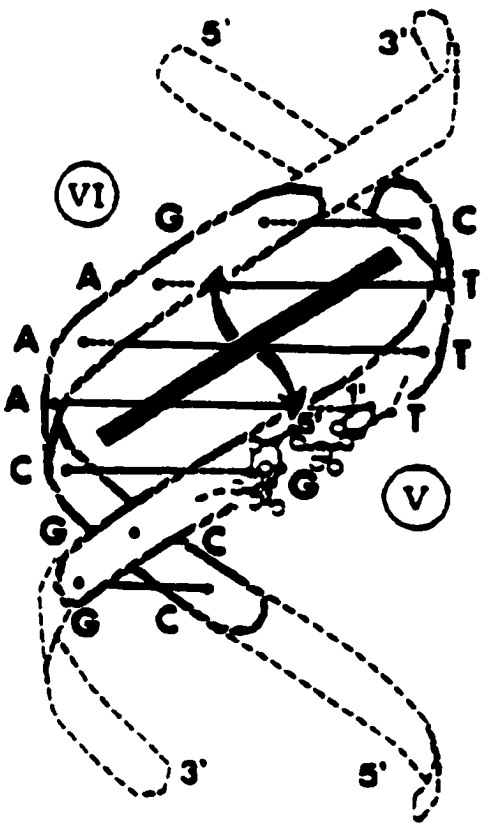

Figure 2.11. Binding Mn(III)-TMPyP/$KHSO_5$ in DNA.

C. Iron Chelation

The amounts of bioavailable iron can affect human health in two major areas. The first and most important aspect of iron bioavailability is iron deficiency, which usually leads to low hemoglobin levels and anemia. Women and children are particularly susceptible to this because of Fe loss by menstruation and an enhanced requirement for growth.[155] Secondly, too much iron, or iron overload, occurs in very special situations, but is hard to treat readily. Three forms of iron excess have been known. The first type of iron overload occurs by acute iron poisoning, especially for child. The second type is a specific form of chronic iron overload, hereditary hemochromatosis, which is a disorder due to slow accumulation of excessive body iron loads. The third type is a chronic iron overload resulting from multiple blood transfusions for chronic anemia such as β-thalassaemia.[156] This disease is a major public health problem in the Mediterranean area, the Middle East, the Indian subcontinent and the Far East. Other anemias including sickle cell diseases, aplastic anemia, sideroblastic anemia, and myelofibrosis, may also lead to transfusional iron overload.

In the past 20 years, a large variety of iron-chelating ligands with oxygen donors, such as desferrioxamine, have been systemically tested as potential oral active drugs. HBED (*N,N'*-(bis-hydroxybenzyl)ethyllediamine-*N,N'*-diacetic acid) (**Fig. 2.12, 129**), an analogue of EDTA with two phenolates replacing two carboxylate groups, is one of them. It has a significantly higher log *K* value for Fe(III) (complex formation constant) than EDTA. It is well absorbed orally and is effective in rodent assays, but it is remarkably less effective in primates and in

patient trials.[157] The chelating abilities of PIH (pyridoxyl isonicotonyl hydrazide, **Fig 2.12, 130**) and analogues were studied by Webb et al.[158]

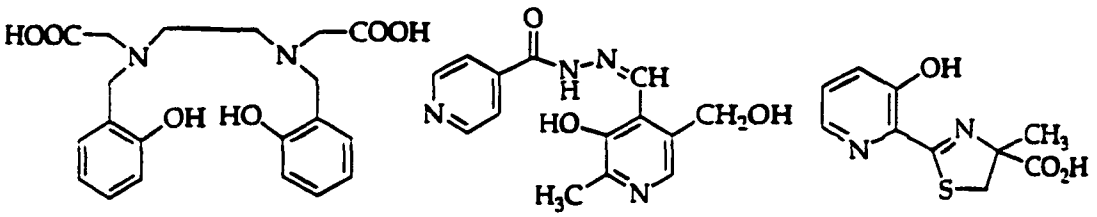

129 **130** **131**

Figure 2.12. HBED and PIH.

Desferrithiocin **131** is one of few siderophores which is not in the hydroxamate or catecholate class, and forms a stable 2:1 complex with iron (K 4 x 10^{29} M^{-2}).[159] This compound is effective in iron mobilization both in rat and in primate models but unfortunately shows nephrotoxicity. Raymond et al.[160] reported hydroxypyridinones (1-hydroxy-2-pyridinone, 3-hydroxy-2-pyridinone, 3-hydroxy-4-pyridinone, **132, 133,** and **134**, respectively) as the most promising oral iron-chelating reagents because of their binding properties and the result of biological trials. The 1,2-dimethyl derivative**135**[161] of **134** has been tested clinically since 1989 by different thalassaemia hospitals. Also the 1,2-diethyl analogue (CP94) has been extensively investigated and showed a higher Fe(III) mobilization. A new class of hydroxypyridinones **136** was prepared by introduction of hydroxy alkyl groups in 2-position, resulting lower ligand p*K*a through intramolecular hydrogen bonding.[162] This new class of hydroxypyridinones is very promising in their ability to remove iron *in vivo*.

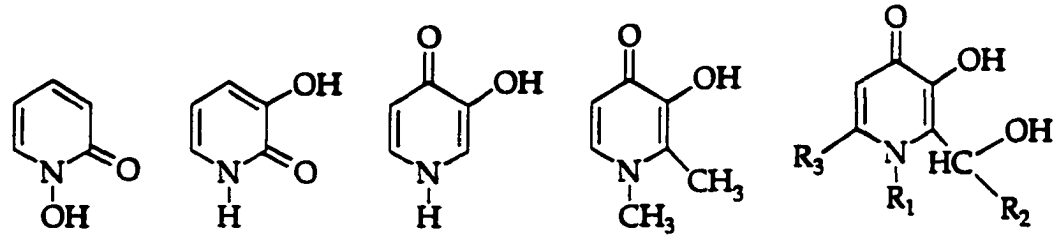

132 133 134 135 136

Figure 2.13. Hydroxypyridinones.

A new potential tridentate oral chelator (4-(3,5-bis(2-hydroxyphenyl)-1,2,4-triazol-1-yl)benzoic acid) **137** which combines high oral potency and tolerability[163] has been proposed. It forms mono- and bis-iron complexes with extremely high formation constants.

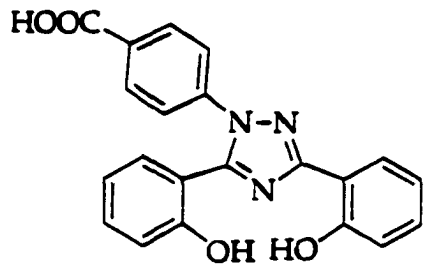

137

Figure 2.14. 4-(3,5-bis(2-hydroxyphenyl)-1,2,4-triazol-1-yl)benzoic acid.

D. Iron Deprivation in Cancer Therapy

Because large amounts of iron are needed for growth of cells, iron deprivation strategies have been receiving increased interest in inhibition of tumor cell growth. Iron depletion therapeutic strategies in treatments of human tumor cells are currently being explored. Some of these methods are depicted in **Figure 2.15.**

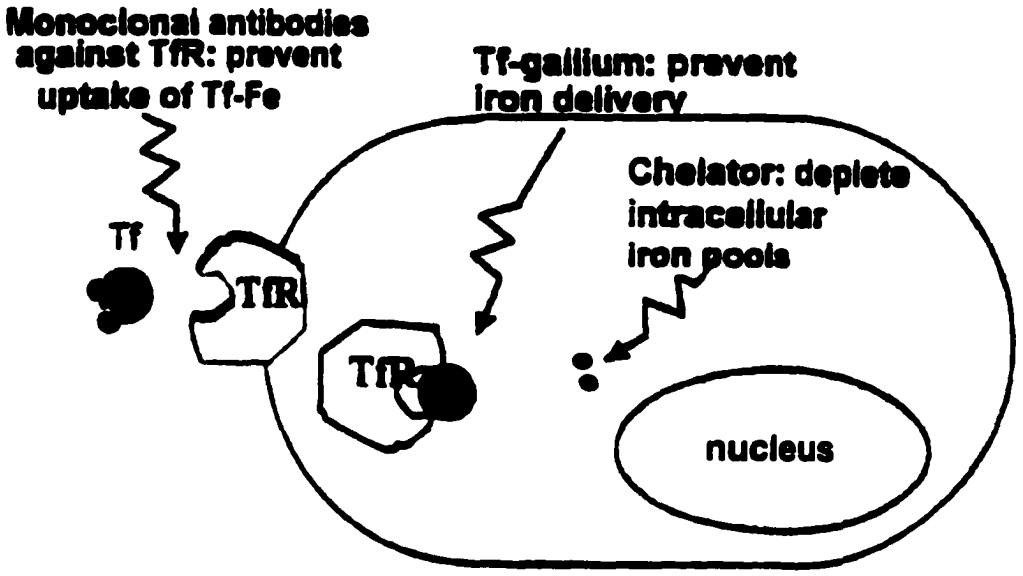

Figure 2.15. Strategies for iron depletion in tumor cells.

The iron chelator desferrioxamine, used in conditions of iron overload, has been used in the treatment of various tumor cells. Gallium also is in clinical use in treatment of bladder cancer because of its ability to replace iron in transferrin, resulting in iron deprivation.[164, 165] Some antitransferrin receptor antibodies, which are able to inhibit a pathway of cellular iron uptake, has been

investigated for their potential to inhibit growth of tumor cells.[166]

Most studies of anti-proliferative effects of iron chelators have been focused on utilizing desferrioxamine, because its clinical effects are well known. However, desferrioxamine has shown a limited activity as a single agent in the treatment of human cancer. The PIH (pyridoxyl isonicotinoyl hydrazide, **Fig. 2.12, 130**) family has been examined as anti-proliferative agents, which demonstrated its effectiveness in inhibiting the growth of cultured cells.[167] The importance of lipophilicity of the iron-chelators in anti-proliferative activity was found in the systematic study of a group of PIH analogues. In addition, a recent study demonstrated that for some PIH derivatives, cytotoxicity was not correlated with iron chelation efficiency but with ability of chelators to mobilize iron from essential pools.[167]

E. Fe-Mediated Oxidative Dehydrogenation

Oxidative dehydrogenation of secondary amines coordinated to transition-metal ions has been reported with Ru(III),[168] Ru(II),[169, 170] Fe(II),[171, 172, 173] Fe(III),[174, 175] Ni(II),[176] Cu(II),[177] Co(II),[178] and Os(IV),[179] and has been the subject of extensive studies for the last three decades. Stadtman reported that the oxidative degradation of proteins, which is one of the possible causes of aging, is catalyzed by iron.[180]

The introduction of one double bond into the coordinated ligand requires a two-electron oxidation, and these reactions have been known to proceed via higher oxidation states, such as Ni(III), Fe(III), and Os(III). On other hand, a direct oxidative dehydrogenation of some trivalent metal ions, Fe(III)[174] and Os(III),[168] complexes was observed affording an introduction of an imine group into the coordinated ligands.

Iron has unique features that make it easy to study metal mediated oxidative dehydrogenation reaction for the following reasons. First, the Fe(III) state is readily accessible ($E^\circ = 0.77$). Secondly, Fe(II) low-spin state is more stable than Fe(III) low-spin state thermodynamically and kinetically from ligand-field considerations. Thirdly, after the oxidative dehydrogenation occurs and iron becomes the bivalent state, the low-spin Fe(II) complex is inert to substitution reaction resulting in easy isolation and characterization.[172]

Goedken[172] and Goto[175] reported a transient Fe(III) species which undergoes metal ion mediated oxidative dehydrogenation of the amine ligand to yield a di-imino coordinated complex in the reaction of tetracyanodiamine Fe(II)

complex with oxidizing agents (**Scheme 2.13**). They isolated $[Fe(III)(en)(CN)_4]^-$ as an Fe(III) intermediate in the ligand oxidation reactions under acidic conditions with Cl_2 or $[Fe(CN)_6]^{3-}$ as oxidants.

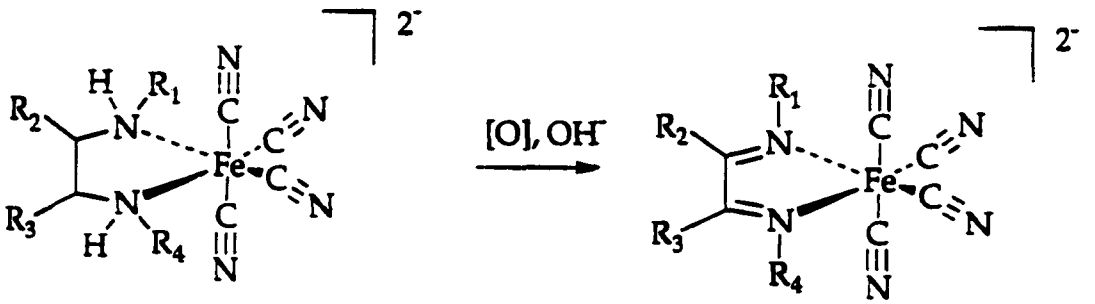

$[O] = O_2, H_2O_2, Cl_2, OCl^-$

Me_2en = *N,N'*dimethylenediamine

Scheme 2.13. Oxidative dehydrogenation of $[Fe(diamine)(CN)_4]^{2-}$.

The oxidative dehydrogenation of $[Fe(Me_6[14]4,11\text{-}dieneN_4)(CH_3CN)]^{2+}$ **138** affording a tris-imino complex $[Fe(Me_6[14]1,4,11\text{-}trieneN_4)(CH_3CN)]^{2+}$ **140** and a tetra-imino complex $[Fe(Me_6[14]1,4,8,11\text{-}trieneN_4)(CH_3CN)]^{2+}$ **141** on exposure of the tris-imino to air for 24 h was investigated by Busch et al. (**Scheme 2.14 (a)**).[171] The intermediate Fe(III) complex, $[Fe(Me_6[14]4,11\text{-}dieneN_4)(CH_3CN)](ClO_4)_3$ **139** was isolated as a precipitate that separates prior to ligand oxidation. The Fe(III) complex was reduced to Fe(II) with an oxidized ligand by addition of small amount of water. They proposed that the central ferric ion abstracts an electron from one of coordinated secondary amine groups generating a radical and a proton. When an external oxidizing agent, O_2 or H_2O_2, is available, it oxidizes the radical followed by the ionization of a second proton consummating the process (**Scheme 2.14 (b)**).

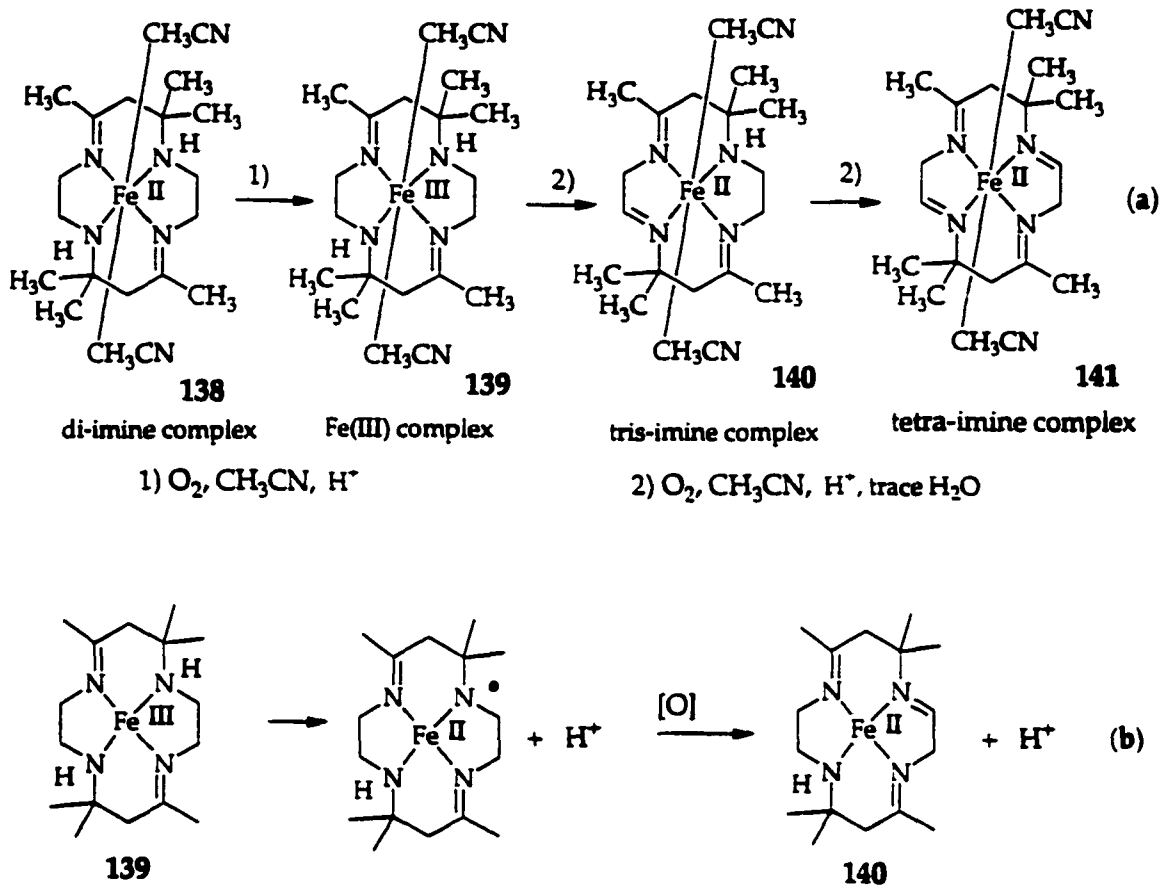

Scheme 2.14. (a) Formation of **140** and **141**; (b) proposed mechanism for oxidative dehydrogenation of **138**.

In the presence of an external oxidant (H_2O_2 or O_2), a decomposition of the deep blue $[Fe(III)L(L\text{-}H)]^{2+}$ **142 (Fig 2.16)** (L = [9]aneN$_3$ and L-H = N-deprotonated form of ligand L) to produce quantitatively one equivalent of an oxidative dehydrogenated ligand and $[Fe(III)L(OH_2)_3]^{3+}$ was investigated by Pohl et al.[174] The electronic ground state of **146** was identified as low-spin amidoiron(III) species according to EPR spectroscopy. They suggested that the amidoiron(III) intermediates are the primary reactive species in the oxidative dehydrogenation of primary or secondary amine coordinated to iron(III)

complexes, yielding mono-imino or di-imino Fe(II) complexes.

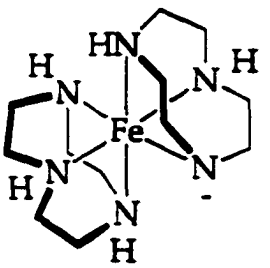

142

Figure 2.16. Low-spin amidoiron(III) complex, $[Fe(III)L(L\text{-}H)]^{2+}$.

Oxidation of *mer*-$Na[Fe(CN)_3(2\text{-}DPA)]^-$ **143** and *fac*-$Na[Fe(CN)_3(2\text{-}DPA)]^-$ **144** (2-DPA = di(2-pyridylmethyl)amine)) with $(NH_4)_2S_2O_8$ to produce a deep red dehydrogenated product, *mer*-$Na[Fe(CN)_3(2\text{-}DPA - 2H)]^-$ **145**, and *fac*-$Na[Fe(CN)_3(2\text{-}DPA)]^0$ was investigated by Goto et al. (**Scheme 2.15**).[173] They also observed that the oxidation of **143** with H_2O_2 (30%) yields **145** too. They proposed a mechanism that consists of 1) oxidation of the central metal ion, and 2) a disproportionation of the deprotonated species of the metal-oxidized species yielding iron(II) species, iron(III) aminyl species and/or iron(IV) species: the latter undergo deprotonation to yield the ligand-dehydrogenated iron(II) complex. The faster disproportionation process for **143** than **144** was explained by the steric effect of producing the deprotonated species or the planar intermediate on the way to the coordinated imine.

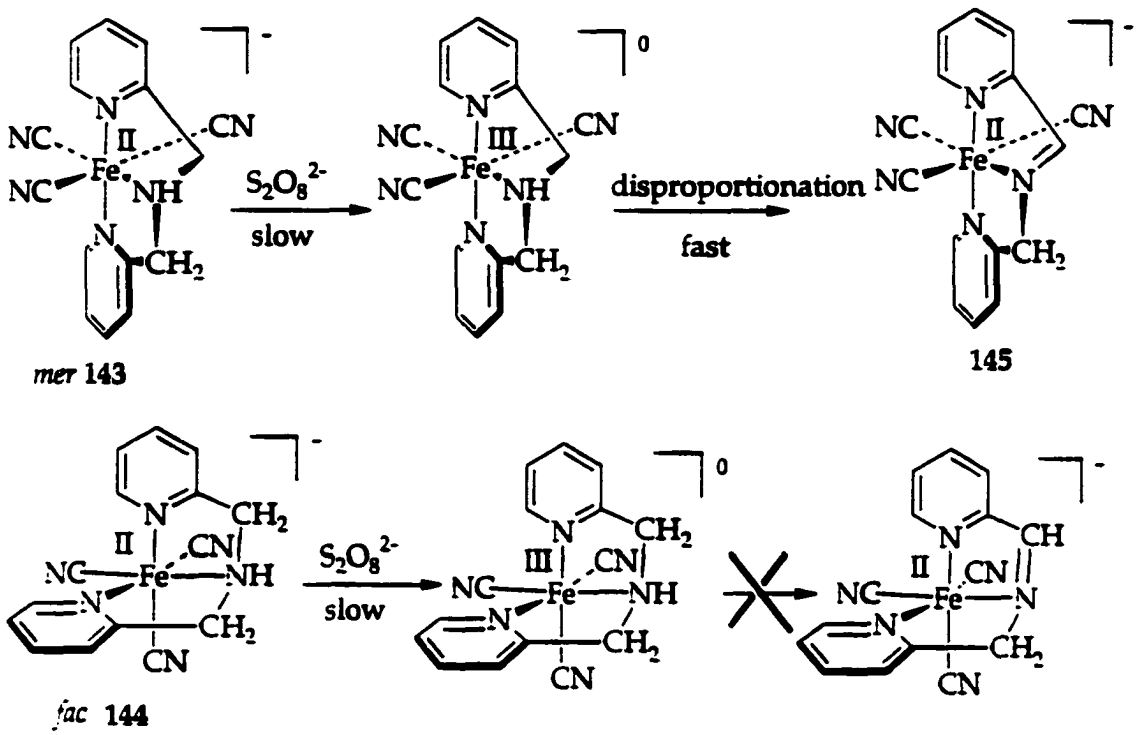

Scheme 2.15. A proposed mechanism of oxidative dehydrogenation of **143** and **144**.

Experimental Section

A. Materials and Methods

All the materials listed below were of a research grade or a spectroquality grade in the highest purity available and were generally used without further purification except Et_2O. Et_2O was distilled from Na and used immediately. DMSO-*d6* andD_2O were obtained from Cambridge Isotope Laboratories. 2-Deoxy-D-ribose and adenosine-5'-triphosphate were obtained from Sigma. $FeCl_2 \bullet 4H_2O$, $Fe(ClO_4)_2 \bullet 6H_2O$, $FeCl_3 \bullet 6H_2O$, $Fe(ClO_4)_3 \bullet 6H_2O$, $NaBPh_4$, anhydrous MeOH, Na_2HPO_4, KH_2PO_4, NaCl, KCl, 2-thiobarbituric acid, 2,2'-bipyridine, $CaCl_2$, $MgCl_2 \bullet 6H_2O$, $Zn(ClO_4)_2 \bullet 6H_2O$, $Mn(ClO_4)_2 \bullet 6H_2O$, $Cu(ClO_4)_2 \bullet 6H_2O$, and anhydrous grade DMSO and DMF were purchased from Aldrich. H_2O_2, HNO_3, and glacial acetic acid were obtained from Fisher Scientific. EtOH was purchased from Pharmco. CH_2Cl_2 and $CHCl_3$ were obtained from EM Science. Deionized water was obtained through reversed-osmosis followed by anion and cation exchange on an E-pure from Barnstend.

All ligands, derived from tach framework and used in this study, were synthesized by Dr. Brechbiel et al.[9, 51] at NIH and kindly donated to this group to investigate biological applications and structures of the first row transition metal complexes of tach derivatives.

^1H and ^{13}C NMR spectra were obtained using a Bruker AM360 instrument. Chemical shifts are reported in ppm on the δ scale relative to TMS. Proton chemical shifts are annotated as follows: ppm (multiplicity or spin system, integral, and assignment). All of the UV-vis electronic spectra were measured

using a Cary 5 Varian UV-vis spectrometer or a Hewlett-Packard 8453 spectrometer with 1 mL or 3 mL quartz cuvettes (1cm path-length). All of the vibrational spectra were measured using a Nicolet 205 FT-IR spectrometer with KBr pellets. Fast atom bombardment (FAB-MS) mass spectra were taken on an Extrel 4000 at NIH. Elemental analysis was performed by the UNH Instrumentation Center, Atlantic Microlabs (Atlanta, Georgia) or by Galbraith Laboratories (Knoxville, Tennessee).

Note In the reactions of iron salts ($FeCl_2 \bullet 4H_2O$, $Fe(ClO_4)_2 \bullet 6H_2O$, $FeCl_3 \bullet 6H_2O$, and $Fe(ClO_4)_3 \bullet 6H_2O$) and tachpyr at different conditions and exchanges of anions with $NaBPh_4$, identical cationic compounds with different anions were produced. In order to clarify the composition of the complexes, numbering of the complexes will be focused on the identity of the cationic compounds followed by the anion. Therefore, all non-oxidized Fe(II) complex of tachpyr will be referred as **146**$(X)_2$ (**Fig. 2.23**), [Fe(tachpyr)]$(X)_2$, all mono-imino Fe(II) complex as **147**$(X)_2$ (**Fig. 2.20**), [Fe(tachpyr-ox-2]$(X)_2$, the di-imino Fe(II) complex as **148**$(X)_2$ (**Fig. 2.20**), [Fe(tachpyr-ox-4]$(X)_2$, and the tris-imino Fe(II) complex as **149**$(X)_2$ (**Fig. 2.23**), [Fe(tachpyr-ox-6]$(X)_2$. The tris-imino Fe(II) complex, [Fe(tachpyr-ox-6]$^{2+}$, was obtained by two different methods. They will be referred differently in this study according to the method of preparations to distinguish them. The tris-imino Fe(II) complex generated through oxidative dehydrogenation will be referred as **149**$(BPh_4)_2$, [Fe(tachpyr-ox-6)]$(BPh_4)_2$, and the other one obtained by direct reaction of $Fe(ClO_4)_2 \bullet 6H_2O$ with the tachimpyr ligand which has three 2-pyridylimine arms (tach-N=CH-py, **Fig. 2.25 (b)**) will be referred as **149**,

[Fe(tachimpyr)]$(ClO_4)_2$. Therefore, the tachpyr-ox-*6* and tachimpyr are identical ligands, but only the tachpyr-ox-*6* is generated through iron mediated oxidative dehydrogenation.

B. Preparation of Metal Complexes

Preparation of [Fe(tachpyr)] (146)$(Cl)_2$. A pale green solution of $FeCl_2 \bullet 4H_2O$ (0.0229 g, 1.15 x 10^{-4} mol) in MeOH (2 mL) was degassed in a Schlenk flask by purging with N_2 for 5 min. A similarly degassed yellow solution of tachpyr (0.0464 g, 1.15 x 10^{-4} mol) in MeOH (2 mL) was added. The mixture attained a brown color while stirring for 30 min at 0°C under N_2. Layering with Et_2O produced a brown precipitate that was isolated by filtration under N_2, dried under reduced pressure, and stored under N_2 in a Schlenk flask. Air-sensitivity of the product precluded yield measurement and accurate elemental analysis of samples submitted in vials. ^{1}H NMR (DMSO-d_6, 25 °C): δ 7.80, 7.58, 7.26, 6.98 (t, d, t, d, 4H, $C_5\underline{H}_4N$); 5.55 (t, 1H, N$\underline{H}$-CH_2-py); 4.43 (dd, A$\underline{M}$X, 1H, NH-C$\underline{H}_2$-py), 4.10 (dd, AM$\underline{X}$, 1H, NH-C$\underline{H}_2$-py); 3.07 (s, $\underline{A}$MM'XX', 1H, cyclohexyl methine H); 2.09 (d, A$\underline{MM}$'XX', 1H, equatorial cyclohexyl methylene H's diastereotopic); 1.86 (d, AMM'$\underline{XX}$', 1H, axial cyclohexyl methylene H's, diastereotopic).

Conversion of 146$(Cl)_2$ to a mixture of (146)$(Cl)_2$ and [Fe(tachpyr-ox-2)] (147)$(Cl)_2$. Complex **146**$(Cl)_2$ (brown solid) was exposed to air for 1 h at 25 °C. A color change from brown to greenish brown occurred. The product was identified as a mixture of **146**$(Cl)_2$ and **147**$(Cl)_2$ by ^{1}H NMR spectroscopy.

Preparation of a mixture of [Fe(tachpyr-ox-2)] (147)$(BPh_4)_2$ and [Fe(tachpyr-ox-4)] (148)$(BPh_4)_2$ from $FeCl_2 \bullet 4H_2O$ and tachpyr. To $FeCl_2 \bullet 4H_2O$ (0.0179 g, 9.01 x 10^{-5} mol) in MeOH (2 mL) was added tachpyr (0.0363 g, 9.01 x 10^{-5} mol) in MeOH

(2 mL) affording a dark brownish green solution. After standing for 0.5 h, a solution of $NaBPh_4$ in MeOH is added into the mixture affording a blue-purple precipitate. This was isolated by decanting the supernatant, dissolved in CH_3CN and filtered, and dried under reduced pressure affording a blue-purple solid in 69.3% yield (0.0149 g, 2.82×10^{-5} mol). ^1H NMR (DMSO-d_6, 25°C); δ 9.40, 9.38,9.30 (s, 3 imine H, RN=C(H)-py); numerous peaks from 8.5 δ to 7.3 δ for pyridyl protons; 4 peaks from 6.3 δ to 5.5 δ for (t, 1H, N<u>H</u>-CH_2-py); multiplets from 5.0 δ to 4.3 δ for (2H, NH-C<u>H_2</u>-py); numerous peaks from 1.5 δ to 4.3 δ for (1H, cyclohexyl methine H) and (2H, cyclohexyl methylene H's).

Preparation of a mixture of [Fe(tachpyr-ox-2)] (147)$(ClO_4)_2$ and [Fe(tachpyr-ox-4)] (148)$(ClO_4)_2$ from $Fe(ClO_4)_2 \cdot 6H_2O$ and tachpyr. To $Fe(ClO_4)_2 \cdot 6H_2O$ (0.0306 g, 8.44×10^{-5} mol) in MeOH (2 mL) was added tachpyr (0.0340 g, 8.44×10^{-5} mol) in MeOH (2 mL) affording a dark green solution. After standing for 10 h, a dark green precipitate and a green solution were formed. The precipitate was isolated and dried under reduced pressure affording a dark brown-green solid in 65.0% yield (0.0420 g, 6.35×10^{-5} mol). Anal. Calcd for $C_{25}H_{32}C_{12}FeN_6O_9$ (147$(ClO_4)_2 \cdot$MeOH): C, 43.69; H, 4.69; N, 12.23. Anal. Calcd for $C_{25}H_{30}C_{12}FeN_6O_9$ (148$(ClO_4)_2 \cdot$MeOH): C, 43.82; H, 4.41; N, 12.26. Found: C, 43.53; H, 4.47; N, 12.07. MS (FAB/thioglycerol): 456 (M - $2ClO_4^-$) for $[Fe(tachpyr\text{-}ox\text{-}2)]^{2+}$ and 454 (M - $2ClO_4^-$) for $[Fe(tachpyr\text{-}ox\text{-}4)]^{2+}$). ^1H NMR spectroscopy of mixtures of 147$(ClO_4)_2$ and 148$(ClO_4)_2$ was almost identical to ^1H NMR spectra of [Fe(tachpyr-ox-2)] (146)$(BPh_4)_2$ and [Fe(tachpyr-ox-4)] (147)$(BPh_4)_2$ except peaks from counter anions.

Preparation of a mixture of [Fe(tachpyr-ox-2)] (147)$(BPh_4)_2$ and [Fe(tachpyr-ox-4)] (148)$(BPh_4)_2$ from $FeCl_3 \bullet 6H_2O$ and tachpyr. To a yellow solution of $FeCl_3 \bullet 6H_2O$ (0.0174 g, 6.43×10^{-5} mol) in MeOH (2 mL) was added a yellow solution of tachpyr (0.0259 g, 6.43×10^{-5} mol) in MeOH (2 mL) affording a gradual color change from yellow to dark green. After standing for 0.5 h, Et_2O (12 mL) was added into the mixture to form a green precipitate and a green solution. The isolated green solid was dissolved in MeOH (2 mL), treated with $NaBPh_4$ (0.05 g in 2 mL of MeOH) giving a dark green precipitate. The precipitate was isolated and dried under reduced pressure affording the product in 56.1% yield (0.0243 g, 4.60×10^{-5} mol) as a green solid. ^1H NMR (DMSO-d_6, 25°C); δ 9.33, 9.31, 9.17 (s, 3 imine H, RN=C(*H*)-py); numerous peaks from 8.5 δ to 6.0 δ for pyridyl protons; 7.17, 6.90, 6.77 (br s, t, t, $B(C_6H_5)_4$); 3 peaks from 5.0 δ to 4.5 δ for (1H, cyclohexyl methine H); 4 peaks from 4.5 δ to 4.0 δ for (d, 2H, py-CH_2-NH); numerous peaks from 1.5 δ to 3.5 δ (2H, cyclohexyl methylene H's).

Preparation of a mixture of [Fe(tachpyr-ox-2)] (147)$(BPh_4)_2$ and [Fe(tachpyr-ox-4)] (148)$(BPh_4)_2$ from $Fe(ClO_4)_3 \bullet 6H_2O$ and tachpyr. To a yellowish red solution of $Fe(ClO_4)_3 \bullet 6H_2O$ (0.0310 g, 6.73×10^{-5} mol) in MeOH (2 mL) was added a yellow solution of tachpyr (0.0271 g, 6.73×10^{-5} mol) in MeOH (2 mL) affording gradual color change from yellowish red to dark green solution. After standing for 0.5 h, Et_2O (12 mL) was added into the mixture to form a green precipitate and a green solution. The precipitate was isolated by decanting the supernatant and dried under reduced pressure. The solid was dissolved in MeOH (2 mL),

and treated with $NaBPh_4$ (0.05 g in 2 mL of MeOH), giving a dark green precipitate. The precipitate was isolated and dried under reduced pressure affording the product in 76.2% yield (0.0443 g, 6.74×10^{-5} mol) as a green solid, whose ^1H NMR spectrum in DMSO-d_6 indicates a mixture of **147**$(BPh_4)_2$ and **148**$(BPh_4)_2$.

Preparation of [Fe(tachpyr-ox-*6*)] (149)$(BPh_4)_2$. To a green solution of $FeCl_2 \bullet 4H_2O$ (0.0219 g, 1.10×10^{-4} mol) in MeOH (2 mL) was added a yellow solution of tachpyr (0.0443 g, 1.10×10^{-4} mol) in MeOH (2 mL) affording a dark brownish green solution. Adding 4 drops of H_2O_2 (30%) gave a bluish purple solution that was let stand one hour and then layered with Et_2O (10 mL), forming a purple precipitate immediately. The precipitate was purified by decanting the supernatant, taking the solid up in acetone (5 mL), filtering, and drying under reduced pressure, then repeating the acetone extraction and drying process to give a purple solid. The solid was dissolved in MeOH (2 mL) and treated with $NaBPh_4$ (0.05 g in 2 mL of MeOH) giving a purple precipitate which was isolated and dried under reduced pressure. This solid was extracted into acetone (5 mL), filtered and dried under reduced pressure. The solid was washed with CH_2Cl_2 (5 mL) and dried under reduced pressure affording the product in 35.5% yield (0.0301 g, 4.79×10^{-5} mol) as a purple solid. ^1H NMR (DMSO-d_6, 25 °C): δ 9.18 (s, 1H, N=C$\underline{H}$-py) 8.38, 8.22, 7.59, 6.69 (d, t, t, d, 4H, $C_5\underline{H}_4N$); 7.59, 6.90, 6.77 (s, t, t, $B(C_6\underline{H}_5)_4$); 4.79 (s, $\underline{A}$MM'XX', 1H, cyclohexyl methine H); 2.57 (d, A$\underline{MM}$'XX', 1H, equatorial cyclohexyl methylene H's diastereotopic); 1.79 (d, AMM'$\underline{XX}$', 1H, ^2J = 14.6 Hz, axial cyclohexyl methylene H's, diastereotopic). HPLC: single peak, R.T. = 18.5 min. UV (MeOH) 582 nm (ε = 5220), 328 nm (ε = 2950). FT-IR (cm^{-1}, in

KBr) 3430 br s (H_2O), 1656 m(C=N), 1582 s (py).

Preparation of [Fe(tachimpyr)]$(ClO_4)_2 \bullet 2H_2O \bullet$MeOH (149). To a yellow solution of $Fe(ClO_4)_2 \bullet 6H_2O$ (0.0336 g, 9.26 x 10^{-5} mol) in MeOH (2 mL) was added a brown solution of tachimpyr (0.0367 g, 9.26 x 10^{-5} mol) in MeOH (2 mL), giving a purple solution and a purple precipitate. This was isolated by decanting supernatant, dried under reduced pressure, washed with CH_2Cl_2, and dried again. A 64.4% yield (0.0453 g, 6.95 x 10^{-5} mol) of a purple solid was obtained. Anal. Calcd for $C_{25}H_{32}Cl_2FeN_6O_{11}$: C, 41.74; H, 4.48; N, 11.68. Found: C, 41.83; H, 4.04; N, 11.14. ^{1}H NMR (DMSO-*d6*, 25 °C): δ 9.27 (s, 1H, N=C*H*-py) 8.40, 8.24, 7.62, 6.65 (d, t, t, d, 4H, C_5H_4N); 4.84 (s, *A*MM'XX', 1H, cyclohexyl methine H); 2.63 (d, A*MM*'XX', 1H, equatorial cyclohexyl methylene H's diastereotopic); 1.82 (d, AMM'*XX*', 1H, ^2J = 14.6 Hz, axial cyclohexyl methylene H's, diastereotopic). ^{13}C NMR: δ 174.45 (N=*C*H-py); 162.42, 158.66, 143.82, 134.62, 132.30 (C_5H_4N); 66.58, 45.16 (cyclohexyl carbons). MS (FAB/thioglycerol): 452 (M - 2$(ClO_4)^-$. FT-IR (cm^{-1}, in KBr) 3500-2800 br s (H_2O), 1641 m (C=N), 1580 s (py), 1085 s (ClO_4^-).

Attempted preparation of a mixture of [Fe(tach(C-Me)$_3$pyr)]$(ClO_4)_2$ (150) and [Fe(tach(C-Me)$_3$pyr-ox-2)]$(ClO_4)_2$ (151) from $Fe(ClO_4)_2 \bullet 6H_2O$ and (+/-)tach(C-Me)$_3$pyr. To a yellow solution of $Fe(ClO_4)_2 \bullet 6H_2O$ (0.0465 g, 1.28 x 10^{-4} mol) in MeOH (2 mL) was added a yellow solution of (+/-)tach(C-Me)$_3$pyr (0.0569 g, 1.28 x 10^{-4} mol) in MeOH (2 mL), affording immediately a brown solution which gradually changes its color to green after 5 min. After standing for 1/2 h, Et_2O (12 mL) was added to from a green precipitate and a green solution. The

precipitate was isolated by decanting the supernatant, washed with Et_2O, and dried under reduced pressure affording a green solid in 72.3% yield (0.0645 g, 9.25×10^{-5} mol). ^1H NMR (DMSO-*d6*, 25°C); multiplets from 8.5 δ to 5.5 δ for pyridyl protons; 4.96, 4.70, 4.29 (br s, AMM'XX', 1H, cyclohexyl methine H); 4.43, 4.16, 3.79 (br s, 1H, py-C(H)CH_3-N*H*); 3.22, 3.11, 2.92 (1H, py-C*H*(CH_3)-NH); 2.73 (s, 3H, py-C(C*H*$_3$)=N-R); multiplets from 1.5 δ to 2.5 δ for (1H, cyclohexyl methine H) and (2H, cyclohexyl methylene H's); 1.39, 1.34 (d, 3H, 6H, py-CH(C*H*$_3$)-NH-R).

Preparation of [Fe(tach(C-Me)$_3$pyr-ox-*6*)](ClO$_4$)$_2$ (153) from a mixture of 150 and 151. To a green solution of a mixture of **150** and **151** in MeOH (2 mL) is added 8 drops of H_2O_2 (30 %) affording a bluish purple solution and purple prisms. After standing two hours, crystals were isolated, washed with Et_2O, and dried under reduced pressure giving a purple solid in 52.7% yield (0.0340 g, 4.90×10^{-5} mol). Prisms for X-ray study were obtained by vapor diffusion of Et_2O into a solution of product in CH_3CN. Anal. Calcd for $C_{27}H_{30}Cl_2FeN_6O_8$ (**153**): C, 46.77; H, 4.36; N, 12.12. Found: C, 46.99; H, 4.46; N, 12.09. ^1H NMR (DMSO-d_6, 25 °C): δ 8.51, 8.22, 7.58, 6.24 (d, t, t, d, 4H, C_5H_4N); 5.04 (s, AMM'XX', 1H, cyclohexyl methine H); 2.79 (s, 3H, py-C(C*H*$_3$)=N-R); 2.53 (d, A*MM*'XX', 1H, equatorial cyclohexyl methylene H's diastereotopic); 1.73 (d, AMM'*XX*', 1H, ^2J = 13.8 Hz, axial cyclohexyl methylene H's, diastereotopic). ^{13}C NMR: δ 174.17 (N=*C*(CH_3)-py); 159.10, 153.12, 138.33, 127.98, 126.96 (*C*$_5$H$_4$N); 54.70, 37.26 (cyclohexyl carbons); 17.80 (py-C(*C*H$_3$)=N-R). MS (FAB/NBA/glycerol): 494 (M - $2ClO_4$).

Preparation of [Fe(tach(C-Me)$_3$pyr-ox-4)](ClO$_4$)$_2$ (152) from Fe(ClO$_4$)$_2$•6H$_2$O and (+/-)tach(C-Me)$_3$pyr. To Fe(ClO$_4$)$_2$•6H$_2$O (0.0418 g, 1.15 x 10^{-4} mol) in MeOH (2 mL) was added (+/-)tach(C-Me)$_3$pyr (0.0512 g, 1.15 x 10^{-4} mol) in MeOH (2 mL) affording immediately a brown solution. While exposing a mixture to air for 2 d, purple prisms were formed. These were isolated, washed with Et$_2$O, and dried under reduced pressure giving a purple solid in 70.6% yield (0.0563 g, 8.12 x 10^{-5} mol). Crystals for X-ray study were obtained by vapor diffusion of Et$_2$O into a solution of product in CH$_3$CN. Anal. Calcd for $C_{27}H_{32}Cl_2FeN_6O_8$ ([Fe(tach(C-Me)$_3$py -ox-4)](ClO$_4$)$_2$): C, 46.64; H, 4.64; N, 12.09. Found: C, 46.71; H, 4.59; N, 12.10. ^{1}H NMR (DMSO-d_6, 25°C); multiplets from 8.5 δ to 5.5 δ for pyridyl protons; 4.96, 4.70 (br s, AMM'XX', 1H, cyclohexyl methine H's on oxidized pendant arms); 4.54 (br s, 1H, py-C(H)CH$_3$-N*H*); 4.46 (1H, py-C*H*(CH$_3$)-NH); 3.15 (br s, AMM'XX', 1H, cyclohexyl methine H from non-oxidized pendant arms); 2.78, 2.74 (s, 3H, py-C(C*H*$_3$)=N-R on oxidized pendant arms); multiplets from 1.5 δ to 2.5 δ for (1H, cyclohexyl methine H) and (2H, cyclohexyl methylene H's); 1.36 (d, 3H, 6H, py-CH(C*H*$_3$)-NH-R from a non-oxidized pendant arm). MS (FAB/NBA/DMSO): 496 (M - 2ClO$_4^-$).

Preparation of a mixture of [Fe(tach(C-Me)$_3$pyr-ox-4)](ClO$_4$)$_2$ (152) and [Fe(tach(C-Me)$_3$pyr-ox-6)](ClO$_4$)$_2$ (153) from Fe(ClO$_4$)$_3$•6H$_2$O and (+/-)tach(C-Me)$_3$pyr. To a yellow solution of Fe(ClO$_4$)$_3$•6H$_2$O (0.033 g, 7.2 x 10^{-5} mol) in MeOH (2 mL) was added a yellow solution of (+/-)tach(C-Me)$_3$pyr (0.032 g, 7.2 x 10^{-5} mol) in MeOH (2 mL) affording immediately a brown solution which was turned into green solution after 2 minutes. While exposing the mixture to air for

2 d, purple microcrystals were formed. These were isolated by decanting supernatant, washed with Et_2O, and dried under reduced pressure giving a purple solid in 65.3 % yield (0.0033 g, 4.8 x 10^{-6} mol). ^1H NMR (DMSO-d_6, 25°C); multiplets from 8.5 δ to 5.5 δ for pyridyl protons; 5.13, 4.74 (br s, AMM'XX', 1H, cyclohexyl methine H's on oxidized pendant arms); 4.54 (br s, 1H, py-C(H)CH_3-N*H*); 4.45 (1H, py-C*H*(CH_3)-NH); 3.15 (br s, AMM'XX', 1H, cyclohexyl methine H from non-oxidized pendant arms); 2.77, 2.73 (s, 3H, py-C(C*H*$_3$)=N-R on oxidized pendant arms); multiplets from 1.5 δ to 2.5 δ for (1H, cyclohexyl methine H) and (2H, cyclohexyl methylene H's); 1.35 (d, d, 3H, 6H, py-CH(C*H*$_3$)-NH-R from the non-oxidized pendant arm).

Preparation of [Fe(tach(C-Me)$_3$pyr-ox-*6*)](ClO$_4$)$_2$ (153) from the mixture of 152 and 153. The mixture of **152** and **153** was dissolved in CH_3CN, and Et_2O was vapor diffused into it resulting in the formation of purple prisms. These were dried under reduced pressure giving a purple solid in 54.2 % yield (0.0027 g, 3.9 x 10^{-6} mol). Anal. Calcd for $C_{27}H_{30}Cl_2FeN_6O_8$: C, 46.77; H, 4.36; N, 12.12. Found: C, 46.92; H, 4.43; N, 12.06. ^1H NMR (DMSO-d_6, 25 °C): δ 8.50, 8.21, 7.56, 6.22 (d, t, t, d, 4H, C_5H_4N); 5.01 (s, AMM'XX', 1H, cyclohexyl methine H); 2.77 (s, 3H, py-C(C*H*$_3$)=N-R); 2.50 (overlapped with solvent , A*MM*'XX', 1H, equatorial cyclohexyl methylene H's diastereotopic); 1.70 (d, AMM'*XX*', 1H, ^2J = 14.2 Hz, axial cyclohexyl methylene H's, diastereotopic). MS (FAB/NBA/DMSO): 494 (M - 2ClO_4^-).

Preparation of [Fe(tach-Me$_3$pyr)](ClO$_4$)$_2$ (154) from Fe(ClO$_4$)$_2$•6H$_2$O and tach-

Me_3pyr. To a pale yellow solution of $Fe(ClO_4)_2 \bullet 6H_2O$ (0.0374 g, 1.03×10^{-4} mol) in MeOH (2 mL) was added a pale yellow solution of (N-Me_3)tachpyr (0.0458 g, 1.03×10^{-4} mol) in MeOH (2 mL) affording a brownish green solution. After standing for 3 hours, gray-green microcrystals were deposited. The supernatant was decanted, and the solid was washed with Et_2O and dried under reduced pressure affording a green solid in 77.7% yield (0.0647 g, 9.27 x 10-5 mol). Anal. Calcd for $C_{27}H_{38}Cl_2FeN_6O_9$ (**142**$\bullet H_2O$): C, 45.21; H, 5.34; N, 11.71. Found: C, 44.90; H, 5.08; N, 11.88. UV-vis (CH_3CN) 595 nm (ε = 144.5). μ_{eff} = 5.078 at 25°C. MS (FAB/Glycerol/DMSO): 500 (M - $2ClO_4^-$).

Reaction of the Fe(III)–ATP (1:3) (155) complex with tachpyr. The Fe(III)-ATP complex was prepared by using method of Chasteen et al.[181] To a solution of ATP disodium salt (1.82 g, 3.30×10^{-3} mol) in 0.1 M HEPES/Na buffer (pH 7.0, 20 mL) was added 6.14 mL of $FeCl_3$ (0.179 M) solution in 1 M HCl (pale yellow), while maintaining the pH at 7.0 using 1.0 N NaOH. A deeper yellow solution was obtained. The total volume was made up to 100 mL. To this Fe-ATP complex solution (1 mL) was added tachpyr (3 eqiv based on Fe(III), 0.0133 g, 3.3 x 10^{-5} mol) in 10 mL deionized water giving a color change from yellow to green after 5 min. The mixture was stood for 48 h after which it was identified as **147**$(Cl)_2$ and **148**$(Cl)_2$ by the UV-vis spectroscopy.

Attempted study of Oxidation of Deoxyribose by Hydroxyl Radical Mediated by Fe(II) Complexes see Appendix D

Preliminary Competition Study of Zn(II) and Fe(II) for tachpyr Ligand see Appendix E

C. Tumor Cell Cytotoxicity of tachpyr Derivatives

A novel chelator, tachpyr, and its derivatives were investigated for their potential as an anti-cancer drug in the close collaboration with Dr. Suzy Torti at Wake Forest University of School of medicine.

[Fe(tachpyr-ox-2)] (147)$(Cl)_2$ and [Fe(tachpyr-ox-4)] (148)$(Cl)_2$ from $FeCl_2 \bullet 4H_2O$ and tachpyr were prepared by using $FeCl_2 \bullet 4H_2O$ instead of $Fe(ClO_4) \bullet 6H_2O$ and by following the method described above for the preparation of **147**$(ClO_4)_2$ and **148**$(ClO_4)_2$.

Preparation of [Zn(tachpyr)]$(ClO_4)_2 \bullet CH_3OH$ (250), [Mn(tachpyr)]$(ClO_4)_2$(271), and [Cu(tachpyr)]$(ClO_4)_2$ (257A). See experimental section in **Chapter 3.**

Preliminary preparation of [Ca(tachpyr)]Cl_2 from $CaCl_2$and tachpyr. To a clear solution of $CaCl_2$ (0.037 g, 9.2×10^{-5} mol) in MeOH (2 mL) was added to a yellow solution of tachpyr (0.010 g, 9.2×10^{-5} mol) in MeOH (2 mL) affording a yellow suspension immediately which was disappeared upon swirling. A yellow precipitate was formed by adding Et_2O into a mixture, isolated, and dried under reduced pressure giving a pale yellow solid. This was dissolved in MeOH and filtered, and Et_2O was diffused into the filtrate giving white prisms. These were isolated and dried under reduced pressure affording a white solid in 67.5 % yield (0.032 g, 6.2×10^{-5} mol). ^1H NMR (DMSO-d_6, 25° C): δ 8.45, 8.35, 7.87, 7.78 (d, t, d,

t, 4H, $C_5\underline{H}_4N$); 6.65 (br s, $\underline{A}XY$, 1H, $N\underline{H}$-CH_2-py); 4.49 (m (two dd), $AX\underline{Y}$, 2H, NH-$C\underline{H}_2$-py); 3.66 (br s, $\underline{A}MM'XX'$, 1H, cyclohexyl methine H's); 2.53 (br d, $A\underline{M}M'XX'$, 1H, equatorial cyclohexyl methylene H diastereotopic), 2.13 (br d, $AMM'\underline{X}X'$, 1H, axial cyclohexyl methylene H's, diastereotopic).

Preliminary preparation of [Mg(tachpyr)]Cl_2 from $MgCl_2 \cdot 6H_2O$ and tachpyr. To $MgCl_2 \cdot 6H_2O$ (0.011 g, 5.6×10^{-5} mol) in MeOH (2 mL) was added to a yellow solution of tachpyr (0.023 g, 5.6×10^{-5} mol) in MeOH (2 mL) affording a yellow solution. A pale yellow precipitate was formed by adding Et_2O in to the mixture, isolated by decanting supernatant, and dried under reduced pressure giving a pale yellow solid. The yellow solid was dissolved in MeOH, and Et_2O was diffused into MeOH solution of a crude product giving a white prism shape crystalline. The white crystalline was isolated by decanting supernatant, purified by washing with CH_2Cl_2, and dried under reduced pressure affording 50.4 % yield (0.014 g, 2.8×10^{-5} mol) as a white solid.

Preparation of tachpyr$\cdot 5HNO_3$. To tachpyr (0.1769 g, 4.39×10^{-4} mol) in MeOH (4 mL) was added eight equiv of HNO_3 (70%, 0.220 mL) affording a sticky white precipitate. This was sonicated for 1 min and decanted to give a white solid. MeOH (4 mL) was added to the solid, followed by vigorous scratching to partially break up the solid. Addition of Et_2O (4 mL) gave a milky white suspension and a white solid. This was sonicated for 5 min, allowed to settle, and decanted. Two more washings with Et_2O (8 mL each) and sonications (5 min) were carried out, after which scratching gave a homogeneous white solid that was isolated and dried under reduced pressure (yield 0.260 g). The

substance should be stored in a desiccator at room temperature, where it yellows slightly over several weeks without any discernible change in properties. The composition of product may vary slightly in number of nitrate anions and degree of hydration. It should always be characterized by elemental analysis. One preparation similar to the above gave tachpyr•5HNO_3•H_2O. Anal. Calcd for $C_{24}H_{37}N_{11}O_{16}$: C, 39.19; H, 5.07; N, 20.94, Found: C, 39.62; H, 5.06; N, 20.97.

Nitrate salts of tach-Me_3pyr and tach-Et_3pyr can be prepared by using a same method described above.

D. Partition Coefficients of tachpyr

Octanol-water partition coefficients were determined for the tachpyr ligand by dissolving the ligand (0.0017g, 4.2×10^{-6} mol) in octanol (10 mL) in a screw-cap vial. To this vial was added deionized (10 mL). The mixture was stirred for 18 h, allowed to stand overnight, and poured into a separation funnel. The two layers were separated and stored in two individual vials. The absorption values at 260 nm were then compared directly between octanol and water layers giving partition coefficient, log $P_{Oct./H_2O}$, of – 0.1.

Results

A. Complex Formation and Ligand Oxidation in the Reactions of Fe(II) and Fe(III) with tachpyr Ligand

A.1. Ligands

Novel hexadentate tach derivatives (tach-R_3pyr) were prepared by adding three 2-pyridylmethyl arms to tach.[95] The choice was based upon the desire to form cationic complexes while maintaining five-membered chelate rings in the complex.[182] Tach was alkylated by reaction with the appropriate aldehyde to form the respective tris(imine), and a routine borohydride reduction followed to provide a novel hexadentate tachpyr (**158**) (R = H). Tach-Me_3pyr (**159**) (R = Me) and tach-Et_3pyr (**160**) (R = Et) were prepared by alkylation of tach-R_3 with 2-chloromethylpyridine.[1]

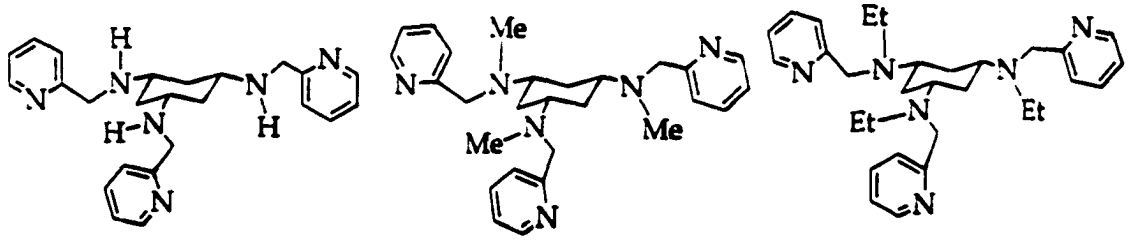

158 **159** **160**

Figure 2.17. Tachpyr derivatives.

The tachpyr and its *N,N',N''*-alkylated derivatives coordinate as neutral ligands, so no deprotonation is needed. To an alcoholic solution of the ligand was added the metal ion in alcohol to form the appropriate metal complex. The

formation of complexes can be detected by ^1H NMR spectroscopy if applicable.

A.2. Reaction of $Fe(II)Cl_2 \cdot 4H_2O$ and tachpyr

Many different reaction conditions were used for the reactions of Fe (II or III) salts (Cl_2 or $(ClO_4)_2$) with tachpyr to investigate the tachpyr oxidation that Fe promotes. The reactions of iron salts and tachpyr are summarized and presented in **Scheme 2.16.**

1) When $Fe(II)Cl_2 \cdot 4H_2O$ in MeOH reacted with tachpyr in MeOH in the presence of oxygen it generated a dark brown-green solution to which air was bubbled for 10 min and Et_2O was added affording a dark green precipitate. ^1H spectra of the dark green precipitate are very complex with some extent of line broadening and indicate the presence of at least two different species of Fe(II) complexes according to the number of peaks (**Fig. 2.18 (a)**). It is even difficult to observe a splitting pattern of pyridyl protons because of the broadness of peaks. Many efforts have been made to separate those complexes without success. However, in the ^1H NMR spectra, there were very distinctive peaks around δ 9.5 (**Fig. 2.18 (a)**), which were not observed in ^1H NMR spectra of other divalent diamagnetic metal ions, Zn(II) (**Fig. 2.18 (b)**) and Ca(II).

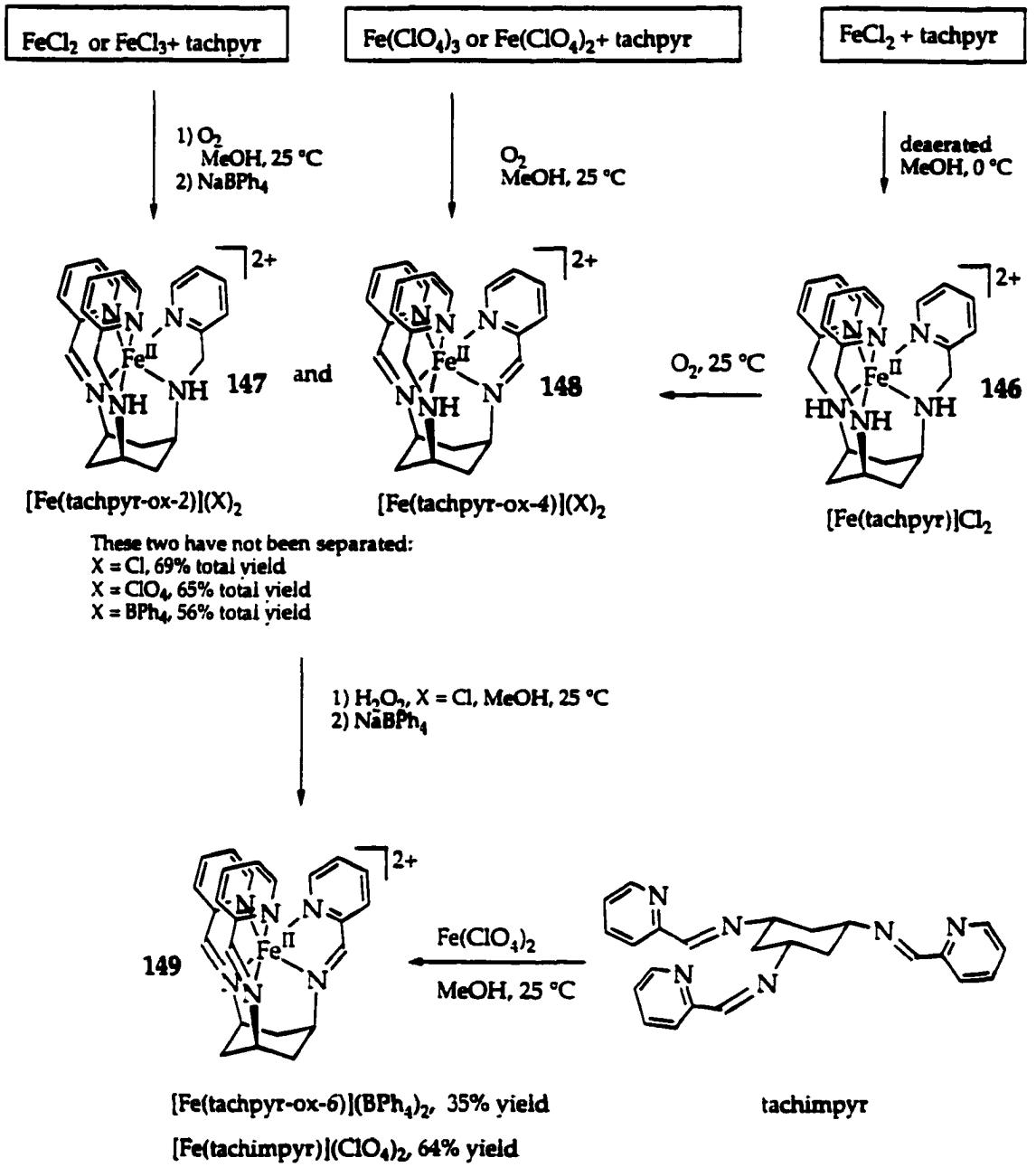

Scheme 2.16. Reactions of iron salts and tachpyr, complex formation, and ligand oxidation.

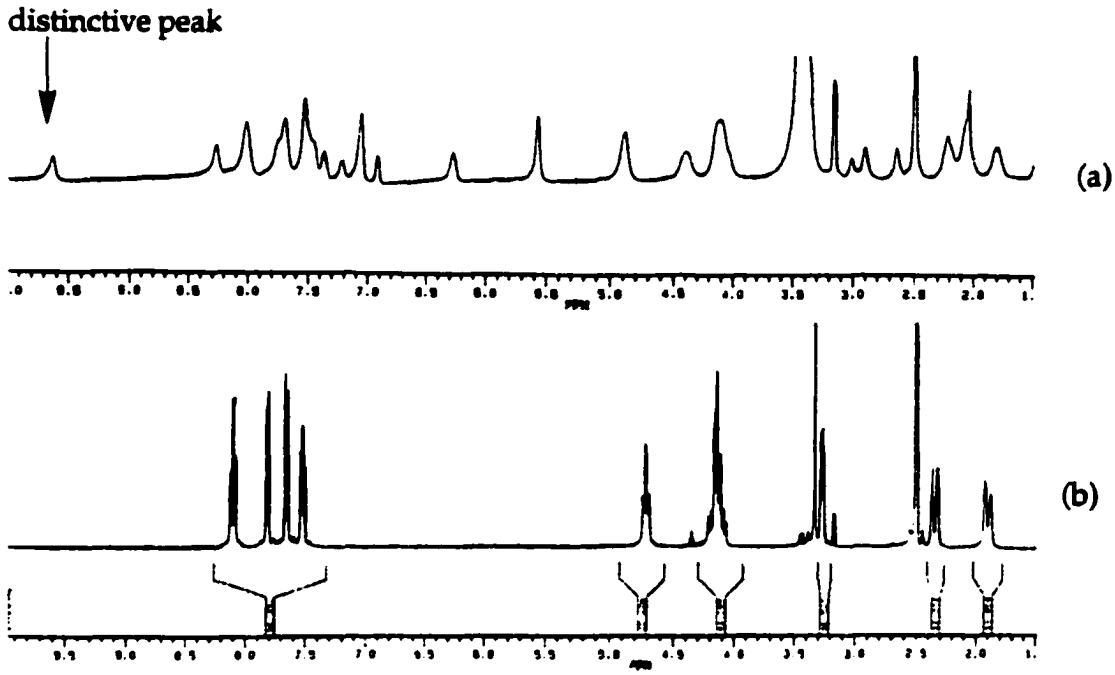

Figure 2.18. ^{1}H NMR spectra of (a) Fe(II) complex of tachpyr after bubbling air 10 min, (b) [Zn(tachpyr)]$(ClO_4)_2$.

2) When Fe(II)$Cl_2 \cdot 4H_2O$ in a mixture of MeOH (2 mL) and Et_2O (6 mL) was reacted with tachpyr in a mixture of MeOH (2 mL) and Et_2O (6 mL) in the presence of oxygen, a dark green-brown precipitate formed immediately and was isolated. Its ^{1}H NMR spectrum presented very broad peaks (**Fig. 2.19 (a)**), even broader than those in **Figure 2.18 (a)**. However, it showed a distinctive peak around δ 9.5.

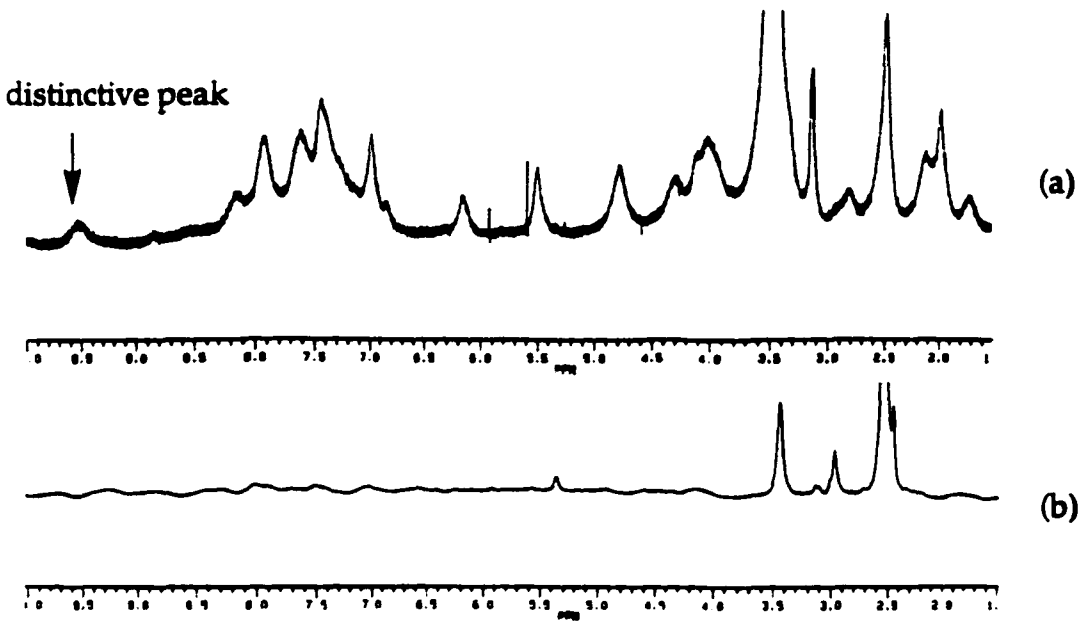

Figure 2.19. ^{1}H NMR spectra of Fe(II) complexes of tachpyr; (a) precipitation just after mixing reactants, (b) N_2 gas purged after mixing.

3) A reaction of Fe(II)$Cl_2 \bullet 4H_2O$ in MeOH and tachpyr in MeOH in the presence of oxygen afforded a brown-green solution that was purged with nitrogen gas for 1/2 h, giving a dark green oily material. ^{1}H NMR of the isolated oily material showed only a peak for solvent (DMSO) at 2.5 ppm and a peak for water at 3.35 ppm (**Fig. 2.19 (b)**), suggesting the formation of a paramagnetic Fe complex. Replacement of Cl^- anions by addition of excess of $NaBPh_4$ in MeOH gave a purple precipitate. This was isolated, washed with MeOH, and dried under reduced pressure giving a purple solid. ^{1}H NMR spectrum of the purple solid presented a very complex spectrum with three distinctive peaks (δ 9.58, 9.27, and 9.26) (**Fig. 2.21**) which were assigned as imine protons (R-N=C*H*-py).[171, 173] The product was inferred to be an inseparable mixture of mono-imino **147**$(BPh_4)_2$ and di-imino **148**$(BPh_4)_2$ (**Fig. 2.20**) complexes resulting from oxidative dehydrogenation.

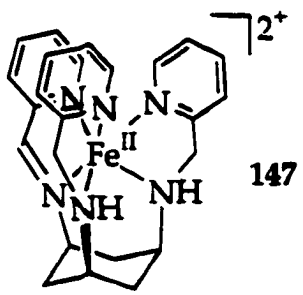

147

[Fe(tachpyr-ox-2)](BPh$_4$)$_2$

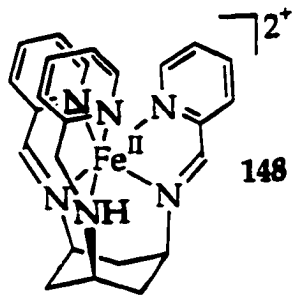

148

[Fe(tachpyr-ox-4)](BPh$_4$)$_2$

Figure 2.20. Mono-imino **147**(BPh$_4$)$_2$ and di-imino **148**(BPh$_4$)$_2$ Fe(II) tachpyr complexes.

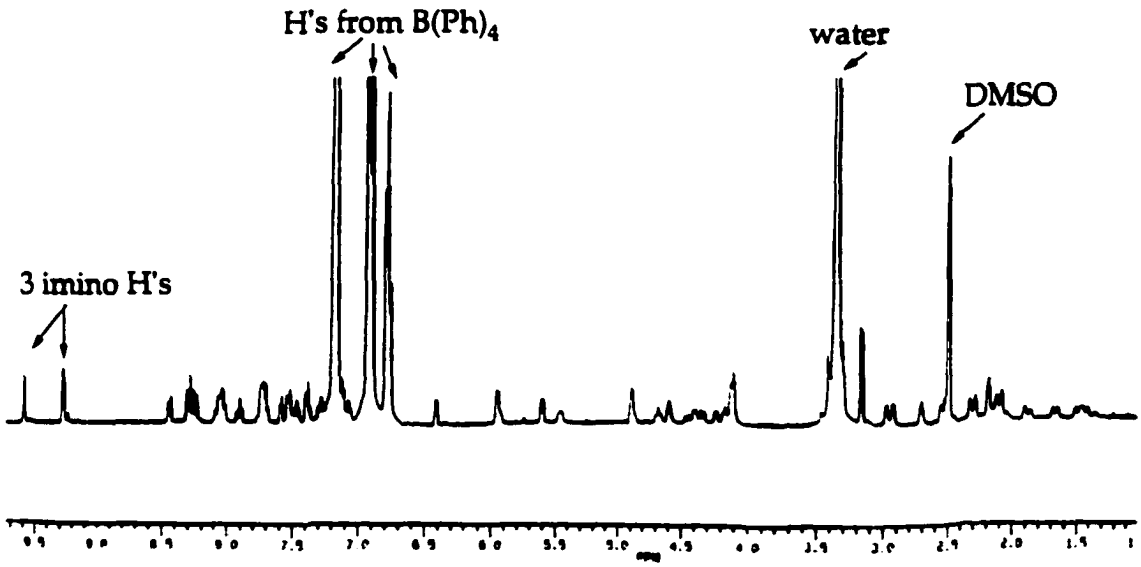

Figure 2.21. ^{1}H NMR of a mixture of mono-imino **147**(BPh$_4$)$_2$ and di-imino **148**(BPh$_4$)$_2$ Fe(II) tachpyr complexes.

4) To dark brown-green solution of a mixture of Fe(II)Cl$_2$•4H$_2$O and tachpyr in MeOH in the presence of oxygen was added excess of NaBPh$_4$ in MeOH, affording a dark blue-purple precipitate which was filtered after adding Et$_2$O to obtain more precipitates. The isolated blue-purple precipitate has a

similar ^{1}H NMR spectrum (**Fig. 2.22**) of **147**$(BPh_4)_2$ and **148**$(BPh_4)_2$ in **Figure 2.21**, indicating formation identical products.

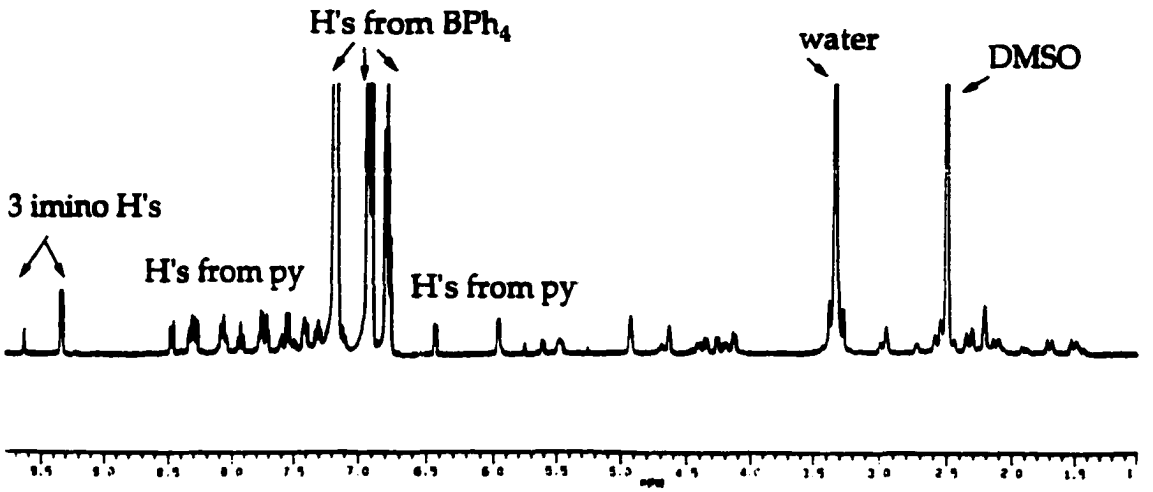

Figure 2.22. ^{1}H NMR of mono-imino **147**$(BPh_4)_2$ and di-imino **148**$(BPh_4)_2$.

5) A tris-imino Fe(II) tachpyr complex **149**$(BPh_4)_2$, [Fe(tachpyr-ox-6)]$(BPh_4)_2$ (**Fig. 2.23**), was obtained by adding H_2O_2 (30%) (4-5 drops) into a mixture of $FeCl_2 \bullet 4H_2O$ and tachpyr in MeOH to force the oxidation followed by the anion change with BPh_4 and purification. ^{1}H NMR indicated that all three 2-pyridylmethyl arms are oxidatively dehydrogenated, affording three 2-pyridylimine arms which present a very simple ^{1}H NMR spectrum (**Fig. 2.24**). FT-IR spectra also support the formation of an imino complex by presenting C=N stretching at 1656.3 cm^{-1} which can not be observed from the tachpyr ligand and [In(tachpyr)]$(ClO_4)_3$ in which three 2-pyridylmethyl arms are not oxidized. The tris-imino Fe(II) complex **149**, [Fe(tachimpyr)]$(ClO_4)_2$, and **149**$(BPh_4)_2$, [Fe(tachpyr-ox-6)]$(BPh_4)_2$, are identical complexes except the counter anions. The **149** was first prepared directly from pyridine-2-carboxaldehyde, tach, $FeSO_4$, and

$HClO_4$ (Fig. 2.25 (a)).[183] ^1H NMR spectrum of **149** is very similar to that of **149**$(BPh_4)_2$ except peaks for the counter anions.

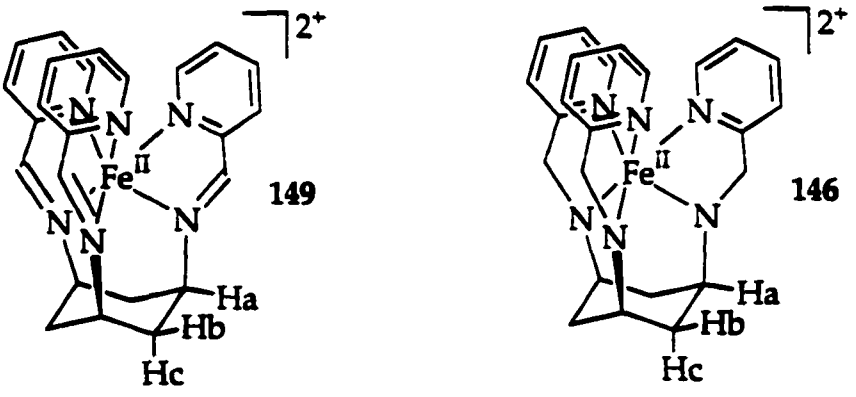

[Fe(tachpyr-ox-6)]$(BPh_4)_2$ [Fe(tachpyr)]Cl_2

Figure 2.23. Tris-imino **149**$(BPh_4)_2$, and non-oxidized Fe(II) tachpyr complex.

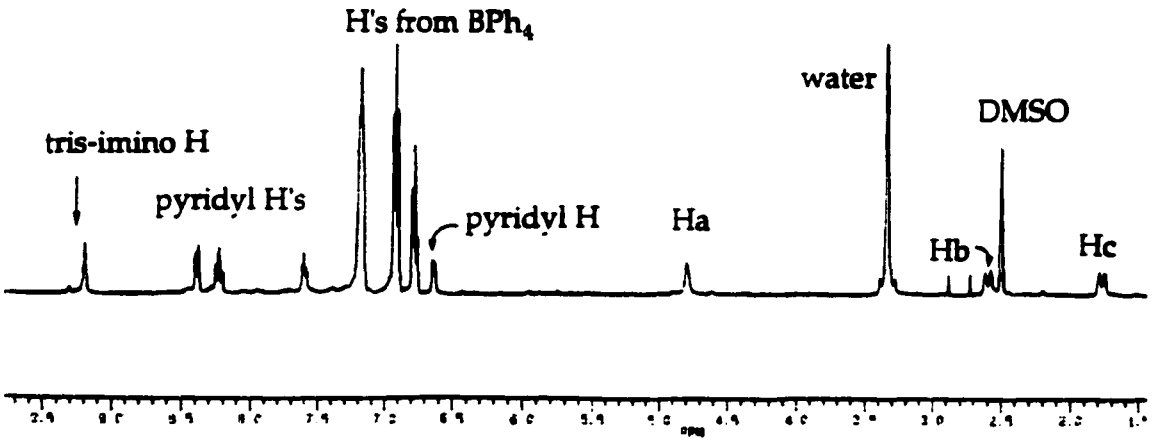

Figure 2.24. ^1H NMR of **149**$(BPh_4)_2$.

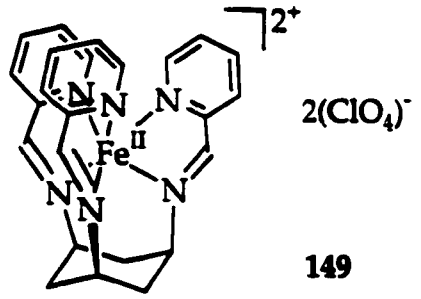

149

[Fe(tachimpyr)](ClO$_4$)$_2$

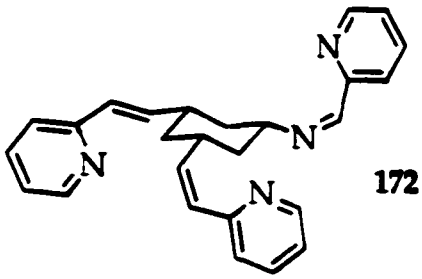

172

tachimpyr ligand

Figure 2.25. (a) **149**, [Fe(tachimpyr)](ClO$_4$)$_2$, (b) tachimpyr ligand.

6) Non-oxidized Fe(II) tachpyr complex **146 (Fig. 2.23)** as a brown precipitate was obtained by the reaction of $FeCl_2 \bullet 4H_2O$ in MeOH degassed with N_2 and tachpyr in MeOH degassed with N_2 at 0°C and under N_2 gas. The brown precipitate is air-sensitive, so only ^{1}H NMR was used to characterize it. The ^{1}H NMR spectrum of the product **(Fig. 2.26)** is consistent with that of other tachpyr complexes of metals e.g., Hg^{2+}, Cd^{2+}, and Ca^{2+}.

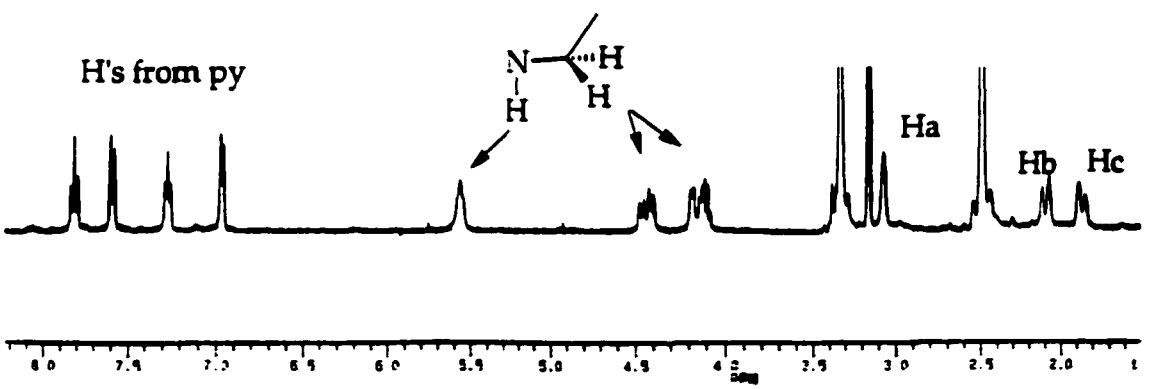

Figure 2.26. ^{1}H NMR of non-oxidized [Fe(tachpyr)] **146**(Cl)$_2$.

Upon exposure to air for 2h, brown Fe(II) tachpyr complex turned to a green-blue oil which was isolated and dried under reduced pressure. ^{1}H NMR (**Fig. 2.27**) indicated a mixture of **146**$(Cl)_2$, [Fe(tachpyr)]Cl_2, and **147**$(Cl)_2$, [Fe(tachpyr-ox-2)]Cl_2.

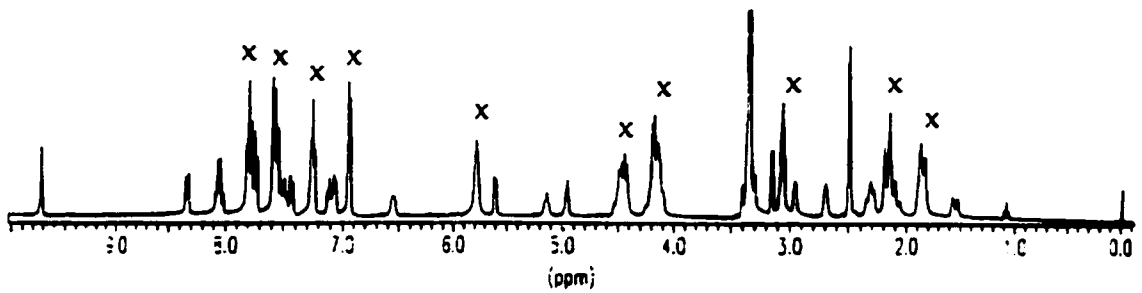

x = peaks from [Fetachpyr]Cl_2

Figure 2.27. ^{1}H NMR of the mixture of **146**$(Cl)_2$ and **147**$(Cl)_2$.

A.3. Reaction of Fe(III)$Cl_3 \bullet 4H_2O$ and tachpyr

1) MeOH solutions of Fe(III)$Cl_3 \bullet 6H_2O$ and tachpyr reacted in the presence of oxygen to form a dark green solution from which a green precipitate was isolated by precipitation with Et_2O (12 mL). The ^{1}H NMR spectrum of this precipitate (**Fig. 2.28 (a)**) suggested presence of the paramagnetic ferric state (d^5). The presence of an imine proton, however, was observed around δ 9.5. The precipitate was dissolved in MeOH and treated with excess of $NaBPh_4$ affording a blue solid that was identified as a di-imino Fe(II) tachpyr complex **148**$(Cl)_2$ (**Fig. 2.20**) according to its ^{1}H NMR (**Fig. 2.28 (b)**).

2) When N_2 gas was purged into the mixture of Fe(III)$Cl_3 \bullet 6H_2O$ and tachpyr in MeOH a gradual color change was observed from yellow to brown-

green then to dark green. A green precipitate was isolated by addition of EtO (12 mL), which gave a ^{1}H NMR spectrum almost identical to that in **Figure 2.28 (a)**, suggesting presence of iron(III). After the precipitate in MeOH was treated with $NaBPh_4$, a blue-purple precipitate was formed. Its ^{1}H NMR (not presented) is almost identical to that of **147**$(BPh_4)_2$ and **148**$(BPh_4)_2$ (**Fig. 2.21**), indicating the formation of a mixture of a mono-imino and di-imino Fe(II) tachpyr complexes, **147**$(BPh_4)_2$ and **148**$(BPh_4)_2$.

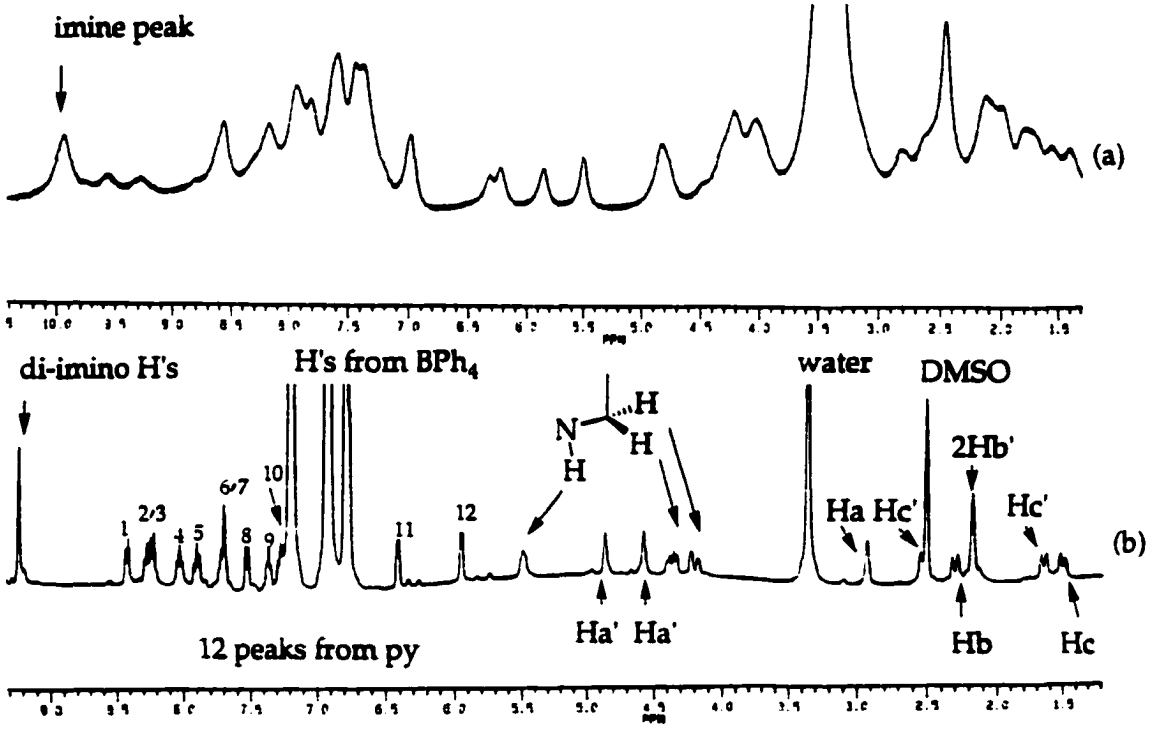

Figure 2.28. ^{1}H NMR spectra of (a) just after mixing, (b) after treatment with $NaBPh_4$, formation of di-imino Fe(II) complex **148**$(BPh_4)_2$.

A.4. Reaction between $Fe(II)(ClO_4)_2 \cdot 6H_2O$ and tachpyr

1) The reaction of $Fe(II)(ClO_4)_2 \cdot 6H_2O$ and tachpyr in MeOH in the presence of oxygen formed a dark brown-green solution immediately. The color of the mixture changed from dark brown-green to green after it was exposed to

air for 1/2 h. After exposing it to air for 16 h, a green precipitate was formed. Its ^{1}H NMR spectrum (**Fig. 2.29 (a)**) indicates the formation of a mixture of mono- and di-imino Fe(II) complexes, **147**$(ClO_4)_2$ and **148**$(ClO_4)_2$. However, the majority of the product is **147**$(ClO_4)_2$ according to the integration.

2) When the reaction mixture of Fe(II)$(ClO_4)_2 \bullet 6H_2O$ and tachpyr in MeOH was exposed to air for 2 d, the formation of a dark blue plates was observed. The ^{1}H NMR (**Fig. 2.29 (b)**) spectra of the crystals indicates a mixture of **147**$(ClO_4)_2$ and **148**$(ClO_4)_2$, however, the amount of **148**$(ClO_4)_2$ is significantly increased compared to those in **Figure 2.29 (a)**.

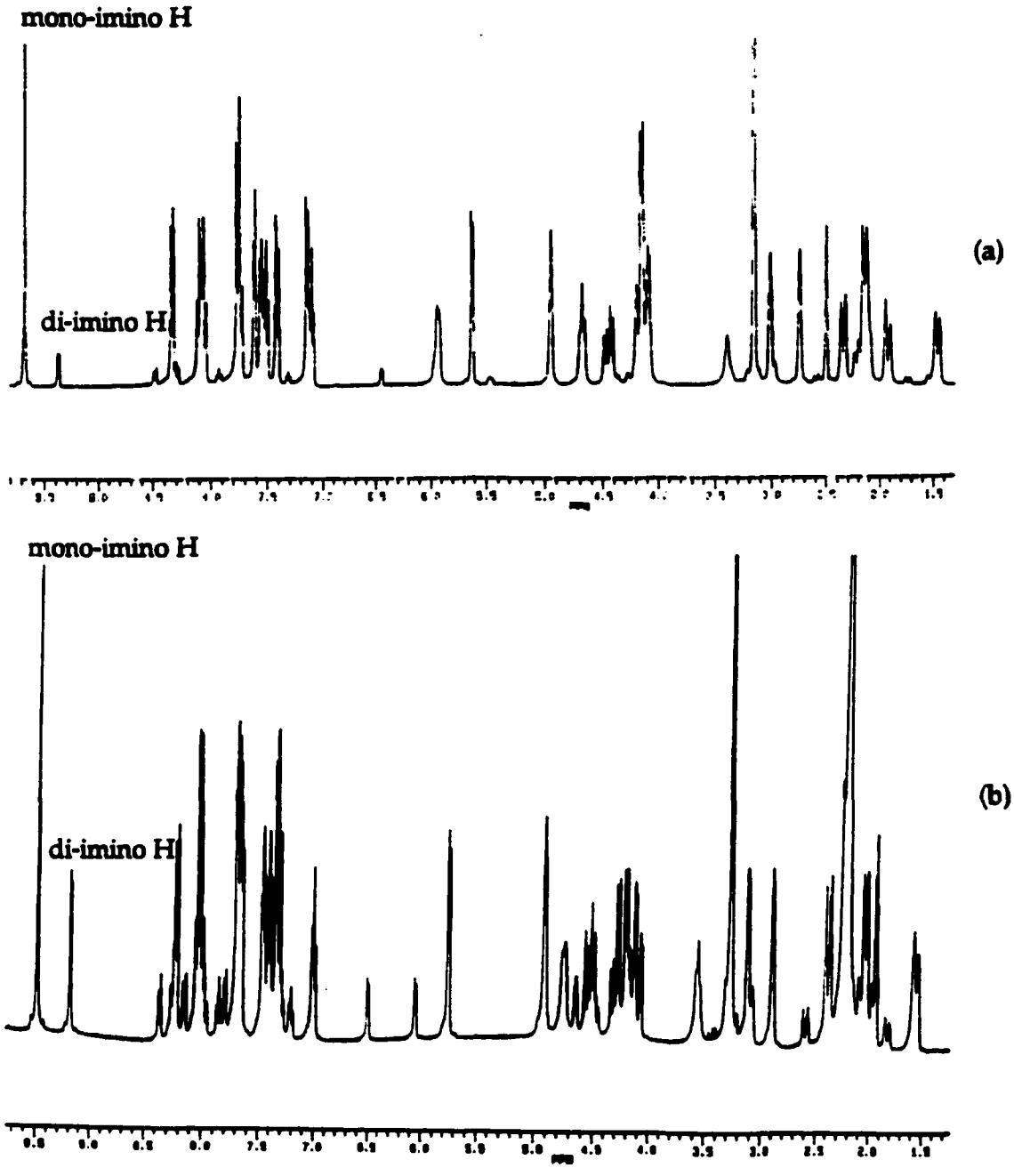

Figure 2.29. ^{1}H NMR (a) a mixture of **147**$(ClO_4)_2$ and **148**$(ClO_4)_2$ after 16 h exposure to air (b) a mixture of **147**$(ClO_4)_2$ and **148**$(ClO_4)_2$ after 2 d exposure to air.

3) A brown-green precipitate was formed immediately from a reaction o

$Fe(II)(ClO_4)_2$ and tachpyr in a mixture of $MeOH/Et_2O$ (2 mL : 6 mL), isolated, and dried under reduced pressure affording a dark green solid. The ^1H NMR spectrum of a solid (**Fig. 2.30**) indicates a mixture of a non-oxidized Fe(II) tachpyr complex **146**$(ClO_4)_2$, [Fe(tachpyr)]$(ClO_4)_2$, as a major product and a mono-imino Fe(II) tachpyr complex **147**$(ClO_4)_2$, [Fetachpyr-ox-2]$(ClO_4)_2$, as a minor product.

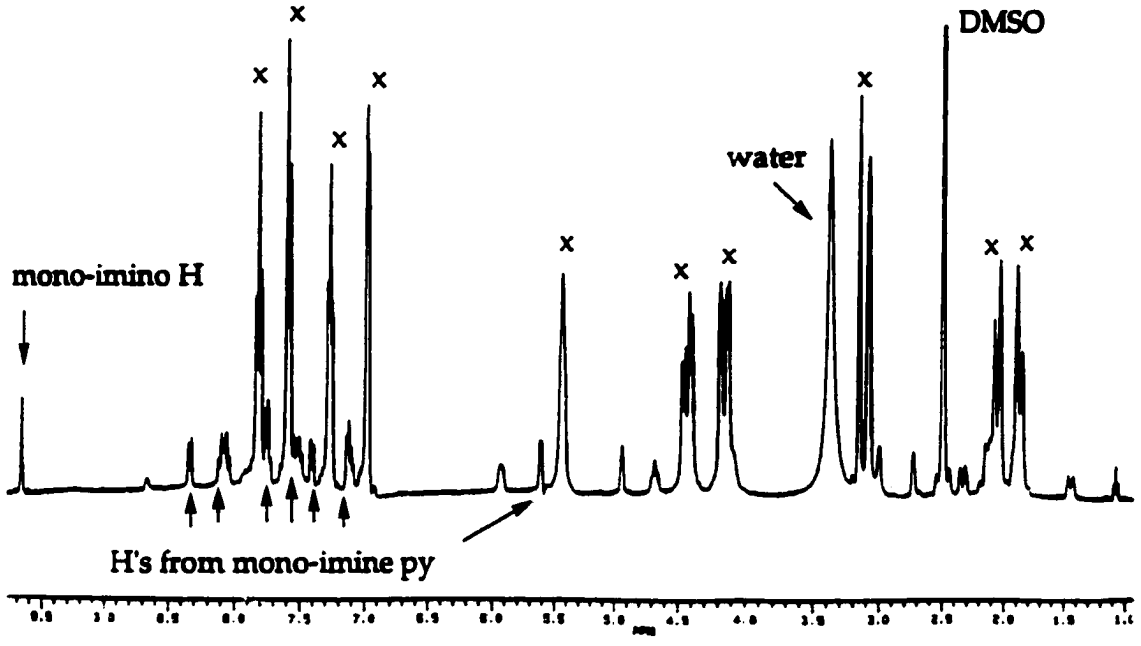

Figure 2.30. ^1H NMR of a mixture of **146**$(ClO_4)_2$ and **147**$(ClO_4)_2$.

4) To support the assignments of the imino peaks in the ^1H NMR spectra, a mixture of a mono- and di-imino Fe(II) tachpyr complexes **147**$(ClO_4)_2$ and **148**$(ClO_4)_2$ was added to an equal amount of tris-imino Fe(II) tachimpyr complex **149** in MeOH. The ^1H NMR spectra of the mixture (**Fig. 2.31**) clearly distinguished the chemical shift differences of the imino protons from the three complexes. A singlet at δ 9.64 arose from the mono-imino complex, two singlets

at δ 9.35 from the di-imino complex, and a singlet at δ 9.25 from the tris-imino complex.

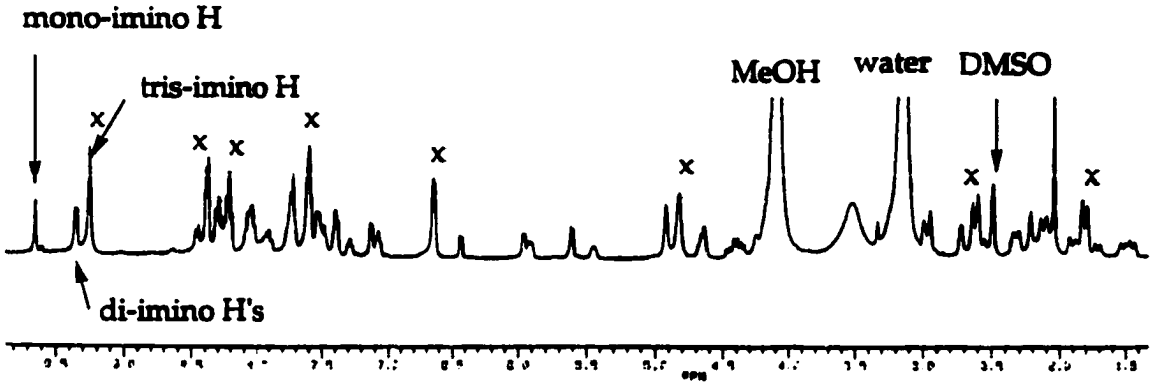

Figure 2.31. ^{1}H NMR spectrum of a mixture of mono-, di-, and tris-imino Fe(II) tachpyr complexes.

A.5. Reaction of $Fe(III)(ClO_4)_2 \cdot 6H_2O$ and tachpyr

A mixture of **147**$(ClO_4)_2$ and **148**$(ClO_4)_2$ was obtained by the reaction between $Fe(III)(ClO_4)_2 \cdot 6H_2O$ in MeOH and tachpyr in MeOH either in the presence of oxygen or purging N_2 gas into the mixture for 1/2h. ^{1}H NMR spectra of the green oily solid indicate that the product is a mixture of equal amount **147**$(ClO_4)_2$ and **148**$(ClO_4)_2$ according to the integration. When it was treated with excess of $NaBPh_4$ in MeOH and H_2O_2 (30%) (5 drops), the formation of a mixture of a di-imino and tris-imino Fe(II) complexes, **148**$(BPh_4)_2$ and **149**$(BPh_4)_2$, was observed based on the ^{1}H NMR spectra (**Fig. 2.32**).

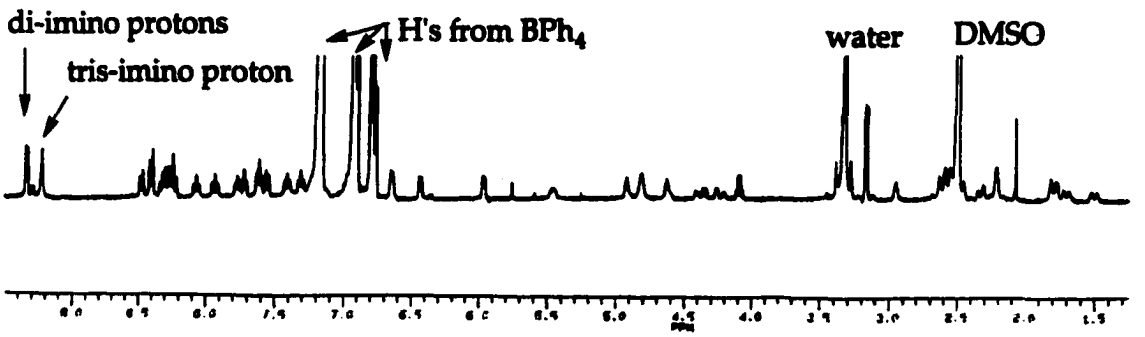

Figure 2.32. ^1H NMR of a mixture of the di- and tris-imino Fe(II) complexes, **148**$(BPh_4)_2$ and **149**$(BPh_4)_2$.

A.6. Electronic and Vibrational Spectra of Fe(II)tachpyr Complexes

The electronic spectra of the mixture of **146**$(ClO_4)_2$ and **147**$(ClO_4)_2$, [Fe(tachpyr)]$(ClO_4)_2$ and [Fe(tachpyr-ox-2)]$(ClO_4)_2$, and of the mixture of **147**$(ClO_4)_2$ and **148**$(ClO_4)_2$, [Fe(tachpyr-ox-2)]$(ClO_4)_2$ and [Fe(tachpyr-ox-4)]$(ClO_4)_2$, were obtained and presented in **Figure 2.33 (a)** and **(b)**, respectively. UV-vis spectra of the tris-imino Fe(II) complex **149** **(Fig. 2.34)**, [Fe(tachimpyr)]$(ClO_4)_2$, was also obtained. Results of the electronic spectra of Fe(II) tachpyr complexes and their molar absorptivity in anhydrous MeOH are presented in **Table 2.2.** The electronic spectral data of **149** compare well to those reported previously[184] and those in tris-imino complex **153**, [Fe(tach(C-Me)$_3$pyr-ox-*6*)], which has also two charge-transfer absorptions at 374 nm (26.7 kK, ε = 2572) and 588 nm (17.0 kK, ε = 9125) **(Fig. 2.42 (b))**.

All UV-vis spectra have two charge-transfer bands as absorption maxima in the visible region and possibly three absorption maxima below 300 nm. Because the absorption maxima below 300 nm were also observed in UV-vis spectra of the free ligand and non-oxidized metal complexes, they were

attributed to the electronic transitions from the ligand. An intense absorption around 600 nm (ε = 1735 ~ 9305) is characteristic of metal-ligand charge-transfer bands observed for other iron(II) complexes of α,α′-diimines. The higher energy band around 380 nm (ε = 4821 ~ 5185) is presumably associated with a metal-ligand charge-transfer (pyridine).[171] A shoulder around 500 nm starts to appear and its intensity is increased as the number of the oxidized ligand are increased. This shoulder is a characteristic of octahedral $[Fe(II)(\alpha,\alpha'\text{-diimine})_3]^{2+}$ systems but no attempts has been made further to assign it.[184]

Table 2.2. Results of the electronic spectra of Fe(II) tachpyr complexes and their molar absorptivity (ε) in anhydrous MeOH.

Metal complex	Low energy charge-transfer band (ε =L mol^{-1} cm^{-1})	High energy charge-transfer band (ε =L mol^{-1} cm^{-1})
$[Fe(tachpyr)]^{2+}$ and $[Fe(tachpyr\text{-}ox\text{-}2)]^{2+}$	603 nm (1735)	422 nm (4821)
$[Fe(tachpyr\text{-}ox\text{-}2)]^{2+}$ and $[Fe(tachpyr\text{-}ox\text{-}4)]^{2+}$	605 nm (6869) 523nm (2261)*	385 nm (5185)
$[Fe(tachimpyr)]^{2+}$	578 nm (9305) 530 nm (6326)*	327 nm (4843)
$[Fe(py_3tach)]^{2+}$[184]	574 nm (12300) 534 nm (9000)*	362 nm (3300)

* shoulder. py_3tach = tachimpyr[184]

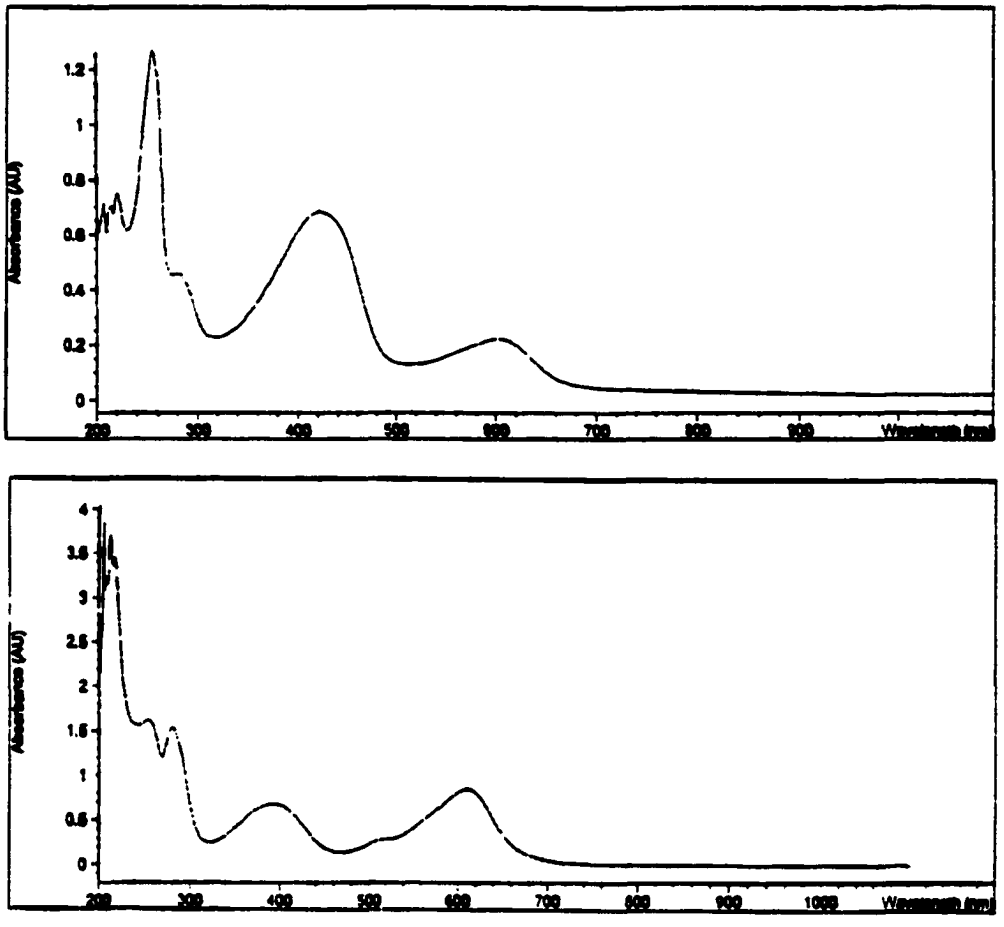

Figure 2.33. (a) UV-vis spectra of the mixture of **146**$(ClO_4)_2$ and **147**$(ClO_4)_2$, (b) UV-vis spectra of the mixture of **147**$(ClO_4)_2$ and **148**$(ClO_4)_2$.

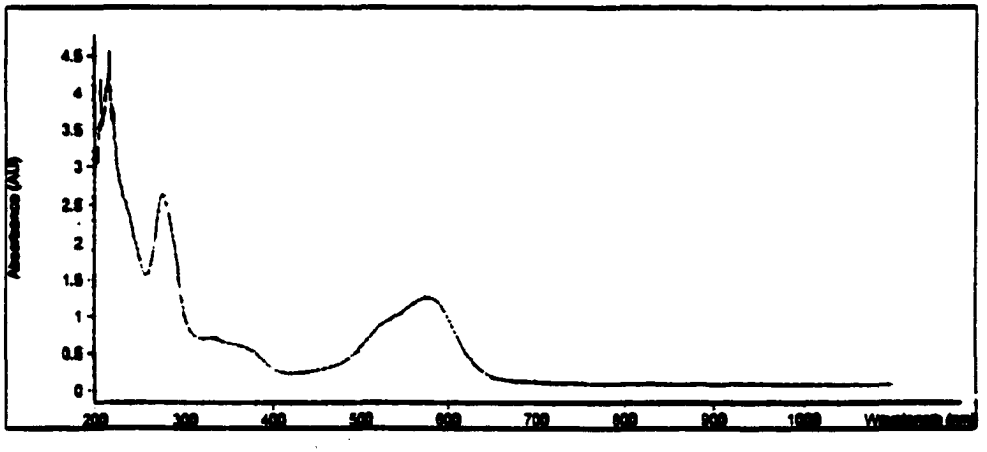

Figure 2.34. UV-vis spectra of **149**, [Fe(tachimpyr)]$(ClO_4)_2$.

The IR spectrum of the mixture **147**$(Cl)_2$ and **148**$(Cl)_2$ was obtained and presented in **Figure 2.35 (a)**. The IR spectrum of **149**$(BPh_4)_2$ **(Fig. 2.35 (b))** was also obtained and compared to identical (except anions) tris-imino complex **149**, $[Fe(tachimpyr)](ClO_4)_2$, prepared by the direct reaction of tachimpyr and $Fe(II)(ClO_4)_2 \cdot 6H_2O$.

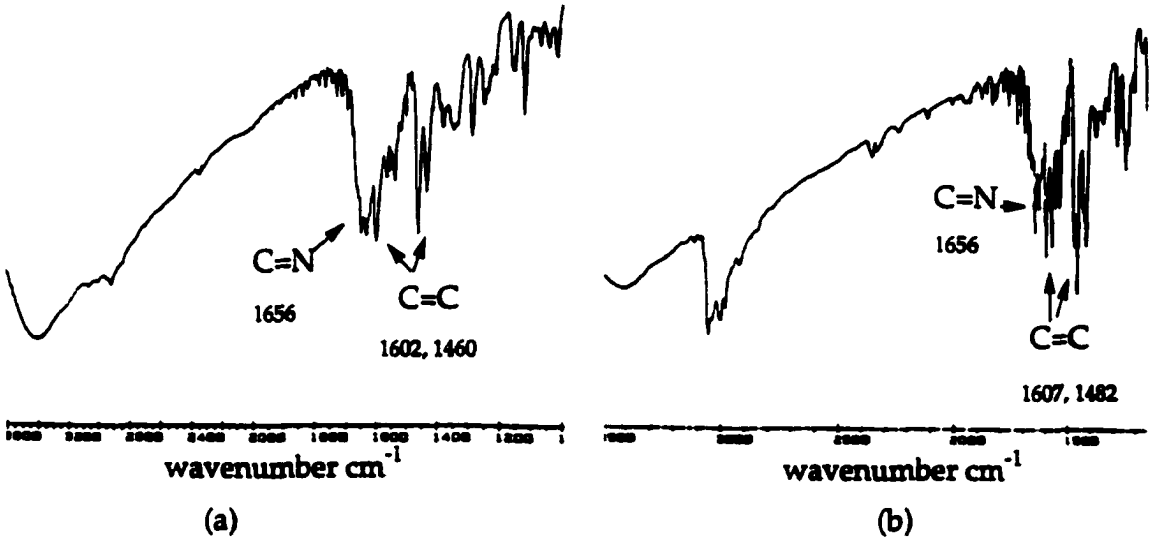

Figure 2.35. IR spectra of (a) the mixture of **147**$(Cl)_2$ and **148**$(Cl)_2$, (b) **149**$(BPh_4)_2$.

B. Complex Formation and Ligand Oxidation in the Reactions of Fe(II) and Fe(III) with (+/-)tach(C-Me)$_3$pyr Ligand

B.1. Properties of (+/-)tach(C-Me)$_3$pyr

For the further investigation of the oxidative dehydrogenation reaction, (+/-)tach(C-Me)$_3$pyr ligand was prepared. The (+/-)tach(C-Me)$_3$pyr ligand **161** has a methyl group on the methylene bridge of tachpyr (**Fig. 2.36**) providing only one proton available for oxidative dehydrogenation, which would make oxidative dehydrogenation slow In an unsymmetrical ligand with three stereo-centers, there would be eight possible stereo-isomers (RRR, RRS, RSR, RSS, SRS, SSR, SRR, and SSS), the threefold symmetry of the ligand reduces these to two enantiomeric pairs ((RRR, SSS) and (RRS, SSR)). The ^{1}H NMR spectrum of the free ligand clearly indicates the presence of two different isomers in equal amounts. Because of smaller repulsions caused by methyl groups and adjacent protons on the tach amine nitrogen and the cyclohexyl ring in the RRS and SSR isomers the RRR and SSS isomers are expected form a well-shaped metal complex more readily than RRS and SSR isomers. However, once either isomer is coordinated to iron metal ion followed by the ligand oxidation, chirality on carbon atoms will be lost leading to an identical imino complex.

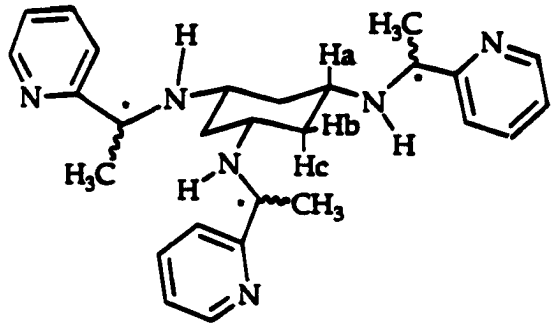

161

Figure 2.36. The (+/-)tach(C-Me)$_3$pyr ligand.

B.2. Reaction of Fe(II)(ClO$_4$)$_2$•6H$_2$O and (+/-)tach(C-Me)$_3$pyr

Various reaction conditions were used for the reactions of Fe(II) and Fe(III) with (+/-)tach(C-Me)$_3$pyr to investigate oxidative dehydrogenation reaction mediated by iron ion. The reactions of Fe(II or III) perchlorate salts and (+/-)tach(C-Me)$_3$pyr is presented in **Scheme 2.17.**

1) A brown-green precipitate was obtained by adding Et_2O (12 mL) into a mixture of Fe(II)(ClO$_4$)$_2$•6H$_2$O and (+/-)tach(C-Me)$_3$pyr in MeOH, which was capped and stored at 5° C for 14 h,. The ^{1}H NMR spectrum of the precipitate **(Fig. 2.37)** shows very broad but simple peaks suggesting the formation of a non-oxidized Fe(II) complex **150** with some Fe(III) byproducts.

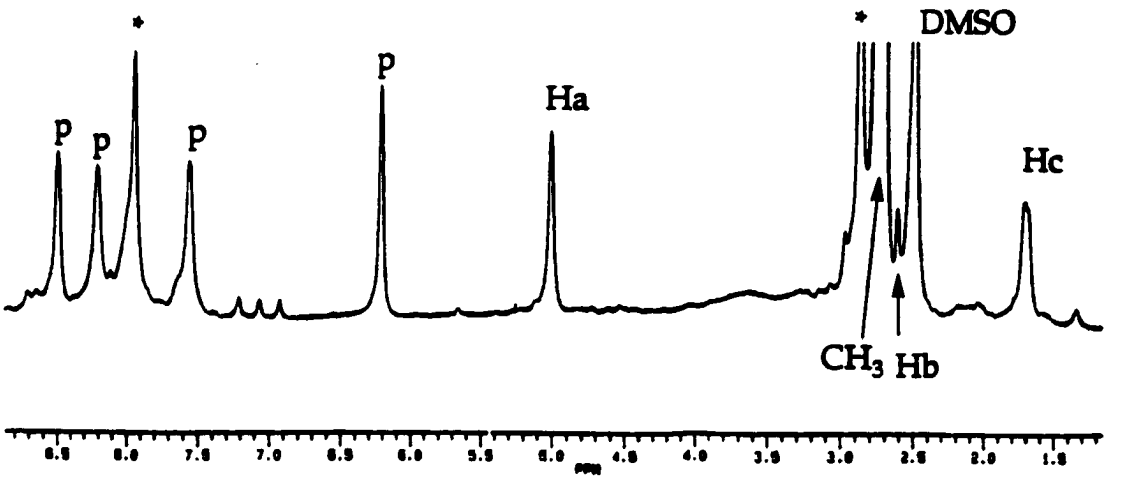

Figure 2.37. ^{1}H NMR of a mixture of a non-oxidized Fe(II) complex **150** and some Fe(III) byproducts.

2) A green precipitate was obtained by adding Et_2O (12 mL) into a mixture, exposed to air for 1/2 h, of $Fe(II)(ClO_4)_2 \cdot 6H_2O$ and (+/-)tach(C-Me)$_3$pyr in MeOH. No attempts were made to definitively to assign the spectra of this solid. The ^{1}H NMR spectrum of the solid (**Fig 2.38 (b)**) showed sharp peaks with clear coupling patterns, suggesting the formation of a diamagnetic Fe(II) complex which is assumed as a mixture of a non-oxidized Fe(II) complex and a mono-imino Fe(II) complex **150** and **151** (**Fig 2.38 (a)**, [Fe(tach(C-Me)$_3$pyr](ClO$_4$)$_2$ and [Fe(tach(C-Me)$_3$pyr-ox-2)](ClO$_4$)$_2$. The methyl protons (N(H)-C(H)C$\underline{H}_3$-py) in **150** or on non-oxidized arms in **151** show a doublet around δ 1.4 as a result of coupling with a proton (N(H)-C($\underline{H}$)CH$_3$-py) on an adjacent carbon. On the other hand, the methyl protons (N=C(C$\underline{H}_3$)-py) on an oxidized arm show a distinctive singlet since there is no proton to couple with after the ligand oxidation occurs and shift to the downfield around δ 2.7.

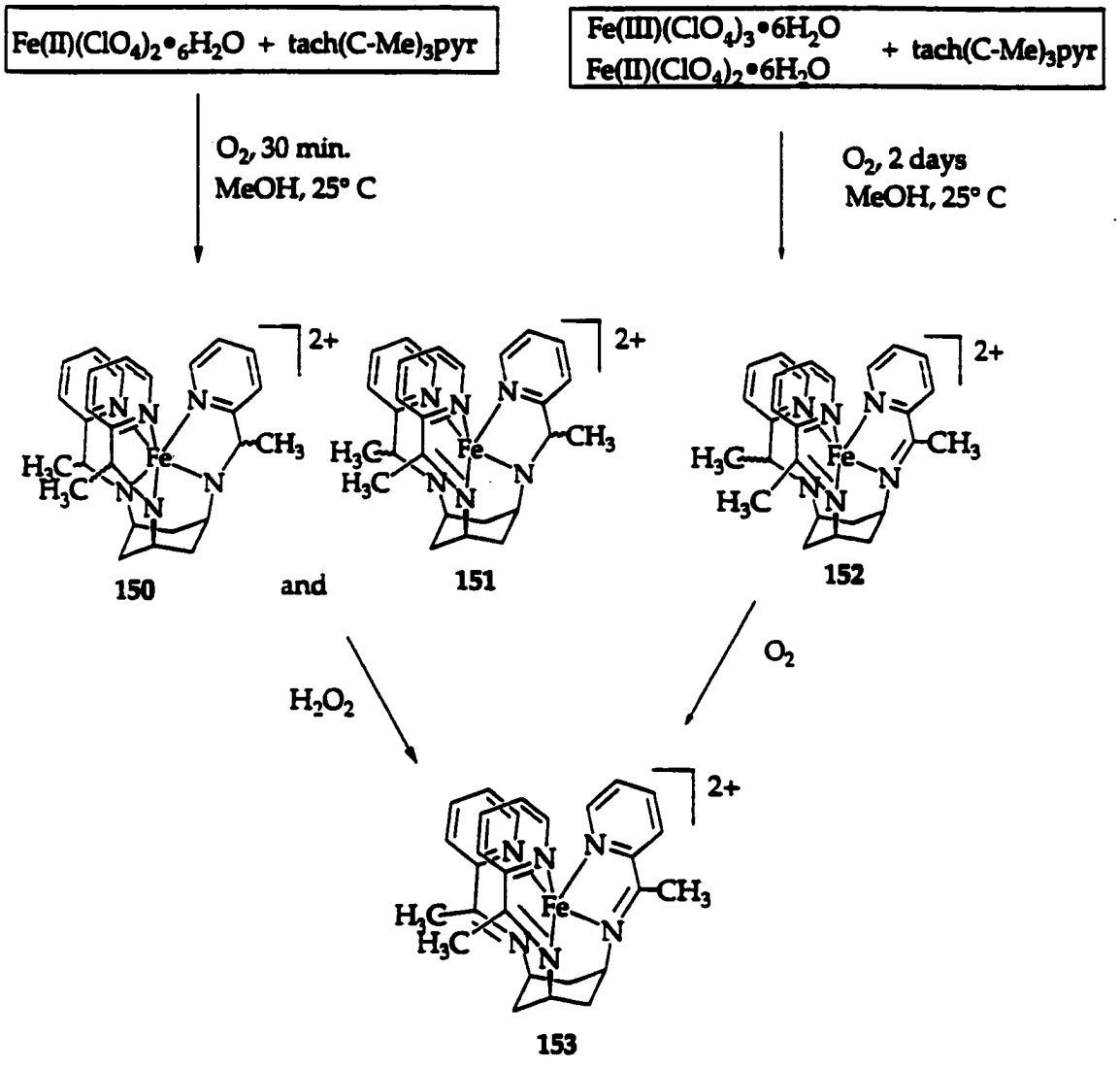

Scheme 2.17. Reaction of iron salts and (+/-)tach(C-Me)$_3$pyr, complex formation, and ligand oxidation.

To a green solution of the mixture of **150** and **151** in MeOH was added 8 drops of H_2O_2 (30%) affording purple prisms that give a ^{1}H NMR spectrum of a tris-imino Fe(II) complex **153**, [Fe(tach(C-Me)$_3$pyr-ox-*6*)](ClO$_4$)$_2$, (**Fig 2.39**). The ^{13}C NMR, FAB-MS spectra, and elemental analysis result were also consistent with the structure of **153**. X-ray suitable single crystals of [Fe(tach(C-Me)$_3$pyr-ox-*6*)] were obtained by vapor Et_2O diffusion into a CH_3CN solution of **153**.

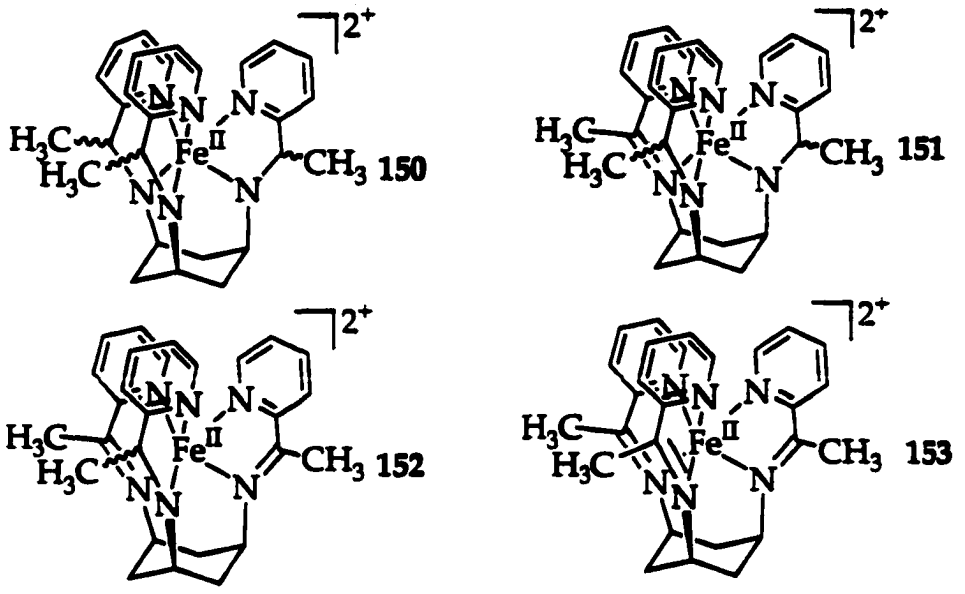

(a)

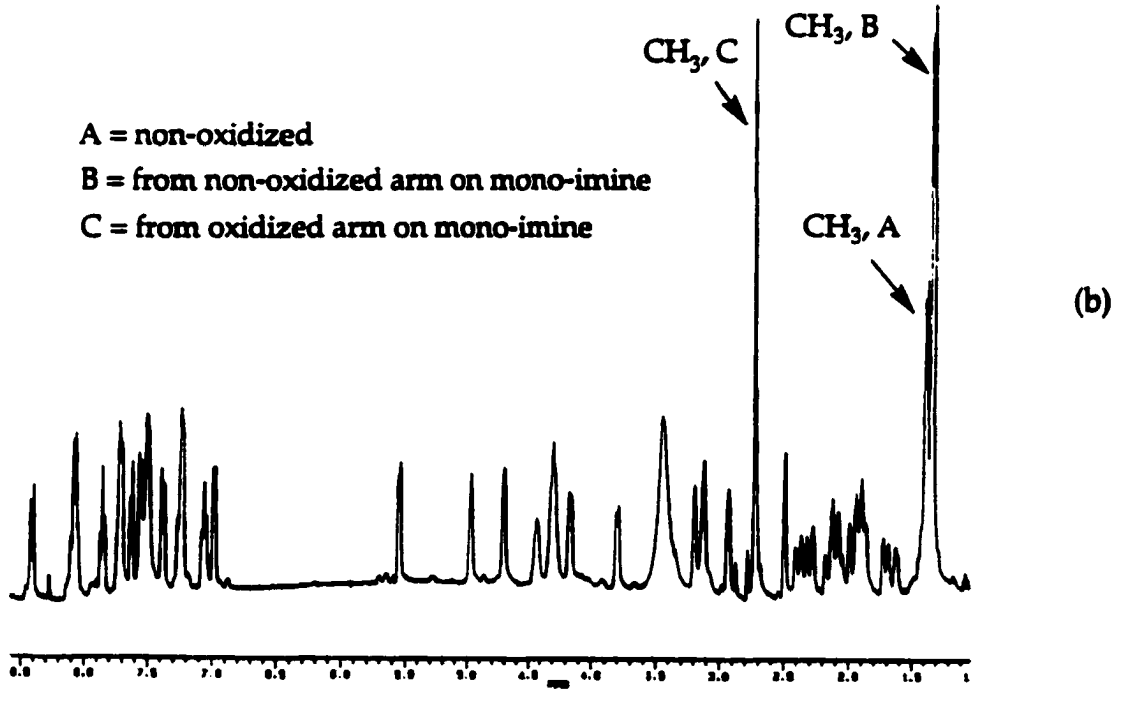

(b)

Figure 2.38. (a) non-oxidized (150), mono- (151), di- (152), and tris-imino (153) tach(C-Me)$_3$pyr Fe(II) complexes, (b) ^{1}H NMR of a possible mixture of 150 and 151.

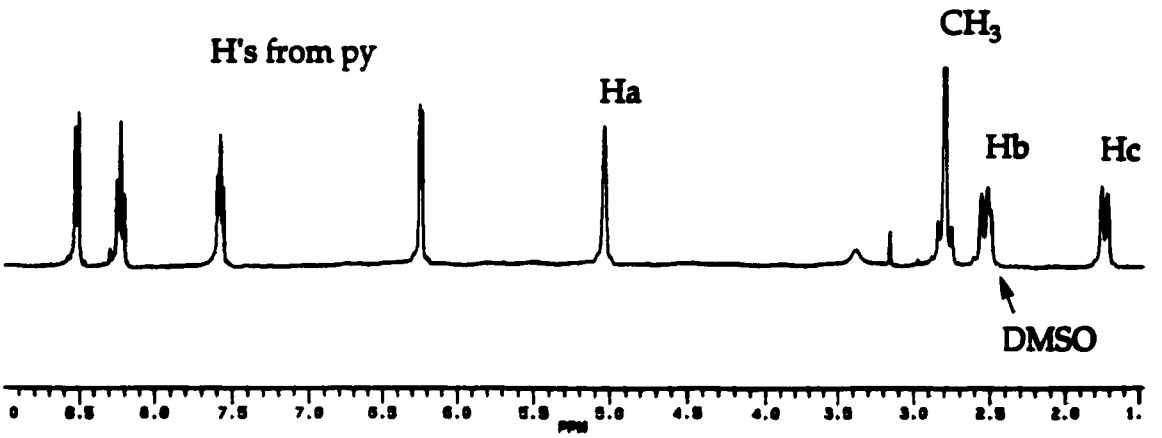

Figure 2.39. ^{1}H NMR of tris-imino complex **153.**

3) By exposing the reaction mixture of $Fe(II)(ClO_4)_2 \cdot 6H_2O$ and (+/-)tach(C-Me)$_3$pyr in MeOH to air for 2 d, purple prisms were formed and isolated. ^{1}H NMR of the purple prisms (**Fig. 2.40**) shows the formation of **152**, $[Fe(tach(C\text{-}Me)_3pyr\text{-}ox\text{-}4)](ClO_4)_2$, which was characterized by FAB-MS and elemental analysis. Because of the presence of 12 peaks between δ 5.5 and 8.7 as pyridyl protons (four peaks for each pyridine ring) and three distinguished methyl proton peaks (two around δ 2.7 as a singlet and one at δ 1.4 as a doublet), **152** in solution does not seem to have any symmetry. Crystals of **152** were obtained by vapor Et_2O diffusion into CH_3CN solution, however, they were not analyzed.

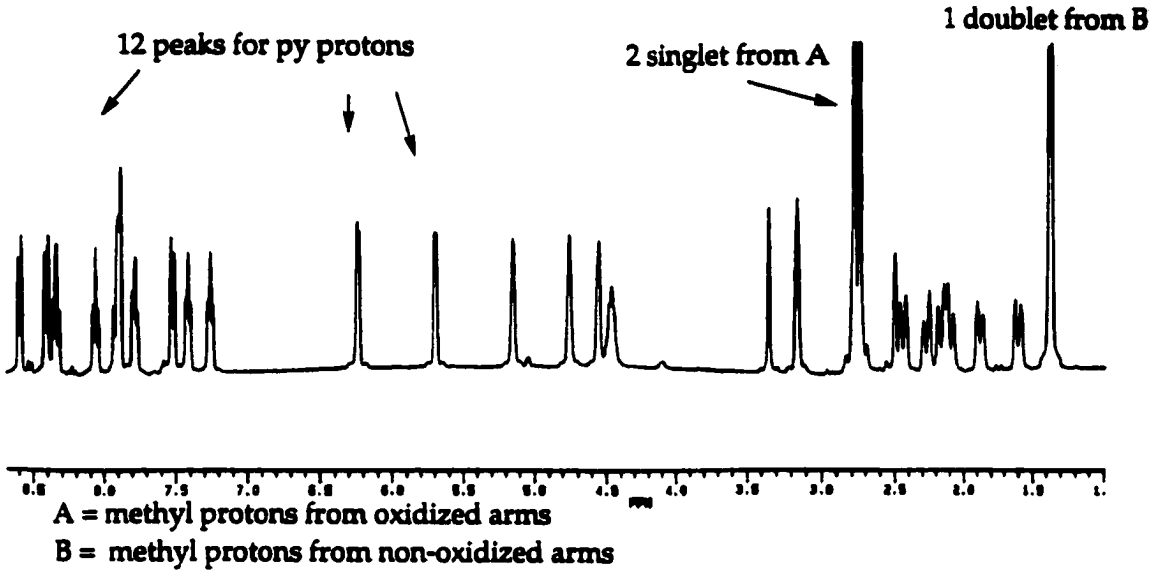

Figure 2.40. ^{1}H NMR of di-imino Fe(II) complex **152**.

B.3. Reaction between $Fe(III)(ClO_4)_3 \cdot 6H_2O$ and (+/-)tach(C-Me)$_3$pyr

1) ^{1}H NMR of brown solid obtained immediately by adding Et_2O (12 mL) to a mixture of $Fe(III)(ClO_4)_3 \cdot 6H_2O$ and (+/-)tach(C-Me)$_3$pyr in MeOH presented even broader peaks than those in **Figure 2.37**.

2) The reaction mixture of $Fe(III)(ClO_4)_3 \cdot 6H_2O$ and (+/-)tach(C-Me)$_3$pyr in MeOH was exposed to air for 2 d affording purple prisms identified as a mixture of **152** (a major), [Fe(tach(C-Me)$_3$pyr-ox-4)]$(ClO_4)_2$, and **153** (a minor), [Fe(tach(C-Me)$_3$pyr-ox-6)]$(ClO_4)_2$, by ^{1}H NMR spectrum (**Fig. 2.41 (a)**). Purple prisms obtained from recrystallization of the mixture of **152** and **153** were identified as the tris-imino complex **153** by ^{1}H NMR spectroscopy, the FAB-MS spectrum, and elemental analysis. The formation of **153** from the mixture of **152** and **153** during the processes of recrystallization can be explained by an extended exposure of the complex solution to air in the processes of the purification and the

recrystallization.

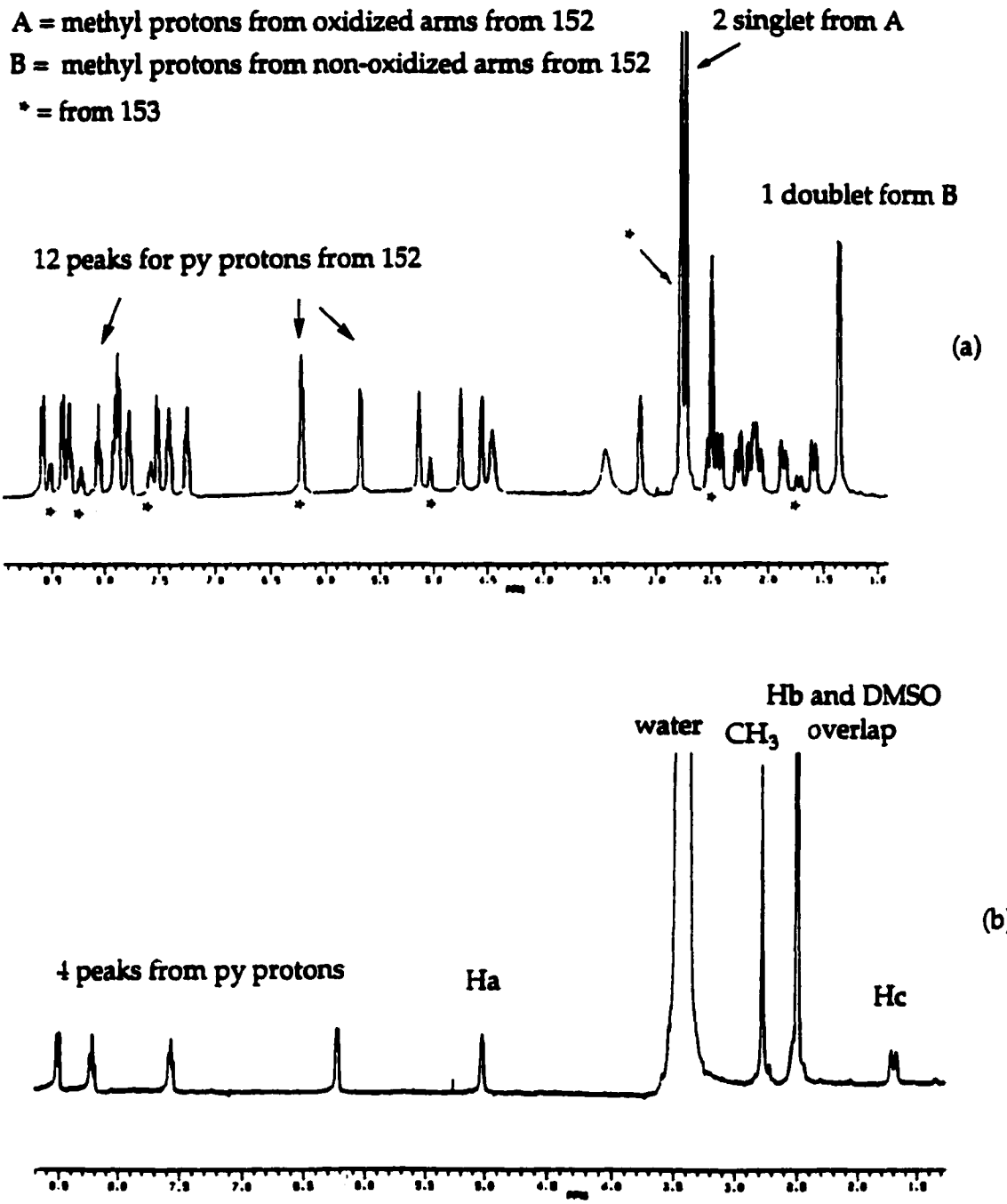

Figure 2.41. ^{1}H NMR of (a) a mixture of **152** and **153**, (b) **153**.

The electronic spectra of the mixture of **150** and **151**, [Fe(tach(C-Me)$_3$pyr](ClO$_4$)$_2$ and [Fe(tach(C-Me)$_3$pyr-ox-2)](ClO$_4$)$_2$, and **153**, [Fe(tach(C-

$Me)_3$pyr-ox-6)]$(ClO_4)_2$, were obtained and presented in **Figure 2.42 (a) and (b).** Results of the electronic spectra of Fe(II) complexes of tach(C-Me)$_3$pyr and their molar absorptivity in anhydrous MeOH are presented in **Table 2.3.**

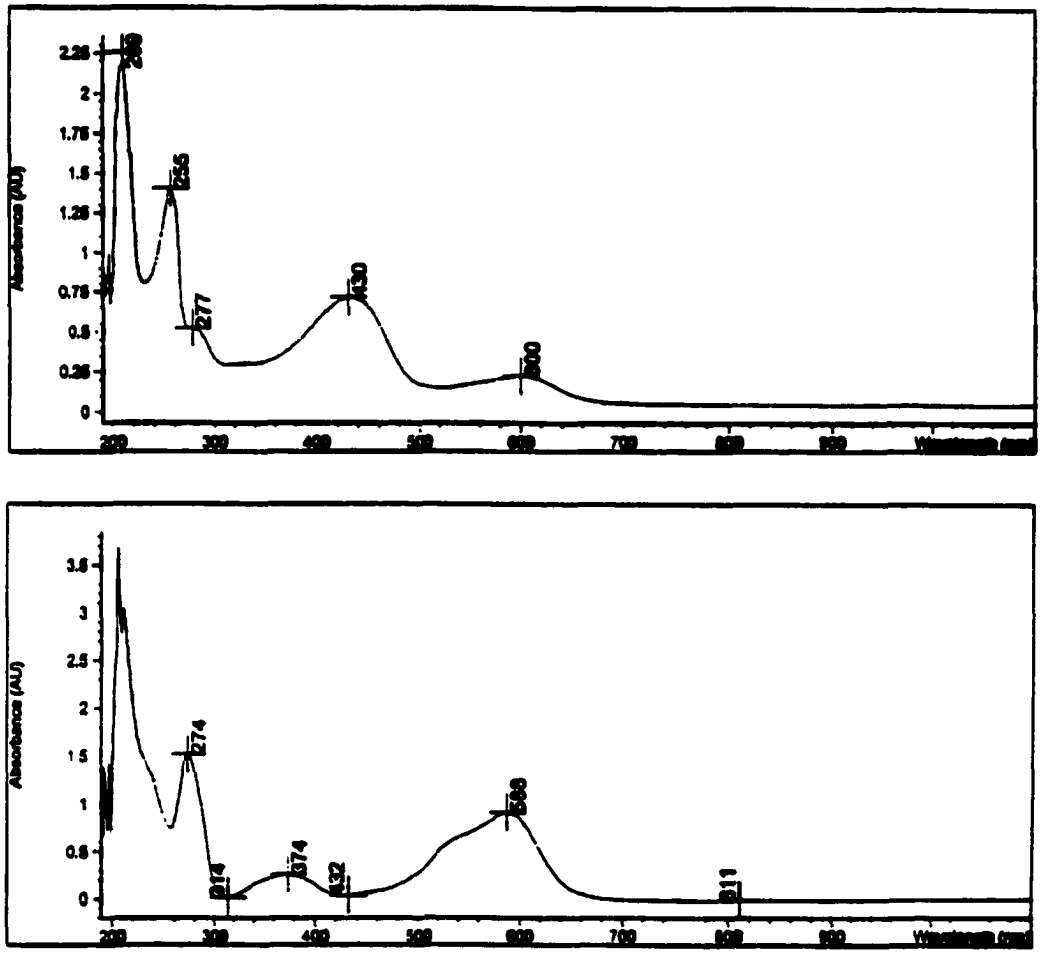

(a)

(b)

Figure 2.42.. UV-vis spectra of (a) a mixture of 150 and 151, (b) a tris-imino complex 153.

Table 2.3. Results of the electronic spectra of Fe(II) tach(C-Me)$_3$pyr complexes and their molar absorptivity (ε) in anhydrous MeOH.

Metal complex	Low energy charge-transfer band (ε = L mol^{-1} cm^{-1})	High energy charge-transfer band (ε = L mol^{-1} cm^{-1})
[Fe(tach(C-Me)$_3$pyr]$^{4+}$ and [Fe(tach(C-Me)$_3$pyr-ox-2)]	600 nm (2255)	430 nm (7152)
[Fe(tach(C-Me)$_3$pyr-ox-6)]$^{2+}$	588 nm (9125) 528 nm (5930)*	374 nm (2572)

*shoulder

C. X-ray Structure of [Fe(tach(C-Me)$_3$pyr-ox-6](ClO$_4$)$_2$ (153)

Crystals of **153** consist of the dication [Fe(tach(C-Me)$_3$pyr-ox-*6*)]$^{2+}$ and perchlorate anions. The ORTEP view of [Fe(tach(C-Me)$_3$pyr-ox-*6*)](ClO$_4$)$_2$ (**153**) is depicted in **Figure 2.43.** Selected bond distances and angles of **153** are in **Table 2.4.** A summary of crystallographic and data collection parameters for **153** is given in **Appendix A-2.**

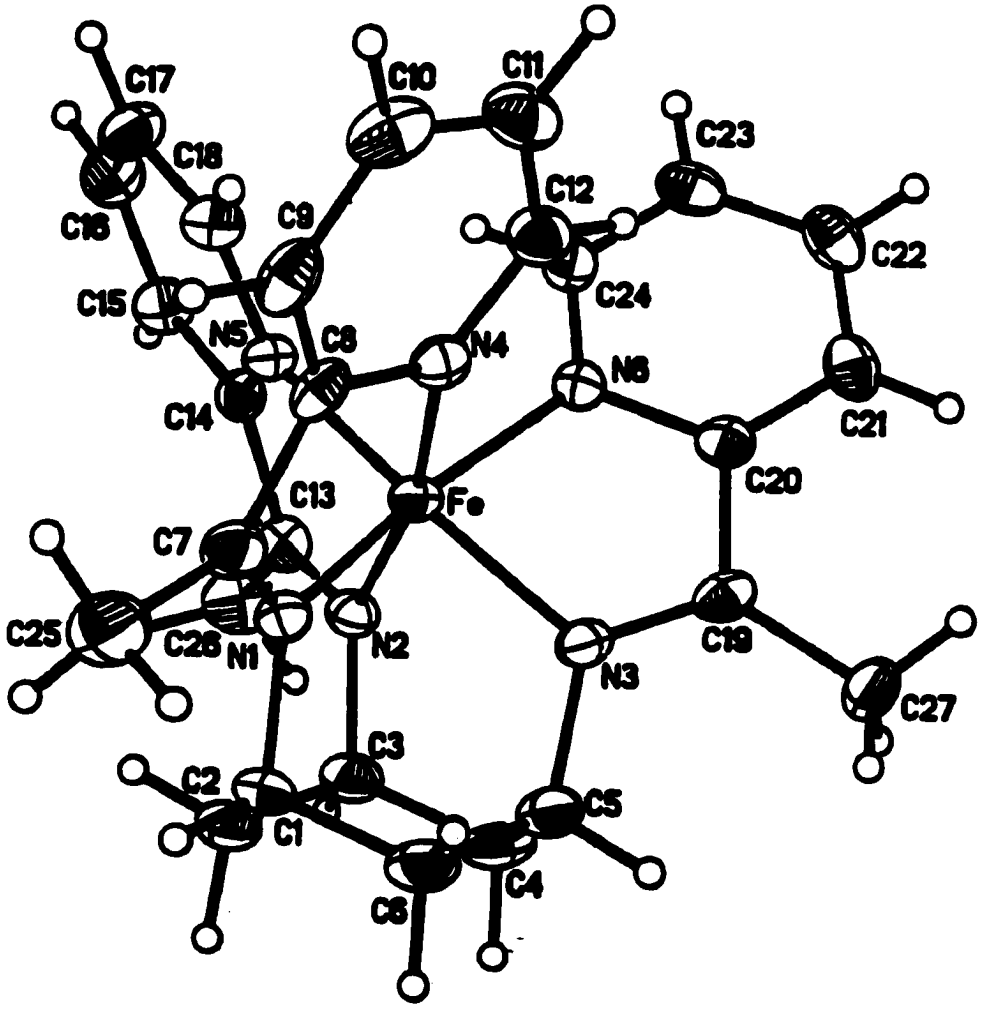

Figure 2.43. ORTEP view of [Fe(tach(C-Me)$_3$pyr-ox-*6*](ClO$_4$)$_2$ (**153**) showing 50% probability of thermal ellipsoids.

Table 2.4. Selected bond distances [Å] and angles [°] for [Fe(tach(C-Me)$_3$pyr-ox-6](ClO$_4$)$_2$ (**153**).

Fe-N(1)	1.906(3)	Fe-N(2)	1.924(3)	Fe-N(3)	1.929(3)
Fe- N(5)	1.974(3)	Fe-N(6)	1.981(3)	Fe-N(4)	1.987(3)
N(1)-C(7)	1.300(5)	N(l)-C(1)	1.496(5)	N(4)-C(12)	1.338(5)
N(4)-C(8)	1.364(5)	C(1)-C(2)	1.534(6)	C(1)-C(6)	1.541(5)
C(7)-C(8)	1.475(5)	C(7)-C(25)	1.494(5)	C(8)-C(9)	1.378(5)
C(9)-C(10)	1.388(6)	C(l0)-C(11)	1.379(6)	C(11)-C(12)	1.392(5)

N(l)-Fe-N(2)	91.65(14)	N(l)-Fe-N(3)	91.82(13)
N(l)-Fe-N(5)	98.11(14)	N(l)-Fe-N(4)	80.66(13)
N(l)-Fe-N(6)	167.70(14)	C(7)-N(l)-C(1)	120.0(3)
C(7)-N(l)-Fe	118.2(3)	C(l)-N(l)-Fe	119.7(2)
C(12)-N(4)-C(8)	118.6(3)	C(12)-N(4)-Fe	128.8(3)
C(8)-N(4)-Fe	111.7(2)	N(l)-C(l)-C(2)	113.1(3)
N(l)-C(l)-C(6)	104.5(3)	C(2)-C(1)-C(6)	111.2(3)
C(l)-C(2)-C(3)	113.1(3)		

C(1)-C(2)-C(3)-C(4)	52.6(4)	C(2)-C(3)-C(4)-C(5)	53.0(4)
C(3)-C(4)-C(S)-C(6)	53.9(4)	C(4)-C(5)-C(6)-C(1)	53.8(4)
C(5)-C(6)-C(1)-C(2)	53.7(4)	C(6)-C(1)-C(2)-C(3)	52.6(4)
N(1)-X(1)-X(2)-N(4)	44.9(2)	N(2)-X(1)-X(2)-N(5)	44.9(2)
N(3)-X(1)-X(2)-N(6)	44.6(2)	N(2)-X(1)-X(2)-N(6)	74.8(2)

Discussion

A. Reaction of Iron Salts and tachpyr Ligand and Ligand Oxidation

A.1. Metal Complex Formation

The non-oxidized complex [Fe(tachpyr)]$(Cl)_2$ **146**$(Cl)_2$ is formed at 0° C with exclusion of oxygen and is oxidized from exposure to air at room temperature for 2h resulting in the formation of an inseparable mixture of **146**$(Cl)_2$ and a mono-imino Fe(II) complex **147**$(Cl)_2$, [Fe(tachpyr-ox-2)]$(Cl)_2$. Iron (II or III) chloride salts react with tachpyr in MeOH in the presence of oxygen affording a brown-green solid that is very hard to identify by ^1H NMR spectra because of the line broadening, presumably due to paramagnetic Fe(III) byproducts or intermediates. By treatment of the mixture of **146**$(Cl)_2$ and **147**$(Cl)_2$ with excess of $NaBPh_4$ in MeOH, a brown-green solid was formed as an inseparable mixture of **147**$(BPh_4)_2$ and **148**$(BPh_4)_2$. However, iron (II or III) perchlorate salts react with tachpyr in MeOH in the presence of oxygen affording **147**$(ClO_4)_2$ and **148**$(ClO_4)_2$ as a green precipitate without treatment with $NaBPh_4$. The mixture of **147**$(BPh_4)_2$ and **148**$(BPh_4)_2$ is further oxidized leading to the formation of **149**$(BPh_4)_2$, [Fe(tachpyr-ox-6)]$(BPh_4)_2$, by adding an oxidizing reagent H_2O_2 (30%).

A.2. Proposed Mechanism of Ligand Oxidation

Very broad peaks with a distinctive imine peak ^1H NMR spectra (**Fig. 2.19 (a)**) were obtained from the precipitate formed between Fe(II)$Cl_2 \cdot 4H_2O$ in a mixture of MeOH (2 mL) and Et_2O (6 mL) and tachpyr in a mixture of MeOH (2

mL) and Et_2O (6 mL) in the presence of oxygen. A typical paramagnetic ^1H NMR was obtained when N_2 gas was purged for 1/2 h into a mixture of $Fe(II)Cl_2 \bullet 4H_2O$ in MeOH and tachpyr in MeOH. These observations are very indicative for the formation of an Fe(III) tachpyr intermediate complex, $[Fe(tachpyr)]^{3+}$ **162** (**Scheme 2.19**), from the reaction between $FeCl_2$ and tachpyr ligand. However, further characterizations are needed to confirm its identity. It is proposed that the non-oxidized **146**$(Cl)_2$ formed immediately reacts with external oxidants, H_2O_2 or O_2, yielding a Fe(III) complex **162**. The mechanism of the oxidation of $[FeL_2]^{2+}$ by H_2O_2 was also proposed as an outer-sphere one-electron-transfer process in the rate-determining step with successive rapid reduction of the OH• radical intermediate by a second $[FeL_2]^{2+}$ (L = [9]aneN_3) by Pohl et al. (**Scheme 2.18**).[174]

$$[FeL_2]^{2+} + H_2O_2 \xrightarrow{\text{slow}} [FeL_2]^{3+} + OH\bullet + OH^-$$

$$[FeL_2]^{2+} + OH\bullet \xrightarrow{\text{fast}} [FeL_2]^{3+} + OH^-$$

Scheme 2.18. Oxidation of a Fe(II) complex by H_2O_2 to form a Fe(III) complex.

The Fe(III) intermediate is then reduced by abstraction of an electron from one of coordinated secondary amine groups generating an aminyliron(II) radical dication **163** and a proton.[171] The aminyliron(II) radical dication **163** then reacts further with the external oxidant to form an inseparable mixture of non-oxidized and mono-imino Fe(II) complex, **146** and **147**, by exposing it to air for 2 h (**Scheme 2.19**). The magnetic moment (1.792 B.M.) of the precipitate, identified as a mixture of **146** and **147**, obtained from a mixture of $Fe(II)(ClO_4)_2 \bullet 6H_2O$ and

tachpyr in a mixture of MeOH/Et_2O (2 mL : 6 mL) may also suggest the existence of **162.**

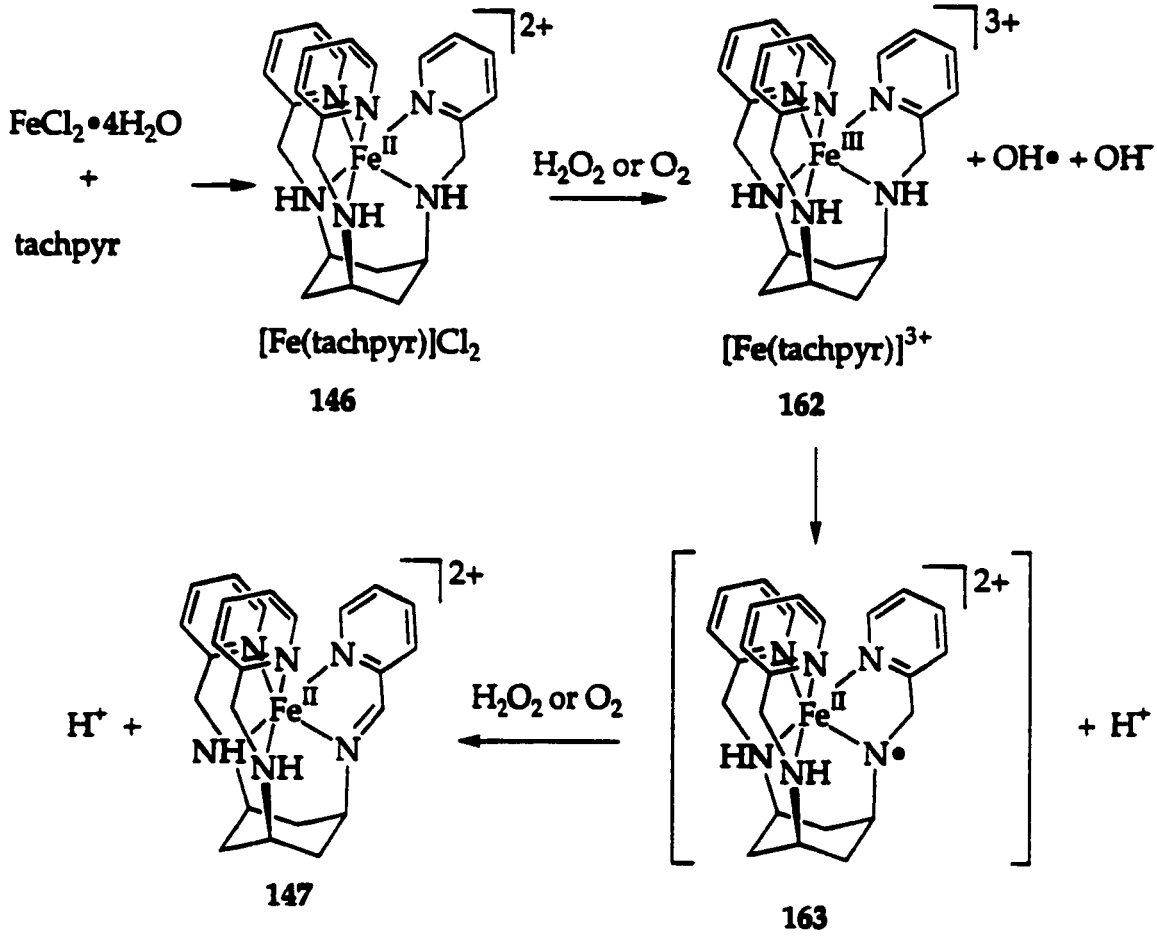

Scheme 2.19. Proposed mechanism of the oxidative dehydrogenation of [Fe(II)tachpyr] complex.

The oxidative dehydrogenation reactions observed from the reaction of Fe(III) salts with tachpyr are faster than those from the reaction of Fe(II) salts with tachpyr ligand. This observation is reasonable since the immediate product generated by the reactions of Fe(III) salts and tachpyr ligand would be Fe(III) an intermediate for the oxidative dehydrogenation reaction without oxidation of

central metal ion (Fe^{3+}) as observed in [Fe(II)(tachpyr)] complexes. However, in the reaction between $FeCl_3 \bullet 4H_2O$ and tachpyr, it is necessary to exchange the counter anion of the products (Cl^-) with $NaBPh_4$ for a faster deposition and isolation of the product. The mechanism for these reactions is similar to proposed mechanism (**Scheme 2.19**) for the reaction between Fe(II) salts and tachpyr ligand without the oxidation process (Fe^{2+} -> Fe^{3+}) of a central metal ion prior to an oxidative dehydrogenation.

A.3. Electronic and Vibrational Spectra of Fe(II) tachpyr Complexes

The electronic spectra of the mixture of **146** and **147** (**Fig. 2.33 (a)**), $[Fe(tachpyr)]^{2+}$ and $[Fe(tachpyr\text{-}ox\text{-}2)]^{2+}$, and of the mixture of **147** and **148** (**Fig. 2.33 (b)**), $[Fe(tachpyr\text{-}ox\text{-}2)]^{2+}$ and $[Fe(tachpyr\text{-}ox\text{-}4)]^{2+}$, are similar to each other with a difference in intensity of the metal-ligand charge-transfer band. Both of spectra show two charge-transfer bands at 422 nm (23.7 kK, ε = 4821 L mol^{-1} cm^{-1}) and 603 nm (16.6 kK, ε = 1735) in the mixture of **146** and **147** and at 385 nm (25.9 kK, ε = 5185) and 605 nm (16.5 kK, ε = 6869) the mixture of **147** and **148**. The *d-d* absorption bands in these complexes are presumably obscured by those charge-transfer absorptions.[185]

The intensity of the charge-transfer band at higher energy is not changed significantly, but it shifts to higher energy, from 422 nm to 385 nm, with increasing oxidation of the ligand. This trend also observed in the oxidative dehydrogenation of *mer*-$Na[Fe(CN)_3(2\text{-}DPA)]$ (DPA = bis(2-pyridylmethyl)amine, **44** (**Fig. 1.17**)).[173] Because this band is not observed in alkyl di-imino Fe(II) complexes[171, 186] but observed in Fe(II) complexes with

pyridyl donors such as bipy, tachimpyr,[184] and DPA,[173] it is assumed to be an electron transfer from metal to π^* system of a pyridyl ring. The transition energy of this charge-transfer seems to enhanced with an increased number of the oxidized ligand due to the formation of a conjugated α,α'-diimine system.

On the other hand, the location of the charge-transfer band at lower energy appeared at 600 nm is independent on the number of the oxidized ligands, however, the intensity of those band is affected by the degree of oxidation. The mixture of **147** and **148** has a three times larger molar absorptivity (6869 L mol^{-1} cm^{-1}) at 605 nm than that of the mixture of **146** and **147** (1735 L mol^{-1} cm^{-1}) at 603 nm. A similar trend was found in electronic spectra of the [Fe([14]1,11-dieneN$_4$(CH_3CN)$_2$], the [Fe([14]1,4,11-trieneN$_4$(CH_3CN)$_2$], and [Fe([14]1,4,8,11-tetraeneN$_4$(CH_3CN)$_2$] complexes[171] and of *mer*-Na[Fe(CN)$_3$(2-DPA)](**Fig. 2.47**).[173]

The UV-vis spectra of **149** (**Fig. 2.34**), [Fe(tachimpyr)](ClO_4)$_2$, was also obtained and presents two charge-transfer bands at 327 nm (30.5 kK, ε = 4843 L mol^{-1} cm^{-1}) and 578 nm (17.3 kK, ε = 9305) with a shoulder. The higher energy charge-transfer band is further shifted, and the intensity of the lower energy band is more increased with the increased numbers of oxidized ligands, which is consistent with trends described above.

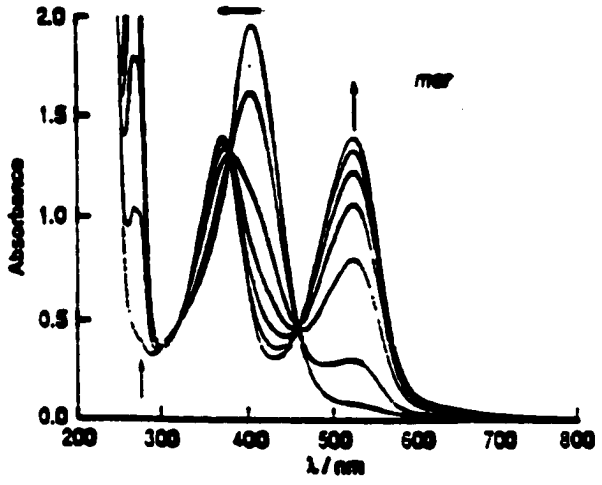

Figure 2.44. UV-vis spectra of oxidative dehydrogenation of *mer*-Na[Fe(CN)$_3$(2-DPA)].

The infrared spectrum of the free tachpyr shows N-H and C=C stretching absorptions at 3320 and 1597 cm^{-1} (**Fig. 2.45 (a)**), respectively. As tachpyr coordinates to metal ion and forms a non-oxidized metal complex, [M(tachpyr)]$^{n+}$, IR spectra of non-oxidized metal complex would be similar to that of the free ligand. The non-oxidized Fe(II) complex of tachpyr **146**, [Fe(tachpyr)]$^{2+}$, is too air sensitive to be characterized by IR spectroscopy. However, other non-oxidized tachpyr metal complex, i.e. [In(tachpyr)]$^{3+}$, would provide IR spectral information of non-oxidized of **146**. The IR spectrum of [In(tachpyr)]$^{3+}$ (**Fig. 2.45 (b)**) shows a broad N-H absorption at 3380 cm^{-1} due to a H-bonding and a sharp C=C stretching absorption at 1607 cm^{-1}, identical to pyridine stretching reported in [Fe(tachimpyr)]$^{2+}$, without a imine stretching (C=N) ~1650 cm^{-1}.

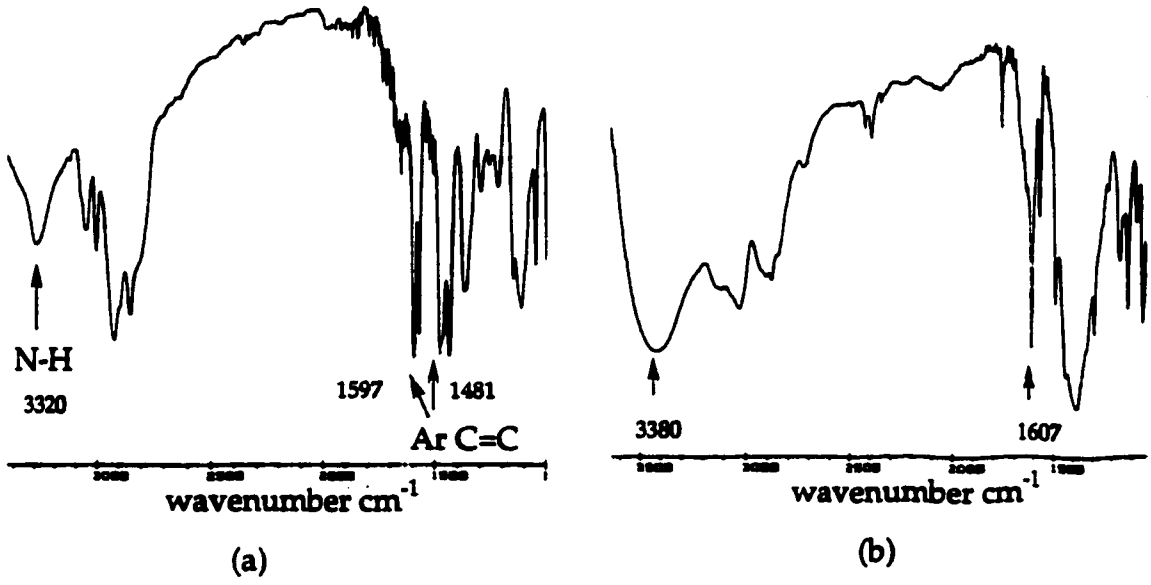

Figure 2.45. IR spectra of (a) free tachpyr ligand, (b) $[In(tachpyr)](NO_3)_3$.

As coordinated tachpyr is oxidized to form imino complexes, IR spectra of the totally oxidized ligand complex should show no N-H absorption and a new C=N stretching band around 1650 cm^{-1}. The IR spectrum of the mono- and di-imino Fe(II) tachpyr mixture (**Fig. 2.35 (a)**), **147** and **148**, shows a very informative peak at 1656 cm^{-1} indicating the formation of oxidized ligands along with the aromatic C=C stretching peaks at 1602 and 1462 cm^{-1}. However, the presence or absence of N-H bands could not be established. The IR spectrum of tris-imino Fe(II) tachpyr complex **149**$(BPh_4)_2$ (**Fig. 2.35 (b)**), [Fe(tachpyr-ox-*6*)]$(BPh_4)_2$, prepared through oxidative dehydrogenation presents a distinctive imine peak at 1656 cm^{-1}. The IR spectra of **149**, $[Fe(tachimpyr)]^{2+}$, prepared by direct reaction of tachimpyr and $Fe(II)(ClO_4)_2 \cdot 6H_2O$ shows identical spectroscopic data of **149**$(BPh_4)_2$, [Fe(tachpyr-ox-*6*)]$(BPh_4)_2$. Those imine stretching bands compare well to 1652 cm^{-1} in **141** (**Scheme 2.14**)[171] and 1620 cm^{-1} in $[Fe(CN)_4(Me_2en)]^{2-}$ (Me^2en = *N,N'*-dimethylenediamine, **Scheme 2.13**).[172]

B. Reaction of Iron(II/III) perchlorate and (+/-)tach(C-Me)$_3$pyr Ligand and Ligand Oxidation

A mixture of a non-oxidized **150**, [Fe(tach(C-Me)$_3$pyr)](ClO$_4$)$_2$, and a mono-imino Fe(II) complex **151**, [Fe(tach(C-Me)$_3$pyr-ox-2)](ClO$_4$)$_2$, was possibly formed while exposing the reaction mixture of Fe(II)(ClO$_4$)$_2$•6H$_2$O and (+/-)tach(C-Me)$_3$pyr in MeOH to air at room temperature for 1/2 h. An attempt to obtain only **150** was not made, however, it may be obtained when the reaction is carried out at low temperature (0° C) with an exclusion of O$_2$. The mixture of **150** and **151** was further oxidized with H$_2$O$_2$ (30%) resulting the formation of tris-imino complex **153**, [Fe(tach(C-Me)$_3$pyr-ox-6)](ClO$_4$)$_2$. Two days exposure of the mixture of Fe(ClO$_4$)$_2$ and (+/-)tach(C-Me)$_3$pyr in MeOH affords purple prisms, the di-imino complex **152**, [Fe(tach(C-Me)$_3$pyr-ox-4)](ClO$_4$)$_2$, while the mixture of Fe(ClO$_4$)$_3$ and (+/-)tach(C-Me)$_3$pyr in MeOH affords the mixture of **152** (a major) and **153** (a minor), which is further oxidized to **153** in the purification and recrystallization processes.

The electronic spectra of the mixture of non-oxidized Fe(II) complex and a mono-imino Fe(II) complex **150** and **151** (**Fig 2.42 (a)**) and tris-imino complex **153** were obtained. The *d-d* absorption bands in these complexes are also obscured by those charge-transfer absorptions.[185] The mixture of **150** and **151** has two charge-transfer absorptions at 430 nm (23.2 kK, ε = 7152 L mol^{-1} cm^{-1}) and 600 nm (16.7 kK, ε = 2255) (**Fig 2.42 (a)**), and tris-imino complex **153** has also two charge-transfer absorptions at 374 nm (26.7 kK, ε = 2572) and 588 nm (17.0 kK, ε = 9125) (**Fig. 2.42 (b)**).

The low-energy band shifts to higher energy from 430 nm to 374 nm and an enhanced intensity on the high energy band from 2255 to 9125 L mol^{-1} cm^{-1} with an increased number of the oxidized ligand are also observed. These trends are similar to those observed in the tachpyr reactions. The mechanism of the iron-mediated oxidative dehydrogenation of the coordinated (+/-)tach(C-Me)$_3$pyr ligand is assumed to be similar to that of the tachpyr ligand oxidation reaction.

C. X-ray Structure of [Fe(tach(C-Me)$_3$pyr-ox-6](ClO$_4$)$_2$ (153)

An extremely large number and wide range of iron(II) complexes are known. This d^6 configuration is one of the most important oxidation states of iron along with iron(III) (d^5). Even though there are examples of four, five and eight coordinated iron(II) complexes, most iron(II) complexes have an octahedral geometry.[185]

Most complexes of the type $[Fe(\alpha,\alpha'\text{-diimine})_3]^{2+}$ give stable low-spin and diamagnetic pseudooctahedral complexes.[187] Because of good σ donor abilities, appropriate π back-bonding properties and chelate effects, α,α′-diimine ligands are classified as high-field ligands and are comparable in strength to the cyanide ion. Most $[Fe(\alpha,\alpha'\text{-diimine})_3]^{2+}$ complexes have a characteristic metal-to-ligand charge transfer absorption in the visible region of the spectrum with a molar absorptivity of ~ 10^4.[185]

(+/-)Tach(C-Me)$_3$pyr ligand provides six nitrogen donor atoms, iron coordination, and promotion of oxidation by iron in presence of O_2 results in the diamagnetic low-spin, Fe(II) complex **153**. X-ray crystallography shows that the coordination geometry of FeN_6 in **153** (**Fig. 2.43**) is best described as a distorted octahedron. The twist angles (α) (see introduction in **Chapter 3**) in **153** are 44.9(2), 44.9(2), and 44.6(2) ° and are well compared to that of 43° in $[Fe(py_3TPN)]^{2+}$ (py_3TPN = 1,1,1-tris(pyridine-2-aldimimomethyl)ethane)[188] and smaller than that of 54° in $[Fe((py)_3tren)]^{2+}$ ($(py)_3tren$ = tris(4-[2-pyridyl]-3-aza-3-butenyl]amine).[189]

The bond lengths of Fe-N (tach imine) in **153** range from 1.906(3) to

1.929(3) Å and well compared to 1.942, 1.95(6), and 1.95(2) Å in $[Fe(py)_3tren]^{2+}$,[189] $[Fe(gmi)_3]^{2+}$ (gmi = *N,N'*-dimethylglyoxal diimine), and $[Fe(bmi)_3]^{2+}$ (bmi = *N,N'*-dimethyl-2,3-butanedione diimine),[190] respectively. The bond lengths of Fe-N (pyridyl) in **153** range from 1.974(3) to 1.987(3) Å and comparable to 1.96(6), 1.97(6), and 1.966 Å in $[Fe(phen)_3]^{2+}$ (phen = 1,10-phenanthroline), $[Fe(bipy)_3]^{2+}$ (bipy = 2,2'-bipyridine), and in $[Fe(py)_3tren]^{2+}$,[189, 190] respectively. The bond lengths of $(CH_3)C=N$ (tach imine) in **153** range from 1.294(5) to 1.300(5) and are well compared to 1.27(2) 1.29(2), and 1.277(3) Å and in $[Fe(gmi)_3]^{2+}$, $[Fe(bmi)_3]^{2+}$,[190] and $[Fe(py)_3tren]^{2+}$.[191]

D. Reductive Mobilization of Fe(III) by tachpyr from Fe(III)(ATP)$_3$

Tachpyr appears to deplete iron from cells, and one of the proposed cytoplasmic forms of iron is an Fe-ATP complex. Therefore $[Fe(III)(ATP)_3]^{3-}$ was prepared by using a method previously reported[181], investigated reaction with tachpyr, and characterized by UV-vis spectroscopy. A color change from yellow to green was observed after three equiv of tachpyr was added into a yellow solution of Fe(III)(ATP)$_3$ in Hepes buffer (pH 7.4), suggesting formation of the iron tachpyr complex. The reaction was stopped 48 h after addition of tachpyr. The UV-vis spectrum of the mixture (**Fig. 2.46 (b)**) is very similar to that of the mixture of **147** and **148** (**Fig. 2.33 (b)**), $[Fe(tachpyr\text{-}ox\text{-}2)]^{2+}$ and $[Fe(tachpyr\text{-}ox\text{-}4)]^{2+}$. It indicates that Fe(III) in Fe(III)(ATP)$_3$ complex is liberated and reduced to Fe(II) with coordination of tachpyr followed by oxidative dehydrogenation leading to a mixture of mono- and di-imine Fe(II) tachpyr complexes. No attempt was made to determine the extent of iron removal from Fe(III)(ATP)^3.

Iron chelators able to permeate membranes are proposed to make a complex with intracellular iron, either Fe(II) or Fe(III), that exists in the intracellular iron pool.[192] Because Fe(III) is reduced to Fe(II) in the reaction with tachpyr, a new mode iron capture by reduction of Fe(III) from cytoplasmic sources such as Fe(III)-ATP can be postulated.

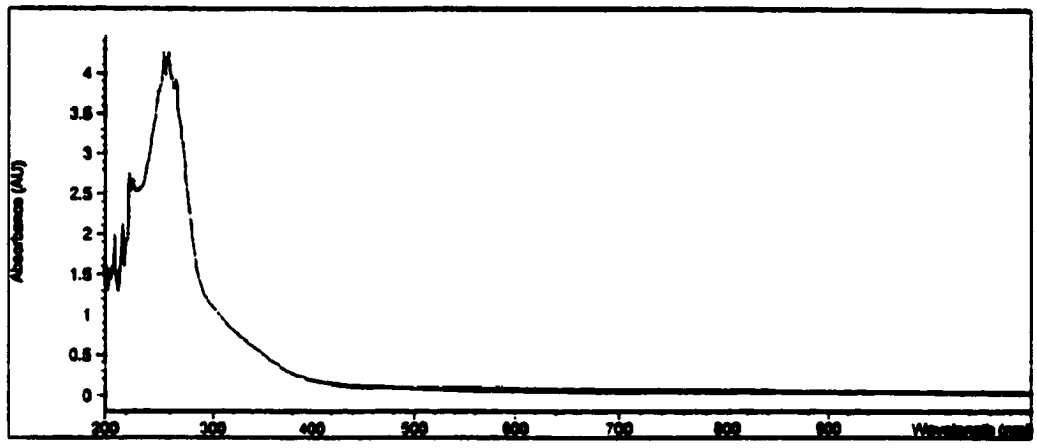

(a)

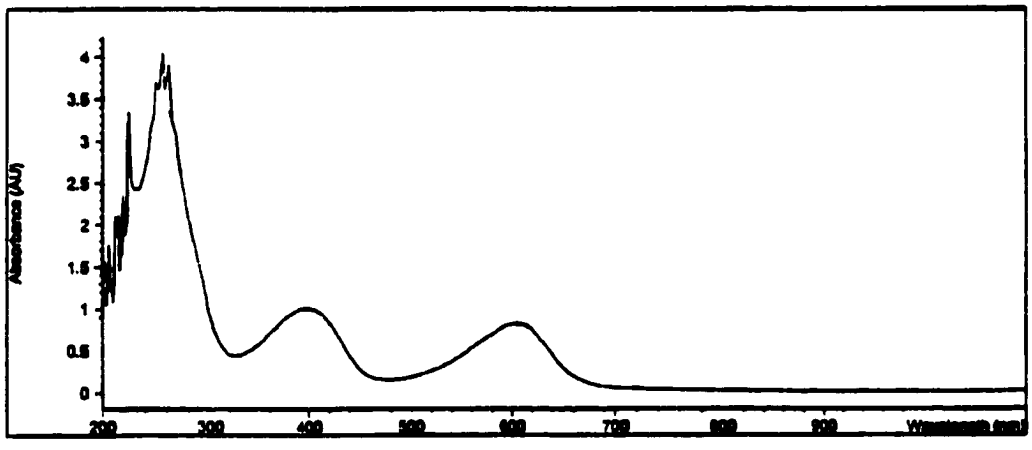

(b)

Figure 2.46. UV-vis spectra of (a) $Fe(III)(ATP)_3$; (b) $Fe(III)(ATP)_3$ + tachpyr after 48 h.

E. Tumor Cell Cytotoxicity of tachpyr Derivatives

The collaborative investigation of the novel chelators, tachpyr and its derivatives, for their potential as an anti-cancer drug with Prof. Suzy Torti at the Wake Forest University of School of Medicine has been undertaken. Metal complexes and nitrate salts of tachpyr and derivatives were prepared and provided by the author for tests. The results of the study of iron chelation for cancer therapy are summarized herein.

Tachpyr and its derivatives are different from most iron chelators such as siderophores that generally contain oxygen donor atoms.[193] They contain six nitrogen donor atoms and form relatively rigid hexa-coordinate iron complexes. Tachpyr and derivatives have a different chemical structure from other ligands, such as desferrioxamine and PIH, explored as anti-tumor therapeutics. Unlike either of these chelators, tachpyr reacts not only with Fe(II) but also Fe(III) by a process of oxidative dehydrogenation, resulting in formation of Fe(II) α,α'-di-imino complexes.

The fundamental biological properties and iron-depleting mode of action of tachpyr were examined by measuring the effects of tachpyr on growing cells in culture and comparing them with desferrioxamine (**Fig. 2.47**). Tachpyr was more potent with the average IC_{50} value of 4.6 ± 2.0 μmol/L than desferrioxamine with IC_{50} value of 70 μmol/L, suggesting an effective dose in the range reported for the most effective PIH analogs (1-7 μmol/L).[194] The lipophilicity value of - 0.1 of tachpyr (octanol-water partition coefficient; log P_{oct/H_2O}) suggests its ability to penetrate biological membranes and may partially explain the lower value of IC_{50} of tachpyr with enhanced permeability compared

to desferrioxamine. Additionally or alternatively, the reductive properties of tachpyr may give it greater access to key intracellular iron pools, increasing its iron chelating properties.

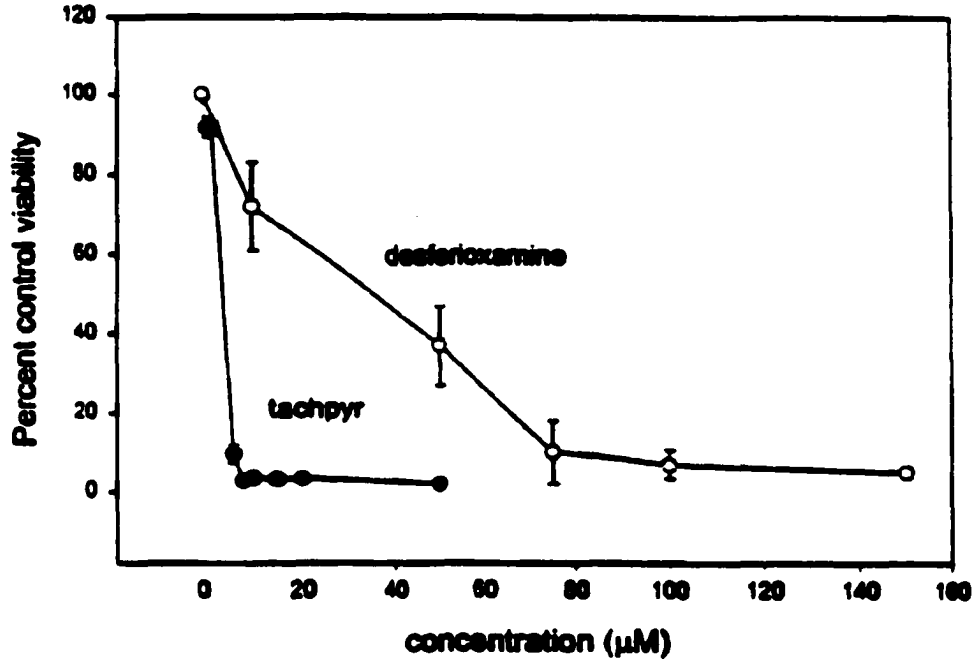

Figure 2.47. Comparative cytotoxicity effect of tachpyr and desferrioxamine on cultures MBT2 bladder cells.

Tachpyr complexes of several biologically important metal ions, Ca(II), Mn(II), Mg(II), Fe(II), Zn(II) and Cu(II), were prepared and their effects on mouse bladder cancer cell lines were compared to that of tachpyr to investigate the relationship between the iron deprivation and tachpyr cytotoxicity. It is expected that tachpyr would bind Ca(II), Mn(II), and Mg(II) less tightly than Fe(II), Zn(II), and Cu(II) based on HSAB (hard and soft acid and base) considerations. As predicted, the Ca(II), Mn(II), and Mg(II) tachpyr complexes were toxic, on the other hand, the Zn(II), Fe(II), and Cu(II) complexes were not

toxic (**Table 2.5**).

Table 2.5. Effects of metal complexes of tachpyr on viability

Drug (all at 100 μM)	Percent viability
None	100
tachpyr	11.3 ± 0.8
$[Mg(tachpyr)]^{2+}$	7.6 ± 0.7
$[Ca(tachpyr)]^{2+}$	5.5 ± 0.5
$[Mn(tachpyr)]^{2+}$	8.5 ± 1.1
$[Cu(tachpyr)]^{2+}$	107 ± 7.0
$[Zn(tachpyr)]^{2+}$	114 ± 4.2
$[Fe(tachpyr)]^{2+}$	82.3 ± 5.0

Since metal-tachpyr complexes can not cross the cell membrane because they are cationic, it is postulated that the toxicity of the Ca(II), Mn(II), and Mg(II) complexes arises from the liberation of free tachpyr by transmetallation of the metal ion to a ligand with greater affinity for those metals (such as apotransferrin). It is also proposed that for Zn(II), Cu(II), and Fe(II) complexes of tachpyr this reaction does not occur appreciably due to strong binding of tachpyr to those metal ions and their great stability.

Involvement of iron chelation in the cytotoxic mechanism of tachpyr was further investigated with alkylated derivatives of tachpyr which have methyl or ethyl groups instead of hydrogen atoms on tach amine nitrogens N, N′, and N″ (**Fig. 2.27**). The reaction of tach-Me_3pyr with $Fe(ClO_4)_2 \cdot 6H_2O$ in dry MeOH

affords pale green paramagnetic microcrystals whose analytical data are consistent with the formation of [Fe(tach-Me_3pyr)]$(ClO_4)_2$ (**154**). The magnetic moment of **154** was obtained by using Evans method (see introduction of **Chapter 3**). It indicates that **154** is a high-spin Fe(II) (d^6) complex with μ_{eff} of 5.078 B.M.[189, 195] The spin state of **154** indicates that metal-ligand interactions are weak, attributed to the steric effect of the methyl groups on the cyclohexyl amine nitrogens. The interaction of $Fe(ClO_4)_3 \bullet 6H_2O$ with tach-Me_3pyr in dry MeOH generate a green oily material that gives a very broad ^1H NMR signals. Those broad signals are attributed to a weak interaction of high-spin Fe(III) and ligand. Many attempts have been made to prepare a fully characterized Fe(II) complex of tach-Et_3pyr **160** without success. ^1H NMR spectra of the mixture of **160** and $Fe(ClO_4)_2 \bullet 6H_2O$ or $Fe(ClO_4)_3 \bullet 6H_2O$ in dry MeOH are broad and can not be interpreted, suggesting presence of high-spin Fe(II) or Fe(III).

However, the preparation of [Cu(tach-Me_3pyr)]$(ClO_4)_2$, [Zn(tach-Me_3pyr)]$(ClO_4)_2$, [Cu(tach-Et_3pyr)]$(ClO_4)_2$, and [Zn(tach-Et_3pyr]$(ClO_4)_2$ (see experimental section in **Chapter 3**) were successful, and those metal complexes were fully characterized by elemental analysis and mass spectroscopy, suggesting a stronger interactions than in reaction of Fe(III) and tach-Me_3pyr. The cytotoxicity of tach-Me_3pyr and of tach-Et_3pyr along with tachpyr was examined to assess further the role of iron chelation in the cytotoxicity mechanism of tachpyr. The *N*-alkylated derivatives of tachpyr were not toxic (**Fig. 2.48**). These results strongly indicate that the iron is the premier target of tachpyr since *N*-alkylation qualitatively inhibits the reaction of tachpyr with iron but not with Zn(II) and Cu(II) and the ability to interact with iron plays an

important role in the cytotoxicity of tachpyr. Biological data also indicate that iron is a target of tachpyr. Tachpyr selectively represses the synthesis of both the H and L subunits of ferritin, a distinctive property of iron chelators, which is consistent with iron depletion as a major consequence of tachpyr activity.[194] A future study should quantitatively address relative binding ability of tachpyr and tach-Me_3pyr, perhaps through competition experiments.

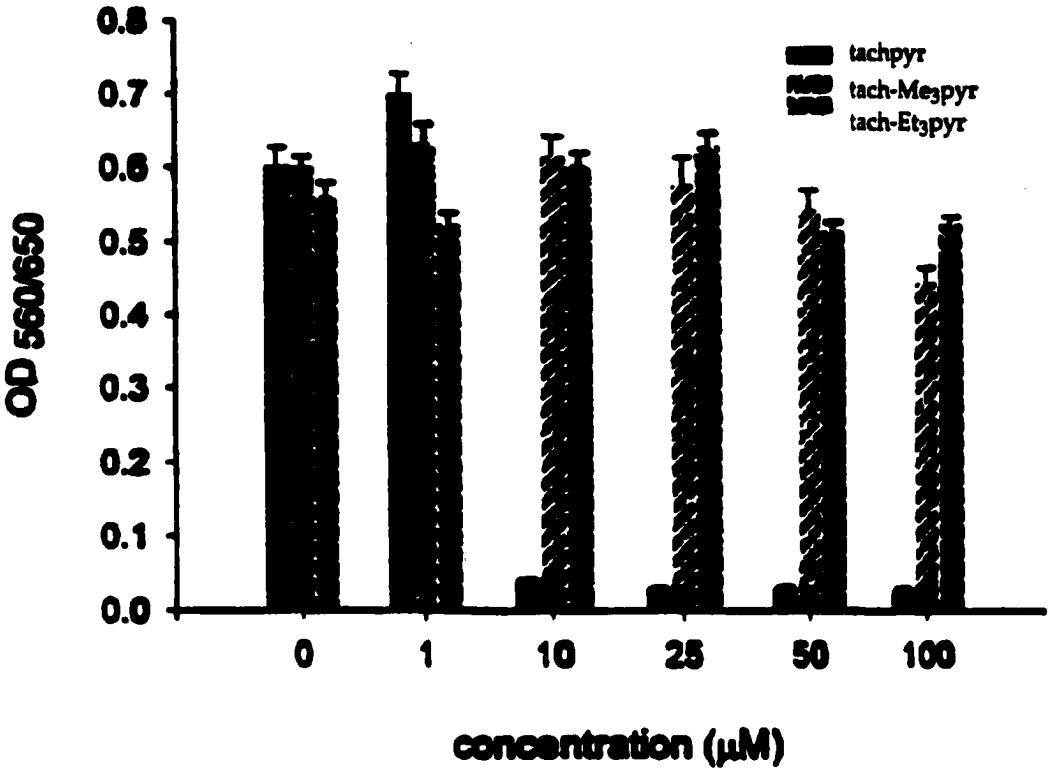

Figure 2.48. The cytotoxicity test of tachpyr and its alkylated derivatives.

Conclusion

Tachpyr and (+/-)tach(C-Me)$_3$pyr react with Fe(II) and Fe(III) to form Fe(II) complexes. Iron-mediated oxidative dehydrogenation of coordinated tachpyr in the presence of O_2 results in the formation of a mixture of corresponding mono- and di-imino Fe(II) complexes. Tris-imino complexes are obtained by more aggressive oxidation of the substances by H_2O_2 or air. Fe(III) reacts with both ligands and is reduced to Fe(II) resulting in imino Fe(II) complexes similar to those derived from Fe(II). The Fe(II) imino complexes show characteristic charge-transfer bands in the UV-vis spectra and a distinctive vibration from a newly-formed C=N bond in the IR spectra. ^{1}H NMR spectroscopy is very useful to distinguish the extent of oxidation of the ligands, because each imino complexes have distinctive imino proton signals. The coordination geometry of [Fe(tach(C-Me)$_3$pyr)](ClO$_4$)$_2$ **153** is described as a slightly distorted octahedron with an average twist angle of 44.8(6)°. Mixtures of Fe and tach chelators are believed to produce hydroxyl radicals because they degrade deoxyribose. Fe complexes of fully oxidized tach chelators, which can not undergo oxidative dehydrogenation, do not degrade deoxyribose.

Cytotoxicy tests suggest that tachpyr has great potential for treatment of cancer through an iron depletion mechanism. One or more of the abilities of tachpyr to coordinate iron, to reduce Fe(III) to Fe(II), and to produce hydroxyl radicals, may be required for its cytotoxic effect. The further evaluation of tachpyr and its derivatives as an anti-tumor agent may be fruitful. Further study of the redox mechanism of iron-tach chelator interaction may allow the above abilities to be tuned. Further understanding of the biological mechanism may also result.

TRANSITION METAL COMPLEXES OF NOVEL LIGANDS DERIVED FROM THE *CIS,CIS*-1,3,5-TRIAMINOCYCLOHEXANE (TACH) FRAMEWORK: STRUCTURAL AND BIOLOGICAL STUDIES

BY

GYUNGSE PARK

B.S., KOREA UNIVERSITY, 1991
M.S., WAYNE STATE UNIVERSITY, 1995

DISSERTATION

Volume 2

Chapter 3

Submitted to the University of New Hampshire
In Partial Fulfillment of
the Requirements for the Degree of

Doctor of Philosophy

in

Chemistry

September, 2000

TABLE OF CONTENTS

Experimental Section

Results

Discussion

CHAPTER 3

TRANSITION (M = Mn(II), Fe(II), Co(II), Co(III), Ni(II), AND Cu(II)) AND GROUP IIB (Zn(II), Cd(II), AND Hg(II)) METAL COMPLEXES OF NOVEL LIGANDS DERIVED FROM THE *CIS,CIS*-1,3,5-TRIAMINOCYCLOHEXANE (TACH) FRAMEWORK

Summary

This chapter focuses on the synthesis, characterization, and structures of the divalent transition and Group IIB metal complexes of novel ligands based on the tach framework. These studies were undertaken to investigate effects of different metal ions on the coordination geometry of hexadentate tach-based hexa-nitrogen donor ligands. In collaboration with Dr. Brechbiel at NIH, effects of variation in tach ligands structure on the metal complex structure are described.

Introduction

In this introduction, the properties and coordination chemistry of the first *d*-block transition metal elements will be addressed, and brief history of tach-based ligands and their metal complexes will be given.

A. Chemistry of Transition Metal Elements

The transition elements may be defined strictly as elements that have partly filled *d* or *f* shells.[196] The transition elements have a number of distinctive chemical properties that are entirely, or largely, distinguished from other groups of elements.

- They are all metals.
- They are all hard (except iron) and malleable. In addition, they have high melting and boiling points and conduct heat and electricity well.
- They exhibit variable valence, with a few exceptions, and their ions and compounds are generally colored. Many of their compounds possess unpaired electrons.
- They have an unparalleled propensity for forming coordination compounds with Lewis bases.

The transition metal elements are classified into three main groups: (a) the main transition elements or d-block elements, (b) the lanthanide elements and (c) the actinide elements. There is an important distinction between the three classes of the transition elements according to electronic structures. The *d*-block elements have partially-filled *d* shells, 3*d*, 4*d*, or 5*d*. These *d* orbitals project well out to the periphery of the atoms and ions so that the electrons occupying them

are strongly influenced by the surroundings of the atoms and ions, and in turn, are able to influence the environments very significantly. Therefore, many of the properties of an ion with a partially filled *d* shell are quite sensitive to the number and arrangement of the *d* electrons present. However, the 4*f* orbitals in the lanthanide elements are rather deeply buried in the atoms and ions. The electrons that occupy them are largely screened from the surroundings by the overlaying shells (5*s*, 5*p*) of electrons. Therefore, interactions of the 4*f* electrons and the surroundings of the atom or the ion are relatively less significant. The behavior of the actinide elements lies between those of two types because the 5*f* orbitals are not as well shielded as the 4*f* orbitals and not so exposed as the *d* orbitals.[196]

The main transition group or *d* block includes the elements that have partially filled *d* shells only. Thus the lightest member of the transition elements is the scandium having the outer electron configuration of $4s^2 3d$. The eight succeeding elements, Ti, V, Cr, Mn, Fe, Co, Ni, and Cu, all have partially filled *d* shells either in the ground state of the free atom (except Cu) or in one or more of their chemically important ions (except Sc). This group of elements is called the first transition series and main interest of this chapter. The group 2B elements, or group 12 elements, Zn, Cd, and Hg have a filled $(n\text{-}1)d$ shell plus two *ns* electrons. These elements form no compounds in which the 3*d*, 4*d*, or 5*d* shell is ionized, and are not classified as transition elements.[196]

B. Various Coordination Numbers

A coordination compound, or complex, is formed when a Lewis base (ligand) is attached to a Lewis acid (acceptor) by means of a "lone-pair" of electrons. The ligand is composed of a number of atoms, but the atom that is directly attached to the acceptor is called the "donor atom". Ligands are most conveniently classified according to the number of donor atoms which they contain and are known as mono-, bi-, tri-, tetra-, penta-, and hexa-dentate accordingly as the number is 1, 2, 3, 4, 5, or 6.[197]

The important factors determining the most favorable coordination number for a particular metal and ligand are summarized below.[197, 198]

- VSEPR (valence shell electron-pair repulsion) arguments for the representative elements.
- Occupancy of *d* orbitals. LFSE (ligand field stabilization energy) and angular overlap energy calculations.
- Steric interference by large ligands, causing crowding around the central metal.
- The attraction between the metal and ligands should exceed the destabilizing repulsions between the ligands. Therefore a high cation charge and a low ligand charge should consequently favor a high coordination number, e.g. halides ions usually favor higher coordination numbers than O2-.
- The more polarizable the ligand the lower the coordination number required to satisfy the particular cation. If back-donation of charge from the cation to

the ligand via suitable π orbitals is possible, then more ligands can be accommodated.

B.1. Coordination Number 1

Coordination number 1 is rare, except in ion pairs in the gas phase. Cu(I) and Ag(I) complexes of 2,4,6-$Ph_3C_6H_2^-$ (5′-phenyl-*m*-terphenyl-2′-yl) have a single coordination number and a very bulky ligand which prevents any bridging between metals.[199] A mono-coordinate transient species $VO^{2+}$is also known.

B.2. Coordination number 2

Coordination number 2 is also rare. Examples of this coordination number are virtually confined to linear ($D_{\infty h}$) complexes of Cu(I), Ag(I), Au(I), and Hg(II). The best known example is $[Ag(NH_3)_2]^+$ in which silver(I) is d^{10} so the only electrons to be considered in the VSEPR theory are those forming the bonds with the ammonia ligands. For reasons of ligand bulk, some d^5, d^6, or d^7 complexes, $[Mn(N(SiMePh_2)_2)_2]$, $[Fe(N(SiMe_2Ph_2)_2)_2]$, and $[Co(N(SiMePh_2)_2)_2]$,[200, 201] with coordination number 2 are also known.

B.3. Coordination number 3

Coordination number 3 is also more likely with d^{10} ions due to electronic factors, including $[Au(PPh_3)_3]^+$, $[Au(PPh_2)Cl]$, and $[Cu(SPPh_3)_3]^+$,[202] commonly forming a planar trigonal structure (D_{3h}). Other compounds tridentate due to ligand bulkiness, e.g., ligands as triphenylphosphine (PPh_3) and di(trimethylsily)amide ($N(SiMe)_3^-$) are bulky enough to prevent larger

coordination numbers. All the first row transition metals except Mn(III) form three coordinated compounds which are close to trigonal planar geometry, although the VSEPR predicts some T- shaped complex.

B.4. Coordination number 4[203]

This coordination number is very common and usually gives rise to stereochemistry of either tetrahedral (T_d) or square planar (D_{4h}). Crowding around small ions of high positive charge prevents octahedral shapes, as for Mn(VII) and Cr(VI), and large ligands can prevent higher coordination numbers. The tetrahedral geometry is common amongst complexes of transition metals of d^0, d^5 and d^{10} ions. Because there is a spherically symmetrical electron configuration about the central atom, the ligand arrangement is sterically determined as tetrahedral. BF_4^-, MnO_4^-, CrO_4^{2-}, $TiCl_4$, $[Ni(CO)_4]$, and $[Cu(py)_4]^+$ exemplify this type of geometry. However, many tetrahedral transition metal complexes such as $[Co(PF_3)_4]^-$, $[NiCl_4]^{2-}$, and $[NiCl_2(PPh_3)_2]$, that have other d^n configurations, are also known.

Square planar geometry is another possibility for four-coordinate species of a central cation, particularly with the d^8 configuration, e.g., Pd(II), Pt(II) and Ni(II). Other d^8 transition metal ions known to form square planar complexes are $[AgF_4]^-$ and $[RhCl(PPh_3)_3]$. The difference in energy between tetrahedral and square planar forms is small, and some Ni(II) (d^8) and Cu(II) (d^9) compounds can have tetrahedral, square planar, or intermediate shapes depending on both the ligand and the counteranion in the crystal.

B.5. Coordination number 5[204]

Five-coordinate complexes are common and are now known for all configurations from d^1 to d^9. The square pyramidal (C_{4v}) and trigonal bipyramidal (D_{3h}) geometries are typical for coordination number 5. The energy difference between the trigonal bipyramid and the square pyramid is very small, thus many complexes with this coordination number have structures intermediate between the two extremes, or exhibit an interconversion between the two (e.g., the Berry pseudorotation).[3] Nuclear magnetic resonance spectrometry (^{13}C and ^{19}F, respectively) shows only one peak each for the $Fe(CO)_5$ and PF_5 complexes, indicating that they are fluxional on the NMR time scale. In the solid state, both are trigonal bipyramidal.

B.6. Coordination number 6[205]

Six is the most common coordination number of transition elements. The octahedral six-coordinate structure is far more common than the trigonal prismatic one. Intermediate structures also occur and can be defined by the "twist angle (α)" (Fig. 3.1) which is the angle through which one face of an octahedron has been rotated with respect to the opposite face, as viewed along a threefold axis of the octahedron. A twist angle of 60° converts an ideal octahedral into an ideal trigonal prismatic geometry.

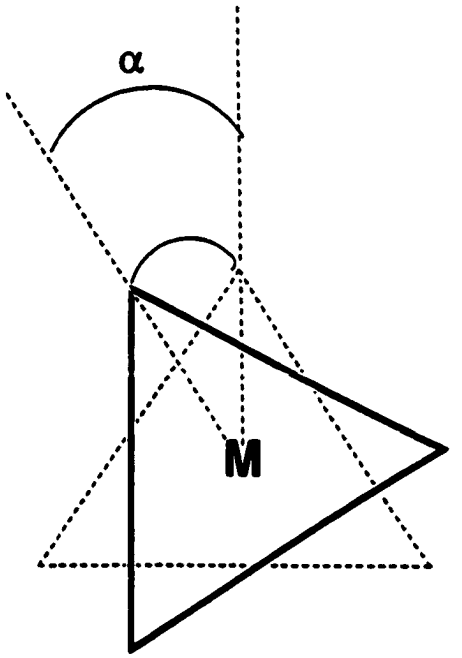

Figure 3.1. Twist angle (α).

Both trigonal and tetragonal distortions of the octahedral geometry are known. These mean compression or elongation along the threefold or fourfold axis of the octahedron, respectively (**Fig. 3.2**).

Jahn-Teller distortion is also predicted to occur in situations in which degenerate orbitals are asymmetrically occupied. Distortion of the octahedral geometry is commonly observed if the e_g orbitals are asymmetrically occupied. The d^4 (high-spin), d^7 (low-spin), and d^9 are the configurations that most likely give rise to observable Jahn-Teller distortions. The most common distortion is the elongation of bonds along one axis.

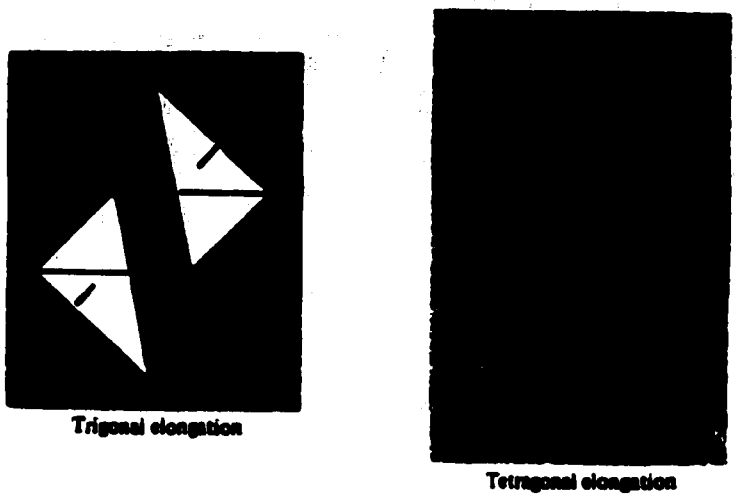

Figure 3.2. Distortions of the octahedral geometry.

B.7. Coordination numbers 7 and 8[206, 207]

Seven-coordinate complexes typically exhibit pentagonal bipyramidal (D_{5h}), capped trigonal prismatic (C_{2v}), or capped octahedral (C_{3v}) (**Fig. 3.3**) geometries. The last two may be conceptualized as the addition of a seventh ligand to one of the rectangular faces of a trigonal prism, or to a triangular face of an octahedron, respectively.

The two most important eight-coordinate structures are the square antiprism (D_{4h}) and the dodecahedron (D_2d). Again, these forms are energetically very similar; distortions from the idealized structures make it difficult to specify one or other.

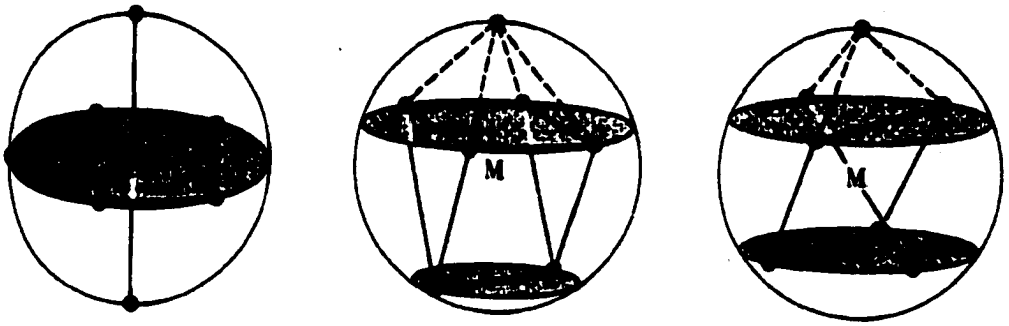

Figure 3.3. The three main stereochemistries for seven-coordination.

C. Coordination chemistry of the First-Row Transition Elements

The factors that can be used for determining the stability of transition metal complexes are generalized from the overwhelming amount of quantitative measurements. Some of these are as follows:

- Irving-Williams order. The stability is generally greater for a metal with oxidation state of +3 rather than +2 for a given metal and ligand due to a larger attraction between the metal ion and the ligand. The stability of divalent transition metal complexes is usually the reverse of the order for the cation radii (Irving-Williams order). This order is consistent with the fact that the coordinate bond is mostly electrostatic for metals in oxidation states +2 and +3. Mn(II) < Fe(II) < Co(II) < Ni(II) < Cu(II) > Zn(II)
- HSAB (hard-soft acid and base). Some metal ions (known as class-a acceptors or as 'hard acids") are any cations with large positive charge (3+ or larger) or those whose *d* electrons are relatively unavailable for π bonding and form their most stable complexes with ligands containing hard base donor atoms. Others (known as class-b acceptors or as "soft acids") are those whose *d* electrons are readily available for π bonding and form their most stable complexes with ligands whose donor atoms are soft base donor atoms.[208] In addition, the more massive the atom, the softer it is likely to be. This is due to the large number of inner electrons shielding the outer ones, making the atom more polarizable. The class-b ions are primarily 1+ and 2+ ions with filled or nearly filled d orbitals, and most are in the second and third row of the transition elements. The metals of group IA and IIA along with the inner

transition elements and early members of the transition series (Groups IIIA – VA) fall into class-a. The transition elements Rh, Pd, Ag, Ir, Pt, Au, and Hg comprise class-b, while the remaining transition elements may be regarded as borderline.

- Chelate effect. In comparing the stability of complexes formed by different ligands, one of the most important factors is the possible formation of chelate ring. If L (monodentate) and L-L (bidentate) are present in similar concentration and are competing for two coordination sites on the metal, the probability of either of them coordinating to the first site may be taken as equal. However, once one end of L-L has become attached it is much more likely that second site will be won by its other end than by L, simple because its other end is held close to the second site and its effective coordination is therefore much higher than of L.[209] This chelate effect is attributed to the entropy and enthalpy difference. The chelate effect is usually most pronounced for five- and six-membered rings.

Since all tach derivatives have nitrogen donor atoms of three or six and complexation was attempted with divalent transition metal elements, this part of the introduction will be focused on the divalent transition metal complexes of ligands with nitrogen donor atoms.

C.1. Coordination chemistry of Mn(II)

Coordination chemistry of manganese has been neglected because of the dominance of the Mn(II) state and the lack of a reliable guide to the structure of the coordination polyhedron from any technique other than the X-ray method.

However, because of its biological role, especially in photosynthesis[210] and oxidative DNA cleavage, interest has recently been aroused. The great majority of Mn(II) compounds are high-spin (half-filled d^5 configuration) and in the ^6S ground state, and its *d-d* transitions are forbidden by both the LaPorte and the spin state selection rules.

Many Mn(II) compounds are sensitive to oxidation by molecular oxygen, and its sensitivity to oxygen and the product of this reaction are a major reason for the increasing interest in manganese chemistry.[211] Both Mn(III) and Mn(IV) have been properly characterized in a number of systems, and it appears that +4 oxidation state is more accessible to manganese than iron. The higher oxidation states V, VI, and VII are all known, and are largely represented in the chemistry of the oxo ligand manganates. Manganese with a variety of oxidation states is a subject of magnetic moment study. The theoretical "spin only" and experimental magnetic moments for oxidation states of +2, +3, and +4 are presented in **Table 3.1** and **Table 3.2**, respectively. Monomeric species typically have moments close to the spin only values. Most known Mn(II) and Mn(III) are high-spin, however with cyano ligand few low-spin species are known. It is, however, not possible to deduce stereochemistry of the metal complexes from magnetic moment information, but, it gives insights into spin state and may help to confirm the oxidation state.

Table 3.1 Theoretical magnetic moments for Mn(II), Mn(III), and Mn(IV) in Bohr magnetons.[211]

Oxidation states	Spin free	Spin paired (*Oh*)
Mn(II)	5.92	1.73
Mn(III)	4.90	2.83
Mn(IV)	3.87	3.87

Table 3.2 Experimental room temperature magnetic moment (in B.M.) of some Mn(II), Mn(III), and Mn(IV) complexes.[211]

Oxidation state	complex	Spin state	stereochemistry	μ_{eff}
Mn(II)	$[Mn(py)_6]Br_2$	Spin free	*Oh*	6.00
	$(pyH)_2[MnCl_4]$	Spin free	*Td*	5.95
	$K_4[Mn(CN)_6]$	Spin paired	*Oh*	1.80
Mn(III)	$[Mn(acac)_3]$	Spin free	*Oh*	4.95
	$K_3[Mn(CN)_6]$	Spin paired	*Oh*	3.18
Mn(IV)	$K_2[MnF_6]$	Spin free	*Oh*	3.90
	$K_2[Mn(CN)_6]$	Spin free	*Oh*	3.94

Manganese(II) is the dominant oxidation state of manganese. Manganese is the first transition metal for which +2 is the common oxidation state which is a feature of the remaining first row transition metals from iron to zinc. Manganese(II) is more stable than expected, and this is ascribed to the stable half-filled *d* electron shell of the high-spin compounds. In many of its features,

the chemistry of manganese(II) spans that of the alkaline earth metals and the later first row transition metals. These are all related to the more significantly ionic bonding for manganese and to the size of the metal ion. Manganese(II) is quite distinctively a hard acid, and has a preference for O donor rather than N donor ligands so that amino acid compounds are simply those of substituted carboxylates.

The coordination geometries of Mn(II) are quite variable because of the lack of LFSE for the high-spin d^5 configuration. Ligand steric and electronic effects are the major factors in defining the geometries of Mn(II). Coordination geometries and spin states of Mn(II) complexes are summarized in **Table 3.3.**

Table 3.3. Coordination polyhedra and spin states for manganese(II)[211].

Coordination Number	Donor Atoms
High-spin Polyhedra (μ_{eff} = 5.8 - 6 2 B.M.)	
8	$[O_8][N_8][N_4O_4]$
7	$[N_7][N_5O_2][N_2O_5]$
6 (Octahedral)	$[N_6][N_xO_{6-x}][O_6][P_6Cl_2][P_4Br_2][P_2I_4]$ $[S_6][S_4N_2][S_4Cl_2][F_6][Cl_6][Br_6][I_6]$ $[X_xO_{6-x}][X_xN_{6-x}]$ and [X, O, N] (X = Cl, Br)
6 (Trigonal Prismatic)	$[O_6][N_6]$
5*	$[C_3N_2][N_5][N_2O_3][O_5][N_4X][N_3X_2]$ $[N_2X_3][N_2OX_2]$ (X = Cl, Br)
4 (Tetrahedral)	$[C_4][N_4][C_3N][C_2N_2][C_3P][C_2P_2][S_4]$ $[N_2O_2][O_4][X_4][X_3N]$ (X = Cl Br, I)
4 (Planar)	$[N_4][O_4]$
3 (Planar)	$[C_3][N_3][N_2O][O_3][X_3]$ (X = Cl, Br)
2 (Linear)	$[X_2][H_2]$ (X = Cl, Br)
Intermediate Spin Polyhedra (μ_{eff} ~ 4 B.M.)	
4 (Planar)	$[N_4]$
Low-spin Polyhedra (μ_{eff} = 1.8 – 2.2 B.M.)	
6 (Octahedral)	$[C_6][C_5N][C_2P_4][Cl_2P_4][N_3O_3]$

It is hard to distinguish the various ideal polyhedra. Constrains within molecules usually adopt intermediate shape.

C.1.1. Mn(II) complexes of tridentate nitrogen donor ligands

In the 1:1 Mn(II) complexes of tridentate nitrogen donor ligands, five-coordinate monomeric $[MnX_2L]$ (X = halides, and L = N_3 ligand) structures are dominant. Stability constants in aqueous solution are known for dien (bis(2-aminoethyl)amine) **164**, bis(2-pyridylmethyl)amine **44**, and terpy (2,2′,2″-terpyridyl) **165**. The determined log K_1's and log K_2's are, respectively: 4.0 and 2.8; 3.5 and 2.6; and 4.4 (K_2 not measured for terpy).[212] The 2:1 species are bis-ligand octahedral, $[MnN_6]X_2$.

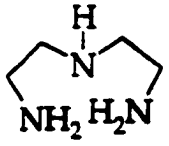

164

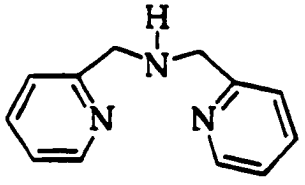

44

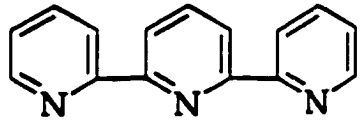

165

Figure 3.4 (bis(2-aminoethyl)amine) **164**, bis(2-pyridylmethyl)amine **44**, and terpy (2,2′,2″-terpyridyl) **165**.

Four neutral molecules $[Mn(N_3)_2]^0$ were produced by loss of the hydrazone protons from **166** and are high-spin.[213] Fifty eight compounds of $[MnX_2L]$ (X = Cl, Br, I or NCS, and L = variation of **166** or related ligands using quinoyl, benzthiazyl or oxime moiety) were produced. They had colors ranging from yellow, through orange, to brown, and are all high-spin.[213]

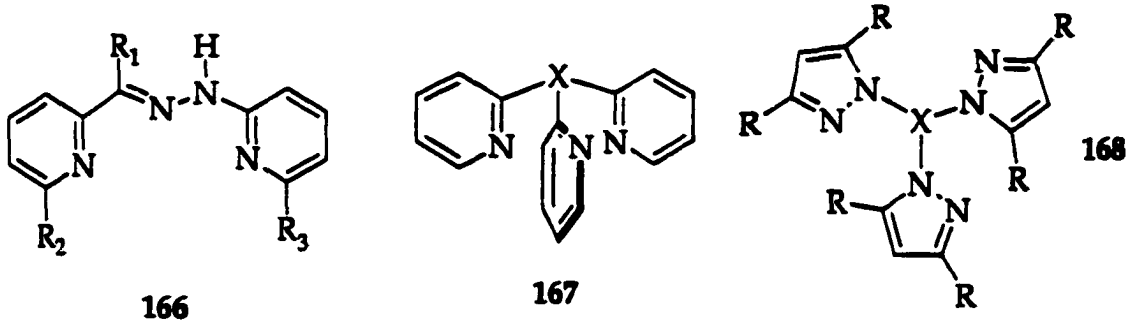

166 167 168

Figure 3.5. Various linear tridentate nitrogen donor ligands.

An octahedron high-spin complex $[MnL_2](ClO_4)_2$ was produced for **167** (X = C-OH), and a five-coordinate monomer $[MnLCl_2]$ (L = **167** and X =N) is known.[214] Colorless high-spin octahedral Mn(II) complexes $[MnN_6]^0$ with monoanion **168** (R = H or Me, X = GaMe, BH, or B-pyrazoyl) were also produced.[215]

C.1.2. Mn(II) complexes of hexadentate nitrogen donor ligands

The linear hexadentate ligand **169** gave bright yellow crystals of the high-spin Mn(II) complex $[MnL)X_2$ (X = NCS or I, n = 2 or 3). Bifurcated ligand **170** (n = 2) forms a 1:1 species identified as a seven-coordinate polyhedron $[Mn(N_6)H_2O]^{2+}$, on the other hand **170** (n =3) forms binuclear species $[Mn_2(N_6)]^{4+}$ in water. The pyridyl ligand **171** has a log *K* of 10.27 and the solid compound $[MnL](ClO_4)_2 \bullet H_2O$[212] has been isolated as yellowish needles with the octahedral coordination geometry. Two tripod ligands, **172** (tachimpyr) (tachimpyr = cis,cis-1,3,5-tris(pyridine-2-carboxaldimino)cyclohexane) and **173**, form trigonal prismatic six-coordinate Mn(II) complexes with yellow colors rather than the octahedral coordination.

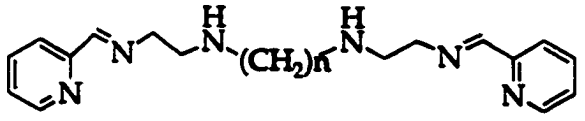

169

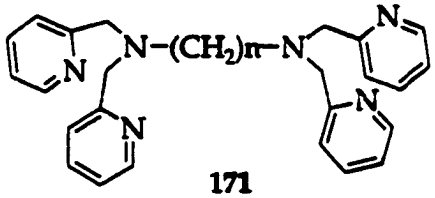

171

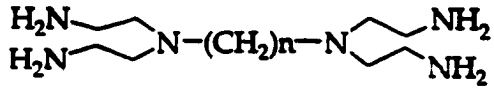

170

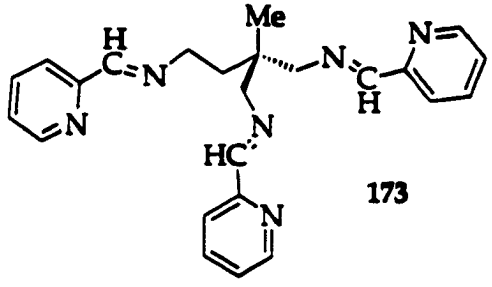

173

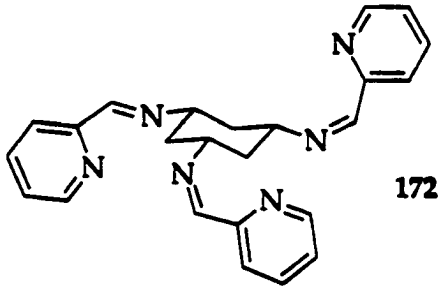

172

Figure 3.6 Hexadentate nitrogen ligands.

C.2. Coordination Chemistry of Fe(II)

C.2.1. Oxidation states of Iron

The chemistry of iron is very versatile, and various roles of irons can be easily found in active centers of biological systems such as oxygen and electron transfer in nitrogenase, many oxidases and in metalloenzymes such as hydrogenases and reductases. Iron compounds have various oxidation states from –II (d^{10}) to VI (d^2) and a variety of coordination chemistries. The most common oxidation states in complexes of a conventional coordination type are II (d^6) and III (d^5), ferrous and ferric, respectively. **Table 3.4** illustrates the kinds of

complexes and stereochemistries formed with iron in different oxidation states. Low oxidation states in iron complexes are formed by π acceptor ligands such as phosphines and carbon monoxide.

Most iron(II) complexes have an octahedral geometry, although four-, five-, seven-, and eight-coordinate Fe(II) complexes are known. Tetrahedral Fe(II) complexes include $[FeCl_4]^{2-}$, $[Fe(OPPh_3)_4]^{2+}$, $[Fe(OP(Nme_2)_3)_4]^{2+}$, while square planar Fe(II) complexes are formed with tetradentate nitrogen donor macrocycles of which the most familiar are the porphyrins.[185] Many five-coordinate high-spin Fe(II) complexes are known having tetradentate nitrogen donor macrocyclic ligands with a halide as the fifth coordination. Five-coordinate Fe(II) complexes with tripod ligands such as $[Fe(N(CH_2CH_2PPh_2)_3)X]^+$ show both high-spin and low-spin complexes.[216]

The iron(II) $^5D_2$ ground state is split by the octahedral field into the $^5F_{2g}$ and $^5E_{2g}$ states. High-spin octahedral iron(II) complexes typically have magnetic moments of about 5.2 B.M. and show a broad transition ($^5F_{2g}$ ->$^5E_{2g}$) in the UV-vis region of the spectrum. With strong field ligands, spin paring can take place to afford diamagnetic low-spin iron(II) complexes having magnetic moments that are typically less than 1.0 B.M. These low-spin iron(II) complexes are usually intensely colored (red or purple) due to strong metal-ligand charge transfer bands that obscure *d-d* transitions.[217] Also, the low-spin iron(II) complexes are also usually thermodynamically stable and kinetically inert, which is consistent with their large crystal field stabilization energy.

Table 3.4. Various oxidation states and coordination chemistries of iron.[185]

Oxidation states	coordination number	complex	coordination geometry
-II (d^{10})	4	$[Fe(CO)_4]2-$	Tetrahedral
0 (d^8)	5	$[Fe(CO)_3(PPh_3)_2]$	Trigonal bipyramidal
I (d^7)	5	$[Fe(dppe)_2H]$[a]	Square pyramidal
II (d^6)	4	$[FeBr_2(PPh_3)_2]$	Tetrahedral
	5	$[FeBr(Me_6tren)]^+$	Trigonal bipyramidal
	5	$[Fe(ClO_4)(OAsMe_3)_4]^+$	Square pyramidal
	6	$[Fe(phen)_3]^{2+}$	Octahedral
	7	$[Fe(HPAP)(H_2O)_2]^{2+}$ [d]	Pentagonal bipyramidal
	8	$[Fe(1,8\text{-naph})_4]^{2+}$ [b]	Dodecahedral
III (d^5)	3	$[Fe(N(SiMe_3)_2)_3]$	Trigonal planar
	4	$[FeCl_4]^-$	Tetrahedral
	5	$[FeCl(dtc)_2]$[c]	Square pyramidal
	5	$[Fe(N_3)_5]^{2-}$	Trigonal bipyramidal
	6	$[Fe(phen)_3]^{3+}$	Octahedral
	7	$[Fe(edta)(H_2O)]^-$	Pentagonal bipyramidal
	8	$[Fe(NO_3)_4]^-$	Dodecahedral
IV (d^4)	4	[Fe(1-norbornyl)$_4$]	Tetrahedral
	6	$[Fe(diars)_2Cl_2]^{2+}$	Octahedral
V (d^3)	4	FeO_4^{3-}	Tetrahedral
VI (d^2)	4	FeO_4^{2-}	Tetrahedral

[a] dppe = 1,2-bis(diphenyphosphino)ethane. [b] 1,8-naph = 1,8-naphthyridine. [c] dtc = dithiocarbamate. [d] HPAP = macrocycle from 2,9-di(1-methylhydrazino)-1,10 phenanthroline and 2,6-diacetylpyridine

An eight-coordinate Fe(II) complex is rare, but $[Fe(naph)_4]^{2+}$ is well characterized as a high-spin distorted dodecahedral.[218] Seven-coordination is more common than eight-coordination, and is known in several macrocyclic complexes.[219]

C.2.2. Fe(II) complexes of tridentate nitrogen donor ligands

The tridentate ligand terpy **165** (**Fig. 3.4**) forms mono and bis complexes with Fe(II). According to X-ray powder data $[Fe(terpy)X_2]$ (X = Br and I)[220] is a five-coordinate structure. Fe(II) with an excess of terpy forms the very stable low-spin bis complex.[221] The tridentate hydrazone **173** derived from pyridine aldehyde also forms low-spin bis complexes,[222] as do the tridentate ligands **174** and **175**.[223]

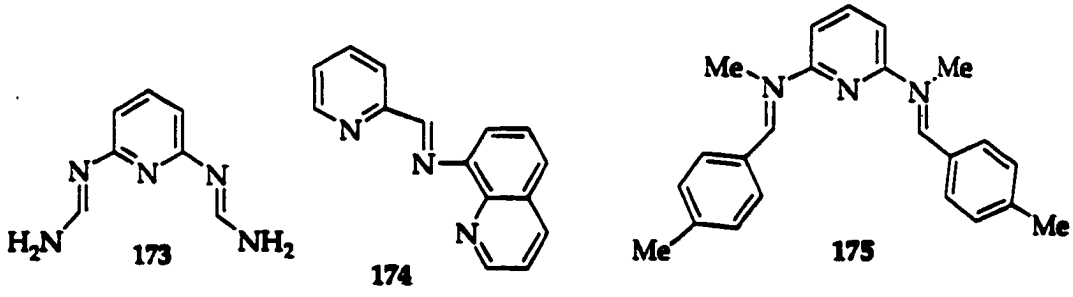

173 174 175

Figure 3.7. Tridentate nitrogen donor ligands.

Reaction of 2-aminomethylpyridine **176** with sodium pyruvate and Fe(II) in an aqueous medium give the complex containing the tridentate ligand **177** and α-alanine rather than the expected complex containing **178**.because isomerization

to the conjugated imine takes place followed by the trasamination with another molecule of **176**.

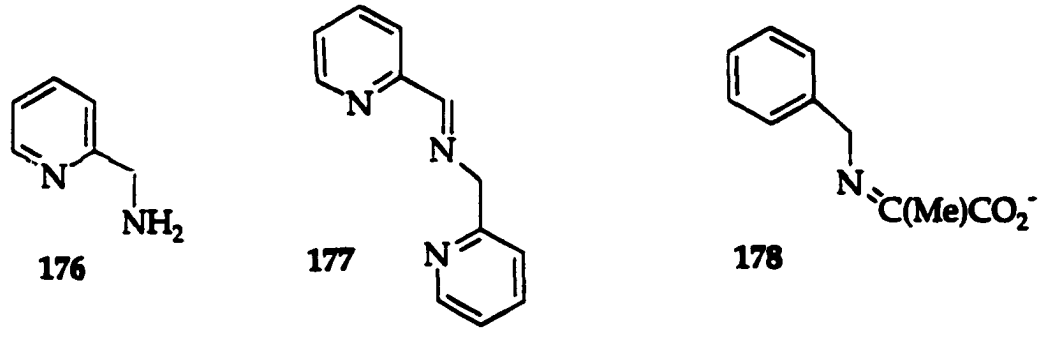

176 **177** **178**

Figure 3.8. Formation of a tridentate ligand**177**.

The bis Fe(II) complex of bispicam **179** is red and low-spin. Tridentate ligands, **180**, and **181**, derived from 1,10-phenanthroline have also been prepared. The 2-amidoxime **180** has a strong ligand field and the Fe(II) complex of **180** is low-spin. Spin cross-over is shown in **181** being depending on the nature of R_1 and R_2.[224] Several 1,10-phenanthroline derivatives, **182** and **183**, with a five-membered heterocyclic group in the 2-position have been prepared, and most of their bis Fe(II) complexes display temperature dependant spin cross-over behavior. The Fe(II) complex of **182** is a high-spin, and it undergoes a spin change at low temperature. The bis complex of **183** is predominantly low-spin at room temperature (~1.8 B.M.) but the magnetic moment gradually increases as the temperature is raised.[225] The macrocyclic triamine [9]aneN_3 **191 (Fig. 3.12)** reacts with $FeCl_2$ to afford a blue precipitate, [Fe([9]aneN_3)$_2$]Cl_2, which is diamagnetic and stable in aqueous solution.[226]

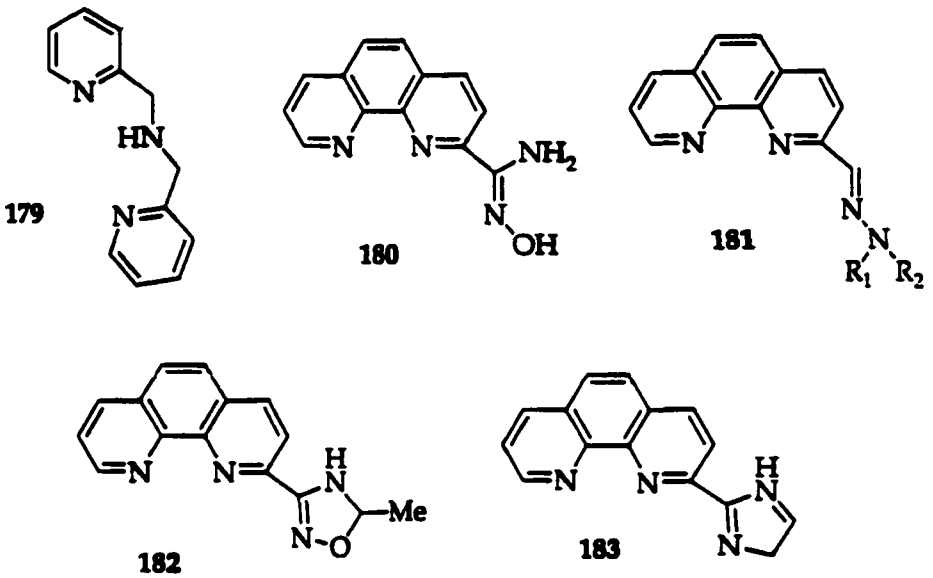

Figure 3.9. Tridentate nitrogen donor ligands.

C.2.3. Fe(II) complexes of hexadentate nitrogen donor ligands

Fe(II) complexes of the linear hexadentate nitrogen donor ligands **184** (R =H and Ph) form low-spin complexes, even though they contain only two di-imine units.[227] The hexadentate ligand **185** forms a well-characterized purple low-spin complex, but a spin cross-over is observed with methyl substituted pyridine rings adjacent to the nitrogen atoms. The Fe(II) complex of **186** forms a red low-spin complex when $n = 3$ and R =H, but a high-spin complex for $n = 2$ and R = Me.[228] With pendant pyridylmethyl groups, triazamacrocyles **187** provide six nitrogen donor atoms. These form the pseudooctahedral low-spin Fe(II) complexes when $n = m = 2$, but high-spin complexes are formed with an expanded ligand having $n = m = 3$.[229] The hexadentate ligands **188** and **172** also form Fe(II) complexes, affording a distorted octahedral complex and octahedral complex respectively.[184, 188]

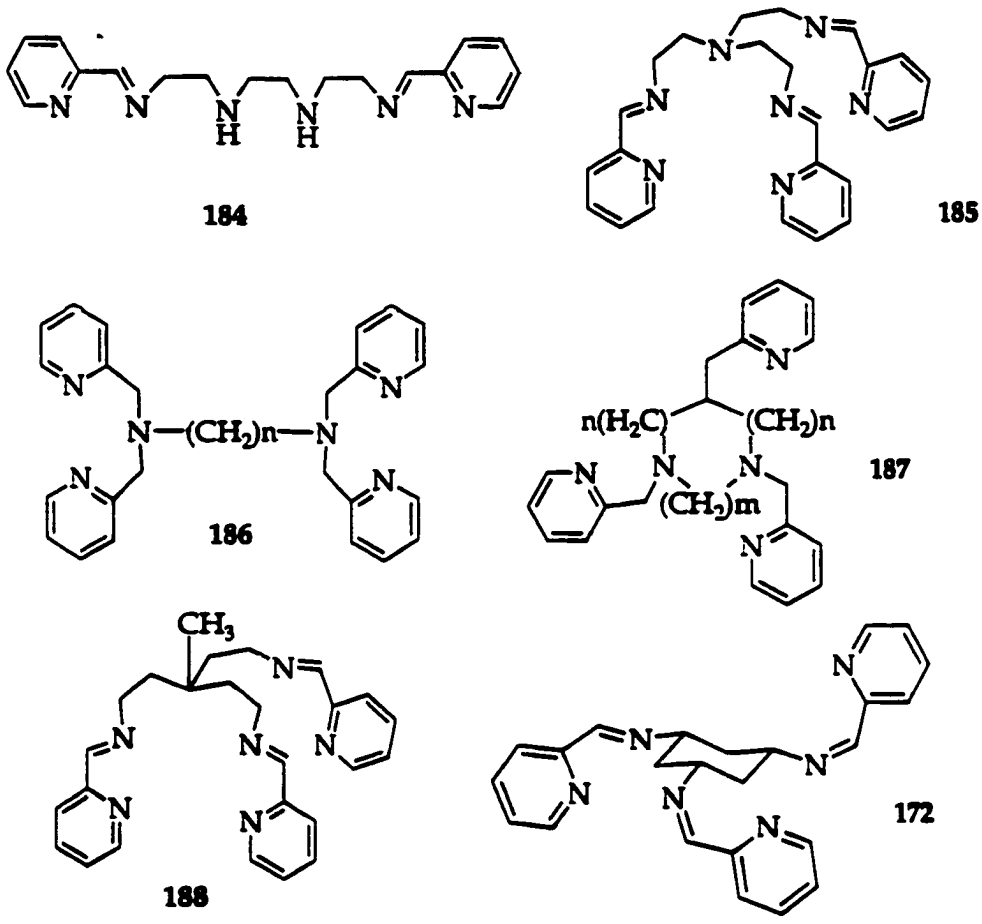

Figure 3.10. Selected hexadentate nitrogen donor ligands.

C.2.4. Fe(III) complexes of nitrogen donor ligands

Most Fe(III) complexes are octahedral like Fe(II), however, four-(tetrahedral) and five coordination are well-known (**Table 3.4**) Some macro cyclic nitrogen ligands can form the uncommon seven-coordinate complexes,[230] as can $[Fe(edta)(H_2O)]^-$.[231] The $[Fe(NO_3)_4]^-$ complex has eight-coordination. Iron(III) has a higher affinity for oxygen than nitrogen due to its hardness. Fe(II), which prefers nitrogen donor atoms, is a softer metal than Fe(III). In most

octahedral monomeric Fe(III) complexes, the spin state is high-spin with magnetic moments of the spin-free value, as found in $[Fe(acac)_3]$. Low-spin Fe(III) complexes, $[Fe(CN)_6]^{3-}$ and $[Fe(phen)_3]^{3+}$, with very high field ligands are known. Like low-spin Fe(II) complexes, low-spin Fe(III) complexes are more kinetically inert than their high-spin complexes.[185] The spin cross-over behavior of Fe(II) complexes is also known in Fe(III) complexes. A variety of Fe(III) dithiocarbamate complexes of the type $[Fe(S_2CNR_2)_3]$ display high-spin/low-spin cross-over behavior.[232] The spin forbidden *d-d* transitions of Fe(III) complexes are little known because of the near-UV charge transfer bands that tail into the visible region of the spectrum.

C.3. Coordination Chemistry of Co(II) and Co(III)

The most common oxidation states of cobalt are II (d^7) and III (d^6), but few compounds represent the oxidation states of IV (d^5) and V (d^4). Coordination chemistry of cobalt(II) is rich. It forms mostly either octahedral or tetrahedral but five-coordinate and square species are also known. Due to the small stability difference between octahedral and tetrahedral Co(II) complexes, there are several cases in which the two geometries with same ligand are both known and may be in equilibrium.233 Cobalt(III) forms exceedingly numerous complexes. Due to relatively slow ligand-exchange reaction of Co(III) complexes, they have been extensively investigated in the isomerism, mode of reaction, and general property studies of octahedral complexes.[233] The oxidation states and stereochemistries of cobalt are summarized in **Table 3.5.**

Cobalt(II) (d^7) ion have both high-spin ($t_{2g}^5 e_g^2$) and low-spin ($t_{2g}^6 e_g^1$) states with different magnetic moments. With considerable orbital contribution, the effective magnetic moments for high-spin octahedral Co(II) complexes are between 4.7 and 5.2 B.M. However, the electron configuration for low-spin Co(II) complexes is mainly $t_{2g}^6 e_g^1$, and a Jahn-Teller distortion would be expected, giving theses complexes magnetic moments in the range of 1.8 – 2.00 B.M.233

All known octahedral Co(III) complexes, including $[Co(H_2O)_6]^{3+}$ and $[Co(NH_3)_6]^{3+}$, have diamagnetic ground states, except for $[Co(H_2O)_3F_3]$ and $[CoF_6]^{3-}$, which are paramagnetic with four unpaired electron.

Table 3.5. Various oxidation states and coordination chemistries of Cobalt.[233]

Oxidation states	coordination number	complex	coordination geometry
-I (d^{10})	4	$[Co(CO)_4]^-$	Tetrahedral
0 (d^9)	4	$K_4[Co(CN)_4]$	Tetrahedral
I (d^8)	3	[(tempo)Co(CO)$_2$]	Planar
	4	$[CoBr(PR_3)_3]$	Tetrahedral
	5	$[Co(CO)_3(PR_3)_2]^+$	Trigonal bipyramidal
	5	$[Co(NCPh)_5](ClO_4)$	Square pyramidal
	6	$[Co(NH_3)_6]^{2+}$	Octahedral
II (d^7)	3	$[Co(OCBu_3)_2(N(SiMe_3)_2)]^-$	Trigonal
	4	$[CoBr_2(PR_3)_2]$	Tetrahedral
	4	$[Co(py)_4]$	Square planar
	5	$[Co(Me_6tren)Br]^+$	Trigonal bipyramidal
	5	$[Co(CN)_5]^{3-}$	Square pyramidal
	6	$[Co(NH_3)_6]^{2+}$	Octahedral
	8	$(Ph_4As)_2[Co(NO_3)_4]$	Dodecahedral
III (d^6)	4	$[CoW_{12}O_{40}]^{5-}$	Tetrahedral
	4	$[Co(SR)_4]^-$	Square planar
	5	[Co(corrole)(PPh$_3$)] [a]	Square pyramidal
	5	CoCl(TC-4,4) [b]	Trigonal bipyramidal
	6	$[Co(en)_2Cl_2]^+$	Octahedral
IV (d^5)	4	[Co(1-norbornyl)$_4$]	Tetrahedral
	6	$[CoF_6]^{2-}$	Octahedral
V	4	$[Co(1\text{-norbornyl})_4]^+$	Tetrahedral

[a] corrole = tetrapyrrolic macrocycle

[b] TC-4,4 =

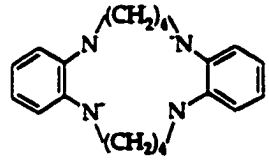

C.3.1. Co(II) complexes of tridentate and hexadentate nitrogen donor ligands

The terpy (2,2',2"-terpyridyl) **165** (**Fig. 3.4**) makes bis Co(II) complexes of the type $[Co(terpy)_2]X_2$, resulting spin cross-over complexes (μ_{eff} = 2.96 B.M.) with X = Br^-, NO_3^- and high-spin complexes (μ_{eff} = 4.49 B.M.) with X = Cl^- and ClO_4^- .[234] The coordination geometries of $[Co(terpy)_2]Br_2 \bullet 3H_2O$ and $[Co(terpy)_2](NCS)_2 \bullet 2H_2O$ are of the distorted octahedron.[235]

The tridentate ligand bis(2-methylaminoethyl)methylamine (Me_5dien) **189**, which is a pentamethyl derivative of bis(2-aminoethyl)amine (dien) **164** (**Fig. 3.4**), forms five-coordinate Co(II) complexes of the type [Co(**189**)X_2] (X = Cl^-, Br^-, and I^-). The coordination geometry of $[Co(Me_5dien)Cl_2]$ is almost intermediate between the two idealized geometries of trigonal bipyramid and square pyramid.[236] A tetraethyl derivatives of dien Et_4dien **190**, 1,1,7,7-tetraethyldiethyleletriamine, also makes five-coordinate complexes with two halides (Cl and Br) affording slightly distorted trigonal bipyramid high-spin Co(II) complexes $[Co(Et_4dien)Cl_2]$.[237]

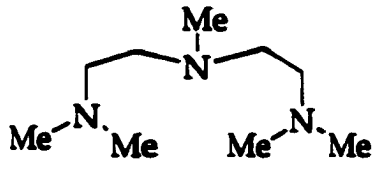

189

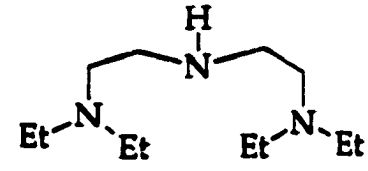

190

Figure 3.11. Me_5dien **189** and Et_4dien **190**.

Nonoyama[238] reported a series of triazacycloalkane bis(thiocyanato)Co(II) complexes which, depending on the ring size of the macrocycle (**Fig. 3.12**), are monomeric five-coordinate with two μ-thiocyanato bridges or binuclear six-coordinate species with two terminal NCS ligands. The facial tridentates [9]aneN$_3$ **191** form bis high-spin Co(II) complexes with a distorted octahedron geometry.[239]

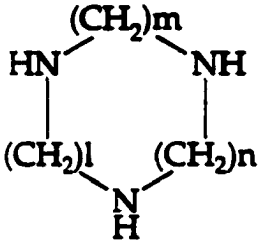

monomeric	l	m	n
	2	2	4
	2	3	4
	3	3	3

dimeric	l	m	n
	2	2	5
	2	2	6
	2	3	5
	3	3	4

191 l, m, and n = 2

Figure 3.12. A series of triazacycloalkane ligands.

There are a few cobalt(II) complexes having a hexadentate nitrogen donor ligand. The symmetrical cage ligand sep **192** (sep = sepulchrate) forms a high-spin Co(II) complex $[Co(sep)]^{2+}$ in which the polyhedron CoN_6 is classified as a distorted octahedral.[240] $[Co(sar)]^{2+}$ (sar = sarcophagine **193**) and its derivatives[241] have been prepared. The coordination geometry of $[Co(di(amH)sar)]^{2+}$ (di(amH)sar = **194**) is almost intermediate between the two ideal geometries, octahedral and trigonal prismatic.[240]

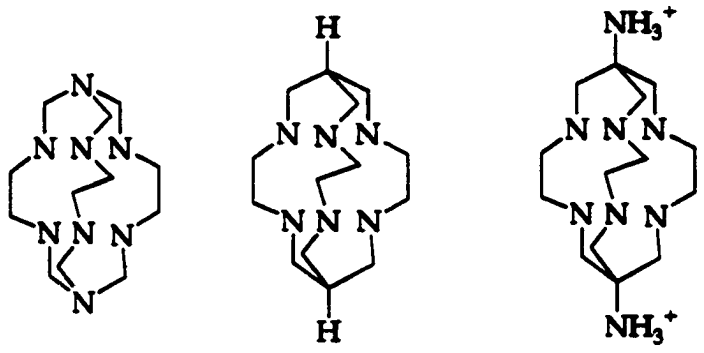

192 193 194

Figure 3.13. Hexadentate cage ligands.

C.3.2. Co(III) Complexes of Tridentate and hexadentate nitrogen donor ligands

The bis Co(III) complexes of dien **164** (**Fig. 3.4**) were prepared with Cl^-, Br^-, NO_3^-, and ClO_4^- counter ions as three geometric isomers: *mer*, unsymmetrical *fac* (*asym-fac*), and symmetrical *fac* (*sym-fac*) (**Fig. 3.14**).[242, 243] The isomer distribution was independent of the anion with a *mer*, *asym-fac*, and *sym-fac* ratio of ~ 64: 29:7.[242]

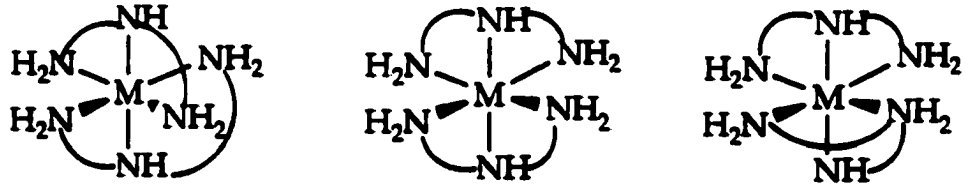

mer *sym-fac* *asym-fac*

Figure 3.14. Three isomers of $[Co(dien)_2]^{3+}$.

The mixture of *mer* and *fac* isomers of $[Co(pet)_2]^{3+}$ (pet = 1,6,-diamino-3-azahexane **195**) were prepared. Only the *mer* isomer of $[Co(dpt)_2]^{3+}$ (dpt = 1,7,-diamino-4-azahexane **196**),[244] and a only the *sym-fac* isomer of $[Co(medien)_2]^{3+}$ (medien = 3-methyl-1,5,-diamino-3-azahexane **197**) were produced.[245]

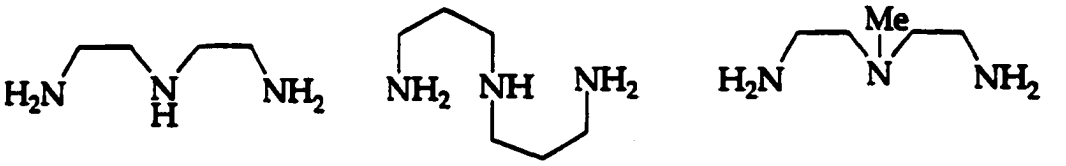

195 **196** **197**

Figure 3.15. Linear tridentate ligands.

A mixture of *sym-fac* and *asym-fac* isomers of $[Co(tap)_2]^{3+}$ (tap = 1,2,3-triaminopropane **198** (a branched tridentate ligand) were prepared and separated affording a 45:55 ratio with an abundance of the *asym-fac* isomers.[246] Tamp **199**, a methylated tap at the 2-position, also forms a mixture of *sym-fac* and *asym-fac* isomers (65:35 ratio) of the Co(III) complex. The two isomers have been separated, and each isomer was characterized by ^{13}C NMR spectroscopy. In this spectra the *asym-fac* isomer shows four signals, and the *sym-fac* isomer shows only three. The $[Co(tame)_2]^{3+}$ complex (tame = **200**) is slightly trigonally twisted (twist angle = 55.8°); the twist apparently relives some proton-proton non-bond interactions between the ligands.[247]

The Co(III) complex of [9]aneN_3 (tacn) **191** (**Fig. 3.12**) was prepared, but the solid structure is not known. The conformation of the Co(III) complex of metacn **201**, methylated tacn at the 2-position, is dictated by the presence of

methyl group in the axial position. Therefore R-metacn forms conformers with λ rings and S-metach forms δ rings. In the X-ray structure of $[Co(R\text{-}metacn)_2]^{3+}$ the two ligands are rotated 7.6° toward a trigonal prismatic structure.[248]

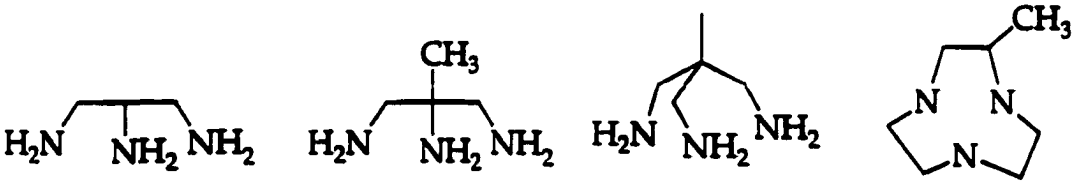

198 199 200 201

Figure 3.16. Tridentate nitrogen donor ligands.

The linear hexadentate ligand, linpen **202**, can form eight geometric isomers of Co(III) complexes $[Co(lipen)]^{3+}$. One of the isomers, f4-RSSR, was identified by X-ray crystallography.[249] However, the dtah ligand **203**, similar to lipen, forms a single isomer of C1 symmetry, indicating, unlike lipen, the coordination of dtah is highly stereospecific.[250] A crystal structure of the Co(III) complex of taetacn **204** shows a single isomer with Δ (λ,δ) conformer in which the λ conformation is for the five-membered ring in the tacn moiety and the δ conformation is for the en ring.[251] Tae-en **205**, the amine analogue of edta, also called penten, is able to form only a single geometric isomer when acting as a hexadentate ligand. The X-ray structure established that the $[Co(tae\text{-}en)]^{3+}$ is the ΛΔΛ (or just Λ) isomer.[252] The symmetrical cage ligands, sep **192** and **193** (**Fig. 3.13**), and their derivatives also form general Co(III) complexes.[253] The bimacorcyclic ligand dtne **206**, consists of two tacn ligands joined by an ethyl link

between two amines. Each tacn moiety is constrained to coordinate facially, and thus the (mono) Co(III) complexes of dtne are limited to a single isomer.[254]

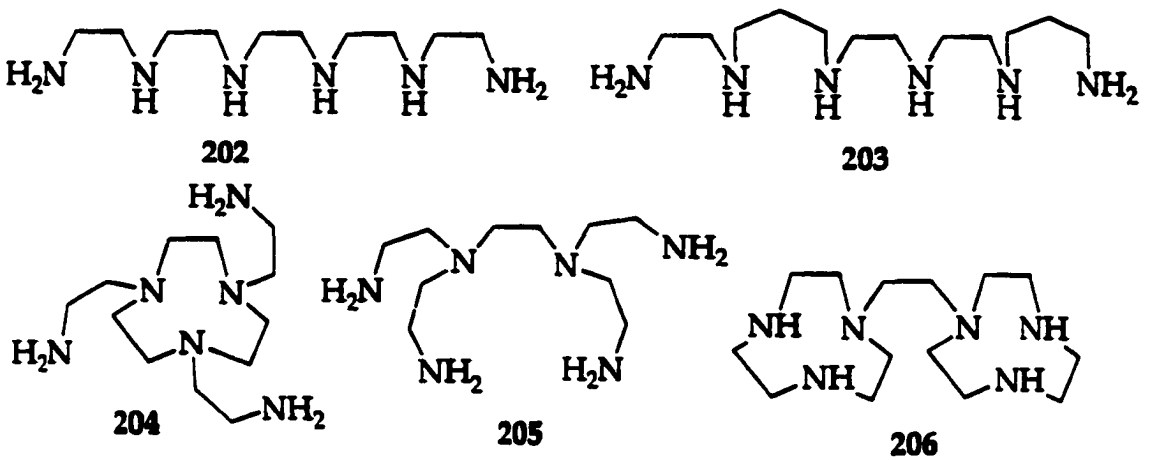

Figure 3.17. Hexadenate nitrogen donor ligands.

C.4. Coordination chemistry of Ni(II)

The maximum oxidation state that nickel can reach is IV (d^6), but the most common oxidation state of nickel is II (d^8). Comparatively, very few compounds with the lowest (-I) and to the higher (III and IV) oxidation states are known.[255] **Table 3.7** represents oxidation states and stereochemistries of nickel compounds revealing the reluctance of this element to form compounds with high coordination numbers. A coordination number higher than six is hardly achieved in the coordination chemistry of nickel. The overwhelming majority of Ni(II) complexes have coordination numbers of four, five, and six exhibiting stereochemistries which often exist simultaneously in equilibrium with each other.

The spin-only magnetic moment for Ni(II) (d^8) complexes is 2.83 B.M., however, larger values are generally observed due to orbital contributions derived from the mixing of the ground state of low-lying excited states under spin orbital operator or the degenerated ground states.[255] The magnetic moments usually observed at room temperature for Ni(II) complexes are listed in Table 3.6.

Table 3.6. Typical values of the effective magnetic moment at room temperature of Ni(II) complexes in various coordination environments.[255]

Coordination	μ_{eff} (B.M.)
Octahedral	2.9-3.3
Trigonal bipyramidal	3.2-3.8
Square pyramidal	3.2-3.4
Tetrahedral	3.2-4.0
Square planar	diamagnetic

Table 3.7. Oxidation states and stereochemistries of nickel.[255]

Oxidation states	coordination number	complex	coordination geometry
0 (d^{10})	2	[Ni(1,3-diarylimidazolyidene)$_2$]	Linear
	3	[Ni(P(OC$_6$H$_4$-O-Me)$_3$)$_3$]	?
	4	[Ni(CN)$_4$]$^{4-}$	Tetrahedral
	5	[NiH(P(OEt)$_3$)$_4$]$^+$	?
I (d^9)	4	[Ni(PPh$_3$)$_3$Br]	Tetrahedral
II (d^8)	3	[Ni(NPh$_2$)$_3$]$^-$	Trigonal planar
	4[a]	[NiBr$_2$(PEt$_3$)$_2$]	Square planar
	4[a]	[NiCl$_4$]$^{2-}$	Tetrahedral
	5	[Ni(CN)$_5$]$^{3-}$	Square pyramid
	5	[NiX(trident)]$^+$	Trigonal bipyramid
	6[a]	[Ni(NH$_3$)$_6$]$^{2+}$	Octahedral
	6	NiAs	Trigonal prismatic
III (d^7)	5	[NiBr$_3$(PR)$_2$]	Trigonal bipyramid
	6	[Ni(diars)$_2$Cl$_2$]$^+$	Distorted Octahedral
IV (d^6)	6	[Ni(Bu$_2$(dtc))$_3$]$^+$	Distorted Octahedral

[a]Most common states

C.4.1. Ni(II) complexes of tridentate nitrogen donor ligands

Numerous nickel(II) complexes with tridentate amines have been described. In general, direct synthesis from nickel salts and the appropriate ligand using H_2O, MeOH, EtOH or butanol as a reaction medium have generated solid complexes.[255] The dien **164** (**Fig. 3.4**) forms octahedral bis Ni(II) complexes of the type $[Ni(dien)_2]^{2+}$ (X = Cl, ClO_4, and NO_3).[256, 257] The complexes of dien having five-membered chelate rings are more stable than the corresponding complexes of dpt **196** (**Fig. 3.15**) with six-membered chelate rings, according to the stability constant measurements.[258] In both the $[NiL_2]^{2+}$ (L = dien or dpt) complexes *mer*-isomers are predominant, and the two ligands lie in orthogonal planes. The Me_3dien **207**, alkylated derivatives of dien, also form a bis octahedral complex $[Ni(Me_3dien)_2]X_2$ (X = I or ClO_4)[259] or five coordinate Ni(II) complexes $[[NiX_2(Me_3dien)]$ (X = Cl, Br, or I).[260] The alkylated dpt ligands, Me_3dpt **208** and Medpt **209**) also form five-coordinate Ni(II) complexes, $[NiX_2(Me_3dpt)]$ (X = Cl, Br, or NCS))[259] and $[NiX_2(Medpt)]$ (X= Cl, Br, and I)[261], respectively.

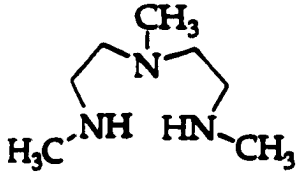

207

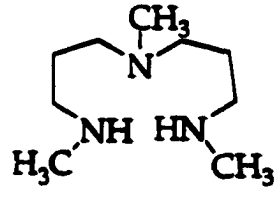

208

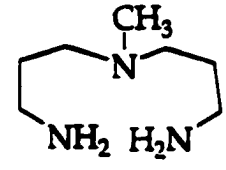

209

Figure 3.18. Tridentate nitrogen donor ligands.

Various triazacycloalkane ligands with different sizes of aliphatic chains form five- coordinate Ni(II) complexes of the type $[NiX_2L]$.[262] The mononuclear, six-coordinate Ni(II) complex containing two [9]aneN$_3$ **191** (**Fig. 3.12**), shows the octahedral geometry with three typical absorptions in the electronic spectrum.[99] A bis Ni(II) complex of tach $[Ni(tach)_2]X_2$ (tach = 1,3,5-triaminocyclohexane and X = ClO_4 and Cl) also shows octahedral geometry.[263] Bis adducts of terpy **165** (**Fig. 3.4**) $[Ni(terpy)_2]X_2$ (X = Cl, Br) can be obtained in EtOH solutions. The mono adducts can be obtained by thermal decomposition of the corresponding bis adducts, or, by reaction of excess nickel salts with ligand in water-MeOH solutions. The $[Ni(terpy)_2]X_2$ complexes are six-coordinate whereas the mono adducts $[NiLX_2]$ are five-coordinate.[264] The X-ray structure of the [dibromo(bis(6-methyl-2-pyridylmethyl)amine)], 6-methylated **44** (**Fig. 3.4**), Ni(II) complex has shown that the Ni(II) is five-coordinate in an approximate trigonal bipyramidal geometry, having the bromine atoms lying in the basal plane.[265]

C.4.2. Ni(II) complexes of hexadentate nitrogen donor ligands

Ni(II) complexes of hexadentate Schiff base ligands are known. When the ligand 5,8-dimethyl-1,12-di(2'-pyridyl)-1,2,5,8,11,12-hexaazadodeca-2,10-dien **210** (**Fig. 3.19**) is allowed to react with Ni(II), the octahedral complex $[NiL](ClO_4)_2$ is formed.[266] The ligand 1,12-di(8'-quinolyl)-2,5,8,11-tetraazadodeca-1,11-diene **211** also forms the octahedral Ni(II) complex.[267]

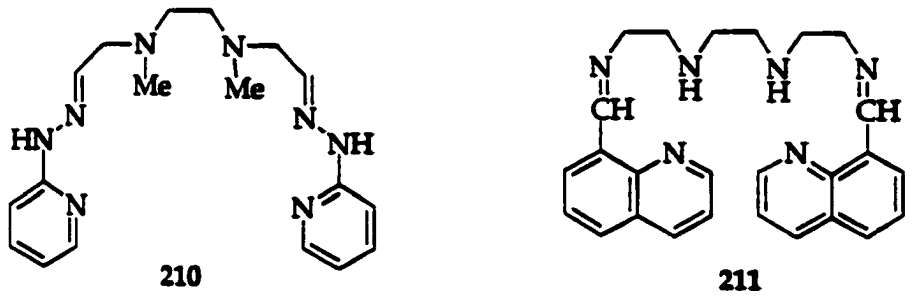

210 211

Figure 3.19. Hexadentate Schiff base ligands.

The hexadentate ligand fluoroboratotris(2-carboxaldimino-6-pyridyl)phosphine (PccBF) **212** (**Fig. 3.20**), containing three pyridyl-2-aldimine groups, forms a six-coordinate trigonal prismatic geometry with twist angle of 1.6°.[268] The structure of the Ni(II) complex with 1,1,1,-tris(2-carboxaldiminomethylpyridine)ethane **213** is almost an intermediate between two geometries of octahedral and trigonal prismatic (ϕ = 36°).[184] However, the Ni(II) complex of tris(1-(2-pyridyl)-2-azabuten-4-yl)amine **214** is nearly octahedral with twist angle of 51°.[269]

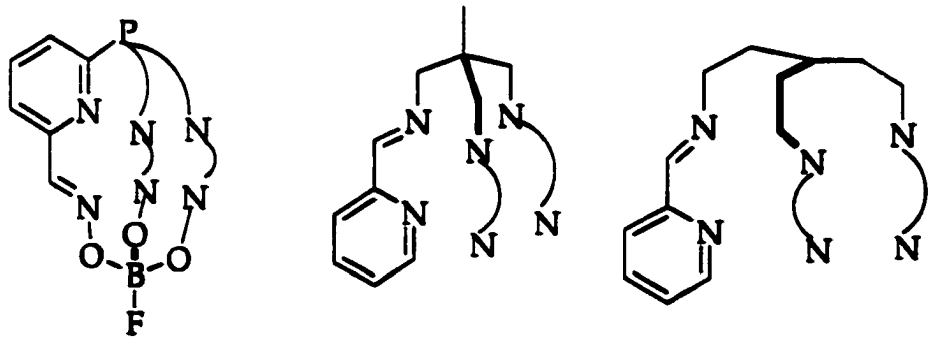

212 213 214

Figure 3.20. Hexadentate nitrogen donor ligands. For clarity reasons, only one chelating ring is correctly presented on each structure.

C.5. Coordination chemistry of Cu(II)

Table 3.8 is a list of typical compounds of the copper element. The electronic configuration of copper is $4s^2 3d^9$. Copper is a typical transition element. The ions in various oxidation states readily form complexes yielding an extensive variety of coordination chemistry. Copper can have oxidation states of copper(0) in the metal, copper(I) in cuprous compounds, copper(II) in cupric compounds, copper(III), and (IV). The oxidation states of copper(0) and copper(IV) are extremely rare, and only about 30 copper(III) compounds has been characterized.[3] The copper(I) and copper(II) oxidation states are the most abundant oxidation states. Copper(II) is more stable between these two states under normal conditions, whereas the copper(I) is less extensive and is readily oxidized to the copper(II). Copper(II) oxidation states is not only the most stable oxidation states, but also is the most fruitful in the formation of complexes.[3]

The d^9 configuration of Cu(II) make itself subject to Jahn-Teller distortion if placed in a cubic environment. In six-coordinate Cu(II) complexes, the octahedron is usually severely distorted with typical elongation along one fourfold axis, so that there is a planar array of four short Cu-L bonds and two long trans Cu-L bonds. There are many cases in which octahedral Cu(II) complexes execute a dynamic Jahn-Teller behavior, where the direction of the elongation varies rapidly.[270] Switching of the direction of the elongation with pressure change has also been observed by Simmons and coworkers.[271] The individual copper(II) ions give the effective magnetic moment of 1.73 B.M.. In practice, the experimental values at room temperature lie in the range 1.8-2.0 B.M.[272]

Table 3.8. Oxidation states and stereochemistries of copper compounds.[273]

Oxidation states	coordination number	complex	coordination geometry
1 (d^{10})	2	$[CuCl_2]^-$	Linear
	3	$[Cu(CN)_3]^{2-}$	Trigonal planar
	4	$[Cu(py)_4]^+$	Tetrahedral
II (d^9)	4	$Cs_2[CuCl_4]$	Tetrahedral
	4	$[EtNH_3]_2[CuCl_4]$	Square planar
	5	$[Cu(bipy)_2I]^+$	Trigonal bipyramid
	5	$[(Cu(DMGH)_2)_2]^a$	Square pyramid
	6	$K_2Pb[Cu(NO_2)_6]$	Octahedral
	7	$[Cu(H_2O)_2(dps)]^{2+,b}$	Pentagonal bipyramidal
III (d^8)	4	$[CuBr_2(S_2CN^tBu_2)]$	Square planar
	6	$[CuF6]^{3-}$	Octahedral
IV (d^7)	6	$[CuF6]^{2-}$	?

[a]DMGH = dimethylglyoxime. [b]dps = 2,6-diacetylpyridinebisiemicarbazone

C.5.1. Cu(II) complexes of tridentate and hexadentate nitrogen donor ligands

The most simple tridentate chelate ligand, diethylenetriamine (dien) **164** (**Fig 3.4**), forms mono and bis chelate complexes in which CuN_3 polyhedron forms an approximately planar conformation. The bis dien Cu(II) complexes $[Cu(dien)_2]Br \bullet H_2O$[274] and $[Cu(dien)_2](NO_3)_2$[275] show octahedral geometry.

However, the substituted dien ligands form a bent CuN_3 polyhedron as $[Cu(Et_4dien)(N_3)Br]$ (Et_4dien =190 (Fig. 3.11))[276], affording a trigonal bipyramid complex. The structures of five-coordinated Cu(II) complexes are described in the introduction of Chapter 1.

The most simple tridentate tripod-type ligands generally involve a restricted tetragonal elongation due to the restricted bite of the ligands.[3] The more rigid tridentate chelate ligands such as terpy 165 (Fig. 3.4) form mono and bis tridentate complexes, the distorted five-coordinate $[Cu(terpy)](NO_3)_2$[277] and the six-coordinate compressed rhombic octahedral complex $[Cu(terpy)_2](NO_3)_2$,[278], respectively.

The ligand ebtd (ebtd = *N,N,N',N*-tetrakis(2-benzimidazoylmethyl)1,2-ethane-diamine) forms a hexadentate copper(II) complex $[Cu(ebtd)](BF_4)(BF_3OEt)\bullet H_2O$[279] which has an unusual bicapped square pyramidal stereochemistry on the CuN_6 polyhedron. In general three or more nitrogen donor polydentate chelate ligands form polynuclear copper(II) complexes.[3]

C.6. Coordination chemistry of Zn(II)

Zinc shows similarities with magnesium (the main-group metal) and displays the class-a (hard acid) characteristic in complexing. On the other hand, zinc has a much greater tendency than magnesium to form covalent compounds. It forms stable complexes not only with *O*-donor ligands but also with *N*- and *S*-

donor ligands much like the transition metal elements. Znic(II) is the only important oxidation state of this element.[280]

The zinc(II) does not form π complexes with CO, NO, or olefins because of the stability of its d^{10} configuration due to its inability to provide electrons for back bonding. Compounds of the Zn(II) ions are characteristically diamagnetic and are colorless. The zinc(II) ion with its d^{10} electronic configuration shows no stereochemical preference derived from a ligand field stabilization consideration. It displays a variety of coordination numbers and geometries (Table 3.9).[280]

Table 3.9. Stereochemistry of Zn(II).[281, 280]

Coordination number	complex	coordination geometry
2	$ZnEt_2$	Linear
3	$[ZnMe(NPh_3)]_2$	Planar
4	$[Zn(NH_3)_4]^{2+}$	Tetrahedral
	$[Zn(glycinyl)_2]$	Square planar
5	$[Zn(terpy)Cl_2]$	Trigonal bipyramidal
	$[Zn(acac)_2]\bullet H_2O$	Square pyramidal
6	$[Zn(en)_3]^{2+}$	Octahedral
7	$[Zn(H_2dapp)(H_2O)_2]^{2+,a}$	Pentagonal bipyramidal
8	$[Zn(NO_3)_4]^{2-}$	Distorted dodecahedral

[a] H_2dapp = 2,6-diacetylpyridine(2′-pyridylhydrazone).

C.6.1. Zn(II) complexes of tridentate and hexadentate nitrogen donor ligands

The bis dien Zn(II) complex $[Zn(dien)_2]Br_2$ shows an approximate octahedral coordination geometry.[282] In the presence of excess ligand, the tach ligand forms only the $[Zn(tach)(OH)]^+$ complex.[283] The potentially tridentate ligands tach, [12]aneN_3, and tame **200** (**Fig. 3.16**) form the complex ions $[ZnL]^{2+}$ and show the important role of ligand rigidity in coordination.[284] The tach ligand also form the bis Zn(II) complex $[Zn(tach)_2]^{2+}$ in which the coordination geometry is best described as octahedral.[98]

The ligand 1,4-bis[bis(2-aminoethyl)aminomethyl]benzene **215** provides two tridentate moieties separated by a rigid bridge, affording a dinuclear Zn(II) complex. The tripodal ligand 1,1,1-tris(aminomethyl)ethane **216** forms $[Zn(HL)]^{3+}$, $[ZnL]^{2+}$, $[Zn(L)_2]^{2+}$ cations and the hydroxo species $[Zn(OH)L]^+$.[285] Formation of the 1:1 Zn(II) complexes of triazacycloalkane ligands occur in a single step, the stability of these complexes increases with decreasing ring sizes. The bispicam **179** (**Fig. 3.9**) forms a *fac*-isomer with Zn(II), and ^{13}C NMR spectra demonstrate that NMR techniques are of value in distinguishing between the various geometric isomers.[286]

The hexadentate ligand 1,4,7-tris(*o*-aminobenzyl)-1,4,7-triazacyclononane **217** forms a stable complex with the salt $Zn(ClO_4)_2 \cdot 6H_2O$. The ZnN_6 polyhedron is a distorted trigonal prismatic.[287] The hexadentate ligand fluroboratotris(2-carboxaldimino-6-pyridyl)phosphine (PccBF) **212** (**Fig. 3.20**) and tachimpyr **172** (**Fig. 3.6**) form Zn(II) complexes in which the coordination geometries are nearly trigonal prismatic having twist angles of 2° and 4.3° respectively.[288] However,

the structure of the Zn(II) complex with the py_3tren ligand **218** is somewhat closer to an octahedral rather than the trigonal prismatic ($\phi = 46°$), and, the structure $[Zn(py)_3tame]^{2+}$ is almost an intermediate between octahedral and trigonal prismatic having twist angle of 28°.[188]

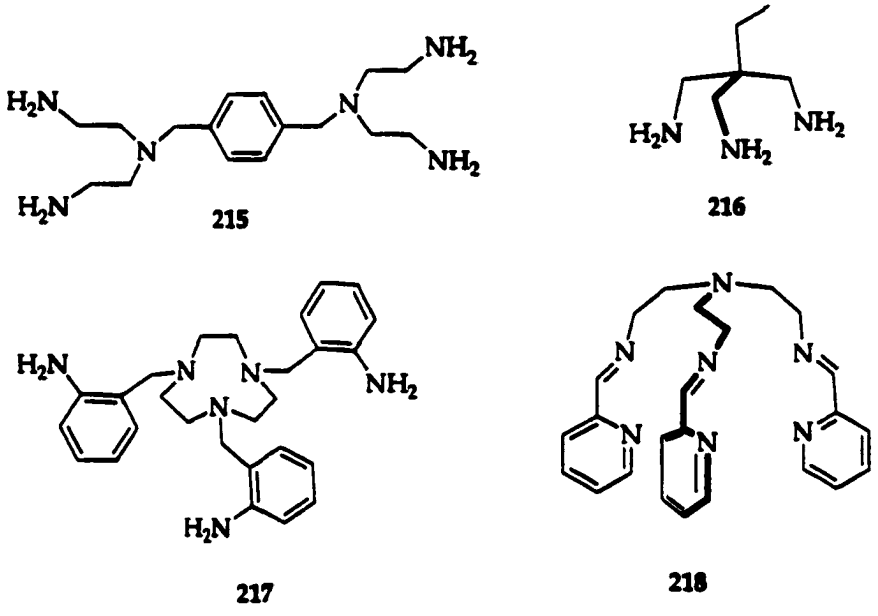

Figure 3.21. Hexadentate nitrogen donor ligands.

D. History of *cis,cis*-1,3,5-triaminocyclohexane (tach) Based Ligands and Their Metal Complexes

The synthesis of *cis,cis*-1,3,5-triaminocyclohexane (referred as tach) was first accomplished by Hassel and Lunde in poor yield via the reduction of the corresponding oxime with sodium in alcohol (**Scheme 3.1**).[289]

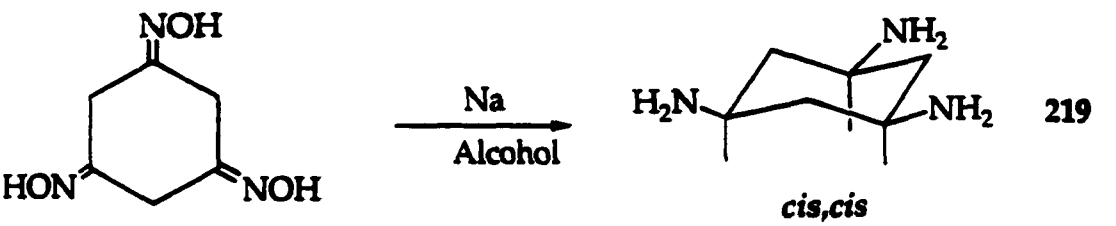

Scheme 3.1. First synthesis of tach.

Although two geometric isomers, *cis,cis* tach and *cis,trans* tach, are possible the product consisted exclusively of the isomer with all amine groups placed in equatorial positions, *cis,cis* tach, according to the X-ray data. A cyclohexyl ring flip of *cis,cis* tach, which requires 5.5 Kcal mol^{-1}, causes the three amine groups to move into a triaxial positions where the nitrogen atoms form an equilateral triangle, whose edge is about 2.5 Å.

The relatively poor preparative procedure was improved via Birch reduction reported by Lions and Martin (**Scheme 3.2**).[290] They believed that only one isomer *cis,cis* tach was obtained. The condensation of **219** with three equivalent pyridine-2-aldehyde in boiling EtOH gave tachimpyr **172** (**Fig. 3.6**) which readily reacted with an aqueous Fe(II) sulfate solution to afford an octahedral $[Fe(tachimpyr)]^{2+}$. The paramagnetic Co(II) complex (4.7 B.M.)

$[Co(tachimpyr)]^{2+}$ and the diamagnetic Co(III) complex $[Co(tachimpyr)]^{3+}$ were also prepared.

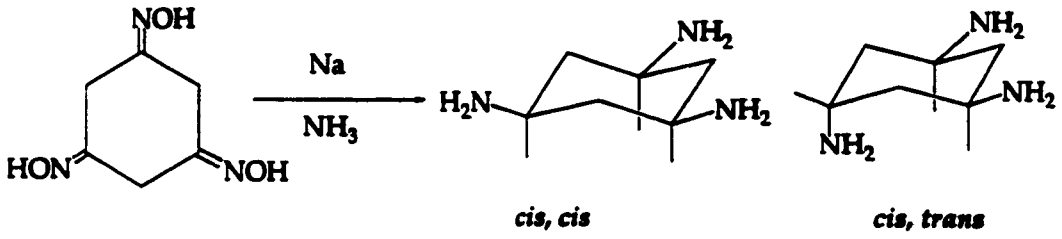

Scheme 3.2. Synthesis of tach ligand by Birch reduction.

Brauner and Schwarzenbach completed potentiometric studies of the tach complex stabilities with a number of metal ions.[291] These results indicated that the facile deprotonation of $[M(tachH)]^{3+}$ yielded $M[(tach)]^{2+}$ (M = Cu, Zn). They had thought that in the former the ligand was a bidentate and in the boat form, but in the latter the loss of a proton enable the ligand to achieve a tridentate and triaxial chair conformation. The formation of the bis complex was not studied in that report. Subsequently, Bosnich and Dwyer, again using the same preparative method for tach, reported the preparation of $[Co(tach)](NO_2)_3$ in an exceptionally high yield.[292]

Wentworth and Felten proved that Birch reduction (**Scheme 3.2**) of the trioxime of α-phloroglucinol produced both possible geometric isomers, *cis,cis* tach and *cis,trans* tach, in nearly equal proportions.[293] They also found that only *cis,cis* tach reacts with Co(III) and Rh(III) to form stable bis complexes and that the decomposition of $[Co(tach)]_2^{3+}$ led to the recovering of the free ligand. The stepwise formation constants for bis complexes $[M(tach)]_2^{n+}$ was also studied which compared favorably to that of the monomeric complexes $[M(tach)]^{n+}$,

except for those cases involving metal ions which possess Jahn-Teller instability.[263, 293] Several bis complexes $[M(tach)]_2^{n+}$ (M = Co(II), Co(III), Rh(III), Zn(II), Cd(II) and Cu(II)) were synthesized as shown in **Figure 3.22.**)

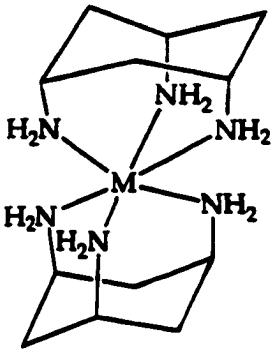

Figure 3.22. Bis complexes of tach $[M(tach)]_2^{n+}$.

Coordination geometries of the Zn(II), Co(II), and Mn(II) complexes of tachimpyr **172** were classified as a trigonal prismatic by a single crystal X-ray diffraction study.[184, 294] However, the patterns of the Ni(II) and Fe(II) compounds are different. Wentworth et al. found that the Ni(II) and Fe(II) complexes respectively have an octahedral or a near-octahedral configuration according to their electronic spectra. Ligand field calculations were used to support this conclusion. The calculations suggested that the tendency toward the octahedral configuration ought to decrease according to: low-spin Fe(II) > Ni(II) > high-spin Co(II) > high-spin Mn(II) = Zn(II). They concluded that there was a competition between two geometries.

A new method for preparation of tach starting from 1,3,5-trinitrobenzene was attempted in early 1970.[295] Starting from tach *cis,cis*-1,3,5-tris(benzylamino)cyclohexane **220** (**Fig. 3.23**), *cis,cis*-1,3,5-

tris(methylamino)cyclohexane **221** (tach-Me_3), and *cis,cis*-1,3,5-triaminocyclohexane-*N,N',N''*-triacetic acid **222** (tachta) were prepared at the same time.[296] The Co(III) complex of **222** was prepared and had an electronic spectrum exhibiting two symmetric absorption maxima at 368 (ε = 148) and 512 nm (ε = 193). The coordination geometry was described as octahedral geometry.[297]

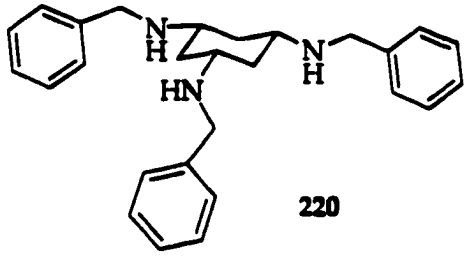

220

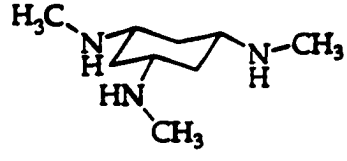

221

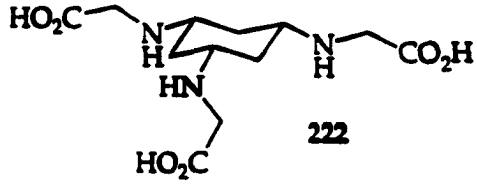

222

Figure 3.23. Tach derivatives.

Analyses of the proton, carbon, and nitrogen NMR spectra of *cis,cis*- and *cis,trans*-1, 3, 5-triaminocyclohexane were studied by Levy et al. The proton spectrum of the isomeric mixture of *cis,cis*- and *cis,trans* was assigned with a 2D COSY experiment.[298] With the 2D J spectrum results the conformation of the two isomers was analyzed. The chemical shifts and coupling constants for both isomers were also reported.[299]

The acid dissociation constants of the trihydrochloride salts of tach, and, the equilibria existing between the ligand and metal ions (M = Ni^{2+}, Cu^{2+}, or Zn^{2+}) were determined in 0.1 M KCl at 25.0° (**Table 3.10**). The electronic spectra of the bis Cu(II) complex $[Cu(tach)_2]^{2+}$ has bands at 8,790 ($\varepsilon = 6$) and 15,750 cm^{-1} ($\varepsilon = 34$).[300]

Table 3.10 Acid dissociation constants of tach and stability constants of its metal complexes in 0.1 M KCl at 25.0°.

Reaction	Constant
$LH_3^{3+} \leftrightarrows LH_2^{2+} + H^+$	$pK_{a3} = 7.17 \pm 0.01$
$LH_2^{2+} \leftrightarrows LH^+ + H^+$	$pK_{a2} = 8.66 \pm 0.01$
$LH^+ \leftrightarrows L + H^+$	$pK_{a1} = 10.16 \pm 0.01$
$Ni^{2+} + L \leftrightarrows NiL^{2+}$	$\log K_{NiL} = 9.88$
$Cu^{2+} + L \leftrightarrows CuL^{2+}$	$\log K_{CuL} = 10.55 \pm 0.03$
$CuL^{2+} + OH^- \leftrightarrows CuLOH^+$	$\log K_{CuLOH} = 6.08 \pm 0.07$
$Zn^{2+} + L \leftrightarrows ZnL^{2+}$	$\log K_{ZnL} = 6.90 \pm 0.05$
$ZnL^{2+} + OH^- \leftrightarrows ZnLOH^+$	$\log K_{ZnLOH} = 5.85 \pm 0.02$

The preparation and structural characterization of a novel octahedral Pt(IV) complex **223** (**Fig. 3. 24**) was produced from the aqueous solution reaction between tach and dichloro(bipy)platinum(II) (bipy = 2,2′-bipyridyl) by Sarneski et al.[301] This complex has two unique properties: in contrast to the normal requirement of strong oxidants to effect this conversion, the platinum(II) to platinum(IV) oxidation occurred under mild conditions (air oxidation); and deprotonation of two amine donors occurred readily in aqueous solution. Such acidity of a coordinated amine is unusual because a similar deprotonation

reaction typically occurs only when a strong base is used. It was reported that this complex contains d^6 platinum that is diamagnetic and prefers octahedral geometry. The loss of two the hydrogen ions makes two additional negative charges on the metal complex, with two chlorides as counter anions this makes a neutral metal complex.

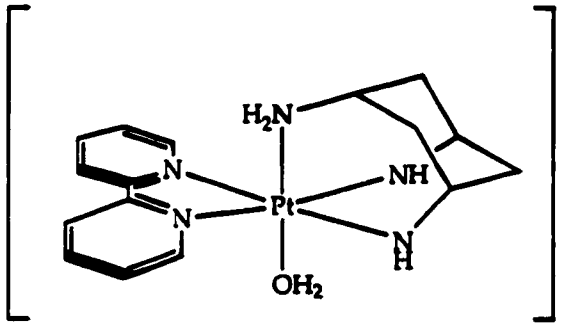

223

Figure 3. 24. $[Pt(bipy)(tach\text{-}H_2)(H_2O)]Cl_2$ complex.

The complex cation $[Cu(tach)_2]^{2+}$ was investigated in two different solids, the perchlorate and nitrate, by X-ray crystallography at room temperature and by EPR spectroscopy between 4 and 300 K. This allowed access to information about the Born-Oppenheimer energy surface of the Jahn-Teller active trigonal Cu(II) complexes with CuN_6 chromophores. The perchlorate salt of bis tach complex $[Cu(tach)_2](ClO_4)_2$ revealed that the CuN_6 octahedron has shown static tetragonal elongation at room temperature, while the nitrate salt of the bis tach complex $[Cu(tach)_2](NO_3)_2$ undergoes dynamic Jahn-Teller distortion.[302] Both complexes have a distorted octahedral stereochemistry. The X-ray structure of $[Co(tach)(dpt)]I_3$ (dpt = 1,7,-diamino-4-azahexane **196**) was obtained by Ishii et al. It shows little distortion from the octahedron.[303]

The synthesis and characterization of zinc complexes of the tach derived ligands tach **219** (**Scheme 3.1**), tach-Me_3 **221** (**Fig. 3.23**), and $C_6H_9(N{=}CHPh)_3$ **224** were reported by Vahrenkamp and coworkers.[98] Generally tach makes 1:1 complexes with ZnX_2 (X = halogen) and $Zn(OAc)_2$ and 2:1 complexes with $Zn(ClO_4)_2$ and $Zn(CF_3SO_3)_2$. Tach-Me_3 **221** did not form 2:1 complexes with zinc salts but formed 1:1 complexes with $ZnCl_2$ and $Zn(NO_3)_2$. Ligand **224** was hydrolyzed in the presence of a zinc salt. Physical properties and spectra indicated that the complexes of ZnX_2 and $Zn(NO_3)_2$ contain tetrahedral $[Zn(tach)X]^+$ cations and a free X anion, while $[Zn(tach)(OAc)_2]\bullet H_2O$ forms octahedral molecular units containing monodentate acetate ligands. According to NMR spectroscopy, the 2:1 complexes $[Zn(tach)_2](CF_3SO_3)_2$ and $[Zn(tach)_2](ClO_4)_2$ are octahedrally coordinated while $[Zn(tach\text{-}H)_2](ClO_4)_2$ is tetrahedrally coordinated.

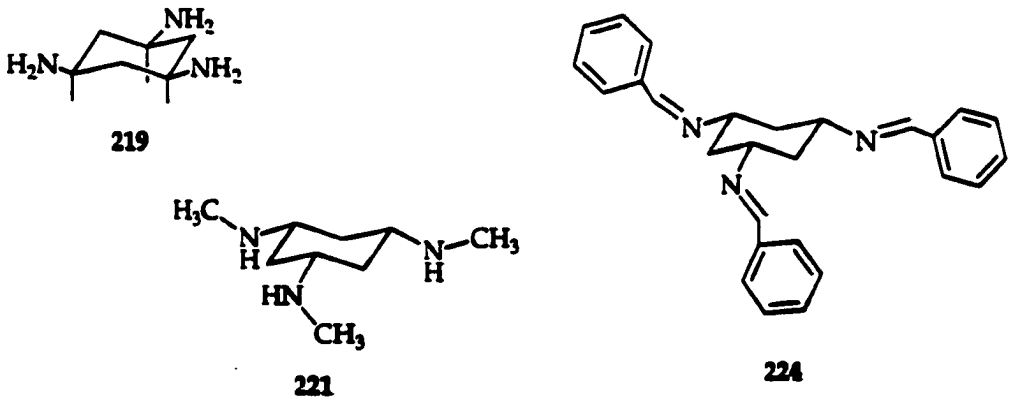

219 **221** **224**

Figure 3.25. Tach derivatives.

A new type of a potentially hexadentate ligand 1,3,5-trideoxy-1,3,5-tris((2-hydroxybenzyl)amino)-*cis*-inositol **225** (H_3thci) (**Scheme 3.3**) was prepared to

elucidate the individual binding properties of metal ions based upon their softness, size, and number of binding atoms.[304] In the complex [ReO(thci)], the amino- and phenoxo group of the two (2-hydroxybenzyl)aminato arms are coordinated in the equatorial positions of a distorted octahedron. The third (hydroxybenzyl)amino moiety does not interact with Re at all. Axial positions of the Re coordination geometry are occupied by the terminal oxygen atom and by a deprotonated hydroxyl group of the cyclohexantriol fragment.[304]

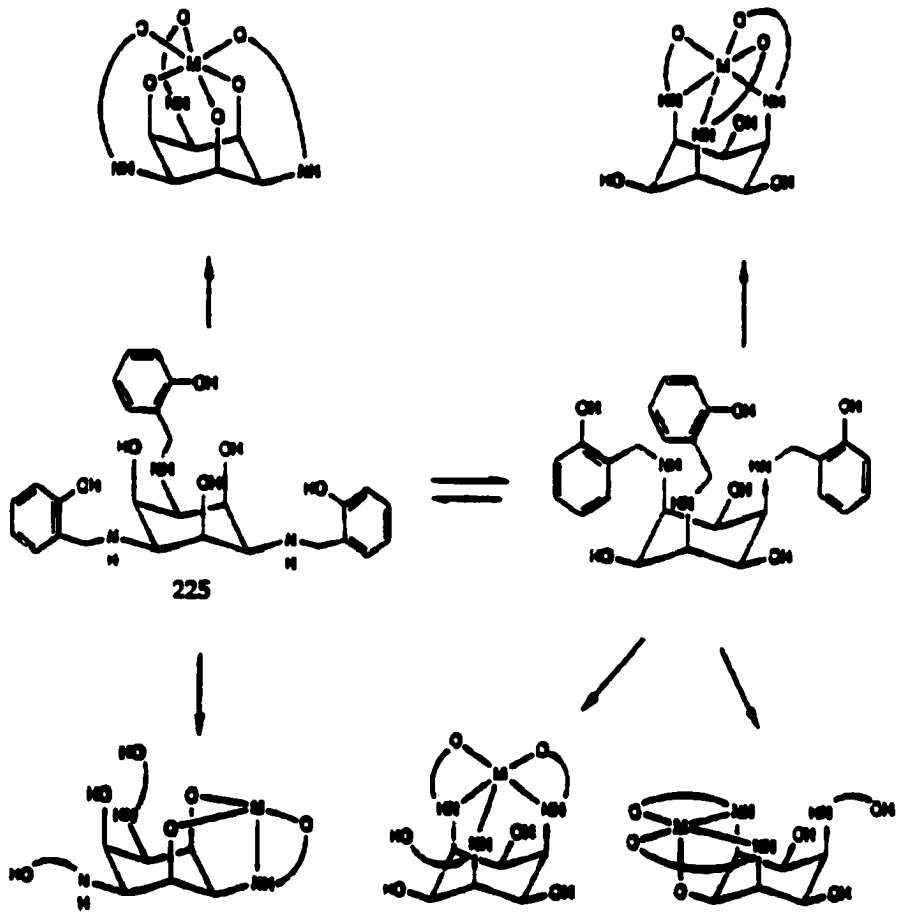

225

Scheme 3.3. Various coordination sites of 1,3,5-trideoxy-1,3,5-tris((2-hydroxybenzyl)amino)-*cis*-inositol **225**.

Bis taci **226** complexes of the type $[M(taci)_2]X_2$ (taci = 1,3,5-triamino-1,3,5-trideoxy-cis-inositol, M = Ni, Cu, Zn, X = NO_3, Br) were prepared from aqueous solutions and characterized by spectroscopic methods. Single-crystal X-ray structures of $[M(taci)_2]Br_2 \bullet 4H_2O$ (M = Ni, Cu, Zn) are isomorphous, and the metals are exclusively bound to three nitrogen donor atoms rather than oxygen donor atoms, forming a MN_6 octahedron. In the case of Cu, a significant distortion corresponding to the usual Jahn-Teller effect was observed.[305] The tdci ligand **227** coordinates to the hard metal ions (Al^{3+}, In^{3+}, Ga^{3+}, and Fe^{3+}), forming $[M(taci)_2]^{3+}$, exclusively through deprotonated alkoxo groups.[306] Here, the bulky $(CH_3)_2N$ groups impede cyclohexyl ring conversion. Formation constants show an increase of stability in the order $Al^{3+} < In^{3+} < Ga^{3+} < Fe^{3+}$. The taci shows its effectiveness for coordination to small and highly charged cations.

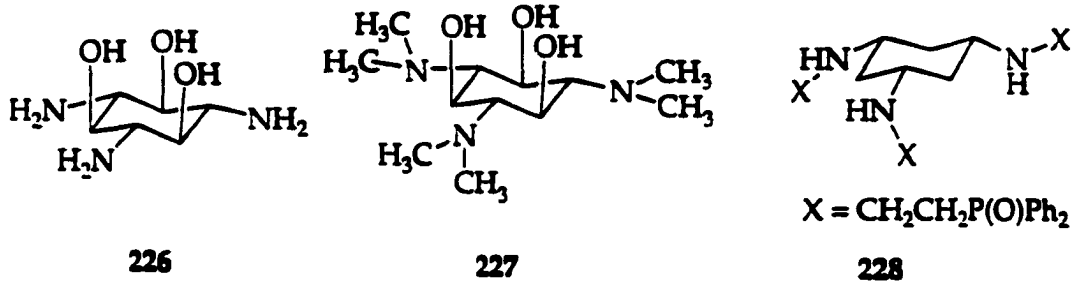

226 **227** **228**

Figure 3.26. Taci and tdci ligands.

The other tach derivative **228**, *cis,cis*-1,3,5-tri[2-(diphenylphosphinyl)ethylamino]cyclohexane, forms complexes with Cu(II) and Co(II). In the Cu(II) complex $[Cu(228)]^{2+}$ the metal ion is penta-coordinated by three nitrogen atoms and two phosphinyl groups of the ligand, affording a

square pyramidal geometry. In the Co(II) complex $[Co(228)]^{2+}$ the Co(II) ion has an octahedral geometry with all donor atoms coordinated.

Roundhill et al. reported an improved synthetic route for the tach (Scheme 3.4) and new hexadentate ligands 229, 230, and 231 designed specifically for complexation with the water-stable trivalent metal ions: Al(III), Ga(III), In(III), and Fe(III).[13, 15]

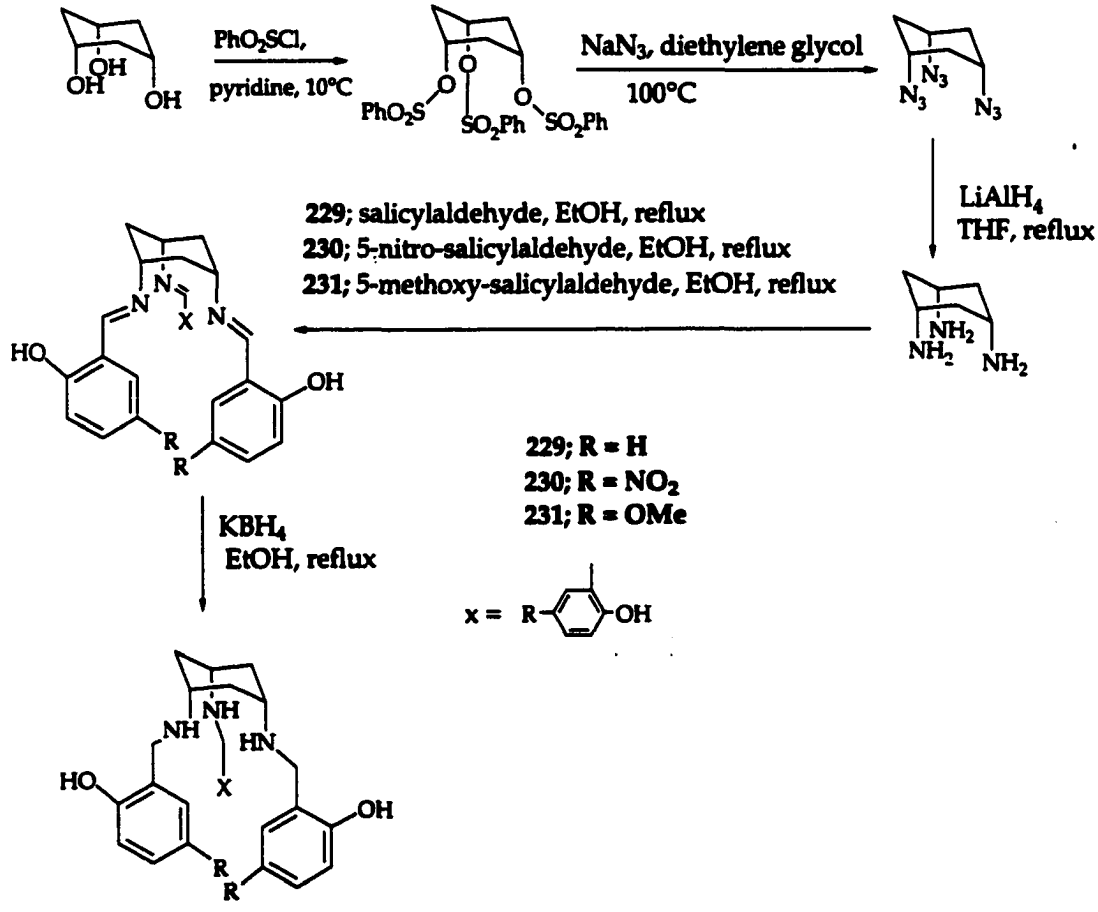

Scheme 3.4. New synthetic route for tach and new hexadentate tach derivatives.

These ligands have phenolate groups appended to the tach backbone and were among the first examples of a non-macrocyclic hexadentate ligand for complexation with trivalent metal ions.[307] The ligands were designed to yield

uncharged complexes when coordinated to these metal ions. X-ray crystal structures of [M(230)] (M = Al(III) and Fe(III)) reveal an uncharged monomeric structure in the solid state. The coordination geometries of both complexes are best described as an octahedron.[13] The magnetic moment of [Fe(230)] is 6.0 B.M., indicating a high-spin Fe(III) complex having a ligand-to-metal charge-transfer band in the 450-500 nm range. The X-ray structures of [M(229)]•xH2O (x = 3, M = Fe; x = 3.5, M = Ga or In) and [Fe(231)] show that in each case the coordination geometry about the central metal ion is octahedral with N_3O_3 ligating atoms.[308] They also reported ^1H and ^{13}C NMR spectral data (δ) for the chelators and their Ga(III) and In(III) complexes.

Fujii et al.[91] investigated the hydrolysis activity of $[Cu(tach)(H_2O)]^{2+}$ **99** (**Fig. 1.27**) for DNA with lithium 2,4-dinitrophenyl ethyl phosphate and 2,4-dinitrophenyl diethyl phosphate at pH 7.0-9.5.[309] The X-ray structure of the Zn(II) complex with tach $[Zn(tach)(OAc)](ClO_4)$ was reported. In this complex $[Zn(tach)(OAc)](ClO_4)$, Zn(II) is surrounded in a tetrahedral coordination environment by three nitrogen atoms from the tach ligand and one oxygen atom of the carbonato ligand.

By condensing tach with aldehydes, a series of triimine ligands **232**, **233**, and **234** were produced by Walton et al.[102] The complexation of the triimine ligands with copper salts cased a selective hydrolysis, producing new monoimine complexes. X-ray structures of Cu(II) complexes of **232**, **233**, and **234** all show a five-coordinate Cu(II) center, having distorted square pyramidal geometry along the longer apical Cu-N bond. From the condensation of tach with cinnamaldehyde a similar triimine ligand **235** (**Scheme 3.6**) was obtained.

Complexation of **232** with zinc chloride in the presence of $NaBPh_4$ forced the hydrolysis of two imine bonds affording a mono-imine complex. The coordination geometry of Zn(II) is highly distorted from regular tetrahedral. Complexation of **232** with zinc sulfate shows an intact ligand coordinated to zinc with a sulfate anion bound to the fourth coordination site of the zinc.[14] The coordination geometry of this Zn(II) complex with **235** is also distorted tetrahedral geometry.

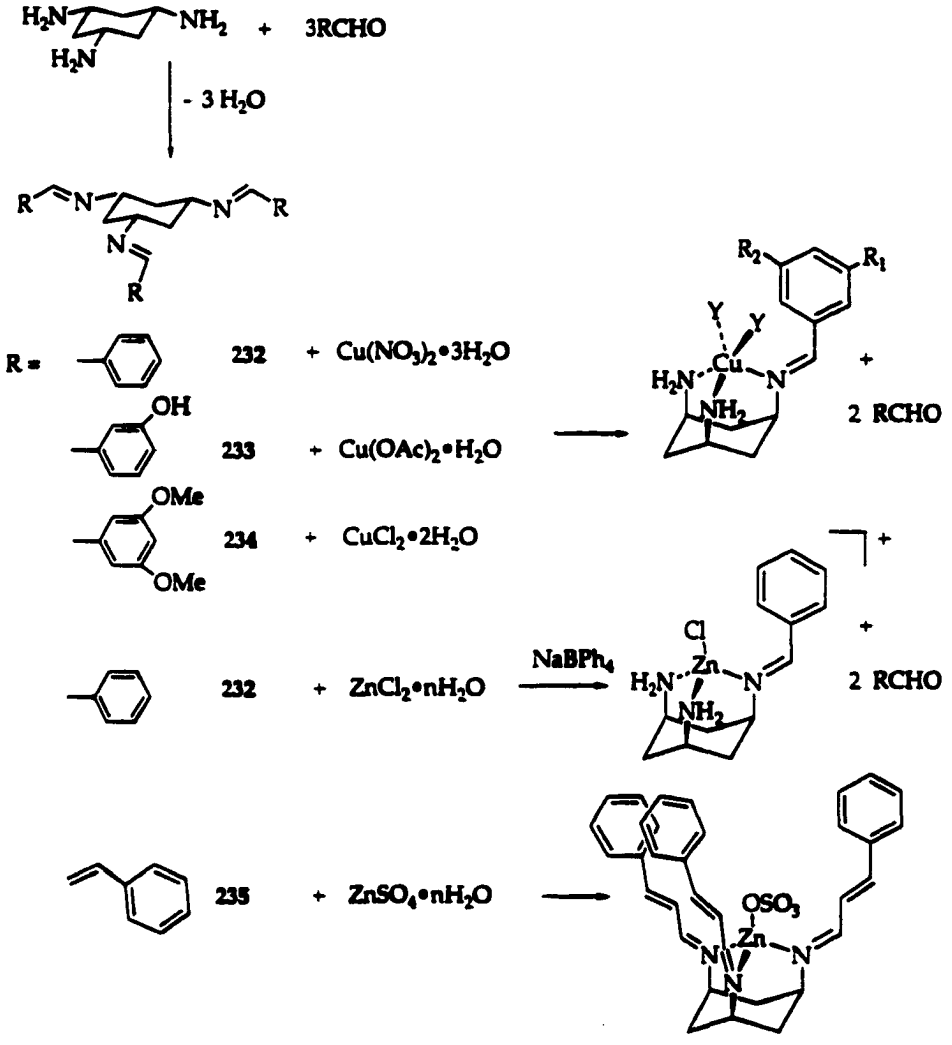

Scheme 3.5 Cu(II) complexes of *r*-1[(*Z*)-(X-benzylidene)amino-k*N*]-*c*-3,*c*-5-diamino-k^2*N*,*N*′-cyclohexane bis(Y)Cu(II)complexes (X = H **232**, 3-hydroxo **233**, and 3,5-dimethoxy **234** and Y = acetato-*k*O, nittrato-*k*O, and dichloro) and Zn(II) complex of **232** and **235**.

E. Ligand Syntheses

All ligands used in this dissertation were synthesized by Dr. Brechbiel et al. at NIH. They were kindly donated to this group for syntheses of metal complexes for the study of their biological applications and structural characteristics. Even though the author of this dissertation is not involved in the ligand syntheses at all, preparative information is provided as background to metal complex synthesis.

E.1. Synthesis of Tach

Several syntheses of *cis,cis* -1,3,5 -triaminocyclohexane (tach) have generated a mixture of products in which the *cis* product predominates.[291, 292] Roundhill et al.[13] prepared tach on a larger scale making use of previously reported Fleischer's method.[299] This has the disadvantage of requiring the potentially hazardous tri(azide) intermediate.

Brechbiel et al.[95] have developed a routine synthesis which avoids these difficulties by starting with the readily available tricarboxylic acid **236**.[310] Recognizing that amines should be directly available via a modified Curtius rearrangement, reported by Yamada, multi gram quantities of the desired *N,N',N"*-tri(benzyl) carbamate **237** were readily synthesized.[311] The CBZ group was efficiently cleaved under typical conditions (by a direct treatment of the solid with 33% HBr/HOAc) to provide the desired tach•3HBr **238** in an 82% yield from the two steps.

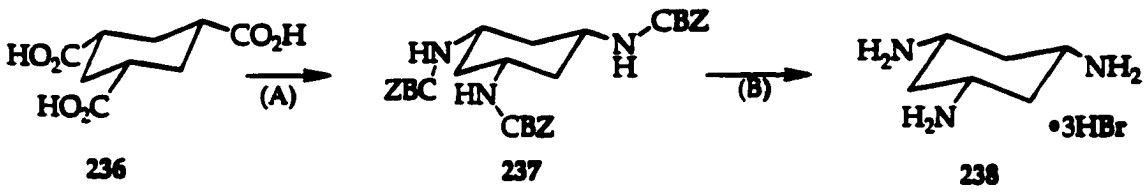

236 237 238

(A) Et_3N, DPPA, Bz-OH (B) HBr/HOAc

Scheme 3.6. Improved tach synthesis route (DPPA = diphenyl phosphoryl azide).

E.2. Synthesis of *N,N',N*-trialkylated tach

Amines of **238** were first monotosylated, allowing the resultant secondary tosylamide to be deprotonated with NaH. These anions were then quenched with the corresponding alkylsulfate (as a source of the methyl, ethyl, and propyl) to afford a functional group transformation. The tosylates were then efficiently removed with HBr in acetic anhydride proving the desired triamines, tach-Me_3•3HBr **239**, tach-Et_3•3HBr **240**, and tach-Pr_3•3HBr **241**, in a good yield.

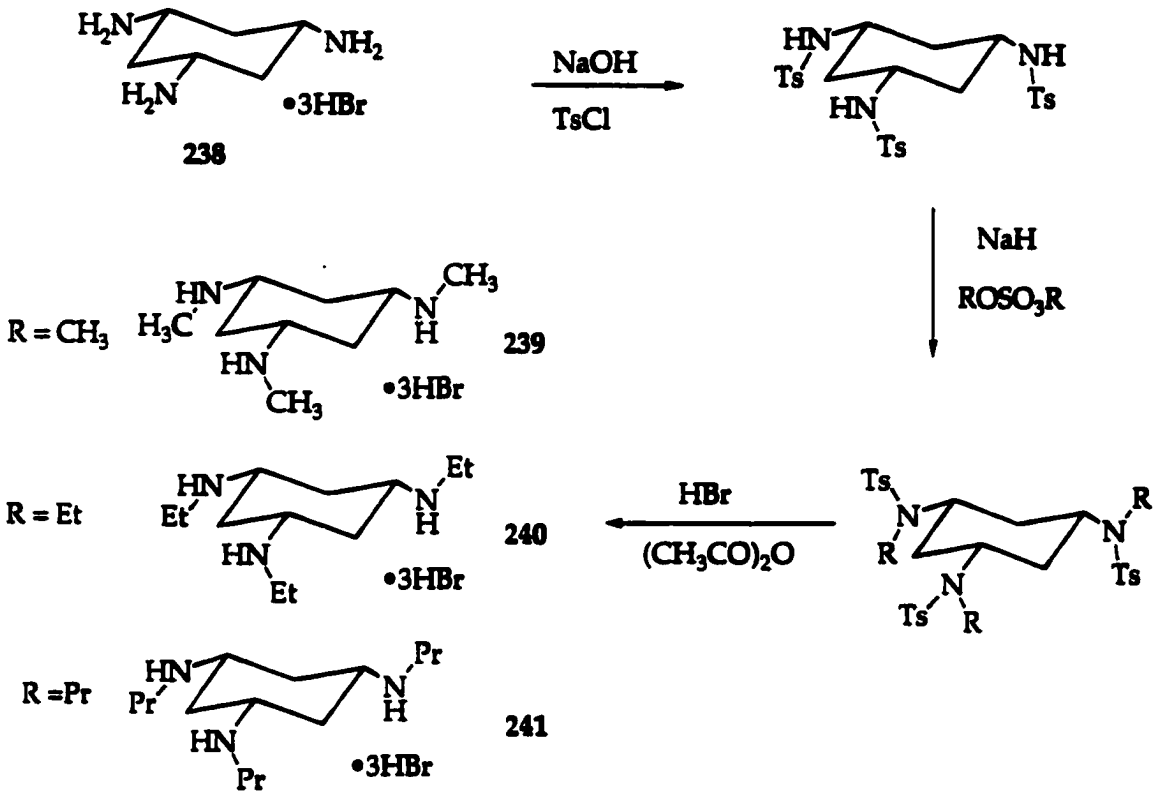

Scheme 3.7. Alkylation of tach: tach-Me_3•3HBr **239**, tach-Et_3•3HBr **240**, and tach-Pr_3•3HBr **241.**

E.3. Syntheses of tachpyr, tach-6-Mepyr, and tachquin

Syntheses of novel tachpyr and tach-6-Mepyr ligands were performed to add more binding sites to the tach framework, increasing its coordination geometry to six. This choice was prompted by the desire to form cationic metal complexes that maintained five membered chelate rings.[182] This was satisfied by the incorporation of three pyridylmethyl arms on the cyclohexyl nitrogen atoms. Tach was reacted with an appropriate aldehyde to form the respective tris(imines), which was then reduced by borohydride to provide the novel hexadentate tachpyr **242**, tach-6-Mepyr **243**, and tachquin **244** ligands.[95]

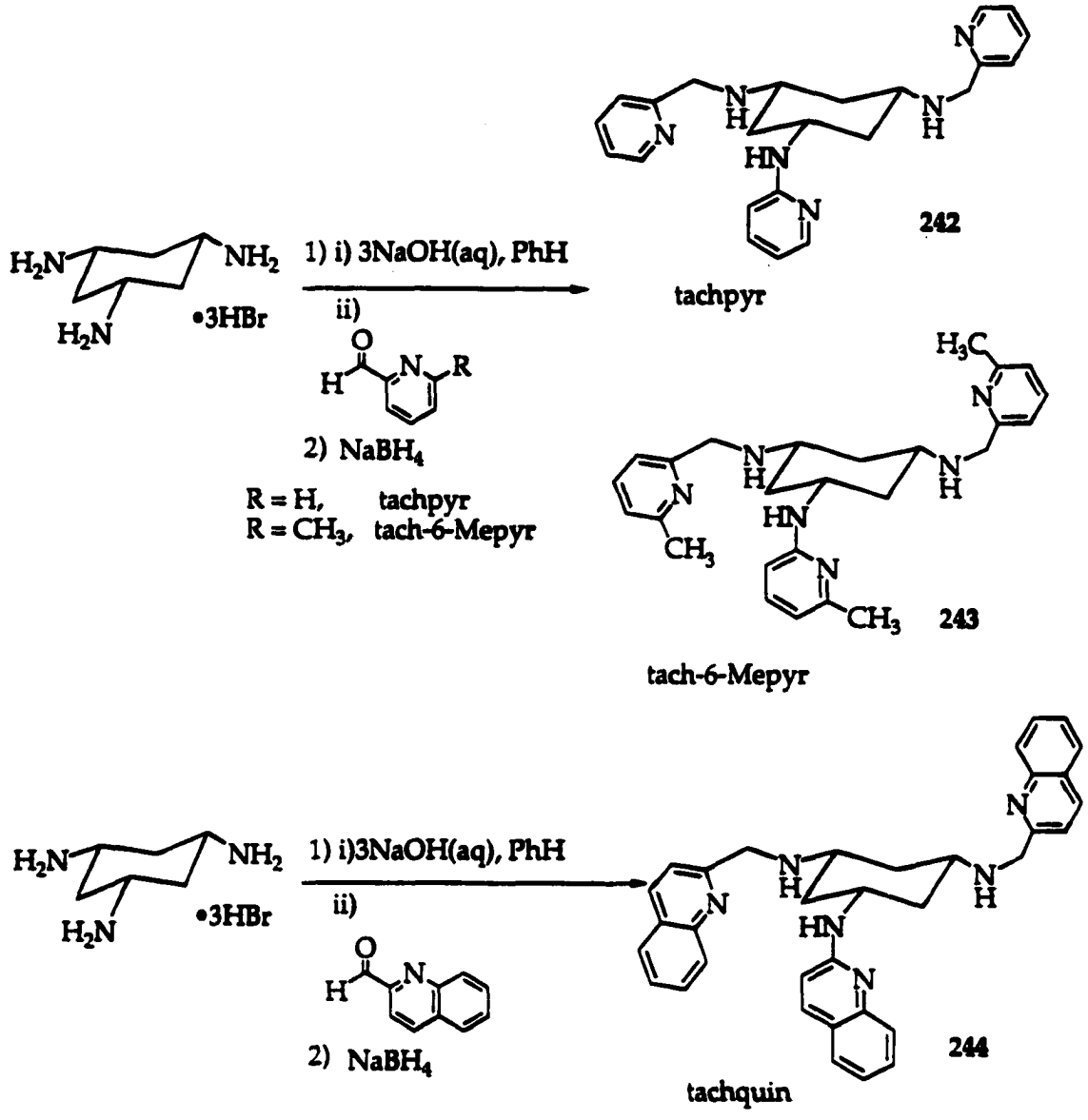

Scheme 3.8. Syntheses of novel hexadentate tach derivatives, tachpyr **242**, tach-6-Mepyr **243**, and tachquin **244**.

E.4. Syntheses of *N,N',N''*-trialkyl-tachpyr

The *N,N',N''*-trialkyl-*N,N',N''*-tris(2-methylpyridyl) derivatives of tach were prepared by the reaction of alkylated tach (tach-Me_3 **239** or tach-Et_3 **240**) with 2-chloromethylpyridine•HCl in dry DMF with excess base. Pure product was isolated by column chromatography on silica gel, affording either tach-

Me_3pyr (or (N-Me)$_3$tachpyr) **245** or tach-Et_3pyr (or (N-Et)$_3$tachpyr) **246** based upon the starting alkylated tach ligand.[1]

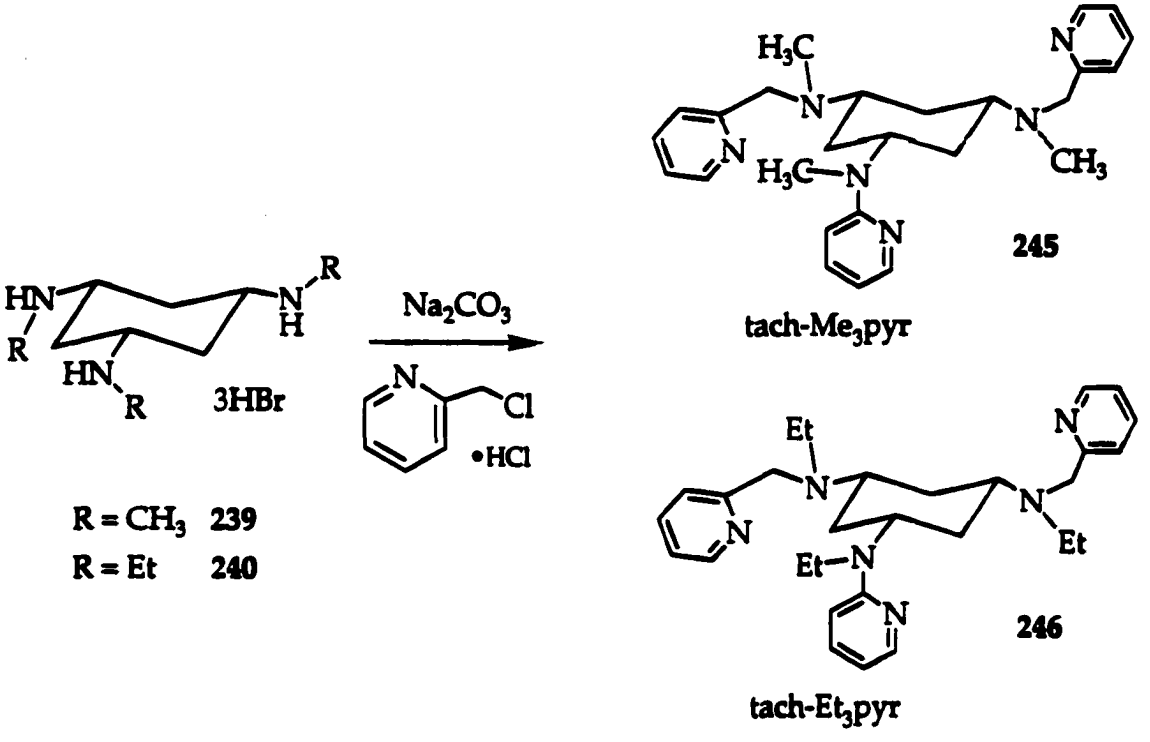

Scheme 3.9. Alkylated tachpyr derivatives; tach-Me_3pyr **245** and tach-Et_3pyr **246**.

E.5. Syntheses of tach Derivatives with 2-aminoethyl Pendant Arms

A set of hexamino tach derivatives, termed tachen ligands, was prepared by an acylation of **238** with the *p*-nitrophenyl activated ester of various amino acids. For the introduction of chiral methyl and benzyl groups, amino acids were chosen, utilizing the readily available substituents, both in nature and synthetic amino acids. The choice of the carbamate protection group afforded an easy deprotection to form the desired product. The final products were isolated from

a borane reduction of amides to afford the new hexadentate tach derivatives, tachen **247**, S,S,S-tachpn **248**, and S,S,S-tachbn **249**, respectively.[312]

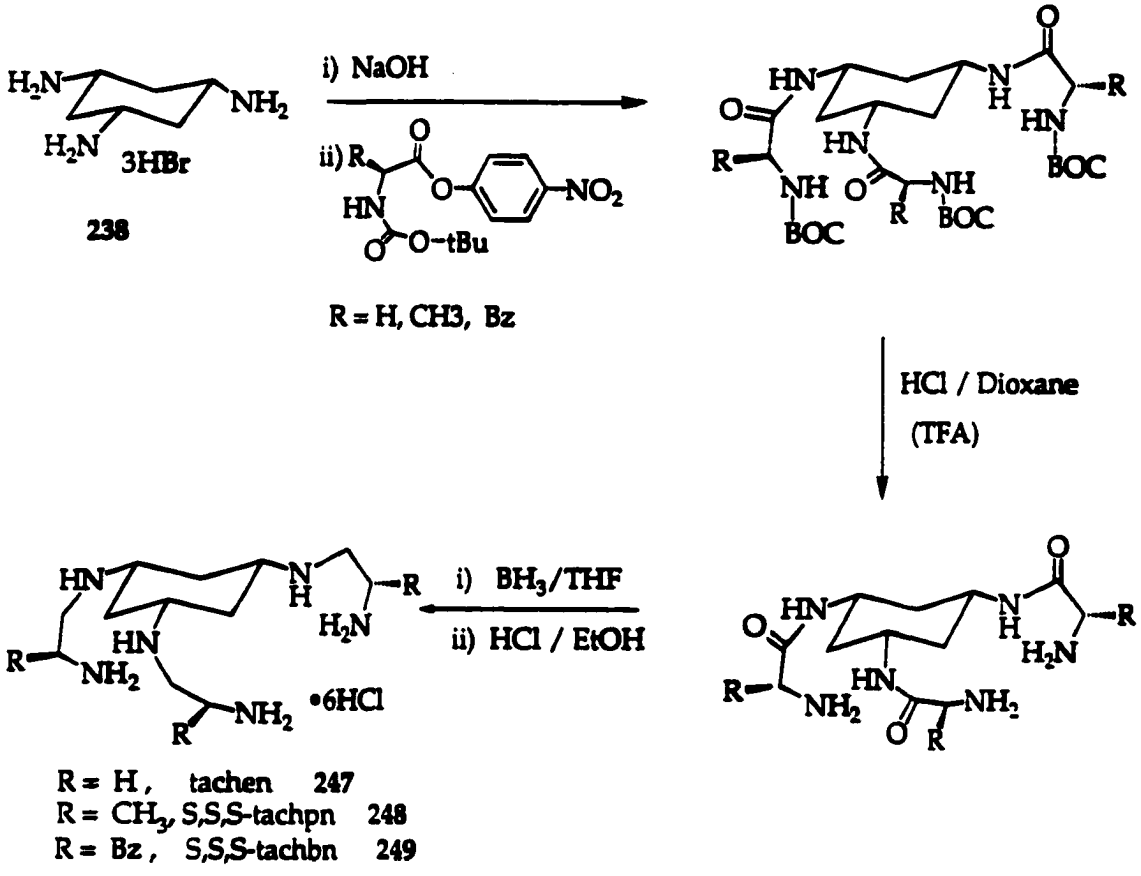

Scheme 3.10. Syntheses of new hexamine tach derivatives; tachen **247**, S,S,S-tachpn **248**, and S,S,S-tachbn **249**. BOC = -C(O)-O-^{t}Bu

F. Complexation and Characterization

The tach-R_3 derivatives and tachen derivatives are hydrochloride or hydrobromide solids. In order to provide lone pairs for coordination to metal ions the salts should be neutralized. The tachen derivatives may be neutralized by adding six equiv of NaOH(aq) (0.1 N) followed by drying under reduced pressure. The free base form of ligands may be extracted into MeOH or EtOH, filtrating out the NaCl or NaBr. More details and an improvement in methods of neutralization are described in **Chapter 1.**

All tach derivatives in the free base form generally coordinate to metal ions readily. Solutions of metal salts react with tach derivatives in alcohol or other solvents to afford complexes.

There are a number of suitable methods for characterization of metal complexes. The author was particularly involved with the application and interpretation of two methods, namely ^{1}H NMR and solution magnetic moment determination. These are discussed further. The formation of tach chelator complexes causes a distinctive change in the splitting pattern of the cyclohexyl protons in ^{1}H MNR. Upon complexation, the cyclohexyl framework undergoes a chair-chair flip that brings the coordinating arms into the axial positions. However, the diagnostic change in ^{1}H NMR spectrum is due to relative positions of cyclohexyl ring protons Ha, Hb, and Hc, which changes their coupling constants (**Scheme 3.11**). A second diagnostic change may occur due to the rigidity associated with metal complexation, which makes protons on the pendant arms diastereotopic.

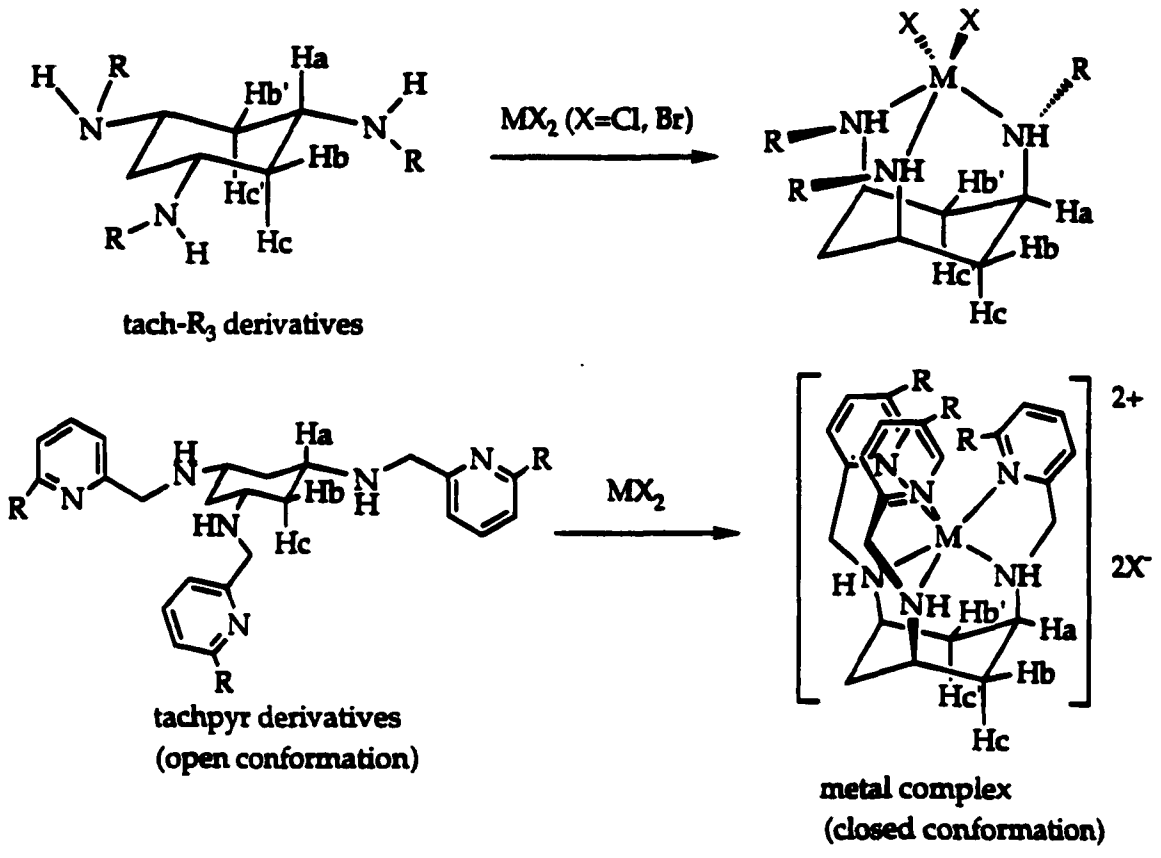

Scheme 3.11. Free ligands (open conformation) and metal complex (closed conformation).

The theoretical ^{1}H NMR splitting patterns the cyclohexyl ring protons for all uncomplexed tach derivatives are as follows: Ha is anti to Hc and gauche to Hb, splitting into a triplet of triplets; Hb is geminal to Hc and gauche to Ha, its splitting pattern should be a doublet of doublets; Hc is geminal to Hb and anti to Ha, its splitting pattern should be a doublet of doublets. Actual ^{1}H NMR spectra of free ligands, however, gives Hc as an apparent quartet, Hb as an apparent doublet, and Ha as an apparent triplet (**Fig. 3.27 (b)**). The spin system for the three protons, Ha, Hb, and Hc, on the cyclohexyl ring of free ligands derived from tach is AMM'XX' since Hb and Hb', and Hc and Hc' are diastereotopic to each other.

The theoretical ^{1}H NMR splitting patterns of the cyclohexyl ring protons for metal complexes can be characterized as follows: Ha is gauche to Hc and Hb, thus it should split into a triplet of triplets; Hb is geminal to Hc and gauche to Ha, its splitting pattern should be a doublet of doublets; Hc is geminal to Hb and anti to Ha, and its splitting pattern should be a doublet of doublets. However the actual ^{1}H NMR spectra of metal complexes give Hc as an apparent doublet, Hb as an apparent doublet, and Ha as an apparent singlet (Fig. 3.27 (a)).

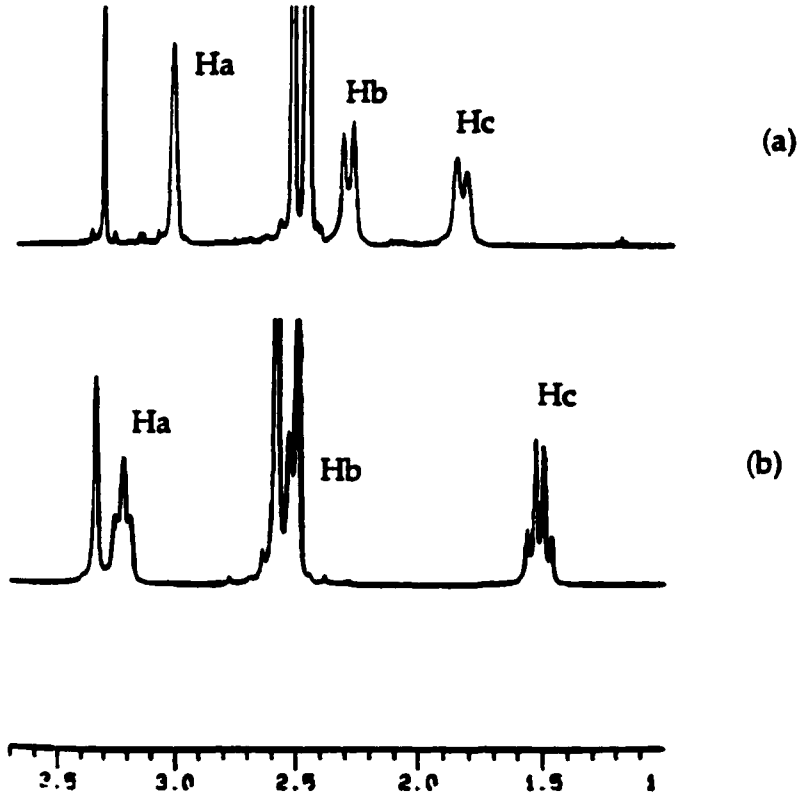

Figure 3.27. ^{1}H NMR spectra showing a splitting pattern change of cyclohexyl protons: (a) $[Zn(tach\text{-}Me_3)]Cl_2$, (b) $tach\text{-}Me_3 \bullet 3HBr$ ligand.

In addition to a change in the splitting pattern of the cyclohexyl ring protons, that obtains for all tach chelators, derivatives of the tachpyr family have another distinctive spectral change upon complexation with metal ions.

Tachpyr-derived ligands have *N*-pendant arms composed of a 2-pyridyl group connected to a cyclohexyl nitrogen via a methylene unit. These methylene protons are chemically and magnetically equivalent before coordination, resulting in a spin system of an A_2. Upon coordination, the nitrogen atoms on the cyclohexyl ring become chiral centers, thus the two methylene protons are now diastereotopic to each other (**Fig. 3.28**).[313, 287] Taking into account coupling to the proton of the cyclohexyl amine, the spin system of the connecting CH_2 and associated NH_A becomes an AXY or AMX (H_A is the amine hydrogen) in the metal complex.

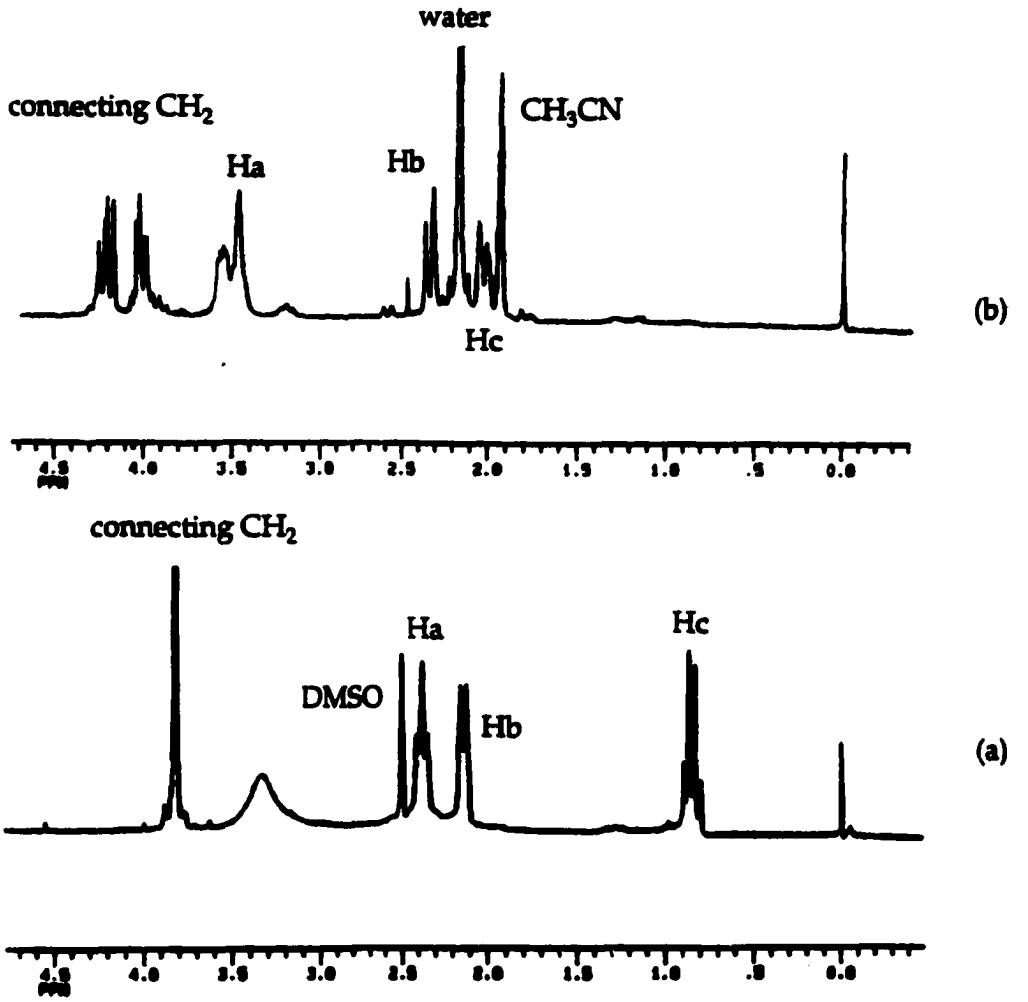

Figure 3.28. ^1H NMR spectra showing a splitting pattern change of methylene protons: (a) tachpyr ligand, (b) $[Cd(tachpyr)](ClO_4)_2$.

A second method that has been effectively applied in this work is the measurement of magnetic moment. A paramagnetic state is generally observed in metal complexes that contain an odd number of electrons or a high-spin state. In this case, ^1H NMR spectroscopy may not be applicable, but determination of magnetic moment may be. A method developed by D. Evans[314] is an indirect NMR study that allows determination of the magnetic moment of the paramagnetic metal complex and its number of unpaired electrons. The presence

of the paramagnetic species will cause a change in the ^1H NMR chemical shift of a non-reactive substance, termed an indicator species. For example, the complex may be dissolved in deuterated solvent and t-butanol used as indicator. A sample of known metal complex concentration is prepared in a 3% t-butanol in deuterated solvent. A sealed capillary tube filled with a standard t-butanol is inserted into the NMR tube with the sample surrounding it. t-Butanol in a sealed capillary tube gives a characteristic indicator peak, a singlet for the three equivalent methyl groups, isolated from t-butanol in deuterated solvent of the metal complex. The observed shift of this peak in Hertz, $\Delta\nu$, will be used to determine the magnetic moment, μ_{eff}, of the complex by using equation (2). The factor Q in (2) depends on the type of magnet used in the NMR spectrometer (Q = 1 for an electromagnet and Q = 2 for a superconducting magnet.

$$\chi_m = \frac{477 \times \Delta\nu}{Q \times \upsilon_I \times \text{concentration}} \qquad (1)$$

$$\mu_{eff} = 2.48 \times \sqrt{\chi_m \times T} \qquad (2)$$

$$N = -1 + \sqrt{\mu_{eff}^2 + 1} \qquad (3)$$

The molar susceptibility, χ_m, is positive if the complex is paramagnetic and υ_I is the frequency in hertz of the radio waves generated by the NMR instrument. T is the temperature in degrees Kelvin, and concentration is the concentration of the paramagnetic sample in mol/L. From the magnetic moment, the number of

unpaired electrons, N, can be calculated by equation (3). Calculation of N may be used to infer the electronic configuration of a metal complex.

Experimental Section

A. Materials and Methods

All the materials listed below were of a research grade or a spectroquality grade in the highest purity available and were generally used without further purification except Et_2O. Et_2O was distilled from Na and used immediately.

Anhydrous grade DMF, MeOH and CH_3CN, and the salts $Zn(ClO_4)_2 \bullet 6H_2O$, $Cd(ClO_4)_2 \bullet 6H_2O$, $Hg(ClO_4)_2$, $Cu(ClO_4)_2 \bullet 6H_2O$, $NiCl_2 \bullet H_2O$, $Ni(ClO_4)_2 \bullet 6H_2O$, $Ni(NO_3)_2 \bullet 6H_2O$, $Co(NO_3)_2 \bullet 6H_2O$, $Co(ClO_4)_2 \bullet 6H_2O$, $Mn(ClO_4)_2 \bullet 6H_2O$, and t-butanol were obtained from Aldrich. Anhydrous grade EtOH was obtained from Pharmco. DMSO-d_6, and CH_3CN-d_3 were obtained from Cambridge Isotope Laboratories. CH_2Cl_2 and $CHCl_3$ were obtained from EM Science.

All of the UV-Vis electronic spectra were measured using a Cary 5 Varian UV-vis spectrometer with 1 mL or 3 mL quartz cuvettes (1cm path-length). All of the vibrational spectra were measured using a Nicolet 205 FT-IR spectrometer with a KBr pellet. Fast atom bombardment (FAB-MS) mass spectra were taken on an Extrel 4000 at NIH. ^1H and ^{13}C NMR spectra were obtained using a Bruker AM360 instrument. Magnetic moment was measure by using a Bruker AM360 instrument ($Q = 2$ and $v_1 = 360 \times 10^6$), DMSO-d_6 as a solvent, and t-butanol as an indicator. Elemental analysis was performed by Atlantic Microlabs (Atlanta, Georgia) or by Galbraith Laboratories (Knoxville, Tennessee).

B. Preparation of Metal Complexes

B.1. Zn(II) complexes of hexadentate tach derivatives

Preparation of [Zn(tachpyr)]$(ClO_4)_2 \bullet CH_3OH$ (250). To a solution of $Zn(ClO_4)_2 \bullet 6H_2O$ (0.0906 g, 2.43×10^{-4} mol) in anhydrous EtOH (3 mL) was added a pale yellow solution of tachpyr (0.0986 g, 2.45×10^{-4} mol) in anhydrous MeOH (3 mL) affording a pale yellow precipitate. After standing for 2 h, the precipitate was isolated by decanting the supernatant and washed with Et_2O and MeOH. The product was dried under reduced pressure affording a white solid in 22.0% yield (0.0370 g, 5.28×10^{-5} mol). Single crystals suitable for X-ray crystallography were grown by Et_2O diffusion into a CH_3CN solution of the metal complex. Anal. Calcd for $C_{24}H_{30}Cl_2N_6O_8Zn \bullet CH_3OH$: C, 42.97; H, 4.90; N, 12.03. Found: C, 42.91; H, 4.67; N, 12.19. ^1H NMR (DMSO-d_6, 25° C): δ 8.11, 7.81, 7.63, 7.50 (t, d, d, t, 4H, ^3J = 7.8 and 5.7 Hz, $C_5\underline{H}_4N$); 4.71 (dd, $\underline{A}XY$, 1H, ^3J = 8.5 and 8.4 Hz, N$\underline{H}$-CH_2); 4.14 (m (two dd), A$\underline{XY}$, 2H, NH-C$\underline{H}_2$-py); 3.26 (br s, $\underline{A}$MM'XX', 1H, cyclohexyl methine H's); 2.34 (br d, A$\underline{MM'}$XX', 1H, equatorial cyclohexyl methylene H's, diastereotopic), 1.90 (br d, AMM'$\underline{XX'}$, 1H, axial cyclohexyl methylene H's, diastereotopic). MS (FAB/glycerol): 465 (M - 2 ClO_4^-).

Preparation of [Zn(tach-Me_3pyr)]$(ClO_4)_2$ (251). To a solution of $Zn(ClO_4)_2 \bullet 6\ H_2O$ (0.0325 g, 8.70×10^{-5} mol) in EtOH (2 mL) was added a yellow solution of tach-Me_3pyr (0.0387 g, 8.70×10^{-5} mol) in MeOH (3 mL) affording a light yellow precipitate immediately. After standing for 1 hour, the precipitate was isolated, washed with EtOH, and dried under reduced pressure affording a white solid

the in 56.6% yield (0.0403 g, 4.60×10^{-5} mol). Single crystals suitable for X-ray crystallography were obtained by Et_2O diffusion into a CH_3CN solution of the complex. Anal. Calcd for $C_{27}H_{36}Cl_2N_6O_8Zn$: C, 45.75; H, 5.20; N, 11.65. Found: C, 45.68; H, 5.20; N, 11.65. ^1H NMR (DMSO-d_6, 25° C): δ 8.16, 7.63 (t, m, 4H, $C_5\underline{H}_4N$); 4.97, 3.68 (d, d, 2H, $N(CH_3)$-$C\underline{H}_2$-Py); 3.13 (br s, $\underline{A}MM'XX'$, 1H, cyclohexyl methine H's); 2.96 (br d, $A\underline{MM'}XX'$, 1H, equatorial cyclohexyl methylene H's, diastereotopic), 2.15 (br d, $AMM'\underline{XX'}$, 1H, axial cyclohexyl methylene H's, diastereotopic); 1.95 (s, 3H,$N(C\underline{H}_3)$-CH_2-Py). MS (FAB/glycerol): 507 (M - 2 ClO_4^-).

Preparation of [Zn(tach-Et$_3$pyr)](ClO$_4$)$_2$ (252). To a solution of $Zn(ClO_4)_2 \bullet 6H_2O$ (0.0612 g, 1.64×10^{-4} mol) in MeOH (3 mL) was added a yellow solution of tach-Et_3pyr (0.0798 g, 1.64×10^{-4} mol) in MeOH (2 mL) affording a yellowish brown precipitate immediately. Et_2O (12 mL) was added into mixture to form more precipitates that were isolated, washed with MeOH, and dissolved in CH_3CN and filtered. This was dried under reduced pressure affording a white solid in 40.7% yield (0.0574 g, 7.64×10^{-5} mol). Colorless crystals were obtained by Et_2O diffusion into a CH_3CN solution of the complex. Anal. Calcd for $C_{30}H_{42}Cl_2N_6O_8Zn$: C, 47.98; H, 5.64; N, 11.19. Found: C, 47.63; H, 5.91; N, 11.12. ^1H NMR (CH_3CN-d_3, 25°C): δ 8.10, 8.06, 7.57, 7.53 (d, t, d, t, 4H, $C_5\underline{H}_4N$); 4.55, 4.09 (d, d, 2H, $N(CH_2CH_3)$-$C\underline{H}_2$-Pyr); 3.39 (br s, $\underline{A}MM'XX'$, 1H, cyclohexyl methine H's)); 2.69 (br d, $A\underline{MM'}XX'$, 1H, equatorial cyclohexyl methylene H's, diastereotopic), 2.05 (br d, $AMM'\underline{XX'}$, 1H, axial cyclohexyl methylene H's, diastereotopic); 2.55, 1.97 (m, m, 2H, $N(C\underline{H}_2CH_3)$-CH_2, diastereotopic); 0.87 (dd, 3H, $N(CH_2C\underline{H}_3)$). ^{13}C

NMR (CH_3CN-d_3, 25°C): δ 161.18, 152.83, 146.02, 131.17, 130.52 ($\underline{C}_5H_4N$); 59.47 ($N(CH_2CH_3)$-$\underline{C}H_2$-Py); 57.11 (1C, cyclohexyl methine C's); 53.43 ($N(\underline{C}H_2CH_3)$-CH_2-py); 32.70 (cyclohexyl methylene C's); 9.98 ($N(CH_2\underline{C}H_3)$-CH_2-py). MS (FAB/glycerol/DMSO): 549 (M - 2 ClO_4^-).

Preparation of [Zn(tach-6-Mepyr)]$(ClO_4)_2 \bullet CH_3OH$ (253). To a solution of $Zn(ClO_4)_2 \bullet 6H_2O$ (0.0493 g, 1.22×10^{-4} mol) in EtOH (4 mL) was added a pale yellow solution of tach-6-Mepyr (0.0540 g, 1.22×10^{-4} mol) in MeOH (4 mL) affording a white precipitate immediately. After standing for 1 hour, the precipitate was isolated and washed with Et_2O and MeOH. This was dried under reduced pressure affording a white solid in 60.3% yield (0.0569 g, 8.05×10^{-5} mol). Single crystals suitable for X-ray crystallography were obtained by Et_2O diffusion into a CH_3CN solution of the complex. Anal. Calcd for $C_{27}H_{36}Cl_2N_6O_8Zn \bullet H_2O$: C, 44.61; H, 5.27; N, 11.56. Found: C, 44.58; H, 5.41; N, 11.74. ^1H NMR (DMSO-d_6, 25° C): δ 7.89, 7.36, 7.34 (t, d, d, 3H, $(CH_3)C_5\underline{H}_3N$); 4.22, 4.05 (d, d, 2H, NH-$C\underline{H}_2$-MePy); 3.07 (br s, $\underline{A}MM'XX'$, 1H, cyclohexyl methine H's); 2.15 (s, 3H, $(C\underline{H}_3)C_5H_3N$) 2.13 (br d, $A\underline{MM'}XX'$, 1H, equatorial cyclohexyl methylene H's, diastereotopic), 1.82 (br d, $AMM'\underline{XX'}$, 1H, axial cyclohexyl methylene H's, diastereotopic). MS (FAB/glycerol): 507 (M - 2 ClO_4^-).

Preparation of [Zn(tachquin)]$(ClO_4)_2 \bullet H_2O$ (254) To a colorless solution of $Zn(ClO_4)_2 \bullet 6H_2O$ (0.0340 g, 9.11×10^{-5} mol) in anhydrous MeOH (2 mL) was added a brown solution of tachquin (0.0986 g, 9.11×10^{-5} mol) in anhydrous MeOH (2 mL) affording a pale yellow precipitate. Et_2O (12 mL) was added to

form more precipitates, which were isolated by decanting supernatant and dried under reduced pressure giving a pale yellow solid. This was dissolved in CH_3CN, and Et_2O was diffused into it giving a yellow precipitate and colorless prisms. The crystals were isolated, washed with Et_2O, and dried under reduced pressure affording a white solid in 39.0% yield (0.0290 g, 3.55×10^{-5} mol). Single crystals suitable for X-ray crystallography were obtained by Et_2O diffusion into a CH_3CN solution of the complex. Anal. Calcd for $C_{36}H_{36}Cl_2N_6O_8Zn \bullet 2H_2O$: C, 50.69; H, 4.73; N, 9.85. Found: C, 50.87; H, 4.82; N, 9.69. ^{1}H NMR (DMSO-d_6, 25° C): δ 8.59, 7.99, 7.65, 7.54, 7.42, 7.15 (d, d, d, d, t, t, 6H, ^{3}J = 8.2 and 7.2 Hz, $C_5\underline{H}_6N$); 4.63 (br s, AXY, 1H, N$\underline{H}$-CH_2); 4.38 (br s, A$\underline{XY}$, 2H, NH-C$\underline{H}_2$-py); 3.20 (br s, AMM'XX', 1H, cyclohexyl methine H's); 2.29 (br d, A$\underline{MM'}$XX', 1H, equatorial cyclohexyl methylene H's, diastereotopic), 1.87 (br d, AMM'$\underline{XX'}$, 1H, axial cyclohexyl methylene H's, diastereotopic).

Preparation of [Zn(tachpn)]$(ClO_4)_2$(255). To a solution of $Zn(ClO_4)_2 \bullet 6H_2O$ (0.0227 g, 6.09×10^{-5} mol) in anhydrous EtOH (2 mL) was added a colorless solution of S,S,S-tachpn (0.0316 g, 6.09×10^{-5} mol) in anhydrous EtOH (5 mL) affording a white precipitate. This was isolated and dried under reduced pressure giving a white solid. The solid was taken up to CH_3CN, and Et_2O was slowly diffused into a CH_3CN solution of the crude product at 5° C, affording small colorless prisms. These were isolated and dried under reduced pressure affording a white solid in 54.3% yield (0.0186 g, 3.29×10^{-5} mol). Anal. Calcd for $C_{15}H_{36}Cl_2N_6O_8Zn \bullet H_2O$: C, 30.91; H, 6.57; N, 14.42. Found: C, 31.13; H, 6.56; N, 13.94. ^{1}H NMR (CH_3CN-d_3, 25° C): δ 3.19 (br s, AMM'XX', 1H, cyclohexyl

methine H's); 3.01(br d, 1H, $NH_2(C\underline{H})$-CH_3); 2.60 (t, 1H, NH-$C\underline{H}_2$-(CH)NH_2CH_3, bridging methylene diastereotopic); 2.57 (t, 1H, NH-$C\underline{H}_2$-(CH)NH_2CH_3, bridging methylene diastereotopic); 2.15 (br d, A$\underline{MM'}$XX', 1H, equatorial cyclohexyl methylene H's, diastereotopic), 1.78 (br d, AMM'$\underline{XX'}$, 1H, axial cyclohexyl methylene H's, diastereotopic); 1.15 (d, 3H, $NH_2(CH)$-$C\underline{H}_3$). ^{13}C NMR (CH_3CN-d_3, 25°C): δ 70.53 (1C, cyclohexyl methine C's); 69.92 (1C, $NH_2(\underline{C}H)$-CH_3); 66.09 (1C, NH-$\underline{C}H_2$-(CH)NH_2CH_3); 50.38 (1C, cyclohexyl methylene C's); 41.83 (1C, $NH_2(CH)$-$\underline{C}H_3$). MS (FAB/m-b): 465 ($M - ClO_4^-$).

Preparation of [Zn(tachbn)](Cl)(ClO_4)•1/2H_2O (256). To a solution of $Zn(ClO_4)_2$•6H_2O (0.0235 g, 6.30 x 10^{-5} mol) in anhydrous MeOH (2 mL) was added a colorless solution of S,S,S-tachbn (0.0470 g, 6.30 x 10^{-5} mol) in anhydrous MeOH (5 mL) affording a colorless solution. White precipitates were formed by adding Et_2O (10 mL) into the reaction mixture, isolated, and dried under reduced pressure giving a white solid. The solid was taken up into CH_3CN (5 mL), filtered, and Et_2O vapor was diffused into filtrate giving colorless prisms suitable for X-ray crystallography. The crystals were isolated and dried under reduced pressure affording a white solid in 49.3% yield (0.0246 g, 3.11x 10^{-5} mol). Anal. Calcd for $C_{33}H_{48}Cl_2N_6O_8Zn$•NaCl•H_2O; C, 49.29; H, 6.27; N, 10.45. Found: C, 49.24; H, 5.98; N, 10.30. ^1H NMR (DMSO-d_6, 25° C): δ 7.34, 7.24, 7.19(t, d, d, AA'MXX', 2H, 1H, 2H,CH_2-$C_6\underline{H}_5$); 3.78 (br t, 1H, $NH_2(C\underline{H})(CH_2)$-$CH_2$-Ph); 3.07 (br s, $\underline{A}$MM'XX', 1H, cyclohexyl methine H's); 2.76 (m, 2H, NH_2-(CH)($C\underline{H}_2$)-CH_2-Ph, bridging methylene H's, diastereotopic); 2.66 (br s, 2H, NH_2-(CH)(CH_2)-$C\underline{H}_2$-Ph); 2.05 (br d, A$\underline{MM'}$XX', 1H, equatorial cyclohexyl methylene H's, diastereotopic);

1.69 (br d, AMM'XX', 1H, axial cyclohexyl methylene H's, diastereotopic). ^{13}C NMR (DMSO-d_6, 25° C): δ 138.02, 129.04, 128.59, 126.45 (1C, 2C, 2C, 1C, CH_2-$\underline{C}_6H_5$); 52.04 (1C, cyclohexyl methine C's); 50.01 (1C, NH_2-($\underline{C}$H)(CH_2)-CH_2-Ph); 49.34 (1C, NH_2-(CH)($\underline{C}H_2$)-CH_2-Ph); 41.83 (1C, NH_2-(CH)(CH_2)-$\underline{C}H_2$-Ph); 30.48 (1C, cyclohexyl methylene C's);. MS (FAB/m-b): 693 (M - ClO_4^-).

B.2. Cu(II) complexes of hexadentate tach derivatives

Preparation of [Cu(tachpyr)]$(ClO_4)_2$•1/2CH_3CN (257). The Cu(II) complex of tachpyr was prepared by using Neng Ye's method with a small modification. To a blue solution of $Cu(ClO_4)_2$•$6H_2O$ (0.0454 g, 1.23 x 10^{-4} mol) in MeOH (2 mL) was added a pale brown solution of tachpyr (0.0794g, 1.23 x 10^{-4} mol) in MeOH (2 mL) affording a blue precipitate. By warming it with a heat gun, the mixture became a clear dark green solution. After standing it for 4 hours at 5°C, dark blue prisms were formed, isolated by decanting the supernatant, washed with Et_2O (5mL), and dried under reduced pressure affording a blue solid. The blue solid was taken up to CH_3CN (4 mL), and vapor Et_2O was diffused into it giving blue prisms in 47.6% yield (0.0389, 5.85 x 10^{-5} mol). Anal. Calcd for $C_{24}H_{30}Cl_2CuN_6O_8$: C, 43.35; H, 4.55; N, 12.64. Found: C, 42.93; H, 4.78; N, 12.54. MS (FAB/glycerol): 465 (M - 2 ClO_4^-). μ_{eff} = 1.557 B.M. at 25°C. UV-vis (CH_3CN) 663 nm (ε = 8.2).

Preparation of [Cu(tachpyr)]$(ClO_4)_2$•CH_3OH (257A). A solution of $Cu(ClO_4)_2$ (0.019 g, 5.0 x 10^{-5} mol) in methanol (2 mL) was added to tachpyr (0.020 g, 5.0 x 10^{-5} mol) in methanol (2 mL) with swirling affording a blue cloudy solution. This

became clear green solution after warming by a heating gun. After standing at room temperature for 2 hours, Et_2O was diffused into the mixture overnight affording green needles. Crystals were isolated, washed with Et_2O and dried under reduced pressure giving a green solid. Green crystals suitable for X-ray crystallography were obtained by layering Et_2O on top of the CH_3CN solution of the complex. Anal. Calcd for $C_{24}H_{32}N_6Cl_2CuO_8$: C, 43.35; H, 4.55; N, 12.64. Found: C, 42.93; H, 4.78; N, 12.54. MS (FAB/glycerol): 465 (M - 2 ClO_4^-).

Preparation of [Cu(tach-Me$_3$pyr)](ClO$_4$)$_2$ (258). To a blue solution of $Cu(ClO_4)_2 \cdot 6H_2O$ (0.0641g, 1.73×10^{-4} mol) in EtOH (3 mL) was added to a yellow solution of tach-Me_3pyr (0.0769g, 1.73×10^{-4} mol) in EtOH (2 mL) affording a blue precipitate immediately. Adding Et_2O (10 mL) generated more blue precipitates. These were isolated and dried under reduced pressure giving a blue solid. This was washed with MeOH (6 mL), dissolved in excess amount of CH_3CN, filtered, and dried under reduced pressure affording a blue solid in 58.2% yield (0.0485 g, 6.86 x 10-4 mol). Single crystals suitable for X-ray crystallography were obtained by Et_2O diffusion into a DMF solution of the complex. Anal. Calcd For $C_{27}H_{36}Cl_2CuN_6O_8$: C, 45.86; H, 5.13; N, 11.89. Found: C, 45.78; H,4.74; N, 12.08. MS (FAB/glycerol): 507 (M - 2 ClO_4^-). μ_{eff} = 1.544 B.M. at 25°C. UV-vis (CH_3CN) 723 nm (ε = 81.4).

Preparation of [Cu(tach-Et$_3$pyr)] (ClO$_4$)$_2$ (259). To a pale blue solution of $Cu(ClO_4)_2 \cdot 6H_2O$ (0.0550 g, 1.49×10^{-4} mol) in a mixture of EtOH/Et_2O (2 mL/4 mL) was added a brown solution of tach-Et_3pyr (0.0723 g, 1.49×10^{-4} mol) in a

mixture of EtOH/Et_2O (2 mL/4 mL) affording a gray-blue precipitate immediately. The precipitate was isolated and dried under reduced pressure affording a pale blue solid. This was washed with EtOH (5 mL) and dissolved in CH_3CN to which Et_2O vapor was diffused giving pale green cubes and dark green precipitates. Crystals were collected manually, washed with MeOH, re-dissolved in CH_3CN, and Et_2O was diffused into CH_3CN solution of the complex giving pale green cubes. After decanting supernatant, the crystals were dried under reduced pressure affording a pale green solid in 54.6% yield (0.0609 g, 8.14 x 10^{-5} mol). Anal. Calcd for $C_{30}H_{42}Cl_2CuN_6O_8$: C, 48.10; H, 5.65; N, 11.22. Found: C, 47.81; H, 5.58; N, 11.21. MS (FAB/DMSO/NBA): 549 (M - 2 ClO_4^-). μ_{eff} = 1.638 B.M. at 25°C. UV-vis (CH_3CN) 734 nm (ε = 85.9).

Preparation of [Cu(tach-6-Mepyr)]$(ClO_4)_2$ (260). The Cu(II) complex of tach-6-Mepyr, [Cu(tach-6-Mepyr)]$(ClO_4)_2$, prepared by Su-jen Lai was washed with Et_2O and CH_3CN, and dissolved in MeOH to which Et_2O was diffused affording blue prisms, which are suitable for X-ray crystallography. Anal. Calcd for $C_{27}H_{38}Cl_2CuN_6O_9$ ([Cu(tach-6-Mepyr)]$(ClO_4)_2 \cdot H_2O$): C, 44.73; H, 5.28; N, 11.59. Found: C, 44.58; H, 5.03; N, 11.57. MS (FAB/DMSO/NBA): 507 (M - 2 ClO_4^-). μ_{eff} = 1.567 B.M. at 25°C. UV-vis (CH_3CN) 698 nm (ε = 237.8) 936 nm (156.8).

Preparation of [Cu(tachbn)]$(ClO_4)_2$ (261). An aqueous solution (3 mL) of S,S,S-tachbn •6HCl (0.0400g, 5.36 x 10^{-5} mol) was neutralized by adding 0.1N NaOH solution (3.21 mL, 1.61 x 10^{-4} mol, 3 equiv). After standing for 1 h, the neutralized ligand was filtrated and dried under reduced pressure for 14 h. The residue was

extracted into EtOH (5mL) and filtered. The filtrate was reacted with a blue solution of $Cu(ClO_4)_2 \cdot 6H_2O$ (0.0199g, 5.36×10^{-5} mol) in EtOH (5ml) affording a clear blue solution. This was dried under reduced pressure giving a blue solid that dissolved in CH_3CN. Blue plates suitable for X-ray crystallography were obtained by Et_2O diffusion into a CH_3CN solution of the complex. Crystals were isolate and dried under reduced pressure giving a blue solid in 45.3% yield (0.0271g, 1.32 x 10-4 mol). Anal. Calcd for $C_{33}H_{50}Cl_2CuN_6O_9$ [Cu(tachbn)]$(ClO_4)_2 \cdot H_2O$: C, 48.98; H, 6.23; N, 10.38. Found: C, 49.03: H, 6.04; N, 10.29. MS (FAB/glycerol): 591 (M - 2 ClO_4^-).

B.3. Ni(II) complexes of hexadentate tach derivatives

Preparation of [Ni(tachpyr)]$(Cl)_2 \cdot CH_3OH$ (262). Using Nicole Tsoupas's method with small modification, the Ni(II) complex of tachpyr was prepared. To a green solution of $NiCl_2 \cdot H_2O$ (0.0524 g, 2.20×10^{-4} mol) in MeOH (2 mL) was added a pale brown solution of tachpyr (0.0888 g, 2.20×10^{-4} mol) in MeOH (2 mL) affording a brown solution immediately. By diffusing Et_2O into the mixture, purple prisms and brown precipitates were formed. Crystals were isolated, washed with Et_2O, and dried under reduced pressure giving a purple solid in 34.7% yield (0.034 g, 6.39 x 10-5 mol). Single crystals suitable for X-ray crystallography were obtained by Et_2O diffusion into a MeOH solution of the complex. Anal. Calcd for $C_{24}H_{30}Cl_2N_6Ni \cdot 3/2H_2O$ ([Ni(tachpyr)]$Cl_2 \cdot 3/2H_2O$): C, 51.55; H, 5.95; N, 15.03. Found: C, 51.65; H, 5.97; N,14.79. MS (FAB/glycerol): 502 (M - 2Cl^-). μ_{eff} = 2.902 B.M. at 25°C. UV-vis (MeOH) 880 nm (ε =11.8), 797 nm (ε =16.0), 511 nm (ε =16.6).

Preparation of [Ni(tach-Me$_3$pyr)](ClO$_4$)$_2$•CH$_3$CN (263). To a green solution of Ni(ClO$_4$)$_2$•6H$_2$O (0.0546 g, 1.49 x 10^{-4} mol) in MeOH (2 mL) was added a yellow solution of tach-Me$_3$pyr (0.0663 g, 1.01 x 10^{-4} mol) in MeOH (2 mL) affording pink microcrystals immediately. After standing for 1/2 hour, the microcrystals were isolated, washed with cold MeOH, and dried under reduced pressure giving a pale pink solid. Pink prisms suitable for X-ray crystallography were obtained by Et$_2$O diffusion into a CH$_3$CN solution of the complex. Crystals were isolated and dried under reduced pressure affording a purple solid in 57.8% yield (0.0604 g, 8.61 x 10^{-5} mol). Anal. Calcd for $C_{27}H_{36}N_6Cl_2NiO_8$: C, 46.18; H, 5.17; N, 11.97. Found: C, 46.42; H, 5.21; N, 11.96. MS (FAB/glycerol): 502 (M - 2 ClO$_4^-$). μ_{eff} = 2.959 B.M. at 25°C. UV-vis (MeOH) 925 nm (ε = 3.4), 814 nm (ε = 8.8), 562 nm (ε = 15.4).

Preparation of [Ni(tach-Et$_3$pyr)](ClO$_4$)$_2$ (264). To a green solution of Ni(ClO$_4$)$_2$•6H$_2$O (0.0445 g, 1.21 x 10^{-4} mol) in a mixture of EtOH (2 mL) and Et$_2$O (4 mL) was added a brown solution of tach-Et$_3$pyr (0.0591 g, 1.21 x 10^{-4} mol) in a mixture of EtOH (2 mL) and Et$_2$O (4 mL) affording a peach precipitate immediately. This was isolated, dried under reduced pressure, washed with MeOH and Et$_2$O, and taken up into CH$_3$CN. Pale purple prisms were obtained by Et$_2$O diffusion into CH$_3$CN solution of the complex, isolated, and dried under reduced pressure affording a pale purple solid in 72.1% yield (0.0649 g, 8.72 x 10^{-5} mol). Anal. Calcd for $C_{30}H_{42}Cl_2N_6NiO_8$: C, 48.41; H, 5.69; N, 11.29. Found: C, 48.14; H, 5.68; N, 11.25. MS (FAB/DMSO/NBA): 544 (M - 2 ClO$_4^-$). μ_{eff} = 2.959

B.M. at 25°C. UV-vis (MeOH) 944 nm (ε = 14.2), 818 nm (ε = 8.6), 574 nm (ε = 16.4).

Preparation of [Ni(tach-6-Mepyr)]$(NO_3)_2 \cdot 1/2\ Et_2O$ (265). To a pale green solution of $Ni(NO_3)_2 \cdot 6H_2O$ (0.0549 g, 1.89×10^{-4} mol) in MeOH (2 mL) was added a pale yellow solution of tach-6-Mepyr (0.0839g, 1.89×10^{-4} mol) in MeOH (2 mL) affording a peach solution. After adding Et_2O (12 mL) and standing 2h, small pale pink microcrystals were formed, isolated, washed with CH_3CN, and dried under reduced pressure giving a pale purple solid. This was dissolved in MeOH followed by vapor Et_2O diffusion, affording pale purple prisms. Crystals were isolated and dried under reduced pressure giving a pale purple solid in 69.8% yield (0.0828 g, 1.32×10^{-5} mol). Anal. Calcd for $C_{27}H_{36}N_8NiO_6$: C, 51.70; H, 5.78; N, 17.86. Found: C, 51.35; H, 5.80; N, 17.83. MS (FAB/DMSO/NBA): 502 (M - 2 NO_3^-). μ_{eff} = 3.087 B.M. at 25°C. UV-vis (MeOH) 927 nm (ε = 23.2), 816 nm (ε = 13.7), 561 nm (ε = 7.8).

Preparation of [Ni(tachpn)]$(ClO_4)_2 \cdot CH_3OH$ (266). The Ni(II) complex of S,S,S-tachpn, [Ni(tachpn)]$(ClO_4)_2$, prepared by Neng Ye was dissolved in MeOH, filtered, and Et_2O was diffused into a MeOH solution of the complex affording pink prisms suitable for X-ray crystallography. Anal. Calcd for $C_{15}H_{36}Cl_2N_6NiO_8$: C, 32.50; H, 6.55; N, 15.16. Found: C, 32.51; H, 6.71; N, 14.98. MS (FAB/m-b): 457 ($M - ClO_4^-$).

B.4. Co(II) complexes of hexadentate tach derivatives

Preparation of a mixture of [Co(tachpyr)]$(NO_3)_3$ (267) and [Co(tachpyr-*ox-n*)]$(NO_3)_3$ (267A). To a pink solution of $Co(NO_3)_2 \cdot 6H_2O$ (0.0518 g, 1.78 x 10^{-4} mol) in a mixture of EtOH/Et_2O (2 mL/4 mL) was added a yellow solution of tachpyr (0.0717 g,1.78 x 10^{-4} mol) in a mixture of EtOH/Et_2O (2 mL/4 mL) affording a pale brown precipitate immediately. After standing 1/2, the precipitate was isolated and dried under reduced pressure giving a brown and a yellow solid. These were washed with CH_3CN (5 mL) and CH_2Cl_2 (5 mL) and dissolved in MeOH. Vapor Et_2O was diffused into a MeOH solution of the complex giving pale yellow plates. These were isolated and dried under reduced pressure affording a yellow solid in 52.8% yield (0.0550g, 9.40 x 10-5 mol). Anal. Calcd for $C_{24}H_{30}CoN_9O_9 \cdot 4/3H_2O$: C, 42.93; H, 4.90; N, 18.77. Found: C, 43.07; H, 4.90; N, 18.77. MS (FAB/glycerol/DMSO): 461 (M -$2NO_3^-$). μ_{eff} = 1.129 B.M. at 25°C. UV-vis (MeOH) 466 nm (ε = 135).

Preparation of [Co(tach-Me_3pyr)]$(NO_3)_2$ (268). To a pink solution of $Co(NO_3)_2 \cdot 6H_2O$ (0.0695 g, 2.39 x 10^{-4} mol) in a mixture of MeOH/Et_2O (2 mL/4 mL) was added a yellow solution of tach-Me_3pyr (0.1062 g, 2.39 x 10^{-4} mol) in a mixture of MeOH/Et_2O (2 mL/4 mL) affording a pink precipitate. More pink precipitates were formed by adding Et_2O (12 mL), isolated, and dried under reduced pressure giving a pink solid. The solid was washed with CH_3CN and Et_2O and dried under reduced pressure affording a pink solid in 67.5% yield (0.1012 g, 1.61 x 10^{-4} mol). Pink crystals were obtained by Et_2O diffusion into a MeOH solution of the complex. Anal. Calcd for $C_{27}H_{36}CoN_8O_6$: C, 51.68; H, 5.78;

N, 17.86. Found: C, 51.50; H, 5.70; N, 17.69. MS (FAB/DMSO/glycerol/H_2O): 503 (M - 2 NO_3^-). μ_{eff} = 4.021 B.M. at 25°C. UV-vis (MeOH) 1032 nm (ε = 7.53), 493 nm (ε = 38.01), 552 nm (ε = 19.18).

Preparation of [Co(tach-Et$_3$pyr)](ClO$_4$)$_2$ (269). To a pink solution of $Co(ClO_4)_2 \cdot 6H_2O$ (0.0549 g, 1.50 x 10^{-4} mol) in a mixture of MeOH/Et_2O (2 mL/6 mL) was added a brown solution of tach-Et_3pyr (0.0730 g, 1.50 x 10^{-4} mol) in a mixture of MeOH/Et_2O (2 mL/6 mL) affording a peach precipitate immediately. The precipitate was isolated and dried under reduced pressure giving a peach solid. This was washed with MeOH (5 mL) and dried under reduced pressure affording a peach solid in 70.9% yield (0.0791 g, 1.06x 10^{-4} mol). Pale pink crystals were obtained by Et_2O diffusion into a CH_3CN solution of the complex. Anal. Calcd for $C_{30}H_{42}Cl_2CoN_6O_8$: C, 48.40; H, 5.69; N, 11.29. Found: C, 48.08; H, 5.74; N, 11.14. MS (FAB/DMSO/NBA): 545 (M - 2 ClO_4^-). μ_{eff} = 4.021 B.M. at 25°C. UV-vis (CH_3CN) 1062 nm (ε = 3.41), 513 nm (ε = 90.4).

Preparation of [Co(tach-6-Mepyr)](NO$_3$)$_2$ (270). To a pink solution of $Co(NO_3)_2 \cdot 6H_2O$ (0.0520 g, 1.79 x 10^{-4} mol) in a mixture of MeOH/Et_2O (2 mL/4 mL) was added a yellow solution of tach-6-Mepyr (0.0794 g, 1.50 x 10^{-4} mol) in a mixture of MeOH/Et_2O (2 mL/4 mL) affording small amount of a pink precipitate immediately. Peach color prisms were formed after standing 14 h, isolated, washed with Et_2O and CH_3CN, and dried under the reduced pressure giving a pale pink solid. The solid was taken up to MeOH (3 mL) to which vapor Et_2O was diffused giving peach prisms. Crystals were isolated and dried under

reduced pressure affording a peach powder in 67.3% yield (0.0756 g, 1.20x 10^{-4} mol). Single crystals suitable for X-ray crystallography were obtained by Et_2O diffusion into a MeOH solution of the complex. Anal. Calcd for $C_{27}H_{36}CoN_8O_6 \bullet 1/2H_2O$ ([Co(tach-6-Mepyr)]$(NO_3)_2 \bullet 1/2H_2O$): C, 450.94; H, 5.86; N, 17.60. Found: C, 51.03; H, 5.65; N, 17.52. MS (FAB/Glycerol/DMSO): 503 (M - 2 NO_3^-). μ_{eff} = 4.998 B.M. at 25°C. UV-vis (MeOH) 1042 nm (ε = 7.6), 494 nm (ε = 28.6).

For the preparation of Fe(II) and Fe(III) complexes of hexadentate tach derivatives, see experimental section of Chapter 2.

B.5. Mn(II) complexes of hexadentate tach derivatives

Preparation of [Mn(tachpyr)]$(ClO_4)_2$ (271). To a solution of $Mn(ClO_4)_2 \bullet 6H_2O$ (0.108 g, 2.99 x 10^{-4} mol) in MeOH (2 mL) was added a yellow solution of tachpyr (0.120g, 2.99 x 10^{-4} mol) in MeOH (2 mL) affording a yellow prisms after 20 min standing. Crystals were isolated and washed with MeOH and EtOH. Colorless prisms were obtained by slow diffusion of Et_2O into a CH_3CN solution of the complex, isolated, and dried under reduced pressure affording a pale yellow solid in 70.5% yield (0.138g, 2.11 x 10-4 mol). Single crystals suitable for X-ray crystallography were obtained by Et_2O diffusion into a CH_3CN solution of the complex. Anal. Calcd for $C_{24}H_{30}Cl_2MnN_6O_8 \bullet 1/2CH_3CN$: C, 44.36; H, 4.69; N, 13.45. Found: C, 44.55; H, 4.30; N, 13.70. MS (FAB/glycerol): 556 (M -ClO_4^-). μ_{eff} = 5.663 B.M. 25°C.

Preparation of [Mn(tach-Me$_3$pyr)](ClO$_4$)$_2$ (272). To a solution of $Mn(ClO_4)_2 \cdot 6H_2O$ (0.0590 g, 1.63×10^{-4} mol) in a mixture of MeOH/Et_2O (2 mL/4 mL) was added a yellow solution of tach-Me$_3$pyr (0.0726 g, 1.63×10^{-4} mol) in a mixture of MeOH/Et_2O (2 mL/4 mL) affording a yellow-white precipitate. The precipitate was isolated and dried under reduced pressure giving a pale yellow solid. This was washed with MeOH and Et_2O and dried under reduced pressure affording a pale yellow solid in 63.2% yield (0.0720 g, 1.03×10^{-4} mol). Pale yellow crystals were obtained by Et_2O diffusion into a CH_3CN solution of the complex. Anal. Calcd for $C_{27}H_{36}Cl_2MnN_6O_8$: C, 46.43; H, 5.20; N, 12.03. Found: C, 46.20; H, 5.15; N, 11.96. MS (FAB/DMSO/glycerol): 598 (M - ClO_4^-). μ_{eff} = 5.829 B.M. at 25°C.

Preparation of [Mn(tach-Et$_3$pyr)](ClO$_4$)$_2$ (273). To a solution of $Mn(ClO_4)_2 \cdot 6H_2O$ (0.0438 g, 1.21×10^{-4} mol) in a mixture of MeOH (2 mL) and Et_2O (4 mL) was added a brown solution of tach-Et$_3$pyr (0.0590 g, 1.21×10^{-4} mol) in a mixture of MeOH/Et_2O (2 mL/6 mL) affording yellow-brown solution. A pale brown precipitate was form by adding Et_2O into the mixture. The precipitate was isolated and dried under reduced pressure giving pale a brown solid. This was washed with CH_2Cl_2 and dissolved in CH_3CN. Vapor Et_2O was diffused into a CH_3CN solution of the complex giving pale brown prisms. Prisms were isolated and dried under reduced pressure affording a pale brown solid in 48.8% yield (0.0437 g, 5.90×10^{-5} mol). Anal. Calcd for $C_{30}H_{42}Cl_2MnN_6O_8$: C, 48.66; H, 5.72; N, 11.35. Found: C, 48.54; H, 5.68; N, 11.29. MS (FAB/DMSO/NBA): 640 (M - ClO_4^-). μ_{eff} = 5.792 B.M. at 25°C.

Preparation of [Mn(tach-6-Mepyr)]$(ClO_4)_2 \bullet CH_3OH$(274). To a solution of $Mn(ClO_4)_2 \bullet 6H_2O$ (0.0899 g, 2.48 x 10^{-4} mol) in MeOH (2 mL) was added a yellow solution of tach-6-Mepyr (0.1103 g, 2.48 x 10^{-4} mol) in MeOH (2 mL) affording a yellow prisms. The crystals were isolated and dried under the reduced pressure giving a pale yellow solid. This was washed with MeOH (5 mL) and Et_2O (5 mL) and dissolved in CH_3CN to which vapor Et_2O was diffused generating yellow prisms. The crystals were isolated and dried under reduced pressure affording a yellow solid in 73.9% yield (0.1280 g, 1.83x 10^{-4} mol). Single crystals suitable for X-ray crystallography were obtained by Et_2O diffusion into a CH_3CN solution of the complex. Anal. Calcd for $C_{27}H_{36}Cl_2MnN_6O_8 \bullet H_2O$: C, 45.26; H, 5.35; N, 11.73. Found: C, 44.93; H, 5.16; N, 11.98. MS (FAB/glycerol): 499 (M - 2 ClO_4^-). μ_{eff} = 5.786 B.M. at 25°C.

B.6. Cd(II) and Hg(II) complexes of tachpyr

Preparation of [Cd(tachpyr)]$(ClO_4)_2$ (275). To a solution of $Cd(ClO_4)_2 \bullet 6H_2O$ (0.088 g, 2.1 x 10^{-4} mol) in anhydrous EtOH (8 mL) was added a yellow solution of tachpyr (0.084 g, 2.1 x 10^{-4} mol) in anhydrous MeOH (8 mL) affording a brown suspension immediately. After standing for 2 hours, feather-shaped crystals precipitated. The product was isolated by decanting the supernatant, washing the residue with Et_2O, and then drying under reduced pressure affording a white solid in 51% yield (0.0763 g, 1.07 x 10^{-4} mol). Single crystals suitable for X-ray crystallography were grown by Et_2O diffusion into the CH_3CN solution of the metal complex. Anal. Calcd for $C_{24}H_{30}CdCl_2N_6O_8$: C, 40.37; H, 4.24; N, 11.77. Found: C, 40.12; H, 4.22; N, 11.48. ^1H NMR (CH_3CN-d_3, 25°C): d 8.80, 7.99, 7.55,

7.49 (d, t, t, d, 4H, ^3J = 7.8 and 5.5 Hz, $C_5\underline{H}_4N$); 4.21 (dd, $\underline{A}$MX, 1H, ^2J = 15.8 Hz, ^3J = 15.8 Hz, NH-$C\underline{H}_2$-py, diastereotopic), 4.01 (dd, A$\underline{M}$X, 1H, ^2J = 15.8 Hz, ^3J = 5.5 Hz, NH-$C\underline{H}_2$-py, diastereotopic); 3.55 (br d (dd), AM$\underline{X}$, 1H, ^3J = 15.8Hz and 5.5 Hz, N$\underline{H}$- CH_2-py); 3.46 (br s, $\underline{A}$MM'XX', 1H, cyclohexyl methine H); 2.28 (br d, A$\underline{MM'}$XX', 1H, equatorial cyclohexyl methylene H's), 2.02 (br d, AMM'$\underline{XX'}$, 1H, axial cyclohexyl methylene H's, diastereotopic). MS (FAB/glycerol): 614 (M - ClO_4^-).

Preparation of [Hg(tachpyr)]$(ClO_4)_2$ (276). To a of $Hg(ClO_4)_2$ (0.038 g, 9.4 x 10^{-5} mol) sonicated (5 min) in anhydrous EtOH (4 mL) was added a yellow solution of tachpyr (0.038 g, 9.4 x 10^{-5} mol) in anhydrous EtOH (2 mL) affording a yellowish-white precipitate. The yellowish-white precipitate was isolated by decanting the supernatant. The residue was washed with Et_2O (4 mL) and dried under reduced pressure giving a pale yellow solid. The crude product was dissolved in CH_3CN (5 mL), and Et_2O was diffused into it forming a mixture of yellow precipitate and white crystals. The white crystals were isolated manually, re-dissolved in CH_3CN (5 mL), and Et_2O was diffused into CH_3CN solution of the crude product forming colorless prisms which were isolated by decanting supernatant and dried under reduced pressure affording a 52% yield (0.0391 g, 4.87 x 10^{-5} mol). Anal. Calcd for $C_{24}H_{30}Cl_2HgN_6O_8$: C, 35.94; H, 3.77; N, 10.48. Found: C, 36.24; H, 3.72; N, 10.39. ^1H NMR (DMSO-d_6, 25°C): d 9.13, 8.06, 7.68 (d, t, m (2H), 4H, ^3J = 7.9 and 5.7 Hz, $C_5\underline{H}_4N$); 4.91 (br d (dd), $\underline{A}$MX, 1H, ^3J = 13.7 Hz and 3.5 Hz, N$\underline{H}$-CH_2-py); 4.35 (dd, A$\underline{M}$X, 1H, ^2J = 13.9 Hz, ^3J = 13.7 Hz, NH-$C\underline{H}_2$-py); 3.94 (dd, AMX, 1H, ^2J = 13.9 Hz, ^3J = 3.5 Hz, NH-$C\underline{H}_2$-py); 3.44 (br s, $\underline{A}$MM'XX', 1H, cyclohexyl methine H); 2.44 (br d, A$\underline{MM'}$XX', 1H, equatorial

cyclohexyl methylene H's), 1.94 (br d, AMM'XX', 1H, axial cyclohexyl methylene H's, diastereotopic). MS (FAB/glycerol): 603 (M - $2ClO_4^-$).

C. X-ray Data Collection, Structure Solution and Refinement for Metal Complexes

All X-ray structures of metal complexes described herein were determined by Dr. Robin Rogers at the University of Alabama. Single crystals suitable for X-ray crystallography of metal complexes were grown by Et_2O diffusion into solutions of the corresponding metal complexes in MeOH, CH_3CN, DMF, and DMSO. Single crystals were mounted on fibers and transferred to the goniometer. The crystals were cooled to -100° C during data collection by using a stream of cold nitrogen gas. Data collection was made on a Siemens SMART diffractometer with a CCD area detector, using graphite monochromated MoKα radiation. The SHELXTL software, version 5, was used for solutions and refinement.[315] Using the program SADABS[335] carried out absorption correction. The molecule was refined by full-matrix least-squares on F^2. ORTEP[316] drawings were made with SHELXTL[315] and ORTEP-3 for Windows.[317]

Results

A. Syntheses of Metal Complexes and NMR Characterization

A.1. Complexes of tachpyr and *N*-alkylated tachpyr.

The molecule *cis,cis*-triaminocyclohexane (tach) has been known for decades as a versatile face-capping N_3 ligand, which can be easily derivatized to give hexadentate ligands.[15, 183] Tachpyr (*N, N', N''*-tris(2-pyridylmethyl) *cis,cis*-1,3,5-triaminocyclohexane) was derived from tach by addition of three *N*-pendant 2-pyridylmethyl arms to generate more binding sites to the tach framework, affording coordination geometry to six.[95] It was believed that the radii (0.75 – 0.97 Å) of first row (middle to late) transition metal elements would fit to tachpyr for metal complexation. Therefore, first row transition metal complexes of tachpyr were prepared to investigate the effects of the metal radii on coordination geometry and their electronic properties. The metal complexes of alkylated tachpyr derivatives, tach-Me_3pyr and tach-Et_3pyr, with divalent first row transition metal elements were also prepared and studied some of their structures and electronic properties.

The tachpyr complexes $[M(tachpyr)](X)_2$ (M = Zn(II) (**250**), Cu(II) (**257**) (**257A**), Ni(II) (**262**), Co(II) (**267**), Mn(II) (**271**), Cd(II) (**275**), and Hg(II) (**276**); X = Cl^-, ClO_4^-, or NO_3^-), the tach-Me_3pyr complexes $[M(tach\text{-}Me_3pyr)](X)_2$ (M = Zn(II) (**251**), Cu(II) (**258**), Ni(II) (**263**), Co(II) (**268**), and Mn(II) (**272**); X = ClO_4^- or NO_3^-), and the tach-Et_3pyr complexes $[M(tach\text{-}Et_3pyr)](X)_2$ (M = Zn(II) (**252**), Cu(II) (**259**), Ni(II) (**264**), Co(II) (**269**), and Mn(II) (**273**); X = ClO_4^-) were prepared by reactions of the respective metal ion salts and the ligand (1:1) in mixture of an

alcohol medium, MeOH, EtOH, or 1:2 mixture of MeOH and Et_2O. All metal complexes were isolated, purified, and crystallized by Et_2O diffusion into CH_3CN, DMF, or MeOH solutions of the metal complexes. The products were characterized by proton NMR, if applicable, electronic spectroscopy, magnetic moment study, elemental analysis, and FAB-Mass spectroscopy.

The formation of metal complexes with a "closed" conformation was easily confirmed by changes in the proton NMR chemical shifts and the splitting patterns of the cyclohexyl protons relative to the respective free ligand which has an "open" conformation of the tach framework (**Scheme 3.11**). The three 2-pyridylmethyl arms of the tachpyr are assumed to coordinate M(II) in either the Λ or Δ configuration.[97] Proton NMR studies indicated that this configuration is static on the NMR time scale at room temperature, as shown by the chemically inequivalent methylene protons (cyclohexyl amine)NH-C*H*$_2$-pyridyl) which form an AMX (or AXY) spin system (usually H_A is the amine hydrogen on tach). ^1H NMR spectra of Zn(II), Cd(II), and Hg(II) complexes of tachpyr are depicted in **Figure 3.29**. Proton NMR data for tachpyr ligand and the Zn(II), Cd(II), and Hg(II) complexes are presented in **Table 3.11**.

In reaction of $Co(NO_3)_2 \cdot 6H_2O$ and the tachpyr ligand to synthesize a divalent cobalt complex, a mixture of the non-oxidized ([Co(tachpyr)]$(NO_3)_3$ (**267**)) and the oxiditively dehydrogenated cobalt(III) complex ([Co(tachpyr-*ox*-*n*)]$(NO_3)_3$ (**267A**)) was generated in the presence of air at ambient pressure. It was characterized by proton NMR (**Fig. 3.56**) and electronic (**Fig. 3.53 (a)**) spectra and its magnetic moment (**Table 3.33**).

Table 3.11. ^{1}H NMR data for the tachpyr ligand L and Zn(II) (250), Cd(II) (275), and Hg(II) (276) tachpyr complexes.

	Proton chemical shifts					
	Pyridine protons C_6H_4N				Methylene protons $NH\text{-}CH_2$	Cyclohexyl protons Ha, Hb, Hc
L	8.46	7.71	7.41	7.20	3.80(s)	2.37(s), 2.12(d), 0.83(q)
250	8.11	7.81	7.63	7.50	4.14(m)	3.26(s), 2.34(d), 1.90(d)
275	8.80	7.99	7.55	7.40	4.21(t), 4.01(dd)	3.46(s), 2.28(d), 2.02(d)
276	9.13	8.06	7.68	7.68	4.35(t), 3.94(dd)	3.44(s), 2.44(d), 1.94(d)

Methylene protons = AMX (or AXY) for the complexes and A_2 for the free ligand, 2H, py-CH_2-NH, diastereotopic; Ha = AMM'XX", 1H, cyclohexyl methine H's; Hb = AMM'XX', 1H, cyclohexyl methylene H's, diastereotopic; Hc = AMM'XX', 1H, cyclohexyl methylene H's, diastereotopic. Chemical shifts are reported in ppm on the δ scale relative to TMS (DMSO-d_6 or CH_3CN-d_3 solutions)

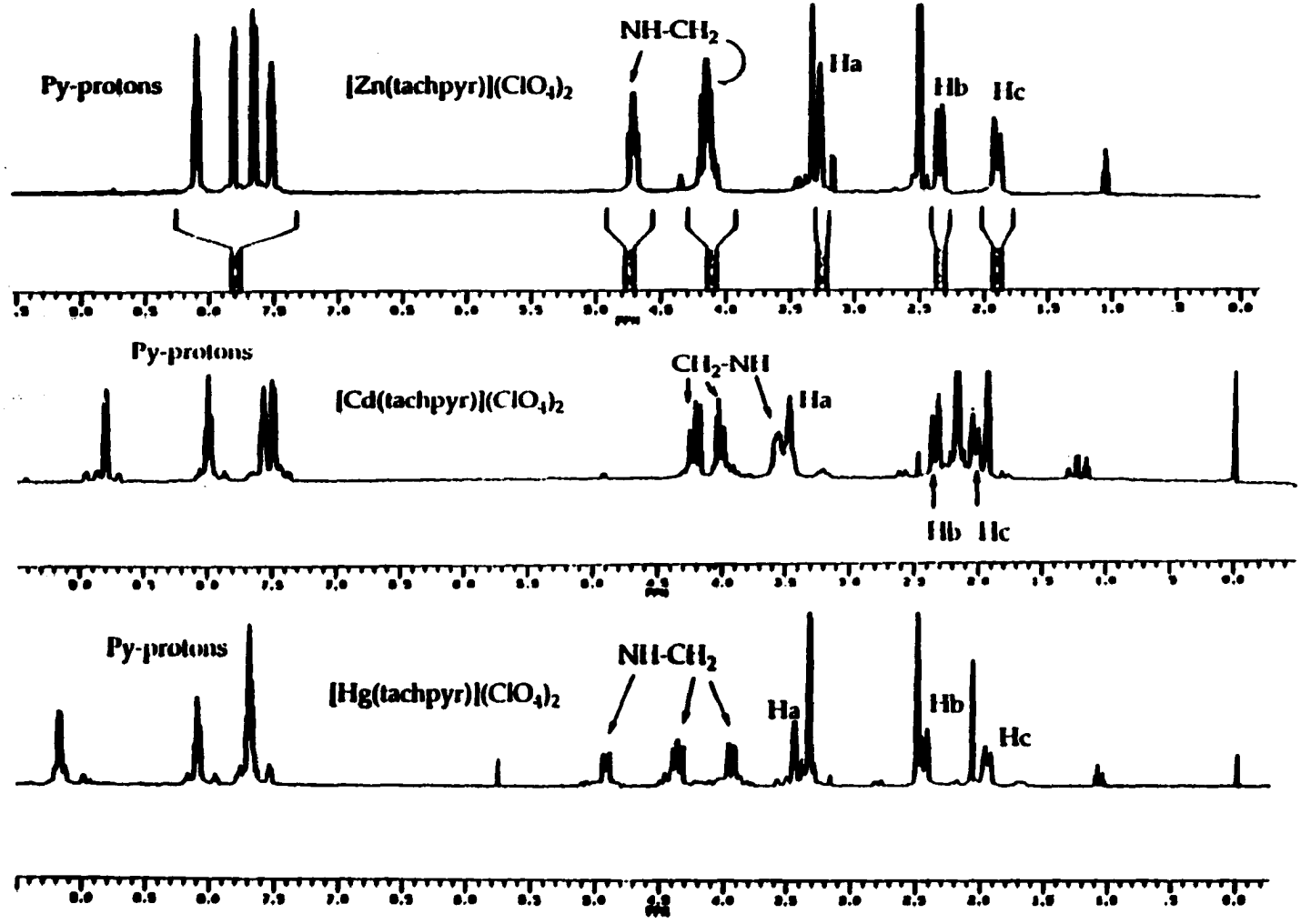

Figure 3.29. ^{1}H NMR spectra of [Zn(tachpyr)](ClO$_4$)$_2$, [Cd(tachpyr)](ClO$_4$)$_2$, and [Hg(tachpyr)](ClO$_4$)$_2$

Because the methylene signals of the ethyl groups of [Zn(tach-Et_3pyr)]$(ClO_4)_2$ (252) are obscured by solvent (Fig. 3.30 (a)), its ^1H-^{13}C HECTOR NMR spectrum was obtained (Fig. 3.31). This clearly identifies ethyl groups and shows the correlation of protons and associated carbons. Therefore, two doublets at 4.55 and 4.09 ppm are assigned to the bridging methylene protons, cyclohexyl ring-N(CH_2CH_3)-CH_2-py, while two multiplets at 2.55 and 1.97 ppm are assigned to the methylene protons on the ethyl groups, cyclohexyl ring-N(CH_2CH_3)-CH_2-py, respectively in ^1H NMR spectrum.

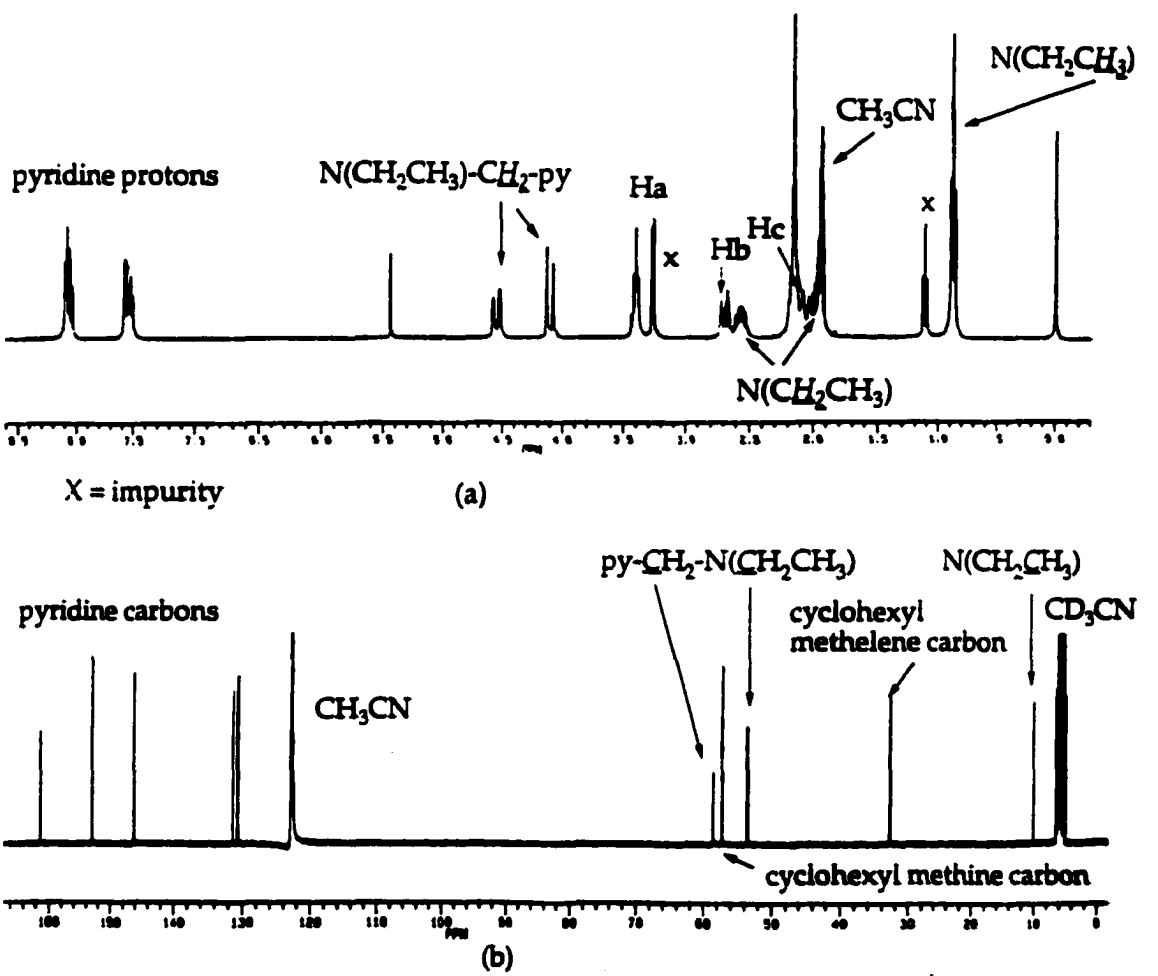

Figure 3.30. (a) ^1H NMR of [Zn(tach-Et_3pyr)]$(ClO_4)_2$ (252); (b) $^{13}C\{^1H\}$ NMR of [Zn(tach-Et_3pyr)]$(ClO_4)_2$ (252) complex.

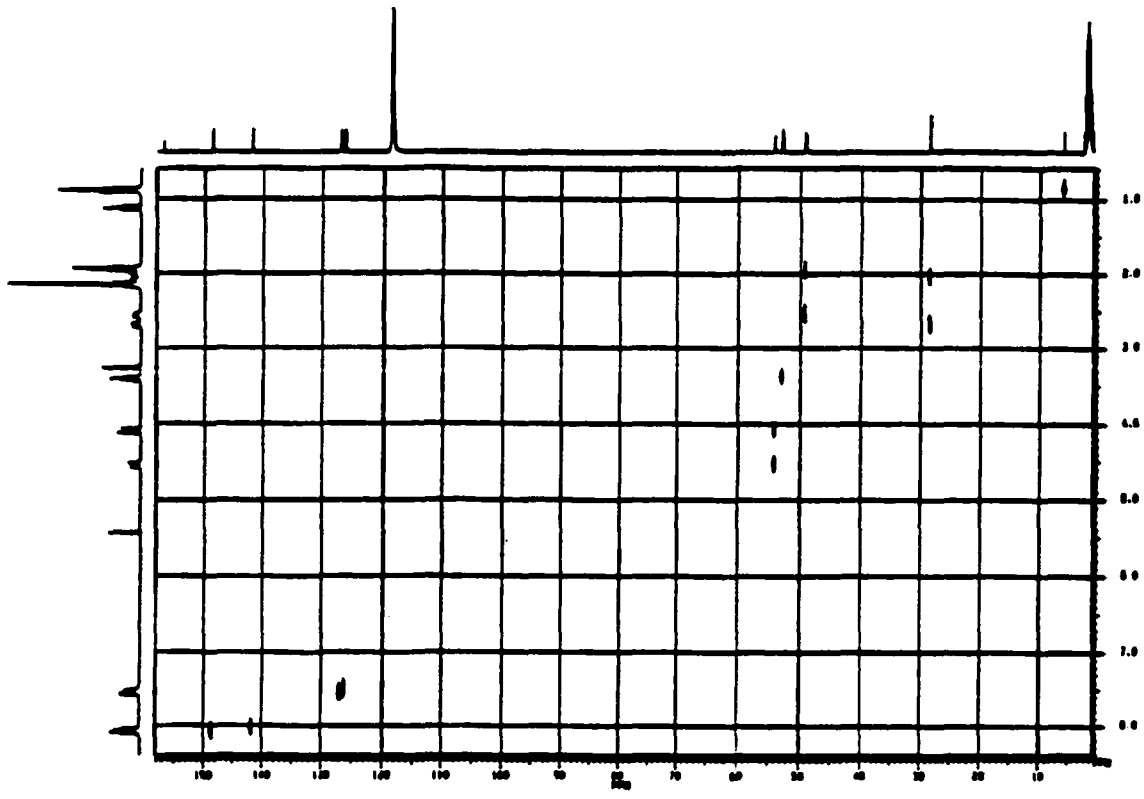

Figure 3.31. ^{1}H-^{13}C HECTOR NMR spectrum of $[Zn(tach\text{-}Et_3pyr)](ClO_4)_2$.

A.2. Complexes of tach-6-Mepyr.

Tach-6-Mepyr ligand, *N,N',N''*-tris(6-methyl-2-methylpyridyl)-*cis,cis*-1,3,5-triaminocyclohexane, were prepared by the reaction of tach neutralized from tach•3HBr **238 (Scheme 3.6)** by azeotropic distillation with 6-methyl-pyridine-2-carboxaldehyde. The tris(imines) produced was reduced by routine borohydride reduction to generate the secondary amines to provide novel hexadentate tach-6-Mepyr **243 (Scheme 3.8).** By the addition of three 6-methyl-2-methylpyridyl arms to the cyclohexyl nitrogen atoms, the tach-6-Mepyr ligand can provide more binding sites to the tach framework, affording coordination geometry to six. The divalent transition metal complexes of tach-6-Mepyr were prepared to

study the effects of metal radii, steric effects of 6-methyl group on pyridine rings, and the electronic property of metal ions on the coordination geometry.

The tach-6-Mepyr complexes [M(tach-6-Mepyr)](X)$_2$ (M = Zn(II) (**253**), Cu(II) (**260**), Ni(II) (**265**), Co(II) (**270**), and Mn(II) (**274**); X = ClO_4^-, or NO_3^-) were prepared by reactions of equimolar amounts of the respective metal ion salts and the ligand in mixture of an alcohol medium, MeOH, EtOH, or 1:2 mixture of MeOH and Et_2O. Isolating and purifying and vapor diffusion of Et_2O into CH_3CN, DMF, or MeOH solutions of the metal complexes obtained single crystals of the metal complexes. These were characterized by proton NMR, if applicable, electronic spectroscopy, magnetic moment study, elemental analysis, and FAB-Mass spectroscopy.

Proton NMR study of **253** (**Fig. 3.32 (a)**) indicated that the metal complex is static on the NMR time scale at room temperature, as shown by the chemically inequivalent methylene protons (cyclohexyl amine)NH-CH_2-pyridyl) which form an AMX (or AXY) spin system (usually H_A is the amine hydrogen on tach). It also shows a chemical shift of methyl groups on the 6-pisitions of the pyridyl rings from 2.42 ppm to 2. 15 ppm upon complexation.

A.3. Complexes of S,S,S-tachpn and S,S,S-tachbn.

The chiral ligands (S,S,S-tachpn•6HCl and S,S,S-tachbn•6HCl) are hydrochloride salts which must be neutralized prior to complexation. The ligands are neutralized with adding 6 equiv of 0.1N NaOH in water followed by drying under reduced pressure. The free base of the ligands was extracted into MeOH or EtOH and filtered to remove the NaCl. The S,S,S-tachpn complexes

[M(tachpn)]$(ClO_4)_2$ (M = Zn(II) (255) and Ni(II) (266)) and the S,S,S-tachbn complexes [M(tachbn)]$(X)_2$ (M = Zn (256) and Cu(II) (261); X = Cl^- and/or ClO_4^-) were prepared from equimolar amounts of the respective metal ion salts and the ligands in either MeOH or EtOH of a mixture of these. Single crystals of metal complexes were obtained from Et_2O diffusion into CH_3CN or CH_3OH solutions. These were characterized by spectroscopy, elemental analysis, X-ray crystallography, and magnetic moment, as appropriate. Notably elemental analysis indicated that the Zn(II) complex of S,S,S-tachbn has mixed counter ions, i.e., [Zn(tachbn)](Cl)(ClO_4), rather than [Zn(tachbn)]$(ClO_4)_2$.

Proton NMR studies of **256** (DMSO-d_6 solvent) and **255** (CH_3CN-d_3 solvent) indicated that the complexes are static on the NMR time scale at room temperature, as shown by the chemically inequivalent methylene protons, (cyclohexyl amine)NH-CH_2-R (R =methyl for S,S,S-tachpn and benzyl for S,S,S-tachbn), which form an AMX (or AXY) spin system (H_A is the amine hydrogen on tach). ^1H NMR spectrum of [Zn(tachpn)]$(ClO_4)_2$ (**255**) complex is depicted in **Figure 3. 32 (b).**

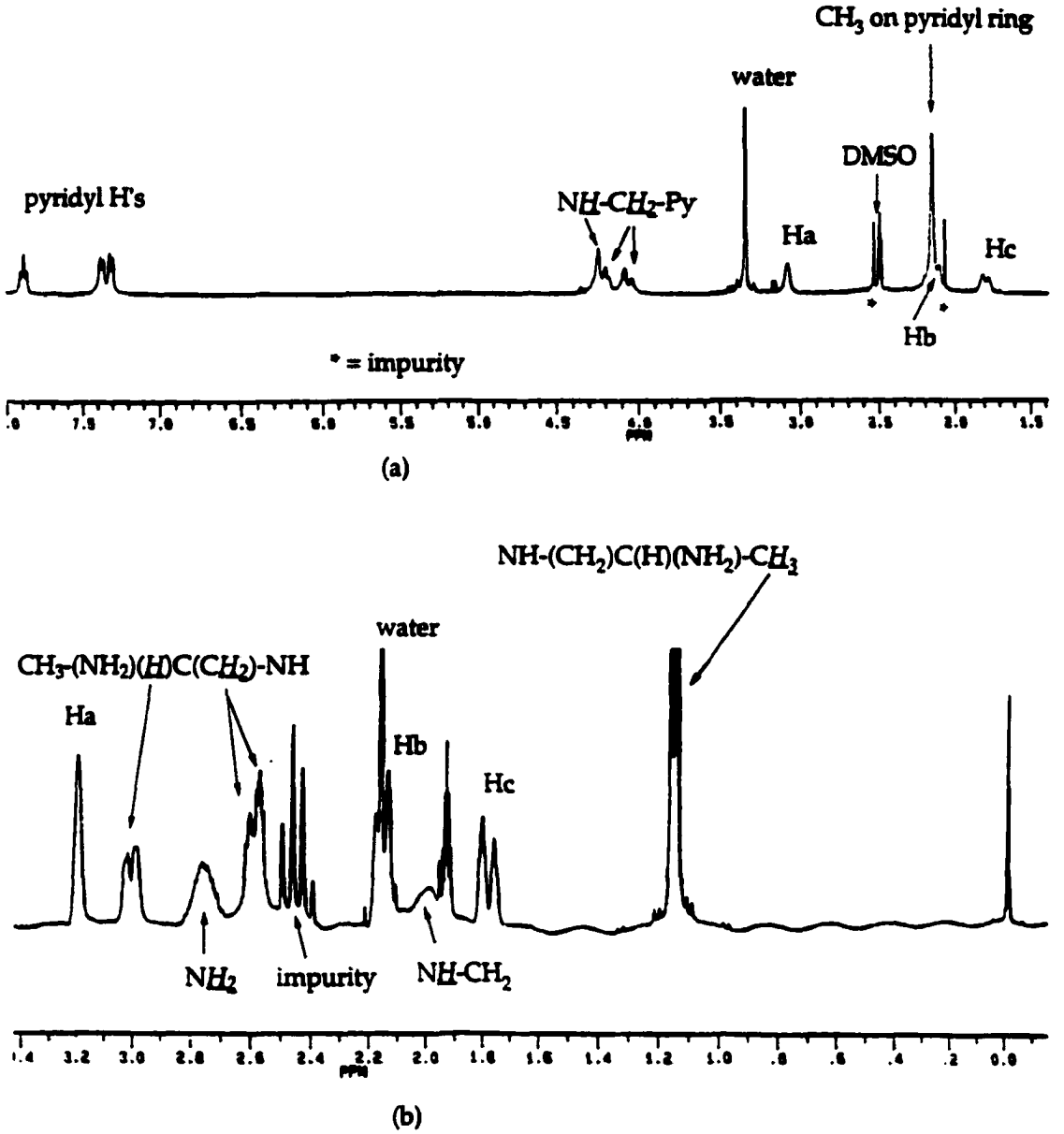

Figure 3.32. ^{1}H NMR of [Zn(tach-6-Mepyr)]$(ClO_4)_2$ **(253)** (a) and [Zn(tachpn)]$(ClO_4)_2$ **(255)** (b).

B. Description of Structures

Crystallographic and data collection parameters of metal complexes are presented in **Appendix A.**

B.1. $[M(tachpyr)](X)_2$ ($M = Zn^{2+}, Cu^{2+}, Ni^{2+}, Mn^{2+}, Cd^{2+}$, and Hg^{2+}, and $X = Cl^-$ for Ni^{2+} and ClO_4^- for other complexes)

B.1.1. $[Zn(tachpyr)](ClO_4)_2 \cdot CH_3OH$ (250). Single crystals[331] suitable for X-ray crystallography were grown by Et_2O diffusion into a CH_3CN solution of the metal complex. The complex **250** crystallizes as a colorless prism in the cubic space group $P2_13$.

The coordination geometry of MN_6 in **250** (**Fig. 3.33**) is best described as a distorted octahedron with the average twist angle (α) (**Fig. 3.1**) of 43.7(2)°. The bond lengths of Zn-N (tach) and Zn-N (pyridyl) in **250** (**Table 3.11**) are 2.160(3) Å and 2.165(4) Å, which compare well with those of other ZnN_6 complexes. Typical Zn-N distances in zinc hexamine complexes are 2.143(5) Å (Zn-N (amine)) and 2.215(5) Å (Zn-N (pyridyl)) in $[Zn(ampy)_3]^{2+}$ (ampy = tris(2-pyridylmethyl)amine)[287] and an average Zn-N distance of 2.23 Å in $[LZn]^{2+}$ (L = 1,4,7-tris(*o*-aminobenzyl)-1,4,7 triazacyclononane).[318]

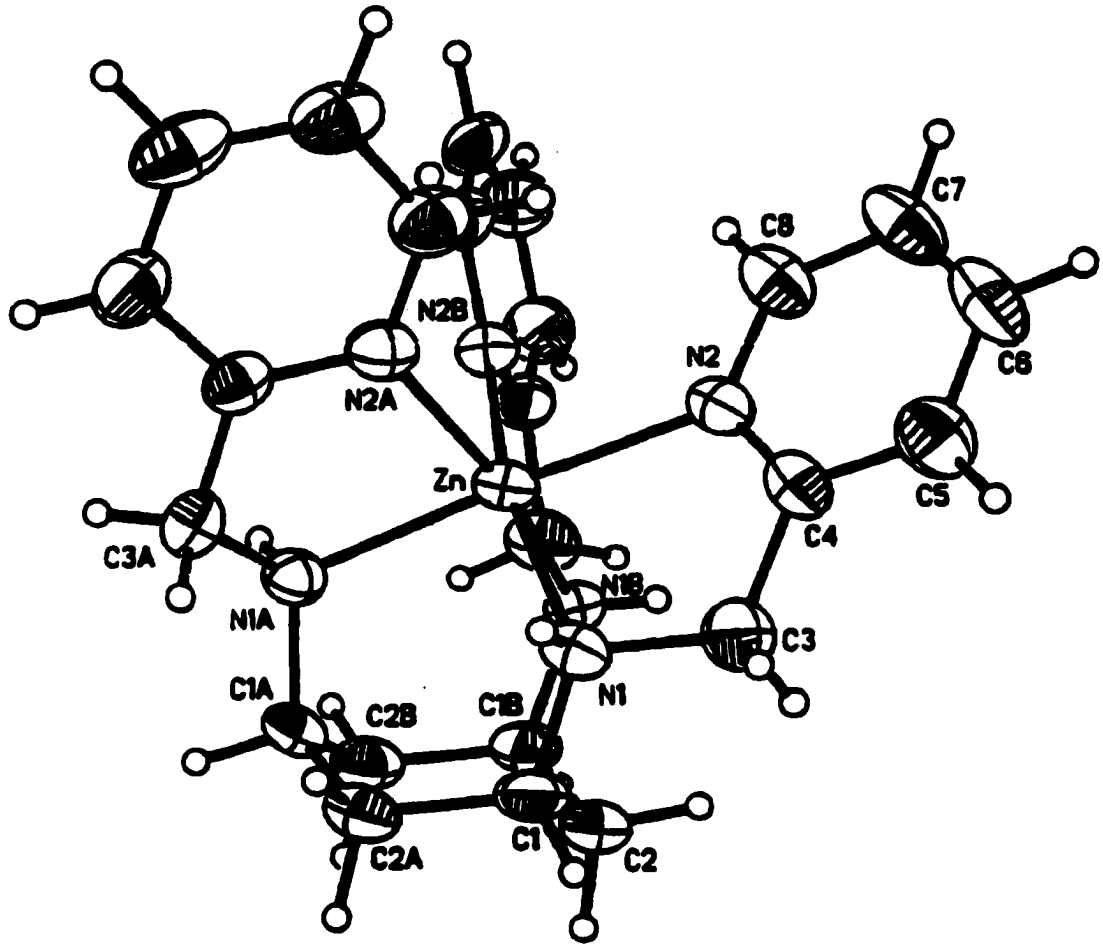

Figure 3.33. ORTEP view of $[Zn(tachpyr)](ClO_4)_2 \cdot CH_3OH$ (250) showing 50% probability of thermal ellipsoids.

Table 3.12. Selected Bond Distances (Å) and Bond Angles (deg) in $[Zn(tachpyr)](ClO_4)_2 \bullet CH_3OH$ (**250**).

Zn-N(1)A	2.160(3)	Zn-N(1)	2.160(3)
Zn-N(1)B	2.160(3)	Zn-N(2)B	2.165(4)
Zn-N(2)A	2.165(4)	Zn-N(2)	2.165(4)
N(1)-C(3)	1.475(5)	N(1)-C(1)	1.486(5)
N(2)-C(2)	1.337(6)	N(2)-C(8)	1.354(5)
C(1)-C(2)A	1.524(7)	C(1)-C(2)	1.528(7)
C(3)-C(4)	1.493(6)	C(5)-C(6)	1.390(7)
N(1)A-Zn-N(1)	90.21(14)	N(1)A-Zn-N(2)B	98.29(14)
N(1)-Zn-N(2)B	166.24(14)	N(1)B-Zn-N(2)B	79.01(14)
N(2)B-Zn-N(2)A	93.97(14)	C(3)-N(l)-C(l)	113.9(4)
C(3)-N(1)-Zn	110.8(3)	C(4)-N(2)-C(8)	117.6(4)
C(4)-N(2)-Zn	114.9(3)	C(8)-N(2)-Zn	126.9(3)
N(1)-C(1)-C(2)A	109.9(2)	N(1)-C(1)-C(2)	114.0(4)
C(2)A-C(l)-C(2)	110.4(5)	C(1)B-C(2)-C(1)	114.2(4)
N(1)-C(3)-C(4)	113.9(4)	N(2)-C(4)-C(5)	122.1(4)
C(4)-C(5)-C(6)	118.7(5)	C(7)-C(8)-N(2)	123.7(5)
N(2)-C(4)-C(3)	117.1(4)	C(5)-C(4)-C(3)	120.7(4)

Symmetry transformation used to generate equivalent atoms: A; z-1/2, -x-3/2, -y-1, and B; -y-3/2, -z-1, x+1/2

B.1.2. [Cu(tachpyr)]$(ClO_4)_2 \cdot 1/2CH_3CN$ (257). Blue prisms[331] suitable for X-ray crystallography were grown by Et_2O diffusion into a CH_3CN solution of the metal complex. The complex **257** crystallizes as a blue prism in the monoclinic space group $P2_1/n$.

The coordination geometry of CuN_6 in **257** (**Fig. 3.34 (a)**) is best described as an elongated tetragonal octahedron that is typical for hexa-coordinate Cu(II). Therefore, two trans nitrogen donors, N(3) (tach) and N(4) (pyridyl), bind weakly to Cu(II) affording longer Cu-N bond distances (**Table 3.13**), 2.245(5) Å for Cu-N(3) and 2.458(5) Å for Cu-N(4), respectively, than four equatorial Cu-N bond distances, 2.032(5) and 2.053(5) Å for Cu-N (pyridyl), 2.033(5) and 2.099(5) Å for Cu-N (tach), respectively.

The bond lengths of four equatorial Cu-N range from 2.032(5) to 2.099(5) Å, and axially elongated Cu-N bond lengths in **257** are 2.245(5) and 2.458(5) Å, respectively. Those bond lengths compare well with those of other CuN_6 complexes. Typical equatorial Cu-N distances in copper(II) hexaamine complexes range from 1.965(5) and 2.085(4) Å and range from 2.061(6) to 2.078(6), respectively, in $[Cu(terpy)_2](NO_3)_2$ (terpy = **165** (**Fig. 3.4**))[319] and in $[Cu(tach)_2](ClO_4)_2$ (tach = **219** (**Scheme 3.1**).[302] The $[Cu(terpy)_2](NO_3)_2$ and $[Cu(tach)_2](ClO_4)_2$ complexes show elongated Cu-N bond distances of 2.288(4) and 2.353(7) Å, which are comparable to those of **257**, 2.245(5) and 2.458(5) Å.

B.1.3. [Cu(tachpyr)]$(ClO_4)_2 \cdot CH_3OH$ (257A). Green crystals[331] suitable for X-ray crystallography were grown by Et_2O diffusion into a CH_3CN solution of the metal complex. The complex **257A** crystallizes as a green crystal in the cubic space group $P2_13$.

The coordination geometry of CuN_6 in **257A** (**Fig. 3.34 (b)**) shows a slightly distorted octahedral geometry rather than a tetragonally elongated octahedral geometry that is typical for hexa-coordinate Cu(II) due to the Jahn-Teller effect. The bond lengths of Cu-N (tach) and Cu-N (pyridyl) in **257A** (**Table 3.13A**) are 2.116(5) Å and 2.143(6) Å, which compare well with those of other Cu(II) complexes which have dynamic Jahn-Teller distortion in the CuN_6 polyhedron.

Typical Cu-N distances in the dynamic Jahn-Teller distorted copper hexamine complexes are 2.173(6) and 2.164(3) Å in $[Cu(tach)_2](NO_3)_2$[302] and range from 2.098(3) to 2.234(3) Å in $[Cu([9]aneN_3)_2][Cu(CN)_3] \cdot 2H_2O$.[320]

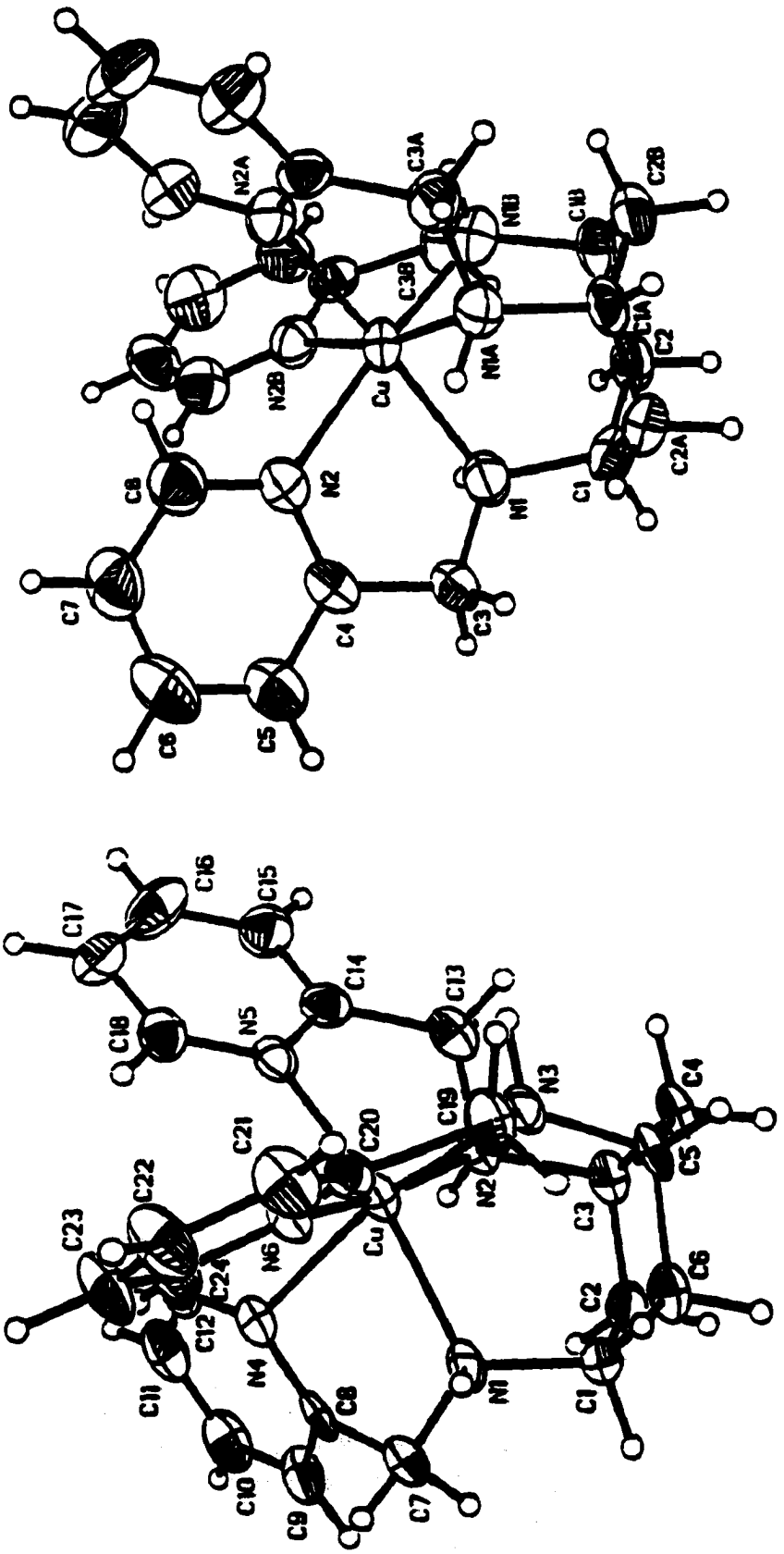

Figure 3.34. ORTEP view of the Cu(II) tachpyr complexes showing 50% probability of thermal ellipsoids: (a) $[Cu(tachpyr)](ClO_4)_2 \cdot 1/2CH_3CN$ (257), (b) $[Cu(tachpyr)](ClO_4)_2 \cdot CH_3OH$ (257A).

Table 3.13. Selected Bond Distances (Å) and Bond Angles (deg) in [Cu(tachpyr)]$(ClO_4)_2 \bullet 1/2CH_3CN$ (257)

Cu-N(6)	2.032(5)	Cu-N(2)	2.033(5)
Cu-N(5)	2.053(5)	Cu-N(1)	2.099(5)
Cu-N(3)	2.245(5)	Cu-N(4)	2.458(5)
N(1)-C(1)	1.494(7)	N(1)-C(7)	1.505(7)
N(4)-C(8)	1.342(8)	N(4)-C(12)	1.355(8)
C(1)-C(2)	1.517(8)	C(1)-C(6)	1.528(8)
C(7)-C(8)	1.497(8)	C(8)-C(9)	1.400(8)
N(6)-Cu-N(2)	168.3(2)	N(6)-Cu-N(5)	97.2(2)
N(2)-Cu-N(5)	81.9(2)	N(6)-Cu-N(1)	91.1(2)
N(2)-Cu-N(1)	93.0(2)	N(5)-Cu-N(l)	163.1(2)
N(5)-Cu-N(3)	105.4(2)	N(1)-Cu-N(3)	90.6(2)
C(1)-N(1)-C(7)	112.4(5)	C(1)-N(1)-Cu	114.1(4)
N(1)-C(1)-C(2)	112.4(5)	N(1)-C(1)-C(6)	110.2(5)
C(2)-C(l)-C(6)	111.3(5)	C(1)-C(2)-C(3)	113.9(5)
N(2)-C(3)-C(4)	113.1(5)	N(2)-C(3)-C(2)	109.4(5)
C(4)-C(3)-C(2)	110.4(5)	C(8)-C(7)-N(1)	115.5(5)
N(4)-C(8)-C(9)	122.0(6)	N(4)-C(12)-C(11)	122.5(6)

Table 3.13A. Selected Bond Distances (Å) and Bond Angles (deg) in $[Cu(tachpyr)](ClO_4)_2 \bullet CH_3OH$ (257A)

Cu-N(1)A	2.116(5)	Cu-N(1)	2.116(5)
Cu-N(1)B	2.116(5)	Cu-N(2)A	2.143(6)
Cu-N(2)	2.143(6)	Cu-N(2)B	2.143(6)
N(1)-C(1)	1.494(9)	N(1)-C(3)	1.466(9)
N(2)-C(4)	1.327(9)	N(2)-C(8)	1.344(9)
C(1)-C(2)	1.503(10)	C(1)-C(2)B	1.546(11)
C(4)-C(5)	1.379(10)	C(5)-C(6)	1.391(13)
N(1)A-Cu-N(1)	91.4(2)	N(1)A-Cu-N(2)A	79.9(2)
N(1)-Cu-N(2)A	96.8(2)	N(1)B-Cu-N(2)A	168.2(2)
N(2)A-Cu-N(2)	93.0(2)	N(1)-Cu-N(1)B	91.4(2)
N(1)-Cu-N(2)	79.9(2)	N(1)A-Cu-N(2)B	96.8(2)
N(1)-Cu-N(2)B	168.2(2)	N(2)A-Cu-N(2)B	93.0(2)
C(3)-N(1)-C(1)	113.5(6)	C(3)-N(1)-Cu	111.5(5)
N(1)-C(1)-C(2)	109.8(6)	N(1)-C(1)-C(2)B	111.9(6)
C(2)-C(l)-C(2)B	112.4(7)	C(1)-C(2)-C(1)A	113.6(7)
N(2)-C(4)-C(3)	117.0(6)	N(2)-C(4)-C(5)	123.3(7)
C(4)-C(5)-C(6)	117.4(8)	C(8)-C(7)-C(6)	118.8(8)
N(2)-C(8)-C(7)	123.1(8)		

Symmetry transformations used to generate equivalent atoms: A; y+1/2, -z-1/2, -x, and B; -z, x-1/2, -y-1/2

B.1.4. [Ni(tachpyr)](Cl)$_2$•CH$_3$OH (262). Purple prisms[332] suitable for X-ray crystallography were grown by Et_2O diffusion into a MeOH solution of the metal complex. The complex **262** crystallizes as a purple prism in the monoclinic space group $P2_1/n$.

The coordination geometry of NiN_6 in **262** (**Fig. 3.35**) is best described as a distorted octahedron with the average twist angle (α) (**Fig. 3.1**) of 45.5°. The bond lengths of Ni-N (tach) in **262** (**Table 3.14**) are 2.099(4) and 2.107(4) Å and the bond lengths of Ni-N (pyridyl) in **262** are 2.118(4), 2.122(4), and 2.127(4) Å. These bond lengths compare well with those of other NiN_6 complexes. Typical Ni-N (amine) distances in nickel hexamine complexes are 2.131(3) and 2.134(2) Å in $[Ni(tach)_2](NO_3)_2$ (tach = **219** (**Scheme 3.1**).[302] The average Ni-N (amine) and Ni-N (pyridyl) distances are 2.109(5) and 2.054(5) Å, respectively, in $[Ni(tmptacn)]^{2+}$ (tmptacn = 1,4,7-tris(2-pyridylmethyl)-1,4,7 triazacyclononane).[321]

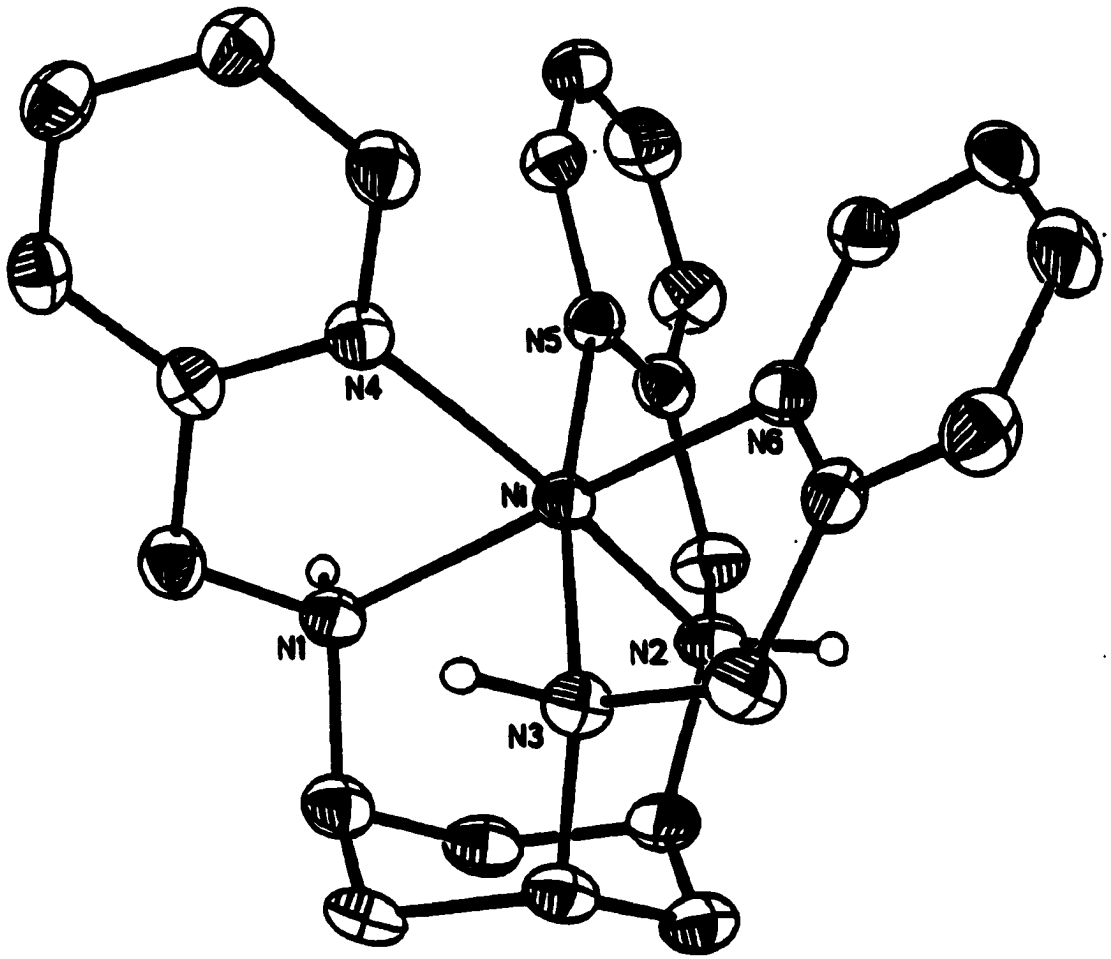

Figure 3.35. ORTEP view of [Ni(tachpyr)](Cl)$_2$•CH$_3$OH (262) showing 50% probability of thermal ellipsoids.

Table 3.14. Selected Bond Distances (Å) and Bond Angles (deg) in [Ni(tachpyr)]$(Cl)_2 \cdot CH_3OH$ (262).

Ni-N(3)	2.099(4)	Ni-N(2)	2.099(4)
Ni-N(1)	2.107(4)	Ni-N(4)	2.118(4)
Ni-N(5)	2.122(4)	Ni-N(6)	2.127(4)
N(1)-C(7)	1.474(6)	N(1)-C(1)	1.492(6)
N(4)-C(8)	1.350(6)	N(4)-C(12)	1.354(6)
C(1)-C(2)	1.522(7)	C(1)-C(6)	1.526(7)
C(7)-C(8)	1.504(7)	C(8)-C(9)	1.380(7)
N(3)-Ni-N(2)	92.7(2)	N(3)-Ni-N(1)	88.8(2)
N(3)-Ni-N(4)	96.6(2)	N(2)-Ni-N(4)	166.1(2)
N(2)-Ni-N(5)	79.7(2)	N(1)-Ni-N(6)	166.8(2)
N(5)-Ni-N(6)	94.7(2)	N(4)-Ni-N(6)	93.9(2)
C(7)-N(1)-C(1)	111.2(4)	C(7)-N(1)-Ni	111.5(3)
C(1)-N(1)-Ni	116.1(3)	N(1)-C(1)-C(6)	113.1(4)
C(2)-C(1)-C(6)	109.5(4)	C(3)-C(2)-C(1)	114.8(4)
N(2)-C(3)-C(4)	109.2(4)	N(2)-C(3)-C(2)	112.5(4)
C(4)-C(3)-C(2)	110.7(4)	C(21)-C(20)-C(19)	120.0(5)
N(4)-C(8)-C(9)	123.0(5)	N(4)-C(12)-C(11)	123.4(5)

B.1.5. [Mn(tachpyr)]$(ClO_4)_2$ (271). Yellow crystals suitable for X-ray crystallography were grown by Et_2O diffusion into a CH_3CN solution of the metal complex. The complex **271** crystallizes as a yellow crystal in the monoclinic space group $P2_1/c$.

The coordination geometry of MnN_6 in **271** (**Fig. 3.36**) is best described as a slightly distorted trigonal-prismatic with the average twist angle (α) (**Fig. 3.1**) of 2.48(2)°. The bond lengths of Mn-N (tach) in **271** (**Table 3.15**) are 2.233(2), 2.236(2), and 2.245(2) Å, and the bond lengths of Mn-N (pyridyl) in **271** are 2.283(2), 2.292(2), and 2.299(2) Å. These bond lengths compare well with those of other MnN_6 complexes. Typical Mn-N (amine) distances in manganese hexamine complexes are 2.266(6) Å in $[Mn(ampy)_3](ClO_4)_2$ (ampy = tris(2-pyridylmethyl)amine)[322] and 2.278(6, 2.291(5), and 2.286(6) Å in $[Mn(tmptacn)]^{2+}$ (tmptacn = 1,4,7-tris(2-pyridylmethyl)-1,4,7 triazacyclononane).[321] The Mn-N (pyridyl) distances are 2.266(5) Å in $[Mn(ampy)_3](ClO_4)_2$(ampy = tris(2-pyridylmethyl)amine)[322] and 2.207(5), 2.203(6), and 2.229(6) Å in $[Mn(tmptacn)]^{2+}$ (tmptacn = 1,4,7-tris(2-pyridylmethyl)-1,4,7 triazacyclononane).[321]

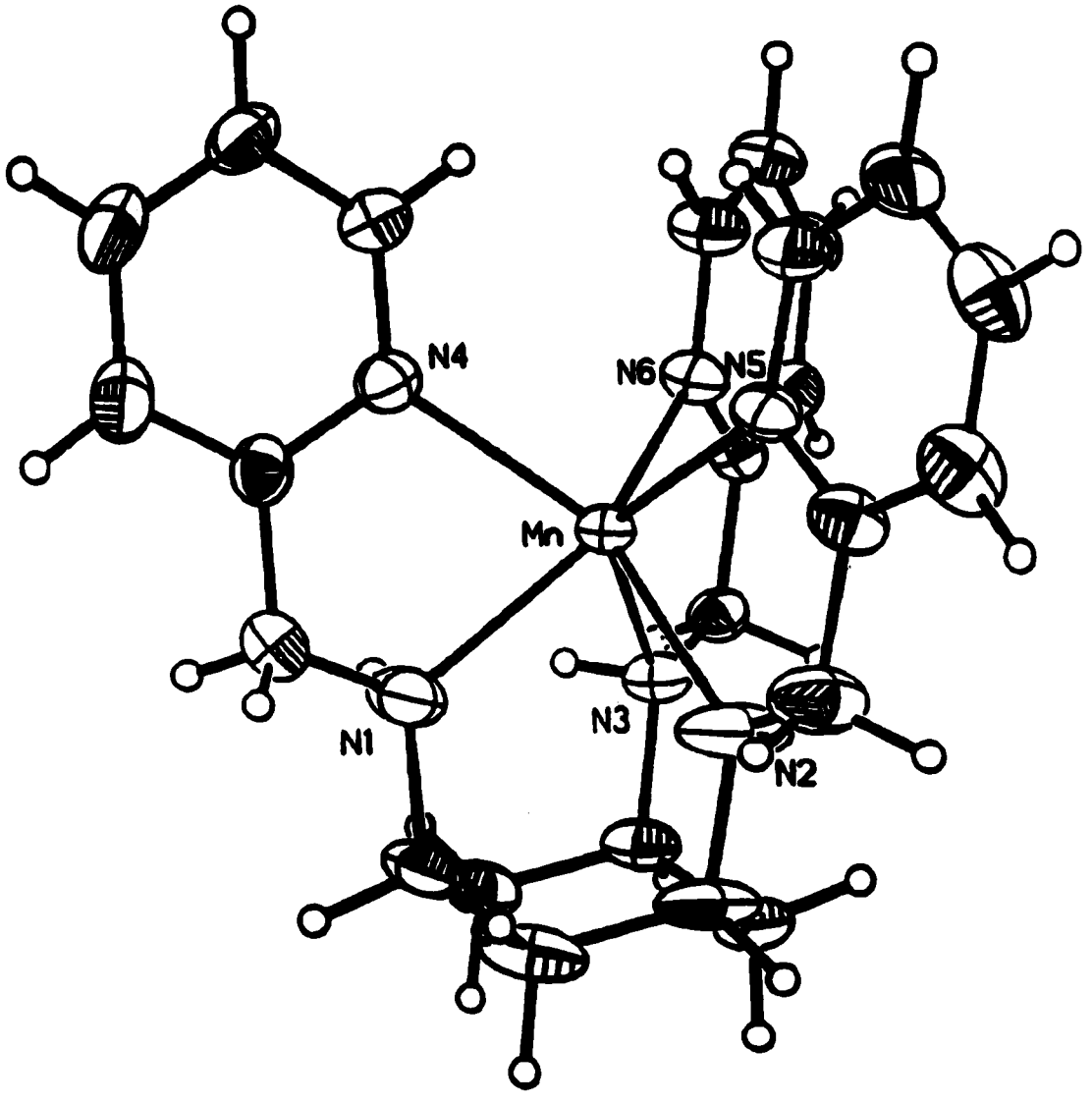

Figure 3.36. ORTEP view of $[Mn(tachpyr)](ClO_4)_2$ **(271)** showing 50% probability of thermal ellipsoids.

Table 3.15. Selected Bond Distances (Å) and Bond Angles (deg) in [Mn(tachpyr)]$(ClO_4)_2$ (271).

Mn-N(3)	2.233(2)	Mn-N(2)	2.236(2)
Mn-N(1)	2.245(2)	Mn-N(6)	2.283(2)
Mn-N(4)	2.292(2)	Mn-N(5)	2.299(2)
N(1)-C(7)	1.283(3)	N(1)-C(1)	1.481(3)
N(4)-C(8)	1.347(3)	N(4)-C(12)	1.347(3)
C(1)-C(2)	1.533(4)	C(1)-C(6)	1.522(3)
C(7)-C(8)	1.483(3)	C(8)-C(9)	1.396(3)
N(3)-Mn-N(2)	80.97(8)	N(3)-Mn-N(1)	81.82(7)
N(3)-Mn-N(6)	73.62(6)	N(2)-Mn-N(4)	131.08(9)
N(2)-Mn-N(5)	72.61(7)	N(1)-Mn-N(6)	135.58(8)
N(6)-Mn-N(5)	94.87(6)	N(6)-Mn-N(4)	97.59(6)
C(7)-N(1)-C(1)	118.8(2)	C(7)-N(1)-Mn	116.4(2)
C(1)-N(1)-Mn	123.3(2)	N(1)-C(1)-C(6)	110.9(2)
C(6)-C(l)-C(2)	110.8(2)	C(3)-C(2)-C(1)	113.9(2)
N(2)-C(3)-C(4)	110.2(2)	N(2)-C(3)-C(2)	110.1(2)
C(4)-C(3)-C(2)	111.2(2)	C(21)-C(20)-C(19)	121.1(2)
N(4)-C(12)-C(11)	123.3(2)	N(4)-C(8)-C(7)	116.2(2)

B.1.6. [Cd(tachpyr)](ClO$_4$)$_2$ (275). Single crystals suitable for X-ray crystallography were grown by Et_2O diffusion a the CH_3CN solution of the metal complex. The complex **275** crystallizes as a colorless crystal in the monoclinic space group $P2_1/c$.

The structures were solved by direct methods. The cyclohexyl group and three nitrogens bonded to it in **275** are disordered and resolved into two orientations with N1-C6 at 60% occupancy and N1′-C6′ at 40% occupancy. The two orientations differ in a twist of the chair conformation of the cyclohexyl ring. High thermal motion was also observed for anions as often found for perchlorate ions. Disorder molecules were not resolvable for these molecules.

The coordination geometry of CdN_6 in **275** (**Fig. 3.37**) is best classified as an intermediate between octahedral and trigonal-prismatic with the average twist angle (α) (**Fig. 3.1**) for two disordered molecule 1 and 2 of 20.8(4)° and 11.4(9)°, respectively. The bond lengths of Cd-N (tach) in **275** (**Table 3.16**) range between 2.302(6) Å and 2.422(6) Å (average 2.36(2) Å). The bond lengths of Cd-N (pyridyl) in **275** range between 2.352(4) Å and 2.361(4) Å (average 2.357(7) Å). These bond lengths compare well with those of other CdN_6 complexes. Typical Cd-N distances in cadmium hexamine complexes are 2.34(2) – 2.42(2) Å (Cd-N in $[Cd(en)_3]^{2+}$ (en = ethylenediamine))[318], and 2.338(3) Å (Cd-N (amine)) and 2.343(4) – 2.370(4) Å (Cd-N (pyridyl)) in $[Cd(bispicam)_2]^{2+}$ (bispicam = bis(2-pyridylmethyl)amine).[286]

Table 3.16. Selected Bond Distances (Å) and Bond Angles (deg) in [Cd(tachpyr)]$(ClO_4)_2$ (275).

Disorder molecule 1			
Cd-N(3)	2.302(6)	Cd-N(5)	2.352(4)
Cd-N(6)	2.359(4)	Cd-N(4)	2.361(4)
Cd-N(2)	2.388(6)	Cd-N(1)	2.400(5)
N(1)-C(7)	1.453(8)	N(4)-C(8)	1.346(10)
N(4)-C(12)	1.350(6)	N(1)-Cd-N(4)	71.2(2)
N(2)-Cd-N(5)	71.0(2)	N(3)-Cd-N(6)	73.0(2)
N(1)-Cd-N(2)	80.2(2)	N(1)-Cd-N(5)	141.9(2)
N(4)-Cd-N(6)	98.20(14)	N(4)-Cd-N(2)	111.1(2)
C(1)-N(1)-Cd	118.2(4)	C(1)-N(1)-C7	114.3(6)
C(8)-N(4)-Cd	114.0(3)	C(12)-N(4)-Cd	125.7(3)
Additional parameters derived from disorder molecule 2			
Cd-N(1')	2.332(13)	Cd-N(2')	2.347(9)
Cd-N(3')	2.422(9)	N(1')-C(7)	1.28(2)
N(1)-C(1')	1.55(2)	N(1')-Cd-N(4)	70.4(3)
N(2')-Cd-N(5)	71.9(2)	N(3')-Cd-N(6)	71.6(2)
N(1')-Cd-N(2')	81.7(5)	N(1')-Cd-N(5)	120.8(6)
N(4)-Cd-N(2')	138.3(3)	C(1')-N(1')-Cd	116.0(9)

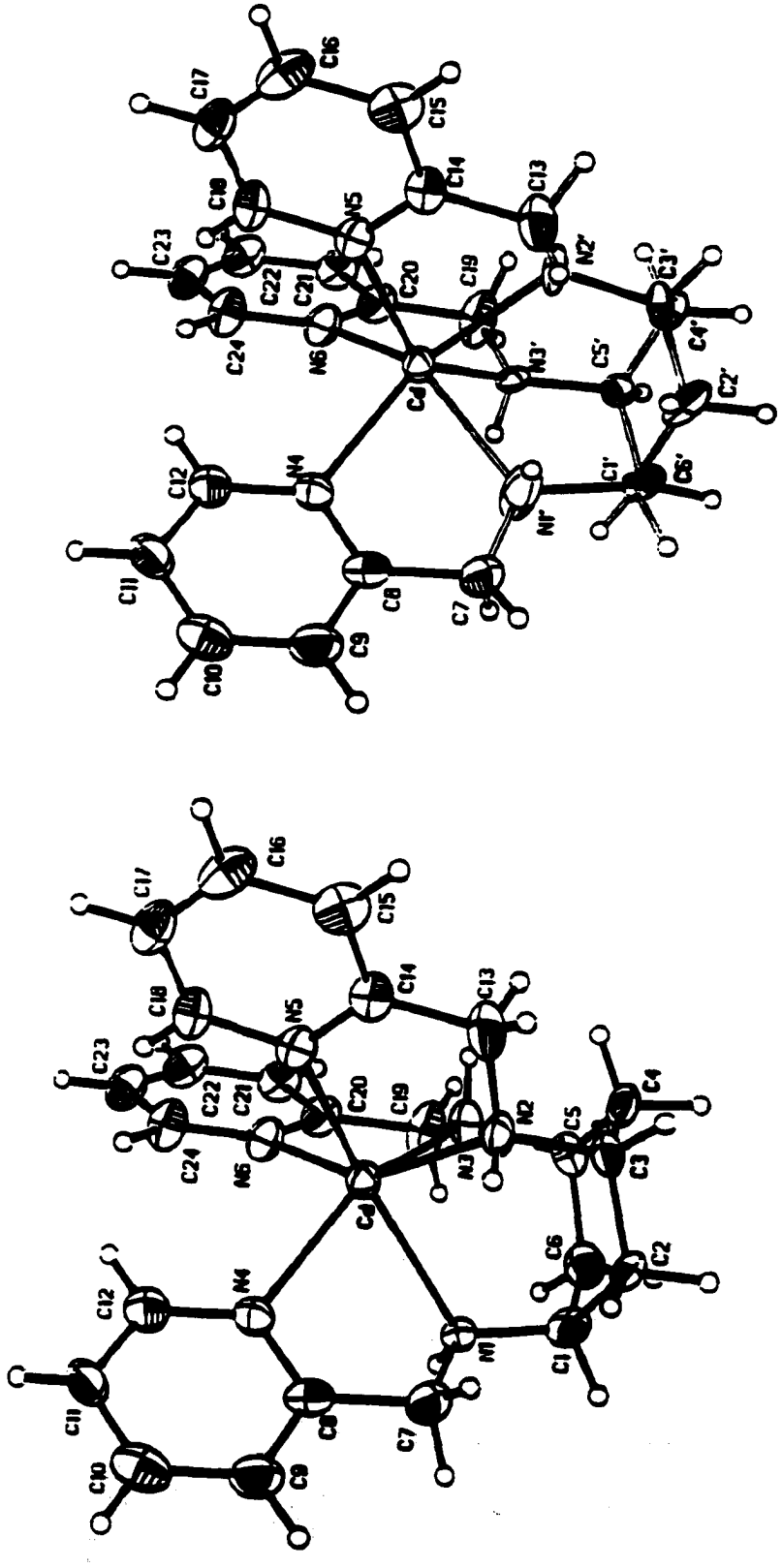

Figure 3.37. ORTEP view (50% probability of thermal ellipsoids) of $[Cd(tachpyr)](ClO_4)_2$ (275) showing two disordered molecules with N1-C6 at 60% occupancy (a) and N1'-C6' at 40% occupancy (b).

B.1.7. [Hg(tachpyr)]$(ClO_4)_2$ (276). Colorless prisms suitable for X-ray crystallography were grown by Et_2O diffusion into a CH_3CN solution of the metal complex. The complex **276** crystallizes as a colorless prism in the monoclinic space group $P2_1/c$.

There is some evidence in the structure of **276** for the disorder observed for [Cd(tachpyr)]$(ClO_4)_2$ **275**, the slight elongation of thermal ellipsoids for N2, N3, and some of the cyclohexyl carbon atoms could not be resolved into a reasonable disorder molecule. The slight elongation of thermal ellipsoids could affect quantitative parameters, although the overall structure is clear.

The coordination geometry of HgN_6 in **276** (**Fig. 3.38**) is best described as a slightly distorted trigonal-prismatic with the average twist angle (α) (**Fig. 3.1**) of 5(1)°. The bond lengths of Hg-N (tach) in **276** (**Table 3.17**) range between 2.335(6) Å and 2.487(6) Å (average 2.420(9) Å). The bond lengths of Hg-N (pyridyl) in **276** range between 2.334(4) Å and 2.461(4) Å (average 2.391(7) Å). These bond lengths compare well with those of other HgN_6 complexes. Typical Hg-N distances in HgN_6 complexes are 2.350(4) – 2.404(4) Å (Hg-N (amine)) and 2.352(4) – 2.557(5) Å (Hg-N (pyridyl)) in $[Hg(bispicam)_2]^{2+}$[323] and an average Hg-N distance of 2.43 Å in $[LHg]^{2+}$ (L = 1,4,7-tris(*o*-aminobenzyl)-1,4,7-triazacyclononane).[287]

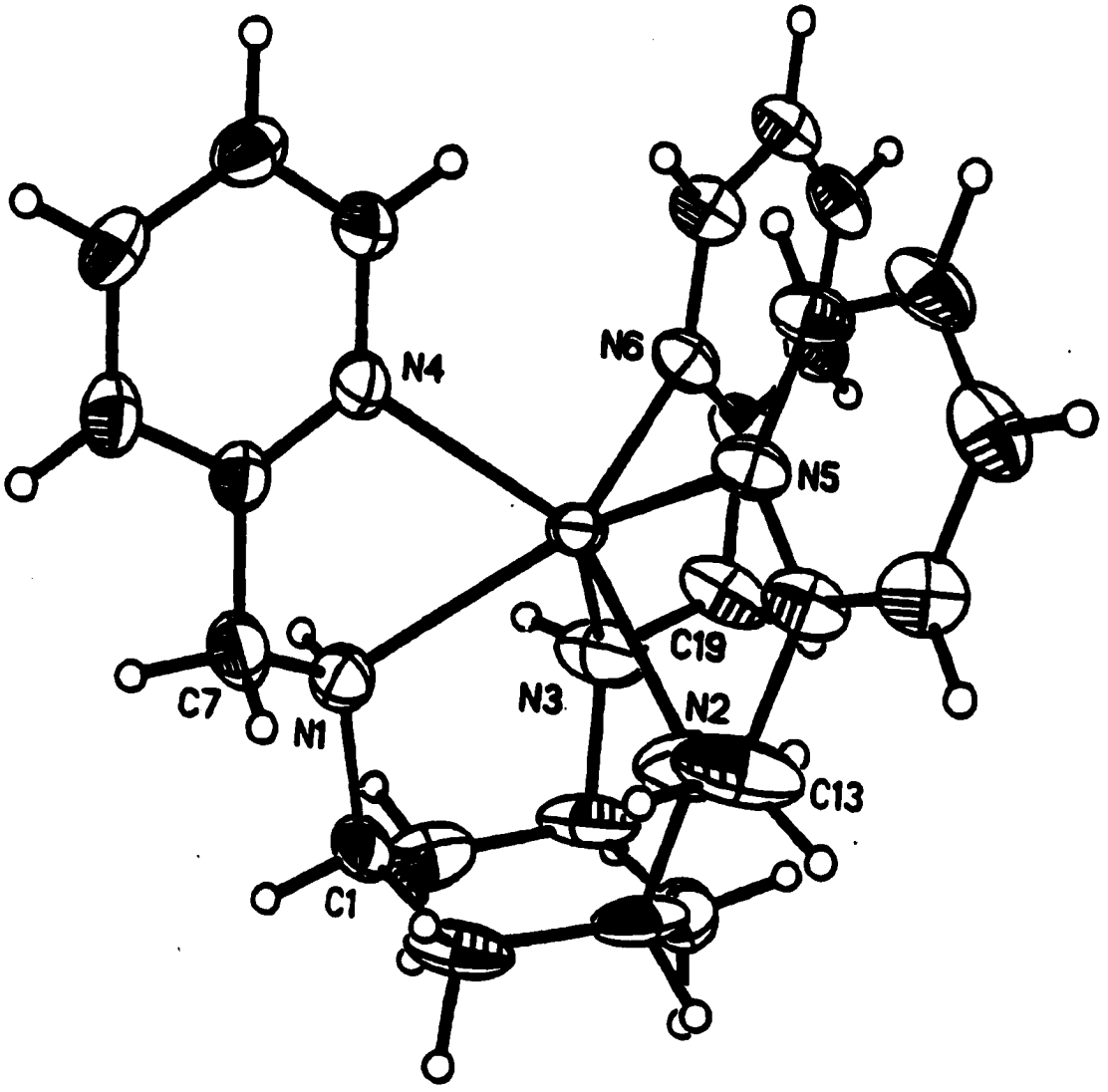

Figure 3.38. ORTEP view of $[Hg(tachpyr)](ClO_4)_2$ (276) showing 50% probability of thermal ellipsoids.

Table 3.17. Selected Bond Distances (Å) and Bond Angles (deg) in [Hg(tachpyr)]$(ClO_4)_2$ (276).

Hg-N(6)	2.334(4)	Hg-N(2)	2.335(6)
Hg-N(4)	2.377(4)	Hg-N(1)	2.438(4)
Hg-N(5)	2.461(4)	Hg-N(3)	2.487(6)
N(1)-C(7)	1.449(7)	N(1)-C(1)	1.502(7)
N(4)-C(8)	1.339(6)	N(4)-C(12)	1.361(7)
C(1)-C(2)	1.540(8)	C(1)-C(6)	1.495(8)
C(7)-C(8)	1.514(7)	C(8)-C(9)	1.389(7)
N(3)-Hg-N(2)	96.95(13)	N(3)-Hg-N(1)	75.0(2)
N(3)-Hg-N(6)	71.0(2)	N(2)-Hg-N(4)	127.9(3)
N(2)-Hg-N(5)	69.4(2)	N(1)-Hg-N(6)	128.21(14)
N(6)-Hg-N(5)	96.95(13)	N(6)-Hg-N(4)	105.5(2)
C(7)-N(1)-C(1)	114.5(4)	C(7)-N(1)-Hg	107.8(3)
C(1)-N(1)-Hg	115.6(3)	N(1)-C(1)-C(2)	114.3(4)
C(6)-C(l)-C(2)	109.8(5)	C(1)-C(2)-C(3)	115.3(5)
N(2)-C(3)-C(4)	108.6(6)	N(2)-C(3)-C(2)	113.6(6)
C(4)-C(3)-C(2)	111.1(5)	C(21)-C(20)-C(19)	120.3(5)
N(4)-C(12)-C(11)	122.9(5)	N(4)-C(8)-C(7)	118.7(4)

B.2. $[M(tach\text{-}Me_3pyr)](X)_2$ ($M = Zn^{2+}$, Cu^{2+}, and Ni^{2+}, and $X = ClO_4^-$)

B.2.1. $[Zn(tach\text{-}Me_3pyr)](ClO_4)_2$ (251). Colorless needles suitable for X-ray crystallography were grown by Et_2O diffusion into a CH_3CN solution of the metal complex. The complex **251** crystallizes as a colorless needle in the trigonal space group *P31c*.

The coordination geometry of ZnN_6 in **251** (**Fig. 3.39**) is best described as a slightly distorted octahedron with the average twist angle (α) (**Fig. 3.1**) of 43.2(2)°. The bond length of Zn-N (tach) and the bond length of Zn-N (pyridyl) in **251** (**Table 3.18**) are 2.228(2) Å and 2.165(2) Å, respectively. These bond lengths are well comparable to 2.160(3) and 2.165(4) Å, Zn-N (tach) and Zn-N (pyridyl), respectively, in $[Zn(tachpyr)](ClO_4)_2$ (**250**).

B.2.2. $[Cu(tach\text{-}Me_3pyr)](ClO_4)_2$ (258). Blue crystals suitable for X-ray crystallography were obtained by Et_2O diffusion into a DMF solution of the complex. The complex **258** crystallizes as a light blue crystal in the monoclinic space group $P2_1$.

The coordination geometry of CuN_6 in **258** (**Fig. 3.40**) is best described as an axially elongated octahedron with the average twist angle(α) (**Fig. 3.1**) of 44.9(3)°. The elongated trans nitrogen donors, N(1) and N(5), bind weakly to Cu(II) affording longer Cu-N bond distances, 2.325(4) Å for Cu-N(1) and 2.336(4) Å for Cu-N(5), respectively, than four equatorial Cu-N bond distances, 2.067(4), 2.071(4), 2.091(4), and 2.159(4) Å, respectively. These bond lengths are well comparable to 2.245(5) and 2.458(5) Å for the axially elongated Cu-N bond

lengths, and to the range from 2.032(5) to 2.099(5) Å for the remaining Cu-N distance in [Cu(tachpyr)]$(ClO_4)_2 \bullet 1/2CH_3CN$ (257).

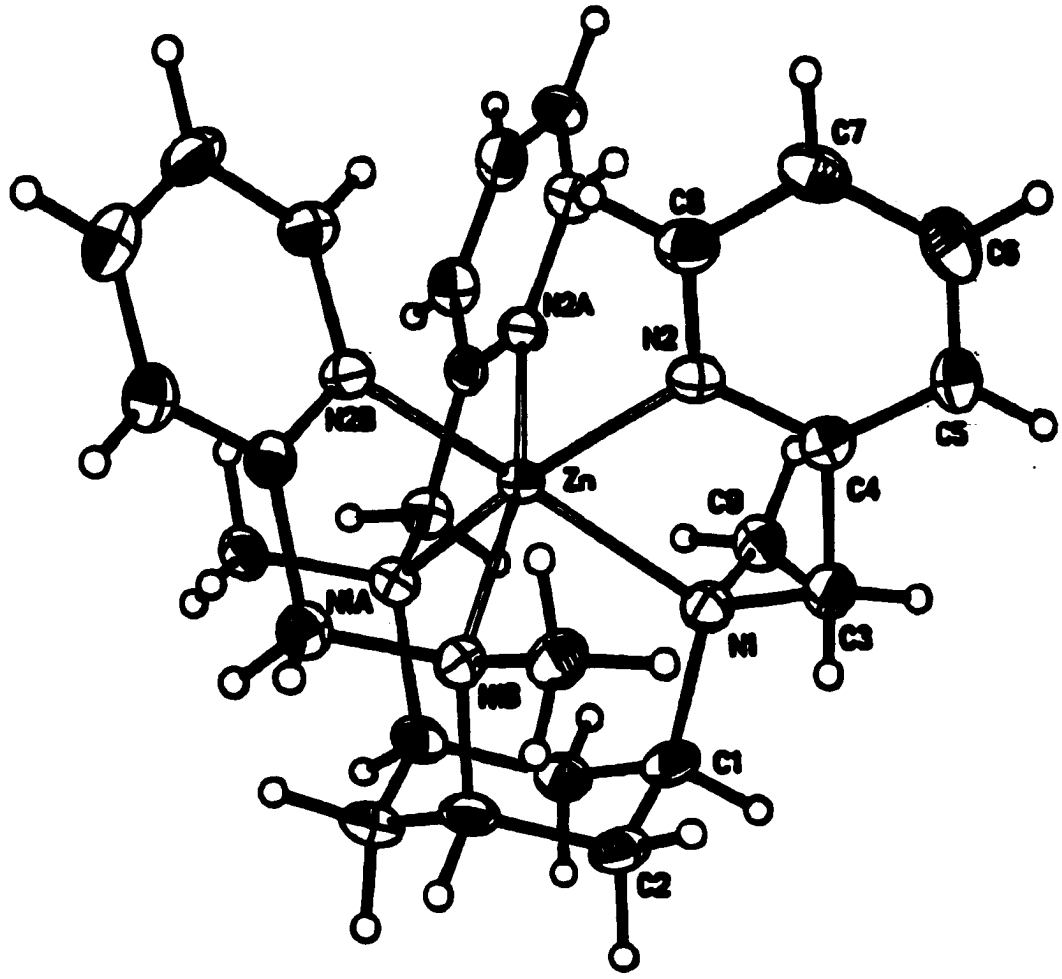

Figure 3.39. ORTEP view of [Zn(tach-Me_3pyr)]$(ClO_4)_2$ (251) showing 50% probability of thermal ellipsoids.

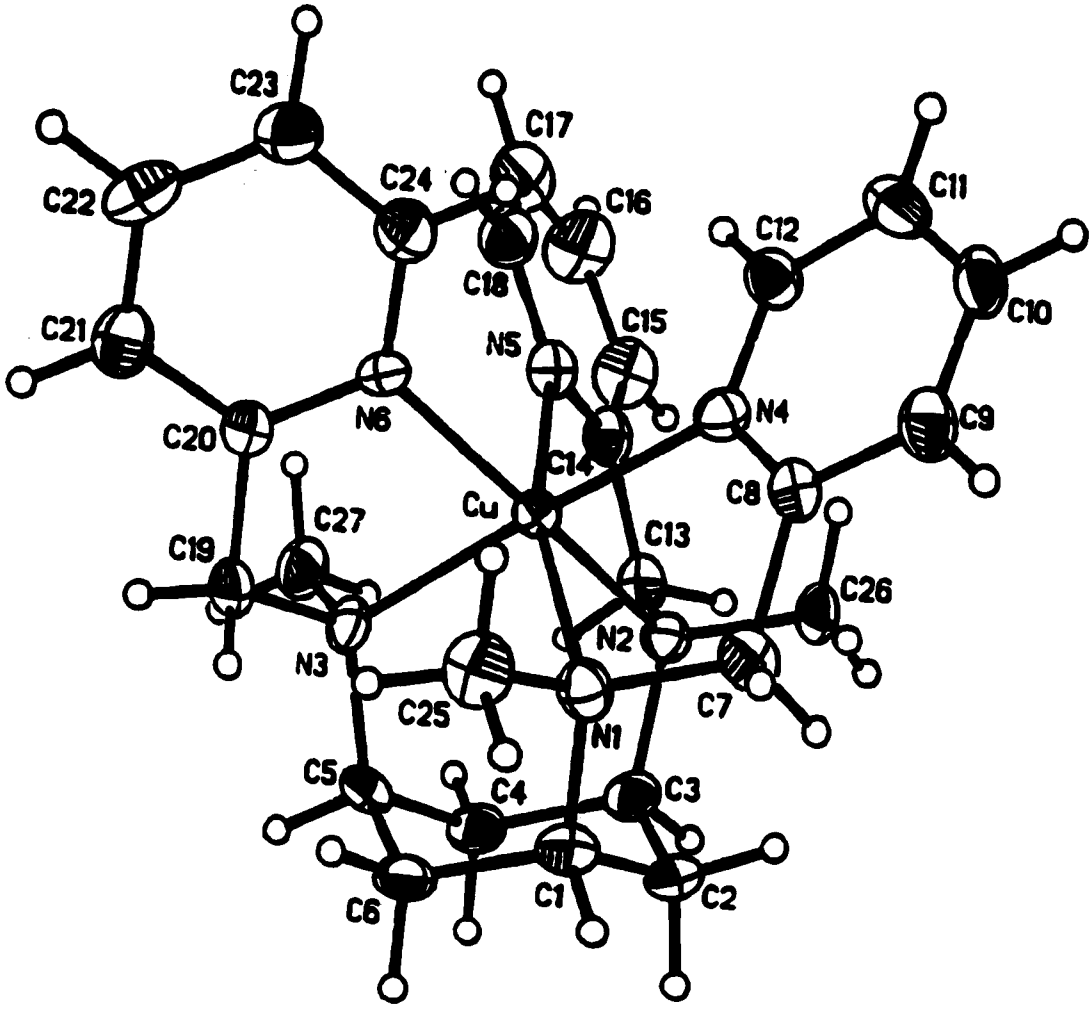

Figure 3.40. ORTEP view of [Cu(tach-Me_3pyr)]$(ClO_4)_2$ (258) showing 50% probability of thermal ellipsoids.

Table 3.18. Selected Bond Distances (Å) and Bond Angles (deg) in [Zn(tach-Me_3pyr)]$(ClO_4)_2$ (251).

Zn-N(2)A	2.165(2)	Zn-N(2)B	2.165(2)
Zn-N(2)	2.165(2)	Zn-N(1)A	2.228(2)
Zn-N(1)B	2.228(2)	Zn-N(1)	2.228(2)
N(1)-C(3)	1.485(3)	N(1)-C(9)	1.490(3)
N(1)-C(1)	1.510(3)	N(2)-C(4)	1.340(3)
C(1)-C(2)	1.532(3)	C(1)-C(2)B	1.531(3)
C(3)-C(4)	1.501(3)	C(7)-C(8)	1.381(3)
N(2)A-Zn-N(2)B	94.57(7)	N(2)A-Zn-N(1)A	77.71(7)
N(2)B-Zn-N(1)A	165.75(6)	N(2)A-Zn-N(1)A	97.95(7)
N(1)A-Zn-N(1)B	91.37(7)	C(3)-N(1)-C(9)	104.4(2)
C(3)-N(1)-C(1)	111.2(2)	C(3)-N(1)-Zn	110.03(13)
C(1)-N(1)-Zn	111.14(13)	N(1)-C(1)-C(2)	114.2(2)
N(1)-C(1)-C(2)B	112.1(2)	C(8)-N(2)-Zn	125.7(2)
C(1)-C(2)-C(1)A	115.8(2)	N(2)-C(3)-C(4)	121.6(2)
C(5)-C(4)-C(3)	120.5(2)	C(6)-C(5)-C(4)	119.2(2)
N(2)-C(8)-C(7)	122.6(2)	N(2)-C(4)-C(3)	117.7(2)

Symmetry transformation used to generate equivalent atoms: A ; -x+y+1, -x+1, z B; -y+1, x-y, z

Table 3.19. Selected Bond Distances (Å) and Bond Angles (deg) in [Cu(tach-Me_3pyr)]$(ClO_4)_2$ (258).

Cu-N(6)	2.067(4)	Cu-N(4)	2.071(4)
Cu-N(3)	2.091(4)	Cu-N(2)	2.159(4)
Cu-N(1)	2.325(4)	Cu-N(5)	2.336(4)
N(1)-C(7)	1.492(6)	N(1)-C(1)	1.499(6)
N(4)-C(8)	1.339(6)	N(4)-C(12)	1.351(7)
C(1)-C(2)	1.534(7)	C(1)-C(6)	1.529(7)
C(7)-C(8)	1.496(7)	C(8)-C(9)	1.394(6)
N(6)-Cu-N(4)	92.5(2)	N(6)-Cu-N(3)	81.7(2)
N(6)-Cu-N(2)	168.12(14)	N(4)-Cu-N(2)	95.0(2)
N(4)-Cu-N(1)	77.8(2)	N(6)-Cu-N(1)	97.9(2)
N(1)-Cu-N(5)	166.16(14)	N(4)-Cu-N(5)	94.3(2)
C(7)-N(1)-C(1)	112.0(4)	C(7)-N(1)-Cu	113.8(3)
C(1)-N(1)-Cu	108.1(3)	N(1)-C(1)-C(2)	115.0(4)
C(6)-C(l)-C(2)	108.6(4)	C(1)-C(2)-C(3)	115.5(4)
N(2)-C(3)-C(4)	114.0(4)	N(2)-C(3)-C(2)	113.3(4)
C(4)-C(3)-C(2)	108.6(4)	C(21)-C(20)-C(19)	122.3(5)
N(4)-C(12)-C(11)	123.0(5)	N(4)-C(8)-C(7)	119.3(4)

B.2.3. [Ni(tach-Me$_3$pyr)](ClO$_4$)$_2$•CH$_3$CN (263). Violet prisms[331] suitable for X-ray crystallography were obtained by Et_2O diffusion into a CH_3CN solution of the complex. The complex **263** crystallizes as a violet prism in the triclinic space group *P-1*.

The coordination geometry of NiN_6 in **263** (**Fig. 3.41**) is best described as a distorted octahedron with the average twist angle (α) (**Fig. 3.1**) of 48.1(3)°. The bond lengths of Ni-N (tach) in **263** (**Table 3.20**) are 2.159(4), 2.170(4), and 2.172(4) Å. The bond lengths of Ni-N (pyridyl) in **263** are 2.106(3), 2.107(4), and 2.108(3) Å. These bond lengths can be compared to 2.099(4), 2.099(4), and 2.107(4) Å, Ni-N (tach), and to 2.118(4), 2.122(4), and 2.127(4) Å, Ni-N (pyridyl), respectively, in [Ni(tachpyr)](Cl)$_2$•CH_3OH (**262**).

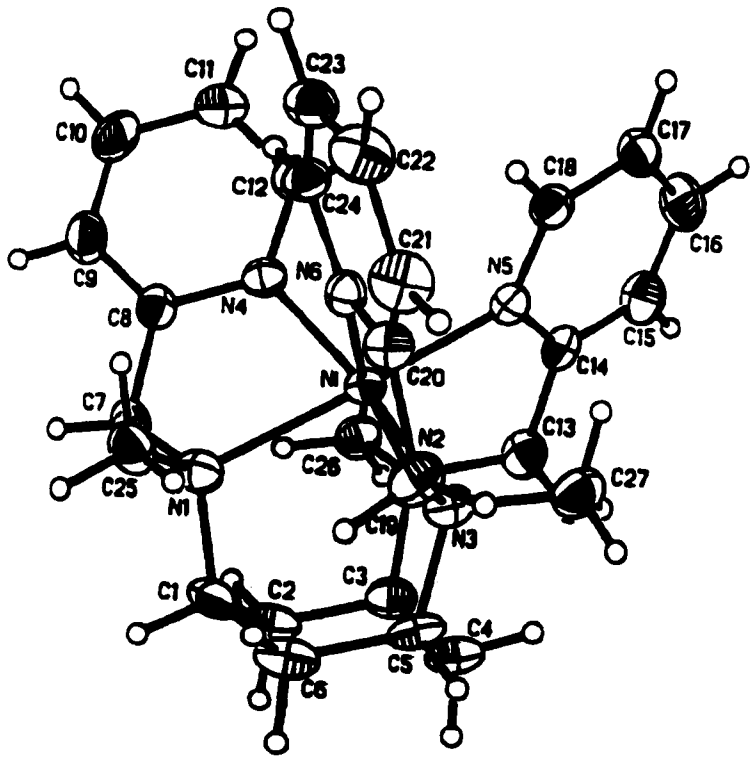

Figure 3.41. ORTEP view of [Ni(tach-Me$_3$pyr)](ClO$_4$)$_2$•CH_3CN (**263**) showing 50% probability of thermal ellipsoids.

Table 3.20. Selected Bond Distances (Å) and Bond Angles (deg) in $[Ni(tach\text{-}Me_3pyr)](ClO_4)_2 \bullet CH_3CN$ (263).

Ni-N(6)	2.106(3)	Ni-N(5)	2.107(4)
Ni-N(4)	2.108(3)	Ni-N(2)	2.159(4)
Ni-N(3)	2.170(4)	Ni-N(1)	2.172(4)
N(1)-C(7)	1.492(6)	N(1)-C(1)	1.503(5)
N(4)-C(8)	1.342(5)	N(4)-C(12)	1.340(5)
C(1)-C(2)	1.536(7)	C(1)-C(6)	1.532(6)
C(7)-C(8)	1.499(6)	C(8)-C(9)	1.383(6)
N(6)-Ni-N(4)	92.75(13)	N(6)-Ni-N(3)	79.74(13)
N(6)-Ni-N(2)	169.80(14)	N(4)-Ni-N(2)	95.01(13)
N(4)-Ni-N(1)	79.84(14)	N(6)-Ni-N(1)	93.97(14)
N(1)-Ni-N(5)	170.62(14)	N(4)-Ni-N(5)	93.79(14)
C(7)-N(1)-C(1)	111.0(3)	C(7)-N(1)-Ni	108.0(3)
C(1)-N(1)-Ni	110.3(3)	N(1)-C(1)-C(2)	113.6(4)
C(6)-C(l)-C(2)	109.2(4)	C(1)-C(2)-C(3)	115.7(4)
N(2)-C(3)-C(4)	113.7(4)	N(2)-C(3)-C(2)	111.4(4)
C(4)-C(3)-C(2)	109.1(4)	C(21)-C(20)-C(19)	121.8(4)
N(4)-C(12)-C(11)	123.2(4)	N(4)-C(8)-C(7)	121.4(4)

B.3. [M(tach-6-Mepyr)](X)$_2$ (M = Zn^{2+}, Cu^{2+}, Ni^{2+}, Co^{2+}, and Mn^{2+}, and X= NO_3^- for Ni^{2+} and Co^{2+} and ClO_4^- for other complexes)

B.3.1. [Zn(tach-6-Mepyr)]$(ClO_4)_2 \bullet CH_3OH$ (253). Orange crystals suitable for X-ray crystallography were obtained by Et_2O diffusion into a CH_3CN solution of the complex. The complex **253** crystallizes as an orange crystal in the triclinic space group *P-1*.

Two independent molecules of **253** crystallize in one asymmetric unit and are not substantially difference in bond lengths and angles. The coordination geometries of two ZnN_6 polyhedrons in **253** (Fig. 3.42) are best described as a slightly distorted octahedron with the average twist angles (α) (**Fig. 3.1**) of 53.9(3)° and 49.5(1)°.

The bond lengths of Zn-N (tach) in molecule 1 of **253** (**Table 3.21**) are 2.128(4), 2.133(4), and 2.136(4) Å. The bond lengths of Zn-N (pyridyl) in molecule 1 of **253** are 2.203(4), 2.216(4), and 2.566(5) Å. These bond lengths can be compared to 2.160(3) Å, Zn-N (tach), and to 2.165(4) Å, Zn-N (pyridyl), respectively, in [Zn(tachpyr)]$(ClO_4)_2 \bullet CH_3OH$ (**250**).

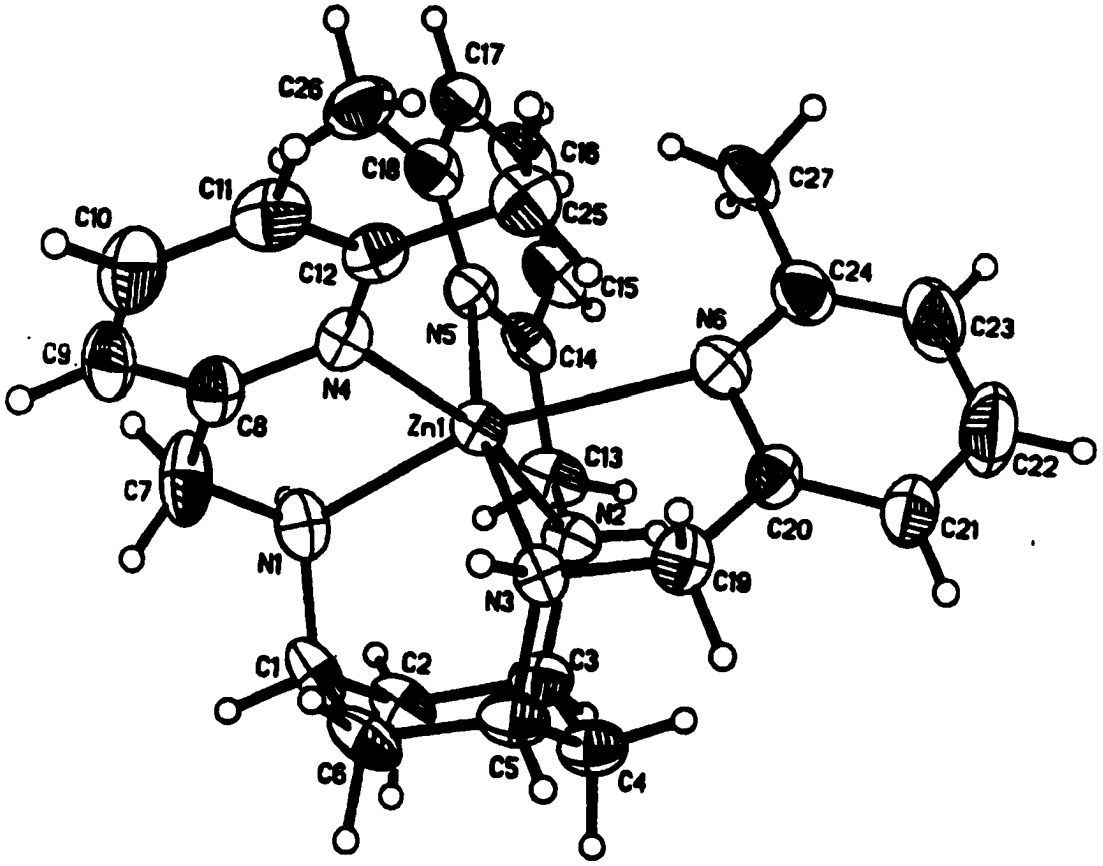

Figure 3.42. ORTEP view of $[Zn(tach\text{-}6\text{-}Mepyr)](ClO_4)_2 \bullet CH_3OH$ **(253)** showing 50% probability of thermal ellipsoids.

Table 3.21. Selected Bond Distances (Å) and Bond Angles (deg) in molecule 1 of [Zn(tach-6-Mepyr)](ClO$_4$)$_2$•CH$_3$OH (253).

Zn-N(1)	2.128(4)	Zn-N(2)	2.133(4)
Zn-N(3)	2.135(4)	Zn-N(5)	2.203(4)
Zn-N(4)	2.216(4)	Zn-N(6)	2.566(5)
N(1)-C(7)	1.469(7)	N(1)-C(1)	1.498(7)
N(4)-C(8)	1.339(7)	N(4)-C(12)	1.364(7)
C(1)-C(2)	1.510(8)	C(1)-C(6)	1.539(8)
C(7)-C(8)	1.499(8)	C(8)-C(9)	1.371(8) Å
N(6)-Zn-N(4)	109.3(2)	N(6)-Zn-N(3)	74.9(2)
N(6)-Zn-N(2)	80.2(2)	N(4)-Zn-N(2)	167.8(2)
N(4)-Zn-N(1)	80.1(2)	N(6)-Zn-N(1)	165.2(2)
N(1)-Zn-N(5)	95.8(2)	N(4)-Zn-N(5)	106.4(2)
C(7)-N(1)-C(1)	114.3(5)	C(7)-N(1)-Zn	111.9(4)
C(1)-N(1)-Zn	112.9(3)	N(1)-C(1)-C(2)	110.0(4)
C(6)-C(5)-C(4)	111.7(5)	C(1)-C(2)-C(3)	114.7(5)
N(2)-C(3)-C(4)	108.9(4)	N(2)-C(3)-C(2)	112.7(5)
C(4)-C(3)-C(2)	109.1(4)	C(21)-C(20)-C(19)	121.8(4)
N(4)-C(12)-C(11)	121.1(5)	N(4)-C(8)-C(7)	119.2(5)
N(4)-C(12)-C(25)	118.1(5)		

B.3.2. [Cu(tach-6-Mepyr)]$(ClO_4)_2 \cdot CH_3OH$ (260). Blue prisms suitable for X-ray crystallography were obtained by Et_2O diffusion into a MeOH solution of the complex. The complex **260** crystallizes as a blue prism in the monoclinic space group $P2_1/n$.

One of three pyridyl nitrogen atom, N(6), is not coordinated to copper(II) ion. The coordination geometry of CuN_5 in **260** (**Fig. 3.43 (a)**) is best described as a distorted trigonal bipyramidal geometry. Two tach amine nitrogen atoms, N(1) and N(3), and one pyridyl nitrogen atom, N(5), occupy equatorial positions of the trigonal bipyramid, while one tach amine nitrogen, N(2), and one pyridyl nitrogen, N(4), occupy apical sites. The in-plane angular distortion, τ (**Fig. 1.4**), is 58.0 % (α = 197.97(13)° and β = 138.16(14)°), indicating the coordination geometry of **260** is slightly closer to a trigonal bipyramid rather than a square pyramidal geometry, and can be compared to that of 60 and 61 % in [Cu(dien)(bipyam)]$(NO_3)_2$ (**Fig. 3.43 (b)**)[324] and [Cu(bipy)$_2$(NCS)](BF_4),[325] respectively.

The bond lengths of Cu-N in **260** compare well with those in other CuN_5 trigonal bipyramidal structures. The bond distances of Cu-N (apical) in **260** (**Table 3.22**) are 2.001(3) and 2.012(3) Å and comparable to those of 1.995(13) and 2.015(14) Å in [Cu(dien)(bipyam)]$(NO_3)_2$[324] and to those of 1.993(7) and 1.980(7) in [Cu(bipy)$_2$(NCS)]$(BF_4)_2$,[325] respectively. The bond distances of Cu-N (equatorial), 2.045(3), 2.103(3), and 2.216(3), in **260** are also comparable to those of 1.988(14), 2.024(14), and 2.125(13) in [Cu(dien)(bipyam)]$(NO_3)_2$ and to those of 1.967(9), 2.069(7), and 2.120(6) in [Cu(bipy)$_2$(NCS)]$(BF_4)_2$.

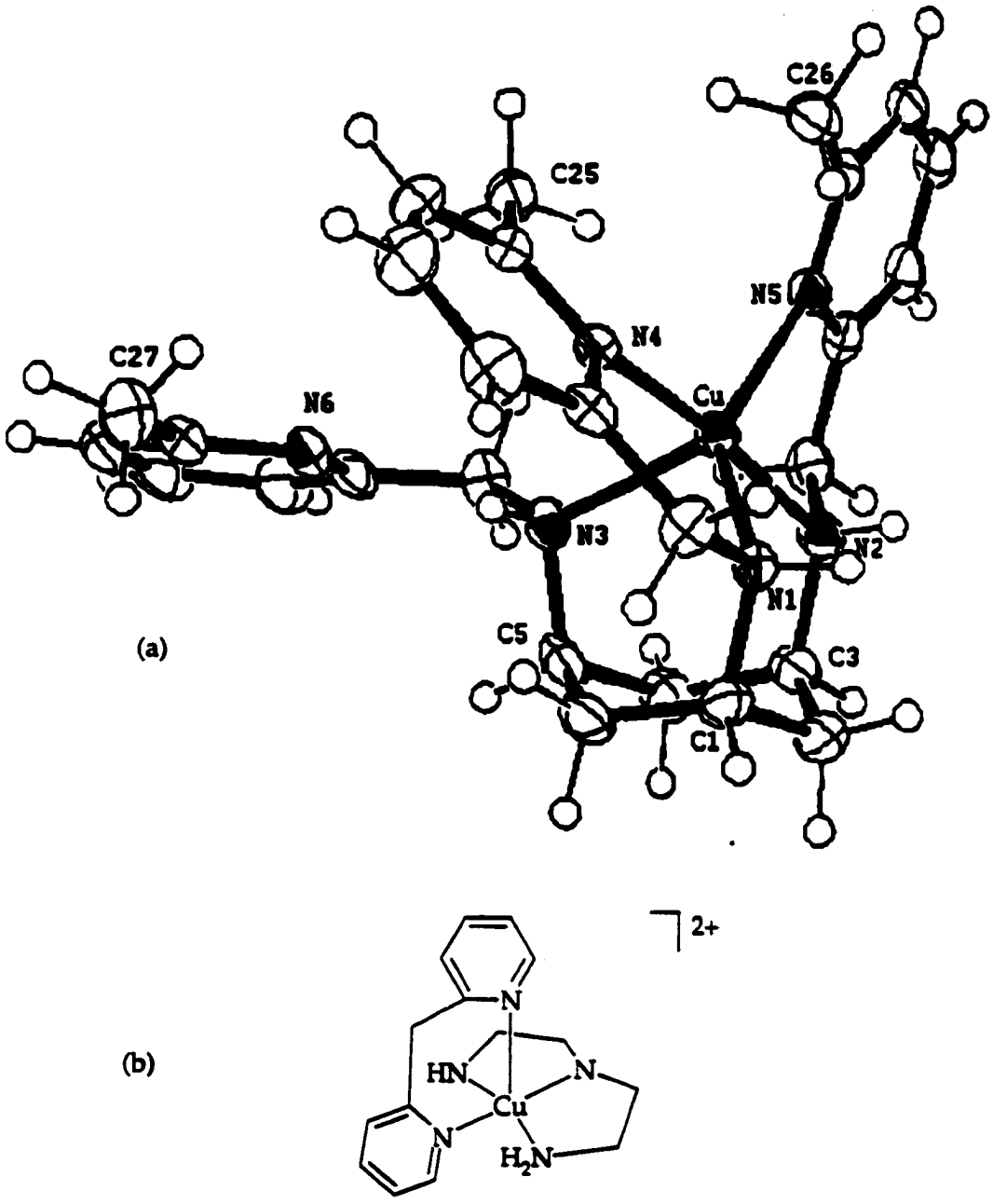

Figure 3.43. (a) ORTEP view of [Cu(tach-6-Mepyr)]$(ClO_4)_2$ (260) showing 50% probability of thermal ellipsoids, (b) [Cu(dien)(bipyam)]$(NO_3)_2$

Table 3.22. Selected Bond Distances (Å) and Bond Angles (deg) in [Cu(tach-6-Mepyr)]$(ClO_4)_2$ (260).

Cu-N(2)	2.001(3)	Cu-N(4)	2.012(3)
Cu-N(1)	2.045(3)	Cu-N(5)	2.103(3)
Cu-N(3)	2.216(3)	N(1)-C(7)	1.479(5)
N(1)-C(1)	1.491(6)	N(4)-C(8)	1.353(5)
N(4)-C(12)	1.365(5)	C(1)-C(2)	1.530(6)
C(1)-C(6)	1.531(7)	C(7)-C(8)	1.505(6)
C(8)-C(9)	1.385(6)	C(24)-C(27)	1.501(8)
N(2)-Cu-N(4)	172.97(13)	N(2)-Cu-N(1)	89.86(14)
N(1)-Cu-N(5)	138.16(14)	N(2)-Cu-N(3)	89.91(14)
N(4)-Cu-N(3)	86.56(13)	N(1)-Cu-N(3)	98.52(14)
N(5)-Cu-N(3)	121.60(13)	N(4)-Cu-N(1)	84.65(13)
C(7)-N(1)-C(1)	114.3(3)	C(7)-N(1)-Cu	110.4(3)
C(1)-N(1)-Cu	112.1(3)	N(1)-C(1)-C(2)	108.8(4)
C(6)-C(5)-C(4)	112.0(4)	C(3)-C(4)-C(5)	113.5(4)
N(2)-C(3)-C(4)	113.4(4)	N(2)-C(3)-C(2)	108.1(4)
C(4)-C(3)-C(2)	110.2(4)	C(21)-C(20)-C(19)	121.1(4)
N(4)-C(12)-C(11)	120.4(4)	N(4)-C(8)-C(7)	121.4(4)
N(4)-C(12)-C(25)	119.3(4)		

B.3.3. [Ni(tach-6-Mepyr)]$(NO_3)_2 \cdot 1/2\ Et_2O$ (265). Pale violet crystals suitable for X-ray crystallography were obtained by Et_2O diffusion into a MeOH solution of the complex. The complex **265** crystallizes as a pale violet crystal in the monoclinic space group $P2_1/n$.

The coordination geometry of NiN_6 in **265** (is best described as a slightly distorted octahedron with the average twist angle (α) (**Fig. 3.1**) of 55.3(3)°. The bond lengths of Ni-N (tach) in **265** (**Table 3.23**) are 2.078(3), 2.099(3), and 2.102(3) Å. The bond lengths of Ni-N (pyridyl) in **265** are 2.191(3), 2.203(3), and 2.267(3) Å. These bond lengths can be compared to 2.099(4) and 2.107(4) Å, Ni-N (tach), and to 2.118(4), 2.122(4), and 2.127(4) Å, Ni-N (pyridyl), respectively, in [Ni(tachpyr)]$(Cl)_2 \cdot CH_3OH$ (**262**).

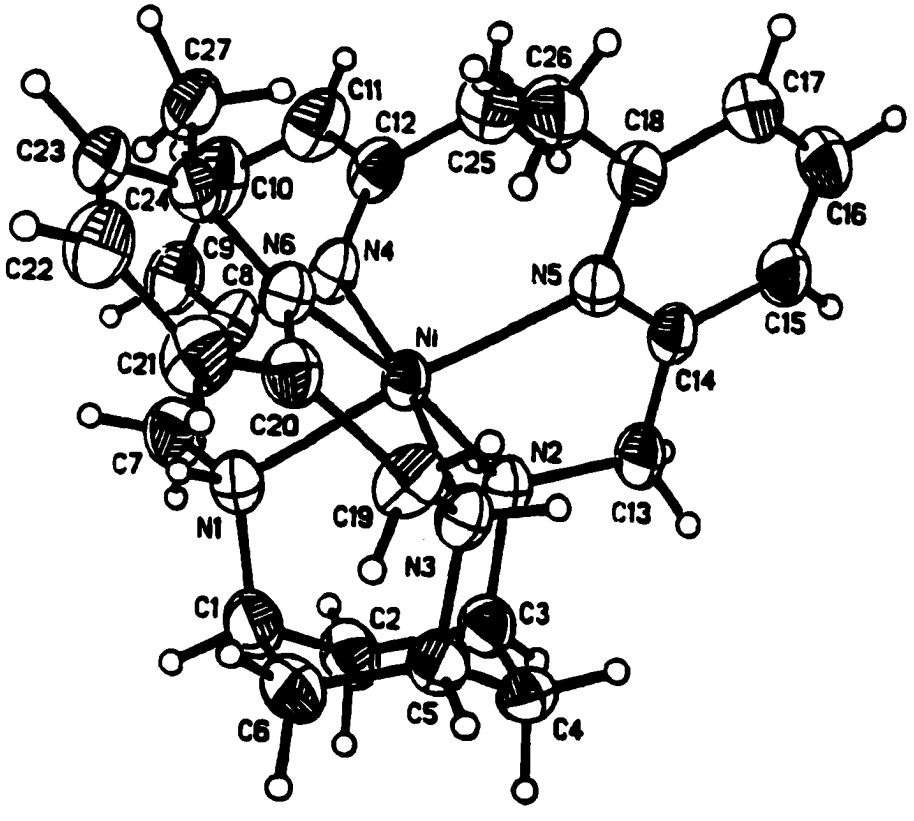

Figure 3.44. ORTEP view of [Ni(tach-6-Mepyr)]$(NO_3)_2 \cdot 1/2\ Et_2O$ (**265**) showing 50% probability of thermal ellipsoids.

Table 3.23. Selected Bond Distances (Å) and Bond Angles (deg) in [Ni(tach-6-Mepyr)]$(NO_3)_2 \bullet 1/2\ Et_2O$ (**265**).

Ni-N(2)	2.078(3)	Ni-N(3)	2.099(3)
Ni-N(1)	2.102(3)	Ni-N(5)	2.191(3)
Ni-N(3)	2.203(3)	Ni-N(4)	2.267(3)
N(1)-C(7)	1.473(5)	N(1)-C(1)	1.483(5)
N(4)-C(8)	1.342(5)	N(4)-C(12)	1.364(5)
C(1)-C(2)	1.523(6)	C(1)-C(6)	1.542(6)
C(7)-C(8)	1.491(6)	C(8)-C(9)	1.392(6)
N(6)-Ni-N(4)	101.56(12)	N(6)-Ni-N(3)	81.44(12)
N(6)-Ni-N(2)	168.74(13)	N(4)-Ni-N(2)	88.00(12)
N(4)-Ni-N(1)	79.65(13)	N(6)-Ni-N(1)	85.20(13)
N(1)-Ni-N(5)	172.50(12)	N(4)-Ni-N(5)	99.53(12)
C(7)-N(1)-C(1)	110.9(3)	C(7)-N(1)-Ni	114.3(3)
C(1)-N(1)-Ni	115.0(2)	N(1)-C(1)-C(2)	110.0(4)
C(6)-C(5)-C(4)	111.7(5)	C(1)-C(2)-C(3)	112.0(4)
N(2)-C(3)-C(4)	113.2(3)	N(2)-C(3)-C(2)	109.9(3)
C(4)-C(3)-C(2)	109.4(3)	C(21)-C(20)-C(19)	117.6(4)
N(4)-C(12)-C(11)	122.2(5)	N(4)-C(8)-C(7)	119.2(5)
N(4)-C(12)-C(25)	119.1(4)		

B.3.4. [Co(tach-6-Mepyr)]$(NO_3)_2$ (270). Red crystals suitable for X-ray crystallography were obtained by Et_2O diffusion into a MeOH solution of the complex. The complex **270** crystallizes as a red crystal in the monoclinic space group $P2_1/c$.

The coordination geometry of CoN_6 in **270** (**Fig. 3.45**) is best described as a slightly distorted octahedron with the average twist angle (α) (**Fig. 3.1**) of 54.7(1)°. The bond lengths of Co-N (tach) in **270** (**Table 3.24**) are 2.1212(13), 2.1510(13), and 2.1517(12) Å, which compare well to those that range from 2.154(9) to 2.169(8) Å in $[Co(sep)]S_2O_6 \bullet H_2O$ (sep = sepulchrate)[240] and those that range from2.124(13) to 2.190(14) Å in $[Co([9]aneN_3)_2]I_2 \bullet 2H_2O$.[239] The bond lengths of Co-N (pyridyl) in **270** are 2.1940(13), 2.2450(12), and 2.3085(13) Å, which are slightly longer than to those in $[Co(terpy)_2](SCN)_2 \bullet 2H_2O$[235], which range from 2.12(2) to 2.17(2) Å, and those in $[Co(bipy)_3]Cl_2 \bullet 2H_2O \bullet EtOH$.[326]

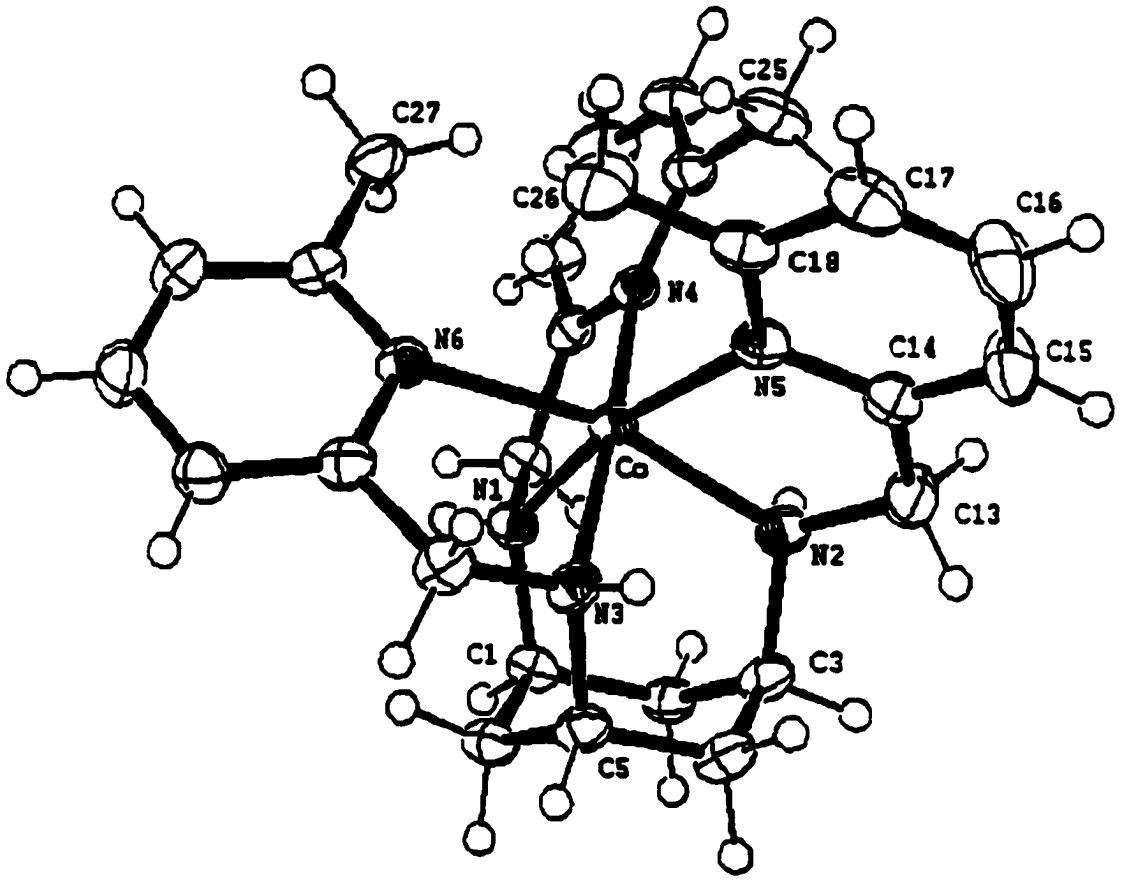

Figure 3.45. ORTEP view of [Co(tach-6-Mepyr)]$(NO_3)_2$ (**270**) showing 50% probability of thermal ellipsoids.

Table 3.24. Selected Bond Distances (Å) and Bond Angles (deg) in [Co(tach-6-Mepyr)]$(NO_3)_2$ (270).

Co-N(1)	2.1212(13)	Co-N(2)	2.1510(13)
Co-N(3)	2.1517(12)	Co-N(5)	2.1940(13)
Co-N(4)	2.2450(12)	Co-N(6)	2.3085(13)
N(1)-C(7)	1.470(2)	N(1)-C(1)	1.497(2)
N(4)-C(8)	1.345(2)	N(4)-C(12)	1.361(2)
C(1)-C(2)	1.530(2)	C(1)-C(6)	1.530(2)
C(7)-C(8)	1.502(2)	C(8)-C(9)	1.395(2)
N(6)-Co-N(4)	100.52(5)	N(6)-Co-N(3)	78.85(5)
N(6)-Co-N(2)	165.14(5)	N(4)-Co-N(2)	89.89(5)
N(4)-Co-N(1)	79.29(5)	N(6)-Co-N(1)	84.05(5)
N(1)-Co-N(5)	167.49(5)	N(4)-Co-N(5)	102.83(5)
C(7)-N(1)-C(1)	112.27(12)	C(7)-N(1)-Co	113.56(9)
C(1)-N(1)-Co	115.66(9)	N(1)-C(1)-C(2)	111.90(12)
C(6)-C(5)-C(4)	111.91(13)	C(2)-C(3)-C(4)	109.92(13)
N(2)-C(3)-C(4)	112.61(13)	N(2)-C(3)-C(2)	109.68(12)
C(17)-C(18)-C(26)	119.9(2)	C(21)-C(20)-C(19)	117.81(14)
N(6)-C(20)-C(19)	117.81(14)	N(6)-C(24)-C(23)	122.1(2)
N(6)-C(24)-C(27)	119.08(14)		

B.3.5. [Mn(tach-6-Mepyr)]$(ClO_4)_2 \bullet CH_3OH$ (274). Colorless crystals suitable for X-ray crystallography were obtained by Et_2O diffusion into a MeOH solution of the complex. The complex **274** crystallizes as a colorless crystal in the triclinic space group *P-1*.

Two independent molecules of **274** crystallize in one asymmetric unit and are not substantially difference in bond lengths and angles. The coordination geometries of two MnN_6 polyhedrons in **274** are best described as a slightly distorted octahedron with the average twist angles (α) (**Fig. 3.1**) of 52.6(3)° and 49.6(1)°. The bond lengths of Mn-N (tach) in molecule 1 of **274** (**Table 3.25**) are 2.235(3), 2.247(3), and 2.262(3) Å, which compare well to those, 2.233(2), 2.236(2), and 2.245(2) Å, in [Mn(tachpyr)]$(ClO_4)_2$ (**271**). The bond lengths of Mn-N (pyridyl) in molecule 1 of **274** are 2.277(3), 2.282(3), and 2.442(3) Å, which compare to those, 2.283(2), 2.292(2), and 2.299(2) Å, in [Mn(tachpyr)]$(ClO_4)_2$ (**271**).

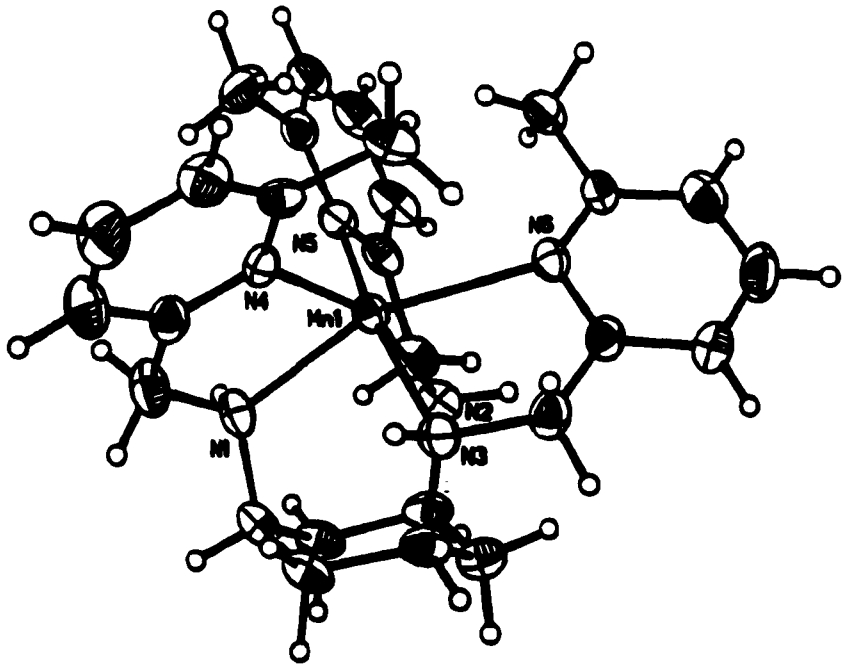

Figure 3.46. ORTEP view of [Mn(tach-6-Mepyr)]$(ClO_4)_2 \bullet CH_3OH$ (**274**) showing 50% probability of thermal ellipsoids.

Table 3.25. Selected Bond Distances (Å) and Bond Angles (deg) in molecule 1 of [Mn(tach-6-Mepyr)]$(ClO_4)_2 \bullet CH_3OH$ (274).

Mn-N(3)	2.235(3)	Mn-N(2)	2.247(3)
Mn-N(1)	2.262(3)	Mn-N(4)	2.277(3)
Mn-N(5)	2.282(3)	Mn-N(6)	2.442(3)
N(1)-C(7)	1.473(5)	N(1)-C(1)	1.498(5)
N(4)-C(8)	1.363(5)	N(4)-C(12)	1.357(5)
C(1)-C(2)	1.534(5)	C(1)-C(6)	1.525(6)
C(7)-C(8)	1.498(6)	C(8)-C(9)	1.385(6)
N(6)-Mn-N(4)	113.38(11)	N(6)-Mn-N(3)	75.46(11)
N(6)-Mn-N(2)	82.43(11)	N(4)-Mn-N(2)	160.69(12)
N(4)-Mn-N(1)	77.11(12)	N(6)-Mn-N(1)	161.11(12)
N(1)-Mn-N(5)	92.11(12)	N(4)-Mn-N(5)	109.70(12)
C(7)-N(1)-C(1)	113.8(3)	C(7)-N(1)-Mn	111.9(2)
C(1)-N(1)-Mn	114.3(2)	N(1)-C(1)-C(2)	109.6(3)
C(6)-C(1)-C(2)	111.3(4)	C(3)-C(2)-C(1)	1115.1(3)
N(2)-C(3)-C(4)	109.5(3)	N(2)-C(3)-C(2)	112.5(3)
C(2)-C(3)-C(4)	111.0(3)	C(21)-C(20)-C(19)	118.9(4)
N(6)-C(20)-C(19)	118.2(3)	N(6)-C(24)-C(23)	121.6(4)
N(6)-C(24)-C(27)	119.1(4)		

B.4. [Zn(tachquin)]$(ClO_4)_2 \bullet H_2O$ (254).

Colorless crystals suitable for X-ray crystallography were obtained by Et_2O diffusion into a CH_3CN solution of the complex. The complex **254** crystallizes as a colorless crystal in the monoclinic space group $P2_1/c$.

One of the 2-methylquinilinyl arms of the ligand is disordered generating two different positions of the 2-methylquinilinyl arm, from C27A to C36A and from C27B to C36B, respectively, coordinated to Zn(II) through identical nitrogen donor atoms, N(3) and N(6). The coordination geometry of ZnN_6 in **254** is best described as a slightly distorted octahedron with the average twist angle (α) (**Fig. 3.1**) of 53.7(8)°. The bond lengths of Zn-N (tach) in **254** (**Table 3.26**) are 2.124(9), 2.135(9), and 2.171(9) Å, which compare well to 2.160(3)Å in [Zn(tachpyr)]$(ClO_4)_2 \bullet CH_3OH$ (**X-3**). The bond lengths of Zn-N (pyridyl) in **254** are 2.198(10), 2.255(9), and 2.296(9) Å, which are significantly longer than 2.165(4) Å in [Zn(tachpyr)]$(ClO_4)_2 \bullet CH_3OH$ (**250**).

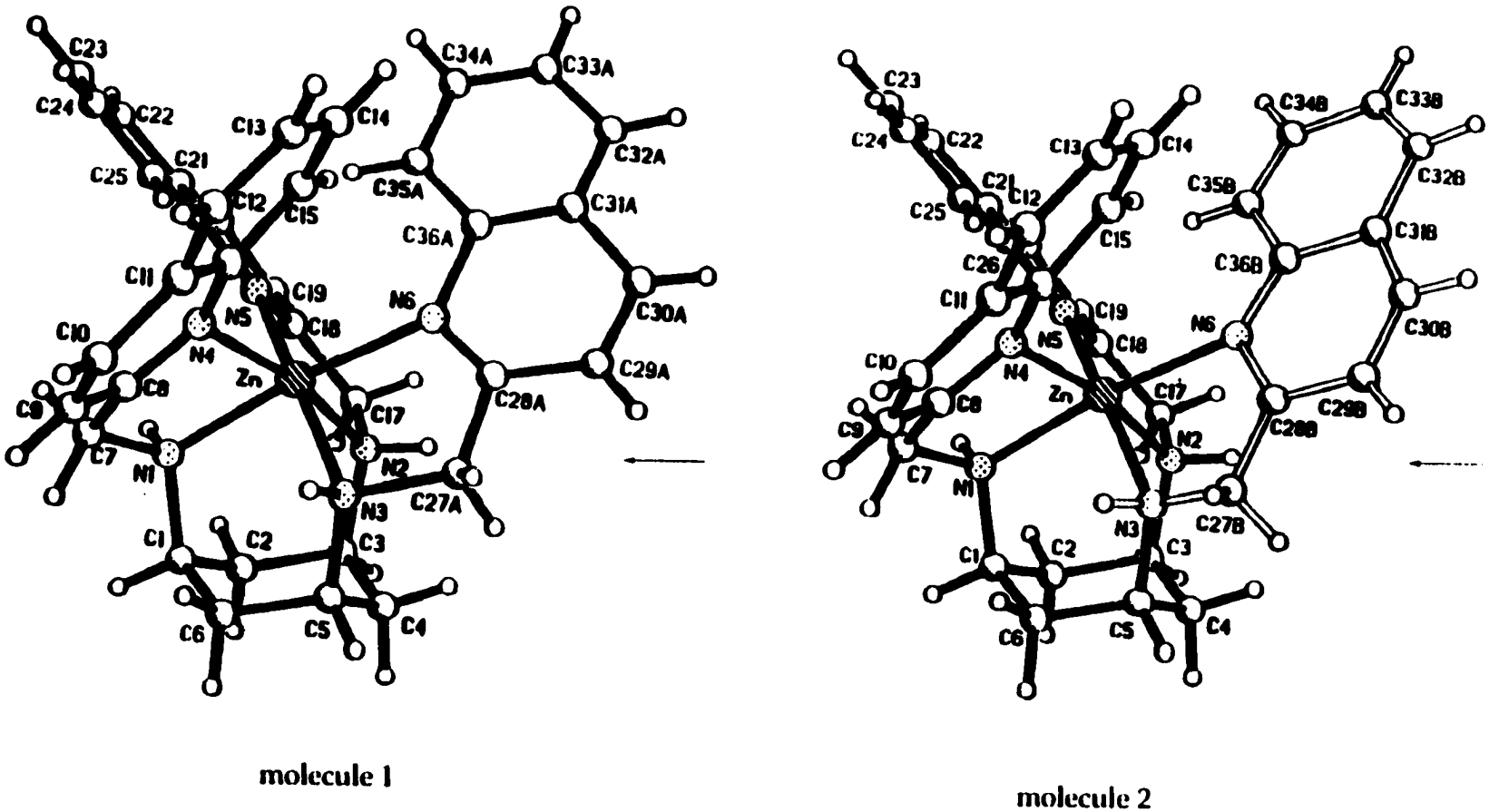

Figure 3.47. ORTEP view (50% probability of thermal ellipsoids) of [Zn(tachquin)]$(ClO_4)_2 \cdot H_2O$ (254) showing two disordered molecules with C27A-C36A (molecule 1) and C27B-C36B (molecule 2).

Table 3.26. Selected Bond Distances (Å) and Bond Angles (deg) in molecule 1 of $[Zn(tachquin)](ClO_4)_2 \bullet H_2O$ (**254**).

Zn-N(1)	2.124(9)	Zn-N(2)	2.135(9)
Zn-N(3)	2.171(9)	Zn-N(6)	2.198(10)
Zn-N(5)	2.255(9)	Zn-N(4)	2.296(9)
N(1)-C(7)	1.497(13)	N(1)-C(1)	1.496(14)
N(4)-C(8)	1.308(14)	N(4)-C(16)	1.390(14)
C(1)-C(2)	1.514(14)	C(1)-C(6)	1.54(2)
C(7)-C(8)	1.54(2)	C(8)-C(9)	1.39(2)
N(6)-Zn-N(4)	96.7(4)	N(6)-Zn-N(3)	79.3(4)
N(6)-Zn-N(2)	90.2(4)	N(4)-Zn-N(2)	169.7(4)
N(4)-Zn-N(1)	79.5(4)	N(6)-Zn-N(1)	168.9(4)
N(1)-Zn-N(5)	86.6(3)	N(4)-Zn-N(5)	104.5(4)
C(7)-N(1)-C(1)	112.6(9)	C(7)-N(1)-Zn	112.3(6)
C(1)-N(1)-Zn	115.3(7)	N(1)-C(1)-C(2)	109.2(9)
C(6)-C(1)-C(2)	111.3(10)	C(3)-C(2)-C(1)	115.2(9)
N(2)-C(3)-C(4)	109.0(9)	N(2)-C(3)-C(4)	109.0(9)
C(2)-C(3)-C(4)	111.8(10)	C(20)-C(19)-C(18)	119.3(12)
N(6)-C(28A)-C(29A)	129(3)	N(6)-C(28A)-C(27A)	117(2)
C(28A)-N(6)-C(36A)	113(2)		

B.5. [M(tachbn)](X)$_2$ (M = Zn^{2+}, and Cu^{2+}, and X= Cl and ClO_4^-)

B.5.1. [Zn(tachbn)](Cl)(ClO_4)•1/2H_2O (256). Colorless prisms suitable for X-ray crystallography were obtained by Et_2O diffusion into the CH_3CN solution of the complex. The complex **256** crystallizes as a colorless prism in the orthorhombic space group $P2_12_12_1$.

In attempts to obtain the [Zn(tachbn)](ClO_4)$_2$ in the reaction of $Zn(ClO_4)_2$•6H_2O and the neutralized S,S,S-tachbn ligand, the product **256** shows a mixed counter anion, a chloride and a perchlorate, rather than two perchlorates. The source of the unexpected Cl^- ion in the complex is attributed to an extraction of the neutralized ligand with wet MeOH. The wet MeOH not only extract the neutralized ligand but also absorb NaCl produced during the neutralization of the ligand, resulting a composition ambiguity of the counter anion. This problem may be avoided by using another neutralization process, azeotropic distillation, or by using anhydrous solvents that can extract the neutralized ligand.

The benzylethylenediamine arms of S,S,S-tachbn are assumed to coordinate Zn(II) in either the Δ or Λ configuration.[327] However, one of the benzylethylenediamine (NH-CH_2-C(H)(NH_2)-CH_2-Ph) arms of the ligand is twisted away from zinc atom. This phenomena is presumably results of the packing processes of a crystallization since the benzyl groups are located with significant distance from the metal ion and do not create any convergence around the Zn(II) ion (see the space-filling model in **Figure 3.28**). The

coordination geometry, Λ(δδδ) isomer, ZnN_6 in **256** (**Fig. 3.48**) is best described as a distorted octahedron with the average twist angle (α) (**Fig. 3.1**) of 43.6(7)°.

The bond lengths of Zn-N (tach) in **256** (**Table 3.27**) range from 2.155(9) to 2.206(10) Å, which compare well with those of other ZnN_6 complexes. Typical Zn-N (amine) distances in zinc hexamine complexes range from 2.182(15) Å to 2.206(10) Å in $[Zn(tach\text{-}Me_3)_2](CF_3SO_3)_2$[98] and from 2.181(4) Å to 2.248(5) Å in $[ZnL](ClO_4)_2$ (L= 1,4,7-tris(o-aminobenzyl)-1,4,7-triazacyclononane).[287]

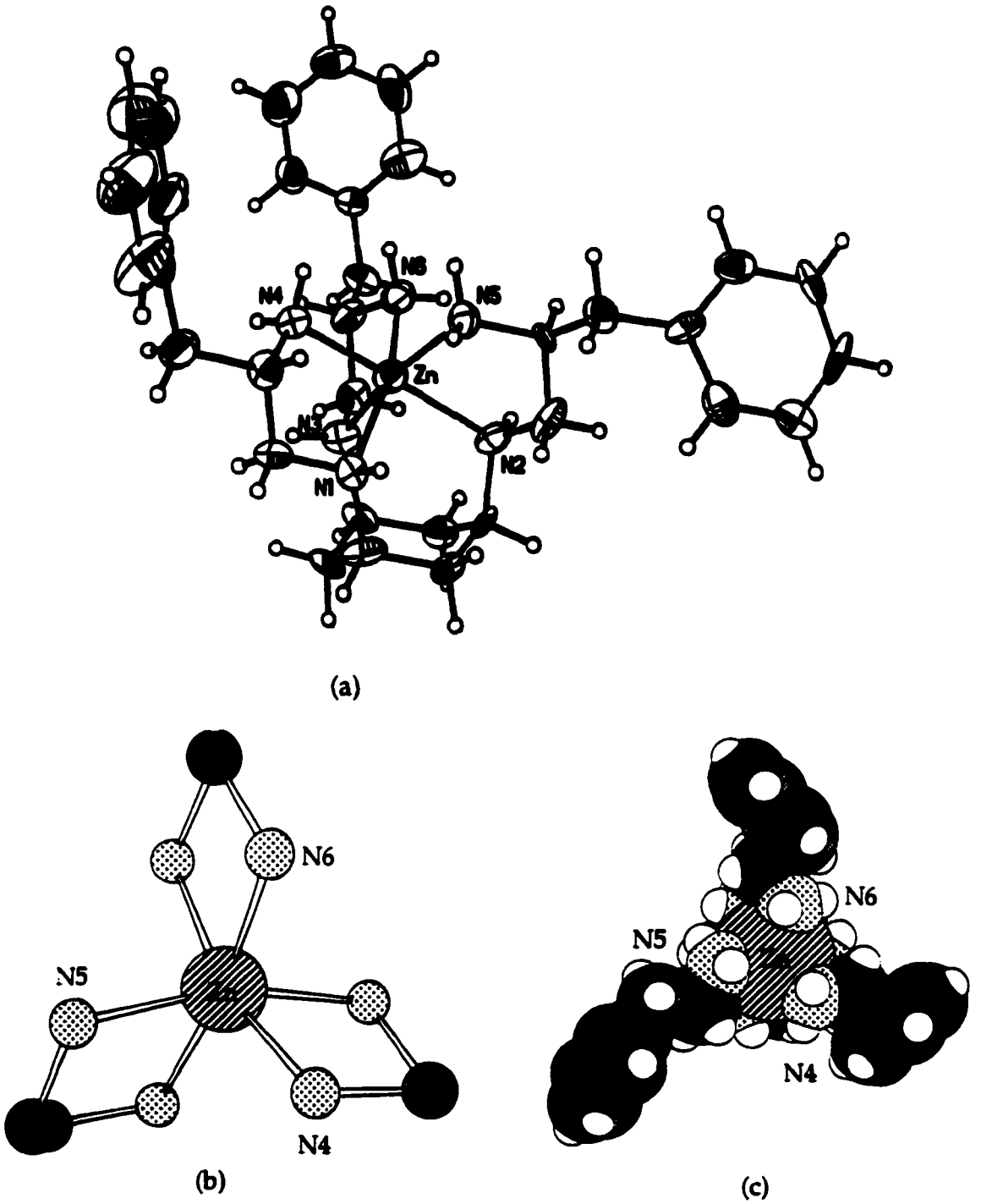

Figure 3.48. (a) ORTEP view of [Zn(tachbn)](Cl)(ClO_4)•1/2H_2O (**256**) showing 50% probability of thermal ellipsoids, (b) coordination geometry Λ(δδδ) of **256**, (c) top vies of space-filling model of **256**.

Table 3.27. Selected Bond Distances (Å) and Bond Angles (deg) in [Zn(tachbn)](Cl)(ClO_4)•1/2H_2O (256).

Zn-N(6)	2.155(9)	Zn-N(5)	2.152(8)
Zn-N(1)	2.195(8)	Zn-N(2)	2.187(9)
Zn-N(4)	2.186(8)	Zn-N(3)	2.206(10)
N(1)-C(7)	1.482(12)	N(1)-C(1)	1.476(12)
N(5)-C(17)	1.495(12)	N(4)-C(8)	1.521(12)
C(1)-C(2)	1.527(14)	C(1)-C(6)	1.50(2)
C(7)-C(8)	1.484(14)	C(8)-C(9)	1.513(14)
C(10)-C(11)	1.38(2)	C(19)-C(24)	1.41(2)
N(6)-Zn-N(4)	94.5(3)	N(6)-Zn-N(3)	79.5(4)
N(6)-Zn-N(2)	99.3(3)	N(4)-Zn-N(2)	164.4(4)
N(4)-Zn-N(1)	79.6(3)	N(6)-Zn-N(1)	163.0(4)
N(1)-Zn-N(5)	97.3(3)	N(4)-Zn-N(5)	90.7(4)
C(7)-N(1)-C(1)	115.4(9)	C(7)-N(1)-Zn	108.2(6)
C(1)-N(1)-Zn	116.4(7)	N(1)-C(1)-C(2)	109.9(10)
C(6)-C(5)-C(4)	111.1(10)	C(3)-C(4)-C(5)	114.5(9)
N(5)-C(17)-C(18)	110.4(9)	N(2)-C(16)-C(17)	111.5(9)
C(16)-C(17)-N(5)	107.6(9)	C(20)-C(19)-C(18)	122.8(12)
N(6)-C(26)-C(25)	106.1(9)	N(6)-C(26)-C(27)	114.5(10)
C(10)-C(11)-C(12)	119(2)	C(21)-C(20)-C(19)	120.9(12)

B.5.2. [Cu(tachbn)]$(ClO_4)_2$ (261). Blue crystals[331] suitable for X-ray crystallography were obtained by Et_2O diffusion into a CH_3CN solution of the complex. The complex **261** crystallizes as a blue crystal in the orthorhombic space group $P2_12_12_1$. One of the benzylethylenediamine (NH-CH_2-C(H)(NH_2)-CH_2-Ph) arms of the ligand is also twisted away from the copper atom like in [Zn(tachbn)](Cl)(ClO_4)•1/2H_2O (**256**).

The coordination geometry, Δ(λλλ) isomer, CuN_6 in **261** (**Fig. 3.49**) is best described as a axially elongated octahedron with the average twist angle (α) (**Fig. 3.1**) of 45.5°. Because of the weak interaction with the copper ion, the axially elongated two apical nitrogen donors, N(2) and N(4), have longer Cu-N bond distances, 2.241(9) Å for Cu-N(2) and 2.332(9) Å for Cu-N(5), respectively, than four equatorial Cu-N bond distances, 2.060(8), 2.075(9), 2.079(8), and 2.103(4) Å, respectively.

The bond lengths Cu-N in **261** (**Table 3.28**) compare well with those of other CuN_6 complexes. Typical Cu-N (equatrial) distances, 2.060(8), 2.075(9), 2.079(8), and 2.103(9) Å, in **261**compare favorably to those range from 2.061(6) to 2.078(6) in [Cu(tach)$_2$](ClO_4)$_2$ (tach = **219** (**Scheme 3.1**)[302] and range from 2.032(5) to 2.099(5) Å in [Cu(tachpyr)](ClO_4)$_2$•1/2CH_3CN (**257**). The axially elongated Cu-N bond lengths, 2.241(9) and 2.332(9) Å , in **261** also compare well to 2.353(7) Å in [Cu(tach)$_2$](ClO_4)$_2$ (tach = **219** (**Scheme 3.1**)[302] and to 2.245(5) and 2.458(5) Å in [Cu(tachpyr)](ClO_4)$_2$•1/2CH_3CN (**257**).

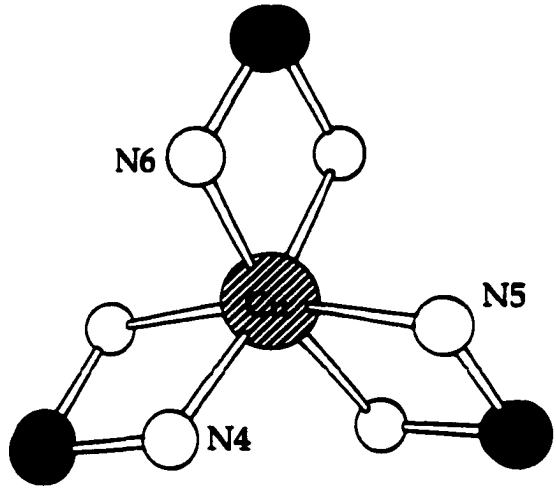

(a)

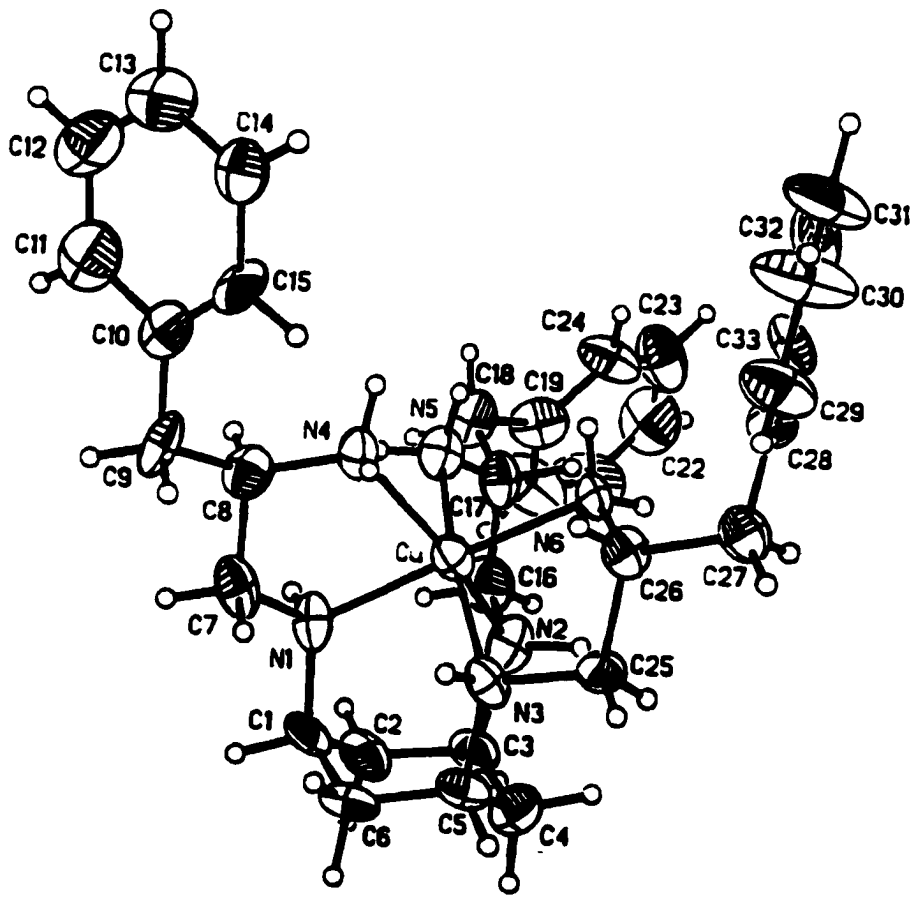

(b)

Figure 3.49. (a) Coordination geometry of $[Cu(tachbn)](ClO_4)_2$ (**261**), (b) ORTEP view of **261** showing 50% probability of thermal ellipsoids.

Table 3.28. Selected Bond Distances (Å) and Bond Angles (deg) in $[Cu(tachbn)](ClO_4)_2$ **(261).**

Cu-N(3)	2.060(8)	Cu-N(5)	2.075(9)
Cu-N(6)	2.079(8)	Cu-N(1)	2.103(9)
Cu-N(2)	2.241(9)	Cu-N(4)	2.332(9)
N(1)-C(7)	1.47(2)	N(1)-C(1)	1.481(14)
N(5)-C(17)	1.480(14)	N(4)-C(8)	1.473(14)
C(1)-C(2)	1.47(2)	C(1)-C(6)	1.54(2)
C(7)-C(8)	1.52(2)	C(8)-C(9)	1.53(2)
C(10)-C(11)	1.41(2)	C(19)-C(24)	1.39(2)
N(6)-Cu-N(4)	91.6(3)	N(6)-Cu-N(3)	83.4(4)
N(6)-Cu-N(2)	99.7(4)	N(4)-Cu-N(2)	165.7(3)
N(4)-Cu-N(1)	80.0(4)	N(6)-Cu-N(1)	168.0(4)
N(1)-Cu-N(5)	95.4(4)	N(4)-Cu-N(5)	91.2(4)
C(7)-N(1)-C(1)	113.0(10)	C(7)-N(1)-Cu	110.0(7)
C(1)-N(1)-Cu	117.2(7)	N(1)-C(1)-C(2)	109.5(11)
C(4)-C(5)-C(6)	110.7(12)	C(3)-C(4)-C(5)	115.1(11)
N(5)-C(17)-C(18)	110.5(10)	N(2)-C(16)-C(17)	112.0(11)
C(16)-C(17)-N(5)	107.0(10)	C(20)-C(19)-C(18)	124(2)
N(6)-C(26)-C(25)	107.1(10)	N(6)-C(26)-C(27)	113.4(11)
C(11)-C(10)-C(9)	119(2)	C(21)-C(20)-C(19)	122(2)

B.6. Structure of [Ni(tachpn)]$(ClO_4)_2 \bullet CH_3OH$ (266)

Light purple prisms suitable for X-ray crystallography were obtained by Et_2O diffusion into the MeOH solution of the complex. The complex **266** crystallizes as a light purple prism in the orthorhombic space group $P2_12_12_1$.

The coordination geometry of NiN_6 in **266** (**Fig. 3.50**) is best described as a distorted octahedron with the average twist angle (α) (**Fig. 3.1**) of 48.7(3)°. The bond lengths of Ni-N (tach) in **266** (**Table 3.29**) range from 2.098(4) to 2.129(4) Å, which compare well with those of other NiN_6 complexes. Typical Ni-N (amine) distances in nickel(II) hexamine complexes are 2.131(3) and 2.134(2) Å in $[Ni(tach)_2](NO_3)_2$ (tach = **219** (**Scheme 3.1**)),[302] and 2.112(3) and 2.136(5) Å in $[Ni(taci)_2]Br_2 \bullet 4H_2O$ (taci = 1,3,5-triamino-1,3,5-trideoxy-*cis*-inositol),[305] and range from 2.104(4) to 2.138(4) Å in $[Ni(en)_3](O_2C_2H_3)_2 \bullet 2H_2O$.[328]

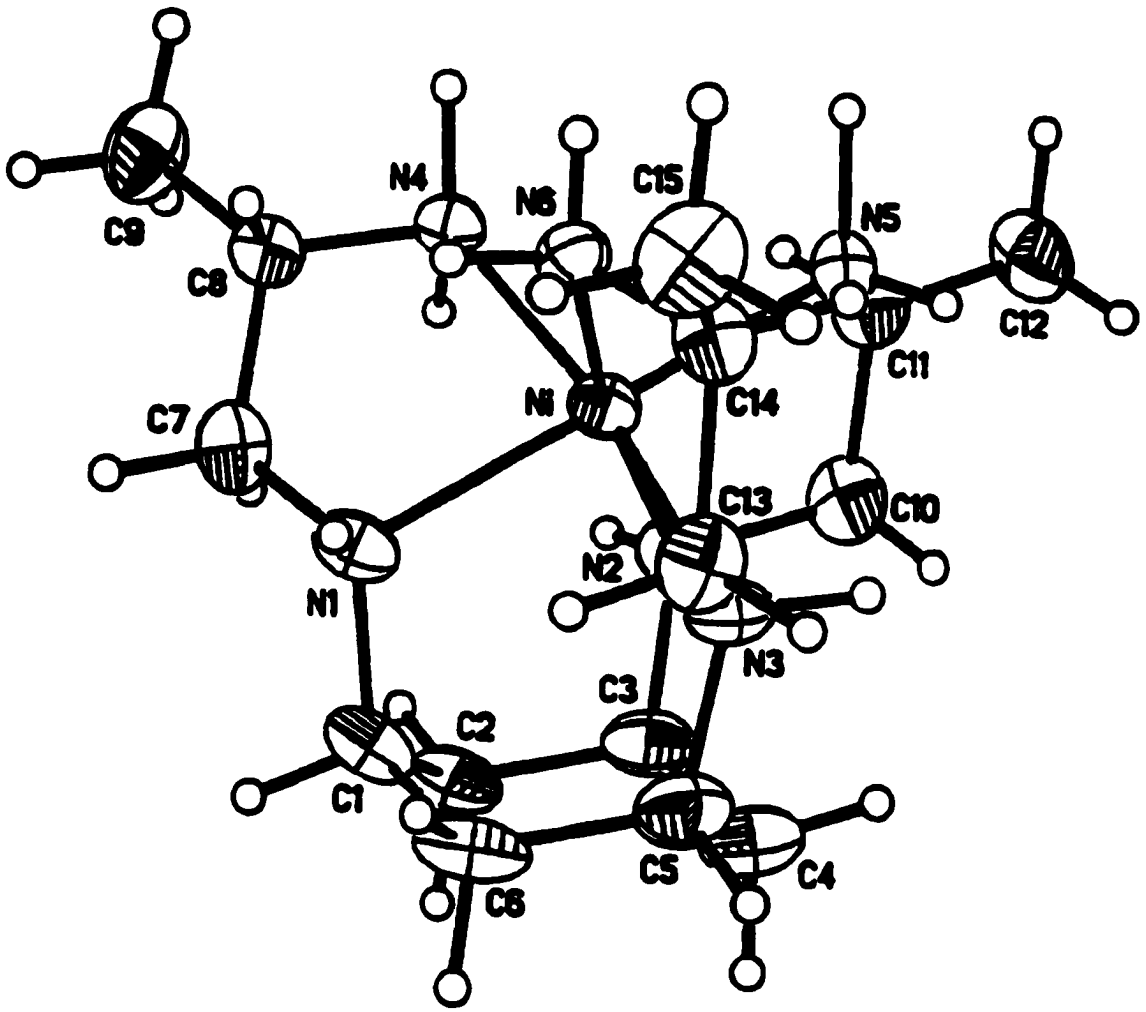

Figure 3.50. ORTEP view of $[Ni(tachpn)](ClO_4)_2 \bullet CH_3OH$ (**266**) showing 50% probability of thermal ellipsoids.

Table 3.29. Selected Bond Distances (Å) and Bond Angles (deg) in $[Ni(tachpn)](ClO_4)_2 \bullet CH_3OH$ (**266**).

Ni-N(3)	2.098(4)	Ni-N(2)	2.113(4)
Ni-N(1)	2.117(4)	Ni-N(6)	2.125(3)
Ni-N(4)	2.129(4)	Ni-N(5)	2.129(4)
N(1)-C(7)	1.475(6)	N(1)-C(1)	1.492(6)
N(5)-C(11)	1.494(6)	N(4)-C(8)	1.484(6)
C(1)-C(2)	1.516(7)	C(1)-C(6)	1.518(7)
C(7)-C(8)	1.514(6)	C(8)-C(9)	1.531(6)
C(10)-C(11)	1.515(7)	C(14)-C(15)	1.523(6)
N(6)-Ni-N(4)	94.2(2)	N(6)-Ni-N(3)	81.84(14)
N(6)-Ni-N(2)	169.9(2)	N(4)-Ni-N(2)	94.1(2)
N(4)-Ni-N(1)	81.92(14)	N(6)-Ni-N(1)	95.67(14)
N(1)-Ni-N(5)	170.63(14)	N(4)-Ni-N(5)	92.20(14)
C(7)-N(1)-C(1)	115.0(4)	C(7)-N(1)-Ni	109.5(3)
C(1)-N(1)-Ni	114.6(3)	N(1)-C(1)-C(2)	113.7(4)
C(4)-C(5)-C(6)	109.6(5)	C(3)-C(4)-C(5)	115.0(5)
N(5)-C(11)-C(10)	107.0(4)	N(2)-C(10)-C(11)	109.6(4)
C(10)-C(11)-C(12)	111.7(4)	N(3)-C(13)-C(14)	109.5(4)
N(6)-C(14)-C(13)	108.1(4)	N(6)-C(14)-C(15)	113.3(4)
C(13)-C(14)-C(15)	112.8(4)		

C. Electronic Absorption Spectroscopy

C.1. Electronic Absorption Spectroscopy of Cu(II) tachpyr Derivatives

The visible-near IR (400 – 1380 nm) spectra of the Cu(II) complexes of tachpyr derivatives, $[Cu(tachpyr)](ClO_4)_2$ (**257**), $[Cu(tach\text{-}Me_3pyr)](ClO_4)_2$ (**258**), $[Cu(tach\text{-}Et_3pyr)](ClO_4)_2$ (**259**), and $[Cu(tach\text{-}6\text{-}Mepyr)](ClO_4)_2$ (**260**), were measured using a Cary 5 Varian spectrometer. The Cu(II) complexes of tachpyr derivatives in a CH_3CN solution have an intense blue color which is attributed to a ligand field *d-d* transitions confirming the presence of a Cu(II) ion, d^9, in these complexes. The visible-near IR spectra of **258** and **259** are very similar to that of **257** except that bands were shifted to lower energy. This fact indicates that the Cu(II) complexes of tachpyr, tach-Me_3pyr, and tach-Et_3pyr have similar structures in a CH_3CN solution and nitrogen atoms in **258** and **259** are weakly coordinated to the Cu(II) ion than those in **257**.

The visible-near IR spectrum of **260** clearly shows two distinct absorption maxima around 700 and 940 nm, while the other complexes show a very broad single absorption maxima around 660nm, 720 nm, and 730 nm for **257**, **258**, and **259**, respectively. The structure of **260** in a solution seems to be different from other Cu(II) complexes of tachpyr derivatives in a solution, which is consistent to its different X-ray structure (trigonal bipyramid) from others (axially elongated octahedrons). The larger intensity of molar absorptivities of **260** due to absence of an inversion center also indicates the maintenance of its structure in a solution. Electronic spectral data of Cu(II) complexes of tachpyr derivatives are summarized in **Table 3.30.** The visible-near IR spectra of **257** and **260** are presented in **Figure 3.51.**

Table 3.30. Electronic spectral data of Cu(II) complexes of tachpyr derivatives.

Compound	*d-d* band V_{max} wavelengths (nm)	ε_{max} (cm^{-1} L mol^{-1})
$[Cu(tachpyr)](ClO_4)_2$	662	93.0
$[Cu(tach\text{-}Me_3pyr)](ClO_4)_2$	723	81.4
$[Cu(tach\text{-}Et_3pyr](ClO_4)_2$	734	85.9
$[Cu(tach\text{-}6\text{-}Mepyr)](ClO_4)_2$	698 936	237.8 156.8

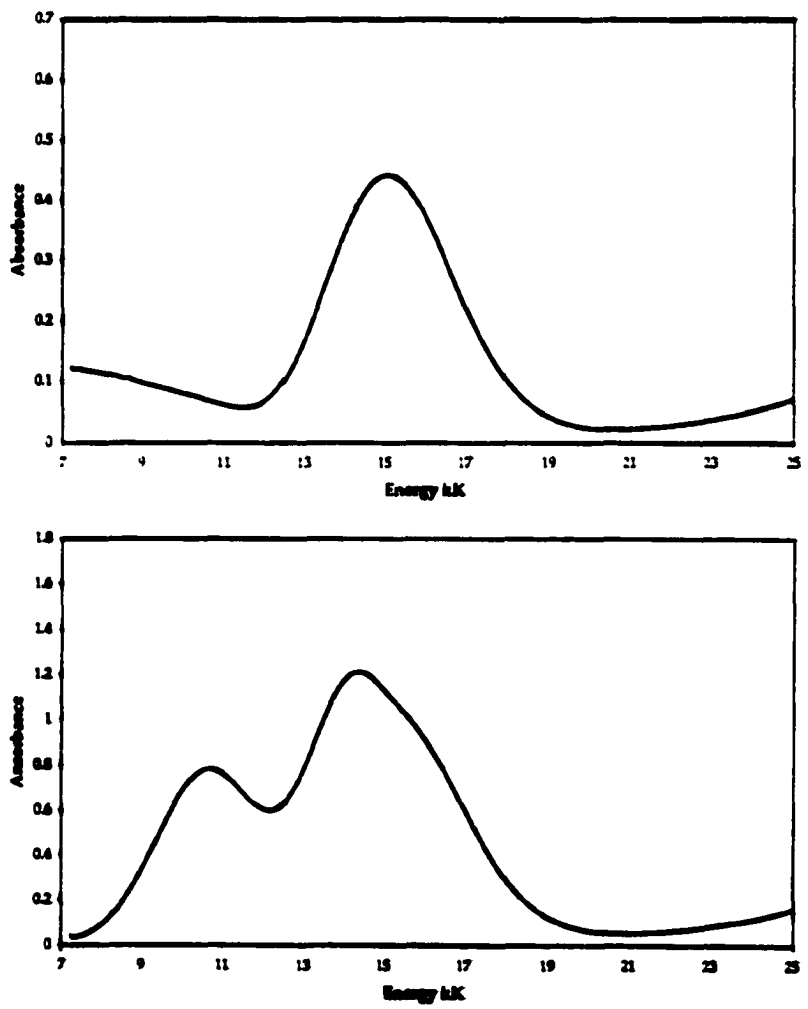

Figure 3.51. Visible-near IR spectra of (a) $[Cu(tachpyr)](ClO_4)_2$ (257); (b) $[Cu(tach\text{-}6\text{-}Mepyr)](ClO_4)_2$ (260).

C.2. Electronic Absorption Spectroscopy of Ni(II) tachpyr Derivatives

The UV-Vis spectra of Ni(II) complexes of tachpyr derivatives, $[Ni(tachpyr)](Cl)_2$ (**262**), $[Ni(tachpyr)](ClO_4)_2$, $[Ni(tach\text{-}Me_3pyr)](ClO_4)_2$ (**263**), $[Cu(tach\text{-}Et_3pyr)](ClO_4)_2$ (**264**), and $[Ni(tach\text{-}6\text{-}Mepyr)](ClO_4)_2$ (**265**), were measured using Cary 5 UV-vis spectrometer. All Ni(II) complexes of tachpyr derivatives in CH_3CN or MeOH solution have a purple color. The UV-Vis spectra of the *N*-alkylated tachpyr complexes, **263** and **264**, are very similar to those of tachpyr complexes $[Ni(tachpyr)](X)_2$ (X = Cl^- **262** or ClO_4^-) except for band shifts to lower energy. Therefore, it was assumed that the structures and electronic properties of these Ni(II) complexes are similar in solution.

The UV-Vis spectra of $[Ni(tachpyr)](Cl)_2$ (**262**) and $[Ni(tachpyr)](ClO_4)_2$ are of typical electronic spectra of Ni(II), d^8, giving two very weak absorption maxima around 800 nm and 500 nm and a very strong absorption maximum around 310 nm as a shoulder. An assignment of the two components of the low energy band around 800nm and 500 nm would attribute one component to the $^3A_{2g}$ -> $^3T_{2g}$ (F) transition and the other to the $^3A_{2g}$ -> $^3T_{1g}$. The lowest energy bands attributed to a spin-allowed *d-d* transition, $^3A_{2g}$ -> $^3T_{2g}$ (F), in *N*-alkylated tachpyr and tachpyr complexes have a shoulder on the lower energy side, which is attributed to the spin-forbidden $^3A_{2g}$ -> ^1E_g (D), enhanced via spin-orbital coupling.[329] On the other hand, the spin forbidden transition is the dominant component of the absorption band in the lowest energy band of $[Ni(tach\text{-}6\text{-}Mepyr)](ClO_4)_2$ (**265**), giving a higher energy shoulder.[330] The stronger intensity of the band around 300 nm compared to those of two spin-allowed *d-d* bands and presence of the shoulder around 310 nm for these complexes are indicative of the

overlapping between the charge transfer band and the spin-allowed $^3A_{2g}$ -> $^3T_{1g}$ (P) transition bands as a shoulder.

The electronic spectral data of Ni(II) complexes of tachpyr derivatives are summarized in **Table 3.31**. The UV-Vis spectra of [Ni(tachpyr)]$(Cl)_2$ (**262**) and [Ni(tach-Me_3pyr)]$(ClO_4)_2$ (**263**) are presented in **Figure 3.52.**

Table 3.31. Electronic spectral data of Ni(II) complexes of tachpyr derivatives and tachimpyr.

Compound	$^3A_{2g}$ -> ^1E_g (D) nm (ε)	$^3A_{2g}$ -> $^3T_{2g}$ (F) nm (ε)	$^3A_{2g}$ -> $^3T_{1g}$ nm (ε)
[Ni(tachpyr)]$(Cl)_2$[a]	880 (11.8)	797 (16.0)	511 (16.6)
[Ni(tach-Me_3pyr)]$(ClO_4)_2$[b]	924 (13.4)	812 (8.6)	561 (14.8)
[Ni(tach-Et_3pyr)]$(ClO_4)_2$[b]	956 (14.1)	820 (8.5)	573 (16.4)
[Ni(tach-6-Mepyr)]$(ClO_4)_2$[b]	927 (23.2)	815 (13.7)	561 (7.8)
[Ni(tachimpyr)]$^{2+}$ 184	900 (27.0)	826 (26.6)	515 (52.8)

[a]in MeOH. [b]in CH_3CN. unit of ε is cm^{-1} L mol^{-1}

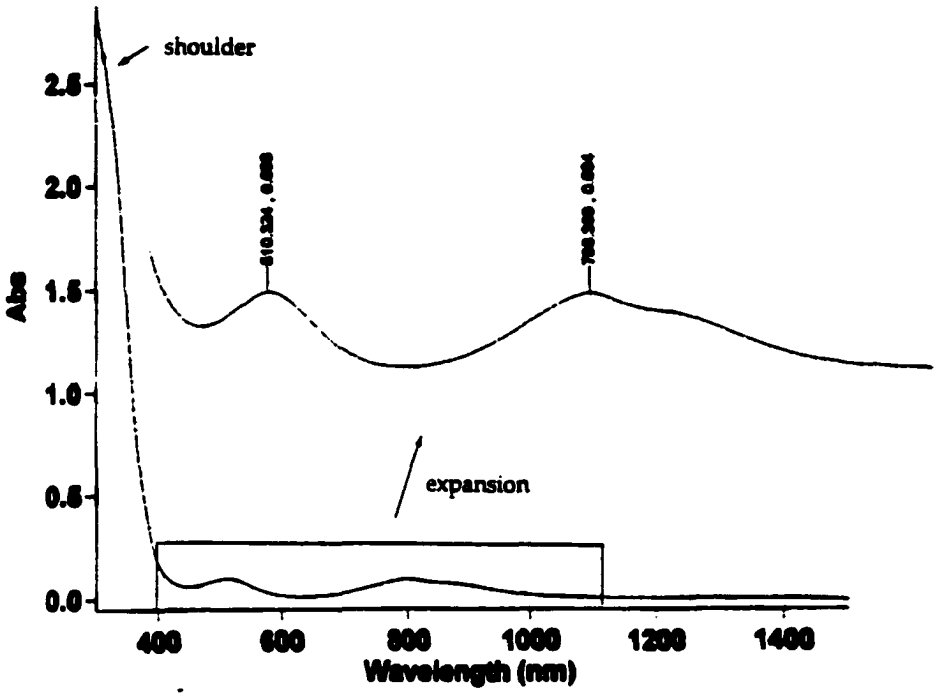

(a) $[Ni(tachpyr)]Cl_2$

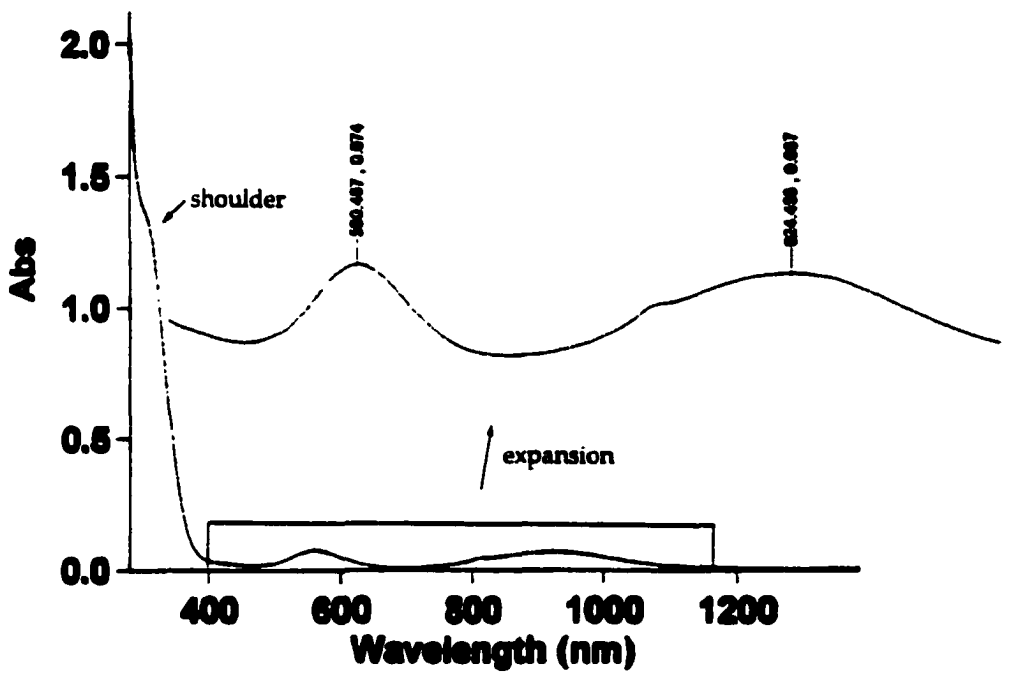

(b) $[Ni(tach\text{-}Me_3pyr)](ClO_4)_2$

Figure. 3.52. UV-Vis spectra (a) $[Ni(tachpyr)](Cl)_2$ **(262)**; (b)$[Ni(tach\text{-}Me_3pyr)](ClO_4)_2$ **(263)**.

C.3. Electronic Absorption Spectroscopy of Co(II) tachpyr Derivatives

The electronic spectral data of Co(II) complexes of tachpyr derivatives, a mixture of [Co(tachpyr)]$(NO_3)_3$ (**267**) and [Co(tachpyr-*ox*-*n*)]$(NO_3)_3$ (**267A**), [Co(tach-Me_3pyr)]$(NO_3)_2$ (**268**), [Co(tach-Et_3pyr)]$(ClO_4)_2$ (**269**), [Co(tach-6-Mepyr)]$(ClO_4)_2$, and [Co(tach-6-Mepyr)]$(NO_3)_2$ (**270**), are presented in **Table 3.32.** The Co(II) complexes of tach-Me_3pyr, tach-Et_3pyr, and tach-6-Mepyr ligands show similar spectra, giving two distinct absorption maxima around 1050 nm and 490 nm which are attributed to low energy component of a spin-allowed $^4T_{1g}$ (F) -> $^4T_{2g}$ transition and high energy component to a spin-allowed $^4T_{1g}$(F) -> $^4T_{1g}$ (P) transition, respectively. The number and intensities of the absorption bands indicate that electronic configuration of these complexes is high-spin Co(II), d^7. There are three spin-allowed transitions, $^4T_{1g}$ (F) -> $^4T_{2g}$, $^4T_{1g}$ (F) -> $^4T_{1g}$ (P), and $^4T_{1g}$ (F) -> $^4A_{2g}$, in the high-spin Co(II) complexes, however, the $^4T_{1g}$ (F) -> $^4A_{2g}$ transition is not observed in any of these spectra since this transition involves a two-electron transition and the intensity is expected to be very small. This transition is probably covered by the spin-allowed transition, $^4T_{1g}$ (F) -> $^4T_{1g}$ (P), and shown as a shoulder on either side of the transition, $^4T_{1g}$ (F) -> $^4T_{1g}$ (P).[336]

The UV-Vis spectrum of a mixture of the mixture of **267** and **267A** is very different from Co(II) complexes of other tachpyr derivatives, presenting a absorption maxima around 470 nm and a shoulder overlapped with a charge transfer band around 360 nm. The electronic configuration of the mixture of **267** and **267A** is assumed to be neither Co(II) with a low-spin state or Co(II) with a high-spin state because there is no spin-allowed transition in Co(II) with a low-spin state, resulting three peaks with very weak intensity, and Co(II) with a high-

spin state would show more than two absorption maxima.[233] Therefore, the electronic configuration of the mixture of **267** and **267A** is assumed to be Co(III) in the low-spin state. Two spin-allowed transitions, $^1A_{1g}$ (F) -> $^1T_{1g}$ at low energy and $^1A_{1g}$ (F) -> $^1T_{2g}$ at high energy, are possible for low-spin Co(III), attributed to one absorption maximum at 465 nm and to a shoulder overlapped with the charge transfer band at 360 nm. The UV-Vis spectra of the mixture of **267** and **267A** and [Co(tach-6-Mepyr)]$(NO_3)_2$ (**270**) complexes are presented in **Figure 3.53.**

Table 3.32. Electronic spectral data of Co(II) and Co(III) complexes of tachpyr derivatives.

Compound	$^4T_{1g}$ (F) -> $^4T_{2g}$ nm (ε)	$^4T_{1g}$ (F) -> $^4T_{1g}$ (P) nm (ε)
[Co(tach-Me_3pyr)]$(NO_3)_2$[a]	1022 (7.74)	491 (43.93) 552 (20.90)*
[Co(tach-Et_3pyr)]$(ClO_4)_2$[b]	1062 (3.41)	513 (90.4)
[Co(tach-6-Mepyr)]$(ClO_4)_2$[a]	1044 (8.0)	461 (51.2) 469 (49.4)*
[Co(tach-6-Mepyr)]$(NO_3)_2$[a]	1042 (7.6)	494 (28.6)
	$^1A_{1g}$ (F) -> $^1T_{1g}$ nm (ε)	$^1A_{1g}$ (F) -> $^1T_{2g}$ nm
[Co(tachpyr)]$(NO_3)_3$ (**267**) and [Co(tachpyr-*ox*-*n*)]$(NO_3)_3$ (**267A**)[a]	466 (135)	360*

[a]in MeOH. [b]in CH_3CN. *shoulder. unit of ε is cm^{-1} L mol^{-1}

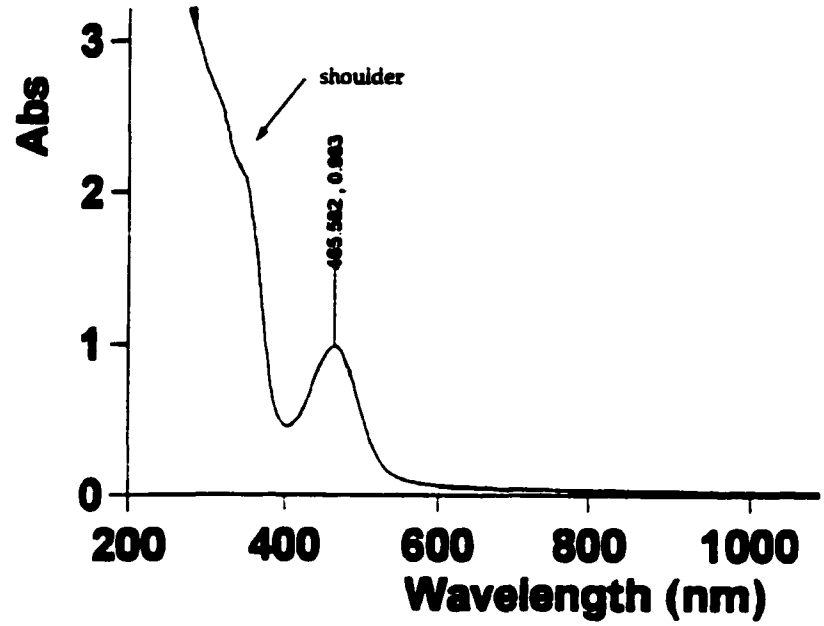

(a)a mixture of $[Co(tachpyr)](NO_3)_3$ (267) and $[Co(tachpyr\text{-}ox\text{-}n)](NO_3)_3$ (267A

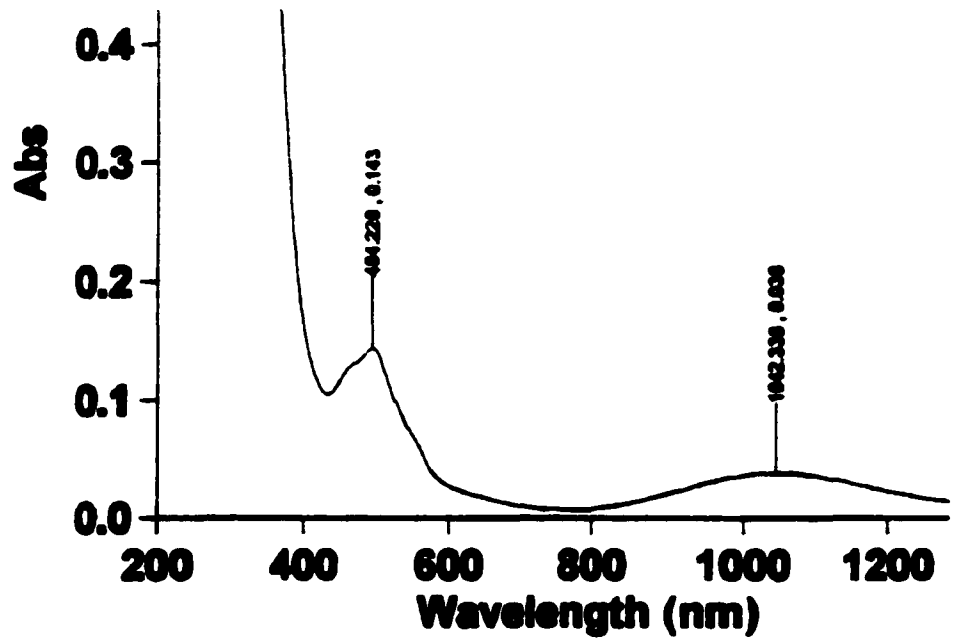

(b) $[Co(tach\text{-}6\text{-}Mepyr)](NO_3)_2$

Figure. 3.53. UV-Vis spectra (a) a mixture of $[Co(tachpyr)](NO_3)_3$ (267) and $[Co(tachpyr\text{-}ox\text{-}n)](NO_3)_3$ (267A); (b) $[Co(tach\text{-}6\text{-}Mepyr)](NO_3)_2$ (270).

D. Magnetic Moment Study

Magnetic susceptibility data for metal complexes of tachpyr derivatives, $[ML]X_2$ (M = Cu^{2+}, Ni^{2+}, Co^{2+}, and Mn^{2+}; L = tachpyr, tach-Me_3pyr, tach-Et_3pyr, and tach-6-Mepyr; X = Cl^-, NO_3^-, or ClO_4^-) were measured at room temperature with use of the Evans method[314, 337] and are presented in **Table 3.33.**

The magnetic moments of the Cu(II) complexes of tachpyr derivatives range from 1.544 to 1.638 B.M. and the number of unpaired electrons in these metal complexes is close to one, indicating that the electronic configuration of these metal complexes is actually Cu(II), d^9. The Ni(II) complexes of tachpyr derivatives present magnetic moments in the range of 2.902 – 3.087 B.M., which are typical for the octahedral Ni(II) complexes.[255] The magnetic moments of Mn(II) complexes of tachpyr derivatives range from 5.663 to 5.829 B.M., which are totally differentiated from low-spin Mn(II) complexes with cyano ligands which provide the spin-paired value of 1.80 B.M. The number of unpaired electrons is close to five, indicating that the electronic configuration in these complexes is high-spin Mn(II), d^5.[211]

The magnetic moment of a mixture of $[Co(tachpyr)]^{3+}$ **(267)** and $[Co(tachpyr\text{-}ox\text{-}n)]^{3+}$ **(267A)** is 1.129 B.M., which is very different from 4.021 B.M. for $[Co(tach\text{-}Me_3pyr)]^{2+}$ **(268)**, 4.128 B.M. for $[Co(tach\text{-}Et_3pyr)]^{2+}$ **(269)**, and 4.341 B.M for $[Co(tach\text{-}6\text{-}Mepyr)]^{2+}$ **(270)** which are that of a high-spin octahedral Co(II) complex, d^7. The number of unpaired electron in the mixture of **267** and **267A** is 0.63, which is also much less than 3.14, 3.24, and 3.45 (for **268, 269, and 270,** respectively). The magnetic moment and the number of unpaired electron

indicate that the electronic configuration of the cobalt ion in the mixture of **267** and **267A** is low-spin Co(III), d^6, which is consistent with its distinctive electronic spectrum.

Table 3.33. Magnetic moment data for metal complexes of tachpyr derivatives.

metal complex	Δν Hz	χm (10^{-3})	μ_{eff} (B. M.)	N	anticipated electronic status
$[Cu(tachpyr)](ClO_4)_2$	38.74	1.346	1.557	0.85	Cu^{2+} (d^9)
$[Cu(tach\text{-}Me_3pyr)](ClO_4)_2$	38.79	1.323	1.544	0.84	Cu^{2+} (d^9)
$[Cu(tach\text{-}Et_3pyr)](ClO_4)_2$	28.48	1.488	1.638	0.92	Cu^{2+} (d^9)
[Cu(tach-6-Mepyr)] $(ClO_4)_2$	23.26	1.363	1.567	0.86	Cu^{2+} (d^9)
$[Ni(tachpyr)](Cl)_2$	80.85	3.563	2.902	2.07	Ni^{2+} (d^8)
$[Ni(tach\text{-}Me_3pyr)](NO_3)_2$	89.19	3.704	2.959	2.12	Ni^{2+} (d^8)
$[Ni(tach\text{-}Et_3pyr)](ClO_4)_2$	93.42	3.937	3.050	2.21	Ni^{2+} (d^8)
[Ni(tach-6-Mepyr)] $(ClO_4)_2$	95.11	4.033	3.087	2.25	Ni^{2+} (d^8)
mixture of $[Co(tachpyr)](NO_3)_3$ and $[Co(tachpyr\text{-}ox\text{-}n)](NO_3)_3$	12.37	0.5392	1.129	0.63	Co^{3+} (d^6) (L.S.)
$[Co(tach\text{-}Me_3pyr)](NO_3)_2$	103.59	8.973	4.021	3.14	Co^{2+} (d^7) (H.S.)
$[Co(tach\text{-}Et_3pyr)](ClO_4)_2$	212.82	9.457	4.128	3.25	Co^{2+} (d^7) (H.S.)
[Co(tach-6-Mepyr)] $(ClO_4)_2$	237.80	10.458	4.341	3.45	Co^{2+} (d^7) (H.S.)
$[Mn(tachpyr)](ClO_4)_2$	318.33	13.570	5.663	4.75	Mn^{2+} (d^5) (H.S.)
$[Mn(tach\text{-}Me_3pyr)](ClO_4)_2$	326.23	14.377	5.829	4.91	Mn^{2+} (d^5) (H.S.)
$[Mn(tach\text{-}Et_3pyr)](ClO_4)_2$	321.13	14.193	5.792	4.88	Mn^{2+} (d^5) (H.S.)
[Mn(tach-6-Mepyr)] $(ClO_4)_2$	333.67	14.165	5.786	4.87	Mn^{2+} (d^5) (H.S.)

N = number of unpaired electron; H.S. = high-spin; L.S. = low-spin

Discussion

A. Effect of Metal Size on Coordination Geometry of $[M^{II}(tachpyr)](ClO_4)_2$, M = Zn, Cd, and Hg (Adapted from "G. Park, N. Ye, R.D. Rogers, M.W. Brechbiel, and R.P. Planalp, *Polyhedron*, 2000, *19*, 1155-1161.")

Ligands that are preorganized or predisposed to bind metal ions form particularly thermodynamically or kinetically stable complexes.[182, 338] The tachpyr ligand, *N,N',N''*-tris(2-pyridylmethyl)-*cis,cis*-1,3,5-triaminocyclohexane, readily makes metal complexes by a ring flip from an open all-equatorial conformation to a closed all-axial conformation (**Scheme 3.11**) encapsulating metal ions ranging in size from Ga^{3+} (six-coordinate ionic radius of 0.76 Å) through many first-row transition elements to In^{3+} (radius = 0.94 Å) in alcoholic or aqueous media.[313, 339]

The complexes $[Zn(tachpyr)](ClO_4)_2 \bullet CH_3OH$ (**250**), $[Cd(tachpyr)](ClO_4)_2$ (**275**), and $[Hg(tachpyr)](ClO_4)_2$ (**276**) were prepared by the reactions of the respective metal ion perchlorate salts, $M(ClO_4)_2 \bullet 6H_2O$ (M = Zn(II) and Cd(II)) or $M(ClO_4)_2$ (M = Hg(II)), and the ligand (1:1) in mixture of MeOH and EtOH. Colorless crystals of **275** and **276** were obtained with reasonable yield (> 50%), however, the yield of colorless crystalline **250** was poor (< 25%).

Tachpyr provides six nitrogens which can coordinate to metal ions, including Group IIB (Zn(II), Cd(II), and Hg(II)). Since these metal ions do not have an electronic preference for either an octahedral or a trigonal-prismatic configuration, the structures of their tachpyr complexes should reflect the conformational preference of tachpyr and non-bonded repulsions between donor groups. The coordination geometry of MN_6 in **250** is best described as a distorted

octahedron, whereas that of **275** is classified as an intermediate between octahedral and trigonal-prismatic and **276** is close to trigonal prismatic. The average "twist angle (α)" (**Fig. 3.1**) of **250** is 43.7(2)°, while those of **275** (disorder molecule 1 and 2) are 20.8(4)° and 11.4(9)° and that of **276** is 5(1)°. Without a major perturbation caused by the metal ion, the tachpyr ligand seems to have a ligand conformation preference towards an octahedral geometry, common among unconstrained hexamine ligands.

As the six-coordinate ionic radius increases from Zn^{2+} (0.88 Å) to Cd^{2+} (1.09 Å) and then to Hg^{2+} (1.16 Å)[340, 341], the 2-pyridylmethyl arms straighten out to accommodate the longer metal-nitrogen bonds, the two nitrogens on each pendant arm come closer to being eclipsed, and the coordination geometry of the metal complexes approaches trigonal-prismatic.

The bond lengths M-N are larger for **275** and **276** than **250**, reflecting the difference in six-coordinate ionic radii from Zn^{2+} in **250** to Cd^{2+} and Hg^{2+} in **275** and **276**. The M-N bond lengths in **276** are slightly longer than those in **275**, which is consistent with a difference in the six-coordinate ionic radii of Hg^{2+} and Cd^{2}+ of 0.07 Å.

Another effect of metal ion radius on the structures of the tachpyr metal complexes is a distortion of the cyclohexyl ring, as manifested in the C-C-C-C torsion angles (β) (**Fig. 3.54**). The torsion angles (β) in **250** range between 52.3(6)° and 52.4(6)° (average 52.35(3)°), in **275** range between 46.1(9)° and 52.7(9)° (average 49(2)°), and in **276** range between 45.1(6)° and 52.9(7)° (average 49(2)°). As the metal ion radius increases, increased distortion of the cyclohexane framework as the cyclohexyl nitrogens are pushed out from the axial positions

occurs as the ligand accommodates the metal. There is no significant difference in the distortion of the C-C-C-C torsion angles (β) between **275** and **276**, which is consistent with the six-coordinate ionic radii of **275** and **276**, which are similar. The structural parameters in **250**, **275**, and **276** are compared and presented in **Table 3.34**.

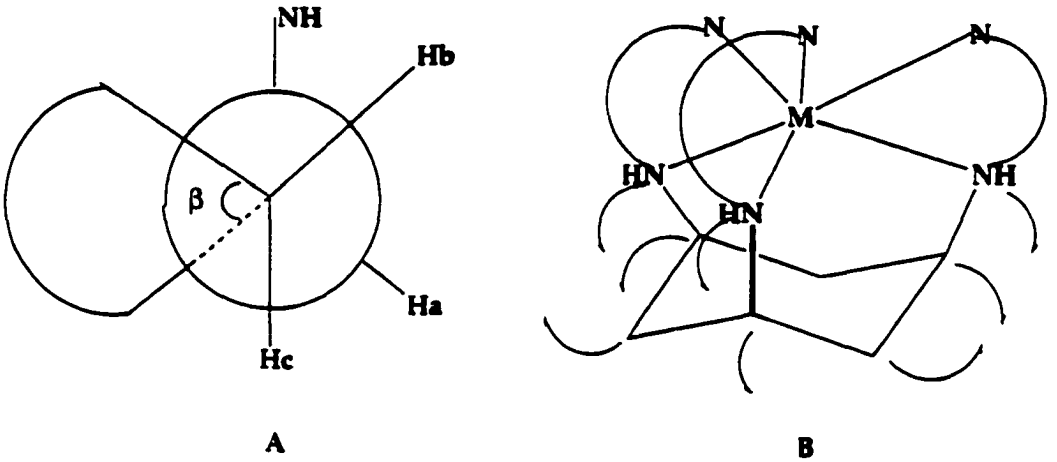

Figure 3.54. A, Torsion angle (β); B, flattening of cyclohexyl ring.

The disorder in **275** indicates the presence of two different stereoisomers formed by two different twist directions (clockwise and counter-clockwise) in the twist of pendant arms. The counter-clockwise twist of the pendant arms forms a Δ(λλλ) isomer, and a clockwise twist of the pendant arms generates a Λ(δδδ) isomer. The Δ(λλλ) and Λ(δδδ) isomers are not enantiomers of each other (**Fig. 3.55**) since the Λ(δδδ) isomer has a smaller twist (average angle = 11.4(9)°), thus is closer to a trigonal-prismatic geometry, than the Δ(λλλ) isomer (average angle = 20.8(4)°). As expected, the presence of two different stereoisomers was not detected in the investigation by the proton NMR at room temperature.

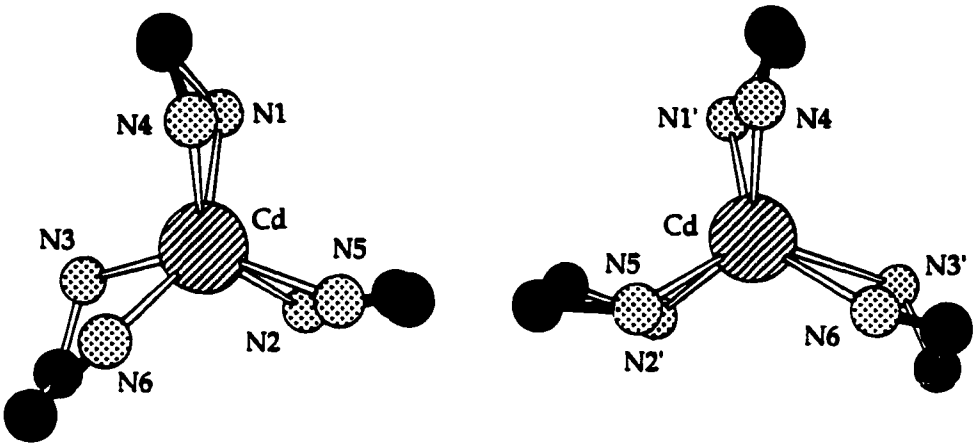

(a) isomer 1 (60%)

(b) isomer 2 (40%)

Figure 3.55. Δ(λλλ) (a) and Λ(δδδ) (b) isomers of $[Cd(tachpyr)](ClO_4)_2$.

The structure of **276** can be defined as a Λ(δδλ) isomer, which is the most stable isomer among of the four Λ diastereomers (δδδ, δδλ, δλλ, and λλλ) due to a combination of steric and entropic factors.[327] Repulsive effects between puckered rings favor a Λ(δδδ) isomer, however the entropy consideration that δδλ and δλλ isomers are three times as probable as the δδδ and λλλ isomers also plays a role.[327]

Table 3.34. Comparison of Structural Parameters in [Zn(tachpyr)]$(ClO_4)_2 \cdot CH_3OH$ (250), [Cd(tachpyr)]$(ClO_4)_2$ (275), and [Hg(tachpyr)]$(ClO_4)_2$ (276).

Parameters	250 (Zn)	275 (Cd) (molecule 1)	275 (Cd) (molecule 2)	276 (Hg)
M-N bond distances, Å				
M-N (tach)	2.160(3)	2.302(6) - 2.400(5)	2.332(13) - 2.422(9)	2.335(6) - 2.487(6)
M-N (pyridyl)	2.165(4)	2.352(4) - 2.361(4)	2.352(4) - 2.361(4)	2.334(4) - 2.461(4)
twist angle α, °	43.7(2)	19.6(2) - 21.7(2) av 20.8(4)	11.0(4) - 12.0(8) av 11.4(9)	3.1(3), 5.0(3), 5.5(2) av 5(1)
C-C-C-C torsion angles	52.3(6), 52.4(6)	46.1(9) - 52.7(9)	49(1) - 52(1)	45.1(6) - 52.9(7)
of cyclohexyl framework, °	av 52.35(3)	av 49(2)	av 49(4)	av 49(2)

B. First Row transition Metal Complexes of tachpyr [M(tachpyr)](X)$_2$, M = Zn (250), Cu (257), Ni (262), Co (267 and 267A), and Mn (271), X = ClO_4^-, Cl^-, or NO_3^-)

The structural parameters and physical properties of **250, 257, 262, 267** and **267A**, and **271** are compared and presented in **Table 3.35.**

Table 3.35. Comparison of physical properties and structural parameters of metal complexes of tachpyr

	250	**257**	**262**	**267 and 267A**	**271**
Oxidation state Atomic radius[b] Å	Zn(II) 0.88	Cu(II) 0.87	Ni(II) 0.83	Co(III)[c] 0.685	Mn(II)[d] 0.97
Electronic maxima nm (ε, cm^{-1} L mol^{-1})		662 (93.0)	880 (11.8) 797 (16.0) 511 (16.6)	466 (135) 360*	
Average M-N (tach) distance Å	2.160(3)	2.245(5)[a] 2.066(7)	2.103(6)		2.238(3)
Average M-N (pyridyl) distance Å	2.165(4)	2.458(5)[a] 2.043(7)	2.122(7)		2.291(3)
Average twist angle, deg	43.7(2)	47.1	45.5		2.48(2)
Average torsion angle, deg	52.35(3)	51.35	52(1)		51.4(7)

*shoulder. [a]tetragonally elongated Cu-N bond lengths. [b]six-coordinate ionic radius.[340, 341] [c]low-spin. [d]high-spin

B.1. Structures and Visible-near IR Electronic Spectra of [M(tachpyr)]2+, M = Zn(II) (250), Ni(II) (262) and Mn(II) (271)

The M-N bond lengths correlate well to the metal radii in **250**, **262**, and **271** (**Table 3.35**). As the six-coordinate ionic radius increases from Ni^{2+} (0.83 Å) to Zn^{2+} (0.88 Å) and then to Mn^{2+} (0.97 Å), the average bond length of M-N (tach) and the average bond length of M-N (pyridyl) increase proportionally. The M-N (tach) bond lengths do not differ from the M-N (pyridyl) bond lengths in these complexes except in the case of Mn(II), where the Mn(II)-N (pyridyl) distances exceed the Mn(II)-N (tach) ones. This may be rationalized as a poorer size fit (the pendant arms can not entirely surround Mn(II)) and/or a poorer hard-soft match (Mn(II) is hard and a pyridine donor is softer than the secondary amine of N (tach).

The coordination geometries of MN_6 in **250** and **262** (M = Zn(II) and Ni(II) respectively) are best described as distorted octahedral, whereas that of **271** (M = Mn(II)) is very close to trigonal prismatic. The average twist angles (α) (**Fig. 3.1**) of **250** and **262** are 43.7(2) and 45.5°, respectively, while that of **271** is 2.48(2)°. The coordination geometries may be explained by differences in metal ion radii (**Table 3.35**), similarly to the structural effects in Cd(II) and Hg(II) tachpyr complexes (Discussion A in **Chapter 3**). Thus, tachpyr adopts to a smaller metal by "wrapping" about the ion, leading to a larger twist angle, a larger dihedral angle of the chelate arm, designated as N(py)-C(py)-C(H_2)-N(tach), and a larger normalized bite.[342] By comparison, the trigonal prismatic coordination geometry in the complex of the larger ion Mn(II) (**271**) is obtained by

"unwrapping" the arms, achieving a smaller dihedral angle, and a smaller normalized bite.[342]

The structure of **250** can be compared to the Zn(II) complex of the related imino ligand, tachimpyr **172** (**Fig. 3.6**), which has a particularly small normalized bite. In order to achieve maximal π-delocalization this ligand tends to toward a planar MN_2C_2 chelating ring, i.e., the dihedral angles N(py)-C(py)-C(imine)-N(imine) are small. Further, its imino nitrogen prefers a planar (sp^2), further disfavoring a twist in chelate arms. Thus, the average twist angle in $[Zn(tachimpyr)](ClO_4)_2$ [288, 294] is 4.5°. In fact, all of the complexes $[M^{II}(tachimpyr)]^{2+}$ (M = Mn, Co, and Zn)[184] are nearly trigonal prismatic. However, the Fe(II) and Ni(II) ions which have greater CFSE than Mn(II), Zn(II), or Co(II), form tachimpyr complexes of intermediate geometry between octahedral and trigonal prismatic, with a twist angle approximately 30°.[184] Thus, electronic factors are also significant in determining coordination geometry.

B.2. Structures of $[Cu(tachpyr)](ClO_4)_2 \cdot 1/2CH_3CN$ (257) and $[Cu(tachpyr)](ClO_4)_2 \cdot CH_3OH$ (257A)

The coordination geometry of CuN_6 in **257** is best described as an axially elongated octahedron that is typical for Jahn-Teller distorted hexa-coordinate Cu(II). The Cu-N bond lengths of two trans nitrogen donors, N(3) (tach) and N(4) (pyridyl) (**Fig. 3.34 (a)**) are longer than the others. The extent of tetragonal distortion in **257** is typical of Cu(II) hexaamine complexes. The tetragonal Jahn-Teller distortion may be quantified by the tetragonality parameter, *T*, defined as

the mean in-plane Cu-N bond length divided by the mean out-of-plane Cu-N bond length.[342] A value of one indicates no tetragonal distortion, while a value greater than one indicates an axial compression and less than one indicates an axial elongation. The tetragonality in **257** is 0.87, which compares favorably to 0.88 in $[Cu([9]aneN_3)_2](CF_3SO_3)_2 \bullet 2H_2O$, 0.87 in $[Cu([9]aneN_3)_2](BPh_4)_2$,[344] and 0.88 in $[Cu(tach)_2](ClO_4)_2$.[302]

Surprisingly, $[Cu(tachpyr)](ClO_4)_2$ may be obtained in a different crystal form as methanol solvate, designated as **257A**. There is no apparent tetragonal distortion in **257A**, which may be attributed to the dynamic Jahn-Teller effect.[302] The bond lengths of the Cu-N (amine) and Cu-N (pyridyl) in **257A** are 2.116(5) and 2.143(6) Å. The bond length of Cu-N (pyridyl) is slightly longer than that of Cu-N (amine), as is observed for the Mn(II) complex of tachpyr.

Other complexes reported to possess a dynamic Jahn-Teller distortion are $[Cu(tach)_2](NO_3)_2$,[302] $[Cu([9]aneN_3)](ClO_4)_2$,[344] and $[Cu([9]aneN_3)][Cu(CN)_3] \bullet 2H_2O$.[320] In all cases, of course, the tetragonality is nearly one (range 0.95 to 1) in these examples and **257A**. The tetragonality of 1.0 for $[Zn(tachpyr)](ClO_4)_2 \bullet CH_3OH$ (**250**) serves as a useful reference for comparison with the structure of **257A** because Zn(II), d^{10}, does not undergo electronically-induced distortions.

B.3. Reaction of Cobalt(II) with tachpyr

In attempts to synthesize [Co(II)(tachpyr)]$(NO_3)_2$ from $Co(NO_3)_2 \bullet 6H_2O$ and tachpyr in MeOH in presence of air, a yellow mixture was obtained. Its composition was tentatively assigned as a mixture of [Co(tachpyr)]$(NO_3)_3$ (**267**) and [Co(tachpyr-*ox*-*n*)]$(NO_3)_3$ (**267A**) (*n* is unspecified). The UV-vis spectrum of the mixture has an absorption maximum at 466 nm (ε = 135) assigned to the $^1A_{1g}$ (F) -> $^1T_{1g}$ transition and a shoulder overlapped with a charge transfer band at 360 nm assigned to the $^1A_{1g}$ (F) -> $^1T_{2g}$ transition, which resemble the absorbances at 467 nm and 339 nm in $[Co(en)_3]^{3+}$.[345] Thus, the mixture presents two spin-allowed transitions, typical of a low-spin Co(III) complex. The magnetic moment of the mixture is 1.129 B.M., which suggests the presence of a paramagnetic substance, such as a small amount of Co(II). The ^1H NMR spectrum of the mixture (**Fig. 3.56**) indicates the presence of imino protons ($\delta > 9$), which would be formed by oxidative dehydrogenation in analogy to the iron-tachpyr system. Because of sharpness of this spectrum, we assign the major state of cobalt as Co(III) (d^6, low-spin).[233] Based on CFSE considerations, low-spin Co(III) is stabilized relative to Co(II).

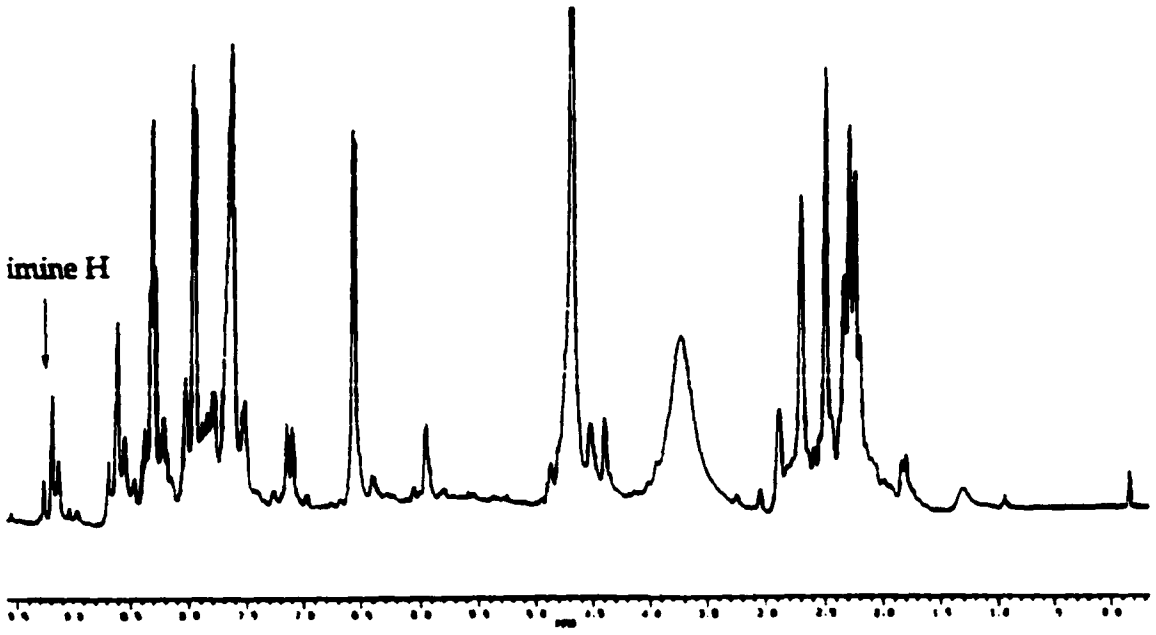

Figure 3.56. ^{1}H NMR spectrum of the mixture of **267** and **267A**.

C. First Row Transition Metal Complexes of tach-Me_3pyr and tach-Et_3pyr: $[M(tach\text{-}Me_3pyr)]^{2+}$ (M = Zn(II) (251), Cu(II) (258), Ni(II) (263), Co(II) (268), Mn(II) (252)) and $[M(tach\text{-}Et_3pyr)]^{2+}$ (M = Zn(II) (259), Ni(II) (264), Co(II) (269), Mn(II) (273))

C.1. Structural analysis of Zn(II) and Ni(II) complexes of tach-Me_3pyr

The structural parameters and physical properties of the Zn(II) and Ni(II) complexes of the tach-Me_3pyr ligand are compared with the Zn(II) and Ni(II) complexes of the tachpyr ligand in **Table 3.36.**

Table 3.36. Comparison of physical properties and structural parameters of the Zn(II) and Ni(II) complexes of tach-Me_3pyr and tachpyr.

	251	**250**	**263**	**262**
Oxidation state	Zn(II)	Zn(II)	Ni(II)	Ni(II)
Atomic radius[a] Å	0.88	0.88	0.83	0.83
Ligand	tach-Me_3pyr	tachpyr	tach-Me_3pyr	tachpyr
Average M-N (tach) distance, Å	2.228(2)	2.160(3)	2.167(7)	2.103(6)
Average M-N (pyridyl) distance, Å	2.165(2)	2.165(4)	2.107(6)	2.122(7)
Average twist angle, deg	43.2(2)	43.7(2)	48.1(3)	45.5[b]
Average torsion angle, deg	52.7(3)	52.35(3)	52(1)	52(1)

[a]six-coordinate ionic radius.[340, 341] [b]ESD unavailable

Differences in the bond lengths of the Ni(II) and Zn(II) complexes of tach-Me_3pyr are clearly related to metal-ion radius, as they are in tachpyr complexes. As the six-coordinate ionic radius increases from Ni^{2+} (0.83 Å) to Zn^{2+} (0.88 Å), the average bond length of M-N (tach) and M-N (pyridyl) increase.

The steric effect of *N*-methylation is evidenced by a greater disparity in M-N (tach) and M-N (pyridyl) bond lengths in the tach-Me_3pyr derivatives than in the tachpyr ones. The bond lengths of M-N (tach) are longer than those M-N (pyridyl) in **252** and **263**, in contrast, the two categories of M-N bond lengths do not differ appreciably in tachpyr derivatives. Bond lengthening of M-N (tach) bonds and shortening of M-N (pyridyl) bonds in tach-Me_3pyr complexes compared to tachpyr complexes are caused by the steric effects of the methyl groups on the cyclohexyl nitrogen atoms. Due to repulsions between the methyl protons and the protons on the adjacent bridging methylene, the cyclohexyl nitrogens are expanded away from the axial positions and coordinate at a greater distance from the metal ions. Consequently, the pendant arms are pushed toward the metal ion, leading the pyridyl nitrogens closer to the metal ions, resulting in a longer M-N (tach) bond than the M-N (pyridyl) bond. The effects of the methyl groups are shown in **Figure 3.57**.

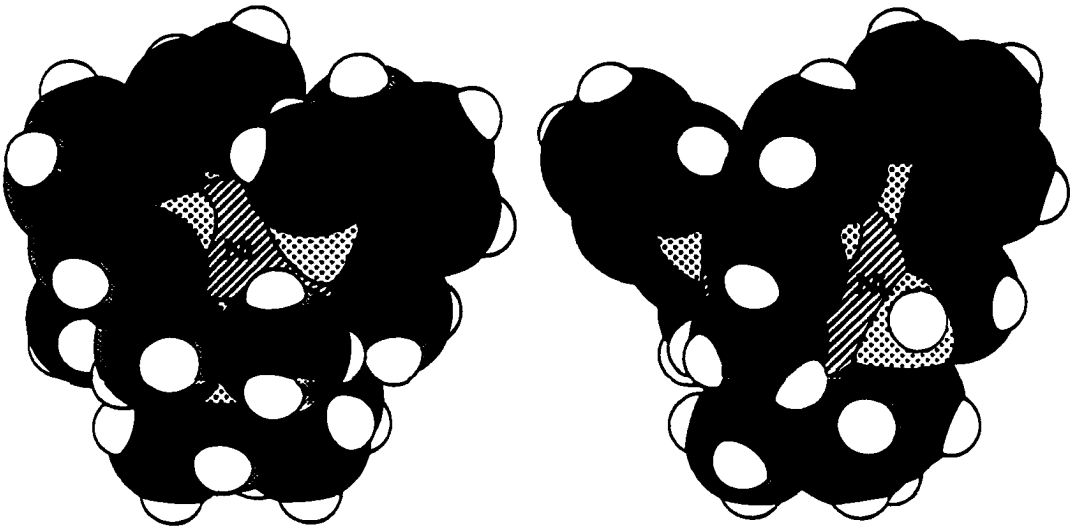

Figure 3.57. Space-filling model of (a) $[Ni(tach\text{-}Me_3pyr)]^{2+}$; (b) $[Ni(tachpyr)]^{2+}$.

Differences in the coordination polyhedra of metal-tach-Me_3pyr (and tachpyr) are related to the respective bonding properties of the Ni(II) and Zn(II) complexes. Compounds **251** and **263** (M = Zn(II) and Ni(II), respectively) possess distorted octahedral coordination polyhedra with average twist angles (α) (**Fig. 3.1**) of 43.2(2) and 48.1(3)°, respectively. The coordination geometry of the $[Ni(tach\text{-}Me_3pyr)]^{2+}$ is closer to octahedral than that of the Zn(II) complex **251** (**Table 3.36**). This is understandable because Ni(II) (O_h, d^8) has Crystal Field Stabilization Energy (CFSE) which creates an larger electronic preference for an octahedral geometry, while Zn(II) (d^{10}) has none. There is no significant difference in the distortion of the C-C-C-C torsion angles (β) between **251** and **263** due to the small difference in the six-coordinate ionic radii of Zn^{2+} (0.88 Å) in **251** and Ni^{2+} (0.83 Å) in **263**.

C.2. Structural analysis of the Cu(II) complex of tach-Me_3pyr (258).

The structural parameters and physical properties of Cu(II) complex of the tach-Me_3pyr ligand are compared Cu(II) complex of the tachpyr ligand in **Table 3.37.**

Table 3.37. Comparison of physical properties and structural parameters of $[Cu(tach\text{-}Me_3pyr)](ClO_4)_2$ (**258**) and $[Cu(tachpyr)](ClO_4)_2 \bullet 1/2CH_3CN$ (**257**).

	258	**257**
Oxidation state Atomic radius[b] Å	Cu(II) 0.87	Cu(II) 0.87
Ligand	tach-Me_3pyr	tachpyr
Magnetic moment B.M.	1.544	1.557
Average M-N (tach) distance Å	2.325(4)[a] 2.125(6)	2.245(5)[a] 2.066(7)
Average M-N (pyridyl) distance Å	2.336(4)[a] 2.069(6)	2.458(5)[a] 2.043(7)
Average twist angle, deg	44.9(3)	47.1
Average torsion angle, deg	55(1)	51.35

[a]tetragonally elongated Cu-N bond lengths. [b]six-coordinate ionic radius.[340,341]

The coordination geometry of CuN_6 in **258** is best described as an axially elongated octahedron as a result of the Jahn-Teller effect, typical for a hexa-coordinate Cu(II) complex. Due to geometric constraints of the tachpyr family, the trans-lengthened bonds must to be one pyridyl nitrogen and one tach nitrogen. In **258 (Fig. 3. 40)**, these are N(1) (tach) (Cu–N = 2.325(4) Å) and N(5)

(pyridyl) (Cu-N = 2.336(4) Å) which are longer than the four equatorial Cu-N distances, 2.0679(4) and 2.071(4) for Cu-N (tach) and 2.091(4) and 2.159(4) Å for Cu-N (pyridyl). The average of elongated Cu-N bond lengths (2.331(6) Å) in **258** is marginally shorter than 2.352(7) in $[Cu(tachpyr)](ClO_4)_2 \bullet 1/2CH_3CN$ (**257**), on the other hand the average of four remaining Cu-N bond lengths (2.097(8) Å) in **258** is clearly longer than 2.05(1) Å in **257**. The extent of Jahn-Teller distortion in **258** is typical amongst CuN_6 compounds. The tetragonality (see discussion B in **Chapter 3**)[342] of 0.90 for **258** compares well to 0.87 in **257**, 0.88 in $[Cu([9]aneN_3)_2](CF_3SO_3) \bullet 2H_2O$, 0.87 in $[Cu([9]aneN_3)_2](BPh_4)_2$,[344] and 0.88 in $[Cu(tach)_2](ClO_4)_2$.[302]

C.3. Visible-near IR spectral analysis of Co(II), Ni(II), and Cu(II) complexes of tach-R_3pyr

Trends in the energies of visible-near IR bands clearly indicate a weakening of metal-ligand interactions in tach-R_3pyr (R = Me and Et) complexes relative to tachpyr. Although no tach-Et_3pyr complexes have been structurally characterized, the trends also indicate that the steric effects decrease in the order tach-Et_3pyr > tach-Me_3pyr > tachpyr. The absorption maxima of the metal complexes of the tachpyr, tach-Me_3pyr, and tach-Et_3pyr ligands are presented in **Table 3.38.**

The Cu(II) complexes of tachpyr, tach-Me_3pyr, and tach-Et_3pyr have absorption maxima at 662, 723, and 734 nm respectively. This trend is also observed in the Ni(II) complexes of tachpyr, tach-Me_3pyr, and tach-Et_3pyr and the Co(II) complexes of tach-Me_3pyr and tach-Et_3pyr. The $^3A_{2g}$ -> ^1E_g (D)

transition (880 nm) in $[Ni(tachpyr)](Cl)_2 \bullet CH_3OH$ (**262**) shifts 44 nm to lower energy in $[Ni(tach\text{-}Me_3pyr)](ClO_4)_2 \bullet CH_3CN$ (**263**) and 76 nm to the lower energy in $[Ni(tach\text{-}Et_3pyr)](ClO_4)_2$ (**264**). As the tach-Me_3pyr ligand is changed to tach-Et_3pyr ligand in the Co(II) complexes, the $^4T_{1g}$ (F) -> $^4T_{2g}$ and $^4T_{1g}$ (F) -> $^4T_{1g}$ (P) transitions shift from 1022 nm to 1062 nm and from 491nm to 513 nm, respectively.

Table 3.38. Electronic absorptions of the metal complexes of the tachpyr, tach-Me_3pyr, and tach-Et_3pyr ligands

	Cu(II) nm (ε = cm^{-1} L mol^{-1})	Ni(II) nm (ε = cm^{-1} L mol^{-1})	Co(II) nm (ε = cm^{-1} L mol^{-1})
tachpyr	662 (93.0)	880 (11.8) 797 (16.0) 511 (16.6)	
tach-Me_3pyr	723 (81.4)	924 (13.4) 812 (8.6) 561 (14.8)	1022 (7.74) 491 (43.93) 552 (20.90)*
tach-Et_3pyr	734 (85.9)	956 (14.1) 820 (8.5) 573 (16.4)	1062 (3.41) 513 (90.4)

D. Divalent Metal Ion Complexes of a tachpyr derivative with sterically hindered pyridine rings, $[M^{II}(tach\text{-}6\text{-}Mepyr)](X)_2$, where M = Zn(II) (253), Cu(II) (260), Ni(II) (265), Co(II) (270), and Mn(II) (274); X = ClO_4^- or NO_3^-

D.1. Structural analysis of tach-6-Mepyr complexes of Zn(II), Ni(II), Co(II), and Mn(II)

The structural parameters and physical properties of **253**, **260**, **265**, **270**, and **274** are presented in **Tables 3.39** and **3.40**.

Table 3.39. Comparison of structural parameters and physical properties of the metal complexes of tach-6-Mepyr.

	253	265	270	274
Oxidation state Atomic radius [c] Å	Zn(II) 0.88	Ni(II) 0.83	Co(II)[d] 0.885	Mn(II)[d] 0.97
Electronic maxima nm (ε, cm^{-1} L mol^{-1})		927 (23.2) 815 (13.7) 561 (7.8)	1042 (7.6) 494 (28.6)	
M-N (tach) distance Å	2.128(4) 2.133(4) 2.136(4)	2.078(3) 2.099(3) 2.102(3)	2.1212(13) 2.1510(13) 2.1517(12)	2.235(3) 2.247(3) 2.262(3)
M-N (pyridyl) distance Å	2.203(4) 2.216(4) 2.566(5)[e]	2.191(3) 2.203(3) 2.267(3)[e]	2.1940(13) 2.2450(12) 2.3085(13)	2.277(3) 2.282(3) 2.442(3)[e]
Average twist angle, deg	53.9(3)[a] 49.5(1)[a]	55.3(3)	54.7(1)	52.6(3)[a] 49.6(1)[a]
Average torsion angle, deg	50(2)[b] 51(2)[b]	53(1)	51.0(5)	49(1)[b] 50(2)[b]

[a]Average twist angles and torsion angles from each of two molecules in **253** and **274**. [b]Average torsion angles and twist angles from each of two molecules in **253** and **274**. [c]six-coordinate ionic radius.[340,341] [d]high-spin complex. [e]asymmetric lengthening.

The tach-6-Mepyr ligand relieves the steric strain caused by the 6-methyl groups through lengthening of M-N (pyridyl) bonds in its metal complexes relative to metal complexes of tachpyr (**Table 3.39** and **3.40**). In the cases of Zn(II), Ni(II), and Mn(II), the lengthening is asymmetric with M-N (pyridyl) distance 0.30 Å longer than the average of the other two for Zn(II), 0.06 Å longer for Ni(II), and 0.16 Å longer for Mn(II). In the case of Cu(II), one arm is entirely dissociated from the metal (**Fig. 3.43**). In the case Co(II) there is a progressive lengthening of M-N (pyridyl) bond lengths, which are 2.1940(13), 2.2450(12), and 2.3085(13) Å.

The steric effects responsible for M-N (pyridyl) bond lengthening in tach-6-Mepyr complexes might be greatest when 6-methyl groups point directly at each other, which would occur in a trigonal prismatic coordination geometry. Therefore, tach-6-Mepyr complexes show substantial twisting of the pendant arms, giving a distorted octahedral geometry and allowing the methyl groups to avoid each other. The average twist angles (α) (**Fig. 3.1**) in **253**, **265**, **270** and **274** (M = Zn(II), Ni(II), Co(II), and Mn(II), respectively) are 53.9(3) and 49.5(1), 55.3(3), 54.7(1), and 52.6(3)° and 49.6(1)°, respectively. The Zn(II) and Mn(II) complexes of tach-6-Mepyr are isostructural, and each complex crystallizes with two independent molecules (molecule 1 and 2) in the asymmetric unit. The coordination geometries of the tach-6-Mepyr complexes do not appear to bear any relationship to metal radii.

The M-N (pyridyl) bond lengths are significantly greater than the M-N (tach) bond lengths in **253**, **265**, **270** and **274**, indicating that steric strain of the 6-methyl groups may be relieved through displacement of pyridyl rings away

from each other. The M-N (pyridyl) bond lengths range 2.203(4)-2.566(5) Å in molecule 1 of **253**, 2.191(3)-2.267(3) Å in **265**, 2.1940(13)-2.3085(13) Å in **270**, and 2.277(3)-2.442(3) Å in molecule 1 of **274**. The bond lengths of M-N (tach) range 2.128(4)-2.136(4) Å in molecule 1 of **253**, 2.078(3)-2.102(3) Å in **265**, 2.1212(13)-2.1517(12) Å in **270**, and 2.235(3)-2.262(3) Å in molecule 1 of **274**. Two space-filling models of the Zn(II) complexes of tach-6-Mepyr and tachpyr are presented in **Figure 3.58** to illustrate the steric effects of the methyl groups.

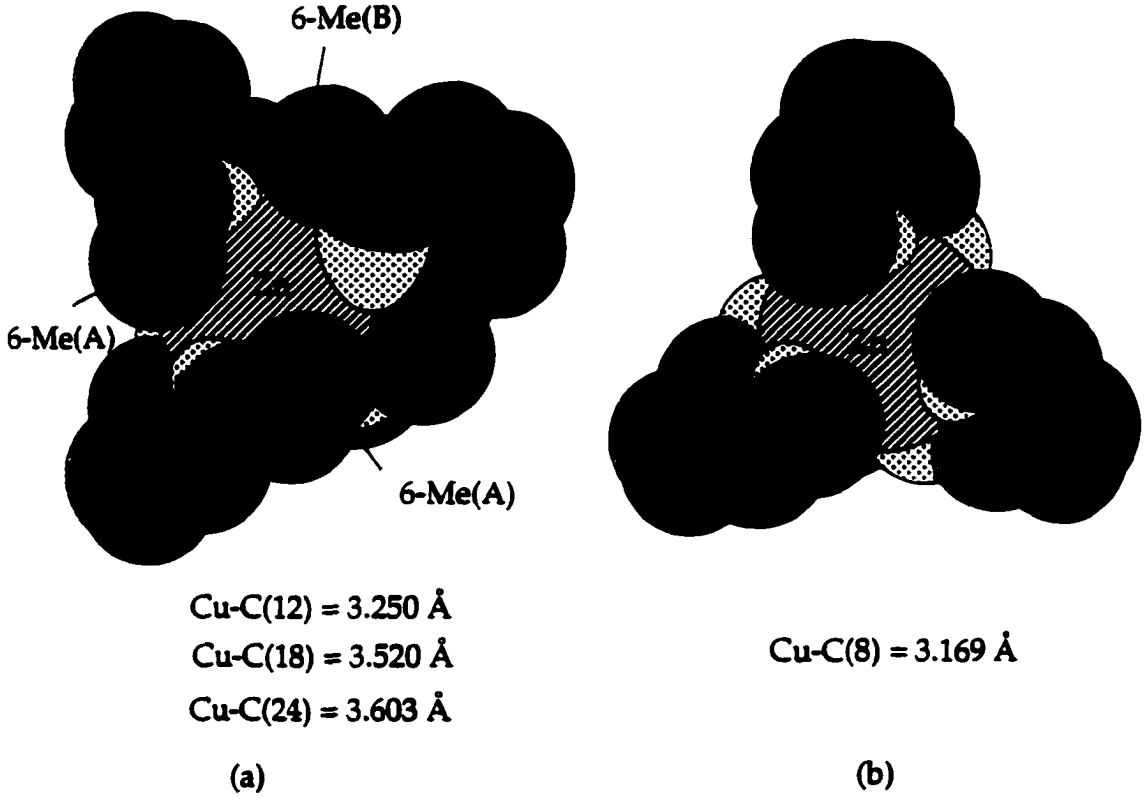

Figure 3.58. Space-filling models of (a) [Zn(tach-6-Mepyr)]$(ClO_4)_2 \bullet CH_3OH$(**253**) in which the two 6-Me(A) create convergence upon complexation as a consequence the 6-Me(B) are located away from metal ions, (b) [Zn(tachpyr)]$(ClO_4)_2 \bullet CH_3OH$ (**250**).

However, the M-N (tach) bond lengths are affected by metal radius. The trends in average M-N (tach) bond length is 2.093(5) Å (Ni(II)) < 2.132(7) Å (Zn(II)) ≈ 2.141(2) Å (Co(II)) < 2.248(5) Å (Mn(II)), which corresponds to the trend in Ni^{2+} (0.83 Å) < Zn^{2+} (0.88 Å) ≈ Co^{2+} (H.S., 0.885 Å) < Mn^{2+} (H.S., 0.97 Å) (**Table 3.40**). There is not significant different in the average bond length of M-N (tach) between **253** and **270**, which is consistent with six-coordinate ionic radii of **253** and **270**. The same effect on the average bond length of the two M-N (pyridyl) from which closely coordinate pyridines is observed but is not significant as in average bond length of M-N (tach). Although the M-N (pyridyl) bond lengths are more irregular, there is a also a general relationship of these bond lengths to metal ion radii.

The lengthening of M-M (pyridyl) bond lengths resulting from 6-methylation of pyridine is accompanied by a marginal shortening of M-N (tach) distances in the cases of Zn(II) and Ni(II) as determined by comparison of these parameters to those of tachpyr complexes. The M-N (tach) bond lengths in **253** and **265** are shorter than those of tachpyr complexes of the corresponding metal ion. The M-N (pyridyl) bond lengths of the tach-6-Mepyr complexes are of course significantly longer than in the related tachpyr complexes. Structural parameters of the complexes of tach-6-Mepyr are compared with those of tachpyr in **Table 3.40** (M = Zn(II), Ni(II), and Mn(II))

The distortion of the cyclohexyl ring caused by displacement of tach nitrogens outward from their axial positions is indicated by the C-C-C-C torsion angles in **Table 3.40**. As the metal ion radius increases from Ni(II) (0.83 Å) to

Mn(II) (high-spin, 0.97 Å), there may be a slightly greater distortion of the cyclohexane framework, as reflected by a marginal decrease in torsion angle.

Table 3.40. Comparison of physical properties and structural parameters of $[M(tach\text{-}6\text{-}Mepyr)]^{2+}$ complexes and $[M(tachpyr)]^{2+}$ where M = Zn(II), Ni(II), and Mn(II).

	253	250	265	262	274	271
Metal ion Atomic radius[b] Å	Zn(II) 0.88	Zn(II) 0.88	Ni(II) 0.83	Ni(II) 0.83	Mn(II)[c] 0.97	Mn(II)[c] 0.97
Ligand	tach-6-Mepyr	tachpyr	tach-6-Mepyr	tachpyr	tach-6-Mepyr	tachpyr
Electronic maxima nm (ε, cm^{-1} L mol^{-1})			927 (23.2) 815 (13.7) 561 (7.8)	880 (11.8) 797 (16.0) 511 (16.6)		
Average M-N (tach) distance Å	2.132(7)	2.160(3)	2.093(5)	2.103(6)	2.248(5)	2.238(3)
Average M-N (pyridyl) distance Å	2.210(6)[a] 2.566(5)	2.165(4)	2.197(4)[a] 2.267(3)	2.122(7)	2.280(4)[a] 2.442(3)	2.291(3)
Average twist angle, deg	53.9(3)[b] 49.5(1)[b]	43.7(2)	55.3(3)	45.5	52.6(3)[b] 49.6(1)[b]	2.48(2)
Average torsion angle, deg	50(2)[b] 51(2)[b]	52.35(3)	53(1)	52(1)	49(1)[b] 50(2)[b]	51.4(7)

[a]average of two short M-N (pyridyl) in tach-6-Mepyr complexes. [b]two averages from two molecules in **253** and **274**. [c]high-spin complex.

D.2. Structural Analysis of [Cu(tach-6-Mepyr)]$(ClO_4)_2$ (260).

The coordination geometry of CuN_5 in **260** is best described as intermediate between trigonal bipyramidal and square pyramidal, but slightly closer to trigonal bipyramidal, where N(2) and N(4) might be considered the apical positions and N(1), N(3), and N(5) form the trigonal plane. The two apical Cu-N distances, 2.000(3) and 2.012(3) Å, are similar, while the trigonal plane Cu-N distances are irregular, 2.045(3), 2.103(3), and 2.216(3) Å. The steric hindrance of tach-6-Mepyr is most apparent in this Cu(II) complex in which the pyridyl nitrogen, N(6), is bent entirely away from copper (**Fig. 3.43**). The complete dissociation of an arm is expected as Cu(II) has a greater tendency to five-coordination than the other ions.[346] The tetragonality in **260**, T^5, is 1.06 and indicates an axially compressed CuN_5 polyhedron, which compares well to 1.04 in [Cu(dien)(bipyam)]$(NO_3)_2$[324] and 1.03 in [Cu(bipy)$_2$(NCS)]$(BF_4)_2$.[325]

D.3. Electronic and Magnetic properties of tach-6-Mepyr Complexes.

The visible-near IR spectra of [Ni(tach-6-Mepyr)]$(NO_3)_2$ (**265**) and [Ni(tachpyr)]$(Cl)_2 \cdot CH_3OH$ (**262**) are very similar, suggesting that they have similar structures in solution (**262** in MeOH and **265** in CH_3CN). The energies of absorption bands in **265** are lower than in **262**, suggesting the nitrogen of **265** are weakly bound relative to those in **262**, consistent with the structural steric effect observed.

The magnetic moments of the Ni(II), Co(II), and Mn(II) complexes of tach-6-Mepyr are consistent with the expected electron configuration of Oh-d^8, high-

spin-Oh-d^7, and high-spin-Oh-d^5, respectively. However, the observed magnetic moments of the Cu(II) tach-6-Mepyr complex is 1.567 B.M., slightly smaller than the spin-only value of 1.73 B.M. and the experimental values of 1.8 – 2.0 B.M.[3]

Conclusion

First row transition metal complexes with tachpyr ligand, *N,N',N''*-tris(2-pyridylmethyl)-*cis,cis*-1,3,5-triaminocyclohexane, exhibit the metal radius effects on the coordination geometry and bond lengths. The tachpyr ligand forms a nearly octahedral complex with Zn(II) and Ni(II), a tetragonally distorted octahedral complex with Cu(II), an intermediate between an octahedron and trigonal prismatic complex with Cd(II), while it forms a nearly trigonal prismatic complex with Mn(II) and a slightly distorted trigonal prismatic complex with Hg(II). Electronic spectra and magnetic susceptibility study confirm the electronic configurations of the metal ions as Ni(II) (d^8), Cu(II) (d^9), Co (III) (low-spin, d^6), and Mn(II) (high-spin, d^5) in solution. Cobalt-mediated oxidative dehydrogenation of coordinated tachpyr in the presence of O_2 is obtained affording the imino Co(III) complexes.

Tach-Me_3pyr ligand, *N,N',N''*-trimethyl-*N,N',N''*-tris(2-methylpyridyl)-*cis,cis*-1,3,5-triaminocyclohexane, exhibit steric effect of the methyl groups on the M-N (tach) bond lengths in Zn(II) and Ni(II) complexes. Thus, while the M-N (tach) bond lengths are shorter than the M-N (pyridyl) ones in $[M^{II}(tachpyr)]^{2+}$ (M = Zn, Ni, and Mn), the order is reversed in $[M^{II}(tach\text{-}Me_3pyr)]^{2+}$ (M = Zn and Ni). The tach-Me_3pyr ligand forms a distorted octahedral complexes with the Ni(II) and Zn(II), while it forms a Jahn-Teller distorted Cu(II) complex.

The steric effects of the methyl groups in the tach-6-Mepyr ligand, *N,N',N''*-tris(6-methyl-2-methylpyridyl)-*cis,cis*-1,3,5-triaminocyclohexane, substantially lengthen one of the three M-N (pyridyl) bond distances. The coordination geometries of the transition metal complexes of tach-6-Mepyr are

distorted octahedral (M = Zn(II), Ni(II), Co(II) and Mn(II)), while it forms a distorted trigonal bipyramidal complexes with Cu(II) as a consequence of a twisted pendant arm away from Cu(II) ion. The electronic configuration of the metal ions are typical Cu(II) (d^9), Ni(II) (d^8), Co(II) (high-spin, d^7), and Mn(II) (high-spin, d^5) according to electronic spectra and the magnetic moments of the complexes.

S,S,S-Tachbn, *N,N',N''*-tris(2-S-amino-3-phenylpropane)-*cis,cis*-1,3,5-triaminocyclohexane, forms a distorted octahedral complex with Zn(II), while it forms a tetragonally distorted octahedral complex with Cu(II). S,S,S-Tachpn, *N,N',N''*-tris(2-S-aminopropane)-*cis,cis*-1,3,5-triaminocyclohexane, forms a distorted octahedral complex with the Ni(II) ion.

The complexation chemistry of tachpyr and a variety of pendant-arm derivatives of tach with first row transition metal elements show a versatility of the metal complexes and different steric effects on coordination geometry. Biological application studies with some of these metal complexes are in progress.

LIST OF REFERENCES

1. Park, G.; Lu, F. H.; Ye, N.; Brechbiel, M. W.; Torti, S. V.; Torti, F. M.; R. P. Planalp, *JBIC* **1998**, 3, 449-457.

2. Cotton, F. A.; Wilkinson, G. *Advanced Inorganic Chemistry*; Wiley: New York, 1988; pp 1336 ff.

3. Hathaway, B. J. *Comprehensive Coordination Chemistry* **1987**, *vol. 5*, 533-774.

4. Duggan, M.; Ray, N.; Hathaway, B. *J. Chem. Soc., Dalton Trans.* **1982**, 1342-1348.

5. Ferguson, J. *Progr. Inorg. Chem.* **1970**, *12*, 159-293.

6. Maslen, H. S.; Waters, T. N. *Coord. Chem. Rev.* **1975**, *17*, 137-176.

7. Hathaway, B. J.; Billing, D. E. *Coord. Chem. Rev.* **1970**, *5*, 143-207.

8. Douglas, B. E.; Mcdaniel, D. H.; Alexander, J. J. *Concepts and models of inorganic chemistry*; John Wiely & Sons: New York, 1993; pp 444-445.

9. Karlin, K. D.; Hayew, J. C.; Juen, S.; Hutchinson, J. P.; Zubieta, J. *Inorg. Chem.* **1982**, *21*, 4106-4108.

10. Wei, N.; Murthy, N. N.; Karlin, K. D. *Inorg. Chem.* **1994**, 33, 6093-6100.

11. de Angelis, S.; Batsanov, A.; Norman, T. J.; Parker, D.; Senanayake, K.; Vepsalainen, J. *J. Chem. Soc., Chem. Commun.* **1995**, 2361.

12. Hegetschweiler, K.; Ghisletta, M.; Fassler, T.; Nesper, R.; Schalle, H.; Rihs, G. *Inorg. Chem.* **1993**, *32*, 2032-2041.

13. Bollinger, J. E.; Mague, J. T.; Roundhill, D. M. *Inorg. Chem.* **1994**, 33, 1241.

14. Greener, B.; Moore, M. H.; Walton, P. H. *J. Chem. Soc., Chem. Commun.* **1996**, 27-28.

15. Bollinger, J. E.; Mague, J. T.; Banks, W. A.; Kastin, A. J.; Roundhill, D. M. *Inorg. Chem.* **1995**, 34, 2143.

16. Radzicka, A.; Wolfenden, R. *Science* **1995**, *267*, 90.

17. Thompson, J.; Kutateladez, T.; Schuster, M.; Venegas, F.; Messmore, J.; Raines, R. *Bioorg. Chem.* **1995**, *23*, 471.

18. Westheimer, F. H. *Science* **1987**, *235*, 1173-1178.

19. Wilcox, D. E. *Chem. Rev.* **1996**, *96*, 2435.

20. Voet, D.; Voet, J. *Biochemistry*; John wiley & sons: New York, 1990.

21. Hegg, E. L.; Mortimore, S. H.; Cheung, C. L.; Huyett, J. E.; Powell, D. R.; Burstyn, J. N. *Inorg. Chem.* **1999**, *38*, 2961-2968.

22. Hegg, E. L.; Burstyn, J. N. *Coord. Chem. Rev.* **1998**, *173*, 133-165.

23. Lippard, S. J.; Berg, J. M. *Principles of bioinorganic chemistry*; Univ Sci Bks: Mill Valley, CA, 1994.

24. Christianson, D. W.; Lipscomb, W. N. *Acc. Chem. Res.* **1989**, 62.

25. Holmes, M. A.; Tronrud, D. E.; Matthews, B. W. *Biochemistry* **1983**, *22*, 236.

26. Matthews, B. W. *Acc. Chem. Res.* **1988**, 333.

27. Holmes, M. A.; Matthews, B. W. *Biochemistry* **1981**, *20*, 6912.

28. Groves, J. T.; Olson, J. R. *Inorg. Chem.* **1985**, *24*, 2715.

29. Vincent, J. B.; Olivier-Lolley, G. L.; Averill, B. A. *Chem. Rev.* **1990**, *90*, 1447.

30. Kim, E. E.; Wyckoff, H. W. *J. Mol. Biol.* **1991**, *218*, 449-464.

31. Strater, N.; Klabunde, T.; Tucker, P.; Witzel, H.; Krebs, B. *Science* **1995**, *268*, 1489.

32. Mueller, E. G.; Crowder, M. W.; Averill, B. A.; Knowles, J. R. *J. Am. Chem. Soc.* **1993**, *115*, 2974.

33. Ganzhorn, A. J.; Chanal, M.-C. *Biochemistry* **1990**, *29*, 6065.

34. Bone, R.; Frank, L.; Springer, J. P.; Pollack, S. J.; Osborne, S.; Atack, J. R.; Knowles, M. R.; McAllister, G.; Ragan, C.; Broughton, H. B.; Baker, R.; Fletcher, S. *Biochemistry* **1994**, *33*, 9460.

35. Bone, R.; Frank, L.; Springer, J. P.; Atack, J. R. *Biochemistry* **1994**, *33*, 9468.

36. Zhang, Y.; Liang, J.; Huang, S.; Ke, H.; Lipscomb, W. N. *Biochemistry* **1993**, *32*, 1844-1857.

37. Domanico, P. L.; Rahil, J. F.; Benkovic, S. J. *Biochemistry* **1985**, *24*, 1623-1628.

38. Welsh, K. M.; jacobyansky, A.; Springs, B.; Cooperman, B. S. *Biochemistry* **1983**, *22*, 2243-2248.

39. Banerjee, A.; Cooperman, B. S. *Inorg. Chim. Acta* **1983**, *79*, 146-148.

40. Welsh, K. M.; Armitage, I.; Cooperman, B. S. *Biochemistry* **1983**, *22*, 1046-1054.

41. Derbyshire, V.; Freemont, P. S.; Sanderson, M. R.; Beese, L.; Friedman, J. M.; Joyce, C. M.; Steitz, T. A. *Science* **1988**, *240*, 199-210.

42. Han, H.; Rifkind, J. M.; Mildvan, A. S. *Biochemistry* **1991**, *30*, 11104-11108.

43. Beese, L. S.; Steitz, T. A. *EMBO J* **1991**, *10*, 25-33.

44. Davies II, J. F.; Hostomska, Z.; Hostomsky, Z.; Jordan, S. R.; Matthews, D. A. *Science* **1988**, *252*, 88-95.

45. Potter, B. V.; Connolly, B. A.; Eckstein, F. *Biochemistry* **1983**, *22*, 1369-1377.

46. Baldwin, G. S.; Vipond, I. B.; Halford, S. E. *Biochemistry* **1995**, *34*, 705-714.

47. Bergstrom, D. E.; Gerry, N. P. *J. Am. Chem. Soc.* **1994**, *116*, 12067.

48. Sutton, P. A.; Buckingham, D. A. *Acc. Chem. Res.* **1987**, *20*, 357-364.

49. Groves, J. T.; Baron, L. A. N. N. *J. Am. Chem. Soc.* **1989**, *111*, 56442-55448.

50. Groves, J. T.; R. Rife Chambers, J. *J. Am. Chem. Soc.* **1984**, *106*, 630-638.

51. Fife, T. H.; Przystas, T. J. *J. Am. Chem. Soc.* **1986**, *108*, 4631-4636.

52. Sayre, L. M.; Reddy, K. V.; Jacobson, A. R.; Tang, W. *Inorg. Chem.* **1992**, *31*, 935.

53. Monteserrat Tetas, Lowenstein, J. M. *Biochemistry* **1963**, *2*, 350.

54. Butcher, W. W.; Westheimer, F. H. *J. Am. Chem. Soc.* **1955**, *77*, 2420.

55. Jones, D. R.; Lindoy, L. F.; Sargeson, A. M. *J. Am. Chem. Soc.* **1983**, *105*, 7327.

56. Kenley, R. A.; Fleming, R. H.; Laine, R. M.; tse, D. S.; Winterle, J. S. *Inorg. Chem.* **1984**, *23*, 1870.

57. Hendry, P.; Sargeson, A. M. *J. Am. Chem. Soc.* **1989**, *111*, 2521.

58. Chin, J.; Zou, X. *J. Am. Chem. Soc.* **1988**, *110*, 223.

59. Chin, J.; Banaszczyk, M.; Jubian, V.; Zou, X. *J. Am. Chem. Soc.* **1989**, *111*, 186-190.

60. Harrowfield, J. M. B.; Jones, D. R.; Lindoy, L. F.; Sargeson, A. M. *J. Am. Chem. Soc.* **1980**, *102*, 7733.

61. Hendry, P.; Sargeson, A. M. *Inorg. Chem.* **1990**, *29*, 92.

62. Hendry, P.; Sargeson, A. M. *Inorg. Chem.* **1990**, *29*, 97.

63. Connolly, J. A.; Kim, J. H.; Banaszczyk, M.; Drouin, M.; Chin, J. *Inorg. Chem.* **1995**, *34*, 1094-1099.

64. Chung, Y.; Akkaya, E. U.; Venkatachalam, T. K.; Czarnik, A. W. *Tetrahedron Lett.* **1990**, *31*, 5413.

65. Vance, D. H.; Czarnik, A. W. *J. Am. Chem. Soc.* **1993**, *115*, 12165.

66. Wall, M.; Hynes, R. C.; Chin, J. *Angew. Chem. Int. Ed. Engl.* **1993**, *32*, 1633-1635.

67. Tsubouchi, A.; Bruice, T. C. *J. Am. Chem. Soc.* **1995**, *117*, 7399.

68. Chapman, W. H.; Breslow, R. *J. Am. Chem. Soc.* **1995**, *117*, 5462.

69. Koike, T.; Inoue, M.; Kimura, E.; Shiro, M. *J. Am. Chem. Soc.* **1996**, *118*, 3091.

70. Gultneh, Y.; Allwar, Ahvazi, B.; Blaise, D.; Butcher, R. J.; Jasinski, J. *Inorg. Chim. Acta* **1996**, *241*, 31.

71. Gultneh, Y.; Khan, A. R.; Blaise, D.; Chaudhry, S.; Ahvazi, B.; Marvey, B. B.; Butcher, R. J. *J. Inorg. Biochem.* **1999**, *75*, 7-18.

72. Bazzicalupi, C.; Bencini, A.; Bianchi, A.; Fusi, V.; Giorgi, C.; paoletti, P.; Valtancoli, B.; Zanchi, D. *Inorg. Chem.* **1997**, *36*, 2784.

73. Bazzicalupi, C.; Bencini, A.; berin, E.; Bianchi, A.; Fedi, V.; Fusi, V.; Giorgi, C.; paoletti, P.; Valtancoli, B. *Inorg. Chem.* **1999**, *38*, 4115.

74. Sigel, H.; Hofstetter, F.; martin, R.; Milburn, R.; Scheller-Krattiger, V.; Scheller, K. *J. Am. Chem. Soc.* **1984**, *106*, 7935.

75. Gellman, S. H.; Petter, R.; Breslow, R. *J. Am. Chem. Soc.* **1986**, *108*, 2388.

76. Norman, P. R. *Inorg. Chim. Acta* **1987**, *130*, 1.

77. Clewley, R. G.; Slebocka-tilk, H.; Brown, R. S. *Inorg. Chim. Acta* **1989**, *157*, 233-238.

78. Kioke, T.; Kimura, E. *J. Am. Chem. Soc.* **1991**, *113*, 8935.

79. Kimura, E.; Kodama, Y.; Koike, T.; Shiro, M. *J. Am. Chem. Soc.* **1995**, *117*, 8304.

80. Kady, I. O.; Tan, B.; Ho, Z.; Scarborough, T. *J. Chem. Soc., Chem. Commun.* **1995**, 1137.

81. Morrow, j. R.; Trogler, W. C. *Inorg. Chem.* **1988**, *27*, 3387-3394.

82. Fife, T. H.; Pujari, M. P. *J. Am. Chem. Soc.* **1988**, *110*, 7790.

83. Wahnon, D.; Hynes, R. C.; Chin, J. *J. Chem. Soc., Chem. Commun.* **1994**, 1441-1442.

84. Kovari, E.; Heitker, J.; Kramer, R. *J. Chem. Soc., Chem. Commun.* **1995**, 1205-1206.

85. Young, M. J.; Wahnon, D.; Hynes, R. C.; Chin, J. *J. Am. Chem. Soc.* **1995**, *117*, 9441-9447.

86. Bunton, C. A.; Scrimin, P.; Tecilla, P. *J. Chem. Soc., Perkin Trans. 2* **1996**, 3, 419-425.

87. Deal, K. A.; Burstyn, J. N. *Inorg. Chem.* **1996**, *35*, 2792-2798.

88. Deal, K. A.; Hengge, A. C.; Burstyn, J. N. *J. Am. Chem. Soc.* **1996**, *118*, 1713-1718.

89. Hegg, E. L.; Deal, K. A.; Kiessling, L. L.; Burstyn, J. N. *Inorg. Chem.* **1997**, *36*, 1715.

90. Hegg, E. L.; Burstyn, J. N. *Inorg. Chem.* **1996**, *35*, 7474-7481.

91. Itoh, T.; Hisada, H.; Usui, Y.; Fujii, Y. *Inorg. Chim. Acta* **1998**, *283*, 51-60.

92. Hay, R. W.; Govan, N. *Polyhedron* **1998**, *17*, 2079-2085.

93. Hay, R. W.; Govan, N. *Polyhedron* **1998**, *17*, 463-468.

94. Ye, N.; Rogers, R. D.; Brechbiel, M. W.; Planalp, R. P. *Polyhedron* **1998**, *17*, 603-606.

95. Bowen, T.; Planalp, R. P.; Brechbiel, M. W. *Bioorg. Med. Chem. Lett.* **1996**, *6*, 807.

96. Park, G.; Lu, F. H.; Shao, J.; Chasteen, N. D.; Rogers, R. D.; Brechbiel, M. W.; Planalp, R. P. *Inorg. Chem.* **in preparation.**

97. Park, G.; Rogers, R.; Brechbiel, M. W.; Planalp, R. P. *Polyhedron* **2000**, *19*, 1155-1161.

98. Brand, U.; Vahrenkamp, H. *Inorg. Chim. Acta* **1992**, *198-200*, 663-669.

99. Yang, R.; Zompa, L. J. *Inorg. Chem.* **1976**, *15*, 1499-1502.

100. Douglas, B. E.; Mcdaniel, D. H.; Alexander, J. J. *Concepts and models of inorganic chemistry*; John Wiely & Son: New York, 1993; pp p404.

101. Shao, J. *dissertation, UNH* **2000**, *chapter 5*, 116-152.

102. Greener, B.; Cronin, L.; Wilson, G. D.; Walton, P. H. *J. Chem. Soc., Dalton Trans.* **1996**, 401-403.

103. Schwindinger, W. F.; Fawcett, T. G.; Lalancette, R. A.; Potenza, J. A.; Schugar, H. J. *Inorg. Chem.* **1980**, *19*, 1379.

104. Bereman, R. D.; Churchill, M. R.; Schaber, P. M.; Winkler, M. E. *Inorg. Chem.* **1979**, *18*, 3122-3125.

105. Deal, K. A.; Park, G. P.; Shao, J.; Chasteen, N. D.; Planalp, R. P.; Brechbiel, M. W. *Inorg. Chem.* **in preparation.**

106. Richardson, D. R.; Ponka, P. *Biochim. Biophys. Acta* **1997**, *1331*, 1-40.

107. Crichton, R. R.; Ward, R. J. **1992**, *Iron and Human Disease*, 23-75.

108. Weinberg, E. D. *Drug Metabolism Rev.* **1990**, *22*, 531-579.

109. Bates, G. W.; Schlabach, M. R. *J. Biol. Chem.* **1975**, *250*, 2177-2181.

110. Torti, S. V.; Planalp, R. P.; Brechbiel, M. W.; Park, G.; Torti, F. M. **1999**, *Molecular Biology of Hematopoiesis 6*, 381.

111. Jacobs, A. *Blood* **1977**, *50*, 433-439.

112. Weaver, J.; Pollack, S. *Biochem. J.* **1989**, *261*, 787-792.

113. Deighton, N.; Hider, R. C. *Biochem. Soc. Trans.* **1989**, *17*, 490.

114. Crichton, R. R. *TIBS* **1984**, *9*, 283-386.

115. Macara, I. G.; Hoy, T. G.; Harrison, P. M. *Biochem. J.* **1972**, *126*, 151-162.

116. Chasteen, N. D.; Antanaitis, C. B.; Aisen, Philip. *J. Biol. Chem.* **1985**, *260*, 2926-2929.

117. Wardeska, J. G.; Viglione, B.; Chasteen, N. D. *J. Biol. Chem.* **1986**, *261*, 6677-6683.

118. Bakker, G. R.; Boyer, R. F. *J. Biol. Chem.* **1986**, *261*, 13182-13185.

119. Munro, H. N.; Linder, M. C. *Physiological Reviews* **1978**, *58*, 317-396.

120. Rohrer, J. S.; Islam, Q. T.; Watt, G. D.; Sayers, D. E.; Theil, E. C. *Biochemistry* **1990**, *29*, 259-264.

121. Fatemi, S. J.; Kadir, F. H.; Williamson, D. J.; Moore, G. R. *Adv. Inorg. Chem.* **1991**, *36*, 409-448.

122. Moore, G. R.; Kadir, F. H.; Al-Massad, F. *J. Inorg. Biochem.* **1992**, *47*, 175-181.

123. Kuhn, L.C.; Hentze, M. W.; *J. Inorg. Biochem.* **1992**, *47*, 183-195.

124. Emery-Goodman, A.; Hirling, H.; Scarpellino, L.; Henderson, B.; Kuhn, L. C. *Nucleic Acids Res.* **1993**, *21*, 1457-1461.

125. Rosch, M. A. D.; Trogler, W. C. *Inorg. Chem.* **1990**, *29*, 2409.

126. Pratviel, G.; Bernadou, J.; Meunier, B. *Angew. Chem. Int. Ed. Engl.* **1995**, *34*, 746.

127. Sigman, D. S.; Graham, D. R.; D'Aurora, V.; Stern, A. M. *J. Biol. Chem.* **1979**, *254*, 12269-12272.

128. Pratviel, G.; Bernadou, J.; Meunier, B. *Adv. Inorg. Chem.* **1998**, *45*, 251.

129. Williams, L. D.; Thivierge, J.; Goldberg, I. H. *Nucleic Acids Res.* **1988**, *16*, 11607-11615.

130. Marshall, L. E.; Graham, D. R.; Reich, K. A.; Sigman, D. S. *Biochemistry* **1981**, *20*, 244-250.

131. Reich, K.; Marshall, L. E.; Graham, D. R.; Sigman, D. S. *J. Am. Chem. Soc.* **1981**, *103*, 3582-3584.

132. Yoon, C.; Kuwabara, M. D.; Spassky, A.; Sigman, D. S. *Biochemistry* **1990**, *29*, 2116-2121.

133. Sugiyama, H.; Xu, C.; Murugesan, N.; Hecht, S. M.; Marel, G. A. v. d.; Boom, J. H. v. *Biochemistry* **1988**, *27*, 58.

134. Burger, R.; Peisach, J.; Horwitz, S. B. *J. Biol. Chem.* **1981**, *256*, 11636.

135. Sam, J. W.; Tang, X.-j.; Peisach, J. *J. Am. Chem. Soc.* **1994**, *116*, 5250.

136. Guajardo, R. J.; Chavez, F.; Farinas, E.; Mascharak, P. K. *J. Am. Chem. Soc.* **1995**, *117*, 3883.

137. Pogozelski, W. K.; McNesse, T. J.; Tullius, T. D. *J. Am. Chem. Soc.* **1995**, *117*, 6428.

138. Walling, C. *Acc. Chem. Res.* **1975**, *8*, 125.

139. Douglas, B. E.; Radanovic, D. J. *Coord. Chem. Rev.* **1993**, *128*, 139-165.

140. Hertzberg, R. P.; Dervan, P. B. *J. Am. Chem. Soc.* **1982**, *104*, 313.

141. Hertzberg, R. P.; Dervan, P. B. *Biochemistry* **1984**, *23*, 3934.

142. Schultz, P. G.; Taylor, J. S.; Dervan, P. B. *J. Am. Chem. Soc.* **1982**, *104*, 6861.

143. Dervan, P. B. *Science* **1986**, *232*, 464-471.

144. Sluka, J. P.; Horvath, S. J.; Bruist, M. F.; Simon, M. I.; Dervan, P. B. *Science* **1987**, *238*, 1129-1132.

145. Sari, M. A.; Battioni, J. P.; Dupre, D.; Mansuy, D.; Pecq, J. B. L. *Biochemistry* **1990**, *29*, 4205-4215.

146. Meng, G. G.; James, B. R.; Skov, K. A.; Korbelik, M. *Can. J. Chem.* **1994**, *72*, 2447-2457.

147. Fiel, R. J.; Beerman, T. A.; mark, E. H.; Datta-Gupta, N. *Biochem. Biophys. Res. Commun.* **1982**, *107*, 1067.

148. Ward, B.; Skorobogaty, A.; Dabrowiak, J. C. *Biochemistry* **1986**, *25*, 6875-6883.

149. Dabrowiak, J. C.; Ward, B.; Goodisman, J. *Biochemistry* **1989**, *28*, 3314-3322.

150. Groves, J. T.; Marla, S. S. *J. Am. Chem. Soc.* **1995**, *117*, 9578-9579.

151. Bernadou, J.; Pratviel, G.; Bennis, F.; Girardet, M.; Meunier, B. *Biochemistry* **1989**, *28*, 7268-7275.

152. Fouquet, E.; Pratviel, G.; Bernadou, J.; Meunier, B. *J. Chem. Soc., Chem. Commun.* **1987**, 1169.

153. Ward, B.; Skorobogaty, A.; Dabrowiak, J. C. *Biochemistry* **1986**, *25*, 7827-7833.

154. Kalayanasundaram, K. *Coord. Chem. Rev.* **1982**, *46*, 159-244.

155. Bothwell, T. H.; Charlton, R. W.; Cook, J. D.; Finch, C. A. *Iron metabolism in man*; Blackwell Sci. Publc.: Oxford London, 1979; pp 44-81.

156. Sarkar, B. *Biological aspects of metals and metal-related diseases*; Raven Press: New York, 1983; pp 263-278.

157. Peter, H. H.; Bergeron, R. J.; Streiff, R. R.; Wiegand, J. *The development of iron chelators for clinical use*; CRC Press: Boca Raton, FL, 1993; pp Chap. 17.

158. Vitolo, L. M. W.; Hefter, G. T.; Clare, B. W.; Webb, J. *Inorg. Chim. Acta* **1990**, *170*, 171-176.

159. Anderegg, G.; Raber, M. *J. Chem. Soc., Chem. Commun.* **1990**, 1194-1196.

160. Scarrow, R. C.; Riley, P. E.; Abu-Dari, K.; White, D. L.; Raymond, K. N. *Inorg. Chem.* **1985**, *24*, 954-967.

161. Porter, J. B.; Hoyes, K. P.; Abeysinghe, R.; Huehns, E. R.; Hider, R. C. *Lancet* **1989**, 156.

162. Liu, Z. D.; Khodr, H.; Lu, S. L.; Liu, D. Y.; Hider, R. C. *9th International Conference on Oral Chelation, Hamburg* **1999**.

163. Nick, H. P.; Acklin, P.; Faller, B.; Jin, Y.; Lattmann, R.; Sergejew, T.; Schnebly, H. P. *9th International Conference on Oral Chelation, Hamburg* **1999**.

164. Foster, B. J.; Clagett-Cerr, K.; Hoth, D.; Leyland-Jones, B. *Cancer Treat. Rep.* **1986**, *70*, 1311-1319.

165. Einhorn, L. H.; Roth, B. J.; Ansari, R.; Dreicer, R.; Gonin, R.; Loehrer, P. J. *J. Clin. Oncology* **1994**, *12*, 2271-2276.

166. Kemp, J. D. *Histol. Histopathol.* **1997**, *12*, 291-296.

167. Richardson, D. R.; Tran, E. H.; Ponka, P. *Blood* **1995**, *86*, 4295.

168. Bernhard, P.; Sargeson, A. M. *J. Am. Chem. Soc.* **1989**, *111*, 597-606.

169. Ridd, M. J.; Keene, F. R. *J. Am. Chem. Soc.* **1981**, *103*, 5733-5740.

170. Mori, T.; Yamamoto, T.; Yamaguchi, M.; Yamagishi, T. *Bull. Chem. Soc. Jpn.* **1997**, *70*, 1069-1075.

171. Goedken, V. L.; Busch, D. H. *J. Am. Chem. Soc.* **1972**, *94*, 7355.

172. Goedken, V. L. *J. Chem. Soc., Chem. Commun.* **1972**, 207-208.

173. Goto, M.; Koga, N.; Ohse, Y.; Kurosaki, H.; Komatsu, T.; Kuroda, Y. *J. Chem. Soc., Chem. Commun.* **1994**, 2015-2016.

174. Pohl, K.; Wieghardt, K.; Kaim, W.; Steenken, S. *Inorg. Chem.* **1988**, *27*, 440-447.

175. Goto, M.; Takeshita, M.; Kanda, N.; Sakai, T.; Goedken, V. L. *Inorg. Chem.* **1985**, *24*, 582-587.

176. Barefield, E. K.; Busch, D. H. *Inorg. Chem.* **1971**, *10*, 108-114.

177. Olson, D. C.; Vasilevskis, J. *Inorg. Chem.* **1971**, *10*, 463-470.

178. Hipp, C. J.; Leonard, L. F.; Lindoy, F.; Busch, D. H. *Inorg. Chem.* **1972**, *11*, 1988-1994.

179. Lay, P. A.; Sargeson, A. M.; Skelton, B. W.; White, A. H. *J. Am. Chem. Soc.* **1982**, *104*, 6161-6164.

180. Stadtman, E. R. *Science* **1992**, *257*, 1220.

181. Mansour, A. N.; Thompson, C.; Theil, E. C.; Chasteen, N. D.; Sayers, D. E. *J. Biol. Chem.* **1985**, *260*, 7975-7979.

182. Hancock, R. D.; Martell, A. E. *Chem. Rev.* **1989**, *89*, 1875.

183. Lions, F.; Martin, K. V. *J. Am. Chem. Soc.* **1957**, *79*, 1572-1575.

184. Gillum, W. O.; Wentworth, R. A. D.; Childers, R. F. *Inorg. Chem.* **1970**, *9*, 1825-1832.

185. Hawker, P. N.; Twigg, M. V. **1987**, *Comprehensive Coordination Chemistry*, 1179-1288, vol. 4.

186. Goto, M.; Takeshita, M.; Sakai, T. *Bull. Chem. Soc. Jpn.* **1981**, *54*, 2491-2495.

187. Cotton, F. A.; Wilkinson, G.; Murillo, C. A.; Bochman, M. *Advanced Inorganic Chemistry*; Wiley: New York, 1999; pp 781ff.

188. Fleischer, E. B.; Gebala, A. E.; Swift, D. R.; Tasker, P. A. *Inorg. Chem.* **1972**, *11*, 2775-2784.

189. Hoselton, M. A.; Wilson, L. J.; Drago, R. S. *J. Am. Chem. Soc.* **1975**, *97*, 1722.

190. Blandamer, M. J.; Burgess, J.; Fawcett, J.; Guardado, P.; Hubbard, C. D.; Nuttall, S.; Prouse, L. J. S.; Radulovic, S.; Russell, D. R. *Inorg. Chem.* **1992**, *31*, 1383-1389.

191. Kirchner, R. M.; Mealli, C.; Bailey, M.; Howe, N.; Torre, L. P.; Wilson, L. J.; Andrews, L. C.; Rose, N. J.; Lingafelter, E. C. *Coord. Chem. Rev.* **1987**, *77*, 89-163.

192. Breuer, W.; Epsztejn, S.; Cabantchik, Z. I. *J. Biol. Chem.* **1995**, *270*, 24209-24215.

193. Crisponi, G.; Nurchi, V. M.; Silvagni, R.; Faa, G. *Polyhedron* **1999**, *18*, 3219-3226.

194. Torti, S. V.; Torti, F. M.; Whitman, S. P.; Brechbiel, M. W.; Park, G.; Planalp, R. P. *Blood* **1998**, *92*, 1384-1389.

195. Chum, H. L.; Vanin, J. A.; Holanda, M. I. D. *Inorg. Chem.* **1982**, *21*, 1146.

196. Cotton, F. A.; Wilkinson, G.; Murillo, C. A.; Bochman, M. *Advanced Inorganic Chemistry*; Wiley: New York, 1999; pp 633ff.

197. Greenwood, N. N.; Earnshaw, A. *Chemistry of the elements*; Pergamon Press: Oxford, 1984; pp p1060.

198. Miessler, G. L.; Tarr, D. A. *Inorganic Chemistry*; Prentice Hall: New Jersey, 1991; pp p343.

199. Lingnau, R.; Strahle, J. *Angew. Chem. Int. Ed. Engl.* **1988**, 436.

200. Bradley, D. C.; Fisher, K. J. *J. Am. Chem. Soc.* **1971**, *93*, 2058.

201. Chen, H.; Bartlett, R. A.; Dias, H. V. R.; Olmstead, M. M.; Power, P. P. *J. Am. Chem. Soc.* **1989**, *111*, 4338-4345.

202. Baenziger, N. C.; Dittemore, K. M.; Doyle, J. R. *Inorg. Chem.* **1974**, *13*, 805.

203. Favas, M. C.; Kepert, D. L. *Progr. Inorg. Chem.* **1980**, *27*, 325.

204. Wood, J. S. *Progr. Inorg. Chem.* **1972**, *16*, 227-486.

205. Kepert, D. L. *Progr. Inorg. Chem.* **1977**, *23*, 1-66.

206. Kepert, D. L. *Progr. Inorg. Chem.* **1979**, *25*, 41-144.

207. Kepert, D. L. *Progr. Inorg. Chem.* **1978**, *24*, 179.

208. Pearson, R. G. *J. Am. Chem. Soc.* **1986**, *108*, 6109-6114.

209. Schwarzenbach, G. *Helv. Chim. Acta* **1952**, *35*, 2344.

210. Lawrence, G. D.; Sawyer, D. T. *Coord. Chem. Rev.* **1978**, *27*, 173-193.

211. Chiswell, B. A.; McKenze, E. D.; Lindoy, L. F. *Comprehensive Coordination Chemistry* **1987**, *Vol.* **4**, 1-122.

212. Anderegg, V. G.; Hubmann, E.; Podder, N. G.; Wenk, F. *Helv. Chim. Acta* **1977**, *60*, 123-140.

213. Chiswell, B.; Litster, D. S. *Inorg. Chim. Acta* **1978**, *29*, 25-36.

214. Kulasingam, G. C.; McWhinnie, W. R. *J. Chem. Soc. sect. A* **1967**, 1253.

215. Jesson, J. P.; Trofimenko, S.; Eaton, D. R. *J. Am. Chem. Soc.* **1967**, *89*, 3148.

216. Sacconi, L.; Vaira, M. D. *Inorg. Chem.* **1978**, *17*, 810.

217. Sanders, N.; Day, P. *J. Chem. Soc. sect. A* **1970**, 1190.

218. Bonder, R. L.; Hendricker, D. G. *Inorg. Chem.* **1973**, *12*, 33.

219. Bishop, M. M.; Lewis, J.; O'Donoghue, T. D.; Raithby, P. R.; Ramsden, J. N. *J. Chem. Soc., Dalton Trans.* **1980**, 1390.

220. Judge, J. S.; Reiff, W. M.; Intille, G. M.; Ballway, P.; W.A. Baker, J. *J. Inorg. Nucl. Chem.* **1967**, *29*, 1711.

221. Brandt, W. W.; Wright, J. P. *J. Am. Chem. Soc.* **1954**, *76*, 3082.

222. Stouffer, R. C.; Busch, D. H. *J. Am. Chem. Soc.* **1956**, *78*, 6016.

223. Blandamer, M. J.; Burgess, J.; Hanines, R. I. *J. Chem. Soc., Dalton Trans.* **1978**, 1001.

224. Goodwin, H. A.; Smith, F. E. *Aust. J. Chem.* **1970**, *23*, 1545.

225. Goodwin, H. A.; Mather, D. W.; Smith, F. E. *Aust. J. Chem.* **1975**, *28*, 33.

226. Wieghardt, K.; Schmidt, W.; Herrmann, W. *Inorg. Chem.* **1983**, *22*, 2953-2956.

227. Decurtins, S.; Felix, F.; Ferguson, J.; Gudel, H. U.; Ludi, A. *J. Am. Chem. Soc.* **1980**, *102*, 4102.

228. Toftlund, H.; Yde-Andersen, S. *Acta Chemica Scandinavica A* **1981**, *35*, 575.

229. Christiansen, L.; Hendrickson, D. N.; Toftlund, H.; Wilson, S. R.; Xie, C.-L. *Inorg. Chem.* **1986**, *25*, 2813.

230. Nelson, S. M.; Bryan, P.; Busch, D. H. *J. Chem. Soc., Chem. Commun.* **1966**, 641.

231. Lind, M. D.; Hoard, J. L. *Inorg. Chem.* **1964**, *3*, 34.

232. Ganguli, P.; Marathe, V. R. *Inorg. Chem.* **1978**, *17*, 543.

233. Cotton, F. A.; Wilkinson, G.; Murillo, C. A.; Bochman, M. *Advanced Inorganic Chemistry*; Wiley: New York, 1999; pp 816ff.

234. Judge, J. S.; W.A. Baker, J. *Inorg. Chim. Acta* **1967**, *1*, 68.

235. Raston, C. L.; White, A. H. *J. Chem. Soc., Dalton Trans.* **1976**, 7-12.

236. Vaira, M. D.; P.L., Orioli. *Inorg. Chem.* **1969**, *8*, 2729-2734.

237. Dori, Z.; Eisenberg, R.; Gray, H. B. *Inorg. Chem.* **1967**, *6*, 483-486.

238. Nonoyama, M.; Sakai, K. *Inorg. Chim. Acta* **1983**, *72*, 57-60.

239. Kuppers, H.; Neves, A.; Pomp, C.; Ventur, D.; Wieghardt, K.; Nuber, B.; Weiss, J. *Inorg. Chem.* **1986**, *25*, 2400-2408.

240. Creaser, I. I.; Geue, R. J.; Harrowfield, J.; Herlt, A. J.; Sargeson, A. M.; Snow, M. R.; Springborg, J. *J. Am. Chem. Soc.* **1982**, *104*, 6016.

241. Comba, P.; Sargeson, A. M.; Engelhardt, L. M.; Harrowfield, J. M.; White, A. H.; Horn, E.; Snow, M. R. *Inorg. Chem.* **1985**, *24*, 2325-2327.

242. Keene, R.; Searle, G. H. *Inorg. Chem.* **1974**, *13*, 2173.

243. Yoshikawa, Y.; Yamaski, K. *Bull. Chem. Soc. Jpn.* **1972**, *45*, 179-184.

244. Hambley, T. W.; Searle, G. H.; Snow, M. R. *Aust. J. Chem.* **1982**, *35*, 1285-1295.

245. Searle, G. H.; Larsen, E. *Acta Chemica Scandinavica A* **1976**, *30*, 143-151.

246. Comba, P.; Hambley, T.; Zipper, L. *Helv. Chim. Acta* **1988**, *71*, 1875.

247. Geue, R. J.; Snow, M. R. *Inorg. Chem.* **1977**, *16*, 231.

248. Mikami, M.; Kuroda, R.; Konno, M.; Saito, Y. *Acta Crystallogr., Sect. B* **1977**, *33*, 1485-1489.

249. Sato, S.; Saito, Y. *Acta Crystallogr., Sect. B* **1975**, *31*, 2456.

250. Angley, M. E.; Dwyr, M.; Lincoln, S. F.; Searle, G. H. *Inorg. Chim. Acta* **1980**, *45*, L91-L93.

251. Taylor, S. G.; Snow, M. R.; Hambley, T. W. *Aust. J. Chem.* **1983**, *36*, 2359-2368.

252. Muto, A.; Marumo, F.; Saito, Y. *Acta Crystallogr., Sect. B* **1970**, *26*, 226.

253. Hendry, P.; Ludi, A. *Adv. Inorg. Chem.* **1990**, *35*, 117.

254. Curtis, N. F.; Gainsford, G. J.; Hambley, T. W.; Lawrance, G. A.; Morgan, K. R.; Siriwardena, A. *J. Chem. Soc., Chem. Commun.* **1987**, 295.

255. Sacconi, L.; Mani, F.; Bencini, A. *Comprehensive Coordination Chemistry* **1987**, *vol. 5*, 1-347.

256. Curtis, N. F.; Powell, H. K. J. *J. Chem. Soc. sect. A* **1968**, 3069.

257. Ciampolini, M.; Paoletti, P.; Sacconi, L. *J. Chem. Soc.* **1961**, 2994.

258. Vacca, A.; Arenare, D.; Paoletti, P. *Inorg. Chem.* **1966**, *5*, 1384.

259. Halfpenny, M. T.; Levason, W.; Mcauliffe, C. A. *Inorg. Chim. Acta* **1979**, *32*, 229-233.

260. Ciampolini, M.; Speroni, G. P. *Inorg. Chem.* **1966**, *5*, 45.

261. Bertini, I.; Johnston, D. L.; W.DeW. Horrocks, J. *Inorg. Chim. Acta* **1970**, *4*, 79.

262. Chaudhuri, P.; Wieghardt, K. *Progr. Inorg. Chem.* **1987**, *35*, 329-436.

263. Wentworth, R. A. D. *Inorg. Chem.* **1968**, *7*, 1030-1032.

264. Judge, J. S.; W.A. Baker, J. *Inorg. Chim. Acta* **1967**, *1*, 239.

265. Rogers, J.; Jacobson, R. A. *J. Chem. Soc. sect. A* **1970**, 1826.

266. Chiswell, B.; Lions, F. *Aust. J. Chem.* **1969**, *22*, 71-81.

267. Dekkers, J.; Goodwin, H. A. *Aust. J. Chem.* **1967**, *20*, 69-75.

268. Parks, J. E.; Wagner, B. E.; Holm, R. H. *Inorg. Chem.* **1971**, *10*, 2472-2478.

269. Donaldson, P. B.; Tasker, P. A. *J. Chem. Soc., Dalton Trans.* **1977**, 1160.

270. Wijinands, P. E. M.; Wood, J. S.; Reedijk, J.; Maaskant, W. J. A. *Inorg. Chem.* **1996**, *35*, 1214-1222.

271. Simmons, C. J.; Hitchmann, M. A.; Stratemeier, H.; Schultz, A. J. *J. Am. Chem. Soc.* **1993**, *115*, 11304-11311.

272. Julve, M.; Verdaguer, M.; Charlot, M.; kahn, O. *Inorg. Chim. Acta* **1984**, *82*, 5-12.

273. Greenwood, N. N.; Earnshaw, A. *Chemistry of the elements*; Pergamon Press: Oxford, 1984; pp 1371.

274. Stephens, F. S. *J. Chem. Soc. sect. A* **1969**, 2233.

275. Stephens, F. S. *J. Chem. Soc. sect. A* **1969**, 883.

276. Ziolo, R. F.; Allen, M. A.; Titus, D. D.; Gray, H. B.; Dori, Z. *Inorg. Chem.* **1972**, *11*, 3044.

277. Allman, R.; Henke, W.; Reinen, D. *Inorg. Chem.* **1978**, *17*, 378.

278. Henke, W.; Kremer, S.; Reinen, D. *Inorg. Chem.* **1983**, *22*, 2858-2863.

279. Birker, P. J.; Hendriks, H. M. J.; Reedijk, J.; Verschoor, G. C. *Inorg. Chem.* **1981**, *20*, 2408.

280. Cotton, F. A.; Wilkinson, G.; Murillo, C. A.; Bochman, M. *Advanced Inorganic Chemistry*; Wiely: New York, 1999; pp 598ff.

281. Greenwood, N. N.; Earnshaw, A. *Chemistry of the elements*; Pergamon Press: Oxford, 1984; pp 1402.

282. Hodgson, P. G.; Penfold, B. R. *J. Chem. Soc., Dalton Trans.* **1974**, 1870.

283. Paoletti, P.; Fabbrizzi, M.; Michelone, M. *Inorg. Chem.* **1976**, *15*, 1451-1452.

284. Fabbrizzi, L.; Micheloni, M.; Paoletti, P. *J. Chem. Soc., Dalton Trans.* **1980**, 1055.

285. Sabatini, A.; Vacca, A. *Coord. Chem. Rev.* **1975**, *16*, 161-169.

286. Glerup, J.; Goodson, P. A.; Hodgson, D. J.; Michelsen, K.; Nielsen, K. M.; Weihe, H. *Inorg. Chem.* **1992**, *31*, 4611-4616.

287. Schlager, O.; Wieghardt, K.; Grondey, H.; Rufinska, A.; Nuber, B. *Inorg. Chem.* **1995**, *34*, 6440-6448.

288. Larsen, E.; La Mar, G. N.; Wagner, B. E.; Parks, J. E.; Holm, R. H. *Inorg. Chem.* **1972**, *11*, 2652.

289. Hassel, O.; Lunde, K. *research (London)* **1950**, *3*, 484.

290. Francis, L.; Martin, K. *J. Am. Chem. Soc.* **1957**, *79*, 2733-2738.

291. Brauner, P. A.; Schwarzenbach, G. *Helv. Chim. Acta* **1962**, *45*, 2030.

292. Bosnich, B.; Dwyer, F. P. *J Australian Chem. Soc.* **1966**, *19*, 2045.

293. Wentworth, R. A. D.; Felten, J. J. *J. Am. Chem. Soc.* **1968**, *90*, 621-626.

294. Gillum, W. O.; Huffman, J. C.; Streib, W. E.; Wentworth, R. A. D. *J. Chem. Soc., Chem. Commun.* **1969**, 843.

295. Stetter, H.; Theisen, D.; Steffens, G. J. *Chem. Ber.* **1970**, *103*, 200-204.

296. Stetter, H.; Bremen, J. *Chem. Ber.* **1973**, *106*, 2523-2529.

297. Zompa, L. J.; Shindler, J. M. *J. Chem. Soc., Chem. Commun.* **1971**, 65-66.

298. Yu, C.; Dumoulin, C. L.; Levy, G. C. *Magn. Reson. Chem.* **1985**, 23, 952.

299. Fleischer, E. B.; Gebala, A. E.; Levey, A.; Taskes, P. A. *J. Org. Chem.* **1971**, *36*, 3042-3044.

300. Childers, R. F.; Wentworth, R. A. D.; Zompa, L. J. *Inorg. Chem.* **1971**, *10*, 302.

301. Sarneski, J. E.; McPhail, A. T.; Onan, K. D. *J. Am. Chem. Soc.* **1977**, *99*, 7376-7378.

302. Ammeter, H.; Bürgi, H. B.; Gamp, E.; Meyer-Sandrin, V.; Jensen, W. P. *Inorg. Chem.* **1979**, *18*, 733.

303. Ishii, M.; Umehara, M.; Nakahara, M. *Bull. Chem. Soc. Jpn.* **1987**, *60*, 1939-1941.

304. Hegetschweiler, K.; Egli, A.; Alberto, R.; Schmalle, H. *Inorg. Chem.* **1992**, *31*, 4027-4028.

305. Hegetschweiler, K.; Gramlich, V.; Ghisletta, M.; Samaras, H. *Inorg. Chem.* **1992**, *31*, 2341.

306. Hegetschweiler, K.; Kradolfer, T.; Gramlich, V.; Hancock, R. D. *Chem. Eur. J.* **1995**, *1*, 74-88.

307. Moore, D. A.; Fanwick, P. E.; Welch, M. J. *Inorg. Chem.* **1990**, *29*, 672.

308. Bollinger, J. E.; Mague, J. T.; O'Connor, C. J.; Banks, W. A.; Roundhill, D. M. *J. Chem. Soc., Dalton Trans.* **1995**, 1677.

309. Itoh, T.; Hisada, H.; Sumiya, T.; Hosono, M.; Usui, Y.; Fujii, Y. *J. Chem. Soc., Chem. Commun.* **1997**, 677-678.

310. Steitz, J. A. *J. Org. Chem.* **1968**, *33*, 2978.

311. Ninomiya, K.; Shioiri, T.; Yamada, S. *Tetrahedron* **1974**, *30*, 2151.

312. Park, G.; Ye, N.; Brechbiel, M.; Planalp, R. **manuscript in preparation.**

313. Hilfiker, K. A.; Rogers, R. D.; Brechbiel, M. W.; Planalp, R. P. *Inorg. Chem.* **1997**, *36*, 4600-4603.

314. Ostfeld, D.; Cohen, I. A. *J. Chem. Educ.* **1972**, *49*, 829-830.

315. Sheldrick, G. M.; *SHELXTL* **1996**, *version 5.05*, Siemens Analytical X-Ray Instruments Inc.

316. Burnett, M. N.; Johnson, C. K. *Oak Ridge National Laboratory Report ORNL-6895*, **1996**.

317. Farrugia, L. J. *J. Appl. Cryst.* **1997**, *30*, 565.

318. Mahadevan, C.; Seshasayee, M.; Sastry, S.; Subrahmanyam, C. *Z. Kristallogr.* **1985**, *171*, 173-178.

319. Allmann, R.; Henke, W.; Reinen, D. *Inorg. Chem.* **1978**, *17*, 378-382.

320. Chaudhuri, P.; Oder, K.; Weighardt, K.; Weiss, J.; Reedijk, J.; Hinrichs, W.; Wood, J.; Ozarowski, A.; Stratemaier, H.; Reinen, D. *Inorg. Chem.* **1986**, *25*, 2951-2958.

321. Wieghardt, K.; Schöffmann, E.; Nuber, B.; Weiss, J. *Inorg. Chem.* **1986**, *25*, 4877.

322. Hodgson, D. J.; Michelsen, K.; Pedersen, E. *Acta Chemica Scandinavica* **1990**, **44**, 1002-1005.

323. Bebout, D. C.; DeLanoy, A. E.; Ehmann, D. E.; Kastner, M. E.; Parrish, D. A.; Butcher, R. J. *Inorg. Chem.* **1998**, *37*, 2952-2959.

324. Ray, N.J.; Hulett, L.; Sheahan, R.; Hathaway, B. J. *J. Chem. Soc., Dalton Trans.* **1981**, 1463-1469.

325. Tyagi, S.; Hathaway, B. J. *J. Chem. Soc., Dalton Trans.* **1981**, 2029-2033.

326. Szalda, D. J.; Creutz, C.; Mahajan, D.; Sutin, N. *Inorg. Chem.* **1983**, *22*, 2372-2379.

327. Cotton, F. A.; Wilkinson, G.; Murillo, C. A.; Bochman, M. *Advanced Inorganic Chemistry*; Wiely: New York, 1999; pp 33ff.

328. Cramer, R. E.; Doorne, W. V.; Huneke, J. T. *Inorg. Chem.* **1976**, *15*, 529-535.

329. Wilson, L. J.; Rose, N. J. *J. Am. Chem. Soc.* **1968**, *90*, 6041.

330. Sarneski, J. E.; Urbach, F. L. *J. Chem. Soc., Chem. Commun.* **1968**, 1025-1026.

331. Single crystals grown by Neng Ye were analyzed for the structure determination.

332. Single crystals grown by Nicole Tsoupas were analyzed for the structure determination.

333. Gellman, S.H.; Petter, R.; Breslow, R. *J. Am. Chem. Soc.* **1986**, *108*, 2388.

334. Kimura, E.; Kodama, Y.; Kodama, T.; Shiro, M. *J. Am. Chem. Soc.* **1995**, *117*, 8304.

335. Sheldrick, G.M. program for semiempirical absorption correction of area detector data, 1996.

336. Jones, W.C.; and Bull, W.E. *J. Chem. Soc. sect. A*, **1968**, 1849.

337. Girolami, G.S.; Rauchfuss, T.B.; Angelici, R.J. *Synthesis and technique in inorganic chemistry*, 3rd Edition, University Science Book, Sausalito, CA 1999.

338. Busch, D. H. *Chem. Rev.*, **1993**, 847-860.

339. Planalp, R.P.; Park, G.; Rogers, R.D.; Brechbiel, M.W. *218th ACS National Meeting*, **1999**, *INOR 516*.

340. Shannon, R.D.; Prewitt, C.T., *Acta Crystallogr., Sect. B*, **1969**, 925.

341. Shannon, R.D. *Acta Crystallogr., Sect. A*, **1976**, 751.

342. Kepert, D.L. *Inorganic stereochemistry* , Springer-Verlag, Berlin, 1982, pp92-111.

343. Hathaway, B.J.; Hodgson, P.G. *J. Inorg. Nucl. Chem.*, **1973**, 4071-4081.

344. Kavana, M.; Powell,D.R.; Burstyn, J.N. *Inorg. Chim. Acta*, **2000**, 351-361.

345. Templeton, D.H.; Zalkin,A.; Ruben, H.W.; Templeton, L.K. *Acta Crystallogr., Sect. B*, **1979**,1608.

346. Wilkins, R.G. *Kinetics and mechanism of reactions of transition metal complexes*, VCH, Weinheim,1991.

347. Nord, G. *Comments Inorg. Chem.*, **1985**, 193-212.

348. Grady, J.K.; Chasteen, N. D.; Harris, D.C. *Anal. Biochem.*, **1988**, 111-115.

349. Coffman, T.J.; Cox, C.D.; Edeker, B.L.; Britigan, B.E. *J. Clin. Invest.*, **1990**, 1030-1037.

350. Halliwell, B. *Free Radical Res. Commun.*, **1990**, 1-32.

APPENDICES

Appendix A

Crystallographic and data collection parameters of metal complexes

Appendix A-1. Crystal data and structure refinement for $[Cu(tach\text{-}Et_3)Cl_{1.2}Br_{0.8}]$ **(108).**

Color / Shape	green / parallelepiped	
Empirical formula	$C_{12}H_{27}Br_{0.80}Cl_{1.20}CuN_3$	
Formula weight	383.37	
Temperature	173(2) K	
Crystal system	Orthorhombic	
Space group	Pnma	
Unit cell dimensions	a = 8.2265(1) Å	$\alpha = 90°$
	b = 12.5313(1) Å	$\beta = 90°$
	c = 15.3587(3) Å	$\gamma = 90°$
Volume	1583.31(4) Å^3	
Z	4	
Density (calculated)	1.608 Mg/m^3	
Absorption coefficient	3.589 mm^{-1}	
Diffractometer / scan	Siemens SMART / CCD area detector	
Radiation / wavelength	Mokα (graphite monochrom.) / 0.71073 Å	
F(000)	790	
Crystal size	0.10 x 0.16 x 0.32 mm	

θ Range for data collection	2.10 to 27.86°
Index ranges	$-10 \leq h \leq 10, -16 \leq k \leq 13, -14 \leq l \leq 20$
Reflections collected	9500
Independent refls.	1952 (R_{int} = 0.0411)
Observed refls.	1551 ([I>2σ(I)])
Absorption correction	SADABS
Range of relat. transm. factors	0.97 and 0. 68
Refinement method	Full-matrix least-squares on F^2
Computing	SHELXTL, Ver. 5
Data / restraints / parameters	1948 / 0 / 100
Goodness-of-fit on F^2	1.070
SHELX-93 weight parameters	0.0461, 1.3522
Final R indices [I>2σ(I)]	R1 = 0.0413, wR2 = 0.0900
R indices (all data)	R1 = 0.0596, wR2 = 0.1000
Extinction coefficient	0.0017(5)
Largest diff. peak and hole	0.614 and -0.594 e $Å^{-3}$

Appendix A-2. Crystal data and structure refinement for [Fe(tach(C-Me_3)pyr-ox-*6*)]$(ClO_4)_2$ **(153).**

Color / Shape	purple / fragment
Empirical formula	$C_{27}H_{30}Cl_2FeN_6O_8$
Formula weight	693.32
Temperature	173(2) K
Crystal system	Orthorhombic
Space group	Fdd2
Unit cell dimensions	a = 22.4811(6) Å α = 90°
	b = 503143(8) Å β = 90°
	c = 10.2095(2) Å γ = 90°
Volume	111548.2(4) Å^3
Z	16
Density (calculated)	1.595 Mg/m^3
Absorption coefficient	0.769 mm^{-1}
Diffractometer / scan	Siemens SMART / CCD area detector
Radiation / wavelength	Mokα (graphite monochrom.) / 0.71073 Å
F(000)	5728
Crystal size	0.18 x 0.26 x 0.38 mm
θ Range for data collection	1.62 to 27.89°
Index ranges	$-29 \le h \le 29, -38 \le k \le 65, -13 \le l \le 13$
Reflections collected	17886
Independent refls.	6678 (R_{int} = 0.0411)
Observed refls.	4809 ([I>2σ(I)])

Absorption correction	SADABS
Range of relat. transm. factors	0.97 and 0.40
Refinement method	Full-matrix least-squares on F^2
Computing	SHELXTL, Ver. 5
Data / restraints / parameters	6675 / 1 / 419
Goodness-of-fit on F^2	0.962
SHELX-93 weight parameters	0.0482, 0.0000
Final R indices [$I>2\sigma(I)$]	R1 = 0.0476, wR2 = 0.0949
R indices (all data)	R1 = 0.0753, wR2 = 0.1067
Absolute structure parameter	0.02(2)
Extinction coefficient	0.000026(14)
Largest diff. peak and hole	0.802 and –0.421 e $Å^{-3}$

Appendix A-3. Crystal data and structure refinement for $[Zn(tachpyr)](ClO_4)_2 \bullet CH_3OH$ **(250).**

Color / Shape	colorless / fragment
Empirical formula	$C_{25}H_{34}Cl_2N_6O_9Zn$
Formula weight	698.85
Temperature	173(2) K
Crystal system	Cubic
Space group	$P2_13$
Unit cell dimensions	a = 14.3088(1) Å $\alpha = 90°$
	b = 14.3088(1) Å $\beta = 90°$
	c = 14.3088(1) Å $\gamma = 90°$
Volume	12929.61(4) $Å^3$
Z	4
Density (calculated)	1.584 Mg/m^3
Absorption coefficient	1.083 mm^{-1}
Diffractometer / scan	Siemens SMART / CCD area detector
Radiation / wavelength	Mokα (graphite monochrom.) / 0.71073 Å
F(000)	1448
Crystal size	0.35 x 0.50 x 0.70 mm
θ Range for data collection	2.01 to 27.81°
Index ranges	$-12 \le h \le 18, -18 \le k \le 16, -18 \le l \le 18$
Reflections collected	18785
Independent refls.	2329 (R_{int} = 0.0411)
Observed refls.	1651 ([I>2σ(I)])

Absorption correction	none
Range of relat. transm. factors	0.97 and 0.40
Refinement method	Full-matrix least-squares on F^2
Computing	SHELXTL, Ver. 5
Data / restraints / parameters	2326 / 0 / 138
Goodness-of-fit on F^2	1.183
SHELX-93 weight parameters	0.0256, 2.1335
Final R indices [$I>2\sigma(I)$]	R1 = 0.0660, wR2 = 0.0898
R indices (all data)	R1 = 0.1084, wR2 = 0.11054
Absolute structure parameter	0.03(2)
Extinction coefficient	0.0004(4)
Largest diff. peak and hole	0.291 and –0.321 e $Å^{-3}$

Appendix A-4. Crystal data and structure refinement for $[Cu(tachpyr)](ClO_4)_2 \bullet 1/2CH_3CN$ (257).

Color / Shape	Blue / fragment	
Empirical formula	$C_{25}H_{31.50}Cl_2CuN_{6.50}O_8$	
Formula weight	685.51	
Temperature	173(2) K	
Crystal system	Monoclinic	
Space group	$P2_1/n$	
Unit cell dimensions	a = 8.4921(2) Å	$\alpha = 90°$
	b = 14.3418(3) Å	$\beta = 99.874(1)°$
	c = 23.9735(6) Å	$\gamma = 90°$
Volume	2876.53(12) Å^3	
Z	4	
Density (calculated)	1.583 Mg/m^3	
Absorption coefficient	1.005 mm^{-1}	
Diffractometer / scan	Siemens SMART / CCD area detector	
Radiation / wavelength	Mokα (graphite monochrom.) / 0.71073 Å	
F(000)	1416	
Crystal size	0.25 x 0.40 x 0.80 mm	
θ Range for data collection	1.66 to 21.72 °	
Index ranges	$-7 \le h \le 8, -14 \le k \le 14, -24 \le l \le 19$	
Reflections collected	10927	
Independent refls.	3360 (R_{int} = 0.0664)	
Observed refls.	2469 ([I>2σ(I)])	

Absorption correction	none
Refinement method	Full-matrix least-squares on F^2
Computing	SHELXTL, Ver. 5
Data / restraints / parameters	3356 / 0 / 399
Goodness-of-fit on F^2	1.064
SHELX-93 weight parameters	0.0533, 6.8212
Final R indices [$I>2\sigma(I)$]	R1 = 0.0548, wR2 = 0.1167
R indices (all data)	R1 = 0.0853, wR2 = 0.1324
Extinction coefficient	0.0001(3)
Largest diff. peak and hole	0.777 and –0.472 e $Å^{-3}$

Appendix A-4A. Crystal data and structure refinement for $[Cu(tachpyr)](ClO_4)_2 \cdot CH_3OH$ (**257A**).

Color / Shape	Blue / plate
Empirical formula	$C_{25}H_{34}Cl_2CuN_6O_9$
Formula weight	697.02
Temperature	173(2) K
Crystal system	Cubic
Space group	$P2_13$
Unit cell dimensions	a = 14.2766(2) Å $\alpha = 90°$
	b = 14.2766(2) Å $\beta = 90°$
	c = 14.2766(2) Å $\gamma = 90°$
Volume	2909.87(7) $Å^3$
Z	4
Density (calculated)	1.591 Mg/m^3
Absorption coefficient	0.997 mm^{-1}
Diffractometer / scan	Siemens SMART / CCD area detector
Radiation / wavelength	Mokα (graphite monochrom.) / 0.71073 Å
F(000)	1444
Crystal size	0.15 x 0.25 x 0.30 mm
θ Range for data collection	2.02 to 21.61 °
Index ranges	$0 \le h \le 9, 0 \le k \le 10, 1 \le l \le 14$
Reflections collected	654
Independent refls.	654 (R_{int} = 0.0000)
Observed refls.	608 ([I>2σ(I)])

Absorption correction	none
Refinement method	Full-matrix least-squares on F^2
Computing	SHELXTL, Ver. 5
Data / restraints / parameters	650 / 0 / 142
Goodness-of-fit on F^2	1.174
SHELX-93 weight parameters	0.0336, 3.6498
Final R indices [$I>2\sigma(I)$]	R1 = 0.0369, wR2 = 0.0788
R indices (all data)	R1 = 0.0427, wR2 = 0.0883
Largest diff. peak and hole	0.263 and –0.180 e $Å^{-3}$

Appendix A-5. Crystal data and structure refinement for $[Ni(tachpyr)](Cl)_2 \bullet CH_3OH$ (262).

Color / Shape	purple / parallelepiped	
Empirical formula	$C_{25}H_{34}Cl_2N_6NiO$	
Formula weight	564.19	
Temperature	173(2) K	
Crystal system	Monoclinic	
Space group	$P2_1/n$	
Unit cell dimensions	a = 9.4103(2) Å	$\alpha = 90°$
	b = 14.5893(3) Å	β = 94.318(1) °
	c = 19.1238(4) Å	$\gamma = 90°$
Volume	2618.05(9) $Å^3$	
Z	4	
Density (calculated)	1.431 Mg/m^3	
Absorption coefficient	0.976 mm^{-1}	
Diffractometer / scan	Siemens SMART / CCD area detector	
Radiation / wavelength	Mokα (graphite monochrom.) / 0.71073 Å	
F(000)	1184	
Crystal size	0.10 x 0.15 x 0.30 mm	
θ Range for data collection	1.76 to 23.30°	
Index ranges	$-10 \le h \le 8, -16 \le k \le 14, -20 \le l \le 21$	
Reflections collected	10411	
Independent refls.	3757 (R_{int} = 0.0535)	

Observed refls.	3496 ([I>2σ(I)])
Absorption correction	none
Refinement method	Full-matrix least-squares on F^2
Computing	SHELXTL, Ver. 5
Data / restraints / parameters	3755 / 0 / 334
Goodness-of-fit on F^2	1.101
SHELX-93 weight parameters	0.1086, 9.3599
Final R indices [I>2σ(I)]	R1 = 0.0581, wR2 = 0.1849
R indices (all data)	R1 = 0.0619, wR2 = 0.1938
Largest diff. peak and hole	1.418 and –0.639 e $Å^{-3}$

Appendix A-6. Crystal data and structure refinement for $[Mn(tachpyr)](ClO_4)_2$ **(271).**

Color / Shape	yellow / fragment
Empirical formula	$C_{24}H_{30}Cl_2MnN_6O_8$
Formula weight	656.38
Temperature	173(2) K
Crystal system	Monoclinic
Space group	$P2_1/c$
Unit cell dimensions	a = 13.4196(2) Å $\alpha = 90°$
	b = 13.8089(1) Å β = 110.406(1) °
	c = 15.2639(1) Å $\gamma = 90°$
Volume	2651.05(5) $Å^3$
Z	4
Density (calculated)	1.645 Mg/m^3
Absorption coefficient	0.762 mm^{-1}
Diffractometer / scan	Siemens SMART / CCD area detector
Radiation / wavelength	Mokα (graphite monochrom.) / 0.71073 Å
F(000)	1356
Crystal size	0.26 x 0.40 x 0.58 mm
θ Range for data collection	1.62 to 27.88°
Index ranges	$-11 \le h \le 17, -18 \le k \le 18, -19 \le l \le 20$
Reflections collected	16540
Independent refls.	6124 (R_{int} = 0.0231)

Observed refls.	5082 ([I>2σ(I)])
Absorption correction	SADAS
Refinement method	Full-matrix least-squares on F^2
Computing	SHELXTL, Ver. 5
Data / restraints / parameters	6119 / 0 / 406
Goodness-of-fit on F^2	1.054
SHELX-93 weight parameters	0.0686, 1.0106
Final R indices [I>2σ(I)]	R1 = 0.0390, wR2 = 0.1088
R indices (all data)	R1 = 0.0489, wR2 = 0.1189
Extinction coefficient	0.0012(5)
Largest diff. peak and hole	0.647 and –0.778 e $Å^{-3}$

Appendix A-7. Crystal data and structure refinement for $[Cd(tachpyr)](ClO_4)_2$ **(275).**

Color / Shape	colorless / fragment	
Empirical formula	$C_{24}H_{30}CdCl_2N_6O_8$	
Formula weight	713.84	
Temperature	173(2) K	
Crystal system	Monoclinic	
Space group	$P2_1/c$	
Unit cell dimensions	a = 13.3620(3) Å	$\alpha = 90°$
	b = 13.9104(3) Å	$\beta = 118.611(1)°$
	c = 15.4736(3) Å	$\gamma = 90°$
Volume	2725.69(10) $Å^3$	
Z	4	
Density (calculated)	1.740 Mg/m^3	
Absorption coefficient	1.058 mm^{-1}	
Diffractometer / scan	Siemens SMART / CCD area detector	
Radiation / wavelength	Mokα (graphite monochrom.) / 0.71073 Å	
F(000)	1448	
Crystal size	0.35 x 0.40 x 0.40 mm	
θ Range for data collection	1.61 to 27.85°	
Index ranges	$-17 \le h \le 15, 0 \le k \le 17, 0 \le l \le 20$	
Reflections collected	6332	
Independent refls.	6332 (R_{int} = 0.0231)	

Observed refls.	5953 ([I>2σ(I)])
Absorption correction	none
Refinement method	Full-matrix least-squares on F^2
Computing	SHELXTL, Ver. 5
Data / restraints / parameters	6329 / 0 / 447
Goodness-of-fit on F^2	1.389
SHELX-93 weight parameters	0.000, 9.3373
Final R indices [I>2σ(I)]	R1 = 0.0645, wR2 = 0.1157
R indices (all data)	R1 = 0.0699, wR2 = 0.1178
Extinction coefficient	0.0004(2)
Largest diff. peak and hole	0.914 and –0.893 e $Å^{-3}$

Appendix A-8. Crystal data and structure refinement for $[Hg(tachpyr)](ClO_4)_2$ (276).

Color / Shape	colorless / parallelepiped	
Empirical formula	$C_{24}H_{30}Cl_2HgN_6O_8$	
Formula weight	802.03	
Temperature	173(2) K	
Crystal system	Monoclinic	
Space group	$P2_1/c$	
Unit cell dimensions	a = 13.3481(4) Å	$\alpha = 90°$
	b = 14.0714(2) Å	$\beta = 109.043(1)°$
	c = 15.4171(4) Å	$\gamma = 90°$
Volume	2737.27(12) Å^3	
Z	4	
Density (calculated)	1.946 Mg/m^3	
Absorption coefficient	5.879 mm^{-1}	
Diffractometer / scan	Siemens SMART / CCD area detector	
Radiation / wavelength	Mokα (graphite monochrom.) / 0.71073 Å	
F(000)	1576	
Crystal size	0.20 x 0.25 x 0.30 mm	
θ Range for data collection	1.61 to 27.82°	
Index ranges	$-17 \le h \le 16, -15 \le k \le 18, -20 \le l \le 19$	
Reflections collected	17006	
Independent refls.	6324 (R_{int} = 0.0231)	
Observed refls.	5068 ([I>2σ(I)])	

Absorption correction	SADABS
Refinement method	Full-matrix least-squares on F^2
Computing	SHELXTL, Ver. 5
Data / restraints / parameters	6319 / 0 / 379
Goodness-of-fit on F^2	1.014
SHELX-93 weight parameters	0.0398, 10.3997
Final R indices [I>2σ(I)]	R1 = 0.0345, wR2 = 0.0816
R indices (all data)	R1 = 0.0469, wR2 = 0.0883
Extinction coefficient	0.00064(10)
Largest diff. peak and hole	2.417 and –1.421 e $Å^{-3}$

Appendix A-9. Crystal data and structure refinement for [Zn(tach-Me_3pyr)]$(ClO_4)_2$ (**251**).

Color / Shape	colorless / needle	
Empirical formula	$C_{27}H_{36}Cl_2N_6O_8Zn$	
Formula weight	708.89	
Temperature	173(2) K	
Crystal system	trigonal	
Space group	P31c	
Unit cell dimensions	a = 11.2593(2) Å	$\alpha = 90°$
	b = 11.2593(2) Å	$\beta = 90°$
	c = 13.5750(4) Å	$\gamma = 120°$
Volume	1490.37(6) $Å^3$	
Z	2	
Density (calculated)	1.580 Mg/m^3	
Absorption coefficient	1.064 mm^{-1}	
Diffractometer / scan	Siemens SMART / CCD area detector	
Radiation / wavelength	Mokα (graphite monochrom.) / 0.71073 Å	
F(000)	736	
Crystal size	0.10 x 0.12 x 0.30 mm	
θ Range for data collection	2.09 to 27.85°	
Index ranges	$-14 \le h \le 12, -13 \le k \le 14, -17 \le l \le 17$	
Reflections collected	9116	
Independent refls.	2300 (R_{int} = 0.0373)	
Observed refls.	1986 ([I>2σ(I)])	

Absorption correction	SADABS
Refinement method	Full-matrix least-squares on F^2
Computing	SHELXTL, Ver. 5
Data / restraints / parameters	2300 / 1 / 139
Goodness-of-fit on F^2	0.985
SHELX-93 weight parameters	0.0290, 0.0000
Final R indices [$I>2\sigma(I)$]	R1 = 0.0275, wR2 = 0.0542
R indices (all data)	R1 = 0.0371, wR2 = 0.0570
Absolute structure parameter	0.038(11)
Extinction coefficient	0.0042(5)
Largest diff. peak and hole	0.222 and –0.295 e $Å^{-3}$

Appendix A-10. Crystal data and structure refinement for [Cu(tach-Me_3pyr)]$(ClO_4)_2$ (258).

Color / Shape	Light blue / fragment	
Empirical formula	$C_{27}H_{36}Cl_2CuN_6O_8$	
Formula weight	707.06	
Temperature	173(2) K	
Crystal system	Monoclinic	
Space group	$P2_1$	
Unit cell dimensions	a = 9.4286(3) Å	α = 90°
	b = 17.1595(5) Å	β = 109.868(1)°
	c = 9.6558(3) Å	γ = 90°
Volume	1469.23(8) Å^3	
Z	2	
Density (calculated)	1.598 Mg/m^3	
Absorption coefficient	0.986 mm^{-1}	
Diffractometer / scan	Siemens SMART / CCD area detector	
Radiation / wavelength	Mokα (graphite monochrom.) / 0.71073 Å	
F(000)	734	
Crystal size	0.25 x 0.30 x 0.37 mm	
θ Range for data collection	2.24 to 27.90°	
Index ranges	$-9 \le h \le 12$, $-18 \le k \le 22$, $-12 \le l \le 9$	
Reflections collected	9397	
Independent refls.	5523 (R_{int} = 0.0285)	
Observed refls.	4816 ([I>2σ(I)])	

Absorption correction	SADABS
Refinement method	Full-matrix least-squares on F^2
Computing	SHELXTL, Ver. 5
Data / restraints / parameters	5516 / 1 / 409
Goodness-of-fit on F^2	1.039
SHELX-93 weight parameters	0.0290, 0.0000
Final R indices [I>2σ(I)]	R1 = 0.0473, wR2 = 0.1189
R indices (all data)	R1 = 0.0561, wR2 = 0.1287
Absolute structure parameter	0.05(2)
Extinction coefficient	0.0050(13)
Largest diff. peak and hole	1.291 and -0.535 e $Å^{-3}$

Appendix A-11. Crystal data and structure refinement for [Ni(tach-Me_3pyr)]$(ClO_4)_2 \cdot CH_3CN$ **(263).**

Color / Shape	Violet / parallelepiped	
Empirical formula	$C_{29}H_{39}Cl_2N_7NiO_8$	
Formula weight	743.28	
Temperature	173(2) K	
Crystal system	Triclinic	
Space group	P1	
Unit cell dimensions	a = 9.9925(7) Å	α = 75.553(1)°
	b = 10.2145(7) Å	β = 86.028(1)°
	c = 18.1508(13) Å	γ = 61.606(1)°
Volume	1575.6(2) $Å^3$	
Z	2	
Density (calculated)	1.567 Mg/m^3	
Absorption coefficient	0.848 mm^{-1}	
Diffractometer / scan	Siemens SMART / CCD area detector	
Radiation / wavelength	Mokα (graphite monochrom.) / 0.71073 Å	
F(000)	776	
Crystal size	0.08 x 0.10 x 0.18 mm	
θ Range for data collection	1.16 to 27.90°	
Index ranges	$-12 \le h \le 12, -7 \le k \le 13, -18 \le l \le 23$	
Reflections collected	10108	
Independent refls.	7011 (R_{int} = 0.0323)	
Observed refls.	4168 ([I>2σ(I)])	

Absorption correction	none
Refinement method	Full-matrix least-squares on F^2
Computing	SHELXTL, Ver. 5
Data / restraints / parameters	7006 / 1 / 434
Goodness-of-fit on F^2	1.051
SHELX-93 weight parameters	0.0414, 2.1430
Final R indices [$I>2\sigma(I)$]	R1 = 0.0612, wR2 = 0.1125
R indices (all data)	R1 = 0.1249, wR2 = 0.1465
Extinction coefficient	0.0013(6)
Largest diff. peak and hole	0.727 and -0.475 e $Å^{-3}$

Appendix A-12. Crystal data and structure refinement for [Zn(tach-6-Mepyr)]$(ClO_4)_2 \bullet CH_3OH$ **(253).**

Color / Shape	Orange / fragment	
Empirical formula	$C_{27.50}H_{39.50}Cl_2N_6O_9Zn$	
Formula weight	734.42	
Temperature	173(2) K	
Crystal system	Triclinic	
Space group	P1	
Unit cell dimensions	a = 9.4081(4) Å	α = 96.581(1)°
	b = 17.6239(8) Å	β = 95.722(1)°
	c = 19.1521(8) Å	γ = 95.383(1)°
Volume	3121.1(2) $Å^3$	
Z	4	
Density (calculated)	1.563 Mg/m^3	
Absorption coefficient	1.021 mm^{-1}	
Diffractometer / scan	Siemens SMART / CCD area detector	
Radiation / wavelength	Mokα (graphite monochrom.) / 0.71073 Å	
F(000)	1530	
Crystal size	0.06 x 0.08 x 0.49 mm	
θ Range for data collection	1.08 to 27.97°	
Index ranges	$-12 \le h \le 11$, $-23 \le k \le 23$, $-25 \le l \le 17$	
Reflections collected	19752	
Independent refls.	13665 (R_{int} = 0.0431)	
Observed refls.	7146 ([I>2σ(I)])	

Absorption correction	SADABS
Refinement method	Full-matrix least-squares on F^2
Computing	SHELXTL, Ver. 5
Data / restraints / parameters	13660 / 1 / 883
Goodness-of-fit on F^2	1.027
SHELX-93 weight parameters	0.0636, 3.0624
Final R indices [I>2σ(I)]	R1 = 0.0698, wR2 = 0.1346
R indices (all data)	R1 = 0.1596, wR2 = 0.1817
Extinction coefficient	0.0008(3)
Largest diff. peak and hole	0.986 and –0.656 e $Å^{-3}$

Appendix A-13. Crystal data and structure refinement for [Cu(tach-6-Mepyr)]$(ClO_4)_2$ (260).

Color / Shape	bright blue / parallelepiped	
Empirical formula	$C_{27}H_{36}Cl_2CuN_6O_8$	
Formula weight	707.06	
Temperature	173(2) K	
Crystal system	Monoclinic	
Space group	$P2_1/n$	
Unit cell dimensions	a = 11.3207(5) Å	$\alpha = 90°$
	b = 19.5193(9) Å	β = 112.2010 (1)°
	c = 14.6157(7) Å	$\gamma = 90°$
Volume	2990.2(2) Å^3	
Z	4	
Density (calculated)	1.571 Mg/m^3	
Absorption coefficient	0.969 mm^{-1}	
Diffractometer / scan	Siemens SMART / CCD area detector	
Radiation / wavelength	Mokα (graphite monochrom.) / 0.71073 Å	
F(000)	1468	
Crystal size	0.10 x 0.14 x 0.30 mm	
θ Range for data collection	1.83 to 27.88°	
Index ranges	$-14 \le h \le 14, -24 \le k \le 25, -19 \le l \le 11$	
Reflections collected	18765	
Independent refls.	6904 (R_{int} = 0.0478)	
Observed refls.	4834 ([I>2σ(I)])	

Absorption correction	SADABS
Refinement method	Full-matrix least-squares on F^2
Computing	SHELXTL, Ver. 5
Data / restraints / parameters	6894 / 0 / 405
Goodness-of-fit on F^2	0.943
SHELX-93 weight parameters	0.0929
Final R indices [$I>2\sigma(I)$]	R1 = 0.0598, wR2 = 0.1471
R indices (all data)	R1 = 0.0971, wR2 = 0.1827
Extinction coefficient	0.0005(3)
Largest diff. peak and hole	1.211 and -1.136 e $Å^{-3}$

Appendix A-14. Crystal data and structure refinement for [Ni(tach-6-Mepyr)]$(NO_3)_2 \bullet 1/2\ Et_2O$ **(265).**

Color / Shape	Pale violet / fragment	
Empirical formula	$C_{29}H_{41}Cl_2N_8O_{6.50}$	
Formula weight	664.41	
Temperature	173(2) K	
Crystal system	Monoclinic	
Space group	$P2_1/n$	
Unit cell dimensions	a = 12.0745(4) Å	$\alpha = 90°$
	b = 16.6907(5) Å	β = 92.280 (1)°
	c = 15.0261(5) Å	$\gamma = 90°$
Volume	3025.8(2) Å^3	
Z	4	
Density (calculated)	1.458 Mg/m^3	
Absorption coefficient	0.700 mm^{-1}	
Diffractometer / scan	Siemens SMART / CCD area detector	
Radiation / wavelength	Mokα (graphite monochrom.) / 0.71073 Å	
F(000)	1404	
Crystal size	0.24 x 0.35 x 0.40 mm	
θ Range for data collection	1.82 to 27.88°	
Index ranges	$-15 \le h \le 11, -21 \le k \le 21, -19 \le l \le 19$	
Reflections collected	18825	
Independent refls.	6953 (R_{int} = 0.0552)	
Observed refls.	3830 ([I>2σ(I)])	

Absorption correction	SADABS
Refinement method	Full-matrix least-squares on F^2
Computing	SHELXTL, Ver. 5
Data / restraints / parameters	6151 / 0 / 419
Goodness-of-fit on F^2	1.054
SHELX-93 weight parameters	0.0760, 1.5449
Final R indices [I>2σ(I)]	R1 = 0.0710, wR2 = 0.1473
R indices (all data)	R1 = 0.1438, wR2 = 0.1907
Extinction coefficient	0.0009(4)
Largest diff. peak and hole	0.715 and -0.386 e $Å^{-3}$

Appendix A-15. Crystal data and structure refinement for [Co(tach-6-Mepyr)]$(NO_3)_2$ (270).

Color / Shape	red / plate	
Empirical formula	$C_{27}H_{36}CoN_8O_6$	
Formula weight	627.57	
Temperature	173(2) K	
Crystal system	Monoclinic	
Space group	$P2_1/c$	
Unit cell dimensions	a = 14.4761(7) Å	α = 90°
	b = 12.9509(6) Å	β = 92.2800(10)°
	c = 15.3527(7) Å	γ = 90°
Volume	2876.0(2) Å^3	
Z	4	
Density (calculated)	1.449 Mg/m^3	
Absorption coefficient	0.653 mm^{-1}	
Diffractometer / scan	Siemens SMART / CCD area detector	
Radiation / wavelength	Mokα (graphite monochrom.) / 0.71073 Å	
F(000)	1316	
Crystal size	0.39 x 0.42 x 0.51 mm	
θ Range for data collection	1.41 to 27.95°	
Index ranges	$-18 \le h \le 17, -17 \le k \le 13, -20 \le l \le 20$	
Reflections collected	17516	
Independent refls.	6653 (R_{int} = 0.0228)	
Observed refls.	5676 ([I>2σ(I)])	

Absorption correction	SADABS
Refinement method	Full-matrix least-squares on F^2
Computing	SHELXTL, Ver. 5
Data / restraints / parameters	6648 / 0 / 391
Goodness-of-fit on F^2	0.992
SHELX-93 weight parameters	0.0352
Final R indices [$I>2\sigma(I)$]	R1 = 0.0305, wR2 = 0.0733
R indices (all data)	R1 = 0.0398, wR2 = 0.0821
Extinction coefficient	0.0009(2)
Largest diff. peak and hole	0.317 and -0.288 e $Å^{-3}$

Appendix A-16. Crystal data and structure refinement for [Mn(tach-6-Mepyr)]$(ClO_4)_2$ (274).

Color / Shape	colorless / fragment	
Empirical formula	$C_{27.50}H_{39.50}Cl_2MnN_6O_9$	
Formula weight	723.99	
Temperature	173(2) K	
Crystal system	Triclinic	
Space group	P-1	
Unit cell dimensions	*a* = 9.4981(4) Å	α = 96.52°
	b = 17.6530(7) Å	β = 95.382(1)°
	c = 19.2146(7) Å	(= 94.63°
Volume	3173.1(2) Å3	
Z	4	
Density (calculated)	1.515 Mg/m3	
Absorption coefficient	0.646 mm-1	
Diffractometer / scan	Siemens SMART / CCD area detector	
Radiation / wavelength	Mok((graphite monochrom.) / 0.71073 Å	
F(000)	1510	
Crystal size	0.14 x 0.20 x 0.27 mm	
(Range for data collection	1.07 to 27.88°	
Index ranges	$-12 \le h \le 12, -19 \le k \le 22, -24 \le l \le 20$	
Reflections collected	20018	
Independent refls.	13991 (Rint = 0.0271)	
Observed refls.	8601 ([I>2((I)])	

Absorption correction	SADABS
Refinement method	Full-matrix least-squares on F2
Computing	SHELXTL, Ver. 5
Data / restraints / parameters	13998 / 0 / 883
Goodness-of-fit on F2	0.996
SHELX-93 weight parameters	0.0956, 2.2097
Final R indices [I>2((I)]	R1 = 0.0625, wR2 = 0.1518
R indices (all data)	R1 = 0.1153, wR2 = 0.1903
Extinction coefficient	0.0016(5)
Largest diff. peak and hole	1.601 and -0.528 e Å-3

Appendix A-17. Crystal data and structure refinement for [Zn(tachquin)](ClO4)2•H2O (254)

Color / Shape	colorless / fragment
Empirical formula	C36H38Cl2N6O9Zn
Formula weight	834.99
Temperature	173(2) K
Crystal system	Monoclinic
Space group	P21/c
Unit cell dimensions	a = 19.4136(13) Å (= 90°
	b = 16.2968(11) Å (= 98.662(2)°
	c = 11.8519(8) Å (= 90°
Volume	3706.9(4) $Å^3$
Z	4
Density (calculated)	1.496 Mg/m^3
Absorption coefficient	0.870 mm^{-1}
Diffractometer / scan	Siemens SMART / CCD area detector
Radiation / wavelength	Mokα (graphite monochrom.) / 0.71073 Å
F(000)	1728
Crystal size	0.20 x 0.32 x 0.40 mm
θ Range for data collection	1.06 to 20.41°
Index ranges	$-19 \le h \le 18, -15 \le k \le 15, -11 \le l \le 10$
Reflections collected	12064
Independent refls.	3651 (R_{int} = 0.00965)
Observed refls.	2190 ([I>2σ(I)])

Absorption correction	SADABS
Refinement method	Full-matrix least-squares on F^2
Computing	SHELXTL, Ver. 5
Data / restraints / parameters	3305 / 0 / 525
Goodness-of-fit on F^2	1.076
SHELX-93 weight parameters	0.1420, 0.0000
Final R indices [$I>2\sigma(I)$]	R1 = 0.0827, wR2 = 0.2042
R indices (all data)	R1 = 0.1463, wR2 = 0.2614
Extinction coefficient	0.0000(6)
Largest diff. peak and hole	1.060 and -0.430e $Å^{-3}$

Appendix A-18. Crystal data and structure refinement for $[Zn(tachbn)](Cl)(ClO_4)\bullet 1/2H_2O$ (256).

Color / Shape	colorless / parallelepiped	
Empirical formula	$C_{33}H_{49}Cl_2N_6O_{4.50}Zn$	
Formula weight	738.05	
Temperature	173(2) K	
Crystal system	Orthorhombic	
Space group	$P2_12_12_1$	
Unit cell dimensions	a = 14.260(2) Å	$\alpha = 90°$
	b = 14790(2) Å	$\beta = 90°$
	c = 17.453(2) Å	$\gamma = 90°$
Volume	3681.1(8) Å^3	
Z	4	
Density (calculated)	1.332 Mg/m^3	
Absorption coefficient	0.857 mm^{-1}	
Diffractometer / scan	Siemens SMART / CCD area detector	
Radiation / wavelength	Mokα (graphite monochrom.) / 0.71073 Å	
F(000)	1556	
Crystal size	0.10 x 0.12 x 0.32 mm	
θ Range for data collection	1.80 to 23.25°	
Index ranges	$-15 \le h \le 15, -16 \le k \le 14, -17 \le l \le 19$	
Reflections collected	16854	
Independent refls.	5296 (R_{int} = 0.2310)	
Observed refls.	2500 ([I>2σ(I)])	

Absorption correction	SADABS
Refinement method	Full-matrix least-squares on F^2
Computing	SHELXTL, Ver. 5
Data / restraints / parameters	4462 / 0 / 443
Goodness-of-fit on F^2	0.953
SHELX-93 weight parameters	0.0638, 0.0000
Final R indices [$I>2\sigma(I)$]	R1 = 0.0827, wR2 = 0.1314
R indices (all data)	R1 = 0.2121, wR2 = 0.1934
Extinction coefficient	0.0032(6)
Largest diff. peak and hole	0.346 and -0.352 e $Å^{-3}$

Appendix A-19. Crystal data and structure refinement for $[Cu(tachbn)](ClO_4)_2$ **(261).**

Color / Shape	blue /plate
Empirical formula	$C_{33}H_{48}Cl_2CuN_6O_8$
Formula weight	791.21
Temperature	173(2) K
Crystal system	Orthorhombic
Space group	$P2_12_12_1$
Unit cell dimensions	a = 13.3903(11) Å $\alpha = 90°$
	b = 16.0536(12) Å $\beta = 90°$
	c = 17.8755(14) Å $\gamma = 90°$
Volume	3842.6(5) $Å^3$
Z	4
Density (calculated)	1.368 Mg/m^3
Absorption coefficient	0.762 mm^{-1}
Diffractometer / scan	Siemens SMART / CCD area detector
Radiation / wavelength	Mokα (graphite monochrom.) / 0.71073 Å
F(000)	1660
Crystal size	0.15 x 0.20 x 0.40 mm
θ Range for data collection	1.70 to 19.93°
Index ranges	$0 \le h \le 12, 0 \le k \le 15, 0 \le l \le 17$
Reflections collected	2033
Independent refls.	2033 (Rint = 0.0000)
Observed refls.	1501 ([I>2σ(I)])

Absorption correction	none
Refinement method	Full-matrix least-squares on F^2
Computing	SHELXTL, Ver. 5
Data / restraints / parameters	2027 / 0 / 447
Goodness-of-fit on F2	1.110
SHELX-93 weight parameters	0.0517, 1.9805
Final R indices [I>2((I)]	R1 = 0.0506, wR2 = 0.0979
R indices (all data)	R1 = 0.0908, wR2 = 0.1198
Extinction coefficient	0.0000(6)
Largest diff. peak and hole	0.311 and -0.274 e $Å^{-3}$

Appendix A-20. Crystal data and structure refinement for $[Ni(tachpn)](ClO_4)_2 \bullet CH_3OH$ **(266).**

Color / Shape	light purple /parallelepiped
Empirical formula	$C_{16}H_{40}Cl_2N_6NiO_9$
Formula weight	590.15
Temperature	173(2) K
Crystal system	Orthorhombic
Space group	$P2_12_12_1$
Unit cell dimensions	a = 9.4038(6) Å $\alpha = 90°$
	b = 13.7359(9) Å $\beta = 90°$
	c = 20.1269(13) Å $\gamma = 90°$
Volume	2599.8(3) $Å^3$
Z	4
Density (calculated)	1.508 Mg/m^3
Absorption coefficient	1.007 mm^{-1}
Diffractometer / scan	Siemens SMART / CCD area detector
Radiation / wavelength	Mok((graphite monochrom.) / 0.71073 Å
F(000)	1248
Crystal size	0.04 x 0.12 x 0.28 mm
θ Range for data collection	1.79 to 27.92°
Index ranges	$-12 \le h \le 8, -16 \le k \le 17, -26 \le l \le 25$
Reflections collected	16433

Observed refls.	4006 ([I>2σ(I)])
Absorption correction	SADABS
Refinement method	Full-matrix least-squares on F^2
Computing	SHELXTL, Ver. 5
Data / restraints / parameters	6063 / 0 / 342
Goodness-of-fit on F^2	1.032
SHELX-93 weight parameters	0.0427, 0.0000
Final R indices [I>2σ(I)]	R1 = 0.0561, wR2 = 0.0907
R indices (all data)	R1 = 0.1067, wR2 = 0.1084
Extinction coefficient	0.0012(3)
Largest diff. peak and hole	0.424 and -0.425 e $Å^{-3}$

Appendix B. Figures of ligands.

tach•3HBr 238

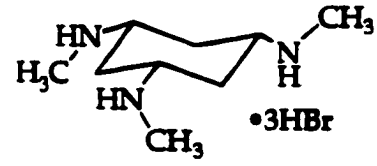

tach-Me_3•3HBr 239

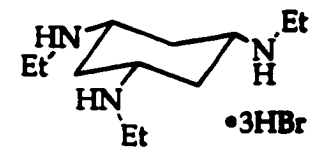

tach-Et_3•3HBr 240

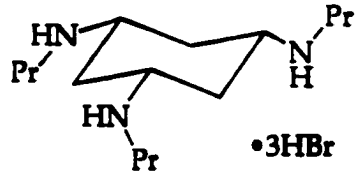

tach-Pr_3•3HBr 241

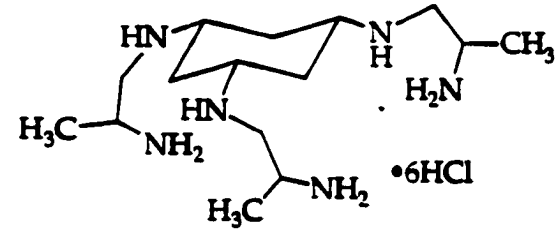

tachpn•6HCl 248

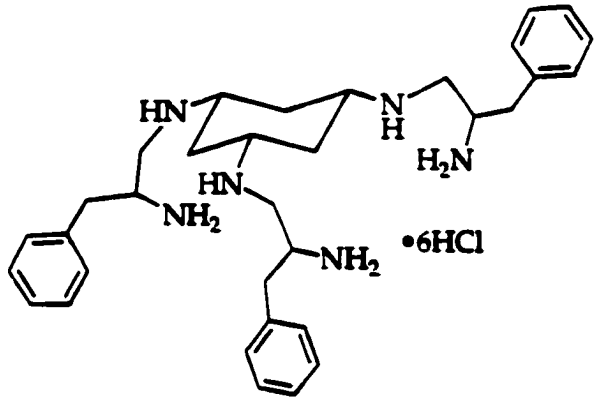

tachbn•6HCl 249

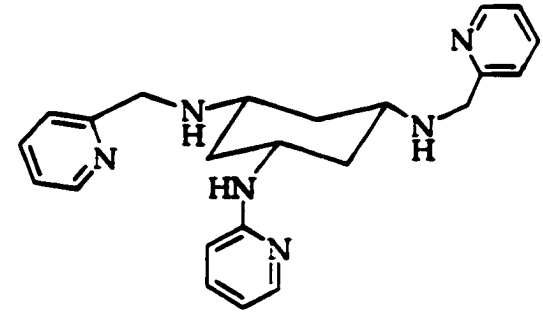

tachpyr 242

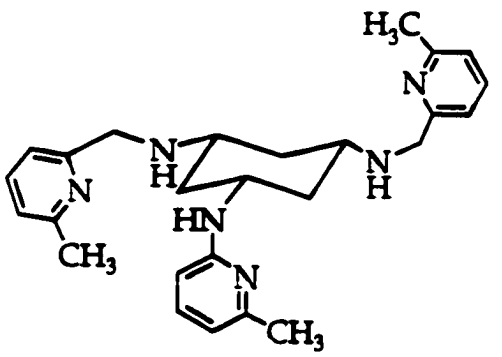

tach-6-Mepyr 243

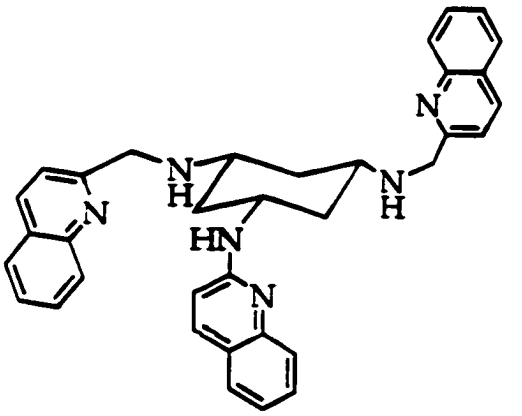

tachquin 244

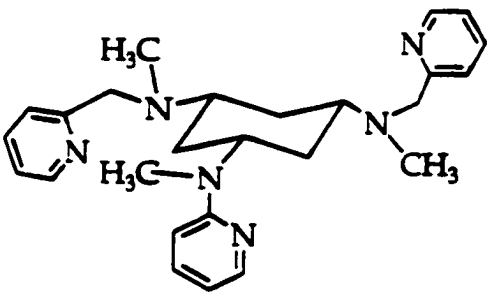

tach-Me$_3$pyr 245

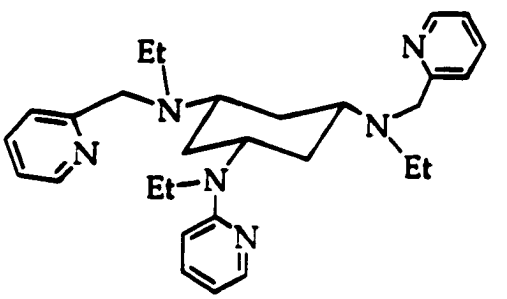

tach-Et$_3$pyr 246

Appendix C.

Attempted Preparation of [Zn(tach-R_3)X_2]

[Zn(tach-Me_3)Cl_2]•1/3H_2O.

A mixture of tach-Me_3•3HBr (0.206 g, 4.97 x 10^{-4} mol) in water (10 mL), Na_2CO_3•H_2O (0.0925g, 7.46 x 10^{-4} mol, 1.5 equiv) in water (10 mL), and benzene (100 mL) was stirred and heated in a 250 mL round-bottomed flask fitted with a Dean-Stark trap with a water-cooled condenser. Benzene-water azeotrope was distilled for 14h with collection of ca. 21.4 mL of water. The benzene layer was transferred to another 250 mL round-bottomed flask and removed by the rotary-evaporator to give tach-Me_3 as a yellow oil. This was dissolved in MeOH (2 mL) and added to a clear solution of $ZnCl_2$ (0.0677 g, 4.97 x 10^{-4} mol) in MeOH (2 mL) affording a clear solution. A white precipitate was formed by adding Et_2O (12 mL), isolated by decanting the supernatant, and dried under reduced pressure giving a white solid. The solid was taken up in MeOH (5 mL), and Et_2O was diffused into it forming clear prisms. Crystal was isolated and dried under reduced pressure giving a white solid (0.102 g, 3.24x 10^{-4} mol, 65.2%). Anal. Calcd for $C_9H_{21}Cl_2N_3Zn$•1/3H_2O ([Zn(tach-Me_3)Cl_2]•1/3H_2O): C, 34.48; H, 6.96; N, 13.40. Found: C, 34.59; H, 6.78; N, 13.20. ^{1}H NMR (DMSO-d_6, 25° C): d 5.17 (s, 1H N$\underline{H}$-CH_3); 3.01 (s, $\underline{A}$MM'XX', 1H, cyclohexyl methine H); 2.43 (d, NH-C$\underline{H_3}$); 2.25 (d, A$\underline{MM}$'XX', 1H, equatorial cyclohexyl methylene H's diastereotopic); 1.90 (d, AMM'$\underline{XX}$', 1H, axial cyclohexyl methylene H's, diastereotopic). ^{13}C NMR (DMSO-d_6, 25° C): d 53.5 (equatorial cyclohexyl methylene C); 34.5 (axial cyclohexyl methylene C).

[Zn(tach-Me_3)$Cl_{1.5}Br_{0.5}$]•1/5 H_2O. An aqueous solution (2 mL) of tach-Me_3•3HBr (0.0559 g, 1.34 x 10^{-4} mol) was neutralized by adding 0.100N NaOH solution (4.02 mL, 4.02 x 10^{-4} mol, 3 equiv). The neutralized ligand was dried under reduced pressure for 10 h and extracted into of $CHCl_3$ (6 mL). This solution was filtered and dried under reduced pressure. The resulting white solid was taken up in $CHCl_3$ (3 mL) and added to a clear solution of $ZnCl_2$ (0.0183 g, 1.34 x 10^{-4} mol) in anhydrous MeOH (2 mL) affording a clear solution. A white precipitate was formed by adding Et_2O (12 mL), isolated, and dried under reduced pressure giving a white solid. The solid was dissolved in MeOH (6 mL) and Et_2O vapor was diffused into the MeOH solution of the solid forming clear prisms which was isolated and dried under reduced pressure a white solid (0.0162 g, 4.88 x 10^{-5} mol, 36.2%). Anal. Calcd for $C_{12}H_{27}Br_{0.5}Cl_{1.5}N_3Zn$•1/5 H_2O ([Zn(tach-Me_3)$Cl_{1.5}Br_{0.5}$]•1/5 H_2O): C, 34.42; H, 6.47; N, 12.60. Found: C, 32.82; H, 6.43; N, 12.17. ^{1}H NMR (DMSO-d_6, 25° C): δ 5.19 (s, 1H N<u>*H*</u>-CH_3); 3.01 (s, <u>*A*</u>MM'XX', 1H, cyclohexyl methine H); 2.42 (d, NH-C<u>*H*</u>$_3$); 2.24 (d, A<u>*MM*</u>'XX', 1H, equatorial cyclohexyl methylene H's diastereotopic); 1.78 (d, AMM'<u>*XX*</u>', 1H, axial cyclohexyl methylene H's, diastereotopic).

[Zn(tach-Me_3)](OAc)$_2$. A mixture of tach-Me_3•3HBr (0.0720 g, 1.71 x 10^{-4} mol) in water (5 mL), Na_2CO_3•H_2O (0.0318 g, 2.56 x 10^{-4} mol, 1.5 equiv) in water (5 mL), and benzene (90 mL) was stirred and heated for 14h in a 250 mL round-bottomed flask fitted with a Dean-Stark trap with a water-cooled condenser. After discarding a collected water layer, the benzene layer was transferred to another 250 mL round-bottomed flask and removed by a rotary evaporator to give tach-Me_3 as a yellow oil. This was dissolved in MeOH (2 mL) and added to a clear

solution of $Zn(OAc)\bullet 2H_2O$ (0.0375 g, 1.71×10^{-4} mol) in MeOH (2 mL) affording a clear solution. The mixture was dried under reduced pressure giving a yellow oily substance that was taken up in CH_2Cl_2. A white precipitate was formed by adding Et_2O (12 mL), isolated, and dried under reduced pressure giving a white solid (0.0414 g, 1.17×10^{-4} mol, 68.3%). ^1H NMR (DMSO-d_6, 25° C): δ 4.54 (s, 1H N*H*-CH_3); 2.86 (s, *A*MM'XX', 1H, cyclohexyl methine H); 2.30 (d, NH-C*H*$_3$); 2.21 (d, A*MM*'XX', 1H, equatorial cyclohexyl methylene H's diastereotopic); 1.74 (s, C*H*$_3$COO$^-$); 1.59(d, AMM'*XX*', 1H, axial cyclohexyl methylene H's, diastereotopic). ^{13}C NMR ($CDCl_3$, 25° C): d 179.8 (CH_3*C*OO$^-$); 53.6(equatorial cyclohexyl methylene C); 40.7 (NH-*C*H_3); 35.7 (axial cyclohexyl methylene C); 23.1(*C*H_3COO$^-$).

[Zn(tach-Et$_3$)Cl$_2$]. A mixture of tach-$Et_3\bullet 3HBr$ (0.628 g, 1.38×10^{-4} mol) in water (5 mL), $Na_2CO_3\bullet H_2O$ (0.0273 g, 2.07×10^{-4} mol, 1.5 equiv) in water (5 mL), and benzene (100 mL) was stirred and heated in a 250 mL round-bottomed flask fitted with a Dean-Stark trap with a water-cooled condenser. Benzene-water azeotrope was distilled for 14h with collection of ca. 12.0 mL of water. The benzene layer was dried under reduced pressure to give tach-Et_3 as a white solid. To a $ZnCl_2$ (0.0179 g, 1.38×10^{-4} mol) in a mixture of $MeOH/Et_2O$ (3 mL/6 mL) was added a pale yellow solution of the neutralized tach-Et_3 in a mixture of $MeOH/Et_2O$ (2 mL/4 mL) affording a clear solution. The mixture was dried under reduced pressure giving a white solid that was taken up in MeOH. A white precipitate was formed by adding Et_2O (12 mL), isolated, and dried under reduced pressure giving a white solid (0.0304 g, 8.63×10^{-5} mol, 62.5%). ^1H NMR (DMSO-d_6, 25° C): δ 4.85 (s, 1H N*H*-CH_3); 3.34 (s, *A*MM'XX', 1H, cyclohexyl

methine H); 2.87 (br s, 2H, NH-C$\underline{H}_2$-CH$_3$); 2.27 (d, A$\underline{MM}$'XX', 1H, equatorial cyclohexyl methylene H's diastereotopic); 1.74 (d, AMM'$\underline{XX}$', 1H, axial cyclohexyl methylene H's, diastereotopic); 1.19 (t, 3H, NH-CH$_2$-C$\underline{H}_3$).

Attempted preparation of Zn(II) Metal Complexes with tach-Me$_3$ and tach-Et$_3$ Ligands

A number of mononuclear Zn(II) complexes have been used and shown to promote activated phosphate ester hydrolysis.[333, 334] The syntheses of Zn(II) complexes of tach-Me$_3$ and tach-Et$_3$ ligands were attempted and preliminarily characterized in order to investigate their structures and the activities as a catalyst in the hydrolysis of the phosphate diesters.

The composition ambiguity of anions in Zn(II) complexes of tach derivatives [Zn(tach-R$_3$)X$_2$] (R = Me or Et) was also observed with NaOH neutralization and has been avoided by adopting the benzene-water azeotropic distillation as a method for neutralization which increases the yield of final products additionally. Combining alcoholic solutions of ZnCl$_2$, ZnBr$_2$, and Zn(OAc)$_2$ with an alcoholic or chlorinated solution of the neutralized tach-R$_3$ (R = methyl or ethyl) did not lead to the precipitation of the complexes as for Cu(II) analogues. However, the precipitation of the complexes was achieved by adding an excess of Et$_2$O (ca. 12 mL), and metal complexes were obtained through a purification process from those precipitates. The synthesis of Zn(II) complexes of tach-Pr$_3$•3HBr and tach-Np$_3$•3HBr has not been attempted because of anticipated poor solubility of those complexes in aqueous media.

The formation of Zn(II) complexes of the alkylated tach derivatives

$[Zn(tach\text{-}R_3)X_2]$ (R = methyl or ethyl) can be easily detected by changes in the chemical shift and the splitting patterns of cyclohexyl protons relative to free tach-R_3 ligands in ^1H NMR. (See introduction in **Chapter 3**). Proton NMR studies indicate that coordination spheres of $[Zn(tach\text{-}R_3)X_2]$ complexes are rigid on the NMR time scale at room temperature.

The Zn(II) complexes of the trialkylated tach derivatives $[Zn(tach\text{-}R_3)X_2]$ (R = methyl or ethyl, and X = Cl or Br) have shown a poor solubility in aqueous solvents, which is disfavored for the study of hydrolysis. Therefore attempts to increase the solubility by changing anions have been tried, and the synthesis of $[Zn(tach\text{-}Me_3)X_2]$ (X = OAc) have been successful. Unfortunately, the solubility of $[Zn(tach\text{-}Me_3)X_2]$ (X = OAc) in aqueous mediums is not improved.

Appendix D.

Attempted study of Oxidation of Deoxyribose by Hydroxyl Radical Mediated by Fe(II) Complexes

Preparation of $[Fe(bipy)_3](ClO_4)_2$[347] (156) from $Fe(ClO_4)_2 \cdot 6H_2O$ and 2,2'-bipyridine To a yellow solution of $Fe(ClO_4)_2 \cdot 6H_2O$ (0.0457 g, 1.26×10^{-4} mol) in MeOH (2 mL) is added a solution of 2,2'-bipyridine (0.0197 g, 1.26×10^{-4} mol) in MeOH (2 mL) affording a red-purple solution. A red-purple precipitate formed from addition of Et_2O (14 mL) to the mixture, isolated by decanting supernatant, and dried under reduced pressure giving maroon color solid.

$[Fe(tachimpyr)](Cl)_2$ (157) was prepared as described as above except using $FeCl_2 \cdot 4H_2O$ instead of $Fe(ClO_4)_2 \cdot 6H_2O$.

PBS Buffer (0.1 M) was prepared by dissolving Na_2HPO_4 (1.1357g, 8.0×10^{-3} mol), KH_2PO_4 (0.2722g, 2.0×10^{-3} mol), NaCl (0.7762g, 1.4×10^{-2} mol), and KCl (0.0745 g, 1.0×10^{-3} mol) in e-pure water (100 mL). The pH of the PBS buffer was adjusted at 7.4.

Deoxyribose oxidation was performed using a slight modification of the methods of Chasteen et al.[348] The TBA assay for measuring the oxidation of deoxyribose by hydroxyl radical was performed by adding 0.5 mL of 5 mM deoxyribose to 0.5 mL of 0.1M phosphate buffer, pH 7.4, in 0.14M NaCl.

To a degassed clear solution of 10 mM $FeCl_2 \bullet 4H_2O$ (0.3 mL) in 0.1M PBS was added 0.3 mL of 20 mM degassed chelator (tachpn, tach-Me_3pyr, (+/-)tach(C-Me)$_3$pyr, and tachpyr) affording samples with a final concentration of 5 mM Fe^{2+}. For preparation of 5 mM $[Fe(tachbn)]^{2+}$, 0.5 mL of 13 mM of tachbn and 0.5 mL of 6.5 mM $FeCl_2 \bullet 4H_2O$ were used. 5 mM sample solutions of $[Fe(bipy)_3](ClO_4)_2$ and $[Fe(tachimpyr)](Cl)_2$ was prepared by dissolving metal complexes in PBS. 5 mM $FeCl_2 \bullet 4H_2O$ in PBS was used as a positive control.

Two aliquots (0.1 mL each) from each sample above (mixture of $FeCl_2 \bullet 4H_2O$ and chelator, or metal complexes) were taken and placed in two different vials for a TBA assay and a blank. To each aliquot in the different vials was added a mixture of 5 mM deoxyribose (0.5 mL) and 0.1M phosphate buffer (0.5 mL), pH 7.4, in 0.14 M NaCl. For the $[Fe(tachbn)]^{2+}$ sample, 0.325 mL of 5 mM deoxyribose and 0.325 mL of 0.1M PBS were used.

The TBA assay samples were then incubated at 37°C for 15 min, along with the blanks. After incubation, 1 mL of 1% (w/v) TBA in 0.05 M NaOH (0.65 mL for the $[Fe(tachbn)]^{2+}$ sample) was added to only TBA assay, followed by 1 mL of glacial acetic acid. For blanks 1 mL of PBS and 1 mL of glacial acetic acid (0.65 mL each for the $[Fe(tachbn)]^{2+}$ sample) were added. Both samples and blanks were then heated 1 hour at 100°C and cooled. The absorbance at 532nm, a measure of OH• radical production, was then read for each sample against their blanks.

Preliminary Results and Discussion of Oxidation of Deoxyribose by Hydroxyl Radical Mediated by Fe(II) Complexes of the Hexadentate Tach Derivatives

Oxidation of sugar deoxyribose caused by attacks of hydroxyl radicals was measured by deoxyribose/thiobarbituric acid (TBA) assay.[348, 349] Hydroxyl radicals not scavenged by other components of the reaction mixture attack the sugar deoxyribose and degrade it into a series of fragments. Some or all of fragments then react with TBA on heating to give a TBA-malondialdehyde adduct which is a pink chromophore with an absorbance maximum of 532 nm.[350] The magnitude of hydroxyl radicals formed correlates with amount of TBA- malondialdehyde adducts.

By adding a chelator to a solution of Fe(II), followed by addition of a deoxyribose solution, sample solutions of final concentrations of 5 mM Fe(II), 2.5 mM deoxyribose, and 10 mM chelators were prepared in PBS (2 mL). Each sample solution was incubated for 15 min at 37° C in air and was divided into two aliquots (1 mL) (one of them was used for a blank). To only one aliquot was added 1 mL of 1% (w/v) TBA in 0.05 M NaOH. The other aliquot, served as a blank, was added 1 mL of PBS. Glacial acetic acid (1 mL) was added to both the sample and the blank, which were heated for 1 hour at 100° C, and cooled at room temperature and examined by UV-vis spectroscopy.

Hydroxyl radicals are formed from the Fe(II), molecular oxygen dissolved in sample solutions, and tach derivatives in PBS. The absorbance at 532 nm was measured for each sample against their blanks and is presented in **Table A1.** UV-vis spectra of samples are shown in **Figure A1** and **A2.**

Table A1. TBA- malondialdehyde adduct production from the Fe(II) mediated oxidation of deoxyribose.

Metal complex	Absorbance at 532 nm
positive control ($FeCl_2$)	0.606
Fe + tachbn	0.461
Fe + tachpn	0.368
Fe + tachpyr	0.411
Fe + tach-Me_3pyr	0.309
Fe(tachimpyr)	0.144
Fe + (+/-)tach(C-Me)$_3$pyr (1:2)	0.499
Fe + (+/-)tach(C-Me)$_3$pyr (1:1)	0.398
Fe(tach(C-Me)$_3$pyr-ox-*6*)	0.040
negative control (without Fe(II))	0.044

The absorbance at 532 nm observed as a result of the formation of TBA-malondialdehyde adduct may indicate that the hydroxyl radical formation correlates with the oxidative dehydrogenation process. More production of TBA-malondialdehyde adduct was observed with tach derivatives, tachbn, tachpn, tachpyr, and (+/-)tach(C-Me)$_3$pyr, known to undergo the oxidative dehydrogenation reaction. The other hand, tach-Me_3pyr ligand without a tendency for oxidative dehydrogenation produced is less active than other tach derivatives mentioned above and produces a less amount of TBA-malondialdehyde adducts. The marginal activity of tach-Me_3pyr in the production of hydroxyl radicals, however, may be result of its electronic state

(Fe(II), high-spin) and liability of its Fe(II) complex. Presumably because of the weak binding of tach-Me_3pyr to Fe(II) ions, some of Fe(II) metal ions are liberated from $[(\text{tach-Me}_3\text{pyr})]^{2+}$ complex forming $[Fe(H_2O)_6]^{2+}$ which is available for the production of hydroxyl radical through the Fenton reaction (**Scheme 2.9**). The fully oxidized Fe(II) complexes, $[Fe(\text{tach(C-Me)}_3\text{pyr-ox-6})]^{2+}$ and $[Fe(\text{tachimpyr})]^{2+}$, are relatively inactive due to lack of further available oxidative dehydrogenation and strong bindings to Fe(II).

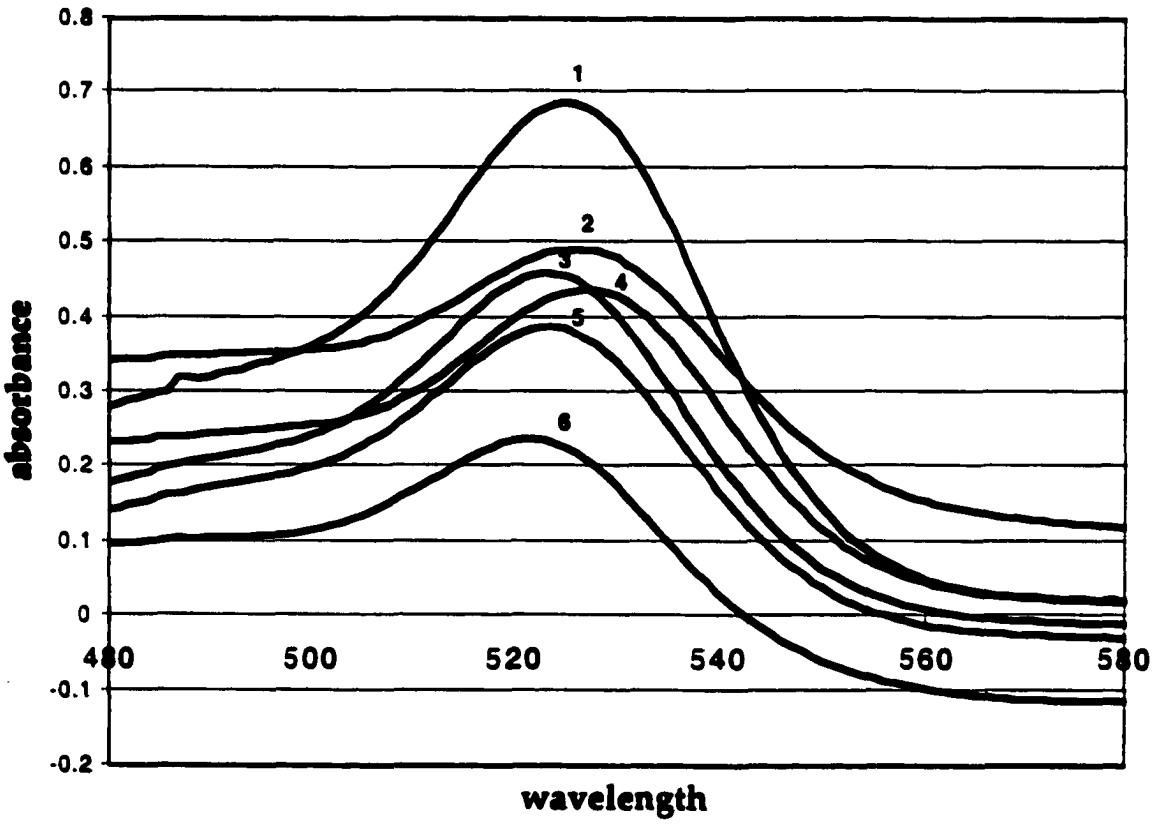

Figure A1. UV-vis spectra of the degraded deoxyribose by Fe(II) tach derivatives. 1 = positive control ($FeCl_2$); 2= Fe(tachbn); 3= Fe(tachpn); 4 = Fe(tachpyr); 5 = Fe(tach-Me_3pyr); 6 = Fe(tachimpyr).

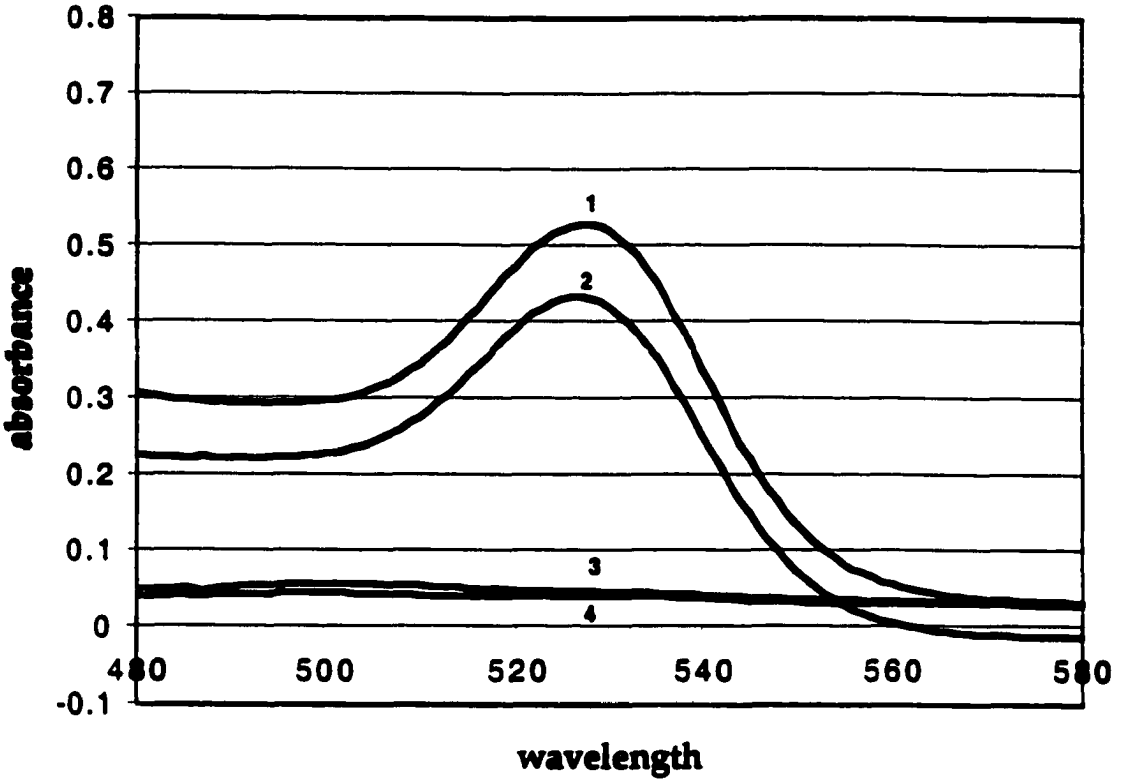

Figure A2. UV-vis spectra of the degraded deoxyribose by Fe(II) tach derivatives. 1 = Fe + (+/-)tach(C-Me)$_3$pyr (1:2), 2 = Fe + (+/-)tach(C-Me)$_3$pyr (1:1); 3 = negative control (without Fe(II)); 4 = Fe(tach(C-Me)$_3$pyr-ox-6).

Appendix E.

Preliminary Competition Study of Zn(II) and Fe(II) for tachpyr Ligand

A Zn(II) and Fe(II) ion pool was prepared by mixing 1 mL of 0.03 M $FeCl_2 \bullet 4H_2O$ solution in 0.1 M PBS and 1 mL of 0.15 M $ZnCl_2$ solution in 0.1 M PBS. To a Zn(II) and Fe(II) ion pool is added 1 mL of 0.03 M tachpyr solution in 0.1 M PBS affording yellow solution with a final concentration of 0.01 M tachpyr, 0.05 M Zn(II), and 0.01 M Fe(II). For a positive control, 1 mL of 0.02 M tachpyr is added into 1 mL of 0.02 M $FeCl_2 \bullet 4H_2O$ in 0.1 M PBS affording brown solution with a final concentration of 0.01 M tachpyr and 0.01 M Fe(II). 0.01 M tachpyr solution was used as a blank.

The Zn(II) and Fe(II) competition sample, sample for the positive control, and a blank were incubated at 37 °C with stirring under the air pressure. UV-vis spectra were taken after 0, 1.5, 4.0, 5.5, 8.0, 12.0, 24.0, and 48.0 hours of incubation. Samples for UV-vis spectra were prepared by diluting 0.2 mL of each sample with 1.8 mL of PBS. Each diluted sample (0.2 mL) was further diluted by adding extra 2 mL of 0.1 M PBS in order to get acceptable spectra.

Preliminary Result of Competition Study of Zn(II) and Fe(II) for tachpyr Ligand

A yellow solution with final concentration 0.01 M tachpyr, 0.05 M Zn(II), and 0.01 M Fe(II) was prepared by adding 0.03 M tachpyr solution (1 mL) in 0.1 M PBS to a Zn and Fe ion pool prepared by mixing 0.03 M $FeCl_2 \bullet 4H_2O$ (1 mL) in and 0.15 M $ZnCl_2$ (1 mL) in 0.1 M PBS. UV-vis spectrum of the yellow solution shows no formation of $[Fe(tachpyr)]^{2+}$ because of lacks of two characteristic

charge-transfer bands around 400 nm and 600 nm. However, a positive control sample prepared by mixing 0.02 M tachpyr (1 mL) with 0.02 $FeCl_2 \cdot 4H_2O$ (1 mL) clearly shows the formation of [Fe(tachpyr)] with the characteristic charge transfer bands at 438 nm and 604 nm. The formation of $[Fe(tachpyr)]^{2+}$ from the ion pool is noticed because of a weak charge transfer band around 425 nm after 4 h incubation at 37° C. The UV-vis spectrum obtained after 48 h incubation under O_2 from the Zn(II) and Fe(II) ion pool clearly presents $[Fe(tachpyr)]^{2+}$complex showing two characteristic charge-transfer bands at 400nm and 600 nm with increased absorbances. The identity of Fe(II) tachpyr complex is assumed as the mixture of **146** and **147** (**Fig. 2.33 (a)**), $[Fe(tachpyr)]^{2+}$ and $[Fe(tachpyr\text{-}ox\text{-}2)]^{2+}$, according to the location of two charge transfer bands and their intensity. After 48 h incubation with O_2 at 37° C, ca. 65% of complex formed is the Fe(II) complex.

UV-vis spectrum obtained from Fe positive control with 48 h incubation under O_2 is very similar to of the mixture of **147** and **148** (**Fig. 2.33 (b)**) in MeOH, $[Fe(tachpyr\text{-}ox\text{-}2)]^{2+}$ and $[Fe(tachpyr\text{-}ox\text{-}4)]^{2+}$, indicating a similar oxidative dehydrogenation reaction occurred in aqueous medium. A band shift of a charge transfer band to higher energy occurs from 420 nm (4 h) to 380 nm (48 h) with an increased incubation, indicating longer incubation with O_2 more oxidized ligand formed. The intensity of band at lower energy is also increased with longer incubation but the location of band is not changed at 600 nm. Selected UV-vis spectra from the ion pool and the Fe positive control are presented in **Figure 2.46.**

These findings suggest that the formation of Zn(II) tachpyr complex is thermodynamically favored but kinetically unstable. Once Zn(II) ion forms a

complex with tachpyr, some extent of Zn(II) is released from metal complexes liberating tachpyr ligand that forms a kinetically stable metal complex with available Fe(II) ion and then undergo the oxidative dehydrogenation reaction to form even more stable metal complexes, imino complexes.

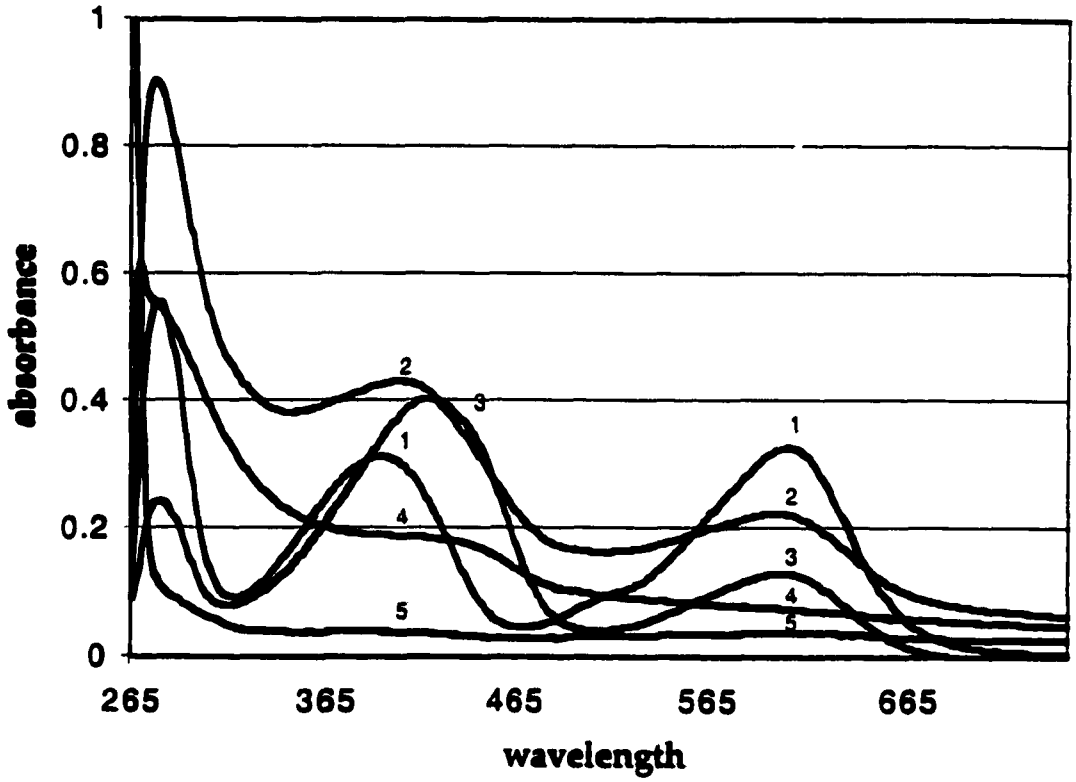

Figure A3. Selected UV-vis spectra from ion pool and Fe(II) positive control samples. **1**, Fe(II) + tachpyr (48 h); **2**, Zn(II) and Fe(II) (5:1) + tachpyr (48 h); **3**, Fe(II) + tachpyr (4 h); **4**, Zn(II) and Fe(II) (5:1) + tachpyr (4 h); **5**, tachpyr only.